

# โครงการ

กลศาสตร์ของท่อลำเลียงของใหลที่ยึดหดตัวได้ในสามมิติ (Mechanics of Three-Dimensional Extensible Marine Risers Transporting Fluid)

โดย ศ. ดร. สมชาย ชูชีพสกุล และคณะ

## รายงานวิจัยฉบับสมบูรณ์

## โครงการกลศาสตร์ของท่อลำเลียงของใหลที่ยืดหดตัวได้ในสามมิติ (MECHANICS OF THREE-DIMENSIONAL EXTENSIBLE MARINE RISERS TRANSPORTING FLUID)

	คณะผู้วิจัย	สังกัด
1.	ศ. คร. สมชาย ชูชีพสกุล	มหาวิทยาลัยเทคโนโลยีพระจอมเกล้าธนบุรี
2.	รศ. คร. นคร ภู่วโรคม	มหาวิทยาลัยธรรมศาสตร์
3.	คร. ทินกร มนต์ประภัสสร	มหาวิทยาลัยเอเชียอาคเนย์
4.	คร. จุลพจน์ จิรวัชรเคช	มหาวิทยาลัยเทคโนโลยีพระจอมเกล้าธนบุรี
5.	คร. หูชัย สุจิรวรกุล	มหาวิทยาลัยเทคโนโลยีพระจอมเกล้าชนบุรี
6.	นายบุญชัย ผึ้งใผ่งาม	สูนย์กลางสถาบันเทคโนโลยีราชมงคล
7.	นางสุชาคา ไวยวุทธิ	มหาวิทยาลัยเทคโนโลยีพระจอมเกล้าธนบุรี
8.	นายทวิช พูลเงิน	มหาวิทยาลัยเทคโนโลยีพระจอมเกล้าธนบุรี
9.	นายบุญมี ชินนาบุญ	มหาวิทยาลัยเทคโนโลยีพระจอมเกล้าชนบุรี
10	. นายนรากร ศรีนิล	มหาวิทยาลัยเทคโนโลยีพระจอมเกล้าชนบุรี
11	. นายชัยณรงค์ อธิสกุล	มหาวิทยาลัยเทคโนโลยีพระจอมเกล้าธนบุรี
12	. นายสุรเคช แก้วประเสริฐ	มหาวิทยาลัยเทคโนโลยีพระจอมเกล้าธนบุรี
13	. นายชัยนันทน์ มะชรา	มหาวิทยาลัยเทคโนโลยีพระจอมเกล้าชนบุรี
14	. นาย อรุณ สุวรรณชีวะศิริ	มหาวิทยาลัยเทค โน โลยีพระจอมเกล้าธนบุรี
15	. นายยศ สมพรเจริญสุข	มหาวิทยาลัยเทค โน โลยีพระจอมเกล้าชนบุรี
16	. นายศักดิ์รัตน์ แก้วอุ่นเรือน	กรมโยชาชิการ
17	'. นายไพโรจน์ วรรณสวัสคิ้กุล	หน่วยงานเอกชน
18	. นายปริญญา แซ่อุ๋ย	หน่วยงานเอกชน

สนับสนุนโดยสำนักงานกองทุนสนับสนุนการวิจัย

19. นายสุวิทย์ รัตนศรีกูล หน่วยงานเอกชน

#### ABSTRACT

This research presents a three-dimensional model formulation of extensible marine risers/pipes transporting fluid and parametric studies of the effects of axial deformation and internal flow on the behaviors of risers/pipes. The variational model formulation is developed based on the new idea employing from the axially deformable elastica theory and from the view of continuum mechanics in three descriptions namely, the total Lagrangian, the updated Lagrangian, and the Eulerlian. By the principle of virtual work-energy, the governing dynamic equilibrium equations are derived in the Cartesian coordinate and are validated by the vectorial summation of forces and moments. Based on the hybrid approach and the state space formulation, the finite element method is used to solve these equations. The three-dimensional nonlinear static analysis and the two-dimensional dynamic analysis are carried out in order to explore these effects on the nonlinear static behavior, the dynamic stability, and the nonlinear oscillations of the pipe under a tidal current and a regular incoming wave, respectively. The parametric studies have demonstrated the effects of axial deformation and fluid transportation in many points of view. The results of this study show that the axial deformation reduces large deflections and nonlinear responses of the pipe, but increases the static and dynamic stabilities of the pipe, while the transported fluid affects on the contrary. The advantages of the present model are related to the flexibility offered in choosing the independent variable, and to the possibility of applying them to numerous elastica problems, including some biomechanics applications.

**KEYWORDS:** Three-dimensional Marine Risers / Large Strain Formulations / Variational Formulation / Elastica / Transported Fluid / Finite Element Method

### บทคัดย่อ

งวนวิจัยนี้เสนอแบบจำลองของท่อลำเลียงของไหลที่ยืดตัวได้ในสามมิติและการศึกษาผล กระทบของการยืดตัวมากในแนวแกนและผลกระทบเนื่องจากของไหลภายในท่อที่มีต่อพลติกรรมของ ท่อ แบบจำลองดังกล่าวได้พัฒนาขึ้นจากวิธีการแปรผันและทฤษฎีอีลาสติคคาที่เสียรูปได้มากในแนว แกนซึ่งอยู่บนพื้นฐานกลศาสตร์วัสคุที่เสียรูปได้ โดยพิจารณามุมมองแบบโททอลลากรองจ์ อัพเคท ลากรองจ์ และออยเลอร์ จากหลักการพลังงานเสมือนทำให้ได้มาซึ่งสมการสมคุลเชิงพลศาสตร์ซึ่ง ครอบคลุมปัญหาในระบบพิกัดการ์ทีเซียน ความถูกต้องของสมการซึ่งครอบคลุมปัญหานี้ได้รับ การตรวสอบ โดยการพิจารณาสมคุลของแรงและ โมเมนต์ที่กระทำต่อชิ้นส่วนท่อลำเลียงในสภาวะการ เคลื่อนที่ซึ่งขึ้นกับเวลา การแก้สมการเหล่านี้กระทำโดยใช้วิธีการไฟในต์เอลิเมนต์ในการคำนวณและ วิเคราะห์ผลทางสถิตศาสตร์ในสามมิติ และผลทางพลศาสตร์ในสองมิติ ผลจากการวิเคราะห์ทำให้ สามารถศึกษาผลกระทบของการเสียรูปมากในแนวแกน และผลกระทบของการลำเลียงของไหลในท่อ ที่มีต่อพฤติกรรมแบบสถิตที่ไม่เป็นเชิงเส้น และเสถียรภาพเชิงพลศาสตร์ รวมถึงพฤติกรรมการสั่นแบบ ไม่เป็นเชิงเส้นของท่อลำเลียงของไหลในทะเลภายใต้กระแสน้ำและสภาวะคลื่นปกติ ผลการวิเคราะห์ สรุปได้ดังนี้ การเสียรูปในแนวแกนของท่อลำเลียงทำให้การแอ่นตัวมากมีค่าลดลง และการตอบสนอง แบบไม่เป็นเชิงเส้นต่างๆมีค่าลดลง ประกอบกับทำให้เสถียรภาพของท่อมีค่ามากขึ้น ในขณะที่การ ลำเลียงของไหลภายในท่อให้ผลกระทบในทางตรงกันข้าม แบบจำลองนี้มีจุดเด่นอยู่ที่ความสะควกใน การเลือกใช้ตัวแปรอิสระให้เข้ากับการวิเคราะห์ปัญหาในแต่ละประเภท นอกจากนี้ยังมีความเป็นไปได้ ที่จะประยุกต์ใช้กับปัญหาบางอย่างในกลศาสตร์ชีวภาพ และปัญหาแบบต่างๆอีกมากในกลศาสตร์ของ โครงสร้างอีลาสติคคา

กำลำคัญ: ท่อลำเลียงของไหลในทะเลที่เสียรูปในสามมิติ / แบบจำลองที่พิจารณาความเครียดมีค่า มาก / วิธีการแปรผัน / อีลาสติคคา / การลำเลียงของไหล / วิธีการไฟในต์เอลิเมนต์

#### **EXECUTIVE SUMMARY**

#### RESESEARCH SIGNIFICANCE AND PROBLEM STATEMENT

The increase of global energy consumption in recent years has urged to find the new resources and leaded to the exploration of underwater resources in the ultra deep ocean. This situation has prompted a substantial level of research activity in the fields of deep offshore engineering and marine technology. Exploration in the very deep ocean required more sophisticated equipment as well as the structural system that can withstand severe environments than those in normal condition. The exploration system, which is commonly used in the operations, is the floating structure or platform, which has marine riser as a linkage between the structure and sea floor. Thus, marine riser is the major component of the offshore/ocean drilling system and it serves two main purposes; one is to convey fluid, the other is to guide the drilling string from the platform to the wellhead at the sea floor. A failure of the riser system cause not only severe environmental pollution but also significant financial consequences. Recent offshore technology development has revealed that the marine riser has been used for water depths greater than 1000 m. This challenges the researchers and design engineers to enhance the performance of the marine riser, thus researchers and engineers must have a complete understanding of the behavior of marine riser to be operated in the ultra deep ocean.

#### **OBJECTIVE OF RESEARCH**

The objectives of this research project are as follows.

- 1. To develop a 3-D model formulation of marine riser/pipe experiencing large displacement and large axial deformation in three-dimensional space based on the virtual work-energy principle and elastica theory.
- 2. To study the effect of large strain deformation and fluid transportation on static equilibrium configurations and dynamic behaviors of the riser/pipe.
- 3. To investigate structural motion stability of the riser.
- 4. To study the response of the riser due to current and wave forces.

#### RESEARCH METHODOLOGY AND RESULTS

Based on the variational formulation, the total virtual work of the riser consists of the virtual work of the internal forces of the riser and the virtual work done of the external forces acting on the riser. The virtual work of the internal forces composes of the strain energies due to large axial, bending, and twisting deformations. The virtual work of the external forces composes of the virtual work of the apparent weight, hydrodynamics pressure, and inertia of the pipe and transported fluid. Large axial strain formulation is emphasized in this research study. Three deformation descriptions, namely the total Lagragian, the updated Lagragian, and the Eulerian, are used to obtain the variational formulation for three different views. The apparent tension concept and the dynamic interactions between fluid and pipe are used to derive the virtual work of the external forces of the riser pipe. The formulation is validated by the vectorial formulation, which considers the equilibrium of forces and moments of a three-dimensional riser/pipe segment.

The numerical investigation presented in this research report covers two main results; the first is of 3-D static analysis and the other is of 2-D dynamic analysis. The finite element method based on the updated Lagrangian formulation is used to solve the problem numerically for both static and dynamic analyses.

The catenary cable and the nonlinear beam problems are used to verify and validate of the model and accuracy of the computer program developed in this work. Several numerical examples of the 3-D static analysis are presented to demonstrate the significance of the large axial and nonlinear deformation of the riser. For 2-D dynamic analysis, a thorough investigation has been carried out for the effects of large axial deformation and transported fluid on the natural frequencies as well as on the nonlinear response of the riser due to current and wave forces. Stability of motion of the linearized system is explained based on the Liapunov stability definitions for the cases of stable and unstable motions.

#### FUTURE WORK AND RECOMMENDATION

The numerical results for 3-D marine riser have been reported only for the case of large displacement static analysis, which excludes the effect of torsional deformation. However, a thorough investigation the effects of large axial deformation and internal fluid flow on nonlinear static and nonlinear dynamic behaviors has yet to be done and will be carried out in the near future. The model formulation developed in this study can readily handle for the aforementioned cases but it requires extensive numerical investigation. Such investigation for the 3-D riser has not been reported elsewhere in the open literature. Finally, there is a possibility of applying the model formulation developed in this research study, with some modifications, to some biomechanics problems such as the three-dimensional structure of supercoiled DNA, and arteries and veins conveying fluid blood inside the human body.

### กิตติกรรมประกาศ

คณะผู้วิจัยใคร่ขอขอบคุณสำนักงานกองทุนสนับสนุนการวิจัย (สกว.) ที่ให้การ สนับสนุนเงินทุนวิจัยในนามของทุนเมธีวิจัยอาวุโสภายใต้ โครงการกลศาสตร์ของท่อลำเลียงของ ไหลที่ยืดหดตัวได้ในสามมิติ โดยมี ศาสตราจารย์ คร. สมชาย ชูชีพสกุล เป็นหัวหน้าโครงการ และขอขอบคุณมหาวิทยาลัยเทคโนโลยีพระจอมเกล้าธนบุรี และภาควิชาวิศวกรรมโยธา ที่ให้การ สนับสนุนในค้านสถานที่รวมทั้งค่าสาธารณูปโภค

ภารกิจในการสร้างผลงานวิชาการรวมทั้งการสร้างนักวิจัยที่มีคุณภาพจะ ไม่สามารถ เกิดขึ้นได้ หากไม่ได้รับการสนับสนุนเงินทุนวิจัยจาก สกว. ในฐานะหัวหน้าโครงการวิจัยที่ได้รับ เกียรติและความไว้วางใจจาก สกว. จึงใคร่ขอขอบคุณ สกว. ไว้ ณ โอกาสนี้

## **CONTENTS**

	Page
Abstract	i
บทคัดย่อ	ii
Executive Summary	iii
กิตติกรรมประกาศ	vi
Contents	vii
Introduction	1
Model Formulations of Three-Dimensional Flexible Marine Risers Transporting Fluid	1 15
Solution Methods	66
Results and Discussions	87
Conclusions	121
References	123
ผลงานที่ได้จากโครงการ	133
Appendix: Reprints and Manuscripts	139

.

#### 1. INTRODUCTION

#### 1.1 STATEMENT OF THE PROBLEM

In the past five decades, flexible riser pipes have been employed extensively in numerous offshore engineering applications. The most vital function of these is to transport fluids that are drilled from beneath the ocean floor such as oil, gas, hydrocarbon and other crude resources, up to the production platform or drilling ship. In the deep-ocean mining industry, flexible pipes play a role of the main module in the production system as shown in Figure 1.1(a). In moderate sea-depth applications, they are often used as the secondary part in cooperating with rigid risers as shown in Figures 1.1(b) and 1.1(c).

In the literature, there are many papers related to analysis of flexible marine riser pipes as reviewed by Chakrabarti and Frampton (1982), Ertas and Kozik (1987), Jain (1994) and Patel and Seyed (1995). The mathematical riser models have been developed continually: from two-dimensional models to three-dimensional models, from linear models to nonlinear models. However, it is remarkable that most of them omit the effects of axial deformation of the pipe and fluid transportation. Furthermore, all of them did not included the nonlinear terms of the large axial strain in their model formulations.

As will be reviewed and discussed in this work, the individual effects of axial deformations, and fluid transportation could be significant to behavior of low flexible pipes. It is therefore conceivable that the combined action of all the effects becomes more important on behavior of highly flexible pipes. In such cases, those effects should be carefully examined in three-dimensional based upon the large strain analysis.

#### 1.2 LITERATURE REVIEW

The marine riser was first used in 1949 in the Mohole project (National Engineering and Science Company, 1965), whereas the first technical paper on riser analysis was carried out by St. Denis and Armijo (1955). The numerous research papers published on this subject since may be summarized chronologically.

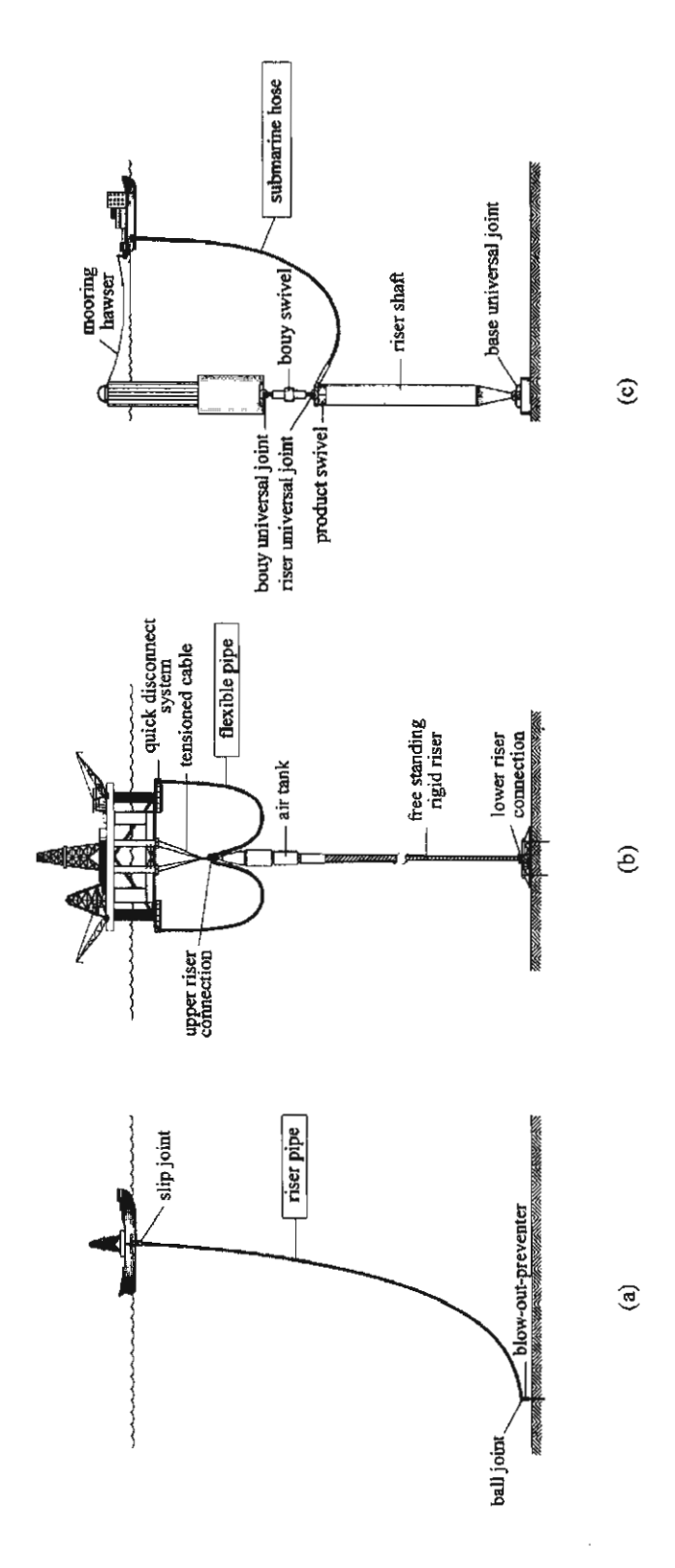


Figure 1.1 Flexible Marine Riser Pipes
(a) a Marine Riser (b) a Flexible Pipe (c) a Hoseline

In the 1960s, research work dealt predominantly with two-dimensional, linear static analysis (Fischer and Ludwig (1966), Gosse and Barksdale (1969)) and two-dimensional, linear dynamic analysis (National Engineering and Science Company (1965), Graham et al. (1965)) that did not take the relative hydrodynamic forces into consideration.

In the 1970s, the research work was escalated on various types of dynamic analyses and methods of solution as demonstrated in Table 1.1. In addition to the time domain analysis via the finite difference solution, the frequency domain analysis and the nondeterministic random vibration analysis had drawn the attention of several authors as well as the finite element method (Gardner and Kotch (1976)) and the modal analysis (Dareing and Huang (1979)). Although the paper by Bennett and Metcalf (1977) was oriented towards nonlinear dynamics, their work was still based on linear static solutions. The computer programs for the three-dimensional riser analysis, NONSAP (Bathe et al., 1974) and NASTRAN (Gnone et al., 1975) also originated in this period. Literature review on the marine riser analyses from 1950 to 1980 was given in the paper by Chakrabarti and Frampton (1982).

In the 1980s, researchers began to focus on three-dimensional large displacement analysis and nonlinear dynamic analysis. As shown in Table 1.1, most papers in this period were aimed at presenting the mathematical models for three-dimensional nonlinear analysis. Several papers were presented to indicate significances of three-dimensional analysis and nonlinear analysis (Natvig (1980), Felippa and Chung (1981), Bernitsas (1982), Safai (1983), Bernitsas et al. (1985), Huang and Chucheepsakul (1985), Owen and Qin (1987), Kokarakis and Bernitsas (1987), Bernitsas and Kokarakis (1988), O'Brien and Mcnamara (1989)). The finite element method was in widespread use for the spatial solution, whereas the numerical integration methods for time history analysis were favored as well as the modal transformation method for frequency domain analysis.

In this period, researches on the marine pipes considering the effect of axial deformation in the variational formulation were published by Felippa and Chung (1981), Irani, Modi and Weit (1987) and O'Brien and McNamara (1989). Researches that included the effect of axial deformation in the vectorial formulation were performed by Bernitsas and coauthors (Bernitsas et al. (1985), Kokarakis and

Bernitsas (1987), Bernitsas and Kokarakis (1988)). The effect of fluid transportation or internal flow were specifically studied by Irani et al. (1987), Moe and Chucheepsakul (1988) and Patel and Seyed (1989). The commercial package for the three-dimensional riser analysis, FLEXCOM-3D (Marine Computation Services International, 1989) was also launched in this period.

In the 1990s, research work on riser analysis had the trend of study of specific problems. Huang and Leonard (1990), Karamanos and Tassoulas (1991), and Hah et al. (1992) investigated the stability of the marine riser pipes. The developments of random dynamics and other types of the hydrodynamic loading were studied by Trim (1990) and Thampi and Niedzwecki (1992). A number of authors extended three-dimensional nonlinear analyses of marine risers by including accessory themes such as various types of boundary conditions (Oran (1992), Chung et al.(1994a), Chung et al. (1994b), Chung and Cheng (1996)), seabed contact problems (Tikhonov et al., 1996), as well as other coordinate systems (Huyse et al. (1997), Ngiam (1997)). In the same period, Wu and Lou (1991), Seyed and Patel (1992), Huang (1993), Chucheepsakul and Huang (1994), and Moe et al. (1994) explored the effects of internal flow. Jain (1994) and Patel and Seyed (1995) reviewed the analysis and modeling of the flexible riser.

Above is an overview of previous research work concerning marine riser pipe analysis. This research work is relevant to marine pipes that take into consideration the in-depth effects of axial deformation, radial deformation, and fluid transportation. A more detailed review of these subjects is given as follows.

#### 1.2.1 Three-dimensional model formulation

The three-dimensional models of the marine riser have been presented in many research works. Most of them used the theory of the space curved rod that can be found in the elasticity books such as Love (1944), Antman (1991), and Atanackovic (1997), which serve as the basic theory for the three-dimensional marine riser analysis.

To obtain the governing equations or the equation of motion of the marine pipe, there are at least three difference approaches: First, the direct equilibration based on D' Alembert's principle, Second, the variational method

based on the virtual work principle. Third, the variational method based on the Hamilton's principle.

The first approach is the most favorite method that can be found in many research works, for example, Bernitsas (1982), Bernitsas, Kokarakis, and Imron (1985), Kokarakis and Bernitsas (1987), Patrikalakis and Kriezis (1987), O'Brien, McNamara and Dunne (1988), Bernitsas and Kokarakis (1988), and Bernitsas and Vlahopoulos (1989). The three-dimensional model formulation of marine riser that based on the principle of virtual work can be found in the works of Felippa and Chung (1981) and Huang and Kang (1991). The research works that used the Hamilton's principle to formulate their governing equation are found in Doll and Mote (1976), and Atadan et al. (1997).

From the literature mentioned above, most of them used the arc-length as the independent variable. Therefore, the problem is limited to the case of specified arc-length or the total arc-length known prior. In the real situation, the arc-length of the marine riser may be unknown or changed due to the large displacement or large axial deformation while the top tension is specified, therefore the formulation that use the arc-length as the independent variable may be not convenient for numerical analysis. To solve this problem, the sea depth may be used to be the independent variable. Chucheepsakul and Huang (1985) is the pioneer in using the sea depth as the independent variable in the formulation. Huang and Kang (1991) extended the model to the three-dimensional formulation including the effect of torsion. However, the effect of internal flow and the axial deformation are neglected in that work.

#### 1.2.2 Significance of the Effect of Axial Deformation

The effect of axial deformation on marine cables was investigated by Huang (1992), Chucheepsakul et al. (1995) and Chucheepsakul and Huang (1997). On the suspended cables, they were studied by Huddleston (1981), Shih and Tadjbakhsh (1984), Burgess and Triantafyllou (1988), Lin and Perkins (1995), Triantafyllou and Yue (1994), Tjavaras and Triantafyllou (1996), and Tjavaras et al. (1998). However, for marine pipes, it is only the low flexible pipes on which the effect of axial deformation has been explored.

On static behavior, the effect of axial deformation is to increase large

displacements of low-tensioned cables due to extensibility domination, and to reduce large displacements of high-tensioned cables due to pre-stressing domination (Chucheepsakul et al. (1995), Chucheepsakul and Huang (1997)). Although Bernitsas et al. (1985) and Bernitsas and Kokarakis (1988) found that the effect of axial deformation on the static behavior of the low flexible pipes was rather small, they did not provide evidence of the same result with the highly flexible pipes.

The effect of axial deformation on the dynamic behavior is to decrease nonlinear responses as reported by Chung et al. (1994a), Chung and Cheng (1996), Chung and Whitney (1983). It reduces the natural frequencies (Chucheepsakul and Huang, 1997), and provokes the elastic mode transitions of cable vibrations (Burgess and Triantafyllou (1988), Lin and Perkins (1995)). If the stress-strain relation is hysteretic, the effect of axial deformation can amplify damping of the dynamic strain in the axial direction (Triantafyllou and Yue,1994). Several papers by Chung and coauthors (Chung et al. (1994a), Chung and Cheng (1996), Chung and Whitney (1983)) highlighted the fact that the effect of axial deformation is crucial to dynamic behavior of low flexible pipe, and should be considered in the design of the pipe.

The interesting point in all the previous research is that the effect of axial deformation has been investigated based on small strain analysis, which assumes that the strains are small, and can be approximated by the binomial expansion. However, this approach is proper if, and only if the axial strain is small compared to unity (Fung, 1965). For highly flexible pipes, such a constraint is no longer confidential. Thus, this dissertation proposes large strain modeling in which the relative elongations or the square-root expressions of large strains are adopted.

#### 1.2.3 Significance of the Effects of Fluid Transportation

Although fluid transportation is the main function of marine riser pipes, marine riser analysis from the middle of 1950s to the end of 1970s gives little attention on the influence of fluid transportation. In the same period, research concerning mechanics of pipes conveying fluid had grown rapidly. Research work related to vibrations of straight and curved pipes can be found in the papers by Housner (1952), Gregory and Païdoussis (1966), Païdoussis (1970), Doll and Mote

(1976) and so on. It was reported that the internal flow reduced stability of the pipe and acted on the pipe like the end follower force (Thompson and Lunn, 1981). As a result, the internal flow can engender divergence instability or statical buckling of simply supported pipes (Holmes, 1978), and can induce flutter instability or snaking behavior of cantilever pipes (Gregory and Païdoussis, 1966).

The lack of connection between research work on marine pipes and pipes conveying fluid brings about a misconception by some authors. When the effects of internal flow on marine pipes were examined in the early of 1980s, it was considered that the internal flow induced only the friction force to act on the pipe wall. However, researchers concerned with pipes conveying fluid such as Gregory and Paï doussis (1966), Païdoussis (1970) and Thompson and Lunn (1981) had been well aware that the internal friction force did not act directly on the pipe, but transmitted the internal pressure into the pipe wall, which yielded tensioning and pressure drop (Païdoussis, 1998). In addition, the internal flow generated not only the effects of pressure, but also other fictitious forces such as Coriolis and centrifugal forces.

By the end of 1980s, the effects of fluid transportation on behavior of marine pipes began to draw specific interest from a number of researchers, and the misconception was dispelled. Several interesting effects of fluid transportation were reported. It was found that the internal flow reduced structural stiffness, provided negative damping (Irani et al., 1987), and induced additional large displacements of the pipes (Chucheepsakul and Huang, 1994). The natural frequencies of the pipes are slightly reduced at a low speed of internal flow, but significantly reduced at a high flow speed (Moe and Chucheepsakul (1988), Wu and Lou (1991)). The internal slug flow can induce the significant cyclic fatigue loading in deep water (Patel and Seyed, 1989). The marine riser pipe transporting fluid buckles by the divergence instability (Chucheepsakul et al., 1999).

However, the three-dimensional model formulations used in most of those works do not consider geometric nonlinearity and axial deformation of the pipes. In this research work, these objects have been taken into account in large strain analysis of marine risers. Therefore, the novelties of this work are the large strain model formulation of the three-dimensional extensible flexible marine risers/pipes transporting fluid and the unveiling of the interaction between the transported fluid and the pipe subjected to large axial deformations.

#### 1.3 OBJECTIVES

The objectives of this research work are as follows:

- 1.3.1 To introduce and illuminate the mathematical principles for large strain analysis of the flexible marine riser pipes that are subjected to the combined action of axial and fluid transportation from viewpoints of the total Lagrangian, the updated Lagrangian and the Eulerian mechanics.
- 1.3.2 To show how to formulate large strain three-dimensional models in the Cartesian coordinates by using the axially deformable elastica theory.
- 1.3.3 To examine the in-depth effects of axial deformations and fluid transportation on behaviors of the marine pipes with large displacements.

#### 1.4 ASSUMPTIONS AND SCOPE

The following assumptions and scope are stipulated in the present study:

- 1.4.1 The material made of the riser/pipe is linearly elastic.
- 1.4.2 At the undeformed state, the pipes are straight, and have no residual stresses.
- 1.4.3 The pipe cross sections remain circular after change of cross-sectional size due to the axial deformation effect.
- 1.4.4 Longitudinal strain is large, while the effect of shear strain is small and can be neglected, so that the Kirchhoff's rod theories can be employed.
- 1.4.5 Every cross section remains plane and remains perpendicular to the axis.
- 1.4.6 Radial lines of the sections remain straight and radial as the cross section rotates about the axis.
- 1.4.7 The internal and external fluids are inviscid, incompressible and irrotational. Their densities are uniform along arc-lengths of the riser.
  - 1.4.8 The internal flow is the one-dimensional plug laminar flow.

- 1.4.9 Morison's equation is adopted for evaluating external hydrodynamic forces of external fluid.
  - 1.4.10 The effect of rotary inertia is negligible.
- 1.4.10 The pipe connections due to construction are presumed to be homogeneous with the pipe body, and have the same properties.
- 1.4.11 The effect of wind flow over the sea surface is negligible for deep-water riser pipe analysis.
- 1.4.12 Structural model. The riser pipe is pinned at the bottom end by the ball joint of wellhead at seabed, and is held at the top end by the slip joint beneath the vessel. The slip joint allows the pipe to change its length as the vessel heaves and moves laterally. The surrounding kill and choke lines are assumed to make no contribution to the structural stiffness. The rotational stiffness at the top end of the riser and the ship motion compared to the water depth are small and negligible, so the top end could be modeled as the slip joint with hinge. The ball joint at the bottom end can not rotate freely around the tangential direction, but can rotate freely around any other direction perpendicular to the tangent.
- 1.4.13 Research methodology. The nonlinear static analysis, the natural frequency analysis and the nonlinear vibration analysis are rendered for studying the effects of axial deformation, and fluid transportation on behaviors of the pipe as shown in Figure 1.2. The nonlinearity in the vibration analysis is due to the nonlinear hydrodynamic damping. The large strains and large displacements are fully treated in the nonlinear static analysis, whereas the linear dynamic strains and the small amplitude vibrations are assumed in the natural frequency analysis and the nonlinear vibration analysis.
- 1.4.14 Current flow. The current is tidal. Its velocity profile can be expressed in form of the polynomial functions of water depth (Larsen, 1976).
- 1.4.15 Wave flow. The wave is regular incoming, and can be described by Airy's wave theory (Chen and Lin, 1989).

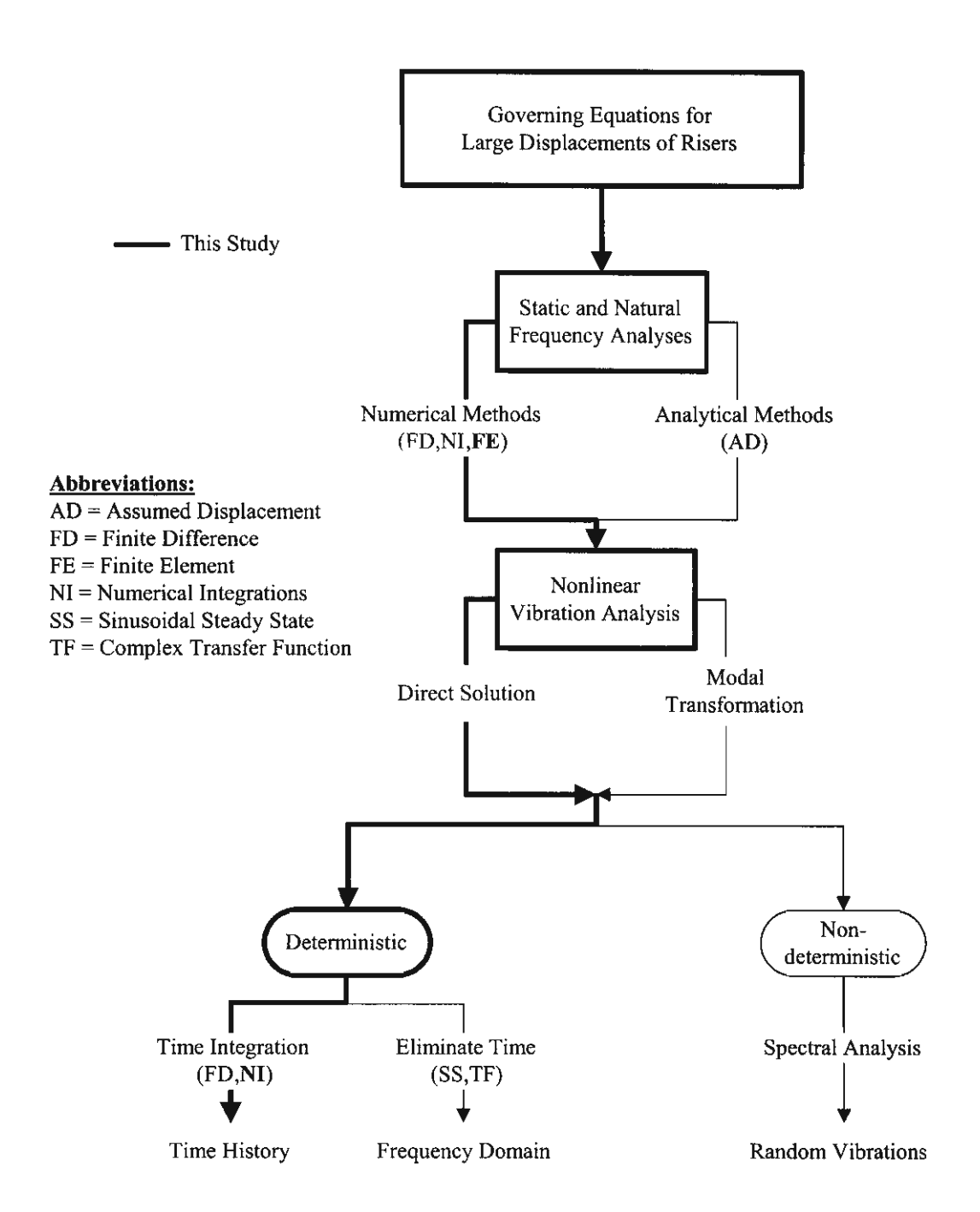


Figure 1.2 Methods of Marine Riser Analysis

Table 1.1 Summary of Paper Review on Riser Pipe Analysis

_	K
Elongation) (Tension) Radial	Bendii
(10) (11)	(6)
z	Y
z -	<b>~</b>
z 	٨
z	Y
z -	Y
2	, Y
z -	¥
7	¥
z -	Y
z 	>
z _	>
Z	Y
z	>
Z	гр,тн ү
	¥
Z	٨
2	>

Table 1.1 Summary of Paper Review on Riser Pipe Analysis (Continued)

			uc	noit	Sol. Technique	hnique	ədA		Deformation	nation		Γ,	Static loads	loads	Dynamic loads	c loads	pa		
Year	Reference	S=static D=dynamic	No. Dimensio	Large Deformat	Spatial	remporal	Dynamic sol	Bending.	Elongation (Tension)	Radial noilemolab	noizroT	woft Ismestri	Current	Horz. Offset	Мачея	Ship motion	ozinasnil gariCl	Wave theory	Boundary conditions
(E)	(2)	(3)	(4)	(5)	(9)	(3)	(8)	6)	(10)	(11)	(12)	(13)	(14)	(13)	(91)	(17)	(18)	(61)	(20)
77	Bennet and Metcaif [12]	D	2	z	FD	Z	ТН	<b>*</b>	I	Z		z	γ	-	>	>	z		Spring-Free
77	Maison and Lea [80]	О		2	FE	FD	TH	>	_	z	z	z	٨	Y2	<b>&gt;</b>	<b>&gt;</b>	z	S	
77	Paulling [81]	D	3	Z	FE	SS	FD	٨	-	z	٨	z	z		<b>*</b>	٨	Y	L	Spring-Free
78	Chou et al. [82]	Q	2	z	FD	Z	TH.	<b>&gt;</b>	-	z	•	z	٧١		У3	>	Z	Г	Pinned-Free
78	Young et al. [83]	۵	2	z	FD	SS	FD	٨	_	z		z"	Y		۲۱,3	<b>&gt;</b>	Y	Г	
79	Kirk et al. [84]	SD	2	z	ΑD	MT	FD	<b>&gt;</b>	ı	z		z	γ	٧١	43	>	٨	L	Pinned-Pinned
79	Dareing and Huang [11]	D	2	z	QΥ	MT	FD	<b>*</b>	1	z		z	γ	Y!	Y3	<b>*</b>	٨	ľ	Pinned-Pinned
80	Krolikowski and Gay [85]	Q	2	z		SS	FD	٨	-	z		z	Y2	Ϋ́	Y1,3	<b>*</b>	Y	L	Ball-Ball
80	Bemitsas [86]	0	3	۲3	AD			¥	-	z	¥	z							
98	Natvig [15]	D	2	72	ž	Z	ТH	Y	-	z		z	γ		<b>*</b>	¥	¥	L	Forced-Forced
81	Etok and Kirk [87]	SD	2	z	Φ	TM	55	<b>&gt;</b>	-	z		z	>	Y1,2	ү3	>	<b>&gt;</b>	1	Pinned-Pinned
8.1	Felippa and Chung [16]	s	е	٨١	FE	,	,	>	ш	z	>	z	>			,	>		Fixed-Free
82	Bernitsas [17]	SD	ы	۲3				>	-	z	>	z						·	
83	Safai [18]	۵	ы	7.2	표	Z	Ŧ	>	-	z	<b>&gt;</b>	z			>	z	z		Ball-Free
85	Huang and Chuchecpsakul [20]	S	2	۲۱	世		٠	<b>&gt;</b>	-	z	•	z	>	*			,	٠,	Slip-Pinned
85	Kirk [88]	۵	2	z	AD.	MT	G	>	5	z		z	٠	Υ	٨	z	Y	L	Pinned-Pinned
85	Bernitsas et al. [19]	S	ъ	۲۱	FE		•	>	Э	z	>	z	¥	À	•	٠	-	•	Pinned-Pinned

Table 1.1 Summary of Paper Review on Riser Pipe Analysis (Continued)

		uo —		noil	Sol. Technique	hnique	Abe		Deformation	nation		A	Static loads	loads	Dynamic loads	c loads	po	A	
Reference S=static D=dynamic No. Dimensio Large Deforma	D=dynamic No. Dimensio	erronage Deforme	lating2		Temporal		Dynamic sol t	Bending	Elongation (Tension)	Radial deformation	noizioT	voft lametral	Current	Horz. Offset	Waves	notiom qid2	Drag lineaniza	Mave theory	Boundary conditions (Top-Bottom)
(2) (3) (4) (5) (6) (7)	(4) (5) (6)	(5) (6)	(9)		0		(8)	(6)	(10)	(11)	(12)	(13)	(14)	(15)	(16)	(17)	(18)	(19)	(20)
Owen and Qin [21] D 3 Y3 FE NI	3 Y3 FE	y3 FE	표		Z	=	TH	<b>&gt;</b>	1	z	<b>*</b>	z	Y	٨	Y	z	•••		Pinned-Pinned
Kokarakis and Bernitsas [22] D 3 Y2 FE	D 3 Y2 FE	72 圧	丑			ž	H	۲	I	z	<b>*</b>	Υı	¥	¥	<b>.</b>		•		
Irani et al. [25] D 3 N FE N	3 N FE	N	FE		2	T.W	FD	<b>&gt;</b>	ш	z	Ý	Y1	Y	¥	٨	z	λ	L	Pinned-Pinned
Bernitsas and Kokarakis [23] S 3 YI FE -	S 3 YI FE	YI FE	FE		'		1	٨	ш	z	<b>×</b>	z	٨	<b>*</b>	•				Pinned-Pinned
Moe and Chucheepsakul [26] D 2 N AD FE	D 2 N AD,FE	N AD,FE	AD,FE				,	z	-	z	ı	١٨	٨	<b>,</b>	,			1	Pinned-Pinned
Ahmad and Datta [89] D 2 N FE N	2 N FE	Z	뜐		_	ž	Ŧ	٨		z		z	<b>,</b>	>	۴۱۶	>-	z	Ĺ	Spring-Spring
O'Brien and Monamara [24] SD 3 Y3 FE N	SD 3 Y3 FE	Y3 FE	85		~	Z	TH.	Y	Е	2	*	z	٨	٨	٨				
Patel and Seyed [27] SD 2 YI FE MT	2 YI FE	Y1 FE	Ħ		Σ	Ļ	Œ	¥	1	z	1	¥2	>	>	>	>	>		
Spanos et al. [90] D 2 YI FE NI	2 YI FE	YI FE	표		Z		FD	γ	1	z		z	Y		<b>&gt;</b>	٨	>		Fixed-Ball
Trim [32] D 2 N FE Ni	2 N FE	Z E	FE		z		RV	٨	1	z		z	Y	¥	٠	>		ı	Pinned-Pinned
Huang and Kang [91] SD 3 YI FE	3 Y1 FE	Y1 FE	FE		'		•	٨	-	z	<b>,</b>	z	٨	Y	•	,	,	,	Pinned-Pinned
Wu and Lou [41] SD 2 N NI N	Z N NI	z	ī			Ī	ТН	Y	_	z		١٨	<b>*</b>	Y	>	<b>*</b>			Pinned-Pinned
Chung et al. [35, 36] SD 3 Y3 FE NI	3 Y3 FE	Y3 FE	표		z		H	¥	E	z	Α.	z	٨		<b>*</b>	>			Fixed-Motion
Chucheepsakul and Huang [44] S 2 Y1 FE -	S 2 Y1 FE	Y1 FE	FE		'		•	Y	1	2	•	١٨	¥	٨	•	•		,	Slip-Pinned
Tikhonov et al. [38] D 3 Y3 NI NI	3 Y3 NI	Y3 NI	ī		Ž		표	Y	E	z	<b>,</b>	Z	٨	<b>&gt;</b>	<b>*</b>	z			Fixed-Fixed
Atxandam et al. [92] D 3 YI NI NI	3 Y1 M	Y1 NI	Z		z		표	¥	E	z	٨	1,k	Y	<b>*</b>	Y	*			Fixed-Free
Huyse et al. [39] S 3 Y1 AD -	3 YI AD	YI AD	QA.		'		-	z	-	z	•	2	Y	٨		•		,	Shp-Ball

Notes of Abbreviations in Table 1.1:

nnn	= Random   2 = Irregular   2 = Paceular	4 = Fourier Series 5 = Static Time Slice	6 = Wave Elevation Record	L = Linear Wave Theory	S = Stoke's Fifth Order								
Column	(16)			(19)									
	TH = Time History  FD = Frequency Domain	= Inextensible Analysis	= Extensible Analysis	= Steady Flow	= Slug Flow		= Any Profile	= Stepwise Linear	= Multidirectional		= Static	= Periodic	
q			ш	) 1	7		1	7	Э		1	7	
Column	8)	(10)		(13)			(14)				(15)		
	ALL Y = Yes N = No	= Static = Dynamic	= Static and Dynamic	AD = Assumed Displacement	= Finite Difference	= Finite Element	= Numerical Integration	= Complex Transfer Functions		= Finite Difference	= Numerical Integration	[ = Modal Transformation	= Sinusoidal Steady State
	> Z	7	3	AD	FD	FE	Z	TF		Œ	Z	MT	SS
Column	ALL	(5)		(9)						6			

# 2. MODEL FORMULATIONS OF THREE-DIMENSIONAL FLEXIBLE MARINE RISERS TRANSPORTIG FLUID

This section presents the large strain model formulation of threedimensional flexible marine risers transporting fluid. The elastica theory of extensible rod and the kinematics theory of mass transported on the moving frame are used to obtain the model formulation.

In section 2.1, the behavior of the flexible marine risers and the physical description of the model formulation are introduced. The concept of large strain measurement in the three deformation descriptions referring to the Cartesian coordinate is discussed in section 2.2.

It is realized that the change of the large axial strain is not only effect on the differential arc-length of the riser but also effect on the property changes of the riser cross section and transporting fluid velocity, which is discussed in section 2.3. In section 2.4, the extensible elastica theorems for the Hookean material riser corresponding to the three deformation descriptors is preformed. The effect of hydrostatic pressures and hydrodynamic pressures is reviewed in section 2.5 and 2.6, respectively.

In section 2.7, the elastica theory, the apparent tension concept and the dynamic interactions between fluid and risers are used to formulate the variational formulations, which are validated by vectorial formulation in section 2.8. For the sake of generality in obtaining the model solution, the nonlinear dynamic model based on the strong form is derived in section 2.9. In section 2.10, eliminating the time-dependent terms in nonlinear dynamic model, the nonlinear static model is derived.

One conspicuous feature of the present formulation is flexibility of the model that allows users to select the independent variable to suit solution of their own problems, therefore the guideline for choosing the independent variable is discussed in section 2.11. Finally, the implementation of the present models is covered in section 2.12.

# 2.1 BEHAVIOR OF THE FLEXIBLE MARINE RISERS AND PHYSICAL DESCRIPTION OF THE MODEL FORMULATION

The large displacement and large deformation behaviors of a flexible marine riser transporting fluid are depicted in Figure 2.1. Firstly the riser is at rest and unstretched at the undeformed configuration. Then, the riser is subjected to the time-independent loads and its configuration changes to equilibrium configuration that is the initial condition before the dynamic actions occur. Finally, at the displaced configuration, dynamic actions such as wave, unsteady current, and unsteady internal flow disturb the riser to sustain vibration about the equilibrium configuration.

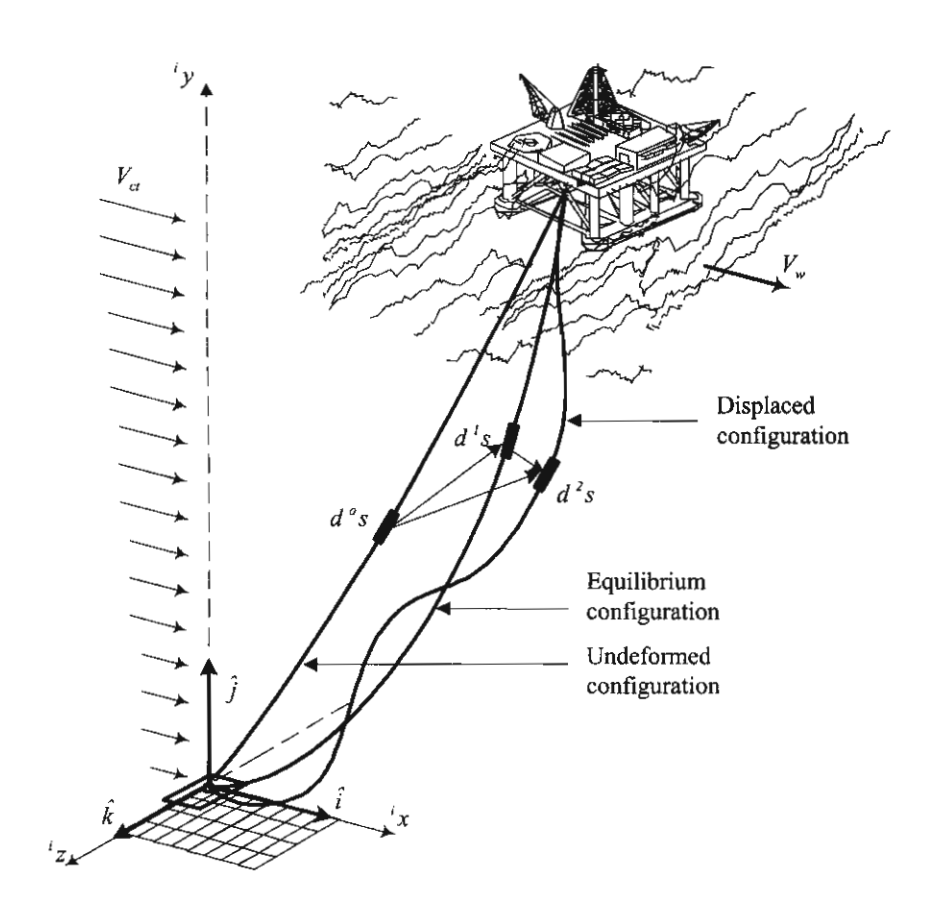


Figure 2.1 Three configurations of marine riser.

The marine riser is modeled as a three-dimensional rod with a ball joint at the bottom end and a slip joint at the top end. In this study, three orthogonal coordinate systems are used to define position, motion, and deformation of an extensible marine riser. The orthogonal triad system  $\hat{t}, \hat{n}, \hat{b}$  and the cross-sectional principal axes system  ${}^ix_1, {}^ix_2, {}^ix_3$  with unit normal vector  ${}^ie_1, {}^ie_2, {}^ie_3$  are used as the local coordinate. The fixed cartesian system  ${}^ix, {}^iy, {}^iz$  with unit normal vector  $\hat{i}, \hat{j}, \hat{k}$  is used as the global coordinate. The left superscript represents the state of marine riser where 0 represents the undeformed state, 1 represents the equilibrium state and 2 represents the displaced state, therefore,  $i \in (0, 1, 2)$ .

Figure 2.2 shows the segments of the extensible marine riser in three states. Since the centerline of the riser at any time t is, in general, a three-dimensional curve and can be described by one parameter, the parameter  $\alpha$ ,  $\alpha \in \{{}^{i}x, {}^{i}y, {}^{i}z, {}^{i}s\}$ , that is employed in the formulation for the sake of generality. Therefore if  ${}^{i}x, {}^{i}y$ , and  ${}^{i}z$  are the coordinates of a point along the marine riser at time t, then  ${}^{i}x = {}^{i}x(\alpha, {}^{i}t)$ ,  ${}^{i}y = {}^{i}y(\alpha, {}^{i}t)$ , and  ${}^{i}z = {}^{i}z(\alpha, {}^{i}t)$ . The partial derivatives with respect to  $\alpha$  and time  ${}^{i}t$  are represented by superscripts (') and ('), respectively.

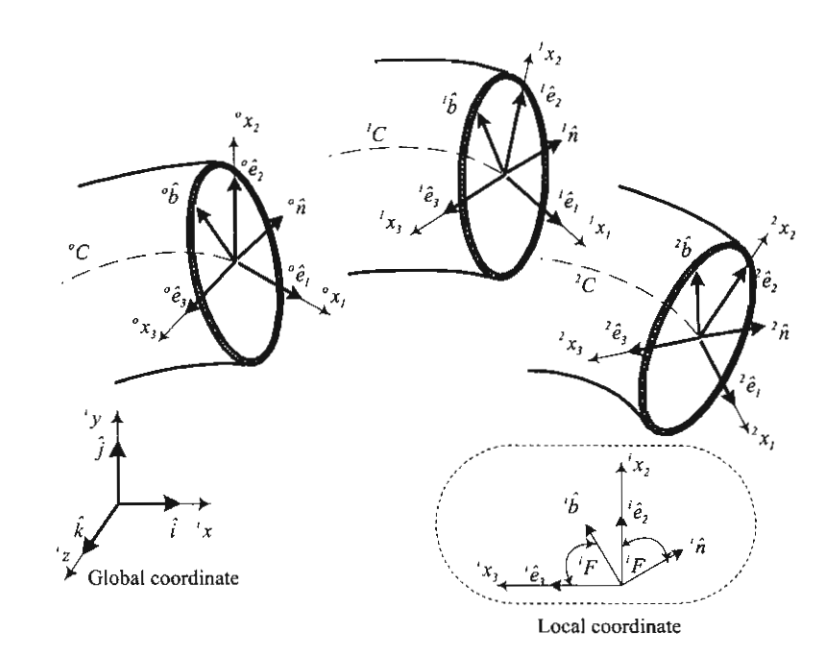


Figure 2.2 Segments of the extensible marine riser in three states.

#### 2.2 MEASUREMENT OF LARGE AXIAL STRAINS

In Cartesian coordinate, the relations of differential arc-length at the undeformed state, the equilibrium state and the displaced state  $({}^{o}s', {}^{l}s'and {}^{2}s')$  can be expressed as

$${}^{o}s' = \sqrt{{}^{o}x'^{2} + {}^{o}y'^{2} + {}^{o}z'^{2}}$$

$${}^{l}s' = \sqrt{{}^{l}x'^{2} + {}^{l}y'^{2} + {}^{l}z'^{2}} = \sqrt{({}^{o}x' + {}^{l}u')^{2} + ({}^{o}y' + {}^{l}v')^{2} + ({}^{o}z' + {}^{l}w')^{2}}$$

$${}^{2}s' = \sqrt{{}^{2}x'^{2} + {}^{2}y'^{2} + {}^{2}z'^{2}} = \sqrt{({}^{o}x' + {}^{2}u')^{2} + ({}^{o}y' + {}^{2}v')^{2} + ({}^{o}z' + {}^{2}w')^{2}}$$

$${}^{2}s' = \sqrt{({}^{o}x' + {}^{l}u' + u')^{2} + ({}^{o}y' + {}^{l}v' + v')^{2} + ({}^{o}z' + {}^{l}w' + w')^{2}}$$
(2.1 a-d)

According to the mechanics of deformable bodies, the definition of axial strain can be provided in three forms, namely the Total Lagrangian Descriptor, the Updated Lagrangian Descriptor, and the Eulerian Descriptor. Each of these forms can be demonstrated as follows.

#### Total Lagrangian Descriptor (TLD)

The coordinate that follows motion and deformation of a deformable body with respect to position, direction, and size of the body at the original state (or undeformed state herein) is said to be the total Lagrangian descriptor.

Total strain
$${}^{2}\overline{\varepsilon} = \frac{d^{2}s - d^{\circ}s}{d^{\circ}s} = \frac{d^{2}s}{d^{\circ}s} - 1 = \sqrt{1 + 2\binom{2}{2}L} - 1$$
Static strain
$${}^{I}\overline{\varepsilon} = \frac{d^{I}s - d^{\circ}s}{d^{\circ}s} = \frac{d^{I}s}{d^{\circ}s} - 1 = \sqrt{1 + 2\binom{2}{2}L} - 1$$
Dynamic strain
$$\overline{\varepsilon} = \frac{d^{2}s - d^{I}s}{d^{\circ}s} = \sqrt{1 + 2\binom{2}{2}L} - \sqrt{1 + 2\binom{2}{2}L}$$
(2.2 a-c)

The Green strains in each state that represents in equation (2.2) can be derived in the terms of displacements of the riser as follows.

$${}^{2}L = \frac{1}{\left({}^{o}s'\right)^{2}} \left({}^{o}x'\left({}^{2}u'\right) + {}^{o}y'\left({}^{2}v'\right) + {}^{o}z'\left({}^{2}w'\right) + \frac{\left({}^{2}u'\right)^{2}}{2} + \frac{\left({}^{2}v'\right)^{2}}{2} + \frac{\left({}^{2}w'\right)^{2}}{2}\right)$$

$${}^{1}L = \frac{1}{\left({}^{2}s'\right)^{2}} \left({}^{o}x'\left({}^{1}u'\right) + {}^{o}y'\left({}^{1}v'\right) + {}^{o}z'\left({}^{1}w'\right) + \frac{\left({}^{1}u'\right)^{2}}{2} + \frac{\left({}^{1}v'\right)^{2}}{2} + \frac{\left({}^{1}w'\right)^{2}}{2}\right)$$

$$L = {}^{2}L - {}^{1}L = \frac{1}{{}^{o}s'^{2}} \left({}^{1}x'u' + {}^{1}y'v' + {}^{1}z'w' + \frac{u'^{2}}{2} + \frac{v'^{2}}{2} + \frac{w'^{2}}{2}\right)$$

$$(2.3 \text{ a-c})$$

#### Updated Lagrangian Descriptor (ULD)

The coordinate that follows motion and deformation of a deformable body with respect to position, direction, and size of the body at the intermediate state (or equilibrium state, the last known deformed configuration herein) is said to be the updated Lagrangian descriptor.

Total strain
$${}^{2}\varepsilon = \frac{d^{2}s - d^{o}s}{d^{I}s} = \sqrt{1 + 2\upsilon} - \sqrt{1 - 2({}^{I}\upsilon)}$$
Static strain
$${}^{I}\varepsilon = \frac{d^{I}s - d^{o}s}{d^{I}s} = 1 - \frac{d^{o}s}{d^{I}s} = 1 - \sqrt{1 - 2({}^{I}\upsilon)}$$
Dynamic strain
$$\varepsilon = \frac{d^{2}s - d^{I}s}{d^{I}s} = \frac{d^{2}s}{d^{I}s} - 1 = \sqrt{1 + 2\upsilon} - 1 \tag{2.4 a-c}$$

The updated Green strains in each state that represents in equation (2.4) can be derived in the term of displacements of the riser which relate to the Green strains as

$${}^{2}v = {}^{1}v + v = {}^{2}L\left(\frac{{}^{o}s'}{{}^{s}s'}\right)^{2}, {}^{1}v = {}^{1}L\left(\frac{{}^{o}s'}{{}^{s}s'}\right)^{2}, \ v = {}^{2}v - {}^{1}v = L\left(\frac{{}^{o}s'}{{}^{s}s'}\right)^{2}$$
 (2.5 a-c)

#### Eulerian Descriptor (ED)

The coordinate that follows motion and deformation of a deformable body with respect to position, direction, and size of the body at the final state (or the displaced state herein) is said to be the Eulerian descriptor (ED).

Total strain
$${}^{2E}\varepsilon = \frac{d^2s - d^os}{d^2s} = 1 - \frac{d^os}{d^2s} = 1 - \sqrt{1 - 2\binom{2}{E}}$$
Static strain
$${}^{1E}\varepsilon = \frac{d^1s - d^os}{d^2s} = \sqrt{1 - 2E} - \sqrt{1 - 2\binom{2}{E}}$$
Dynamic strain
$${}^{E}\varepsilon = \frac{d^2s - d^1s}{d^2s} = 1 - \frac{d^1s}{d^2s} = 1 - \sqrt{1 - 2E}$$
(2.6 a-c)

The Almansi strains in each state that represents in equation (2.6) can be derived in terms of displacements of the riser which relate to the Green strains as

$${}^{2}E = {}^{2}L\left(\frac{{}^{o}S'}{{}^{2}S'}\right)^{2}, {}^{1}E = {}^{1}L\left(\frac{{}^{o}S'}{{}^{2}S'}\right)^{2}, E = {}^{2}E - {}^{1}E = L\left(\frac{{}^{o}S'}{{}^{2}S'}\right)^{2}$$
 (2.7 a-c)

From the definition of axial strain discussed above, the large axial strains are measured by mean of relative elongation that can be called as engineering strains. The square-root expressions in equations (2.2), (2.4) and (2.6) indicated that the large axial strains are function of the Green strains  $^{i}L$ , the updated Green strains  $^{i}v$ , and the Almansi strains  $^{i}E$ . In nonlinear dynamic analysis with large amplitude vibrations and large strain of the flexible marine riser, the square-root expressions in the large axial strain definitions have to be included in the formulation without approximations.

In the case of the vibration problems with large amplitudes but strain is not highly large, the approximate large strain can be used in numerical analysis. By utilizing the two-term approximation of the binomial series, the approximate large total strains can be expressed as follows.

For TLD: 
$${}^{2}\overline{\varepsilon} = {}^{l}\overline{\varepsilon} + \left(\frac{{}^{2}s'}{{}^{l}s'} - 1\right)\left(1 + {}^{l}\overline{\varepsilon}\right) = {}^{l}\overline{\varepsilon} + \left(\sqrt{1 + 2\upsilon} - 1\right)\left(1 + {}^{l}\overline{\varepsilon}\right) \approx {}^{l}\overline{\varepsilon} + \upsilon\left(1 + {}^{l}\overline{\varepsilon}\right)$$

For ULD:  ${}^{2}\varepsilon = {}^{l}\varepsilon + \left(\sqrt{1 + 2\upsilon} - 1\right) \approx {}^{l}\varepsilon + \upsilon$ 

For ED:  ${}^{2E}\varepsilon = {}^{lE}\varepsilon + \left(1 - \frac{{}^{l}s'}{{}^{2}s'}\right) = {}^{lE}\varepsilon + \left(1 - \frac{1}{\sqrt{1 + 2\upsilon}}\right) \approx {}^{lE}\varepsilon + \upsilon$  (2.8 a-c)

Although the approximate large dynamic strains are used, the nonlinear dynamic with large amplitude vibration is complicated and it is difficult to find the solutions. To simplify this problem to be the linear dynamic with small amplitude vibration, the total strain can be expressed same as the equation (2.8) but the updated dynamic Green strain (v) can be neglected the higher order terms as

$$\upsilon = \frac{1}{('s')^2} ('x'u' + 'y'v' + 'z'w')$$
 (2.9)

In the most research works, the large displacement analysis has been investigated by using the small strain assumption. Therefore, the engineering strains can be approximated as

$$^{2}\overline{\varepsilon} \approx ^{2}L, ^{2}\varepsilon \approx ^{2}\upsilon, ^{2E}\varepsilon \approx ^{2}E$$
 (2.10 a-c)

# 2.3 THE PROPERTY CHANGES OF THE RISER CROSS SECTION AND TRANSPORTING FLUID VELOCITY

The change of the large axial strain among three states leads to relations of differential arc-length of the riser, cross-sectional properties of the riser and internal flow velocity of transported fluid as shown in this section.

#### a) Relations of differential arc-length of the riser

TLD; 
$$d^{o}s = \frac{d^{l}s}{l + l^{l}\overline{\varepsilon}} = \frac{d^{2}s}{l + e^{2}\overline{\varepsilon}}$$
ULD; 
$$\frac{d^{o}s}{l - e^{l}\varepsilon} = d^{l}s = \frac{d^{2}s}{l + \varepsilon}$$
ED; 
$$\frac{d^{o}s}{l - e^{2}\varepsilon} = \frac{d^{l}s}{l - e^{2}\varepsilon} = d^{2}s \qquad (2.11 \text{ a-c})$$

#### b) Relations of cross-sectional properties of the riser

Since the riser volume is conserved, the cross-sectional areas of the riser at the three states,  ${}^{i}A_{p}$ , can be related to each other as

TLD; 
$${}^{\circ}A_{p} = {}^{I}A_{p} \left( 1 + {}^{I}\overline{\varepsilon} \right) = {}^{2}A_{p} \left( 1 + {}^{2}\overline{\varepsilon} \right)$$
ULD; 
$${}^{\circ}A_{p} = \frac{{}^{I}A_{p}}{\left( 1 - {}^{I}\varepsilon \right)} = \frac{{}^{2}A_{p} \left( 1 + \varepsilon \right)}{\left( 1 - {}^{I}\varepsilon \right)}$$
ED; 
$${}^{\circ}A_{p} = \frac{{}^{I}A_{p}}{\left( 1 - {}^{IE}\varepsilon \right)} = \frac{{}^{2}A_{p}}{\left( 1 - {}^{2E}\varepsilon \right)}$$
 (2.12 a-c)

The relations of diameter,  $\binom{i}{D_p}$ , moment of inertia,  $\binom{i}{I_p}$ , and polar moment of inertia,  $\binom{i}{J_p}$ , of the circular riser among the three states determined corresponding to equations (2.12 a-c) are shown below.

TLD; 
$${}^{o}D_{p} = {}^{I}D_{p}\sqrt{I + {}^{I}\overline{\varepsilon}} = {}^{2}D_{p}\sqrt{I + {}^{2}\overline{\varepsilon}}$$
,  ${}^{o}I_{p} = {}^{I}I_{p}(I + {}^{I}\overline{\varepsilon})^{2} = {}^{2}I_{p}(I + {}^{2}\overline{\varepsilon})^{2}$ , (2.13 a-c)

$${}^{o}J_{p} = {}^{I}J_{p}(I + {}^{I}\overline{\varepsilon})^{2} = {}^{2}J_{p}(I + {}^{2}\overline{\varepsilon})^{2} = {}^{2}I_{p}(I + {}^{2}\overline{\varepsilon})^{2},$$

$${}^{o}D_{p} = \frac{{}^{I}D_{p}}{\sqrt{I - {}^{I}\varepsilon}} = {}^{2}D_{p}\sqrt{\frac{I + \varepsilon}{I - {}^{I}\varepsilon}}, {}^{o}I_{p} = \frac{{}^{I}I_{p}}{(I - {}^{I}\varepsilon)^{2}} = {}^{2}I_{p}\frac{(I + \varepsilon)^{2}}{(I - {}^{I}\varepsilon)^{2}},$$

$${}^{o}J_{p} = \frac{{}^{I}J_{p}}{(I - {}^{I}\varepsilon)^{2}} = {}^{2}J_{p}\frac{(I + \varepsilon)^{2}}{(I - {}^{I}\varepsilon)^{2}} = \frac{{}^{2}I_{p}}{(I - {}^{2}\varepsilon)^{2}},$$

ED; 
$${}^{o}D_{p} = \frac{{}^{I}D_{p}}{\sqrt{I - {}^{I}\varepsilon}\varepsilon} = \frac{{}^{2}D_{p}}{\sqrt{I - {}^{2}\varepsilon}\varepsilon}, {}^{o}I_{p} = \frac{{}^{I}I_{p}}{(I - {}^{I}\varepsilon\varepsilon)^{2}} = \frac{{}^{2}I_{p}}{(I - {}^{2}\varepsilon\varepsilon)^{2}},$$

$${}^{o}J_{p} = \frac{{}^{I}J_{p}}{(I - {}^{I}\varepsilon\varepsilon)^{2}} = \frac{{}^{2}J_{p}}{(I - {}^{2}\varepsilon\varepsilon)^{2}}$$
(2.15 a-c)

### c) Relations of internal flow velocity of transported fluid

By substituting equation (2.12) into the continuity equation of the fluid flow in the control volume riser, the relationships of internal flow velocities at the three states are obtained as

TLD; 
$${}^{o}V_{i} = \frac{{}^{\prime}V_{i}}{I + {}^{\prime}\overline{\varepsilon}} = \frac{{}^{2}V_{i}}{I + {}^{2}\overline{\varepsilon}}$$

ULD; 
$${}^{o}V_{i} = {}^{l}V_{i} \left( 1 - {}^{l}\varepsilon \right) = \frac{{}^{2}V_{i} \left( 1 - {}^{l}\varepsilon \right)}{\left( 1 + \varepsilon \right)}$$
ED; 
$${}^{o}V_{i} = {}^{l}V_{i} \left( 1 - {}^{lE}\varepsilon \right) = {}^{2}V_{i} \left( 1 - {}^{2E}\varepsilon \right)$$
 (2.16 a-c)

#### 2.4 THE EXTENSIBLE ELASTICA THEORY

The word "elastica" is the equilibrium (stable and unstable) shape of a bar with large displacement, stable, linear elasticity, no section change, axial and shear deformation neglected. In the case of extensible elastica, the material remains linearly elastic while the strain maybe large. The extensible elastica theory (Chucheepsakul et al., 2003) provided in this section is used to develop the large strain formulations of three-dimensional extensible flexible riser, which will be discussed later.

Theorem 1: When the TLD is adopted to describe deformation of the riser, the fiber strain, the constitutive relations and the virtual strain energy are expressed as follows

$${}^{2}\overline{\varepsilon}_{\zeta} = {}^{2}\overline{\varepsilon} + \zeta \left[ {}^{2}\kappa \left( 1 + {}^{2}\overline{\varepsilon} \right) - {}^{o}\kappa \right]$$

$${}^{2}N = E^{o}A_{p}{}^{2}\overline{\varepsilon} , {}^{2}M = E^{o}I_{p} \left[ {}^{2}\kappa \left( 1 + {}^{2}\overline{\varepsilon} \right) - {}^{o}\kappa \right] ,$$

$${}^{2}T = G^{o}J_{p} \left[ {}^{2}\tau \left( 1 + {}^{2}\overline{\varepsilon} \right) - {}^{o}\tau \right] ,$$

$$\delta U = \int_{\sigma_{s}} \left\{ {}^{2}N\delta^{2}\overline{\varepsilon} + {}^{2}M\delta \left[ {}^{2}\kappa \left( 1 + {}^{2}\overline{\varepsilon} \right) - {}^{o}\kappa \right] + {}^{2}T\delta \left[ {}^{2}\tau \left( 1 + {}^{2}\overline{\varepsilon} \right) - {}^{o}\tau \right] \right\} d^{2}s$$

$$\delta U = \int_{\alpha} \left[ {}^{2}N\delta^{2}s' + {}^{2}M\delta \left( {}^{2}\theta' - {}^{o}\theta' \right) + {}^{2}T\delta \left( {}^{2}\phi' - {}^{o}\phi' \right) + {}^{2}T\delta \left( {}^{2}\psi' - {}^{o}\psi' \right) \right] d\alpha$$

$$(2.17 a-f)$$

Theorem 2: When the ULD is adopted to describe deformation of the riser, the fiber strain, the constitutive relations and the virtual strain energy are expressed as follows

$${}^{2}\varepsilon_{\zeta} = {}^{2}\varepsilon + \zeta \left[ {}^{2}\kappa (1+\varepsilon) - {}^{o}\kappa (1 - {}^{I}\varepsilon) \right]$$

$${}^{2}N = E^{I}A_{p}{}^{2}\varepsilon , {}^{2}M = E^{I}I_{p} \left[ {}^{2}\kappa (1+\varepsilon) - {}^{o}\kappa (1 - {}^{I}\varepsilon) \right],$$

$${}^{2}T = G^{I}J_{p} \left[ {}^{2}\tau (1+\varepsilon) - {}^{o}\tau (1 - {}^{I}\varepsilon) \right],$$

$$\delta U = \int_{s} \left\{ {}^{2}N\delta^{2}\varepsilon + {}^{2}M\delta \left[ {}^{2}\kappa \left( 1 + \varepsilon \right) - {}^{o}\kappa \left( 1 - {}^{I}\varepsilon \right) \right] \right.$$

$$\left. + {}^{2}T\delta \left[ {}^{2}\tau \left( 1 + \varepsilon \right) - {}^{o}\tau \left( 1 - {}^{I}\varepsilon \right) \right] \right\} d^{I}s$$

$$\delta U = \int_{\alpha} \left[ {}^{2}N\delta^{2}s' + {}^{2}M\delta \left( {}^{2}\theta' - {}^{o}\theta' \right) + {}^{2}T\delta \left( {}^{2}\phi' - {}^{o}\phi' \right) + {}^{2}T\delta \left( {}^{2}\psi' - {}^{o}\psi' \right) \right] d\alpha$$

$$(2.18 a-f)$$

Theorem 3: When the ED is adopted to describe deformation of the riser, the fiber strain, the constitutive relations and the virtual strain energy are expressed as follows

$${}^{2E}\varepsilon_{\zeta} = {}^{2E}\varepsilon + \zeta \left[ {}^{2}\kappa - {}^{o}\kappa \left( I - {}^{2E}\varepsilon \right) \right]$$

$${}^{2}N = E^{2}A_{p} {}^{2E}\varepsilon , {}^{2}M = E^{2}I_{p} \left[ {}^{2}\kappa - {}^{o}\kappa \left( I - {}^{2E}\varepsilon \right) \right],$$

$${}^{2}T = G^{2}J_{p} \left[ {}^{2}\tau - {}^{o}\tau \left( I - {}^{2E}\varepsilon \right) \right],$$

$$\delta U = \int_{i_{s}} \left\{ {}^{2}N\delta^{2}\overline{\varepsilon} + {}^{2}M\delta \left[ {}^{2}\kappa - {}^{o}\kappa \left( I - {}^{2E}\varepsilon \right) \right] \right\} d^{2}s$$

$$+ {}^{2}T\delta \left[ {}^{2}\tau - {}^{o}\tau \left( I - {}^{2E}\varepsilon \right) \right] \right\} d^{2}s$$

$$\delta U = \int_{\alpha} \left[ {}^{2}N\delta^{2}s' + {}^{2}M\delta \left( {}^{2}\theta' - {}^{o}\theta' \right) + {}^{2}T\delta \left( {}^{2}\phi' - {}^{o}\phi' \right) + {}^{2}T\delta \left( {}^{2}\psi' - {}^{o}\psi' \right) \right] d\alpha$$

$$(2.19 a-f)$$

in which  $\varepsilon_{\zeta}$  is the axial strain at any fiber radius  $(\zeta)$ , E is the elastic modulus, G is the shear modulus, N is the axial force, M is the bending moment, T is the torque, and U is the strain energies due to axial force, bending moments, and torsion of the riser.

#### 2.5 EFFECTS OF HYDROSTAITIC PRESSURES

Hydrostatic pressures are the pressures of still fluids. In the past, the hydrostatic pressure effects on marine riser pipe analysis were tackled via the effective tension concept proposed by Spark (1984), as will be described in section 2.5.1. However, because the effective tension concept limits  $\nu = 0.5$ , thus the apparent tension concept (Chucheepsakul et al., 2003) has proposed instead in order to cover all values of the Poisson's ratio, as will be explained in section 2.5.2. This research offers a more advanced technique on treating the hydrostatic pressure effects.

#### 2.5.1 The Effective Tension Concept

First of all, the Archimedes' principle is recalled and used to explain the effective tension concept. Consider Figure 2.3(a), the equilibrium of water column element proves that the enclosing external pressure field is equivalent to the buoyancy force  $\rho_w g \forall_w$  (see Figure 2.3(a3)), where  $\rho_w$  is the water density, g the gravitational acceleration, and  $\forall_w$  the volume of water column. In contrast, the enclosing internal pressure field will thus induce the weight  $\rho_w g \forall_w$  against the buoyant force (see Figure 2.3(a5)). These tenets are so-called the Archimedes' principle.

It is remarkable that Archimedes' principle is usable with the enclosing pressure fields. However, unlike the water column, the pressure fields of external and internal fluids surround only the external and internal side surfaces of the riser segment, as seen in Figure 2.3(b1). Both ends cut of the riser segment are not subjected to the pressure fields, which are called the missing pressures, and thus Archimedes' principle cannot be used straightforwardly. Sparks (1984) solved this problem by proposing the superposition technique as follows:

Step 1. The first step of the superposition technique is separating all forces acting on the real system of the riser as shown in Figure 2.3(b1) into the two sets of forces as shown in Figures 2.3(b2) and 2.3(b3). The missing pressures are added in at the both ends of the riser segment in Figure 2.3(b2) to result in the pressure fields enclosing the riser segment. However, the added pressures are non-existent, so they must be removed for balance by applying the opposite pressure fields at the both ends of the riser in Figure 2.3(b3).

Step 2. Since the previous step yields the pressured fields enclosing the riser segment in Figure 2.3(b2), Archimedes's principle is now applicable. Therefore, the external pressure induces the buoyant force  $-\rho_e \forall_e g$ , and the internal pressure yields the internal fluid weight  $\rho_i \forall_i g$  as shown in Figure 2.3(b4). Summation of these forces with the aerial weight of the riser segment produces the total weight of the effective system, which is so-called the effective weight. Therefore, the expression of the effective weight per unit length  $w_e$  is obtained as

$$w_a = (\rho_p A_p - \rho_e A_e + \rho_i A_i)g \tag{2.20}$$

Step 3. Summation between the true-wall tension and the balance forces of the missing pressures in Figure 2.3(b3) yields the total tension of the effective system, which is referred to as the effective tension, as shown in Figure 2.3(b5). Therefore, the expression of the effective tension  $N_a$  is obtained as

$$N_{e} = N + p_{e}A_{e} - p_{i}A_{i} \tag{2.21}$$

Step 4. Integrating the forces acting on Figures 2.3(b4) and 2.3(b5) together, one obtains the effective system of the riser, which is subjected to the effective weight and the effective tension as shown in Figure 2.3(b6).

Casting equations (2.20) and (2.21) into the general forms for the three deformation descriptors, one can establish Proposition 2.1.

**Proposition 2.1.** According to the effective tension concept, the real system of the submerged riser subjected to hydrostatic external and internal pressures is equivalent to the effective system of an empty onshore riser that is subjected to the effective weight and the effective tension

$$^{i}w_{a} = (\rho_{B}{}^{i}A_{B} - \rho_{a}{}^{i}A_{a} + \rho_{i}{}^{i}A_{i})g,$$
 (2.22)

$${}^{i}N_{e} = E^{i}A_{p}\varepsilon = N + p_{e}{}^{i}A_{e} - p_{i}{}^{i}A_{i},$$
 (2.23)

in which  ${}^{i}A_{\alpha} = {}^{o}A_{\alpha}$  for TLD,  ${}^{i}A_{\alpha} = {}^{l}A_{\alpha}$  for ULD,  ${}^{i}A_{\alpha} = {}^{2}A_{\alpha}$  for ED when  $\alpha \in \{P, e, i\}$ .

#### 2.5.2 The Apparent Tension Concept

The apparent tension concept is more accurate in undertaking the hydrostatic pressure effects on elastic body than the effective tension concept. It acknowledges that the riser is an elastic solid, and thus in the polar coordinates the enclosing pressure fields in Figure 2.3(b2) can induce the triaxial stresses: the radial stress  $\sigma_r$ , the circumferential stress  $\sigma_\theta$ , and the tensile stress  $\sigma_z$ . From the theory of elasticity, these triaxial stresses provoke the axial strain and the tension in the form

$$\varepsilon_{tri} = \left[\sigma_z - v(\sigma_r + \sigma_\theta)\right] / E, \ N_{tri} = EA_p \varepsilon_{tri}$$
 (2.24 a,b)

In Figure 2.3(b2), the riser segment is subjected to the triaxial stresses due to the hydrostatic internal and external pressures  $\sigma_z = \sigma_r = \sigma_\theta = (p_i A_i - p_e A_e)/A_P$ . Consequently, equations (2.24) yield

$$N_{pj} = (2\nu - 1)(p_{e}A_{e} - p_{i}A_{j})$$
(2.24)

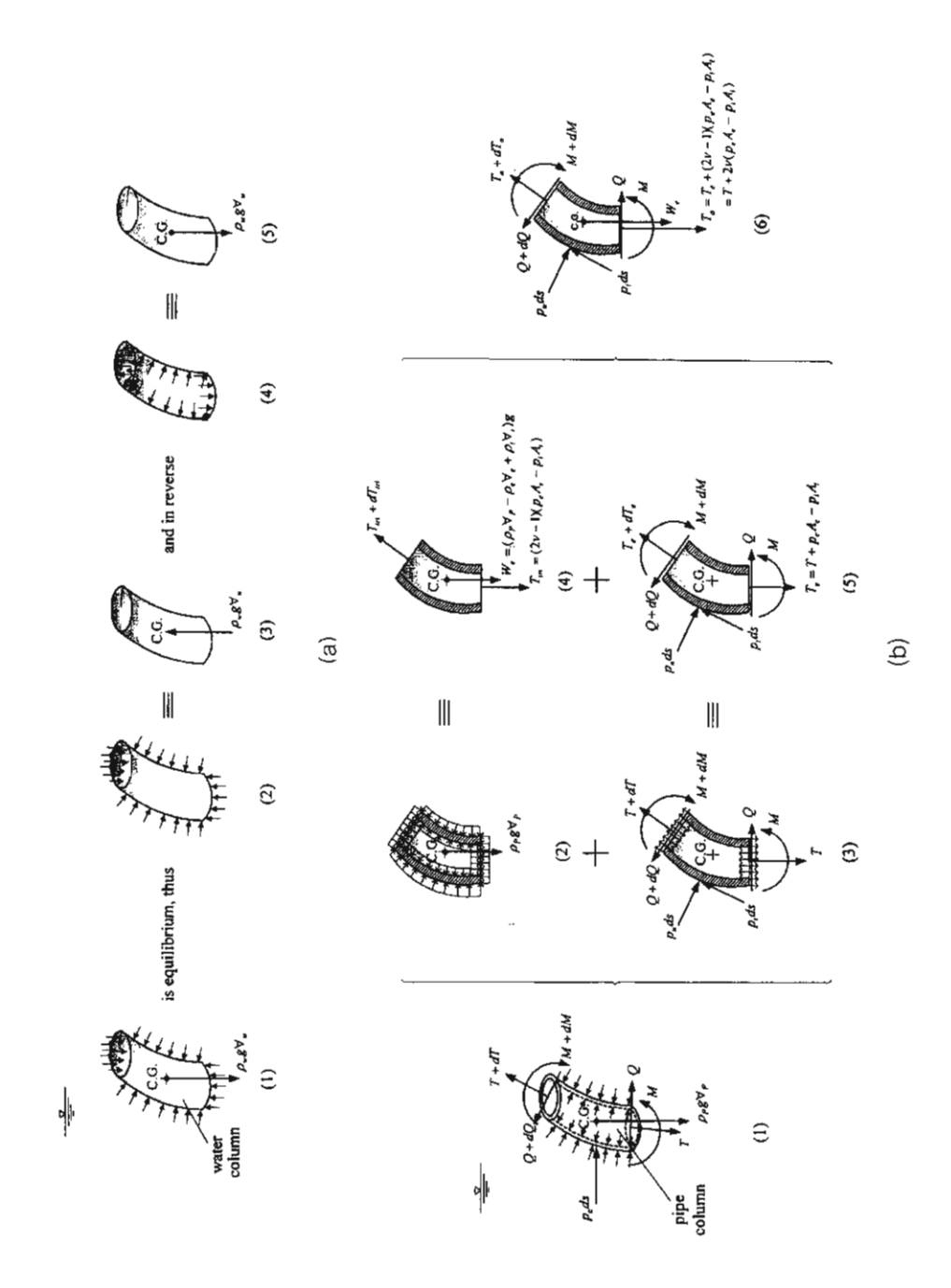


Figure 2.3 Treatments of the Hydrostatic Pressure Effects

(a) Archimedes' Principles (b) the Apparent Tension Concept

For the apparent tension concept, this tension is added into Figures 2.3(b4) and 2.3 (b6), and the system in Figure 2.3(b6) is renamed to the apparent system. The tension acting on the apparent system is called the apparent tension, of which the expression is

$$N_a = N_a + N_{tri} = N + 2\nu(p_a A_a - p_i A_i). \tag{2.25}$$

It is seen that  $N_a = N_e$  if, and only if v = 0.5. This signifies that the effective tension concept is a subset of the apparent tension concept. Although the expressions of the weights acting on the effective and the apparent systems are the same, the weight acting on the apparent system is called the apparent weight.

Casting equation (2.25) into the general forms for the three deformation descriptors, one can establish Proposition 2.2.

**Proposition 2.2.** According to the apparent tension concept, the real system of the submerged riser subjected to hydrostatic external and internal pressures is equivalent to the apparent system of an empty onshore riser that is subjected to the apparent weight and the apparent tension

$$^{i}w_{a} = (\rho_{P}{}^{i}A_{P} - \rho_{e}{}^{i}A_{e} + \rho_{i}{}^{i}A_{i})g,$$
 (2.25)

$${}^{i}N_{a} = E^{i}A_{p}\varepsilon = N + 2\nu(p_{e}{}^{i}A_{e} - p_{i}{}^{i}A_{i})$$
 (2.25)

#### 2.6 EFFECTS OF HYDRODYNAMIC PRESSURES

Hydrodynamic pressures occur due to steady and unsteady flows of external and internal fluids. Steady flows will cause the static forces, while unsteady flows will engender the dynamic forces acting on the riser wall. For the marine riser transporting fluid, the external flow is the horizontal cross flows of ocean current and wave, whereas the internal flow is the tangential flow of transported fluid. In this section, the hydrodynamic forces induced by the horizontal cross flows of current and wave is demonstrated in section 2.6.1, whereas the hydrodynamic forces induced by the tangential flow of transported fluid is derived in section 2.6.2.

## 2.6.1 <u>The Hydrodynamic Forces Due to the Horizontal Cross Flows of</u> Current and Wave

The hydrodynamic forces exerted on flexible marine risers with large displacements in the orthogonal triad system based on the coupled Morison equation (Chakrabarti, 1990) can be expressed as

$$\bar{\mathbf{F}}_{H} = \begin{cases} f_{Ht} \\ f_{Hn} \\ f_{Hbn} \end{cases} = 0.5 \rho_{e}^{2} D_{e} \begin{cases} \pi C_{Dt} \gamma_{t} | \gamma_{t} | \\ C_{Dn} \gamma_{n} | \gamma_{n} | \\ C_{Dbn} \gamma_{bn} | \gamma_{bn} | \end{cases} + \rho_{e}^{2} A_{e} C_{a} \begin{cases} \dot{\gamma}_{t} \\ \dot{\gamma}_{n} \\ \dot{\gamma}_{bn} \end{cases} + \rho_{e}^{2} A_{e} \begin{cases} \dot{V}_{Ht} \\ \dot{V}_{Hn} \\ \dot{V}_{Hbn} \end{cases}$$

$$\frac{1}{\text{Viscous drag force}} \text{ Hydrodynamic mass force mass force} \qquad (2.26)$$

where  $C_{Dt}$ ,  $C_{Dn}$ , and  $C_{Dbn}$  are the tangential, normal, and binormal drag coefficients;  $C_a$  is the added mass coefficient;  $V_{Ht}$ ,  $V_{Hn}$ , and  $V_{Hbn}$  are the tangential, normal and binormal velocities of currents and waves; and  $\gamma_t = V_{Ht} - \dot{u}_t$ ,  $\gamma_n = V_{Hn} - \dot{v}_n$ , and  $\gamma_{bn} = V_{Hbn} - \dot{w}_{bn}$  are the velocities of currents and waves relative to riser velocities  $\dot{u}_t$ ,  $\dot{v}_n$ , and  $\dot{w}_{bn}$  in tangential, normal, and binormal directions, respectively. For large strain analysis, the effect of cross-sectional changes of the riser in equation (2.12) has to be applied to equation (2.26).

To eliminate the difficulty of operating with absolute function in equation (2.26), the signum function is used. Here

$$sgn(\gamma) = \begin{cases} 1 & if \gamma \ge 0 \\ -1 & if \gamma < 0. \end{cases}$$
 (2.27)

With some manipulations, equation (2.26) can be arranged into

$$\vec{F}_{H} = \begin{cases} f_{Hi} \\ f_{Hin} \\ f_{Hbn} \end{cases} = - \begin{bmatrix} C_{a}^{*} & 0 & 0 \\ 0 & C_{a}^{*} & 0 \\ 0 & 0 & C_{a}^{*} \end{bmatrix} \begin{cases} \vec{u}_{l} \\ \vec{v}_{n} \\ \vec{w}_{bn} \end{cases} - \begin{bmatrix} C_{eql}^{*} & 0 & 0 \\ 0 & C_{eqn}^{*} & 0 \\ 0 & 0 & C_{eqbn}^{*} \end{bmatrix} \begin{cases} \vec{u}_{l} \\ \vec{v}_{n} \\ \vec{w}_{bn} \end{cases} \\
+ \begin{cases} C_{Dl}^{*} V_{Hi}^{2} + C_{M}^{*} \vec{V}_{Hi} \\ C_{Dn}^{*} V_{Hin}^{2} + C_{M}^{*} \vec{V}_{Hin} \\ C_{Dbn}^{*} V_{Hin}^{2} + C_{M}^{*} \vec{V}_{Hbn} \end{cases} \tag{2.28}$$

where  $C_{eqt}^*$ ,  $C_{eqn}^*$ ,  $C_{eqbn}^*$  are the coefficients of equivalent tangential, normal, binormal damping, and  $C_{Dt}^*$ ,  $C_{Dn}^*$ ,  $C_{Dbn}^*$  are the coefficients of tangential, normal, and binormal drag forces, and  $C_a^*$ ,  $C_M^*$  are the equivalent coefficients of added mass and inertia forces. They are, respectively, expressed as follows

$$C_{eat}^* = C_{Dt}^* \left[ 2V_{Ht} - \dot{u}_t \right], C_{Dt}^* = 0.5 \rho_e^2 D_e \pi C_{Dt} \cdot sgn(\gamma_t)$$
 (2.29 a,b)

$$C_{eqn}^* = C_{Dn}^* [2V_{Hn} - \dot{v}_n], C_{Dn}^* = 0.5 \rho_e^2 D_e C_{Dn} \cdot sgn(\gamma_n)$$
 (2.29 c,d)

$$C_{eqbn}^* = C_{Dbn}^* \left[ 2V_{Hbn} - \dot{w}_{bn} \right], C_{Dbn}^* = 0.5 \rho_e^2 D_e C_{Dbn} \cdot sgn(\gamma_{bn})$$
 (2.29 f,g)

$$C_a^* = \rho_e^2 A_e C_a, C_M^* = \rho_e^2 A_e C_M$$
 (2.29 h,i)

in which  $C_a$  is the added mass coefficient and  $C_M = I + C_a$  is the inertia coefficient.

In order to transform hydrodynamic force in the orthogonal triad system to the fixed Cartesian coordinate system, Euler's angle (Atanackovic, 1997) is used to find the transformation matrix, which is the orthogonal matrix and can be written as

where

$$a_{1X} = \cos^2 \theta_2 \cos^2 \theta_3 \tag{2.31 a}$$

$$a_{IY} = \cos^2 \theta_2 \sin^2 \theta_3 \cos^2 \theta_1 + \sin^2 \theta_2 \sin^2 \theta_1$$
 (2.31 b)

$$a_{1Z} = \cos^2 \theta_2 \sin^2 \theta_3 \sin^2 \theta_1 - \sin^2 \theta_2 \cos^2 \theta_1$$
 (2.31 c)

$$a_{2X} = -\sin^2\theta_3 \tag{2.31 d}$$

$$a_{2Y} = \cos^2 \theta_1 \cos^2 \theta_3 \tag{2.31 e}$$

$$a_{2Z} = \sin^2 \theta_1 \cos^2 \theta_3 \tag{2.31 f}$$

$$a_{3x} = \cos^2 \theta_3 \sin^2 \theta_2 \tag{2.31 g}$$

$$a_{3Y} = \sin^2 \theta_2 \sin^2 \theta_3 \cos^2 \theta_1 - \cos^2 \theta_2 \sin^2 \theta_1 \tag{2.31 h}$$

$$a_{3Z} = \sin^2 \theta_1 \sin^2 \theta_2 \cos^2 \theta_3 + \cos^2 \theta_1 \cos^2 \theta_2 \tag{2.31 i}$$

Thus, equation (2.28) can be transformed into the fixed Cartesian coordinates system

(2.32)

where  $V_{Hx}$ ,  $V_{Hy}$  and  $V_{Hz}$  are the velocities of external fluid in x, y, and z directions respectively, and

$$C_{eqx}^{*} = C_{eqt}^{*} a_{1X}^{2} + C_{eqn}^{*} a_{2X}^{2} + C_{eqbn}^{*} a_{3X}^{2}$$

$$C_{eqy}^{*} = C_{eqt}^{*} a_{1Y}^{2} + C_{eqn}^{*} a_{2Y}^{2} + C_{eqbn}^{*} a_{3Y}^{2}$$

$$C_{eqz}^{*} = C_{eqt}^{*} a_{1Z}^{2} + C_{eqn}^{*} a_{2Z}^{2} + C_{eqbn}^{*} a_{3Z}^{2}$$

$$(2.33 \text{ a-c})$$

$$C_{eqxy}^{*} = C_{eqt}^{*} a_{1X} a_{1Y} + C_{eqn}^{*} a_{2X} a_{2Y} + C_{eqbn}^{*} a_{3X} a_{3Y}$$

$$C_{eqxz}^{*} = C_{eqt}^{*} a_{1X} a_{1Z} + C_{eqn}^{*} a_{2X} a_{2Z} + C_{eqbn}^{*} a_{3X} a_{3Z}$$

$$C_{eqyz}^{*} = C_{eqt}^{*} a_{1Y} a_{1Z} + C_{eqn}^{*} a_{2Y} a_{2Z} + C_{eqbn}^{*} a_{3Y} a_{3Z}$$

$$(2.34 \text{ a-c})$$

$$C_{Dx}^{*} = C_{Dt}^{*} a_{IX}^{3} + C_{Dn}^{*} a_{2X}^{3} + C_{Dbn}^{*} a_{3X}^{3}$$

$$C_{Dy}^{*} = C_{Dt}^{*} a_{IY}^{3} + C_{Dn}^{*} a_{2Y}^{3} + C_{Dbn}^{*} a_{3Y}^{3}$$

$$C_{Dz}^{*} = C_{Dt}^{*} a_{IZ}^{3} + C_{Dn}^{*} a_{2Z}^{3} + C_{Dbn}^{*} a_{3Z}^{3}$$

$$(2.35 \text{ a-c})$$

$$C_{Dxy1}^{*} = C_{Dt}^{*} a_{1X}^{2} a_{1Y} + C_{Dn}^{*} a_{2X}^{2} a_{2Y} + C_{Dbn}^{*} a_{3X}^{2} a_{3Y}$$

$$C_{Dxz1}^{*} = C_{Dt}^{*} a_{1X}^{2} a_{1Z} + C_{Dn}^{*} a_{2X}^{2} a_{2Z} + C_{Dbn}^{*} a_{3X}^{2} a_{3Z}$$

$$C_{Dyz1}^{*} = C_{Dt}^{*} a_{1Y}^{2} a_{1Z} + C_{Dn}^{*} a_{2Y}^{2} a_{2Z} + C_{Dbn}^{*} a_{3Y}^{2} a_{3Z}$$

$$C_{Dxy2}^{*} = C_{Dt}^{*} a_{1X} a_{1Y}^{2} + C_{Dn}^{*} a_{2X} a_{2Y}^{2} + C_{Dbn}^{*} a_{3X} a_{3Y}^{2}$$

$$C_{Dxz2}^{*} = C_{Dt}^{*} a_{1X} a_{1Z}^{2} + C_{Dn}^{*} a_{2X} a_{2Z}^{2} + C_{Dbn}^{*} a_{3X} a_{3Z}^{2}$$

$$C_{Dyz2}^{*} = C_{Dt}^{*} a_{1Y} a_{1Z}^{2} + C_{Dn}^{*} a_{2Y} a_{2Z}^{2} + C_{Dbn}^{*} a_{3Y} a_{3Z}^{2}$$

$$C_{Dxyz}^{*} = C_{Dt}^{*} a_{1X} a_{1Y} a_{1Z}^{2} + C_{Dn}^{*} a_{2X} a_{2Y} a_{2Z}^{2} + C_{Dbn}^{*} a_{3X} a_{3Y}^{2} a_{3Z}$$

$$C_{Dxyz}^{*} = C_{Dt}^{*} a_{1X} a_{1Y} a_{1Z}^{2} + C_{Dn}^{*} a_{2X} a_{2Y}^{2} a_{2Z}^{2} + C_{Dbn}^{*} a_{3X}^{2} a_{3Y}^{2} a_{3Z}^{2}$$

Equations (2.33 a-c) represent the coefficients of equivalent hydrodynamic damping force in x, y, and z directions. Equations (2.34 a-c) represent the coefficients of equivalent hydrodynamic damping force in x-y, x-z, and y-z planes. Equations (2.35 a-c) represent the coefficients of drag force in x, y, and z directions. Equations (2.36 a-g) represent the coefficients of drag force in x-y, x-z, and y-z planes.

At the equilibrium state, static loading is due only to the steady flow of external fluid. Therefore, the hydrodynamic forces from equations (2.28) and (2.32) are reduced to

$${}^{1}\bar{F}_{H} = \begin{cases} {}^{I}f_{Ht} \\ {}^{I}f_{Hn} \\ {}^{I}f_{Hbn} \end{cases} = \begin{cases} {}^{I}C_{Dt}^{*} {}^{I}V_{Ht}^{2} \\ {}^{I}C_{Dn}^{*} {}^{I}V_{Hn}^{2} \\ {}^{I}C_{Dbn}^{*} {}^{I}V_{Hbn}^{2} \end{cases}$$
(2.37)

$${}^{1}\vec{F}_{H} = \begin{cases} {}^{i}f_{Hx} \\ {}^{i}f_{Hx} \end{cases} = \begin{cases} {}^{i}C_{ox}^{*} {}^{i}V_{ux}^{2} + 2{}^{i}C_{ox}^{*} {}^{i}V_{Hx} {}^{i}V_{Hy} + 2{}^{i}C_{ox}^{*} {}^{i}V_{Hx} {}^{i}V_{Hz} + 2{}^{i}C_{oxx}^{*} {}^{i}V_{Hy} {}^{i}V_{Hz} + {}^{i}C_{oxy}^{*} {}^{i}V_{Hz} + {}^{i}C_{oxy}^{*} {}^{i}V_{Hz}^{2} + {}^{i}C_{oxz}^{*} {}^{i}V_{Hz}^{2} + {}^{i}C$$

In this study, the horizontal cross flows of current and wave, in dynamic analysis, are scoped to be in-plane flows, and the dynamic pressure fields are assumed to be uniform around the cross-section of the riser, but vary along the arclength of the riser. Therefore

$${}^{2}V_{Hx} = {}^{2}V_{c} + {}^{2}V_{w}, {}^{2}V_{Hy} = 0, {}^{2}V_{Hz} = 0,$$
 (2.39 a-c)

$${}^{2}V_{Ht} = {}^{2}V_{Hx}a_{1x}, {}^{2}V_{Hn} = {}^{2}V_{Hx}a_{2x}, {}^{2}V_{Hbn} = 0$$
 (2.40 a-c)

where  ${}^2V_c = {}^2V_c({}^2y)$  is the current velocity, and  ${}^2V_w = {}^2V_w({}^2y,t)$  the wave velocity. The profile of the current velocity may be expressed in the form of polynomial function as

$${}^{2}V_{c} = V_{ct} \left(\frac{{}^{2}y}{{}^{o}y_{t}}\right)^{n}, \qquad (2.41)$$

where  $V_{ct}$  is the current velocity at mean sea level, and  ${}^{o}y_{t}$  are surface sea level. The index n can be varied from 0 to 1 depending upon the current profile. In this study, n = 1/7 is employed for the tidal current profile (Larsen, 1976).

For the regular incoming wave, the velocity of a water particle according to Airy's wave theory may be expressed as

$$^{2}V_{w} = ^{2}V_{wa}\cos\omega_{w}t, \qquad (2.42)$$

where t is the time, and  $\omega_w$  the wave frequency. For deep water ( ${}^o y_t / L \ge 0.5$ ), the velocity amplitude  ${}^2V_{wa} = {}^2V_{wa}({}^2y)$  is given by

$${}^{2}V_{wa} = \varsigma_{a}\omega_{w}e^{k\left[({}^{2}y)-({}^{o}y_{t})\right]}, \tag{2.43}$$

where the wave amplitude

$$\varsigma_a = H/2, \tag{2.44 a}$$

in which H is the wave height, the wave frequency

$$\omega_{w} = 2\pi/T, \qquad (2.44 \text{ b})$$

in which T is the wave period, and the wave number

$$k = 2\pi / L \,, \tag{2.44 c}$$

in which L is the wave length.

Substituting equation (2.39) into (2.32) yields

$$f_{Hx} = -C_a^* \ddot{x} - C_{eqx}^* \dot{x} - C_{eqxy}^* \dot{y} + C_{Dx}^* V_{Hx}^2 + C_M^* \dot{V}_{Hx}, \qquad (2.45 \text{ a})$$

$$f_{Hy} = -C_a^* \ddot{y} - C_{eqy}^* \dot{y} - C_{eqxy}^* \dot{x} + C_{Dxy1}^* V_{Hx}^2 + C_M^* \dot{V}_{Hy}. \tag{2.45 b}$$

$$f_{H_2} = 0$$
 (2.45 c)

Equations (2.32) and (2.45) capture the hydrodynamic pressure effects of both steady and unsteady flows. These equations are exploited for dynamic analysis of the riser.

# 2.6.2 <u>The Hydrodynamic Forces Due to the Tangential Internal Flows of</u> <u>Transported Fluid</u>

Based on the control volume approach of Computational Fluid Dynamics (Shames, 1992), hydrodynamic forces due to flow of transported fluid inside extensible flexible risers with large deformation can be derived as follows. Let  ${}^{i}\bar{\mathbf{V}}_{F}$  and  ${}^{i}\bar{\mathbf{V}}_{P}$  represent the velocity vectors of transported fluid and the riser with respect to the fixed frame of reference, then the velocity vector of transported fluid relative to the riser velocity is given by

$${}^{i}\vec{\mathbf{V}}_{FP} = ({}^{i}V_{FP}){}^{i}\hat{\mathbf{t}} = ({}^{i}V_{FP})\partial^{i}\mathbf{\bar{\tau}}_{P} / \partial^{i}s = {}^{i}\vec{\mathbf{V}}_{F} - {}^{i}\vec{\mathbf{V}}_{P}$$

$$(2.46)$$

where  ${}^{i}V_{FP}$  is the internal flow velocity function:  ${}^{i}V_{FP} = {}^{o}V_{i}$ ,  ${}^{i}V_{FP} = {}^{I}V_{i}$ , and  ${}^{o}V_{FP} = {}^{2}V_{i}$  at the undeformed state, the equilibrium state, and the displaced state, respectively.

From Newton's law of momentum conservation, the hydrodynamic pressures due to internal flow induce the inertial force of transported mass as

$$\int_{\forall_{i}}^{i} \mathbf{\bar{B}}_{i} d \forall_{i} = \int_{\forall_{i}}^{i} \frac{D(\rho_{i}({}^{i} \bar{\nabla}_{F}))}{Dt} d \forall_{i} = \int_{\forall_{i}}^{i} \left[ \frac{D\rho_{i}}{Dt} ({}^{i} \bar{\nabla}_{F}) + \rho_{i} ({}^{i} \bar{\mathbf{a}}_{F}) \right] d \forall_{i}$$
(2.47)

where  ${}^{i}\mathbf{\bar{B}_{i}}$  is the inertial force per unit control volume  $\forall_{i}$ ,  ${}^{i}\mathbf{\bar{a}}_{F}$  the acceleration vector of transported fluid with respect to the fixed frame of reference at each states, and

$$\frac{D(\phantom{x})}{Dt} = \frac{\partial(\phantom{x})}{\partial t} + (^{i}\vec{\nabla}_{FP}.\nabla)(\phantom{x}) = \frac{\partial(\phantom{x})}{\partial t} + \frac{^{i}V_{FP}}{^{i}s'}\frac{\partial(\phantom{x})}{\partial \alpha}$$
(2.48)

It can be proved by Lemma 2.1 that  $D\rho_i/Dt$  vanishes.

**Lemma 2.1.** The conservative condition of transported mass yields  $D\rho_i/Dt = 0$ .

**Proof.** Utilizing equation (2.46), equation (2.47) can be written as

$$\int_{\mathbf{V}_{i}}^{t} \mathbf{\bar{B}}_{i} d \forall_{i} = \int_{\mathbf{V}_{i}}^{t} \left[ \frac{D(\rho_{i}^{i} \mathbf{\bar{V}}_{p})}{Dt} \right] d \forall_{i} + \int_{\mathbf{V}_{i}}^{t} \left[ \frac{D(\rho_{i}^{i} \mathbf{\bar{V}}_{FP})}{Dt} \right] d \forall_{i}$$
(2.49)

From the Reynolds transport theorem (Shames, 1992), the last integral is given by

$$\int_{\forall_{i}} \frac{D(\rho_{i}^{i} \vec{\nabla}_{FP})}{Dt} d\forall_{i} = \frac{\partial}{\partial t} \left[ \int_{\forall_{i}} (\rho_{i}^{i} \vec{\nabla}_{FP}) d\forall_{i} \right] + \bigoplus_{i \neq j} {}^{i} \vec{\nabla}_{FP} (\rho_{i}({}^{i} \vec{\nabla}_{FP}) . d^{i} \vec{A}_{si}), \quad (2.50)$$

where  ${}^{i}A_{si}$  is the internal control surface of the riser.

Employing the Gauss divergence theorem, one can demonstrate that

$$\bigoplus_{i_{A_{i}}} {}^{i} \vec{\nabla}_{FP} \left( \rho_{i} ({}^{i} \vec{\nabla}_{FP}) . d^{i} \vec{A}_{si} \right) = \int_{\nabla_{i}} \left[ \left( \rho_{i} ({}^{i} \vec{\nabla}_{FP}) . \nabla \right)^{i} \vec{\nabla}_{FP} + \nabla . \left( \rho_{i} ({}^{i} \vec{\nabla}_{FP}) \right)^{i} \vec{\nabla}_{FP} \right] d \nabla_{i}$$
(2.51)

Substituting equations (2.51) into (2.50), one obtains

$$\int_{\forall_{i}} \frac{D(\rho_{i}({}^{i}\vec{\nabla}_{FP}))}{Dt} d\forall_{i} = \int_{\forall_{i}} \left\{ \rho_{i} \left[ \frac{\partial^{i}\vec{\nabla}_{FP}}{\partial t} + ({}^{i}\vec{\nabla}_{FP}.\nabla){}^{i}\vec{\nabla}_{FP} \right] \right\}$$

$$+ \left[ \frac{\partial \rho_{i}}{\partial t} + \nabla \cdot \left( \rho_{i} ({}^{i} \vec{\nabla}_{FP}) \right) \right] {}^{i} \vec{\nabla}_{FP} \right\} d \forall_{i} \qquad (2.52)$$

Refer to equation (2.48), the bracketed term (1) is known as the acceleration of transported fluid  $\bar{a}_{FP}$ , whereas following the continuity condition (Shames, 1992) the term (2) is zero due to the continuity condition of conservation of mass. Thereby, equation (2.52) yields

$$\frac{D(\rho_{i}({}^{i}\vec{\nabla}_{FP}))}{Dt} = \rho_{i}({}^{i}\vec{a}_{FP})$$
 (2.53)

But  $\frac{D(\rho_i({}^i\vec{\nabla}_{FP}))}{Dt} = \frac{D\rho_i}{Dt} \cdot ({}^i\vec{\nabla}_{FP}) + \rho_i({}^i\vec{a}_{FP})$  and  ${}^i\vec{\nabla}_{FP} \neq 0$ , thus equation (2.53) is valid if, and only if

$$D\rho_i / Dt = 0 \tag{2.54}$$

Q.E.D.

Using Lemma 2.1 in equation (2.47), one can constitute Proposition 2.3.

**Proposition 2.3**. The internal flow through the moving, deforming control volume of the riser induces the inertial force per unit control volume acting on the riser wall

$${}^{t}\mathbf{\vec{B}}_{i} = \rho_{i}({}^{t}\mathbf{\vec{a}}_{F}), \tag{2.56a}$$

or the inertial force per unit riser-length

$$\overline{\mathbf{f}}_i = m_i \left( {}^i \overline{\mathbf{a}}_F \right), \tag{2.56b}$$

where  $\vec{\mathbf{f}}_i$  is the inertial force, and  $m_i$  the transported mass per unit riser-length.

From equation (2.56), it is seen that determining the inertial force on the transported fluid needs the expression of transported mass acceleration  $\bar{a}_F$ . Based on Eulerian mechanics (Huang, 1993), the velocity and acceleration of transported fluid can be derived as

$$\vec{V}_{F} = \vec{V}_{P} + \vec{V}_{FP} = \frac{\partial \vec{r}_{P}}{\partial t} + \frac{V_{FP}}{^{2}s'} \frac{\partial \vec{r}_{P}}{\partial \alpha}$$
(2.57)

$$\vec{a}_{F} = \vec{a}_{P} + \vec{a}_{FP} = \frac{D\vec{V}_{P}}{Dt} + \frac{D\vec{V}_{FP}}{Dt} = \frac{D}{Dt} \left( \frac{\partial \vec{r}_{p}}{\partial t} \right) + \frac{D}{Dt} \left( \frac{V_{FP}}{^{2}s'} \frac{\partial \vec{r}_{p}}{\partial \alpha} \right)$$

$$= \frac{\partial^{2}\vec{r}_{p}}{\partial t^{2}} + \left( \frac{2V_{FP}}{^{2}s'} \right) \frac{\partial^{2}\vec{r}_{p}}{\partial \alpha \partial t} + \left( \frac{V_{FP}}{^{2}s'} \right)^{2} \frac{\partial^{2}\vec{r}_{p}}{\partial \alpha^{2}} + \left( \frac{\dot{V}_{FP}}{^{2}s'} + \frac{\dot{V}_{FP}V_{FP}'}{\binom{2}s'} - \frac{\dot{V}_{FP}^{2}\dot{s}'}{\binom{2}s'}^{2} - \frac{\dot{V}_{FP}^{2}\dot{s}'}{\binom{2}s'}^{3}}{\delta \alpha} \right) \frac{\partial \vec{r}_{p}}{\partial \alpha}$$

$$(2.58)$$

in which the term (1) is the transported mass acceleration, (2) is the coriolis acceleration, (3) is the centripetal acceleration, (4) is the local acceleration due to unsteady flow, (5) is the convective acceleration due to non-uniform flow, and (6) is the relative accelerations due to local coordinate rotation and displacement.

By using the differential geometry formulas given in appendix and let  $V_i$  be the relative velocity of the transporting fluid, i.e.  $V_i = V_{FP}$ , the velocity and acceleration of transported fluid in the fixed Cartesian coordinate system and the orthogonal triad coordinate system can be expressed as follows

In the fixed Cartesian coordinate system, at the displaced state:

$$\bar{\mathbf{V}}_{F} = \begin{bmatrix} 2\dot{\mathbf{x}} + \frac{V_{i}^{2} 2x'}{2s'} \end{bmatrix} \hat{\mathbf{i}} + \begin{bmatrix} 2\dot{\mathbf{y}} + \frac{V_{i}^{2} 2y'}{2s'} \end{bmatrix} \hat{\mathbf{j}} + \begin{bmatrix} 2\dot{\mathbf{z}} + \frac{V_{i}^{2} 2z'}{2s'} \end{bmatrix} \hat{\mathbf{k}}$$

$$\bar{\mathbf{a}}_{F} = \begin{cases} 2\ddot{\mathbf{x}} + \left[ \left( \frac{2}{2s'} - \frac{(2x')^{2}}{(2s')^{3}} \right)^{2} \dot{\mathbf{x}}' - \left( \frac{2x'^{2} 2y'}{(2s')^{3}} \right)^{2} \dot{\mathbf{y}}' - \left( \frac{2x'^{2} 2z'}{(2s')^{3}} \right)^{2} \dot{\mathbf{z}}' \right] V_{i}$$

$$+ \left[ \frac{(2x''^{2} 2y' - 2x'^{2} 2y'')^{2} y' + (2x''^{2} 2z' - 2x'^{2} 2z'')^{2} z'}{(2s')^{3}} \right] V_{i}^{2} + \left( \frac{DV_{i}}{Dt} \right)^{2} \frac{2x'}{2s'} \right] \hat{\mathbf{i}}$$

$$+ \left[ \frac{2\ddot{\mathbf{y}} + \left[ -\left( \frac{2x'^{2} 2y'}{(2s')^{3}} \right)^{2} \dot{\mathbf{x}}' + \left( \frac{2}{2s'} - \frac{(2y')^{2}}{(2s')^{3}} \right)^{2} \dot{\mathbf{y}}' - \left( \frac{2y'^{2} 2z'}{(2s')^{3}} \right)^{2} \dot{\mathbf{z}}' \right] V_{i}$$

$$+ \left[ \frac{(2y'''^{2} x' - 2y'^{2} x'')^{2} x' + (2y'''^{2} z' - 2y'^{2} z'')^{2} z'}{(2s')^{4}} \right] V_{i}^{2} + \left( \frac{DV_{i}}{Dt} \right)^{2} \frac{2y'}{s'} \right] \hat{\mathbf{j}}$$

$$+ \left\{ {}^{2}\ddot{z} + \left[ -\left( \frac{{}^{2}x'^{2}z'}{\left( {}^{2}s' \right)^{3}} \right)^{2}\dot{x}' - \left( \frac{{}^{2}y'^{2}z'}{\left( {}^{2}s' \right)^{3}} \right)^{2}\dot{y}' + \left( \frac{2}{{}^{2}s'} - \frac{\left( {}^{2}z' \right)^{2}}{\left( {}^{2}s' \right)^{3}} \right)^{2}\dot{z}' \right] V_{i} \right.$$

$$+ \left[ \frac{\left( {}^{2}z''^{2}x' - {}^{2}z'^{2}x'' \right)^{2}x' + \left( {}^{2}z''^{2}y' - {}^{2}z'^{2}y'' \right)^{2}y'}{\left( {}^{2}s' \right)^{4}} \right] V_{i}^{2} + \left( \frac{DV_{i}}{Dt} \right)^{\frac{2}{2}z'} \hat{k}$$

$$(2.60)$$

in which

$$\frac{D(\ )}{Dt} = \frac{\partial(\ )}{\partial t} + \frac{V_i}{^2s'} \frac{\partial(\ )}{\partial \alpha} \tag{2.61}$$

In the orthogonal triad coordinate system, at the displaced state:

$$\vec{\mathbf{V}}_{F} = \begin{bmatrix} {}^{2}\dot{u}_{t} + V_{i} \end{bmatrix} {}^{2}\hat{t} + \begin{bmatrix} {}^{2}\dot{v}_{n} \end{bmatrix} {}^{2}\hat{n} + \begin{bmatrix} {}^{2}\dot{w}_{bn} \end{bmatrix} {}^{2}\hat{b}$$
 (2.62)

$$\vec{a}_{F} = \left[ {}^{2}\vec{u}_{i} + \frac{V_{i}({}^{2}\dot{s}')}{{}^{2}s'} + \dot{V}_{i} + \frac{V_{i}V'_{i}}{{}^{2}s'} \right] {}^{2}\hat{t} + \left[ {}^{2}\ddot{v}_{n} + 2V_{i}({}^{2}\dot{s})({}^{2}\kappa) + V_{i}^{2}({}^{2}\kappa) \right] {}^{2}\hat{n} + \left[ {}^{2}\ddot{w}_{bn} \right] {}^{2}\hat{b} \quad (2.63)$$

At the equilibrium state, the time-dependent terms vanish, the velocity and acceleration of transported fluid in the fixed Cartesian coordinate system and the orthogonal triad coordinate system become

In the fixed Cartesian coordinate system, at the equilibrium state:

$${}^{I}\bar{Q}_{F} = \left[\frac{{}^{I}V_{i}{}^{I}X'}{{}^{I}S'}\right]\hat{i} + \left[\frac{{}^{I}V_{i}{}^{I}y'}{{}^{I}S'}\right]\hat{j} + \left[\frac{{}^{I}V_{i}{}^{I}z'}{{}^{I}S'}\right]\hat{k}$$

$$(2.64)$$

$${}^{I}\bar{a}_{F} = \left\{ \left[\frac{\left({}^{I}X''^{I}y' - {}^{I}X'^{I}y''\right){}^{I}y' + \left({}^{I}X''^{I}z' - {}^{I}X'^{I}z''\right){}^{I}z'}}{\left({}^{I}S'\right)^{4}}\right]\left({}^{I}V_{i}\right)^{2} + \left(\frac{\left({}^{I}V_{i}\right){}^{I}V_{i}'}{{}^{I}S'}\right){}^{I}X'}{\left({}^{I}S'\right)^{4}}\hat{i} + \left\{ \left[\frac{\left({}^{I}Y''^{I}X' - {}^{I}Y'^{I}X''\right){}^{I}X' + \left({}^{I}Y''^{I}z' - {}^{I}Y'^{I}z''\right){}^{I}z'}}{\left({}^{I}S'\right)^{4}}\right]\left({}^{I}V_{i}\right)^{2} + \left(\frac{\left({}^{I}V_{i}\right){}^{I}V_{i}'}{{}^{I}S'}\right){}^{I}X' + \left({}^{I}Z''^{I}Y' - {}^{I}Z'^{I}Y''\right){}^{I}Y'}}{\left({}^{I}S'\right)^{4}}\right]\left({}^{I}V_{i}\right)^{2} + \left(\frac{\left({}^{I}V_{i}\right){}^{I}V_{i}'}{{}^{I}S'}}\right){}^{I}Z'}{\left({}^{I}S'\right)^{4}}\hat{k}$$

$$(2.65)$$

In the orthogonal triad coordinate system, at the equilibrium state:

$${}^{I}\vec{\mathbf{V}}_{F} = \left({}^{I}V_{i}\right){}^{I\partial}\hat{t} \tag{2.66}$$

$$\vec{\mathbf{a}}_{F} = \left[ \frac{\left( {}^{\prime}V_{i} \right) {}^{\prime}V_{i}^{\prime}}{{}^{\prime}S^{\prime}} \right] {}^{\prime}\hat{t} + \left[ \left( {}^{\prime}V_{i} \right)^{2} \left( {}^{\prime}\kappa \right) \right] {}^{\prime}\hat{n}$$
(2.67)

#### 2.7 VIRTUAL WORK FORMULATIONS

Based on the elastica theory, the apparent tension concept and dynamic interactions between fluid and riser, the internal virtual work and external virtual work can be obtained.

#### 2.7.1 Internal Virtual Work

For the overall apparent system, the riser is subjected to the apparent tension  $N_a$  in place of the axial force of the real system. Therefore, applying equations (2.17-2.19) (the extensible elastica theory) to the apparent system yields the stiffness equation of the initially straight riser:

$$\delta({}^{2}U) = \int_{\alpha} {}^{2}N_{a}\delta({}^{2}s') + {}^{2}M\delta({}^{2}\theta') + {}^{2}T\delta({}^{2}\phi') + {}^{2}T\delta({}^{2}\psi') d\alpha \qquad (2.68)$$

where

$${}^{2}N_{a} = \begin{cases} E^{o}A_{p}{}^{2}\overline{\varepsilon} & (\text{TLD}) \\ E^{l}A_{p}{}^{2}\varepsilon & (\text{ULD}), {}^{2}M = {}^{2}B({}^{2}\kappa), {}^{2}B = \begin{cases} E({}^{o}I_{p})(1 + {}^{2}\overline{\varepsilon}) & (\text{TLD}) \\ E({}^{l}I_{p})(1 + \varepsilon) & (\text{ULD}) \end{cases} \\ E({}^{2}I_{p}) & (\text{ED}) \end{cases}$$

$${}^{2}T = {}^{2}C({}^{2}\tau), {}^{2}C = \begin{cases} G({}^{o}J_{p})(1 + {}^{2}\overline{\varepsilon}) & (\text{TLD}) \\ G({}^{I}J_{p})(1 + \varepsilon) & (\text{ULD}) \end{cases}$$

$$G({}^{2}J_{p}) \qquad (\text{ED})$$
(2.69 a-c)

By utilizing the differential geometry expressions and integrating by parts equation (2.68) three times, obtain the four forms of the internal virtual work can be expressed as follows:

Form 1:

$$\begin{split} \delta\left({}^{2}U\right) &= \int_{a}^{1} \left[ \left[ {}^{2}N_{a} \left( \frac{{}^{2}x'}{{}^{2}s'} \right) - {}^{2}M_{a} \left( \frac{{}^{2}\kappa\left({}^{2}x'\right)}{{}^{2}s'} + \frac{{}^{2}s''}{{}^{2}\kappa\left({}^{2}s'\right)^{3}} \frac{\partial}{\partial\alpha} \left( \frac{{}^{2}x'}{{}^{2}s'} \right) \right] \delta\left({}^{2}u'\right) \right. \\ &+ \left[ {}^{2}N_{a} \left( \frac{{}^{2}y'}{{}^{2}s'} \right) - {}^{2}M_{a} \left( \frac{{}^{2}\kappa\left({}^{2}y'\right)}{{}^{2}s'} + \frac{{}^{2}s''}{{}^{2}\kappa\left({}^{2}s'\right)^{3}} \frac{\partial}{\partial\alpha} \left( \frac{{}^{2}y'}{{}^{2}s'} \right) \right] \delta\left({}^{2}v'\right) \right. \\ &+ \left[ {}^{2}N_{a} \left( \frac{{}^{2}z'}{{}^{2}s'} \right) - {}^{2}M_{a} \left( \frac{{}^{2}\kappa\left({}^{2}z'\right)}{{}^{2}s'} + \frac{{}^{2}s''}{{}^{2}\kappa\left({}^{2}s'\right)^{3}} \frac{\partial}{\partial\alpha} \left( \frac{{}^{2}z'}{{}^{2}s'} \right) \right] \delta\left({}^{2}w'\right) \right\} d\alpha \\ &+ \int_{a}^{1} \left\{ \left[ \frac{{}^{2}M_{a}}{{}^{2}\kappa\left({}^{2}s'\right)^{3}} \frac{\partial}{\partial\alpha} \left( \frac{{}^{2}x'}{{}^{2}s'} \right) \right] \delta\left({}^{2}u''\right) + \left[ \frac{{}^{2}M_{a}}{{}^{2}\kappa\left({}^{2}s'\right)^{3}} \frac{\partial}{\partial\alpha} \left( \frac{{}^{2}z'}{{}^{2}s'} \right) \right] \delta\left({}^{2}w''\right) \right\} d\alpha \\ &+ \int_{a}^{1} \left\{ {}^{2}T \left[ \frac{{}^{2}T\left({}^{2}x'\right)}{{}^{2}s'} + \frac{{}^{2}s'}{{}^{2}3} \left( {}^{2}y''\left({}^{2}z''\right) - {}^{2}y''\left({}^{2}z''\right) \right) \right. \\ &+ \left. \left( \frac{{}^{2}M_{a}}{{}^{2}\kappa\left({}^{2}s'\right)^{3}} \frac{\partial}{\partial\alpha} \left( \frac{{}^{2}x'}}{{}^{2}s'} \right) \right] \delta\left({}^{2}w''\right) \right\} d\alpha \\ &+ \int_{a}^{1} \left\{ {}^{2}T\left( {}^{2}T\left({}^{2}x''\right) + \frac{{}^{2}s'}{{}^{2}3} \left( {}^{2}y''\left({}^{2}z''\right) - {}^{2}y''\left({}^{2}z''\right) \right) \right. \\ &+ \left. \left( {}^{2}T\left( {}^{2}T\left({}^{2}x''\right) + \frac{{}^{2}s'}{{}^{2}3} \left( {}^{2}x''\left({}^{2}x''\right) - {}^{2}x''\left({}^{2}x''\right) \right) \right) \right. \\ &+ \left. \left( {}^{2}T\left( {}^{2}T\left({}^{2}T\right) + \frac{{}^{2}S}{{}^{2}3} \left( {}^{2}T\left({}^{2}T\left({}^{2}T\right) - {}^{2}T\left({}^{2}T\left({}^{2}T\right) \right) \right) \right. \right] \delta\left({}^{2}u'\right) \right. \\ &+ \left. \left( {}^{2}T\left( {}^{2}T\left({}^{2}T\right) - {}^{2}T\left({}^{2}T\left({}^{2}T\left({}^{2}T\right) - {}^{2}T\left({}^{2}T\left({}^{2}T\right) \right) \right) \right] \delta\left({}^{2}T\left({}^{2}T\right) \right) \right] \delta\left({}^{2}T\left({}^{2}T\left({}^{2}T\left({}^{2}T\right) - {}^{2}T\left({}^{2}T\left({}^{2}T\left({}^{2}T\right) - {}^{2}T\left({}^{2}T\left({}^{2}T\right) \right) \right) \right] \delta\left({}^{2}T\left({}^{2}T\left({}^{2}T\left({}^{2}T\left({}^{2}T\right) - {}^{2}T\left({}^{2}T\left({}^{2}T\left({}^{2}T\right) - {}^{2}T\left({}^{2}T\left({}^{2}T\left({}^{2}T\right) - {}^{2}T\left({}^{2}T\left({}^{2}T\left({}^{2}T\left({}^{2}T\left({}^{2}T\right) - {}^{2}T\left({}^{2}T\left({}^{2}T\left({}^{2}T\left({}^{2}T\left({}^{2}T\left({}^{2}T\left({}^{2}T\left({}^{2}T\left({}^{2}T\left({}^{2}T$$

$$-2\left(2^{2}\tau\right)\left\{\left(2^{2}x''(2^{2}y')-2^{2}x'(2^{2}y'')\right)\left(2^{2}y'\right)+\left(2^{2}x''(2^{2}z')-2^{2}x'(2^{2}z'')\right)\left(2^{2}z'\right)\right\}\right]\delta\left(2^{2}u''\right)$$

$$+\frac{2^{2}T\left(2^{2}s'\right)}{2}\left[\left(2^{2}x'(2^{2}z'')-2^{2}z'(2^{2}x'')\right)\right]$$

$$-2\left(2^{2}\tau\right)\left\{\left(2^{2}y''(2^{2}z')-2^{2}y'(2^{2}z'')\right)\left(2^{2}z'\right)-\left(2^{2}x''(2^{2}y')-2^{2}x'(2^{2}y'')\right)\left(2^{2}x'\right)\right\}\right]\delta\left(2^{2}v''\right)$$

$$+\frac{2^{2}T\left(2^{2}s'\right)}{2}\left[\left(2^{2}y'(2^{2}x''')-2^{2}x'(2^{2}y''')\right)$$

$$-2\left(2^{2}\tau\right)\left\{-\left(2^{2}x''(2^{2}z')-2^{2}x'(2^{2}z'')\right)\left(2^{2}x'\right)-\left(2^{2}y''(2^{2}z')-2^{2}y'(2^{2}x'')\right)\left(2^{2}y'\right)\right\}\right]\delta\left(2^{2}w''\right)\right\}d\alpha$$

$$+\int_{a}\left\{\frac{2^{2}T\left(2^{2}s'\right)}{2}\left(2^{2}y'(2^{2}z'')-2^{2}z'(2^{2}y'')\right)\delta\left(2^{2}w'''\right)+\frac{2^{2}T\left(2^{2}s'\right)}{2}\left(2^{2}z'(2^{2}x'')-2^{2}x'(2^{2}z'')\right)\delta\left(2^{2}w'''\right)\right\}d\alpha$$

$$+\frac{2^{2}T\left(2^{2}s'\right)}{2}\left(2^{2}x'(2^{2}y'')-2^{2}y'(2^{2}x'')\right)\delta\left(2^{2}w'''\right)\right\}d\alpha$$

$$+\frac{2^{2}T\left(2^{2}s'\right)}{2}\left(2^{2}x'(2^{2}y'')-2^{2}y'(2^{2}x'')\right)\delta\left(2^{2}w'''\right)\right\}d\alpha$$

$$+\frac{2^{2}T\left(2^{2}s'\right)}{2}\left(2^{2}x'(2^{2}y'')-2^{2}y'(2^{2}x'')\right)\delta\left(2^{2}w'''\right)\right\}d\alpha$$

$$+\frac{2^{2}T\left(2^{2}s'\right)}{2}\left(2^{2}x'(2^{2}y'')-2^{2}y'(2^{2}x'')\right)\delta\left(2^{2}w'''\right)\right\}d\alpha$$

$$+\frac{2^{2}T\left(2^{2}s'\right)}{2}\left(2^{2}x'(2^{2}y'')-2^{2}y'(2^{2}x'')\right)\delta\left(2^{2}w'''\right)\right\}d\alpha$$

$$+\frac{2^{2}T\left(2^{2}s'\right)}{2}\left(2^{2}x'(2^{2}y'')-2^{2}y'(2^{2}x'')\right)\delta\left(2^{2}w''\right)\right\}d\alpha$$

$$+\frac{2^{2}T\left(2^{2}s'\right)}{2}\left(2^{2}x'(2^{2}y'')-2^{2}y'(2^{2}x'')\right)\delta\left(2^{2}w'''\right)$$

### Form 2: After a first integration by part

$$\delta({}^{2}U) = \left[\frac{{}^{2}T({}^{2}s')}{{}^{2}\mathfrak{I}}({}^{2}y'({}^{2}z'') - {}^{2}z'({}^{2}y''))\delta({}^{2}u'')\right]_{\alpha_{o}}^{\alpha_{i}} + \left[\frac{{}^{2}T({}^{2}s')}{{}^{2}\mathfrak{I}}({}^{2}z'({}^{2}x'') - {}^{2}x'({}^{2}z''))\delta({}^{2}v'')\right]_{\alpha_{o}}^{\alpha_{i}} + \left[\frac{{}^{2}T({}^{2}s')}{{}^{2}\mathfrak{I}}({}^{2}x'({}^{2}y'') - {}^{2}y'({}^{2}x''))\delta({}^{2}w'')\right]_{\alpha_{o}}^{\alpha_{i}} + \int_{\alpha}^{2}\left[\frac{{}^{2}X'}{{}^{2}S'}\right] - {}^{2}M_{a}\left(\frac{{}^{2}K({}^{2}x')}{{}^{2}S'} + \frac{{}^{2}S''}{{}^{2}K({}^{2}S')}^{3}\frac{\partial}{\partial\alpha}(\frac{{}^{2}X'}{{}^{2}S'})\right)\right]\delta({}^{2}u')$$

$$+ \left[ {}^{2}N_{a} \left( \frac{{}^{2}y'}{{}^{2}s'} \right) - {}^{2}M_{a} \left( \frac{{}^{2}\kappa \left( {}^{2}y' \right)}{{}^{2}s'} + \frac{{}^{2}s''}{{}^{2}\kappa \left( {}^{2}s' \right)^{3}} \frac{\partial}{\partial \alpha} \left( \frac{{}^{2}y'}{{}^{2}s'} \right) \right] \right] \delta \left( {}^{2}v' \right)$$

$$+ \left[ {}^{2}N_{a} \left( \frac{{}^{2}z'}{{}^{2}s'} \right) - {}^{2}M_{a} \left( \frac{{}^{2}\kappa \left( {}^{2}z' \right)}{{}^{2}s'} + \frac{{}^{2}s''}{{}^{2}\kappa \left( {}^{2}s' \right)^{3}} \frac{\partial}{\partial \alpha} \left( \frac{{}^{2}z'}{{}^{2}s'} \right) \right] \delta \left( {}^{2}w' \right) \right\} d\alpha$$

$$+ \int_{a} \left\{ \left[ \frac{{}^{2}M}{{}^{2}\kappa \left( {}^{2}s' \right)^{2}} \frac{\partial}{\partial \alpha} \left( \frac{{}^{2}x'}{{}^{2}s'} \right) \right] \delta \left( {}^{2}u'' \right) + \left[ \frac{{}^{2}M}{{}^{2}\kappa \left( {}^{2}s' \right)^{2}} \frac{\partial}{\partial \alpha} \left( \frac{{}^{2}y'}{{}^{2}s'} \right) \right] \delta \left( {}^{2}v'' \right) \right\} d\alpha$$

$$+ \left[ \frac{{}^{2}M}{{}^{2}\kappa \left( {}^{2}s' \right)^{2}} \frac{\partial}{\partial \alpha} \left( \frac{{}^{2}z'}{{}^{2}s'} \right) \right] \delta \left( {}^{2}w'' \right) + \mathbb{F}_{2z} \delta \left( {}^{2}w'' \right) + \mathbb{F}_{2z} \delta \left( {}^{2}w'' \right) \right\} d\alpha$$

$$+ \int_{a} \left\{ \left\{ \mathbb{F}_{Ix} \delta \left( {}^{2}u' \right) + \mathbb{F}_{Iz} \delta \left( {}^{2}w' \right) + \mathbb{F}_{2z} \delta \left( {}^{2}w'' \right) + \mathbb{F}_{2z} \delta \left( {}^{2}w'' \right) \right\} d\alpha \right\} d\alpha$$

$$+ \int_{a} \left\{ \mathbb{F}_{Ix} \delta \left( {}^{2}w' \right) \right\} d\alpha d\alpha$$

$$+ \int_{a} \left\{ \mathbb{F}_{Ix} \delta \left( {}^{2}w' \right) \right\} d\alpha d\alpha$$

$$(2.71)$$

where

$$\mathbb{F}_{lx} = {}^{2}T \left[ \frac{{}^{2}\tau({}^{2}x')}{{}^{2}s'} + \frac{{}^{2}s'}{{}^{2}\mathfrak{F}} ({}^{2}y''({}^{2}z''') - {}^{2}y'''({}^{2}z'')) + \frac{2({}^{2}s')({}^{2}\tau)}{{}^{2}\mathfrak{F}} (({}^{2}x''({}^{2}y') - {}^{2}x'({}^{2}y''))({}^{2}y'') + ({}^{2}x''({}^{2}z') - {}^{2}x'({}^{2}z''))({}^{2}z'')) \right]$$
(2.72 a)

$$\mathbb{F}_{2x} = \frac{{}^{2}T({}^{2}s')}{{}^{2}\mathfrak{F}} ({}^{2}z'({}^{2}y''') - {}^{2}y'({}^{2}z''')) 
-2({}^{2}\tau) \{ ({}^{2}x''({}^{2}y') - {}^{2}x'({}^{2}y'')) ({}^{2}y') + ({}^{2}x''({}^{2}z') - {}^{2}x'({}^{2}z'')) ({}^{2}z') \} \frac{{}^{2}T({}^{2}s')}{{}^{2}\mathfrak{F}} 
- \left[ \frac{{}^{2}T({}^{2}s')}{{}^{2}\mathfrak{F}} ({}^{2}y'({}^{2}z'') - {}^{2}z'({}^{2}y'')) \right]^{\prime}$$
(2.72 b)

$$\mathbb{F}_{2x} = \frac{-^{2}T(^{2}y'(^{2}z'') - ^{2}z'(^{2}y''))(^{2}s'')}{(^{2}s')^{6}(^{2}\kappa)^{2}}$$
(2.72 c)

$$\mathbb{F}_{Iy} = {}^{2}T \left[ \frac{{}^{2}\tau({}^{2}y')}{{}^{2}s'} - \frac{{}^{2}s'}{{}^{2}\mathfrak{F}} ({}^{2}x''({}^{2}z''') - {}^{2}x'''({}^{2}z'')) \right] \\
+ \frac{2({}^{2}s')({}^{2}\tau)}{{}^{2}\mathfrak{F}} (({}^{2}y''({}^{2}z') - {}^{2}y'({}^{2}z''))({}^{2}z'') - ({}^{2}x''({}^{2}y') - {}^{2}x'({}^{2}y''))({}^{2}x'')) \right] \\
\mathbb{F}_{2y} = \frac{{}^{2}T({}^{2}s')}{{}^{2}\mathfrak{F}} ({}^{2}x'({}^{2}z''') - {}^{2}z'({}^{2}x''')) \tag{2.72 d}$$

$$\mathbb{F}_{2y} = \frac{{}^{2}T\binom{2}{s'}}{{}^{2}\mathfrak{F}} \binom{2}{x'} \binom{2}{z''} - {}^{2}z'\binom{2}{x''}$$

$$-2\binom{2}{t} \left\{ \binom{2}{t}y''\binom{2}{t} - {}^{2}y'\binom{2}{t}y'' \right\} \binom{2}{t} - \binom{2}{t}x''\binom{2}{t}y' - {}^{2}x'\binom{2}{t}y''$$

$$- \left[ \frac{{}^{2}T\binom{2}{s'}}{{}^{2}\mathfrak{F}} \binom{2}{t}z'\binom{2}{t}x'' - {}^{2}x'\binom{2}{t}x'' \right]$$

$$- \left[ \frac{2}{t}\binom{2}{t}x'' - {}^{2}x'\binom{2}{t}x'' - {}^{2}x'\binom{2}{t}x'' \right]$$

$$(2.72 e)$$

$$\mathbb{F}_{2y} = \frac{-^{2}T(^{2}z'(^{2}x'') - ^{2}x'(^{2}z''))(^{2}s'')}{(^{2}s')^{6}(^{2}\kappa)^{2}}$$
(2.72 f)

$$\mathbb{F}_{Iz} = {}^{2}T \left[ \frac{{}^{2}\tau({}^{2}z')}{{}^{2}s'} + \frac{{}^{2}s'}{{}^{2}\mathfrak{F}} ({}^{2}x''({}^{2}y''') - {}^{2}x'''({}^{2}y'')) - \frac{{}^{2}x'''({}^{2}y'')}{{}^{2}\mathfrak{F}} (({}^{2}y''({}^{2}z') - {}^{2}y'({}^{2}z''))({}^{2}y'') + ({}^{2}x''({}^{2}z') - {}^{2}x'({}^{2}z''))({}^{2}x'')) \right]$$
(2.72 g)

$$\mathbb{F}_{2z} = \frac{{}^{2}T({}^{2}s')}{{}^{2}\mathfrak{F}}({}^{2}y'({}^{2}x''') - {}^{2}x'({}^{2}y''')) 
-2({}^{2}\tau)\{-({}^{2}x''({}^{2}z') - {}^{2}x'({}^{2}z''))({}^{2}x') - ({}^{2}y''({}^{2}z') - {}^{2}y'({}^{2}z''))({}^{2}y')\}\frac{{}^{2}T({}^{2}s')}{{}^{2}\mathfrak{F}} 
-\left[\frac{{}^{2}T({}^{2}s')}{{}^{2}\mathfrak{F}}({}^{2}x'({}^{2}y'') - {}^{2}y'({}^{2}x''))\right]'$$
(2.72 h)

$$\mathbb{F}_{2z} = \frac{-^{2}T(^{2}x'(^{2}y'') - ^{2}y'(^{2}x''))(^{2}s'')}{(^{2}s')^{6}(^{2}\kappa)^{2}}$$
(2.72 i)

Form 3: After a second integration by part

$$\delta \begin{pmatrix} {}^{2}U \end{pmatrix} = \begin{bmatrix} {}^{2}T \left( \frac{{}^{2}b_{x}}{\left( {}^{2}s' \right)^{2} {}^{2}K} \delta \left( {}^{2}u'' \right) + \frac{{}^{2}b_{y}}{\left( {}^{2}s' \right)^{2} {}^{2}K} \delta \left( {}^{2}w'' \right) + \frac{{}^{2}b_{z}}{\left( {}^{2}s' \right)^{2} {}^{2}K} \delta \left( {}^{2}w'' \right) \end{bmatrix} \right]_{a_{x}}^{a_{x}}$$

$$+ \begin{bmatrix} \frac{{}^{2}M}{{}^{2}s'} \left( {}^{2}n_{x}\delta \left( {}^{2}u' \right) + {}^{2}n_{y}\delta \left( {}^{2}v' \right) + {}^{2}n_{z}\delta \left( {}^{2}x' \right) \right) \right]_{a_{x}}^{a_{x}}$$

$$+ \int_{a} \left[ \left\{ \left( {}^{2}N_{a} - {}^{2}B \left( {}^{2}K \right)^{2} \right) \left( \frac{{}^{2}x'}{{}^{2}s'} \right) - \frac{{}^{2}B \left( {}^{2}s'' \right)}{\left( {}^{2}s' \right)^{3}} \frac{\partial}{\partial \alpha} \left( \frac{{}^{2}x'}{{}^{2}s'} \right) + \left( \mathbb{F}_{Ix} - \mathbb{F}'_{Ix} \right) \right.$$

$$- \left[ \frac{{}^{2}B}{\left( {}^{2}s' \right)^{2}} \frac{\partial}{\partial \alpha} \left( \frac{{}^{2}x'}{{}^{2}s'} \right) \right] \right] \delta \left( {}^{2}u' \right)$$

$$+ \left\{ \left( {}^{2}N_{a} - {}^{2}B \left( {}^{2}K \right)^{2} \right) \left( \frac{{}^{2}y'}{{}^{2}s'} \right) - \frac{{}^{2}B \left( {}^{2}s'' \right)}{\left( {}^{2}s' \right)^{3}} \frac{\partial}{\partial \alpha} \left( \frac{{}^{2}y'}{{}^{2}s'} \right) + \left( \mathbb{F}_{Iy} - \mathbb{F}'_{2y} \right) \right.$$

$$- \left[ \frac{{}^{2}B}{\left( {}^{2}s' \right)^{2}} \frac{\partial}{\partial \alpha} \left( \frac{{}^{2}y'}{{}^{2}s'} \right) \right] \right\} \delta \left( {}^{2}v' \right)$$

$$+ \left\{ \left( {}^{2}N_{a} - {}^{2}B \left( {}^{2}K \right)^{2} \right) \left( \frac{{}^{2}z'}{{}^{2}s'} \right) - \frac{{}^{2}B \left( {}^{2}s'' \right)}{\left( {}^{2}s' \right)^{3}} \frac{\partial}{\partial \alpha} \left( \frac{{}^{2}z'}{{}^{2}s'} \right) + \left( \mathbb{F}_{Iz} - \mathbb{F}'_{2z} \right) \right.$$

$$- \left[ \frac{{}^{2}B}{\left( {}^{2}s' \right)^{2}} \frac{\partial}{\partial \alpha} \left( \frac{{}^{2}z'}{{}^{2}s'} \right) \right] \right\} \delta \left( {}^{2}w' \right) d\alpha + \int_{\alpha} \left\{ {}^{2}T\delta \left( {}^{2}w' \right) \right\} d\alpha$$

$$(2.73)$$

Form 4: After a third integration by part

$$\delta({}^{2}U) = \begin{bmatrix} {}^{2}T\left(\frac{{}^{2}b_{x}}{\left({}^{2}s'\right)^{2}{}^{2}\kappa}\delta({}^{2}u'') + \frac{{}^{2}b_{y}}{\left({}^{2}s'\right)^{2}{}^{2}\kappa}\delta({}^{2}v'') + \frac{{}^{2}b_{z}}{\left({}^{2}s'\right)^{2}{}^{2}\kappa}\delta({}^{2}w'') \end{bmatrix} \right]_{\alpha_{x}}^{\alpha_{t}}$$

$$+ \mathbb{E}_{2x}\delta({}^{2}u') + \mathbb{E}_{2y}\delta({}^{2}v') + \mathbb{E}_{2z}\delta({}^{2}z') + {}^{2}T\delta({}^{2}\psi)$$

$$+\left[\frac{{}^{2}M}{{}^{2}S'}\left({}^{2}n_{x}\delta\left({}^{2}u'\right)+{}^{2}n_{y}\delta\left({}^{2}v'\right)+{}^{2}n_{z}\delta\left({}^{2}w'\right)\right)\right]_{\alpha_{o}}^{\alpha_{i}}$$

$$+\left[{}^{2}R_{x}\delta\left({}^{2}u\right)+{}^{2}R_{y}\delta\left({}^{2}v\right)+{}^{2}R_{z}\delta\left({}^{2}w\right)\right]_{\alpha_{o}}^{\alpha_{i}}$$

$$+\int_{\alpha}\left[\left\{-{}^{2}R'_{x}\right\}\delta\left({}^{2}u\right)+\left\{-{}^{2}R'_{y}\right\}\delta\left({}^{2}v\right)+\left\{-{}^{2}R'_{z}\right\}\delta\left({}^{2}w\right)+\left\{-{}^{2}T'\right\}\delta\left({}^{2}\psi\right)\right]d\alpha \quad (2.74)$$

where

$$\mathbb{F}_{lx} - \mathbb{F}'_{2x} = {}^{2}T({}^{2}\kappa)({}^{2}b_{x}) \qquad (2.75 \text{ a})$$

$$\mathbb{F}_{ly} - \mathbb{F}'_{2y} = {}^{2}T({}^{2}\kappa)({}^{2}b_{y}) \qquad (2.75 \text{ b})$$

$$\mathbb{F}_{lz} - \mathbb{F}'_{2z} = {}^{2}T({}^{2}\kappa)({}^{2}b_{y}) \qquad (2.75 \text{ b})$$

$$\mathbb{F}_{lz} - \mathbb{F}'_{2z} = {}^{2}T({}^{2}\kappa)({}^{2}b_{z}) \qquad (2.75 \text{ c})$$

$${}^{2}R_{x} = \left[\left({}^{2}N_{a} - {}^{2}B({}^{2}\kappa)^{2}\right)\left({}^{2}\frac{2x'}{2s'}\right) - \frac{{}^{2}B({}^{2}s'')}{({}^{2}s')^{3}}\frac{\partial}{\partial\alpha}\left({}^{2}\frac{2x'}{2s'}\right)\right] + {}^{2}T({}^{2}\kappa)({}^{2}b_{x})$$

$$-\left[\frac{{}^{2}B}{({}^{2}s')^{2}}\frac{\partial}{\partial\alpha}\left({}^{2}\frac{2x'}{2s'}\right) - \frac{{}^{2}B({}^{2}s'')}{({}^{2}s')^{3}}\frac{\partial}{\partial\alpha}\left({}^{2}\frac{2y'}{2s'}\right)\right] + {}^{2}T({}^{2}\kappa)({}^{2}b_{y})$$

$$-\left[\frac{{}^{2}B}{({}^{2}s')^{2}}\frac{\partial}{\partial\alpha}\left({}^{2}\frac{2y'}{2s'}\right) - \frac{{}^{2}B({}^{2}s'')}{({}^{2}s')^{3}}\frac{\partial}{\partial\alpha}\left({}^{2}\frac{2z'}{2s'}\right)\right] + {}^{2}T({}^{2}\kappa)({}^{2}b_{z})$$

$$-\left[\frac{{}^{2}B}{({}^{2}s')^{2}}\frac{\partial}{\partial\alpha}\left({}^{2}\frac{2z'}{2s'}\right) - \frac{{}^{2}B({}^{2}s'')}{({}^{2}s')^{3}}\frac{\partial}{\partial\alpha}\left({}^{2}\frac{2z'}{2s'}\right)\right] + {}^{2}T({}^{2}\kappa)({}^{2}b_{z})$$

$$-\left[\frac{{}^{2}B}{({}^{2}s')^{2}}\frac{\partial}{\partial\alpha}\left({}^{2}\frac{2z'}{2s'}\right) - \frac{{}^{2}B({}^{2}s'')}{({}^{2}s')^{3}}\frac{\partial}{\partial\alpha}\left({}^{2}\frac{2z'}{2s'}\right)\right] + {}^{2}T({}^{2}\kappa)({}^{2}b_{z})$$

$$-\left[\frac{{}^{2}B}{({}^{2}s')^{2}}\frac{\partial}{\partial\alpha}\left({}^{2}\frac{2z'}{2s'}\right) - \frac{{}^{2}B({}^{2}s'')}{({}^{2}s')^{3}}\frac{\partial}{\partial\alpha}\left({}^{2}\frac{2z'}{2s'}\right)\right] + {}^{2}T({}^{2}\kappa)({}^{2}b_{z})$$

#### 2.7.2 External Virtual Work

The external forces exert upon the marine risers are the effective weight, hydrodynamic loading, and inertial forces which depend on deformation of the riser. Therefore, an evaluation of these forces should be done with respect to the current

configuration of the riser. Then the variation of external virtual work evaluating from the free bodies at displaced state is

$$\delta W = \delta W_{w} + \delta W_{H} + \delta W_{I} \tag{2.76}$$

where  $\delta W_w$ ,  $\delta W_H$  and  $\delta W_I$  are the virtual work of the apparent weight, hydrodynamic pressure, and inertial forces of the riser and transported fluid respectively. In the Cartesian coordinates, these expressions are written as follows,

$$\delta W_{w} = -\int_{\alpha} w_{a} \left( {}^{2}s' \right) \delta \left( {}^{2}v \right) d\alpha \tag{2.77}$$

$$\delta W_{H} = \int_{\alpha} \left[ f_{Hx} \left( {}^{2}s' \right) \delta \left( {}^{2}u \right) + f_{Hy} \left( {}^{2}s' \right) \delta \left( {}^{2}v \right) + f_{Hz} \left( {}^{2}s' \right) \delta \left( {}^{2}w \right) \right] d\alpha \tag{2.78}$$

$$\delta W_{I} = - \iint_{a} \left( m_{p} a_{px} + m_{i} a_{Fx} \right) \left( {^{2}s'} \right) \delta \left( {^{2}u} \right) + \left( m_{p} a_{py} + m_{i} a_{Fy} \right) \left( {^{2}s'} \right) \delta \left( {^{2}v} \right)$$

$$+\left(m_{p}a_{pz}+m_{i}a_{Fz}\right)\left({}^{2}s'\right)\delta\left({}^{2}w\right)+m_{p}\left({}^{2}J_{p}\right)\left({}^{2}s'\right)\left({}^{2}\ddot{\psi}\right)\delta\left({}^{2}\psi\right)\right]d\alpha \qquad (2.79)$$

in which  $\vec{a}_p = a_{px}\hat{i} + a_{py}\hat{j} + a_{pz}\hat{k} = \ddot{r} = {}_2\ddot{u}\hat{i} + {}_2\ddot{v}\hat{j} + {}_2\ddot{w}\hat{k}$  and the expressions of hydrodynamic force,  $\vec{F}_H = f_{Hx}\hat{i} + f_{Hy}\hat{j} + f_{Hz}\hat{k}$ , and the accelerate of transporting fluid,  $\vec{a}_F = a_{Fx}\hat{i} + a_{Fy}\hat{j} + a_{Fz}\hat{k}$ , are given by equations (2.32) and (2.60) respectively. Substituting equations (2.77)-(2.79) into equation (2.76) yields

$$\delta W = \int_{\alpha} \left\{ {}^{2}s' \left[ f_{Hx} - m_{p} a_{px} - m_{i} a_{Fx} \right] \delta^{2} u \right\} d\alpha$$

$$+ \int_{\alpha} \left\{ {}^{2}s' \left[ -w_{a} + f_{Hy} - m_{p} a_{py} - m_{i} a_{Fy} \right] \delta^{2} v \right\} d\alpha$$

$$+ \int_{\alpha} \left\{ {}^{2}s' \left[ f_{Hz} - m_{p} a_{pz} - m_{i} a_{Fz} \right] \delta^{2} w \right\} d\alpha$$

$$- \int_{\alpha} \left\{ {}^{2}s' \left[ m_{p} \left( {}^{2}J_{p} \right) \left( {}^{2}\ddot{\psi} \right) \right] \delta \left( {}^{2}\psi \right) \right\} d\alpha$$

$$(2.80)$$

#### 2.7.3 Total Virtual Work

From the principle of virtual work, the total virtual work of the effective system is zero:

$$\delta \pi = \delta U - \delta W = 0 \tag{2.81}$$

Substituting equations (2.70) and (2.80) into equation (2.81) and utilizing the differential geometry expressions in appendix yields the first weak form of the total virtual work expressed in the fixed Cartesian coordinate.

$$\begin{split} \delta\left({}^{2}\pi\right) &= \int_{a}^{\left\{\left[{}^{2}N_{a}\left(\frac{{}^{2}x'}{{}^{2}s'}\right) - {}^{2}M_{a}\left(\frac{{}^{2}\kappa\left({}^{2}x'\right)}{{}^{2}s'} + \frac{{}^{2}s''}{{}^{2}\kappa\left({}^{2}s'\right)^{3}}\frac{\partial}{\partial\alpha}\left(\frac{{}^{2}x'}{{}^{2}s'}\right)\right]\right\} \delta\left({}^{2}u'\right)} \\ &+ \left[{}^{2}N_{a}\left(\frac{{}^{2}y'}{{}^{2}s'}\right) - {}^{2}M_{a}\left(\frac{{}^{2}\kappa\left({}^{2}x'\right)}{{}^{2}s'} + \frac{{}^{2}s''}{{}^{2}\kappa\left({}^{2}s'\right)^{3}}\frac{\partial}{\partial\alpha}\left(\frac{{}^{2}x'}{{}^{2}s'}\right)\right]\right] \delta\left({}^{2}v'\right)} \\ &+ \left[{}^{2}N_{a}\left(\frac{{}^{2}z'}{{}^{2}s'}\right) - {}^{2}M_{a}\left(\frac{{}^{2}\kappa\left({}^{2}z'\right)}{{}^{2}s'} + \frac{{}^{2}s''}{{}^{2}\kappa\left({}^{2}s'\right)^{3}}\frac{\partial}{\partial\alpha}\left(\frac{{}^{2}z'}{{}^{2}s'}\right)\right]\right] \delta\left({}^{2}w'\right)\right\} d\alpha} \\ &+ \int_{a}^{\left\{\left[\frac{{}^{2}M}{{}^{2}\kappa\left({}^{2}s'\right)^{2}}\frac{\partial}{\partial\alpha}\left(\frac{{}^{2}x'}{{}^{2}s'}\right)\right] \delta\left({}^{2}u''\right) + \left[\frac{{}^{2}M}{{}^{2}\kappa\left({}^{2}s'\right)^{2}}\frac{\partial}{\partial\alpha}\left(\frac{{}^{2}y'}{{}^{2}s'}\right)\right] \delta\left({}^{2}w''\right)\right\} d\alpha} \\ &+ \int_{a}^{\left\{{}^{2}T\left[\frac{{}^{2}\tau\left({}^{2}x'\right)}{{}^{2}s'} + \frac{{}^{2}s'}{{}^{2}\Im}\left({}^{2}y''\left({}^{2}z''\right) - {}^{2}y''\left({}^{2}z''\right)\right)\right.} + \left({}^{2}x''\left({}^{2}z'\right) - {}^{2}x'\left({}^{2}z''\right)\right)\right\} \delta\left({}^{2}u'\right)} \\ &+ \frac{{}^{2}\left\{{}^{2}T\left[\frac{{}^{2}\tau\left({}^{2}x'\right)}{{}^{2}s'} + \frac{{}^{2}s'}{{}^{2}\Im}\left({}^{2}x''\left({}^{2}x''\right) - {}^{2}y''\left({}^{2}z''\right)\right)\right.} + \left({}^{2}x''\left({}^{2}z'\right) - {}^{2}x'\left({}^{2}z''\right)\right)\right\} \delta\left({}^{2}u'\right)} \\ &+ \frac{{}^{2}T\left[\frac{{}^{2}\tau\left({}^{2}x'\right)}{{}^{2}s'} - \frac{{}^{2}s'}{{}^{2}\Im}\left({}^{2}x''\left({}^{2}z''\right) - {}^{2}x''\left({}^{2}z''\right)\right)\right.} + \left({}^{2}x''\left({}^{2}z'\right) - {}^{2}x'\left({}^{2}x''\right)\right) \left({}^{2}x''\right)\right] \delta\left({}^{2}u'\right)} \\ &+ \frac{{}^{2}T\left[\frac{{}^{2}\tau\left({}^{2}z'\right)}{{}^{2}s'} - \frac{{}^{2}s'}{{}^{2}\Im}\left({}^{2}x''\left({}^{2}z''\right) - {}^{2}x''\left({}^{2}z''\right)\right)\right] \delta\left({}^{2}u'\right)} + \left({}^{2}x''\left({}^{2}x''\right) - {}^{2}x'\left({}^{2}x''\right)\right) \left({}^{2}x''\right)\right] \delta\left({}^{2}u'\right)} \right] \delta\left({}^{2}u'\right)} \\ &+ \frac{{}^{2}T\left[\frac{{}^{2}\tau\left({}^{2}z'\right)}{{}^{2}S'} - \frac{{}^{2}S'}{{}^{2}\Im}\left({}^{2}x''\left({}^{2}z''\right) - {}^{2}x''\left({}^{2}z''\right)\right) \left({}^{2}x''\right) - {}^{2}x'\left({}^{2}x''\right)\right) \left({}^{2}x''\right)} \right] \delta\left({}^{2}u'\right)} \\ &+ \frac{{}^{2}T\left[\frac{{}^{2}\tau\left({}^{2}x'\right)}{{}^{2}S'} - \frac{{}^{2}S'}{{}^{2}\Im}\left({}^{2}x''\left({}^{2}x''\right) - {}^{2}x''\left({}^{2}x''\right) - {}^{2}x''\left({}^{2}x''\right)\right) \left({}^{2}x''\right)} - {}^{2}x''\left({}^{2}x''\right) - {}^{2}x''\left({}^{2}x''\right) -$$

$$-2\left(2^{2}\tau\right)\left\{\left(2^{2}x''(2^{2}y')-2^{2}x'(2^{2}y'')\right)\left(2^{2}y'\right)+\left(2^{2}x''(2^{2}z')-2^{2}x'(2^{2}y')\right)\left(2^{2}z'\right)\right\}\right]\delta\left(2^{2}u''\right)$$

$$+\frac{2^{2}T\left(2^{2}s'\right)}{2\Im}\left[\left(2^{2}x'(2^{2}z'')-2^{2}y'(2^{2}z'')\right)\left(2^{2}z'\right)-\left(2^{2}x''(2^{2}y')-2^{2}x'(2^{2}y'')\right)\left(2^{2}x'\right)\right\}\right]\delta\left(2^{2}v''\right)$$

$$+\frac{2^{2}T\left(2^{2}s'\right)}{2\Im}\left[\left(2^{2}y'(2^{2}x''')-2^{2}x'(2^{2}y''')\right)$$

$$-2\left(2^{2}\tau\right)\left\{-\left(2^{2}x''(2^{2}z')-2^{2}x'(2^{2}z'')\right)\left(2^{2}x'\right)-\left(2^{2}y''(2^{2}z'')-2^{2}y'(2^{2}z'')\right)\left(2^{2}y'\right)\right\}\right]\delta\left(2^{2}w''\right)\right\}d\alpha$$

$$+\int_{a}\left\{\frac{2^{2}T\left(2^{2}s'\right)}{2\Im}\left(2^{2}y'(2^{2}z'')-2^{2}z'(2^{2}y'')\right)\delta\left(2^{2}w'''\right)+\frac{2^{2}T\left(2^{2}s'\right)}{2\Im}\left(2^{2}z'(2^{2}x'')-2^{2}x'(2^{2}x'')\right)\delta\left(2^{2}w'''\right)$$

$$+\frac{2^{2}T\left(2^{2}s'\right)}{2\Im}\left(2^{2}x'(2^{2}y'')-2^{2}y'(2^{2}x'')\right)\delta\left(2^{2}w'''\right)\right\}d\alpha$$

$$-\int_{a}\left\{2^{2}s'\left[f_{Hx}-m_{p}a_{px}-m_{i}a_{Fx}\right]\delta\left(2^{2}u\right)\right\}d\alpha$$

$$-\int_{a}\left\{2^{2}s'\left[-w_{a}+f_{Hy}-m_{p}a_{py}-m_{i}a_{Fy}\right]\delta\left(2^{2}v\right)\right\}d\alpha$$

$$-\int_{a}\left\{2^{2}s'\left[f_{Hx}-m_{p}a_{px}-m_{i}a_{Fx}\right]\delta\left(2^{2}w\right)\right\}d\alpha$$

$$-\int_{a}\left\{2^{2}s'\left[f_{Hx}-m_{p}a_{px}-m_{i}a_{Fx}\right]\delta\left(2^{2}w\right)\right\}d\alpha$$

$$+\int_{a}\left\{2^{2}s'\left[m_{p}\left(2^{2}J_{p}\right)\left(2^{2}\psi'\right)\right]\delta\left(2^{2}\psi'\right)\right\}d\alpha$$

$$+\int_{a}\left\{2^{2}s'\left[m_{p}\left(2^{2}J_{p}\right)\left(2^{2}\psi'\right)\right]\delta\left(2^{2}w'\right)\right\}d\alpha$$

$$+\int_{a}\left\{2^{2}s'\left[m_{p}\left(2^{2}J_{p}\right)\left(2^{2}\psi'\right)\right]\delta\left(2^{2}w'\right)\right\}d\alpha$$

$$+\int_{a}\left\{2^{2}s'\left[m_{p}\left(2^{2}J_{p}\right)\left(2^{2}\psi'\right)\right]\delta\left(2^{2}w'\right)\right\}d\alpha$$

$$+\int_{a}\left\{2^{2}s'\left[m_{p}\left(2^{2}J_{p}\right)\left(2^{2}\psi'\right)\right]\delta\left(2^{2}w'\right)\right\}d\alpha$$

$$+\int_{a}\left\{2^{2}s'\left[m_{p}\left(2^{2}J_{p}\right)\left(2^{2}\psi'\right)\right]\delta\left(2^{2}w'\right)\right\}d\alpha$$

$$+\int_{a}\left\{2^{2}s'\left[m_{p}\left(2^{2}J_{p}\right)\left(2^{2}\psi'\right)\right]\delta\left(2^{2}w'\right)\right\}d\alpha$$

$$+\int_{a}\left\{2^{2}s'\left[m_{p}\left(2^{2}J_{p}\right)\left(2^{2}\psi'\right)\right]\delta\left(2^{2}w'\right)\right\}d\alpha$$

Integrating by part three times, one obtains the last weak form of the total virtual work as follows.

$$\delta\left({}^{2}\pi\right) = \begin{bmatrix} {}^{2}T\left(\frac{{}^{2}b_{x}}{\left({}^{2}s'\right)^{2}{}^{2}\kappa}\delta\left({}^{2}u''\right) + \frac{{}^{2}b_{y}}{\left({}^{2}s'\right)^{2}{}^{2}\kappa}\delta\left({}^{2}v''\right) + \frac{{}^{2}b_{z}}{\left({}^{2}s'\right)^{2}{}^{2}\kappa}\delta\left({}^{2}w''\right) \end{bmatrix} \right]_{\alpha_{0}}^{\alpha_{1}} + \mathbb{E}_{2x}\delta\left({}^{2}u'\right) + \mathbb{E}_{2y}\delta\left({}^{2}v'\right) + \mathbb{E}_{2z}\delta\left({}^{2}z'\right) + {}^{2}T\delta\left({}^{2}\psi\right)$$
Torque boundary condition (term 4)

$$+ \left[\frac{{}^{2}M}{{}^{2}s'}\left({}^{2}n_{x}\delta\left({}^{2}u'\right) + {}^{2}n_{y}\delta\left({}^{2}v'\right) + {}^{2}n_{z}\delta\left({}^{2}w'\right)\right)\right]_{\alpha_{o}}^{\alpha_{i}}$$

$$+ \left[\frac{{}^{2}R_{x}\delta\left({}^{2}u\right) + {}^{2}R_{y}\delta\left({}^{2}v\right) + {}^{2}R_{z}\delta\left({}^{2}w\right)\right]_{\alpha_{o}}^{\alpha_{i}}$$

$$+ \left[\frac{{}^{2}R_{x}\delta\left({}^{2}u\right) + {}^{2}R_{y}\delta\left({}^{2}v\right) + {}^{2}R_{z}\delta\left({}^{2}w\right)\right]_{\alpha_{o}}^{\alpha_{i}}$$

$$+ \int_{\alpha} \left\{\left\{-{}^{2}R'_{x} - {}^{2}s'\left({}^{2}q_{x}\right)\right\}\delta\left({}^{2}u\right) + \left\{-{}^{2}R'_{y} - {}^{2}s'\left({}^{2}q_{y}\right)\right\}\delta\left({}^{2}v\right) + \left\{-{}^{2}R'_{z} - {}^{2}s'\left({}^{2}q_{y}\right)\right\}\delta\left({}^{2}w\right)\right\} d\alpha (2.83)$$

$$+ \int_{\alpha} \left\{\left\{-{}^{2}R'_{z} - {}^{2}s'\left({}^{2}q_{z}\right)\right\}\delta\left({}^{2}w\right) + \left\{-{}^{2}T' + {}^{2}s'\left[m_{p}\left({}^{2}J_{p}\right)\left({}^{2}\ddot{\psi}\right)\right]\right\}\delta\left({}^{2}\psi\right)\right\} d\alpha (2.83)$$

where

$$^{2}q_{x} = \left[ f_{Hx} - m_{p} a_{px} - m_{i} a_{Fx} \right]$$
 (2.84 a)

$$^{2}q_{y} = \left[-w_{a} + f_{Hy} - m_{p}a_{py} - m_{i}a_{Fy}\right]$$
 (2.84 b)

$$^{2}q_{z} = \left[ f_{Hz} - m_{p} a_{pz} - m_{i} a_{Fz} \right]$$
 (2.84 c)

#### 2.7.4 Euler Equations and Boundary Conditions

Considering the boundary conditions of the problem, two classes of boundary conditions are identified, called essential and natural boundary conditions. The essential boundary conditions are also called geometric boundary conditions and correspond to prescribe displacements and rotations. The natural boundary conditions are also called the force boundary conditions and correspond to prescribe boundary forces and moments. In this problem, the hinge support is applied on top and bottom end, therefore, the essential boundary condition are

$${}^{2}u(\alpha_{o}, {}^{2}t) = 0, {}^{2}u(\alpha_{t}, {}^{2}t) = 0$$
 (2.85 a)

$$^{2}v(\alpha_{\alpha},^{2}t) = 0,^{2}v(\alpha_{t},^{2}t) = 0$$
 (2.85 b)

$$^{2}w(\alpha_{o},^{2}t) = 0,^{2}w(\alpha_{t},^{2}t) = 0$$
 (2.85 c)

To extract from the variational equation, equation (2.83), the governing differential equations and natural boundary conditions can be obtained. One uses the argument that the variations on  ${}^2u$ ,  ${}^2v$ , and  ${}^2w$  are completely arbitrary, except that there can be no variations on the prescribed essential boundary conditions. Hence, because  ${}^2u(\alpha_o, {}^2t)$ ,  ${}^2u(\alpha_t, {}^2t)$ ,  ${}^2v(\alpha_o, {}^2t)$ ,  ${}^2v(\alpha_o, {}^2t)$ ,  ${}^2w(\alpha_o, {}^2t)$ , and  ${}^2w(\alpha_t, {}^2t)$  are prescribed one has  $\delta({}^2u(\alpha_o, {}^2t))$ ,  $\delta({}^2u(\alpha_t, {}^2t))$ ,  $\delta({}^2v(\alpha_o, {}^2t))$ ,  $\delta({}^2v(\alpha_o, {}^2t))$ , and  $\delta({}^2w(\alpha_t, {}^2t))$  are equal to zero and term 2 in equation (2.83) vanishes. Then

$$\left[{}^{2}R_{x}\delta^{2}u + {}^{2}R_{y}\delta^{2}v + {}^{2}R_{z}\delta^{2}w\right]_{\alpha}^{\alpha_{i}} = 0$$
 (2.86)

Considering term 3 in equation (2.83), since the variations on  ${}^{2}u'$ ,  ${}^{2}v'$ , and  ${}^{2}w'$  are completely arbitrary at any point, that means

$$\left[\frac{{}^{2}M}{{}^{2}s'}\left({}^{2}n_{x}\right)\right]_{\alpha_{o}}^{\alpha_{i}} = \left[\frac{{}^{2}B\left({}^{2}\kappa\right)}{{}^{2}s'}\left({}^{2}n_{x}\right)\right]_{\alpha_{i}}^{\alpha_{i}} = 0$$
 (2.87 a)

$$\left[\frac{{}^{2}M}{{}^{2}S'}\left({}^{2}n_{y}\right)\right]_{\alpha_{o}}^{\alpha_{i}} = \left[\frac{{}^{2}B\left({}^{2}\kappa\right)}{{}^{2}S'}\left({}^{2}n_{y}\right)\right]_{\alpha}^{\alpha_{i}} = 0$$
 (2.87 b)

$$\left[\frac{{}^{2}M}{{}^{2}S'}\left({}^{2}n_{z}\right)\right]_{\alpha_{o}}^{\alpha_{i}} = \left[\frac{{}^{2}B\left({}^{2}\kappa\right)}{{}^{2}S'}\left({}^{2}n_{z}\right)\right]_{\alpha_{o}}^{\alpha_{i}} = 0$$
 (2.87 c)

Considering term 4 in equation (2.83), one has

$$\frac{{}^{2}T\left({}^{2}b_{x}\right)}{\left({}^{2}s'\right)^{2}{}^{2}\kappa}\delta\left({}^{2}u''\left(\alpha_{o},{}^{2}t\right)\right) = 0, \frac{{}^{2}T\left({}^{2}b_{y}\right)}{\left({}^{2}s'\right)^{2}{}^{2}\kappa}\delta\left({}^{2}v''\left(\alpha_{o},{}^{2}t\right)\right) = 0,$$

$$\frac{{}^{2}T\left({}^{2}b_{z}\right)}{\left({}^{2}s'\right)^{2}{}^{2}\kappa}\delta\left({}^{2}w''\left(\alpha_{o},{}^{2}t\right)\right) = 0, {}^{2}T\delta\left({}^{2}\psi\left(\alpha_{o},{}^{2}t\right)\right)$$

$$\frac{{}^{2}T\left({}^{2}b_{x}\right)}{\left({}^{2}s'\right)^{2}{}^{2}\kappa}\delta\left({}^{2}u''\left(\alpha_{t},{}^{2}t\right)\right) = 0, \frac{{}^{2}T\left({}^{2}b_{y}\right)}{\left({}^{2}s'\right)^{2}{}^{2}\kappa}\delta\left({}^{2}v''\left(\alpha_{t},{}^{2}t\right)\right) = 0,$$

$$(2.88 a-d)$$

$$\frac{{}^{2}T\left({}^{2}b_{z}\right)}{\left({}^{2}s'\right)^{2}{}^{2}\kappa}\delta\left({}^{2}w''\left(\alpha_{t},{}^{2}t\right)\right) = 0, {}^{2}T\delta\left({}^{2}\psi\left(\alpha_{t},{}^{2}t\right)\right) \tag{2.89 a-d}$$

$$\left[ \mathbb{F}_{2x} \right]_{\alpha_{0}}^{\alpha_{1}} = \left[ \left[ \frac{-^{2}T(^{2}y'^{2}z'' - ^{2}z'^{2}y'')^{2}s''}{(^{2}s')^{6}(^{2}\kappa)^{2}} \right] \right]_{\alpha}^{\alpha_{1}} = 0$$
 (2.90 a)

$$\left[\mathbb{F}_{2y}\right]_{\alpha_{0}}^{\alpha_{1}} = \left[\left(\frac{-^{2}T\left(\frac{^{2}z'^{2}x'' - \frac{^{2}x'^{2}z''}}{\left(\frac{^{2}s'}{\right)^{6}\left(\frac{^{2}\kappa}{\right)^{2}}}\right)^{2}s''}\right)\right]_{\alpha}^{\alpha_{1}} = 0$$
 (2.90 b)

$$\left[ \mathbb{F}_{2z} \right]_{\alpha_{o}}^{\alpha_{i}} = \left[ \left( \frac{-^{2}T \left( {^{2}x'} {^{2}y''} - {^{2}y'} {^{2}x''} \right) {^{2}s''}}{\left( {^{2}s'} \right)^{6} \left( {^{2}\kappa} \right)^{2}} \right) \right]_{\alpha}^{\alpha_{i}} = 0$$
 (2.90 c)

It is true that equation (2.88) will be exact by two arguments. First, the variation of the second derivative of displacements or the variation the twisting angle are equal to zero, i.e.  $\delta\left({}^2u''(\alpha_o,{}^2t)\right) = 0$ ,  $\delta\left({}^2v''(\alpha_o,{}^2t)\right) = 0$ ,  $\delta\left({}^2w''(\alpha_o,{}^2t)\right) = 0$ , and  $\delta\left({}^2\psi\left(\alpha_o,{}^2t\right)\right) = 0$ . Second, the torque at the bottom end is equal to zero, i.e.  ${}^2T\left(\alpha_o,{}^2t\right) = 0$ . In this study, the bottom end of the riser can not rotate around the tangential direction freely, but can rotate freely around any other direction perpendicular to the tangent. Therefore, the second argument can not occur because the torque reaction is not equal to zero, i.e.  ${}^2T\left(\alpha_o,{}^2t\right) \neq 0$ . Consequently, the first argument has been adopted and it can be concluded that the second derivative of the displacement is a constant or equal to zero, i.e.

$$^{2}u''(\alpha_{o},^{2}t) = Const$$
, or  $^{2}u''(\alpha_{o},^{2}t) = 0$   
 $^{2}v''(\alpha_{o},^{2}t) = Const$ , or  $^{2}v''(\alpha_{o},^{2}t) = 0$   
 $^{2}w''(\alpha_{o},^{2}t) = Const$ , or  $^{2}w''(\alpha_{o},^{2}t) = 0$ 

In the same manner, the equation (2.89) will be exact by two arguments in the same manner as equation (2.88). At the top end, however, the riser can rotate

freely around in every direction. Therefore, the first argument can not occur because the torsion at the top end is not equal to zero, i.e.  ${}^2\tau(\alpha_o,{}^2t)\neq 0$ . Since the torsion is function of the second derivative of the displacement, they and their variation are not equal to zero, i.e.

$${}^{2}u''(\alpha_{t}, {}^{2}t) \neq 0$$
, and  $\delta({}^{2}u''(\alpha_{t}, {}^{2}t)) \neq 0$   
 ${}^{2}v''(\alpha_{t}, {}^{2}t) \neq 0$ , and  $\delta({}^{2}v''(\alpha_{t}, {}^{2}t)) \neq 0$   
 ${}^{2}w''(\alpha_{t}, {}^{2}t) \neq 0$ , and  $\delta({}^{2}w''(\alpha_{t}, {}^{2}t)) \neq 0$ 

Consequently, the second argument has been adopted and it can be concluded that, the torque at the top end is equal to zero in the case of no applied external torque. For the most general problem, the external torque may be applied from the environment of the riser. Thus, the natural boundary condition of torque at the top end becomes  ${}^2T(\alpha_t, {}^2t) = T_{ex}$ .

Considering equation (2.90), each term is composed of the second derivative of displacement and torque. From this reason, this condition corresponds to the conditions of equation (2.88) and (2.89).

Since the variations on  ${}^{2}u$ ,  ${}^{2}v$ , and  ${}^{2}w$  are completely arbitrary at any point except at the essential boundary, the governing differential equations are shown in term 1 of equation (2.83) and can be called Euler's equations. By substituting equations (2.75 d)-(2.75 f) into term 1 of equation (2.83), one obtain the governing differential equations in three directions of the fixed cartesian coordinate system as follows.

In x direction:

$$\left[\frac{{}^{2}B}{\left({}^{2}s'\right)^{2}}\frac{\partial}{\partial\alpha}\left({}^{2}x'\right)\right]^{n} - \left[\left({}^{2}N_{a} - {}^{2}B\left({}^{2}\kappa\right)^{2}\right)\frac{{}^{2}x'}{{}^{2}s'} - {}^{2}B\left(\frac{{}^{2}s''}{\left({}^{2}s'\right)^{3}}\right)\frac{\partial}{\partial\alpha}\left(\frac{{}^{2}x'}{{}^{2}s'}\right)\right]^{n} - \left[{}^{2}T\left({}^{2}\kappa\right)\left({}^{2}b_{x}\right)\right]^{n} - \left({}^{2}s'\right)\left({}^{2}q_{x}\right) = 0$$
(2.91)

In y direction:

$$\left[\frac{{}^{2}B}{\left({}^{2}s'\right)^{2}}\frac{\partial}{\partial\alpha}\left({}^{2}\frac{y'}{{}^{2}s'}\right)\right]'' - \left[\left({}^{2}N_{a} - {}^{2}B\left({}^{2}\kappa\right)^{2}\right)\frac{{}^{2}y'}{{}^{2}s'} - {}^{2}B\left(\frac{{}^{2}s''}{\left({}^{2}s'\right)^{3}}\right)\frac{\partial}{\partial\alpha}\left({}^{2}\frac{y'}{{}^{2}s'}\right)\right]' - \left[{}^{2}T\left({}^{2}\kappa\right)\left({}^{2}b_{y}\right)\right]' - \left({}^{2}s'\right)\left({}^{2}q_{y}\right) = 0$$
(2.92)

In z direction:

$$\left[\frac{{}^{2}B}{\left(\frac{2}{s'}\right)^{2}}\frac{\partial}{\partial\alpha}\left(\frac{2}{s'}\right)\right]^{n} - \left[\left(\frac{2}{s}N_{a} - \frac{2}{s}B\left(\frac{2}{s}\kappa\right)^{2}\right)\frac{2}{s'} - \frac{2}{s}B\left(\frac{2}{s'}\right)^{3}\right]\frac{\partial}{\partial\alpha}\left(\frac{2}{s'}\right)^{3} - \left[\left(\frac{2}{s}\kappa\right)\left(\frac{2}{s}\kappa\right)\left(\frac{2}{s}\kappa\right)\right]^{2} - \left(\frac{2}{s}\kappa\right)\left(\frac{2}{s}\kappa\right)\left(\frac{2}{s}\kappa\right) - \left(\frac{2}{s}\kappa\right)\left(\frac{2}{s}\kappa\right)\left(\frac{2}{s}\kappa\right) = 0$$
(2.93)

In twisting rotation

$${}^{2}T' = {}^{2}s' \left[ m_{p} \left( {}^{2}J_{p} \right) \left( {}^{2}\ddot{\psi} \right) \right] \tag{2.94}$$

By using the differential geometry of space curve, equations (2.91)-(2.93) can be written in the vector form as

$$\left[\frac{{}^{2}B}{\left({}^{2}s'\right)^{2}}\frac{\partial}{\partial\alpha}\left({}^{2}\vec{r}'\right)\right]'' - \left[\left({}^{2}N_{a} - {}^{2}B\left({}^{2}\kappa\right)^{2}\right)\frac{{}^{2}\vec{r}'}{{}^{2}s'} - {}^{2}B\left(\frac{{}^{2}s''}{\left({}^{2}s'\right)^{3}}\right)\frac{\partial}{\partial\alpha}\left(\frac{{}^{2}\vec{r}'}{{}^{2}s'}\right)\right]''$$

$$-\left[\frac{^{2}T}{^{2}s'}\left(\frac{^{2}\vec{r}'}{^{2}s'}\times\frac{\partial}{\partial\alpha}\left(\frac{^{2}\vec{r}'}{^{2}s'}\right)\right)\right]'-\left(^{2}s'\right)\left(^{2}\vec{q}\right)=0$$
(2.95)

Note that

$$\frac{{}^{2}\vec{r}'}{{}^{2}s'} = \frac{{}^{2}x'}{{}^{2}s'}\hat{i} + \frac{{}^{2}y'}{{}^{2}s'}\hat{j} + \frac{{}^{2}z'}{{}^{2}s'}\hat{k}$$
 (2.96 a)

$$\frac{\partial}{\partial \alpha} \left( \frac{{}^{2}\vec{r}'}{{}^{2}s'} \right) = \frac{\partial}{\partial \alpha} \left( \frac{{}^{2}x'}{{}^{2}s'} \right) \hat{i} + \frac{\partial}{\partial \alpha} \left( \frac{{}^{2}y'}{{}^{2}s'} \right) \hat{j} + \frac{\partial}{\partial \alpha} \left( \frac{{}^{2}z'}{{}^{2}s'} \right) \hat{k}$$
 (2.96 b)

$$\left(\frac{{}^{2}\vec{r}'}{{}^{2}s'} \times \frac{\partial}{\partial \alpha} \left(\frac{{}^{2}\vec{r}'}{{}^{2}s'}\right)\right) = \left({}^{2}s'\right) \left({}^{2}\kappa\right) \left({}^{2}b_{x}\right) \hat{i} + \left({}^{2}s'\right) \left({}^{2}\kappa\right) \left({}^{2}b_{y}\right) \hat{j} + \left({}^{2}s'\right) \left({}^{2}\kappa\right) \left({}^{2}b_{y}\right) \hat{k} \qquad (2.96 c)$$

If  $\alpha = {}^2s$ , equations (2.94)-(2.95) become

$$^{2}T' = \left\lceil m_{p} \left( ^{2}J_{p} \right) \left( ^{2}\ddot{\psi} \right) \right\rceil \tag{2.97 a}$$

$$\left[{}^{2}B^{2}\bar{r}''\right]'' - \left[\left({}^{2}N_{a} - {}^{2}B\left({}^{2}\kappa\right)^{2}\right){}^{2}\bar{r}'\right]' - \left[{}^{2}T\left({}^{2}\bar{r}'\times{}^{2}\bar{r}''\right)\right]' - {}^{2}\bar{q} = 0$$
 (2.97 b)

which is compatible with the nonlinear dynamic equation given by Kokarakis and Bernitsas (1987).

#### 2.8 VECTORIAL FORMULATION

To validate equation (2.94)-(2.95), one has to use the relation between three orthogonal coordinate systems and two moment differential equations to eliminate shear forces. As a result, it is found that the six equilibrium equations are reduced to three equations and can be arranged in vectorial form as equation (2.95).

Figure 3. shows the riser element of the length  $d^2s$  in displaced state loaded by forces and couples in the cross-sectional principal axes system. Let  ${}^2\bar{R}$  be the vector of an internal force such that  ${}^2\bar{R} = {}^2R_1{}^2\hat{e}_1 + {}^2R_2{}^2\hat{e}_2 + {}^2R_3{}^2\hat{e}_3$  where  ${}^2R_1$  is an axial force,  ${}^2R_2$  and  ${}^2R_3$  are shear forces; let  ${}^2\bar{M}$  be the vector of an internal moment such that  ${}^2\bar{M} = {}^2M_1{}^2\hat{e}_1 + {}^2M_2{}^2\hat{e}_2 + {}^2M_3{}^2\hat{e}_3$  where  ${}^2M_1$  is a twisting moment,  ${}^2M_2$  and  ${}^2M_3$  are bending moments. The vector of an external load, i.e., current and wave force, effective weight, inertial force, is represented by  ${}^2\bar{q} = {}^2q_1{}^2\hat{e}_1 + {}^2q_2{}^2\hat{e}_2 + {}^2q_3{}^2\hat{e}_3$  and the vector of an external distributed moment is represented by  ${}^2\bar{m} = {}^2m_1{}^2\hat{e}_1 + {}^2m_2{}^2\hat{e}_2 + {}^2m_3{}^2\hat{e}_3$ .

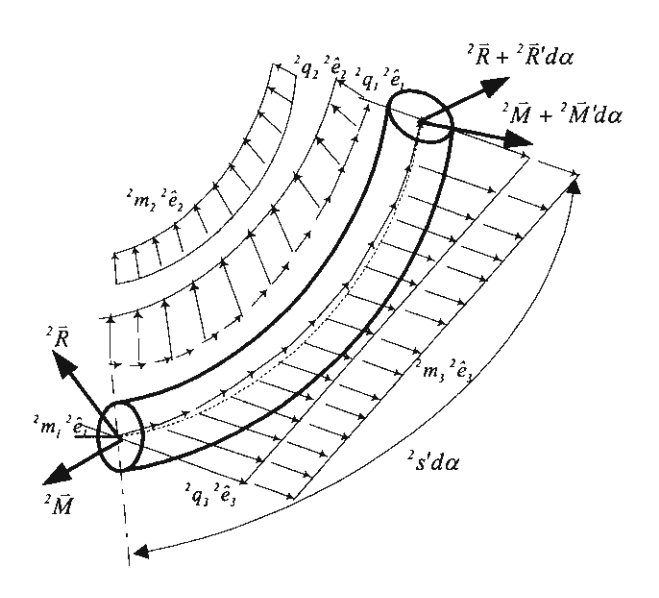


Figure 2.3 Riser differential segment.

Since the riser element is in equilibrium, therefore the sum of forces and the sum of moments equal to zero. Hence, the equilibrium equations in the crosssectional principal axes system are

$$\frac{{}^{2}R'_{1}}{{}^{2}s'} + {}^{2}R_{3}{}^{2}\omega_{2} - {}^{2}R_{2}{}^{2}\omega_{3} = -{}^{2}q_{1}$$
 (2.98 a)

$$\frac{{}^{2}R'_{2}}{{}^{2}s'} + {}^{2}R_{I}{}^{2}\omega_{3} - {}^{2}R_{3}{}^{2}\omega_{I} = -{}^{2}q_{2}$$
 (2.98 b)

$$\frac{{}^{2}R'_{3}}{{}^{2}S'} + {}^{2}R_{2}{}^{2}\omega_{1} - {}^{2}R_{1}{}^{2}\omega_{2} = -{}^{2}q_{3}$$
 (2.98 c)

$$\frac{{}^{2}M'_{I}}{{}^{2}S'} + {}^{2}M_{3}{}^{2}\omega_{2} - {}^{2}M_{2}{}^{2}\omega_{3} = -{}^{2}m_{I} + \left[m_{p}\left({}^{2}J_{p}\right)\left({}^{2}\ddot{\psi}\right)\right]$$
(2.98 d)

$$\frac{{}^{2}M_{2}'}{{}^{2}S'} + {}^{2}M_{1}{}^{2}\omega_{3} - {}^{2}M_{3}{}^{2}\omega_{1} = {}^{2}R_{3} - {}^{2}m_{2}$$
 (2.98 e)

$$\frac{{}^{2}M_{3}'}{{}^{2}s'} + {}^{2}M_{2}{}^{2}\omega_{1} - {}^{2}M_{1}{}^{2}\omega_{2} = -{}^{2}R_{2} - {}^{2}m_{3}$$
 (2.98 f)

It is worth noticing in this formulation that the external forces are assumed to act on the centerline of the riser, therefore the distributed external moments are equal to zero.

By coordinate transformation and shear force elimination, the components of internal force vector in fixed Cartesian coordinate can be derived and written in vectorial form as follows

$${}^{i}\bar{R} = \left[ {}^{i}N_{a} - {}^{i}B({}^{i}\kappa)^{2} \right)^{i}\frac{\vec{r}'}{{}^{i}s'} - {}^{i}B\left(\frac{{}^{i}s''}{\left({}^{i}s'\right)^{3}}\right) \frac{\partial}{\partial\alpha} \left(\frac{{}^{i}\vec{r}'}{{}^{i}s'}\right) \right] - \left[ \frac{{}^{i}B}{\left({}^{i}s'\right)^{2}} \frac{\partial}{\partial\alpha} \left(\frac{{}^{i}\vec{r}'}{{}^{i}s'}\right) \right]' + \left[ \frac{{}^{i}T}{{}^{i}s'} \left(\frac{{}^{i}\vec{r}'}{{}^{i}s'}\right) \frac{\partial}{\partial\alpha} \left(\frac{{}^{i}\vec{r}'}{{}^{i}s'}\right) \right]$$

$$(2.99)$$

Since, the summation of forces in fixed Cartesian coordinate and the summation of moments in tangential axis are

$${}^{2}\vec{R}' + {}^{2}s'({}^{2}\vec{q}') = 0$$
 (2.100 a)

$${}^{2}T' = {}^{2}s' \left[ m_{p} \left( {}^{2}J_{p} \right) \left( {}^{2}\ddot{\psi} \right) \right]$$
 (2.100 b)

therefore, it is confirmed that exact agreement is achieved among the vectorial formulation and the variational formulation.

## 2.9 NONLINEAR DYNAMIC AND LARGE AMPLITUDE VIBRATION MODELS

Based on the variational formulation, the governing equation describing nonlinear dynamics of the flexible marine riser have been achived in the four weak forms and in the one strong form. For the sake of generality in obtaining the finite element model, however, the strong form is used to generate the large amplitude vibration models. The governing equation in displacement-based strong form can be expressed as follows

$${}^{2}s'\left(m_{p}-m_{i}\right)\left\{\frac{\partial^{2}\left(^{2}\bar{r}\right)}{\partial t^{2}}\right\}+{}^{2}s'm_{p}\left\{\begin{pmatrix}0\\2J_{p}\right)\left(^{2}\bar{\psi}'\right)\right\}+{}^{2}s'm_{i}\left(\frac{2V_{i}}{2s'}\right)\left\{\frac{\partial^{2}\left(^{2}\bar{r}\right)}{\partial \alpha \partial t}\right\}$$

$$+\left[\frac{^{2}B}{\left(^{2}s'\right)^{2}}\left\{\frac{\partial}{\partial \alpha}\left(^{2}\frac{\bar{r}'}{2s'}\right)\right\}\right]^{"}-\left[\left(^{2}N_{a}-^{2}B\left(^{2}\kappa\right)^{2}\right)\left\{\frac{^{2}\bar{r}'}{^{2}s'}\right\}-^{2}B\left(\frac{^{2}s''}{^{2}s'}\right)\right\}\left\{\frac{\partial}{\partial \alpha}\left(^{2}\frac{\bar{r}'}{^{2}s'}\right)\right\}\right]^{'}$$

$$-\left[\frac{^{2}T}{^{2}s'}\left\{\left(\frac{^{2}\bar{r}'}{^{2}s'}\times\frac{\partial}{\partial \alpha}\left(^{2}\frac{\bar{r}'}{^{2}s'}\right)\right)\right\}+\left\{0\\^{2}T\right\}\right]^{'}$$

$$+^{2}s'm_{i}\left(\frac{V_{i}}{^{2}s'}\right)^{2}\left\{\frac{\partial^{2}\left(^{2}\bar{r}\right)}{\partial \alpha^{2}}\right\}+^{2}s'm_{i}\left[\frac{V_{i}V_{i}'}{\left(^{2}s'\right)^{2}}-\frac{V_{i}\left(^{2}s'\right)}{\left(^{2}s'\right)^{2}}-\frac{V_{i}^{2}\left(^{2}s''\right)}{\left(^{2}s'\right)^{3}}\right]\left\{\frac{\partial\left(^{2}\bar{r}\right)}{\partial \alpha}\right\}$$

$$=^{2}s'\left\{\frac{^{2}\bar{F}_{H}}{0}\right\}-^{2}s'^{2}w_{a}\hat{J}-^{2}s'm_{i}\left[\frac{\dot{V}_{i}}{^{2}s'}\right]\left\{\frac{\partial\left(^{2}\bar{r}\right)}{\partial \alpha}\right\}$$

$$=^{2}s'\left\{\frac{^{2}\bar{F}_{H}}{0}\right\}-^{2}s'^{2}w_{a}\hat{J}-^{2}s'm_{i}\left[\frac{\dot{V}_{i}}{^{2}s'}\right]\left\{\frac{\partial\left(^{2}\bar{r}\right)}{\partial \alpha}\right\}$$

$$=^{2}s'\left\{\frac{^{2}\bar{F}_{H}}{0}\right\}-^{2}s'^{2}w_{a}\hat{J}-^{2}s'm_{i}\left[\frac{\dot{V}_{i}}{^{2}s'}\right]\left\{\frac{\partial\left(^{2}\bar{r}\right)}{\partial \alpha}\right\}$$

By utilizing the differential geometry of a space curve, each term in equation (2.101 a) are expanded by

$$\begin{split} & {}^{2}s'(m_{p}+m_{i}) \begin{cases} \frac{\partial^{2}(^{2}\bar{r})}{\partial t^{2}} \\ 0 \end{cases} + {}^{2}s'm_{p} \begin{cases} 0 \\ (^{2}J_{p})(^{2}\bar{\psi}) \end{cases} \\ & = \begin{bmatrix} {}^{2}s'(m_{p}+m_{i}) & 0 & 0 & 0 \\ 0 & {}^{2}s'(m_{p}+m_{i}) & 0 & 0 \\ 0 & 0 & {}^{2}s'(m_{p}+m_{i}) & 0 \\ 0 & 0 & 0 & {}^{2}s'(m_{p}+m_{i}) & 0 \\ 0 & 0 & 0 & {}^{2}s'(m_{p}+m_{i}) & 0 \end{cases} \\ & = \begin{bmatrix} {}^{2}\frac{B}{3} & \partial \alpha \begin{pmatrix} {}^{2}\bar{r}' \\ {}^{2}\bar{s}' \end{pmatrix} = \frac{2}{3} & \left[ {}^{2}y')^{2} + {}^{2}(z')^{2} & {}^{2}-z'^{2}y' & {}^{2}-z'^{2}z' \\ {}^{2}z'' & {}^{2}z'' & {}^{2}z'' & {}^{2}z''^{2}z' \\ {}^{2}z'' & {}^{2}z'' & {}^{2}z''^{2}z' & {}^{2}z'^{2}z' \\ {}^{2}z'' & {}^{2}z'' & {}^{2}z''^{2}z' & {}^{2}z''^{2}z' \\ {}^{2}z'' & {}^{2}z'' & {}^{2}z''^{2}z' & {}^{2}z'^{2}z' \\ {}^{2}z'' & {}^{2}z'' & {}^{2}z''^{2}z' & {}^{2}z''^{2}z' \\ {}^{2}z'' & {}^{2}z'' & {}^{2}z''^{2}z' & {}^{2}z'^{2}z' \\ {}^{2}z'' & {}^{2}z'' & {}^{2}z'^{2}z' & {}^{2}z'^{2}z' \\ {}^{2}z'' & {}^{2}z'' & {}^{2}z''^{2}z' & {}^{2}z''^{2}z' \\ {}^{2}z'' & {}^{2}z'' & {}^{2}z'' & {}^{2}z'' \\ {}^{2}z'' & {}^{2}z'' & {}^{2}z''^{2}z' & {}^{2}z'^{2}z' \\ {}^{2}z'' & {}^{2}z'' & {}^{2}z'' & {}^{2}z'' \\ {}^{2}z'' & {}^{2}z'' & {}^{2}z''^{2}z' & {}^{2}z'^{2}z' \\ {}^{2}z'' & {}^{2}z'' & {}^{2}z'' & {}^{2}z'' & {}^{2}z'' \\ {}^{2}z'' & {}^{2}z'' & {}^{2}z'' & {}^{2}z'' & {}^{2}z'' \\ {}^{2}z'' & {}^{2}z'' & {}^{2}z'' & {}^{2}z'' & {}^{2}z'' \\ {}^{2}z'' & {}^{2}z'' & {}^{2}z'' & {}^{2}z'' & {}^{2}z'' \\ {}^{2}z'' & {}^{2}z'' & {}^{2}z'' & {}^{2}z'' & {}^{2}z'' \\ {}^{2}z'' & {}^{2}z'' & {}^{2}z'' & {}^{2}z'' & {}^{2}z'' \\ {}^{2}z'' & {}^{2}z'' & {}^{2}z'' & {}^{2}z'' & {}^{2}z'' \\ {}^{2}z'' & {}^{2}z'' & {}^{2}z'' & {}^{2}z'' & {}^{2}z'' & {}^{2}z'' \\ {}^{2}z'' & {}^{2}z'' & {}^{2}z'' & {}^{2}z'' & {}^{2}z'' & {}^{2}z'' \\ {}^{2}z'' & {}^{2}z'' \\ {}^{2}z'' & {}^{2}z$$

$$= \frac{m_{i}V_{i}^{2}}{\left(\frac{2}{s'}\right)^{3}} \begin{bmatrix} \left(\frac{2}{y'}\right)^{2} + \left(\frac{2}{z'}\right)^{2} & -\frac{2}{x'^{2}}y' & -\frac{2}{x'^{2}}z' \\ -\frac{2}{x'^{2}}y' & \left(\frac{2}{x'}\right)^{2} + \left(\frac{2}{z'}\right)^{2} & -\frac{2}{y'^{2}}z' \\ -\frac{2}{x'^{2}}z' & -\frac{2}{y'^{2}}z' & \left(\frac{2}{x'}\right)^{2} + \left(\frac{2}{y'}\right)^{2} \end{bmatrix} \begin{cases} \frac{2}{2}x'' \\ \frac{2}{2}z'' \end{bmatrix}$$

$$= \frac{2}{s'}m_{i}\left(\frac{V_{i}V_{i}'}{2s'}\right) \frac{\partial \left(\frac{2}{r}\right)}{\partial \alpha} = \frac{m_{i}V_{i}V'}{2s'} \begin{bmatrix} 1 & 0 & 0 \\ 0 & 1 & 0 \\ 0 & 0 & 1 \end{bmatrix} \begin{bmatrix} \frac{2}{x'} \\ \frac{2}{y'} \\ \frac{2}{z'} \end{bmatrix}$$

$$= \frac{m_{i}V_{i}}{\left(\frac{2}{s'}\right)^{2}} \begin{bmatrix} 2\left(\frac{2}{s'}\right)^{2} + \left(\frac{2}{s'}\right)^{2} - \frac{2}{x'^{2}}y' & -\frac{2}{x'^{2}}z' \\ -\frac{2}{x'^{2}}y' & 2\left(\frac{2}{s'}\right)^{2} + \left(\frac{2}{y'}\right)^{2} & -\frac{2}{y'^{2}}z' \\ -\frac{2}{x'^{2}}z' & -\frac{2}{y'^{2}}z' & \left(\frac{2}{s'}\right)^{2} + \left(\frac{2}{z'}\right)^{2} \end{bmatrix} \begin{cases} \frac{2}{x'} \\ \frac{2}{y'} \\ \frac{2}{z'} \end{cases}$$

$$= \frac{m_{i}V_{i}}{\left(\frac{2}{s'}\right)^{2}} \begin{bmatrix} 2\left(\frac{2}{s'}\right)^{2} + \left(\frac{2}{x'}\right)^{2} & -\frac{2}{x'^{2}}y' & -\frac{2}{x'^{2}}z' \\ -\frac{2}{x'^{2}}z' & -\frac{2}{y'^{2}}z' & \left(\frac{2}{s'}\right)^{2} + \left(\frac{2}{z'}\right)^{2} \end{bmatrix} \begin{cases} \frac{2}{s'} \\ \frac{2}{s'} \\ \frac{2}{s'} \end{cases}$$

$$= \frac{2}{s'}m_{i}\left(\frac{\dot{V}_{i}}{\left(\frac{2}{s'}\right)}\right) \frac{\partial \left(\frac{2}{r}\right)}{\partial \alpha} = \frac{2}{s'} \begin{cases} \frac{m_{i}\dot{V}_{i}\left(\frac{2}{s'}\right)}{\frac{2}{s'}} \\ \frac{m_{i}\dot{V}_{i}\left(\frac{2}{s'}\right)}{\frac{2}{s'}} \end{cases}$$

$$(2.102 i)$$

By substituting equations (2.32) and (2.102) into (2.101) together with some manipulation. The nonlinear dynamic, large amplitude model in the Cartesian coordinate system is obtained as

$$\begin{bmatrix}
\mathbf{M} & \mathbf{0} \\
\mathbf{0} & m_{p} \begin{pmatrix} {}^{2}s' \end{pmatrix} \begin{pmatrix} {}^{2}J_{p} \end{pmatrix} \end{bmatrix} \begin{Bmatrix} {}^{2}\ddot{r} \\ {}^{2}\ddot{\psi} \end{Bmatrix} + \begin{bmatrix} \mathbf{C} & \mathbf{0} \\ \mathbf{0} & \mathbf{0} \end{bmatrix} \begin{Bmatrix} {}^{2}\dot{r} \\ {}^{2}\psi \end{Bmatrix} + \begin{bmatrix} \mathbf{G} & \mathbf{0} \\ \mathbf{0} & \mathbf{0} \end{bmatrix} \begin{Bmatrix} {}^{2}\dot{r}' \\ {}^{2}\psi' \end{Bmatrix}$$

$$+ \begin{bmatrix}
 {}^{2}\mathbf{K} & \mathbf{0} \\
 {}^{1}\mathbf{I}^{2}\mathbf{K} & \mathbf{0} \\
 {}^{2}\psi'' \end{Bmatrix} + \begin{bmatrix}
 {}^{2}\mathbf{K} & \mathbf{0} \\
 {}^{2}\mathbf{I}^{2}\mathbf{K} \\
 {}^{2}\psi'' \end{Bmatrix} + \begin{bmatrix}
 {}^{2}\mathbf{K} & \mathbf{0} \\
 {}^{2}\mathbf{I}^{2}\mathbf{K} \\
 {}^{2}\psi'' \end{Bmatrix} + \begin{bmatrix}
 {}^{2}\mathbf{K} & \mathbf{0} \\
 {}^{2}\mathbf{I}^{2}\mathbf{K} \\
 {}^{2}\psi'' \end{Bmatrix} \end{bmatrix} \begin{pmatrix} {}^{2}\ddot{r}' \\ {}^{2}\psi'' \end{Bmatrix} + \begin{bmatrix}
 {}^{2}\mathbf{K} & \mathbf{0} \\
 {}^{2}\mathbf{I}^{2}\mathbf{K} \\
 {}^{2}\mathbf{I}^{2}\mathbf{K} \end{bmatrix} \begin{pmatrix} {}^{2}\ddot{r}' \\ {}^{2}\psi'' \end{Bmatrix} + \begin{bmatrix}
 {}^{2}\mathbf{K} & \mathbf{0} \\
 {}^{2}\mathbf{I}^{2}\mathbf{K} \\
 {}^{2}\mathbf{I}^{2}\mathbf{K} \end{bmatrix} \begin{pmatrix} {}^{2}\ddot{r}' \\ {}^{2}\psi'' \end{Bmatrix} + \begin{bmatrix}
 {}^{2}\mathbf{I}^{2}\mathbf{K} & \mathbf{0} \\
 {}^{2}\mathbf{I}^{2}\mathbf{K} \end{bmatrix} \begin{pmatrix} {}^{2}\ddot{r}' \\ {}^{2}\psi' \end{Bmatrix} = \begin{Bmatrix} {}^{2}\mathbf{I} \\
 {}^{2}\mathbf{I}^{2}\mathbf{I} \\
 {}^{2}\mathbf{I}^{2}\mathbf{I}^{2}\mathbf{I} \\
 {}^{2}\mathbf{I}^{$$

where the total mass matrix is

$$\mathbf{M} = {}^{2}s' \Big( m_{p} + m_{i} + C_{a}^{*} \Big) \begin{bmatrix} I & 0 & 0 \\ 0 & I & 0 \\ 0 & 0 & I \end{bmatrix}$$
 (2.104)

the hydrodynamic damping matrix is

$$\mathbf{C} = {}^{2}S' \begin{bmatrix} C_{eqx}^{*} & C_{eqxy}^{*} & C_{eqxz}^{*} \\ C_{eqxy}^{*} & C_{eqy}^{*} & C_{eqyz}^{*} \\ C_{eqxz}^{*} & C_{eqyz}^{*} & C_{eqz}^{*} \end{bmatrix}$$
(2.105)

the gyroscopic matrix is

$$\mathbf{G} = \frac{m_i V_i}{\binom{2}{s'}^2} \begin{bmatrix} 2\binom{2}{s'}^2 + \binom{2}{x'}^2 & -\frac{2}{x'}^2 y' & -\frac{2}{x'}^2 z' \\ -\frac{2}{x'}^2 y' & 2\binom{2}{s'}^2 + \binom{2}{y'}^2 & -\frac{2}{y'}^2 z' \\ -\frac{2}{x'}^2 z' & -\frac{2}{y'}^2 z' & \binom{2}{s'}^2 + \binom{2}{z'}^2 \end{bmatrix}$$
(2.106)

the torsion stiffness matrix is

$${}_{\mathbf{T}}^{2}\mathbf{K} = \begin{bmatrix} {}_{71}^{2}k_{11} & {}_{71}^{2}k_{12} & {}_{71}^{2}k_{13} & 0 \\ {}_{71}^{2}k_{12} & {}_{71}^{2}k_{22} & {}_{71}^{2}k_{23} & 0 \\ {}_{271}^{2}k_{13} & {}_{71}^{2}k_{23} & {}_{71}^{2}k_{33} & 0 \\ 0 & 0 & 0 & 0 \end{bmatrix} + \begin{bmatrix} 0 & 0 & 0 & {}_{72}^{2}k_{14} \\ 0 & 0 & 0 & {}_{72}^{2}k_{24} \\ 0 & 0 & 0 & {}_{72}^{2}k_{34} \\ 0 & 0 & 0 & {}_{72}^{2}k_{44} \end{bmatrix}$$
(2.107 a)

in which

$${}_{TI}^{2}k_{II} = -\frac{{}^{2}C({}^{2}s')^{6}}{({}^{2}\kappa)^{2}}({}^{2}y'{}^{2}z'' - {}^{2}z'{}^{2}y'')^{2}$$
(2.107 b)

$${}_{TI}^{2}k_{22} = -\frac{{}^{2}C({}^{2}s')^{6}}{({}^{2}\kappa)^{2}}({}^{2}z'{}^{2}x'' - {}^{2}x'{}^{2}z'')^{2}$$
(2.107 c)

$${}_{T_{I}}^{2}k_{33} = -\frac{{}^{2}C({}^{2}s')^{6}}{({}^{2}\kappa)^{2}}({}^{2}x'{}^{2}y'' - {}^{2}y'{}^{2}x'')^{2}$$
(2.107 d)

$${}_{T_{I}}^{2}k_{I2} = {}_{T}^{2}k_{2I} = -\frac{{}^{2}C({}^{2}s')^{6}}{({}^{2}\kappa)^{2}}({}^{2}y'{}^{2}z'' - {}^{2}z'{}^{2}y'')({}^{2}z'{}^{2}x'' - {}^{2}x'{}^{2}z'') \quad (2.107 e)$$

$${}_{T_{I}}^{2}k_{I3} = {}_{T}^{2}k_{3I} = -\frac{{}^{2}C({}^{2}s')^{6}}{({}^{2}\kappa)^{2}}({}^{2}y'{}^{2}z'' - {}^{2}z'{}^{2}y'')({}^{2}x'{}^{2}y'' - {}^{2}y'{}^{2}x'') \quad (2.107 \text{ f})$$

$${}_{T_{1}}^{2}k_{23} = {}_{T}^{2}k_{32} = -\frac{{}^{2}C({}^{2}s')^{6}}{({}^{2}\kappa)^{2}}({}^{2}z'{}^{2}x'' - {}^{2}x'{}^{2}z'')({}^{2}x'{}^{2}y'' - {}^{2}y'{}^{2}x'') \quad (2.107 \text{ g})$$

$${}_{T2}^{2}k_{14} = \frac{{}^{2}C}{\left({}^{2}s'\right)^{2}} \left[ \frac{\left({}^{2}y'\right)\left({}^{2}z''\right) - \left({}^{2}z'\right)\left({}^{2}y''\right)}{\left({}^{2}s'\right)^{2}} \right]$$
(2.107 h)

$${}_{T_2}^2 k_{24} = \frac{{}^2 C}{\left({}^2 s'\right)^2} \left[ \frac{\left({}^2 z'\right) \left({}^2 x''\right) - \left({}^2 x'\right) \left({}^2 z''\right)}{\left({}^2 s'\right)^2} \right]$$
(2.107 i)

$${}_{T2}^{2}k_{34} = \frac{{}^{2}C}{\left({}^{2}s'\right)^{2}} \left[ \frac{\left({}^{2}x'\right)\left({}^{2}y''\right) - \left({}^{2}y'\right)\left({}^{2}x''\right)}{\left({}^{2}s'\right)^{2}} \right]$$
(2.107 j)

$${}_{T2}^{2}k_{44} = {}^{2}C\left(\frac{{}^{2}\tau_{I}}{\left({}^{2}\psi'\right)} + \frac{1}{\left({}^{2}s'\right)}\right)$$
(2.107 k)

the bending stiffness matrices are

$${}_{b1}^{2}\mathbf{K} = \frac{{}^{2}B}{\left({}^{2}s'\right)^{5}} \begin{bmatrix} \left({}^{2}y'\right)^{2} + \left({}^{2}z'\right)^{2} & -{}^{2}x'{}^{2}y' & -{}^{2}x'{}^{2}z' \\ -{}^{2}x'{}^{2}y' & \left({}^{2}x'\right)^{2} + \left({}^{2}z'\right)^{2} & -{}^{2}y'{}^{2}z' \\ -{}^{2}x'{}^{2}z' & -{}^{2}y'{}^{2}z' & \left({}^{2}x'\right)^{2} + \left({}^{2}y'\right)^{2} \end{bmatrix}$$
(2.108 a)

$${}_{\mathbf{b}2}^{2}\mathbf{K} = \begin{bmatrix} {}_{b2}^{2}k_{11} & {}_{b2}^{2}k_{12} & {}_{b2}^{2}k_{13} \\ {}_{b2}^{2}k_{21} & {}_{b2}^{2}k_{22} & {}_{b2}^{2}k_{32} \\ {}_{b2}^{2}k_{13} & {}_{b2}^{2}k_{32} & {}_{b2}^{2}k_{33} \end{bmatrix}$$
(2.108 b)

in which

$${}_{b2}^{2}k_{II} = \frac{{}^{2}B}{\left({}^{2}s'\right)^{7}} \left[ 2\left({}^{2}x''^{2}y' - {}^{2}x'^{2}y''\right){}^{2}x'^{2}y' + 2\left({}^{2}x''^{2}z' - {}^{2}x'^{2}z''\right){}^{2}x'^{2}z'\right]$$
(2.108 c)

$${}_{b2}^{2}k_{22} = \frac{{}^{2}B}{\left({}^{2}s'\right)^{7}} \left[ 2\left({}^{2}y''^{2}z' - {}^{2}y'^{2}z''\right){}^{2}y'^{2}z' - 2\left({}^{2}x''^{2}y' - {}^{2}x'^{2}y''\right){}^{2}x'^{2}y'\right]$$
(2.108 d)

$$_{b2}^{2}k_{33} = \frac{^{2}B}{\left(^{2}s'\right)^{7}} \left[ -2\left(^{2}x''^{2}z' - ^{2}x'^{2}z''\right)^{2}x'^{2}z' - 2\left(^{2}y''^{2}z' - ^{2}y'^{2}z''\right)^{2}y'^{2}z' \right]$$
 (2.108 e)

$${}_{b2}^{2}k_{12} = \frac{{}^{2}B}{\left({}^{2}s'\right)^{7}} \left[ \left({}^{2}x''^{2}y' - {}^{2}x'^{2}y''\right) \left(\left({}^{2}y'\right)^{2} - \left({}^{2}x'\right)^{2}\right) + \left({}^{2}y''^{2}z' - {}^{2}y'^{2}z''\right)^{2}x'^{2}z'\right]$$

$$+ \left( {}^{2}x''^{2}z' - {}^{2}x'^{2}z'' \right) {}^{2}y'^{2}z' \right]$$

$$+ \left( {}^{2}x''^{2}z' - {}^{2}x'^{2}z'' \right) {}^{2}y'^{2}z' \right]$$

$$+ \left( {}^{2}x''^{2}z' - {}^{2}x'^{2}z'' \right) \left( \left( {}^{2}z' \right)^{2} - \left( {}^{2}x' \right)^{2} \right) - \left( {}^{2}y''^{2}z' - {}^{2}y'^{2}z'' \right) {}^{2}x'^{2}y'$$

$$+ \left( {}^{2}x''^{2}y' - {}^{2}x'^{2}y'' \right) {}^{2}y'^{2}z' \right]$$

$$+ \left( {}^{2}x''^{2}y' - {}^{2}x'^{2}y'' \right) {}^{2}y'^{2}z' \right]$$

$$+ \left( {}^{2}x''^{2}y' - {}^{2}x'^{2}y'' \right) {}^{2}y'^{2}z' \right]$$

$$+ \left( {}^{2}x''^{2}z' - {}^{2}x'^{2}z'' \right) {}^{2}x'^{2}z'$$

$$- \left( {}^{2}x''^{2}y' - {}^{2}x'^{2}y'' \right) {}^{2}x'^{2}z' \right]$$

$$+ \left( {}^{2}x''^{2}z' - {}^{2}x'^{2}z'' \right) {}^{2}x'^{2}z'$$

$$+ \left( {}^{2}x''^{2}y' - {}^{2}x'^{2}y'' \right) {}^{2}x'^{2}z' \right]$$

$$+ \left( {}^{2}x''^{2}y' - {}^{2}x'^{2}y'' \right) {}^{2}x'^{2}z'$$

$$+ \left( {}^{2}x''^{2}y' - {}^{2}x'^{2}y'' \right) {}^{2}x'^{2}z' \right]$$

$$+ \left( {}^{2}x''^{2}y' - {}^{2}x'^{2}y'' \right) {}^{2}x'^{2}z'$$

the axial stiffness matrices are

$${}_{NI}^{2}\mathbf{K} = \frac{\left({}^{2}N'_{a} - m_{i}V_{i}^{2}\right)}{\left({}^{2}s'\right)^{3}} \begin{bmatrix} -\left(\left({}^{2}y'\right)^{2} + \left({}^{2}z'\right)^{2}\right) & {}^{2}x'^{2}y' & {}^{2}x'^{2}z' \\ & {}^{2}x'^{2}y' & -\left(\left({}^{2}x'\right)^{2} + \left({}^{2}z'\right)^{2}\right) & {}^{2}y'^{2}z' \\ & {}^{2}x'^{2}z' & {}^{2}y'^{2}z' & -\left(\left({}^{2}y'\right)^{2} + \left({}^{2}x'\right)^{2}\right) \end{bmatrix}$$

$$-\left({}^{2}N'_{a} - m_{i}V_{i}V'_{i}\right) \begin{bmatrix} 1 & 0 & 0 \end{bmatrix}$$

$$(2.109)$$

$${}_{N2}^{2}\mathbf{K} = \frac{-\binom{2}{N_{a}'} - m_{i}V_{i}V_{i}'}{\binom{2}{S'}} \begin{bmatrix} I & 0 & 0 \\ 0 & I & 0 \\ 0 & 0 & I \end{bmatrix}$$
(2.110)

$$\frac{2\bar{\mathbf{f}}}{} = {}^{2}S' \left\{ C_{M}^{*}\dot{V}_{Hx} + C_{Dx}^{*}V_{Hx}^{2} + 2C_{Dxyz}^{*}V_{Hx}V_{Hy} + 2C_{Dxyz}^{*}V_{Hx}V_{Hz} \right.$$

$$\frac{2\bar{\mathbf{f}}}{} = {}^{2}S' \left\{ C_{M}^{*}\dot{V}_{Hy} + C_{Dy}^{*}V_{Hy}^{2} + 2C_{Dxyz}^{*}V_{Hx}V_{Hy} + 2C_{Dxyz}^{*}V_{Hx}V_{Hz} \right.$$

$$\frac{2\bar{\mathbf{f}}}{} = {}^{2}S' \left\{ C_{M}^{*}\dot{V}_{Hy} + C_{Dy}^{*}V_{Hy}^{2} + 2C_{Dxyz}^{*}V_{Hx}V_{Hy} + 2C_{Dxyz}^{*}V_{Hx}V_{Hz} \right.$$

$$\frac{2\bar{\mathbf{f}}}{} = {}^{2}S' \left\{ C_{M}^{*}\dot{V}_{Hy} + C_{Dy}^{*}V_{Hy}^{2} + 2C_{Dxyz}^{*}V_{Hx}V_{Hz} \right.$$

$$\frac{2\bar{\mathbf{f}}}{} = {}^{2}S' \left\{ C_{M}^{*}\dot{V}_{Hy} + C_{Dy}^{*}V_{Hx}V_{Hy} + 2C_{Dxyz}^{*}V_{Hx}V_{Hz} \right.$$

$$\frac{2\bar{\mathbf{f}}}{} = {}^{2}S' \left\{ C_{M}^{*}\dot{V}_{Hy}V_{Hz} + C_{Dxyz}^{*}V_{Hx}V_{Hy} + 2C_{Dxyz}^{*}V_{Hx}V_{Hz} - m_{i}\dot{V}_{i}\left(\frac{2\chi'}{2S'}\right) \right.$$

$$\frac{2\bar{\mathbf{f}}}{} = {}^{2}S' \left\{ C_{M}^{*}\dot{V}_{Hy}V_{Hz} + C_{Dxyz}^{*}V_{Hy}V_{Hz} + C_{Dxyz}^{*}V_{Hy}V_{Hz} - m_{i}\dot{V}_{i}\left(\frac{2\chi'}{2S'}\right) \right.$$

$$\frac{2\bar{\mathbf{f}}}{} = {}^{2}S' \left\{ C_{M}^{*}\dot{V}_{Hy}V_{Hz} + C_{Dxyz}^{*}V_{Hx}V_{Hy} + 2C_{Dxyz}^{*}V_{Hx}V_{Hz} - m_{i}\dot{V}_{i}\left(\frac{2\chi'}{2S'}\right) \right.$$

$$\frac{2\bar{\mathbf{f}}}{} = {}^{2}S' \left\{ C_{M}^{*}\dot{V}_{Hy}V_{Hz} + C_{Dxyz}^{*}V_{Hx}V_{Hy} + 2C_{Dxyz}^{*}V_{Hx}V_{Hz} - m_{i}\dot{V}_{i}\left(\frac{2\chi'}{2S'}\right) \right.$$

$$\frac{2\bar{\mathbf{f}}}{} = {}^{2}S' \left[ C_{M}^{*}\dot{V}_{Hy}V_{Hz} + C_{Dxyz}^{*}V_{Hx}V_{Hy} + 2C_{Dxyz}^{*}V_{Hx}V_{Hz} - m_{i}\dot{V}_{i}\left(\frac{2\chi'}{2S'}\right) \right.$$

$$\frac{2\bar{\mathbf{f}}}{} = {}^{2}S' \left[ C_{M}^{*}\dot{V}_{Hy}V_{Hz} + C_{Dxyz}^{*}V_{Hx}V_{Hy} + 2C_{Dxyz}^{*}V_{Hx}V_{Hz} - m_{i}\dot{V}_{i}\left(\frac{2\chi'}{2S'}\right) \right.$$

$$\frac{2\bar{\mathbf{f}}}{} = {}^{2}S' \left[ C_{M}^{*}\dot{V}_{Hy}V_{Hz} + C_{Dxyz}^{*}V_{Hx}V_{Hy} + 2C_{Dxyz}^{*}V_{Hx}V_{Hz} + C_{Dxyz}^{*}V_{Hx}V_{Hz} - m_{i}\dot{V}_{i}\left(\frac{2\chi'}{2S'}\right) \right.$$

$$\frac{2\bar{\mathbf{f}}}{} = {}^{2}S' \left[ C_{M}^{*}\dot{V}_{Hy}V_{Hz} + C_{Dxyz}^{*}V_{Hx}V_{Hy} + 2C_{Dxyz}^{*}V_{Hx}V_{Hz} + C_{Dxyz}^{*}V_{Hx}V_{Hz} + C_{Dxyz}^{*}V_{Hx}V_{Hz} \right.$$

$$\frac{2\bar{\mathbf{f}}}{} = {}^{2}S' \left[ C_{M}^{*}\dot{V}_{Hy}V_{Hz} + C_{Dxyz}^{*}V_{Hx}V_{Hz} + C_{Dxyz}^{*}V_{Hx}V_{Hz} + C_{Dxyz}^{*}V_{Hx}V_{Hz} \right]$$

$$\frac{2\bar{\mathbf{f}}}{} = {}^{2}S' \left[ C_{M}^{*}\dot{V}_{Hy}V_{Hz} + C_{Dxyz}^{*}V_{Hx}V$$

.

### 2.10 NONLINEAR STATIC EQUILIBRIUM MODEL

The nonlinear static model is obtained by eliminating the time-dependent terms in the nonlinear dynamic equation (2.102) and replacing the variables at the displaced state by ones at the equilibrium state. Therefore, the nonlinear static model can be expressed as follows.

$$+\left[\begin{bmatrix} {}_{11}^{l}\mathbf{K} & \mathbf{0} \\ \mathbf{0} & \mathbf{0} \end{bmatrix} \begin{Bmatrix} {}_{1}\vec{r}'' \\ {}_{1}\psi''' \end{Bmatrix} + \begin{bmatrix} \mathbf{0} & {}_{12}^{l}k_{14} \\ 0 & {}_{12}^{l}k_{24} \\ {}_{12}^{l}k_{34} \\ 0 & 0 & {}_{12}^{l}k_{44} \end{bmatrix} \begin{Bmatrix} {}_{1}\vec{r}' \\ {}_{1}\psi' \end{Bmatrix} \right] + \left[\begin{bmatrix} {}_{\mathbf{b}_{1}}^{l}\mathbf{K} & \mathbf{0} \\ \mathbf{0} & \mathbf{0} \end{bmatrix} \begin{Bmatrix} {}_{1}\vec{r}'' \\ {}_{1}\psi'' \end{Bmatrix} \right] + \left[\begin{bmatrix} {}_{\mathbf{b}_{1}}^{l}\mathbf{K} & \mathbf{0} \\ \mathbf{0} & \mathbf{0} \end{bmatrix} \begin{Bmatrix} {}_{1}\vec{r}'' \\ {}_{1}\psi'' \end{Bmatrix} \right] + \left[\begin{bmatrix} {}_{\mathbf{b}_{1}}^{l}\mathbf{K} & \mathbf{0} \\ \mathbf{0} & \mathbf{0} \end{bmatrix} \begin{Bmatrix} {}_{1}\vec{r}' \\ {}_{1}\psi'' \end{Bmatrix} + \left[\begin{bmatrix} {}_{\mathbf{b}_{1}}^{l}\mathbf{K} & \mathbf{0} \\ \mathbf{0} & \mathbf{0} \end{bmatrix} \begin{Bmatrix} {}_{1}\vec{r}' \\ {}_{1}\psi'' \end{Bmatrix} = \begin{Bmatrix} {}_{1}\vec{\mathbf{f}} \\ \mathbf{0} \end{Bmatrix}$$

$$(2.112)$$

the torsion stiffness matrix is

$${}_{\mathbf{T}}^{I}\mathbf{K} = \begin{bmatrix} {}_{1}{}^{I}k_{11} & {}_{1}{}^{I}k_{12} & {}_{1}{}^{I}k_{13} & 0 \\ {}_{1}{}^{I}k_{12} & {}_{1}{}^{I}k_{22} & {}_{1}{}^{I}k_{23} & 0 \\ {}_{1}{}^{I}k_{13} & {}_{1}{}^{I}k_{23} & {}_{1}{}^{I}k_{33} & 0 \\ 0 & 0 & 0 & 0 \end{bmatrix} + \begin{bmatrix} 0 & 0 & 0 & {}_{1}{}^{I}k_{14} \\ 0 & 0 & 0 & {}_{1}{}^{I}k_{24} \\ 0 & 0 & 0 & {}_{1}{}^{I}k_{24} \\ 0 & 0 & 0 & {}_{1}{}^{I}k_{34} \\ 0 & 0 & 0 & {}_{1}{}^{I}k_{34} \end{bmatrix}$$
 (2.113 a)

in which

 ${}_{T}^{I}k_{II} = -\frac{{}^{I}C({}^{I}s')^{6}}{({}^{I}\kappa)^{2}}({}^{I}y'{}^{I}z'' - {}^{I}z'{}^{I}y'')^{2}$  (2.113 b)

$${}_{T}^{I}k_{22} = -\frac{{}^{I}C({}^{I}s')^{6}}{({}^{I}\kappa)^{2}}({}^{I}z'{}^{I}x'' - {}^{I}x'{}^{I}z'')^{2}$$
(2.113 c)

$${}_{T}^{I}k_{33} = -\frac{{}^{I}C({}^{I}s')^{6}}{({}^{I}\kappa)^{2}}({}^{I}x'{}^{I}y'' - {}^{I}y'{}^{I}x'')^{2}$$
 (2.113 d)

$${}_{T}^{l}k_{l2} = {}_{T}^{l}k_{2l} = -\frac{{}^{l}C({}^{l}s')^{6}}{({}^{l}\kappa)^{2}}({}^{l}y'{}^{l}z'' - {}^{l}z'{}^{l}y'')({}^{l}z'{}^{l}x'' - {}^{l}x'{}^{l}z'') \qquad (2.113 e)$$

$${}_{T}^{l}k_{l3} = {}_{T}^{l}k_{3l} = -\frac{{}^{l}C({}^{l}s')^{6}}{({}^{l}\kappa)^{2}}({}^{l}y'{}^{l}z'' - {}^{l}z'{}^{l}y'')({}^{l}x'{}^{l}y'' - {}^{l}y'{}^{l}x'') \qquad (2.113 f)$$

$${}_{T}^{l}k_{23} = {}_{T}^{l}k_{32} = -\frac{{}_{C}^{l}({}_{s}^{l})^{6}}{({}_{K}^{l})^{2}}({}_{z}^{l}x'' - {}_{x}^{l}x'' z'')({}_{x}^{l}x'' y'' - {}_{y}^{l}x'') \qquad (2.113 g)$$

$${}_{T_{2}}{}^{J}k_{J4} = \frac{{}^{J}C}{\left({}^{J}s'\right)^{2}} \left[ \frac{\left({}^{J}y'\right)\left({}^{J}z''\right) - \left({}^{J}z'\right)\left({}^{J}y''\right)}{\left({}^{J}s'\right)^{2}} \right]$$
(2.113 h)

$${}_{T_{2}}{}^{I}k_{24} = \frac{{}^{I}C}{\left({}^{I}s'\right)^{2}} \left[ \frac{\left({}^{I}z'\right)\left({}^{I}x''\right) - \left({}^{I}x'\right)\left({}^{I}z''\right)}{\left({}^{I}s'\right)^{2}} \right]$$
(2.113 i)

$${}_{T_{2}}{}^{l}k_{34} = \frac{{}^{l}C}{\left({}^{l}s'\right)^{2}} \left[ \frac{\left({}^{l}x'\right)\left({}^{l}y''\right) - \left({}^{l}y'\right)\left({}^{l}x''\right)}{\left({}^{l}s'\right)^{2}} \right]$$
(2.113 j)

$$T_{2}^{I}k_{44} = {}^{I}C\left(\frac{{}^{I}\tau_{I}}{\left({}^{I}\psi'\right)} + \frac{I}{\left({}^{I}s'\right)}\right)$$
 (2.113 k)

the bending stiffness matrices are

$${}_{\mathbf{b}\mathbf{i}}^{I}\mathbf{K} = \frac{{}^{I}B}{\left({}^{I}s'\right)^{5}} \begin{bmatrix} \left({}^{I}y'\right)^{2} + \left({}^{I}z'\right)^{2} & -{}^{I}x'{}^{I}y' & -{}^{I}x'{}^{I}z' \\ -{}^{I}x'{}^{I}y' & \left({}^{I}x'\right)^{2} + \left({}^{I}z'\right)^{2} & -{}^{I}y'{}^{I}z' \\ -{}^{I}x'{}^{I}z' & -{}^{I}y'{}^{I}z' & \left({}^{I}x'\right)^{2} + \left({}^{I}y'\right)^{2} \end{bmatrix} (2.114 \text{ a})$$

$${}_{\mathbf{b2}}^{I}\mathbf{K} = \begin{bmatrix} {}_{b2}^{I}k_{1l} & {}_{b2}^{I}k_{12} & {}_{b2}^{I}k_{13} \\ {}_{b2}^{I}k_{2l} & {}_{b2}^{I}k_{22} & {}_{b2}^{I}k_{32} \\ {}_{b2}^{I}k_{13} & {}_{b2}^{I}k_{32} & {}_{b2}^{I}k_{33} \end{bmatrix}$$
(2.114 b)

in which

$${}_{b2}{}^{l}k_{II} = \frac{{}^{l}B}{\left({}^{l}s'\right)^{7}} \left[ 2\left({}^{l}x''^{I}y' - {}^{l}x'^{I}y''\right){}^{l}x'^{I}y' + 2\left({}^{l}x''^{I}z' - {}^{l}x'^{I}z''\right){}^{l}x'^{I}z'\right]$$
(2.114 c)

$${}_{b2}{}^{l}k_{22} = \frac{{}^{l}B}{\left({}^{l}s'\right)^{7}} \left[ 2\left({}^{l}y'''z' - {}^{l}y''z''\right){}^{l}y'{}^{l}z' - 2\left({}^{l}x'''y' - {}^{l}x''^{l}y''\right){}^{l}x'{}^{l}y'\right]$$
(2.114 d)

$${}_{b2}{}^{l}k_{33} = \frac{{}^{l}B}{\left({}^{l}s'\right)^{2}} \left[ -2\left({}^{l}x''^{l}z' - {}^{l}x'^{l}z''\right){}^{l}x'^{l}z' - 2\left({}^{l}y''^{l}z' - {}^{l}y'^{l}z''\right){}^{l}y'^{l}z'\right]$$
(2.114 e)

$${}_{b2}{}^{I}k_{I2} = \frac{{}^{I}B}{\left({}^{I}s'\right)^{7}} \left[ \left({}^{I}x''^{I}y' - {}^{I}x'^{I}y''\right) \left(\left({}^{I}y'\right)^{2} - \left({}^{I}x'\right)^{2}\right) + \left({}^{I}y''^{I}z' - {}^{I}y'^{I}z''\right) {}^{I}x'^{I}z' + \left({}^{I}x''^{I}z' - {}^{I}x'^{I}z''\right) {}^{I}y'^{I}z'\right]$$

$$(2.114 f)$$

$${}_{b2}{}^{l}k_{l3} = \frac{{}^{l}B}{\left({}^{l}s'\right)^{7}} \left[ \left({}^{l}x'''^{l}z' - {}^{l}x'^{l}z''\right) \left(\left({}^{l}z'\right)^{2} - \left({}^{l}x'\right)^{2}\right) - \left({}^{l}y''^{l}z' - {}^{l}y'^{l}z''\right){}^{l}x'^{l}y'\right]$$

$$+ \left( {}^{I}x''^{I}y' - {}^{I}x'^{I}y'' \right) {}^{I}y'^{I}z' \right]$$

$$= \frac{{}^{I}B}{\left( {}^{I}s' \right)^{2}} \left[ \left( {}^{I}y''^{I}z' - {}^{I}y'^{I}z'' \right) \left( \left( {}^{I}z' \right)^{2} - \left( {}^{I}y' \right)^{2} \right) - \left( {}^{I}x''^{I}z' - {}^{I}x'^{I}z'' \right) {}^{I}x'^{I}y' \right]$$

$$- \left( {}^{I}x''^{I}y' - {}^{I}x'^{I}y'' \right) {}^{I}x'^{I}z' \right]$$
(2.114 h)

the axial stiffness matrices are

$$\mathbf{N}_{\mathbf{I}}^{I}\mathbf{K} = \frac{\left({}^{I}N_{a}^{\prime} - m_{i}V_{i}^{2}\right)}{\left({}^{\prime}s^{\prime}\right)^{3}} \begin{bmatrix} -\left(\left({}^{\prime}y^{\prime}\right)^{2} + \left({}^{\prime}z^{\prime}\right)^{2}\right) & {}^{I}x^{\prime I}y^{\prime} & {}^{I}x^{\prime I}z^{\prime} \\ {}^{I}x^{\prime I}y^{\prime} & -\left(\left({}^{I}x^{\prime}\right)^{2} + \left({}^{I}z^{\prime}\right)^{2}\right) & {}^{I}y^{\prime I}z^{\prime} \\ {}^{I}x^{\prime I}z^{\prime} & {}^{I}y^{\prime I}z^{\prime} & -\left(\left({}^{I}y^{\prime}\right)^{2} + \left({}^{I}x^{\prime}\right)^{2}\right) \end{bmatrix} \tag{2.115}$$

$$\mathbf{N}_{\mathbf{I}}^{I}\mathbf{K} = \frac{-\left({}^{I}N_{a}^{\prime} - m_{i}V_{i}V_{i}^{\prime}\right)}{{}^{I}s^{\prime}} \begin{bmatrix} I & 0 & 0 \\ 0 & I & 0 \\ 0 & 0 & I \end{bmatrix} \tag{2.116}$$

$$\mathbf{I}_{\mathbf{I}}^{I}\mathbf{f} = {}^{I}s^{\prime} \begin{cases} {}^{I}C_{bx}^{*} {}^{I}V_{a}^{2} + 2{}^{I}C_{bxy}^{*} {}^{I}V_{Hx} {}^{I}V_{Hy} + 2{}^{I}C_{bxy}^{*} {}^{I}V_{Hx} {}^{I}V_{Hz} \\ {}^{I}C_{by}^{*} {}^{I}V_{by}^{2} + 2{}^{I}C_{bxy}^{*} {}^{I}V_{Hx} {}^{I}V_{Hy} + 2{}^{I}C_{bxy}^{*} {}^{I}V_{Hx} {}^{I}V_{Hz} \\ {}^{I}C_{bx}^{*} {}^{I}V_{By}^{2} + 2{}^{I}C_{bxy}^{*} {}^{I}V_{Hx} {}^{I}V_{Hy} + 2{}^{I}C_{bxy}^{*} {}^{I}V_{Hx} {}^{I}V_{Hz} \\ {}^{I}C_{bx}^{*} {}^{I}V_{Hy}^{2} {}^{I}V_{Hy} + 2{}^{I}C_{bxy}^{*} {}^{I}V_{Hx} {}^{I}V_{Hz} \\ {}^{I}V_{hy}^{2} {}^{I}V_{Hz} + {}^{I}C_{bxy}^{*} {}^{I}V_{Hz} + {}^{I}C_{bxy}^{*} {}^{I}V_{Hz}^{2} \\ {}^{I}V_{by}^{2} {}^{I}V_{Hz} + {}^{I}C_{bxy}^{*} {}^{I}V_{Hz}^{2} + {}^{I}C_{bxy}^{*} {}^{I}V_{Hz}^{2} - {}^{I}V_{a} \\ {}^{I}V_{hy}^{2} {}^{I}V_{Hz} + {}^{I}C_{bxy}^{*} {}^{I}V_{Hz}^{2} + {}^{I}C_{bxz}^{*} {}^{I}V_{Hz}^{2} \\ {}^{I}V_{hy}^{2} {}^{I}V_{Hz} + {}^{I}C_{bxz}^{*} {}^{I}V_{Hz}^{2} + {}^{I}C_{bxz}^{*} {}^{I}V_{Hy}^{2} \\ {}^{I}V_{Hz}^{2} + {}^{I}C_{bxz}^{*} {}^{I}V_{Hy}^{2} \\ {}^{I}V_{Hz}^{2} + {}^{I}C_{bxz}^{*} {}^{I}V_{Hy}^{2} + {}^{I}C_{bxz}^{*} {}^{I}V_{Hy}^{2} \\ {}^{I}V_{Hz}^{2} + {}^{I}C_{bxz}^{*} {}^{I}V_{Hy}^{2} + {}^{I}C_{bxz}^{*} {}^{I}V_{Hy}^{2} \\ {}^{I}V_{Hz}^{2} + {}^{I}C_{bxz}^{*} {}^{I}V_{Hy}^{2} \\ {}^{I}V$$

## 2.11 CHOICES OF THE INDEPENDENT VARIABLE $\alpha$

One salient feature of the large strain formulations presented in this work is that the independent variable  $\alpha$  used in the formulations provides flexibility in the choice of parameters defining elastic curves. The formulations therefore allow users to select the independent variable that is most efficient for their own problem solution. For example, analysis of flexible marine risers as shown in Figure 2.1, has at least four alternatives for the independent variable  $\alpha$  such as the vertical coordinate y, the in-plane offset distance x, the out-of-plane offset distance z, and the arc length s.

The advantage of using  $\alpha = y$  is that the total water depth or the boundary condition is known initially. While using  $\alpha = x$  or  $\alpha = z$  the boundary condition is known if the offset at the top end of the riser can be assumed to be static, and is unknown if the offset is dynamic. If one uses  $\alpha = s$ , the boundary condition is always unknown, because the total arc-length changes after deformation. The problem for which the boundary condition is unknown, becomes much more difficult, and requires specific treatment.

However, the disadvantage of using  $\alpha = y$  is that if elastic curves after large displacements form like the U-shape or the semi U-shape as shown in Figures 1 (b) and 1(c), the vertical position is no longer a one to one function for all points on the elastic curves. Consequently,  $\alpha = y$  is not an effective choice in this case. Likewise, using  $\alpha = x$  or  $\alpha = z$  encounter the same difficulty when the elastic curves after large displacements develop akin to the C-shape or the semi C-shape. In these troublesome cases, using  $\alpha = s$  becomes the best way, because arc-length is an intrinsic property, and thus is always a one to one function for all points of the elastic curves.

Therefore for flexible marine risers which do not face the problem of elastic curves having a U-shape, such as the high-tensioned risers, using  $\alpha = y$  is sufficient. However, if the risers confront the problem that occurs in the case of low-tensioned risers,  $\alpha = s$  should be employed. It should be noted that in addition to the four alternatives of  $\alpha$  as exemplified earlier, there are still other choices of  $\alpha$  such as the span length, the rotational angle, and so on, which may be employed if efficient.

# 2.12 IMPLEMENTATION OF THE MODEL FORMULATION TO PRACTICAL ENGINEERING PROBLEMS

The present formulations are applicable to large strain analysis not only of flexible marine risers, but also of any kind of engineering structures, which may have the elastica's behavior. The examples of these are listed as follows.

(a) Onshore pipes. The effect of external fluid would be excluded from the present models.

- (b) Submerged pipes. The hydrodynamic pressure effect of external fluid would be excluded.
- (c) Marine cables. Bending rigidity, Torsion rigidity and influence of internal fluid would be excluded.
- (d) Submerged cables. Bending rigidity, Torsion rigidity, influence of internal fluid, and hydrodynamic pressure effect of external fluid would be excluded from the present models.
- (e) Onshore cables and strings. Bending rigidity, Torsion rigidity, and influences of internal and external fluids would be excluded from the present models.
- (g) Elastic rods, long columns, and long beams. Influences of external and internal fluids would be excluded from the present models.

Even though the present models are intended for engineering structures with environment-induced initial curvatures, the models can still be extended to the structures with man-made initial curvatures such as curved beams and arches by considering  $\vec{k} \neq 0$  in application of the extensible elastica theory developed in this study.

### 3. SOLUTION METHODS

In this chapter, the updated Lagrangian descriptor (ULD) is employed for describing the nonlinear behaviors of the riser, and the independent variable  $\alpha = {}^{I}y$  is adopted. For the 3-D nonlinear static analysis, the weak formulation  $\delta^{I}\pi = 0$  is derived and solved by the hybrid finite element method as will be elaborated in section 3.1. For the 2-D dynamic analysis, the ordinary differential equations of motion are derived from the weak formulation  $\delta^{2}\pi = 0$  by the finite element method as will be shown in section 3.2. Based on the state-space formulation obtained from section 3.2, the natural frequency analysis and the time history analysis of the nonlinear vibrations will be carried out in sections 3.3 and 3.4, respectively.

# 3.1 THREE-DIMENSIONAL NONLINEAR STATIC ANALYSIS VIA THE HYBRID FINITE ELEMENT METHOD

The hybrid finite element method herein refers to the finite element solution of the weak formulation that is mixed with the strong formulation. One may question why this method is essential for the nonlinear static analysis of the marine riser. The answer is as follows. For the extensible analysis of most structures, the static axial strain in the weak formulation is determined from the strain-displacement relation such as

$${}^{I}\varepsilon = (d^{I}s - d^{o}s)/d^{I}s. \tag{3.1}$$

However, for extensible marine risers with large displacements this approach may not be applicable, because in practices, marine risers do not have the undeformed configuration as for reference. In other words, for marine risers  $d^{\circ}s$  is nonexistence for use in equation (3.1). The equilibrium state is the only initial state or the first state of marine risers, which is unknown initially, while the undeformed state is the ideal state, which never appears in the real situation. The way to solve this problem is to establish the static axial strain from the constitutive equation

$${}^{l}\varepsilon = {}^{l}N_{a} / E^{l}A_{p}, \qquad (3.2)$$

where the apparent axial force  ${}^{I}N_{a}$  is determined from the equilibrium equations. This approach is called the hybrid method (O'Brien and Mcnamara, 1989).

It should be noted that this problem would not be encountered in the dynamic analysis of the marine riser, because the dynamic axial strain can be determined from the strain-displacement relation

$$\varepsilon = (d^2s - d^1s)/d^1s, \qquad (3.3)$$

where the reference configuration d's in equation (3.3) refers to the equilibrium configuration, which is known from static analysis. Therefore, the hybrid method is not needed for dynamic analysis.

In section 2.7, there are at least four forms of the weak variational formulations to be used. In this study, the second weak formulation is employed. With application of  $\alpha = {}^{t}y$ , and neglecting the time-dependent terms in equation (2.71) and (2.80), the hybrid formulation for nonlinear static analysis is obtained as

$$\delta({}^{l}\pi) = \int_{y_{a}}^{y_{B}} \left\{ \left[ {}^{l}N_{a} \left( \frac{{}^{l}x'}{{}^{l}s'} \right) - {}^{l}B \left( \frac{{}^{l}\kappa}{{}^{l}s'} + \frac{{}^{l}s''}{{}^{l}s'} + \frac{{}^{l}s''}{{}^{l}s'} - \frac{{}^{l}x''({}^{l}s'')}{{}^{l}s'} - \frac{{}^{l}x'({}^{l}s'')}{{}^{l}s'} \right] \right] \delta({}^{l}u')$$

$$+ \left[ {}^{l}N_{a} \left( \frac{{}^{l}z'}{{}^{l}s'} \right) - {}^{l}B \left( \frac{{}^{l}\kappa}{{}^{l}s'} + \frac{{}^{l}s''}{{}^{l}s'} + \frac{{}^{l}s''}{{}^{l}s'} - \frac{{}^{l}z'({}^{l}s'')}{{}^{l}s'} - \frac{{}^{l}z'({}^{l}s'')}{{}^{l}s'} \right] \right] \delta({}^{l}w')$$

$$+ \frac{{}^{l}B}{{}^{l}({}^{l}s')^{2}} \left( \frac{{}^{l}x'''}{{}^{l}s'} - \frac{{}^{l}x'({}^{l}s'')}{{}^{l}(s')^{2}} \right) \delta({}^{l}u'') + \frac{{}^{l}B}{{}^{l}s'} - \frac{{}^{l}z'({}^{l}s'')}{{}^{l}(s')^{2}} \right] \delta({}^{l}w')$$

$$+ {}^{l}\mathbb{F}_{lx}\delta({}^{l}u') + {}^{l}\mathbb{F}_{lz}\delta({}^{l}w') + {}^{l}\mathbb{F}_{lz}\delta({}^{l}u'') + {}^{l}\mathbb{F}_{2z}\delta({}^{l}u'') + {}^{l}\mathbb{F}_{2z}\delta({}^{l}w'') + {}^{l}T\delta({}^{l}\psi')$$

$$+ {}^{l}s'(-{}^{l}f_{Hx} + m_{i}({}^{l}a_{Fx}))\delta({}^{l}u) + {}^{l}s'(-{}^{l}f_{Hz} + m_{i}({}^{l}a_{Fz}))\delta({}^{l}w)$$

$$+ {}^{l}s'(-{}^{l}f_{Hx} + m_{i}({}^{l}a_{Fx}))\delta({}^{l}u) + {}^{l}s'(-{}^{l}f_{Hz} + m_{i}({}^{l}a_{Fz}))\delta({}^{l}w)$$

where

$${}^{I}N_{a}({}^{I}y) = {}^{I}N_{a}({}^{I}y_{H}) + \int_{y}^{y_{H}} \left[ \left( {}^{I}B({}^{I}\kappa) \right)'({}^{I}\kappa) + {}^{I}s'({}^{I}q_{I}) \right] d({}^{I}y), \qquad (3.5 \text{ a})$$

$${}^{\prime}T\left({}^{\prime}y\right) = {}^{\prime}T\left({}^{\prime}y_{H}\right),\tag{3.5 b}$$

$${}^{I}q_{I} = {}^{I}f_{Ht} - {}^{I}m_{i}({}^{I}a_{Ft}) - {}^{I}w_{a}(\frac{{}^{I}y'}{{}^{I}s'}),$$
 (3.5 c)

$${}^{1}f_{Ht} = 0.5 \rho_{e} ({}^{1}D_{e}) \pi C_{Dt} ({}^{1}V_{Ht})^{2},$$
 (3.5 d)

$${}^{I}f_{Hn} = 0.5 \rho_{e} \left( {}^{I}D_{e} \right) C_{Dn} \left( {}^{I}V_{Hn} \right)^{2},$$
 (3.5 e)

$${}^{1}f_{Hbn} = 0.5 \rho_{e} ({}^{1}D_{e}) C_{Dn} ({}^{1}V_{Hbn})^{2},$$
 (3.5 f)

$${}^{1}f_{Hx} = {}^{1}f_{Ht} \left( \frac{{}^{1}x'}{{}^{1}S'} \right) + {}^{1}f_{Hn} \left( {}^{1}n_{x} \right) + {}^{1}f_{Hbn} \left( {}^{1}b_{x} \right), \tag{3.5 g}$$

$${}^{I}f_{Hz} = {}^{I}f_{Ht} \left( \frac{{}^{I}z'}{{}^{I}s'} \right) + {}^{I}f_{Hn} \left( {}^{I}n_{z} \right) + {}^{I}f_{Hbn} \left( {}^{I}b_{z} \right), \tag{3.5 h}$$

$${}^{\prime}a_{Fi} = \frac{{}^{\prime}V_{i}({}^{\prime}V_{i}')}{{}^{\prime}S'},$$
 (3.5 i)

$${}^{I}a_{Fx} = {}^{I}\kappa \left({}^{I}n_{x}\right)\left({}^{I}V_{i}\right)^{2} + \frac{\left({}^{I}V_{i}\right)\left({}^{I}V_{i}'\right)\left({}^{I}x'\right)}{\left({}^{I}s'\right)^{2}},$$
(3.5 j)

$${}^{\prime}a_{Fz} = {}^{\prime}\kappa \left({}^{\prime}n_{z}\right)\left({}^{\prime}V_{i}\right)^{2} + \frac{\left({}^{\prime}V_{i}\right)\left({}^{\prime}V_{i}^{\prime}\right)\left({}^{\prime}z^{\prime}\right)}{\left({}^{\prime}s^{\prime}\right)^{2}}, \tag{3.5 k}$$

$${}^{I}V_{Ht} = {}^{I}V_{Hx} \left( \frac{{}^{I}x'}{{}^{I}s'} \right) + {}^{I}V_{Hz} \left( \frac{{}^{I}z'}{{}^{I}s'} \right), \tag{3.5 l}$$

$${}^{I}V_{Hn} = {}^{I}V_{Hx} \left({}^{I}n_{x}\right) + {}^{I}V_{Hz} \left({}^{I}n_{z}\right),$$
 (3.5 m)

$${}^{1}V_{Hbn} = {}^{1}V_{Hx} ({}^{1}b_{x}) + {}^{1}V_{Hz} ({}^{1}b_{z}),$$
 (3.5 n)

Note that for  $\alpha = {}^{1}y$ ,

$${}^{I}B = E({}^{I}I_{p}), {}^{I}B' = 2E({}^{0}I_{p})(1 + {}^{I}\varepsilon){}^{I}\varepsilon', \qquad (3.6 \text{ a,b})$$

$${}^{\prime}s' = \sqrt{1 + \left({}^{\prime}x'\right)^{2} + \left({}^{\prime}z'\right)^{2}}, \ {}^{\prime}s'' = \frac{{}^{\prime}x'\left({}^{\prime}u''\right) + {}^{\prime}z'\left({}^{\prime}w''\right)}{{}^{\prime}s'}, \tag{3.6 c,d}$$

$${}^{I}\kappa = \frac{I}{\left({}^{I}s'\right)^{3}} \sqrt{\left({}^{I}u''\right)^{2} + \left({}^{I}w''\right)^{2} + \left(\left({}^{I}u''\right)\left({}^{I}z'\right) - \left({}^{I}x'\right)\left({}^{I}w''\right)\right)^{2}} , \qquad (3.6 e)$$

$${}^{I}\kappa' = \frac{1}{\left({}^{I}s'\right)^{6}\left({}^{I}\kappa\right)}\left\{ \left({}^{I}u''\right)\left({}^{I}u'''\right) + \left({}^{I}w'''\right)\left({}^{I}w''''\right)\right\}$$

$$+\left[\left({}^{\prime}u''\right)\left({}^{\prime}z'\right)-\left({}^{\prime}x'\right)\left({}^{\prime}w''\right)\right]\left[\left({}^{\prime}u'''\right)\left({}^{\prime}z'\right)-\left({}^{\prime}x'\right)\left({}^{\prime}w'''\right)\right]\right] -\frac{3\left({}^{\prime}\kappa\right)\left({}^{\prime}s''\right)}{{}^{\prime}s'} \quad (3.6 \text{ f})$$

$${}^{l}\tau = {}^{l}\tau_{I} + \frac{{}^{l}\psi'}{{}^{l}s'}, {}^{l}\tau_{I} = \frac{{}^{(l}w'')({}^{l}u''') - {}^{(l}w''')({}^{l}u'')}{{}^{(l}u'') + {}^{(l}w'')^{2} + {}^{(l}u''')({}^{l}z') - {}^{(l}x')({}^{l}w'')]^{2}}, \quad (3.6 \text{ g,h})$$

$${}^{l}\mathfrak{F}_{lx} = {}^{l}T \left[ \frac{{}^{l}\tau_{I}({}^{l}x')}{{}^{l}s'} + \frac{2({}^{l}s')({}^{l}\tau_{I})}{{}^{l}\mathfrak{I}} \left( {}^{(l}u'')({}^{l}z') - {}^{(l}x')({}^{l}w'') \right) ({}^{l}w'') \right] \quad (3.6 \text{ j})$$

$${}^{l}\mathfrak{F}_{lz} = {}^{l}T \left[ \frac{{}^{l}\tau_{I}({}^{l}z')}{{}^{l}s'} - \frac{2({}^{l}s')({}^{l}\tau_{I})}{{}^{l}\mathfrak{I}} \left( {}^{(l}u'')({}^{l}z') - {}^{(l}x')({}^{l}w'') \right) ({}^{l}u'') \right] \quad (3.6 \text{ k})$$

$${}^{l}\mathfrak{F}_{lz} = \frac{-{}^{l}T({}^{(l}w'')({}^{l}s'')}{{}^{l}\mathfrak{I}} + \frac{{}^{l}T({}^{(l}w'')({}^{l}s'')}{{}^{l}\mathfrak{I}} + \frac{{}^{l}T({}^{(l}u'')({}^{l}s'')}{{}^{l}\mathfrak{I}} + \frac{{}^{l}T({}^{(l}u'')({}^{(l}s''))}{{}^{(l}s'')} + \frac{{}^{l}T({}^{(l}u'')({}^{(l}s'$$

In large strain analysis, the axial strain is one of degree of freedom and the axial force can be derived from constitutive equation.

$${}^{I}N_{a}({}^{I}y) = E({}^{I}A_{p})({}^{I}\varepsilon({}^{I}y))$$
(3.7)

To satisfy both equilibrium equation and constitutive equation, equation (3.7) has to be equal to equation (3.5 a), the constrain equation of this condition may be written as

$$\delta w_c = \int_{y_a}^{y_H} \left\{ E(^{\prime}A_p)^{\prime} \varepsilon(^{\prime}y) - ^{\prime}N_a(^{\prime}y) \right\} \delta(^{\prime}\varepsilon) = 0$$
 (3.8)

This constrain equation may be considered as an equivalent work term and is added directly to the standard virtual work statement; equation (3.4).

From equations (3.4)-(3.8), it is seen that there are four dependent variables ( ${}^{1}u$ ,  ${}^{1}w$ ,  ${}^{1}\psi$ , and  ${}^{1}\varepsilon$ ) and one independent variable ( ${}^{1}y$ ). Along with the essential and the natural boundary conditions of the riser that has the slip joint at top and the ball joint that can not rotate in tangential direction at the bottom end.

at 
$${}^{1}y = 0$$
:  ${}^{1}u = 0$ ,  ${}^{1}w = 0$ ,  ${}^{1}\psi = 0$ , (essential) (3.9 a, b)

$${}^{1}u'' = 0, {}^{1}w'' = 0$$
 (natural) (3.9 c,d)

and at 
$$y = y_t$$
:  $u = 0$ ,  $w = 0$ ,  $\varepsilon = (N_{aH}) / E(A_{pH})$  (essential) (3.10 a-c)

$$^{I}T = {}^{I}T_{H}$$
 (essential) (3.10 d)

$${}^{l}u'' = \theta, {}^{l}w'' = \theta$$
 (natural), (3.10 e,f)

the system of equations (3.4)-(3.10) is the boundary value problem that should be discretized by using the C<sup>2</sup> finite elements so that all the boundary conditions are constrained. Note that the C<sup>m</sup> finite elements are the elements of which derivatives of displacement field through order 'm' are continuous.

However, the higher derivatives of the twisting rotation  ${}^{l}\psi$  and the strain  ${}^{l}\varepsilon$  are equal to order one, thus it is sufficient to approximate the twisting rotation and the strain by the  $C^{1}$  element. Therefore, in this study the elements mixed between the  $C^{1}$  and the  $C^{2}$  elements are used for approximating the displacement vector of  ${}^{l}\psi$ ,  ${}^{l}\varepsilon$ ,  ${}^{l}u$  and  ${}^{l}w$ .

For ease, the third and the fifth order polynomial shape functions are employed to correspond the  $C^1$  and the  $C^2$  finite elements, respectively. Therefore, the displacement vector is expressed as

$$\{ \vec{d} \} = \{ u^{-1} w^{-1} \psi^{-1} \varepsilon \}^{T} = [N] \{ \vec{d}_{n} \},$$
 (3.11)

where the generalized coordinates of the nodal displacements of each element are

and the shape function matrix at the equilibrium state

$$\begin{bmatrix} {}^{I}\mathbf{N} \end{bmatrix} = \begin{bmatrix} {}^{I}N_{51} & {}^{I}N_{52} & {}^{I}N_{53} & 0 & 0 & 0 & 0 & 0 & 0 & 0 \\ \hline 0 & 0 & 0 & {}^{I}N_{51} & {}^{I}N_{52} & {}^{I}N_{53} & 0 & 0 & 0 & 0 \\ \hline 0 & 0 & 0 & 0 & 0 & 0 & {}^{I}N_{31} & {}^{I}N_{32} & 0 & 0 \\ \hline 0 & 0 & 0 & 0 & 0 & 0 & 0 & 0 & {}^{I}N_{31} & {}^{I}N_{32} \end{bmatrix}$$

$$\frac{\begin{vmatrix}
^{1}N_{54} & ^{1}N_{55} & ^{1}N_{56} & 0 & 0 & 0 & 0 & 0 & 0 & 0 \\
\hline
0 & 0 & 0 & ^{1}N_{54} & ^{1}N_{55} & ^{1}N_{56} & 0 & 0 & 0 & 0 \\
\hline
0 & 0 & 0 & 0 & 0 & 0 & ^{1}N_{33} & ^{1}N_{34} & 0 & 0 \\
\hline
0 & 0 & 0 & 0 & 0 & 0 & 0 & 0 & ^{1}N_{33} & ^{1}N_{34}
\end{vmatrix}$$
(3.13)

Note that  ${}^{I}N_{3i}$  and  ${}^{I}N_{5i}$  are the coefficients of the third and the fifth order polynomial shape functions, respectively.

From equation (3.13), the number of degrees of freedom per element is 20. From equation (2.81) and the calculus of variation, one has

$$\delta\left({}^{I}\pi^{(e)}\right) = \sum_{i=1}^{20} \left[\frac{\partial\left({}^{I}\pi^{(e)}\right)}{\partial\left({}^{I}d_{ni}\right)}\right] \delta\left({}^{I}d_{ni}\right) = 0. \tag{3.14}$$

Equation (3.14) yields the twenty equilibrium equations of each element

$$\frac{\partial \binom{1}{\pi^{(e)}}}{\partial \binom{1}{d_{ni}}} = 0, \text{ for } i = 1, 2, \dots, 20.$$

$$(3.15)$$

Substituting equation (3.11) into equations (3.4) and (3.8), the matrix form of equation (3.15) can be obtained as

$$\int_{0}^{h} \left\{ \left[ {}^{l}N_{x} \left( \frac{{}^{l}X'}{{}^{l}S'} \right) - {}^{l}B \left( \frac{{}^{l}K'}{{}^{l}S'} + \frac{{}^{l}S''}{{}^{l}S'} + \frac{{}^{l}S''}{{}^{l}S'} - \frac{{}^{l}X'({}^{l}S'')}{{}^{l}S'} \right] \right\} + {}^{l}\mathbb{F}_{lx} \right] \left[ {}^{l}N'\right]^{T} \begin{cases} l \\ 0 \\ 0 \\ 0 \end{cases}$$

$$+ \left[ {}^{l}N_{x} \left( \frac{{}^{l}Z'}{{}^{l}S'} \right) - {}^{l}B \left( \frac{{}^{l}K'}{{}^{l}S'} + \frac{{}^{l}S''}{{}^{l}S'} + \frac{{}^{l}S''}{{}^{l}S''} - \frac{{}^{l}Z'({}^{l}S'')}{{}^{l}S'} - \frac{{}^{l}Z'({}^{l}S'')}{{}^{l}S'} \right] \right] + {}^{l}\mathbb{F}_{lx} \left[ {}^{l}N'\right]^{T} \begin{cases} 0 \\ l \\ 0 \\ 0 \end{cases}$$

$$+ \left[ \frac{{}^{l}B}{{}^{l}S'} \left( \frac{{}^{l}X''}{{}^{l}S'} - \frac{{}^{l}X'({}^{l}S'')}{{}^{l}(S')^{2}} \right) + {}^{l}\mathbb{F}_{2x} \right] \left[ {}^{l}N''\right]^{T} \begin{cases} 0 \\ 0 \\ 0 \\ 0 \end{cases}$$

$$+ \left[ \frac{{}^{l}B}{{}^{l}S'} \left( \frac{{}^{l}Z''}{{}^{l}S'} - \frac{{}^{l}Z'({}^{l}S'')}{{}^{l}(S')^{2}} \right) + {}^{l}\mathbb{F}_{2x} \right] \left[ {}^{l}N''\right]^{T} \begin{cases} 0 \\ l \\ 0 \\ 0 \end{cases}$$

$$+ \left[ \frac{{}^{l}B}{{}^{l}S'} \left( \frac{{}^{l}Z''}{{}^{l}S'} - \frac{{}^{l}Z'({}^{l}S'')}{{}^{l}(S')^{2}} \right) + {}^{l}\mathbb{F}_{2x} \right] \left[ {}^{l}N''\right]^{T} \begin{cases} 0 \\ l \\ 0 \\ 0 \end{cases}$$

$$+ {}^{l}S'(-{}^{l}f_{hx} + m_{l}({}^{l}a_{Fx})) \left[ {}^{l}N\right]^{T} \begin{cases} 0 \\ 0 \\ 0 \\ 0 \end{cases}$$

$$+ \left[ ({}^{l}A_{p})({}^{l}S) - {}^{l}N_{x} \right] \left[ {}^{l}N\right]^{T} \left[ {}^{l}S' \right] \right] \begin{cases} 0 \\ 0 \\ 0 \end{cases}$$

$$+ \left[ ({}^{l}A_{p})({}^{l}S) - {}^{l}N_{x} \right] \left[ {}^{l}N\right]^{T} \left[ {}^{l}S' \right] \end{cases} \begin{cases} 0 \\ 0 \\ 0 \end{cases}$$

$$+ \left[ ({}^{l}A_{p})({}^{l}S) - {}^{l}N_{x} \right] \left[ {}^{l}N\right]^{T} \left[ {}^{l}S' \right] \end{cases} \begin{cases} 0 \\ 0 \\ 0 \end{cases}$$

$$+ \left[ ({}^{l}A_{p})({}^{l}S) - {}^{l}N_{x} \right] \left[ {}^{l}N\right] \left[ {}^{l}N\right] \right] \begin{cases} 0 \\ 0 \\ 0 \end{cases} \end{cases} \end{cases} \begin{cases} 0 \\ 0 \\ 0 \end{cases}$$

The Fortran-90 codes for solving the system of equation (3.16) has been developed based on the aforementioned finite element method. The solution steps used in the codes can be summarized as follows.

- Step 1 Read the usual data from the data file.
- Step 2 Set the values of constants.
- Step 3 Determine the values of the constant.
- Step 4 Label the node number of all elements.
- Step 5 Initialize the guessed values of all degrees of freedom.
- Step 6 Form the system of finite element equations, in which the procedures are as follows:
- Step 6.1 Calculate the nodal axial forces and the nodal axial strains based on equation (3.5a).
- Step 6.2 Create the element equations based on equation (3.16). The numerical integration is performed by using the fourth-order Gaussian quadrature. The global degrees of freedom are transformed to the local. The third and the fifth order polynomial shape functions are calculated. The shape function matrices are formed. The generalized coordinates of displacements are evaluated. The effects of radial deformation on the changes of cross-sectional properties and velocity of transported fluid are treated. The external loads due to the effects of the hydrostatic and the hydrodynamic pressures are evaluated. The axial and shear forces at the depth 'y are computed.
- Step 6.3 Assemble the element equations obtained from step 6.2 to generate the global system of finite element equations.

Step 6.4 Impose the boundary conditions from equations (3.9) and (3.10).

Step 7 Solve the system of the finite element equations obtained from step 6 by numerical methods. This study utilizes the modified Powell hybrid algorithm based on the MINPACK subroutine HYBRD1 (More et al., 1980) which will correct and update the guessed values of degrees of freedom, and repeat steps 4-7 until the stopping error criterion is satisfied.

Step 8 Save the numerical results in the result files.

#### 3.2 TWO-DIMENSIONAL DYNAMIC ANALYSIS

The second weak formulation is employed for the dynamic analysis as well. From equation (2.81)  $\delta \pi = 0$ , hence the second weak formulation may be decomposed into the following four nonlinear dynamic equilibrium equations.

$$\int_{\alpha} \left\{ \left[ \frac{{}^{2}M}{{}^{2}\kappa \left( {}^{2}s' \right)^{2}} \frac{\partial}{\partial \alpha} \left( \frac{{}^{2}x'}{{}^{2}s'} \right) + {}^{2}\mathbb{F}_{2x} \right] \delta \left( {}^{2}u'' \right) \right. \\
+ \left[ {}^{2}N_{a} \left( \frac{{}^{2}x'}{{}^{2}s'} \right) - {}^{2}M_{a} \left( \frac{{}^{2}\kappa \left( {}^{2}x' \right)}{{}^{2}s'} + \frac{{}^{2}s''}{{}^{2}\kappa \left( {}^{2}s' \right)^{3}} \frac{\partial}{\partial \alpha} \left( \frac{{}^{2}x'}{{}^{2}s'} \right) \right) + {}^{2}\mathbb{F}_{1x} \right] \delta \left( {}^{2}u' \right) \right. \\
+ \left[ {}^{2}N_{a} \left( \frac{{}^{2}y'}{{}^{2}s'} \right) + {}^{2}\mathbb{F}_{2y} \right] \delta \left( {}^{2}v'' \right) \\
+ \left[ {}^{2}N_{a} \left( \frac{{}^{2}y'}{{}^{2}s'} \right) - {}^{2}M_{a} \left( \frac{{}^{2}\kappa \left( {}^{2}y' \right)}{{}^{2}s'} + \frac{{}^{2}s''}{{}^{2}\kappa \left( {}^{2}s' \right)^{3}} \frac{\partial}{\partial \alpha} \left( \frac{{}^{2}y'}{{}^{2}s'} \right) + {}^{2}\mathbb{F}_{1y} \right] \delta \left( {}^{2}v' \right) \\
+ \left[ {}^{2}N_{a} \left( \frac{{}^{2}y'}{{}^{2}s'} \right) - {}^{2}M_{a} \left( \frac{{}^{2}\kappa \left( {}^{2}y' \right)}{{}^{2}s'} + \frac{{}^{2}s''}{{}^{2}\kappa \left( {}^{2}s' \right)^{3}} \frac{\partial}{\partial \alpha} \left( \frac{{}^{2}y'}{{}^{2}s'} \right) \right] + {}^{2}\mathbb{F}_{1y} \right] \delta \left( {}^{2}v' \right) \right.$$

$$\int_{\alpha}^{2} \left\{ \left[ -w_{a} - f_{Hy} - m_{p} a_{py} - m_{i} a_{Fy} \right] \delta\left(^{2}v\right) \right\} d\alpha = 0, \qquad (3.17 \text{ b})$$

$$\int_{\alpha}^{2} \left\{ \left[ \frac{^{2}M}{^{2}\kappa\left(^{2}s'\right)^{2}} \frac{\partial}{\partial\alpha} \left(\frac{^{2}z'}{^{2}s'}\right) + {}^{2}\mathbb{F}_{2w} \right] \delta\left(^{2}w''\right) + \left[ {}^{2}N_{a} \left(\frac{^{2}z'}{^{2}s'}\right) - {}^{2}M_{a} \left(\frac{^{2}\kappa\left(^{2}z'\right)}{^{2}s'} + \frac{^{2}s''}{^{2}\kappa\left(^{2}s'\right)^{3}} \frac{\partial}{\partial\alpha} \left(\frac{^{2}z'}{^{2}s'}\right) \right) + {}^{2}\mathbb{F}_{1z} \right] \delta\left(^{2}w'\right)$$

$${}^{2}s' \left[ f_{Hz} - m_{p} a_{pz} - m_{i} a_{Fz} \right] \delta\left(^{2}w\right) \right\} d\alpha = 0, \qquad (3.17 \text{ c})$$

$$\int_{\alpha}^{2} \left\{ {}^{2}T\delta\left(^{2}\psi'\right) - {}^{2}s'\left(-m_{p}\left(^{2}J_{p}\right)\left(^{2}\ddot{\psi}\right)\right) \delta\left(^{2}\psi\right) \right\} d\alpha = 0, \qquad (3.17 \text{ d})$$

By neglecting the out-of-plane motion and the effect of torsion, the two nonlinear dynamic equilibrium equations for two-dimensional analysis can be expressed as follows

$$\int_{a}^{\left\{\frac{B(^{2}\kappa)}{^{2}s'}\left(\frac{^{2}y'}{^{2}s'}\right)\delta(^{2}u'')\right\} d\alpha = 0, \qquad (3.18 a)$$

$$\int_{a}^{-2s'}\left[f_{Hx} - m_{p}a_{px} - m_{i}a_{Fx}\right]\delta(^{2}u) d\alpha = 0, \qquad (3.18 a)$$

$$\int_{a}^{-2s'}\left[f_{Hx} - m_{p}a_{px} - m_{i}a_{Fx}\right]\delta(^{2}u) d\alpha = 0, \qquad (3.18 b)$$

$$\int_{a}^{-2s'}\left[f_{Hx} - a_{p}a_{px} - a_{px} - a_{px}\right]\delta(^{2}u) d\alpha = 0, \qquad (3.18 b)$$

$$\int_{a}^{-2s'}\left[f_{Hx} - a_{p}a_{px} - a_{px} - a_{px}\right]\delta(^{2}u) d\alpha = 0, \qquad (3.18 b)$$

From the assumption of the linear dynamic strain of the vibrations with infinitesimal amplitudes in equation (2.8) and (2.9), one has

$${}^{2}N_{a} \approx {}^{1}N_{a} + E({}^{1}A_{P})\left(\frac{{}^{1}x'u' + {}^{1}y'v'}{({}^{1}s')^{2}}\right).$$
 (3.19)

By substituting equations (2.45), (2.65), and (3.19) into equations (3.18 a-b) together with neglecting the higher order terms of the vibrations with infinitesimal amplitudes, equations (3.18 a-b) can be expressed as

$$\left\{ \frac{{}^{1}B}{({}^{'}s')^{2}} \left[ ({}^{1}y')^{2} ({}^{2}x'') - (({}^{1}x')({}^{1}y'))({}^{2}y'') \right] \delta({}^{2}u'') \right. \\
+ \left[ \frac{({}^{1}N_{a} - {}^{1}m_{i}({}^{1}V_{i})^{2})({}^{2}x')}{{}^{i}s'} \right] \delta({}^{2}u') \\
+ E({}^{1}A_{p}) \left[ \frac{({}^{1}x')^{2}u' + (({}^{1}x')({}^{1}y'))v'}{({}^{1}s')^{3}} \right] \delta({}^{2}u') \\
- \frac{{}^{1}B({}^{1}K)}{({}^{1}s')^{4}} \left[ (2({}^{1}x')({}^{1}y'))({}^{2}x'') + (({}^{1}y')^{2} - ({}^{1}x')^{2})({}^{2}y'') \right] \delta({}^{2}u') \\
- {}^{1}s' \left[ -{}^{1}C_{a}^{*}({}^{2}\ddot{x}) - {}^{1}C_{eqx}^{*}({}^{2}\dot{x}) - {}^{1}C_{eqxy}^{*}({}^{2}\dot{y}) + {}^{1}C_{Dx}^{*}V_{Hx}^{2} + {}^{1}C_{M}^{*}\dot{V}_{Hx} \right] \delta({}^{2}u) \right\} d\alpha \\
+ {}^{1}s' \left[ ({}^{1}m_{p} + {}^{1}m_{i})({}^{2}\ddot{x}) + {}^{1}m_{i}({}^{1}V_{i}) \left( \frac{2}{s'} - \frac{({}^{1}x')^{2}}{({}^{1}s')^{3}} \right)({}^{2}\dot{x}') \right] \\
+ {}^{1}s' \left[ \left( {}^{1}m_{i}({}^{1}V_{i})({}^{1}V_{i}') \right] ({}^{2}x') + \frac{{}^{1}m_{i}({}^{1}x')}{s'} \frac{DV_{td}}{Dt} \right] \delta({}^{2}u) \right] \\
+ \left[ {}^{1}m_{i}({}^{1}V_{i})({}^{1}V_{i}') \left( {}^{1}s')^{2} \right] ({}^{2}x') + \frac{{}^{1}m_{i}({}^{1}x')}{s'} \frac{DV_{td}}{Dt} \right] \delta({}^{2}u) \right]$$

$$(3.20 a)$$

$$\frac{\frac{i_{B}}{\left(i's'\right)^{2}}\left[-\left(\left(i'x'\right)\left(i'y'\right)\right)\left(i'x''\right)+\left(i'x'\right)^{2}\left(i'y''\right)\right]\delta\left(i'y''\right)}{+\left[\frac{\left(i'N_{a}-i'm_{i}\left(i'V_{i}\right)^{2}\right)\left(i'y'\right)}{i's'}\right]\delta\left(i'y'\right)} + \left[\frac{\left(i'X'\right)\left(i'y'\right)\left(i'y'\right)}{i's'}\right]\delta\left(i'y'\right) + \left[\left(i'y'\right)^{2}\right]v'\right]}\delta\left(i'y'\right) + \left[\frac{i'B\left(i'K\right)}{\left(i's'\right)^{3}}\left[\left(\left(i'y'\right)^{2}-\left(i'x'\right)^{2}\right)\left(i'x'\right)-\left(i'x'\right)\left(i'y'\right)\right)\left(i'y'\right)\right]\delta\left(i'y'\right)}{\left(i's'\right)^{3}}\left[\left(i'y'\right)^{2}-i'C_{eqy}^{*}\left(i'y'\right)-i'C_{eqy}^{*}\left(i'x'\right)+i'C_{Dsy}^{*}V_{ffx}^{*}\right]\delta\left(i'y'\right) + \left[\frac{i'M_{i}\left(i'V_{i}\right)\left(i'x'\right)\left(i'y'\right)}{\left(i's'\right)^{3}}\left(i'x'\right)\right]\delta\left(i'y'\right) + \left[\frac{i'M_{i}\left(i'V_{i}\right)\left(i'Y_{i}\right)\left(i'x'\right)\left(i'y'\right)}{\left(i's'\right)^{3}}\left(i'y'\right)\right]\delta\left(i'y'\right) + \left[\frac{i'M_{i}\left(i'V_{i}\right)\left(i'Y_{i}\right)\left(i'y'\right)}{\left(i's'\right)^{3}}\left(i'y'\right)\right]\delta\left(i'y'\right) + \left[\frac{i'M_{i}\left(i'V_{i}\right)\left(i'Y_{i}\right)\left(i'Y_{i}\right)\left(i'y'\right)}{i's'}\left(i'y'\right)\right]\delta\left(i'y'\right) + \left[\frac{i'M_{i}\left(i'V_{i}\right)\left(i'Y_{i$$

Note that the following relations are used in the derivation of equations (3.20 a,b):

$$-{}^{2}B({}^{2}\kappa)^{2}\left(\frac{{}^{2}x'}{{}^{2}s'}\right) - \frac{{}^{2}B({}^{2}\kappa)({}^{2}s'')}{({}^{2}s')^{2}}\left(\frac{{}^{2}y'}{{}^{2}s'}\right)$$

$$= -\frac{{}^{2}B({}^{2}\kappa)}{({}^{2}s')^{4}}\left[\left(2({}^{2}x')({}^{2}y')\right)({}^{2}x'') + \left(({}^{2}y')^{2} - ({}^{2}x')^{2}\right)({}^{2}y'')\right] \qquad (3.21 \text{ a})$$

$$-{}^{2}B({}^{2}\kappa)^{2}\left(\frac{{}^{2}y'}{{}^{2}s'}\right) + \frac{{}^{2}B({}^{2}\kappa)({}^{2}s'')}{({}^{2}s')^{2}}\left(\frac{{}^{2}x'}{{}^{2}s'}\right)$$

$$= \frac{{}^{2}B({}^{2}\kappa)}{({}^{2}s')^{4}}\left[\left(({}^{2}y')^{2} - ({}^{2}x')^{2}\right)({}^{2}x'') - \left(2({}^{2}x')({}^{2}y')\right)({}^{2}y'')\right] \qquad (3.21 \text{ b})$$

$$\int \left[{}^{4}s'({}^{4}m_{i})({}^{2}V_{i})^{2}\frac{({}^{2}\kappa)({}^{2}y')}{{}^{2}s'}}\right]\delta({}^{2}u)d\alpha$$

$$= \left[\frac{{}^{4}s'}{{}^{2}s'}{}^{4}m_{i}({}^{2}V_{i})^{2}\delta({}^{2}u)\frac{{}^{2}x'}{{}^{2}s'}\right]\delta({}^{2}u)d\alpha$$

$$= \left[\frac{{}^{4}s'}{{}^{2}s'}{}^{4}m_{i}({}^{2}V_{i})^{2}\left(-\frac{({}^{2}\kappa)({}^{2}x')}{{}^{2}s'}\right)\right]\delta({}^{2}v)d\alpha$$

$$= \left[\frac{{}^{4}s'}{{}^{2}s'}{}^{4}m_{i}({}^{2}V_{i})^{2}\delta({}^{2}v)\frac{{}^{2}y'}{{}^{2}s'}\right]_{a_{a_{i}}}^{a_{i}} - \frac{a_{i}}{a_{s}}\left[\left(\frac{{}^{4}s'}{{}^{2}s'}{}^{4}m_{i}({}^{2}V_{i})^{2}\delta({}^{2}v)\right)\frac{{}^{2}\frac{y'}{{}^{2}s'}}\right]d\alpha \qquad (3.21 \text{ d})$$

$${}^{2}s' = \frac{({}^{2}x')({}^{2}u') + ({}^{2}y')({}^{2}v')}{{}^{2}s'}}, \qquad (3.21 \text{ e})$$

$${}^{2}\kappa = \frac{({}^{2}x'')({}^{2}y') - ({}^{2}x')({}^{2}y')}{({}^{2}s')^{3}}. \qquad (3.21 \text{ f})$$

When the time-independent terms in equations (3.17a-c) are eliminated, the equations of the vibrations with infinitesimal amplitudes can be obtained as

$$\left\{ \frac{\frac{i}{B}}{\left(\frac{i}{s'}\right)^{2}} \left[ \left(\frac{i}{y'}\right)^{2} u'' - \left(\left(\frac{i}{x'}\right)\left(\frac{i}{y'}\right)\right) v'' \right] \delta u'' \right. \\
+ \left[ \frac{\left(\frac{i}{N_{a}} - i m_{i} \left(\frac{i}{V_{i}}\right)^{2}\right) \left(u'\right)}{i's'} \right] \delta u' \\
+ E \left(\frac{i}{A_{p}}\right) \left[ \frac{\left(\frac{i}{x'}\right)^{2} u' + \left(\left(\frac{i}{x'}\right)\left(\frac{i}{y'}\right)\right) v'}{\left(\frac{i}{s'}\right)^{3}} \right] \delta u' \\
- \frac{\frac{i}{B} \left(\frac{i}{K}\right)}{\left(\frac{i}{s'}\right)^{4}} \left[ \left(2\left(\frac{i}{x'}\right)\left(\frac{i}{y'}\right)\right) \left(u''\right) + \left(\left(\frac{i}{y'}\right)^{2} - \left(\frac{i}{x'}\right)^{2}\right) \left(v''\right) \right] \delta u' \\
- \frac{i}{s'} \left[ -\frac{i}{C_{a}} \ddot{u} - i C_{eqx}^{*} \dot{u} - i C_{eqxy}^{*} \dot{v} + i C_{Dx}^{*} \left(2V_{c}V_{w} + V_{w}^{2}\right) + i C_{M}^{*} \dot{V}_{w} \right] \delta u \\
+ \frac{i}{s'} \left[ \left(\frac{i}{m_{p}} + i m_{i}\right) \ddot{u} + i m_{i} \left(\frac{i}{V_{i}}\right) \left(\frac{2}{is'} - \frac{\left(\frac{i}{x'}\right)^{2}}{\left(\frac{i}{s'}\right)^{3}}\right) \dot{u}' \right] \delta u \\
+ \frac{i}{s'} \left[ \left(\frac{i}{m_{i}} \left(\frac{i}{V_{i}}\right) \left(\frac{i}{V_{i}}\right)\right] u' + \frac{i}{i} m_{i} \left(\frac{i}{x'}\right) \frac{DV_{id}}{Dt} \right] \delta u \\
+ \left[ \frac{i}{m_{i}} \left(\frac{i}{V_{i}}\right)^{2} u' \right] \delta u \right]^{a_{i}} = 0, \tag{3.22 a}$$

$$\frac{\frac{i}{B}}{\left(\frac{i}{S'}\right)^{2}} \left[ -\left(\left(\frac{i}{X'}\right)\left(\frac{i}{Y'}\right)\right)u'' + \left(\frac{i}{X'}\right)^{2}v'' \right] \delta v'' \\
+ \left[ \frac{\left(\frac{i}{N_{a}} - im_{i}\left(\frac{i}{V_{i}}\right)^{2}\right)v'}{i_{S'}} \right] \delta v' \\
+ E\left(\frac{i}{A_{p}}\right) \left[ \frac{\left(\left(\frac{i}{X'}\right)\left(\frac{i}{Y'}\right)\right)u' + \left(\left(\frac{i}{Y'}\right)^{2}\right)v'}{\left(\frac{i}{S'}\right)^{3}} \right] \delta v' \\
- \frac{\frac{i}{B}\left(\frac{i}{K}\right)}{\left(\frac{i}{S'}\right)^{4}} \left[ \left(\left(\frac{i}{Y'}\right)^{2} - \left(\frac{i}{X'}\right)^{2}\right)u'' - \left(2\left(\frac{i}{X'}\right)\left(\frac{i}{Y'}\right)\right)v'' \right] \delta v' \\
- \frac{i}{S'} \left[ -iC_{a}^{*}\ddot{v} - iC_{eqy}^{*}\dot{v} - iC_{eqy}^{*}\dot{u} + iC_{Dsyl}^{*}\left(2V_{c}V_{w} + V_{w}^{2}\right)\right] \delta v \\
+ \frac{i}{S'} \left[ \left(\frac{i}{m_{p}} + im_{i}\right)\ddot{v} - im_{i}\left(\frac{i}{V_{i}}\right)\left(\frac{i}{S'}\right)^{3}\right) \dot{v}' \\
+ \frac{i}{m_{i}}\left(\frac{i}{V_{i}}\right)\left(\frac{2}{i_{S'}} - \frac{\left(\frac{i}{Y'}\right)^{2}}{\left(\frac{i}{S'}\right)^{3}}\right) \dot{v}' \\
+ \frac{i}{S'} \left[ \left(\frac{i}{m_{i}}\left(\frac{i}{V_{i}}\right)\left(\frac{i}{V_{i}}\right)\right) v' + \frac{i}{i_{S'}}\frac{DV_{ud}}{Dt} \right] \delta v \\
+ \left[ \frac{i}{m_{i}}\left(\frac{i}{V_{i}}\right)^{2}v'}{i_{S'}} \delta v \right]^{a_{i}} = 0, \tag{3.22 b}$$

Along with the boundary conditions at  $^{1}y = 0$ :

$$u(0,t) = v(0,t) = 0$$
 (essential), (3.23 a)

$$u''(0,t) = v''(0,t) = 0$$
 (natural), (3.23 b)

and at 
$${}^{1}y = {}^{o}y_{t}$$
:  $u({}^{o}y_{t}, t) = v({}^{o}y_{t}, t) = 0$  (essential), (3.24 a)

$$u''({}^{\circ}y_{i},t) = v''({}^{\circ}y_{i},t) = 0$$
 (natural), (3.24 b)

and 
$$N_a = N_{aH}$$
 (essential), (3.24 c)

and the initial conditions at time t = 0:

$$u(^{T}y,\theta) = {^{T}u}, \ v(^{T}y,\theta) = {^{T}v},$$
 (3.25 a,b)

$$\dot{u}(^{1}y,0) = 0, \ \dot{v}(^{1}y,0) = 0,$$
 (3.25 c,d)

the system of partial differential equations (3.22 a-b) is the initial-boundary-value problem, which can be transformed to the system of ordinary differential equations by performing the following three steps of the finite element method.

Step 1. By separation of variables, the displacement vector is assumed as

$$\{\boldsymbol{d}\} = \{\boldsymbol{u} \quad \boldsymbol{v}\}^T = \left[\boldsymbol{N}(^T\boldsymbol{y})\right] \{\boldsymbol{d}_n(t)\}, \tag{3.26}$$

where the generalized coordinates of the nodal displacements of an element are

$$\{\boldsymbol{d}_{n}\} = \{u_{1} \quad u_{1}' \quad u_{1}'' \quad v_{1} \quad v_{1}' \quad v_{1}'' \mid u_{2} \quad u_{2}' \quad u_{2}'' \quad v_{2} \quad v_{2}' \quad v_{2}''\}^{T}, \tag{3.27}$$

and the shape function matrix at the displaced state is

$$[\mathbf{N}] = \begin{bmatrix} N_{51} & N_{52} & N_{53} & 0 & 0 & 0 & | N_{54} & N_{55} & N_{56} & 0 & 0 & 0 \\ 0 & 0 & 0 & N_{51} & N_{52} & N_{53} & | 0 & 0 & 0 & N_{54} & N_{55} & N_{56} \end{bmatrix} . (3.28)$$

Note that  $N_{5i}$  is the coefficients of the fifth order polynomial shape function.

Step 2. Substituting equation (3.26) into equations (3.22 a,b), the element equations can be obtained as

$$[\mathbf{m}^{(e)}]\{\ddot{\mathbf{d}}_n\} + ([\mathbf{c}^{(e)}] + [\mathbf{g}^{(e)}])\{\dot{\mathbf{d}}_n\} + [\mathbf{k}^{(e)}]\{\mathbf{d}_n\} = \{\mathbf{f}^{(e)}\},$$
(3.29)

where the element mass matrix is

$$\left[\mathbf{m}^{(e)}\right] = \int_{\alpha} \left\{ \left[\mathbf{N}\right]^{T} \binom{1}{s'} \binom{1}{m_{P}} + \binom{1}{m_{i}} + \binom{1}{c} C_{ao}^{*} \right\} \left[ \begin{pmatrix} 1 & 0 \\ 0 & 1 \end{pmatrix} \right] \left[\mathbf{N}\right] \right\} d\alpha, \qquad (3.30 a)$$

the element hydrodynamic damping matrix is

$$\begin{bmatrix} \mathbf{c}^{(e)} \end{bmatrix} = \int_{\alpha} \left\{ [\mathbf{N}]^T \binom{1}{s'} \begin{bmatrix} {}^{I}C_{eqx}^* & {}^{I}C_{eqxy}^* \\ {}^{I}C_{eqxy}^* & {}^{I}C_{eqy}^* \end{bmatrix} [\mathbf{N}] \right\} d\alpha , \qquad (3.30 b)$$

the element gyroscopic matrix is

$$\begin{bmatrix} \mathbf{g}^{(e)} \end{bmatrix} = \int_{\alpha} \left\{ \begin{bmatrix} \mathbf{N} \end{bmatrix}^{T} m_{i} \binom{t}{V} \right\}_{i} \begin{bmatrix} 2 - \frac{\binom{t}{x'}}{\binom{t}{s'}^{2}} & -\frac{\binom{t}{x'}}{\binom{t}{s'}^{2}} \\ -\frac{\binom{t}{x'}}{\binom{t}{s'}^{2}} & 2 - \frac{\binom{t}{y'}}{\binom{t}{s'}^{2}} \end{bmatrix} \begin{bmatrix} \mathbf{N}' \end{bmatrix} \right\} d\alpha, \quad (3.30 \text{ c})$$

the element stiffness matrix is

$$\begin{bmatrix} \mathbf{k}^{(e)} \end{bmatrix} = \begin{bmatrix} \mathbf{k}_{b1}^{(e)} \end{bmatrix} + \begin{bmatrix} \mathbf{k}_{b2}^{(e)} \end{bmatrix} + \begin{bmatrix} \mathbf{k}_{N1}^{(e)} \end{bmatrix} + \begin{bmatrix} \mathbf{k}_{N2}^{(e)} \end{bmatrix}, \tag{3.30 d}$$

in which the bending stiffness matrix of the fourth order derivative is

$$\begin{bmatrix} \mathbf{k}_{bl}^{(e)} \end{bmatrix} = \int_{\alpha} \left\{ \begin{bmatrix} \mathbf{N}'' \end{bmatrix}^T \frac{{}^{t}B}{\left({}^{t}s'\right)^5} \begin{bmatrix} {}^{t}y' \end{pmatrix}^2 - {}^{t}x' \left({}^{t}y'\right) \\ -{}^{t}x' \left({}^{t}y'\right) & {}^{t}x' \right)^2 \end{bmatrix} \begin{bmatrix} \mathbf{N}'' \end{bmatrix} \right\} d\alpha , \qquad (3.30 e)$$

the bending stiffness matrix of the third order derivative is

$$\left[\mathbf{k}_{b2}^{(e)}\right] = \int_{\alpha} \left\{ \left[\mathbf{N}'\right]^{T} \frac{{}^{\prime}B({}^{\prime}\kappa)}{\left({}^{\prime}s'\right)^{4}} \left[ \frac{2({}^{\prime}x')({}^{\prime}y')}{\left({}^{\prime}y'\right)^{2} - \left({}^{\prime}x'\right)^{2}} - 2({}^{\prime}x')({}^{\prime}y')} \right] \left[\mathbf{N}''\right] \right\} d\alpha, \qquad (3.30 f)$$

the axial stiffness matrix of the second order derivative is

$$\begin{bmatrix} \mathbf{k}_{NI}^{(e)} \end{bmatrix} = \int_{\alpha}^{\infty} \begin{bmatrix} \mathbf{N}' \end{bmatrix}^{T} \begin{pmatrix} \frac{{}^{\prime}N_{a}}{{}^{\prime}s'} \begin{bmatrix} 1 & 0 \\ 0 & 1 \end{bmatrix} - \frac{{}^{\prime}m_{i} ({}^{\prime}V)^{2}}{{}^{\prime}s'} \begin{bmatrix} 1 & 0 \\ 0 & 1 \end{bmatrix} \mathbf{N}' \end{bmatrix} d\alpha , \qquad (3.30 g)$$

$$+ \begin{bmatrix} \mathbf{N}' \end{bmatrix}^{T} \frac{E({}^{\prime}A_{P})}{({}^{\prime}s')^{3}} \begin{bmatrix} ({}^{\prime}x')^{2} & ({}^{\prime}x')({}^{\prime}y') \\ ({}^{\prime}x')({}^{\prime}y') & ({}^{\prime}y')^{2} \end{bmatrix} \mathbf{N}' \end{bmatrix}$$

the axial stiffness matrix of the first order derivative is

$$[\mathbf{k}_{N2}^{(e)}] = \int_{\alpha} \left\{ [\mathbf{N}]^T \left( \frac{{}^{I}m_i \left( {}^{I}V_i \right) \left( {}^{I}V_i' \right)}{\left( {}^{I}s' \right)^2} \begin{bmatrix} 1 & 0 \\ 0 & 1 \end{bmatrix} \right) [\mathbf{N}'] \right\} d\alpha ,$$
 (3.30 h)

the element hydrodynamic excitation vector is

$$\{\mathbf{f}^{(e)}\} = \int_{\alpha} [\mathbf{N}]^{T} {\binom{1}{s'}} \begin{cases} {}^{I}C_{Dx}^{*}(2V_{c}V_{w} + V_{w}^{2}) + {}^{I}C_{M}^{*}\dot{V}_{w} - \frac{{}^{I}m_{i}({}^{I}x')}{{}^{I}s'} \frac{DV_{id}}{Dt} \\ {}^{I}C_{DxyI}^{*}(2V_{c}V_{w} + V_{w}^{2}) - \frac{{}^{I}m_{i}({}^{I}y')}{{}^{I}s'} \frac{DV_{id}}{Dt} \end{cases} d\alpha .$$
 (3.30 i)

Step 3. Assembling the element equations, the global system of finite element equations can be obtained as

$$[\mathbf{M}]\{\ddot{\mathbf{D}}_{n}\} + ([\mathbf{C}] + [\mathbf{G}])\{\dot{\mathbf{D}}_{n}\} + [\mathbf{K}]\{\mathbf{D}_{n}\} = \{\mathbf{F}\}, \tag{3.31}$$

where  $\{\mathbf{D}_n\}, \{\dot{\mathbf{D}}_n\}, \{\mathbf{D}_n\}$  are the global nodal displacement, velocity, and acceleration vectors, respectively. In equation (3.31), the total mass matrix is

$$[\mathbf{M}] = \sum_{i=1}^{nelem} [\mathbf{m}^{(e)}], \qquad (3.32 a)$$

the total hydrodynamic damping matrix is

$$[\mathbf{C}] = \sum_{i=1}^{nelem} [\mathbf{c}^{(e)}], \tag{3.32 b}$$

the total gyroscopic matrix is

$$[\mathbf{G}] = \sum_{i=1}^{nelem} [\mathbf{g}^{(e)}], \qquad (3.32 c)$$

the total stiffness matrix is

$$[\mathbf{K}] = \sum_{i=1}^{nelem} [\mathbf{k}^{(e)}], \qquad (3.32 \text{ d})$$

the total hydrodynamic excitation vector is

$$[\mathbf{F}] = \sum_{i=1}^{nelem} [\mathbf{f}^{(e)}], \qquad (3.32 e)$$

and the global nodal displacement vector is

$$[\mathbf{D}_n] = \sum_{i=1}^{nelem} [\mathbf{d}_n], \tag{3.32 f}$$

in which *nelem* is the number of finite elements.

It is noteworthy that although the assumption of the vibrations with infinitesimal amplitude is adopted, equation (3.31) is still nonlinear. This is because of the nonlinear effects of the hydrodynamic damping and the gyroscopic forces appearing in the damping and the gyroscopic matrices.

To obtain the state space formulation, which is central to the development of nonlinear vibration control theory, the second order model of equation (3.31) must be transformed to the first order model. To achieve this, the following state vector is defined:

$$\{\mathbf{X}_n\} = \begin{cases} \mathbf{D}_n \\ \mathbf{V}_n \end{cases},\tag{3.33}$$

where

$$\{\mathbf{V}_n\} = \{\dot{\mathbf{D}}_n\}. \tag{3.34}$$

Substituting equation (3.34) into (3.31), one obtains

$$[\mathbf{M}]\{\dot{\mathbf{V}}_{n}\} + ([\mathbf{C}] + [\mathbf{G}])\{\mathbf{V}_{n}\} + [\mathbf{K}]\{\mathbf{D}_{n}\} = \{\mathbf{F}\}, \tag{3.35}$$

The system of equations (3.34) and (3.35) can be cast into the matrix form

$$\begin{bmatrix} \mathbf{I} & \mathbf{0} \\ \mathbf{0} & \mathbf{M} \end{bmatrix} \begin{bmatrix} \dot{\mathbf{D}}_n \\ \dot{\mathbf{V}}_n \end{bmatrix} + \begin{bmatrix} \mathbf{0} & -\mathbf{I} \\ \mathbf{K} & \mathbf{C} + \mathbf{G} \end{bmatrix} \begin{bmatrix} \mathbf{D}_n \\ \mathbf{V}_n \end{bmatrix} = \begin{bmatrix} \mathbf{0} \\ \mathbf{F} \end{bmatrix}. \tag{3.36}$$

Equation (3.36) can be manipulated in state space form

$$\{\dot{\mathbf{X}}_n\} = [\mathbf{A}]\{\mathbf{X}_n\} + \{\mathbf{B}\},$$
 (3.37)

where the coefficient matrix or state transition matrix is

$$[\mathbf{A}] = \begin{bmatrix} \mathbf{0} & \mathbf{I} \\ -\mathbf{M}^{-1}\mathbf{K} & -\mathbf{M}^{-1}(\mathbf{C} + \mathbf{G}) \end{bmatrix}, \tag{3.38 a}$$

and the deterministic input matrix is

$$\{\mathbf{B}\} = \begin{Bmatrix} \mathbf{0} \\ \mathbf{M}^{-1}\mathbf{F} \end{Bmatrix}. \tag{3.38 b}$$

The state equation (3.37) is used for the natural frequency analysis in section 3.3, and for the time history analysis in section 3.4.

## 3.3 NATURAL FREQUENCY ANALYSIS

For free vibrations, equation (3.37) is reduced to

$$\{\dot{\mathbf{X}}_n\} = [\mathbf{A}]\{\mathbf{X}_n\},\tag{3.39}$$

where

$$[\mathbf{A}] = \begin{bmatrix} \mathbf{0} & \mathbf{I} \\ -\mathbf{M}^{-1}\mathbf{K} & -\mathbf{M}^{-1}\mathbf{G} \end{bmatrix}. \tag{3.40}$$

Equation (3.39) has the harmonic solution in the exponential form

$$\{\mathbf{X}_n\} = e^{\lambda t} \{\mathbf{X}_{na}\},\tag{3.41}$$

where  $\lambda = \alpha \pm i\omega$  is the complex eigenvalues,  $\omega$  the natural frequency, and  $\{X_{na}\}$  the vector of complex coefficients or initial modal weights.

Inserting equation (3.41) into (3.39) and dividing through by  $e^{\lambda}$ , the general algebraic eigenvalue problem is obtained as

$$[\mathbf{A}]\{\mathbf{X}_n\} = \lambda\{\mathbf{X}_n\},\tag{3.42}$$

in which the matrix [A] is the real, nonsymmetrical matrix. The Fortran-90 codes for implementing the eigenvalue problem of equation (3.42) has been developed based on the QR-algorithm (Press et al., 1992). The steps to the solution used in the codes are as follows:

- Step 1 Compute the element matrices, in which the procedures are as follows:
- Step 1.1 Form the element shape function matrix of equation (3.28).
- Step 1.2 Determine the element mass matrix of equation (3.30 a).
- Step 1.3 Determine the element gyroscopic matrix of equation (3.30 c).
- Step 1.4 Determine the element stiffness matrix of equation (3.30 d).
- Step 2 Assemble the element matrices to obtain the structural matrices of equations (3.32 a,c,d).
- Step 3 Impose the boundary conditions of equations (3.23) and (3.24) by utilizing the index matrix that identifies the dynamic degrees of freedom.
- Step 4 Form the coefficient matrix of equation (3.40).
- Step 5 Solve the eigenvalue problem of equation (3.42). This study uses the implicit double-shifted QR algorithm based on the EISPACK routine

HQR2 (Smith et al., 1976) to compute the eigenvalues and the eigenvectors.

Step 6 Save the numerical results of the eigenvalues and the eigenvectors in the result file.

#### 3.4 NONLINEAR VIBRATION ANALYSIS

From equation (3.30 i), it is seen that the excitations inducing the nonlinear forced vibrations of the marine riser originate from the unsteady flow of ocean wave with velocity  $V_w$  and the unsteady flow of transported fluid with velocity  $V_{id}$ . In chapter 2, the expression of the ocean wave velocity  $V_w$  has been determined by using Airy's wave theory, as shown in section 2.6.1. However, the expression of  $V_{id}$  has not yet been mentioned. This is because the unsteady internal flow depends upon many factors such as: the variation of fluid density along the riser length; the unsteadiness of pump rate; the change of cross section of the riser due to the axial deformation as described in section 2.3. Consequently, the accurate expression of  $V_{id}$  closed to the real circumstances, is considerably more complicated and difficult to resolve by any theory. For simplicity, this study represents the unsteady internal flow velocity  $V_{id}$  as

$$V_{id} = V_{it}t + V_{ia}\cos\omega_i t , \qquad (3.43)$$

where  $V_{ii}$  is the linear velocity amplitude of internal flow,  $V_{ia}$  the wave velocity amplitude of internal flow, and  $\omega_i$  the forcing frequency of internal flow.

From section 3.2, the initial-boundary-value problem of nonlinear vibrations with infinitesimal amplitudes of the marine riser is reduced to the initial-value problem of the state equation (3.37) in association with the initial conditions (3.25) by using the finite element method. This initial-value problem is highly nonlinear owing to the effects of nonlinear hydrodynamic damping. For implementing such an initial-value problem to be solved by numerical integration, the Fortran-90 computer code has been developed following the steps as shown below.

- Step 1 Compute the element matrices, in which the procedures are as steps 1.1 to 1.5:
- Step 1.1 Form the element shape function matrix of equation (3.28).
- Step 1.2 Determine the element mass matrix of equation (3.30 a).
- Step 1.3 Determine the element gyroscopic matrix of equation (3.30 c).
- Step 1.4 Determine the element stiffness matrix of equation (3.30 d).
- Step 1.5 Determine the element hydrodynamic damping matrix of equation (3.30 b) and the element hydrodynamic excitation vector of equation (3.30 i).
- Step 2 Assemble the element matrices to obtain the structural matrices of equations (3.32 a-e).
- Step 3 Impose the boundary conditions of equations (3.23) and (3.24) by utilizing the index matrix that identifies the dynamic degrees of freedom.
- Step 4 Form the coefficient matrix of equation (3.38 a) and the deterministic input matrix of equation (3.38 b).
- Step 5 Integrate the initial-value problem of equation (3.37) in association with the initial conditions (3.25) by the numerical integration. In this study, the Gear's stiff method using the backward differentiation formulas up to order five based on the subroutine DIFSUB (Bathe, 1996) are applied. The numerical values of the first derivatives of the state vector or the left-hand side of equation (3.37) are computed.
- Step 6 Save the numerical results of the dynamic degrees of freedom of the state vector in the result file.

#### 4. RESULTS AND DISCUSSIONS

In this chapter, validation of the numerical results obtained from the solution procedures proposed in chapter 3 is demonstrated in section 4.1. The important results of the three-dimensional static analysis are concluded in section 4.2. The parametric studies are designated in section 4.3. Based on the numerical results of the parametric studies, the effects of axial deformation, and fluid transportation on behaviors of the pipes are explained further in sections 4.4, and 4.5, respectively.

#### 4.1 VALIDATION OF NUMERICAL RESULTS

The accuracy of the solution can be verified in two ways: first, using the direct methods, and second, using the indirect approaches. The direct methods deal with monitoring and controlling the occurring numerical errors, while the indirect ones involve cross-checking with the solutions of the test cases reported in literature.

### 4.1.1 The Direct Methods

In nonlinear static analysis for which the equilibrium equation is  $[{}^{I}\mathbf{K}]\{{}^{I}\mathbf{D}\} = \{{}^{I}\mathbf{R}\}$ , Bathe (1996) showed that there are two kinds of errors to be controlled, namely the load error

$$\{\Delta^{T} \mathbf{R}\} = \{^{T} \mathbf{R}\} - [^{T} \mathbf{K}] \{^{T} \overline{\mathbf{D}}\}, \tag{4.1}$$

and the solution error

$$\{{}^{I}\mathbf{D}\} - \{{}^{I}\mathbf{\overline{D}}\} = [{}^{I}\mathbf{K}]^{-I}\{\Delta^{I}\mathbf{R}\}, \qquad (4.2)$$

where  $\{^{\prime}\overline{\mathbf{D}}\}$  and  $\{^{\prime}\mathbf{D}\}$  are the calculated and the exact degrees of freedom. He also demonstrated that the load error is usually much less than the solution error. Consequently, although the load error seems to indicate an accurate solution, the solution error may still be large, especially if  $[^{\prime}\mathbf{K}]^{-\prime}$  is very large. In this study, for convenience the load error is kept very much small  $\{\Delta^{\prime}\mathbf{R}\} \rightarrow \{\mathbf{0}\}$  in order to approach the solution error to zero. To achieve this, the Frobenius matrix norm of the load error, which has the scalar value

$$\left\|\Delta^{1}\mathbf{R}\right\|_{F}^{2} = \sum_{i=1}^{numdfs} \Delta^{1}R_{i}^{2}, \qquad (4.3)$$

is minimized to less than 10<sup>-12</sup>.

In the natural frequency analysis for which the standard equation is  $[A]{X_n} = \lambda{X_n}$ , the performance index, which was first developed by the EISPACK project at Argonne National Laboratory (Smith et al., 1976), is employed to measure the performance of the EISPACK routine HQR2. The performance index is defined by

$$PI = \max_{1 \le i \le N} \frac{\|AX_{ni} - \lambda_i X_{ni}\|_1}{10\varepsilon \|A\|_1 \|X_{ni}\|_1},$$
(4.4)

where each pair of  $\lambda_i$  and  $X_{ni}$  is the eigenvalue and the corresponding eigenvector of the matrix [A] of order N, and  $\varepsilon$  the precision of arithmetic of the test machine. Note that the norm used in equation (4.4) is a modified form of the 1-norm, namely for the complex vector  $\mathbf{r}$ :

$$\left\|\mathbf{r}\right\|_{1} = \sum_{i=1}^{N} \left\{ \left| \operatorname{Re}(r_{i}) \right| + \left| \operatorname{Im}(r_{i}) \right| \right\}. \tag{4.5}$$

The performance of the EISPACK routine HQR2 in determining eigensolutions is excellent if PI < 1, good if  $1 \le PI < 100$  and poor if  $PI \ge 100$ . In this study, all the performance indexes are found to be less than  $10^{-3}$ , hence the excellent condition of the eigensolutions is definitely achieved.

In the nonlinear vibration analysis, the state space formulation is presented, thus the explicit time integration is preferred. However, the major drawback to the explicit methods is that they are conditionally stable, because the time step has a critical size. This shortcoming is overcome in this study by adopting the automatically adaptive time-step-size algorithm, which is included in the subroutine DIFSUB developed by Gear (1971). By using this algorithm, the time-step-size is automatically improved during the integration process so that the absolute error criterion:

$$\max_{i=1...N} (error_i) \le tol \tag{4.6}$$

is achieved. In this study,  $tol = 10^{-3}$  is set forth, and the corresponding adaptive timestep-sizes are in the range  $10^{-3}$  to  $10^{-1}$  sec.

Table 4.1 Comparisons of In-Plane Natural Frequencies of Test Cases

	$x_t$									
	$\overline{A}$ = Undeformed cross-sectional area $E$ = Elastic modulus $w_a$ suspended cable									
Case 1: the	Nondimension	nal l	Parameter $\frac{\overline{A}}{w_a}$	$\frac{E}{S}$	$\cong 5000, \frac{\sqrt{x_t^2}}{}$	+ . S	$\frac{\overline{y_t^2}}{} \cong 0.95, \Omega$			
Chord Inclination $oldsymbol{\phi}$	Mode No.				Interpolation (This Study*)				Quadratic Interpolation [105]	
7	(0)	4 Elements			0 Elements		20 Elements		Elements	
0°	$\omega_1(\Omega_1)$			0.62 (5.87)		0.62 (5.87)		<u> </u>	60 (5.65)	
	$\omega_2(\Omega_2)$	0.92 (8.75)		0.92 (8.74)		0.92 (8.74)		0.92 (8.77)		
30°	$\omega_1(\Omega_1)$	(	0.58 (6.00)		0.53 (5.43)		0.51 (5.29)		0.50 (5.17)	
	$\omega_2(\Omega_2)$	0	.98 (10.11)	0	0.85 (8.73)	0.81 (8.34)		0.80 (8.17)		
60°	$\omega_1(\Omega_1)$	$\omega_1(\Omega_1)$ 0.30		0.30 (4.05)		0.27 (3.65)		0.	0.27 (3.65)	
	$\omega_2(\Omega_2)$				).46 (6.19)			47 (6.30)		
Case 2: the	e Nondimension	nal l	Parameter $\frac{\overline{A}}{w_a}$	$\frac{E}{S}$	$\approx 2500, \frac{\sqrt{x_t^2}}{}$	+ . S	$\frac{\overline{y_t^2}}{2} \cong 0.98, \Omega$	$\Omega = 0$	$\omega \sqrt{\frac{S}{g}}$	
	~ ~	Fir	nite Element N	1eth	od		Initial-V			
Mode No.	Elements	8 Curve Elements (This Study*)  16 Straight-1 Element [16]					[107][ Extrapolation Method		Continuous Method	
$\omega_1$	0.793		0.809		0.795		0.80		0.811	
$\omega_2$	1.148		1.185		1.155		1.16		1.175	
$\omega_3$	1.620		1.680		1.627		1.63		1.653	
$\omega_4$	1.984	2.090			1.998		1.99		2.027	

<sup>\*</sup> Including the effect of axial deformation

#### 4.1.2 The Indirect Methods

The indirect methods involve comparisons of numerical results with the test cases. This study adopts the two test cases of the suspended cables reported in the papers by Henghold and Russell (1977), Gambhir, Barrington and Batchelor (1978), West, Geschwinder and Suhoski (1975) and West and Caramanico (1973). As shown in Table 4.1, the natural frequencies of the suspended cables calculated from the simplified version of this study are in good agreement with those obtained from other works. Therefore validity of the numerical results is confirmed.

Yet there are other informal checks that are carried out in this work. These include comparisons of the mode shapes of free vibrations of the marine pipes with the results reported by Pesce et al. (1999) and Chucheepsakul (1983); comparisons of the shapes of static equilibrium configurations and bending moment diagrams with the results of Bernitsas et al. (1985); checking the precision of the boundary conditions; checking that if subharmonic and superharmonic oscillations do not occur, the response frequencies should be closed to the hydrodynamic frequencies. The outcomes of these informal checks also manifest validity of the numerical results.

#### 4.2 THREE-DIMENSIONAL STATIC ANALYSIS

This section presents the important results of three-dimensional static analysis of the deep-water risers. The properties of the riser used in the numerical applications are summarized in Table 4.2. The riser is subjected to a tidal current with an exponential velocity profile, Eq. (2.41), acting in the x-direction and a triangular profile in the z-direction as show in Figure 4.1. The velocity of the current at the surface is 0.75 m/s and 1.3 m/s, respectively. The displacement is computed in two different ways. First, the three-dimensional model described in the previous section is used to obtain the results. Second, the two-dimensional model is used to approximate the three-dimensional deformation by vectorial summation of the two-dimensional deformations in the x-y plane and z-y plane.

Table 4.2 Properties of the riser used in the three-dimensional nonlinear static analysis

Property	Value		
Undeformed external diameter of the riser	0.610 m		
Undeformed internal diameter of the riser	0.575 m		
Density of pipe	$7850 \text{ kg/m}^3$		
Density of sea water	$1025 \text{ kg/m}^3$		
Density of internal fluid	$998.3 \text{ kg/m}^3$		
Elastic modulus	$2.07E+10^{11}$		
The ratio of the top tension to the effective weight (TTR)	1.1,1.5		
Sea depth (L)	2500 m		
In-plane offset	0 m		
Out-of-plane offset	0 m		
Normal hydrodynamic drag coefficient	0.7		
Tangential hydrodynamic drag coefficient	0.03		

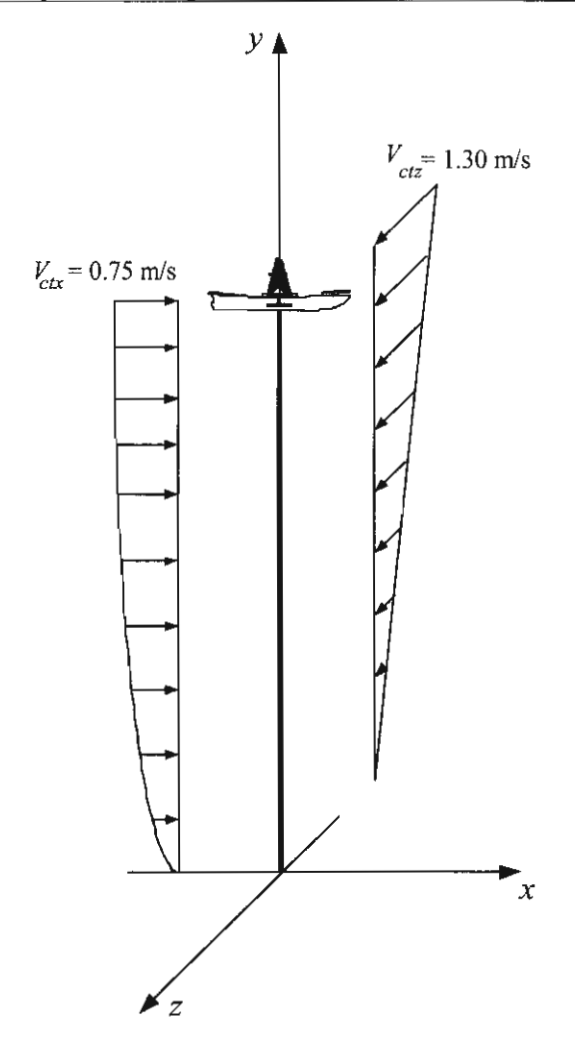


Figure 4.1 Deep-water riser subjected to the tidal and the triangular profile currents

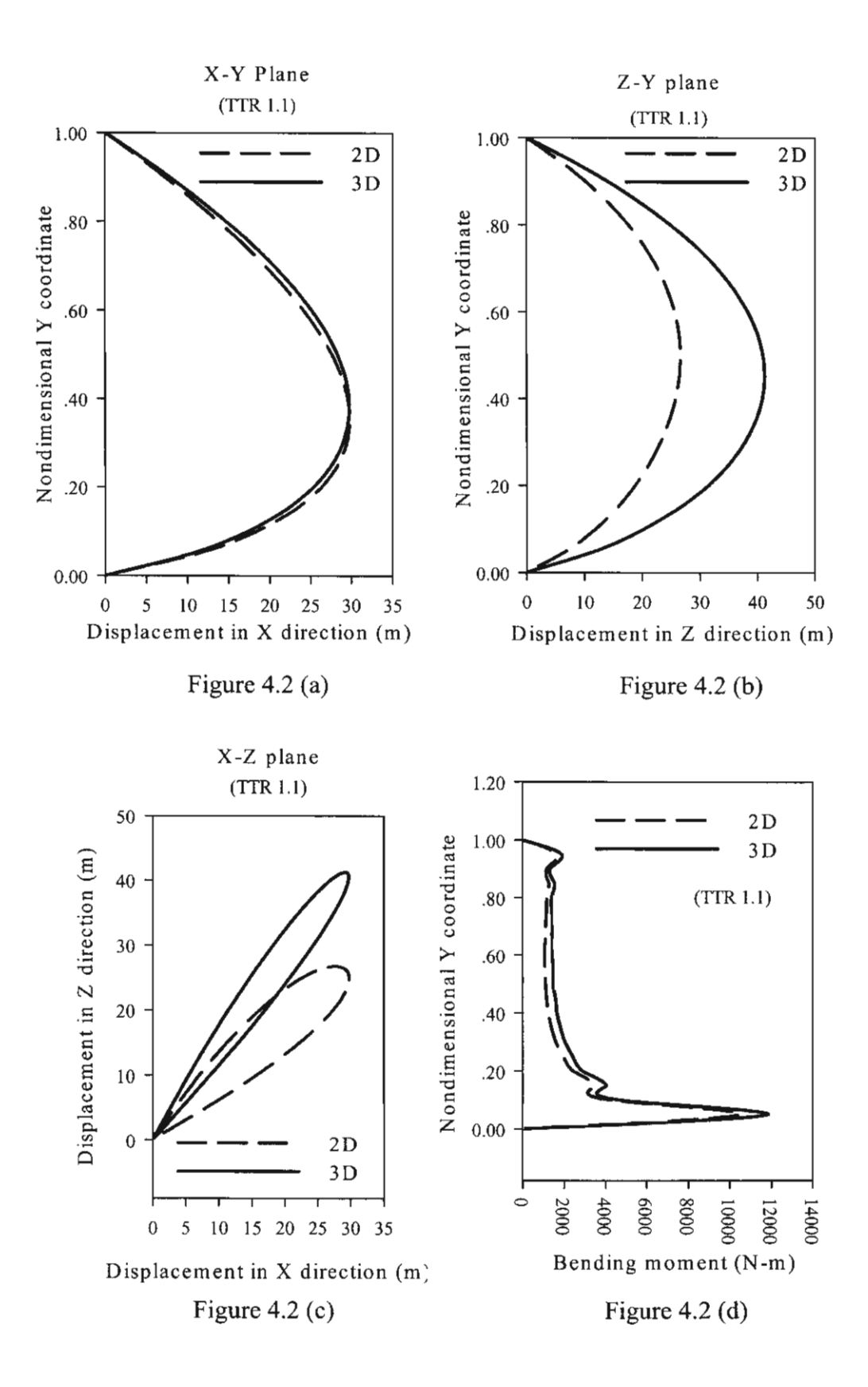


Figure 4.2 Static configurations and bending moment diagram of the deep-water riser subject to the tidal and the linear profile currents with TTR 1.1

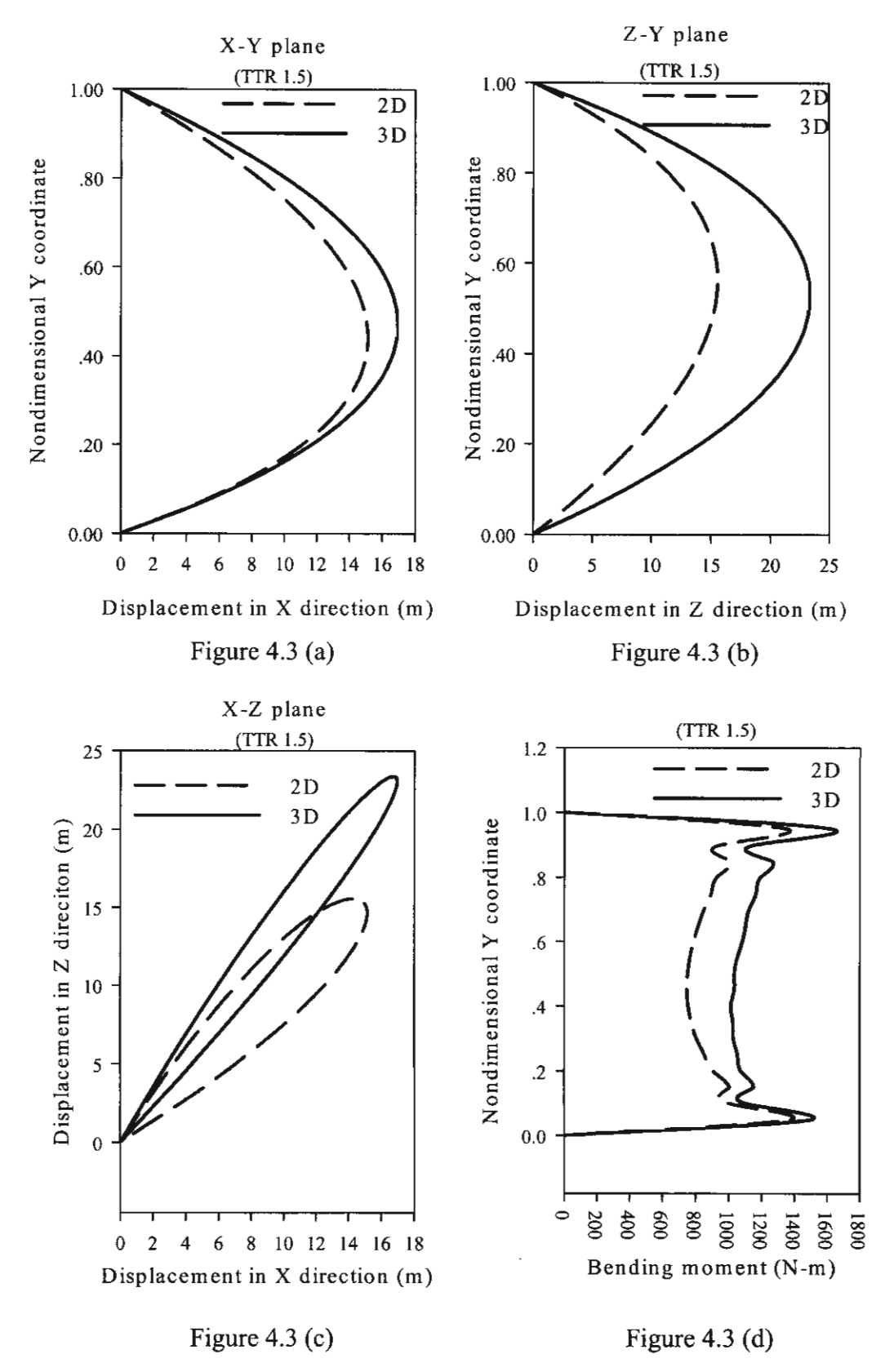


Figure 4.3 Static configurations and bending moment diagram of the deep-water riser subject to the tidal and the linear profile currents with TTR 1.5

Table 4.3 Displacement and bending moment comparison, between twodimensional and three-dimensional nonlinear analysis, of a riser subject to a tidal and a triangular current for TTR 1.1

TTR 1.1	Lateral in-plane displacement (m)		Lateral out-of-plane displacement (m)		Total Lateral Displacement $\sqrt{('x)' + ('z)'}$ (N-m)			Bending moment (N-m)		
Y/L	2-D	3-D	2-D	3-D	2-D	3-D	Diff	2-D	3-D	Diff
1.00	0.00	0.00	0.00	0.00	0.00	0.00	0.00	0.00	0.00	0.00
0.90	7.25	7.84	10.17	14.03	12.48	16.07	3.58	1173.91	1339.68	165.77
0.80	13.77	14.73	17.68	24.99	22.41	29.01	6.60	1176.02	1399.39	223.37
0.70	19.46	20.55	22.79	33.06	29.97	38.93	8.96	1113.45	1443.47	330.01
0.60	24.15	25.14	25.73	38.36	35.29	45.86	10.57	1077.77	1417.98	340.21
0.50	27.62	28.29	26.71	40.97	38.42	49.79	11.36	1104.93	1465.14	360.21
0.40	29.57	29.71	25.88	40.89	39.29	50.54	11.25	1247.05	1654.05	407.00
0.30	29.46	28.99	23.31	37.93	37.57	47.74	10.17	1606.53	2040.57	434.03
0.20	26.39	25.40	18.88	31.58	32.45	40.53	8.08	2424.71	2885.89	461.18
0.10	18.42	17.36	11.97	20.47	21.97	26.84	4.87	4265.35	4798.43	533.07
0.00	0.00	0.00	0.00	0.00	0.00	0.00	0.00	0.00	0.00	0.00

Table 4.4 Displacement and bending moment comparison, between twodimensional and three-dimensional nonlinear analysis, of a riser subject to a tidal and a triangular current for TTR 1.5

TTR 1.5	Lateral in-plane displacement (m)		Lateral out-of-plane displacement (m)		Total Lateral Displacement $\sqrt{('x)^2 + ('z)^2}$ (N-m)			Bending moment (N-m)		
Y/L	2-D	3-D	2-D	3-D	2-D	3-D	Diff	2-D	3-D	Diff
1.00	0.00	0.00	0.00	0.00	0.00	0.00	0.00	0.00	0.00	0.00
0.90	4.57	5.54	6.79	9.34	8.18	10.86	2.67	943.43	1146.53	203.09
0.80	8.43	10.09	11.47	16.13	14.23	19.02	4.79	924.88	1186.98	262.09
0.70	11.51	13.55	14.29	20.59	18.35	24.65	6.30	849.43	1120.26	270.83
0.60	13.71	15.86	15.50	22.92	20.69	27.87	7.18	786.38	1081.12	294.74
0.50	14.94	16.91	15.33	23.30	21.41	28.79	7.38	751.11	1032.66	281.54
0.40	15.04	16.63	14.00	21.90	20.55	27.50	6.95	754.36	1011.89	257.52
0.30	13.86	14.95	11.69	18.83	18.13	24.04	5.91	805.00	1027.03	222.03
0.20	11.15	11.73	8.56	14.15	14.06	18.38	4.32	904.88	1074.19	169.31
0.10	6.64	6.83	4.67	7.90	8.12	10.44	2.33	1001.06	1106.75	105.69
0.00	0.00	0.00	0.00	0.00	0.00	0.00	0.00	0.00	0.00	0.00

95

Figures 4.2 and 4.3 show the plot of the nonlinear static configurations and the bending moment diagram of the deep-water riser that are obtained from the approximate two-dimensional nonlinear analysis and three-dimensional nonlinear analysis for TTR = 1.1 and TTR = 1.5. The ratio of the top tension to the effective weight (TTR) is defined as

$$TTR = \frac{{}^{I}N_{t}}{{}^{o}w_{c}L} \tag{4.7}$$

Tables 4.3 and 4.4 show the numerical comparisons of the lateral displacement and bending moment between the two-dimensional and three-dimensional analyses of the deep-water risers for TTR = 1.1 and TTR = 1.5.

When the top tension is specified and the arc-length of the riser is varied with the magnitude of the large displacement. The lateral displacement and the bending moment computed by the three-dimensional model is higher than the displacement that computed by the two-dimensional model as shown in Figures 4.2 and 4.3. These results are due to the nature of nonlinearity in the model formulation. The linear combination or the superposition method of 2-D cases can not be applied to obtain the same results as those from the deep-water riser experiencing 3-D large displacement.

The increasing of the ratio of the top tension to the effective weight (TTR) reduces the lateral displacement and the bending moment as show in Tables 4.3 and 4.4. Moreover, the results in Tables 4.3 and Table 4.4 indicate that the difference of the lateral displacement and the bending moment between the two-dimensional and three-dimensional analysis are reduced when TTR is increased because the increasing top tension increases the axial deformation, thus reduce the effect of the large displacement. The discussion of the effect of the axial deformation and the effect of the internal flow velocity are discussed in the next section.

From the discussion above, it can be concluded that the coupling of the three-dimensional deformation affects on the large displacement and the bending moment when the in-plane and the out-of-plane loads occur in the same time. Therefore, the three-dimensional model formulation should be used in the general case.

### 4.3 PARAMETRIC STUDIES

The deep-water risers, which are the marine pipe under severe pressure environments, are employed as the specimen of the parametric studies. Their input parameters are given in Table 4.5. The details of the parametric studies are proposed in Table 4.6, where the applied top tension  $N_i$ , and the internal flow velocity  ${}^{o}V_{i}$  are varied to demonstrate the effects of axial deformation, and fluid transportation on the behaviors of the marine pipes, respectively. The reasons for choosing the parameters  $N_i$  and  ${}^{o}V_i$  for use in the parametric studies are that the axial strain  $\varepsilon \propto N_i$  follows the constitutive relation; and the rate of fluid transportation may be represented by the internal flow velocity  ${}^{o}V_i$ .

Table 4.5 Input Parameters of the Deep-Water Riser Specimen

Parameter	Standard Value
Elastic modulus E (N/m²)	0.207x10 <sup>12</sup>
External diameter of the pipe ${}^oD_e$ (m)	0.610
Internal diameter of the pipe ${}^oD_i$ (m)	0.575
Density of pipe material $ ho_p({ m kg/m^3})$	8337.9
Density of external fluid $ ho_e( ext{kg/m}^3)$	1025
Density of internal fluid $ ho_i$ (kg/m $^3$ )	1438
Static in-plane offset ${}^{o}x_{i}$ (m) (see Fig.4.1)	100
Static out-of-plane offset $^{o}z_{i}$ (m) (see Fig.4.1)	0
$^{\circ}y_{i}$ (m) (see Fig.2.1a)	2000
Applied top tension $N_i$ (N)	$0.7x10^{7}$
Normal drag coefficient $C_{Dn}$	2
Tangential drag coefficient $C_{Dt}$	0.1
Current velocity at mean sea level $V_{ct}\left(\mathrm{m/s}\right)$	0.2
Internal flow velocity ${}^{o}V_{i}$ (m/s)	20
Added mass coefficient $C_a$	1.5
Wave amplitude $\varphi_a$ (m)	6
Wave frequency $\omega_{\rm w}$ (rad/sec)	0.6
Wave number $k$	0.03
Linear velocity amplitude of int. flow $V_{it}$ (m/s)	0
Wave velocity amplitude of int. flow $V_{ia}  (\text{m/s})$	0.2
Internal flow frequency $\omega_i$ (rad/sec)	0.05

Table 4.6 Parametric Studies

To Study the Effects of	The Values of Parameters in Table 4.2 are Reserved Constant Except Varying					
Axial deformation	$^{1}N_{t} = 10^{7}, 0.8 \times 10^{7}, 0.7 \times 10^{7}, 0.67 \times 10^{7}, 0.64 \times 10^{7}N$					
Fluid transportation	$^{o}V_{i} = 0, 5, 10, 15, 20 \text{ m/s}$					

# 4.4 EFFECTS OF AXIAL DEFORMATION ON BEHAVIORS OF THE MARINE PIPES

## 4.4.1 Effects of Axial Deformation on Nonlinear Static Behavior

From the parametric study of the axial deformation effects designated in section 4.3, the results are obtained as depicted in Figures 4.4-4.11. The effects of axial deformation on the nonlinear static behavior of the marine pipes are illustrated in Figures 4.4 and 4.5, and can be summarized as follows:

4.4.1.1 Axial deformation reduces the large deflections of the marine pipe. As seen in Figure 4.4, dropping the top tension, which induces a reduction of the axial deformation, increases the sag of the marine pipe. This result is not uncommon for a prestressed structure such as marine pipes. Diminishing degree of prestressing significantly reduces the axial stiffness of the prestressed structure. Consequently, the large deflections are raised.

4.4.1.2 Axial deformation affects behaviors of the marine pipe. The pipe subjected to the large axial deformation due to high pretension behaves as the taut pipe with low sag, whereas the low-tensioned pipe with low axial deformation behaves as the slack pipe with large sag. As shown in Figure 4.4, the pipe in the case where  ${}^{1}N_{t} = 10^{7} N$  is taut, while the pipe subjected to  ${}^{1}N_{t} = 6.4 \times 10^{6} N$  is largely slack, especially at the bottom portion  ${}^{1}y = 0$  - 200 m. The vibration behaviors of the taut and the slack pipes are quite different, as will be discussed later.

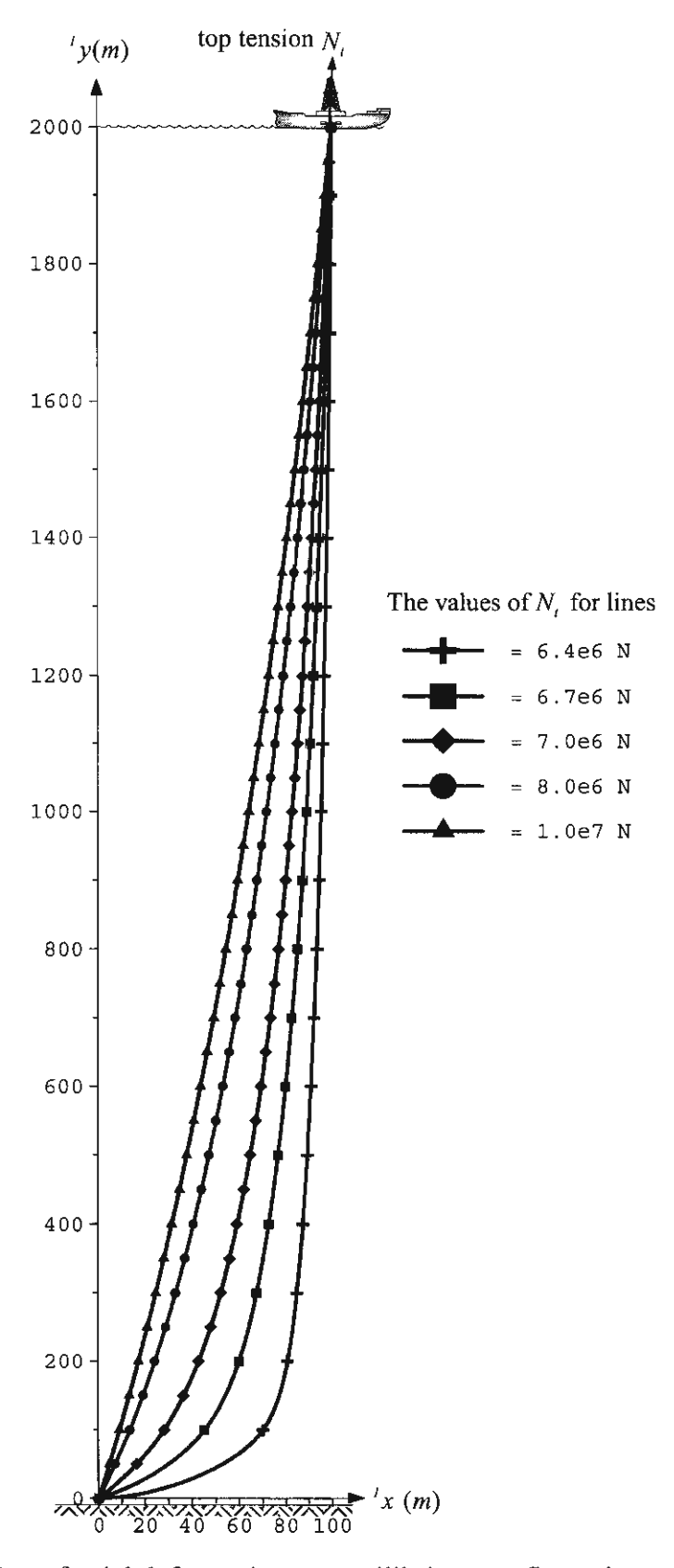


Figure 4.4 Effect of axial deformation on equilibrium configurations of the pipe

- 4.4.1.3 The allowable range of axial deformation indicates the design patterns of the marine pipe. In Figure 4.4, the effective design criterion belongs to the condition  $0.7 \times 10^7 < {}^{1}N_{t} < 10^7 N$ . The pipe is overdesigned if  ${}^{1}N_{t} > 10^7 N$  is devised, and underdesigned if  ${}^{1}N_{t} < 0.7 \times 10^7 N$  is adopted. Overdesign is uneconomical, while underdesign results in the divergence instability of the pipe.
- 4.4.1.4 Axial deformation reduces the rotations of the marine pipe particularly at the large sag region. As shown in Figure 4.5 (a), the pipe that is taut due to high axial deformation ( ${}^{I}N_{I} = 10^{7} N$ ), gains much less rotation of the bottom support than the pipe that is slack due to low axial deformation ( ${}^{I}N_{I} = 6.4 \times 10^{6} N$ ).
- 4.4.1.5 Axial deformation increases the axial strain in the marine pipe. Figure 4.5 (b) manifests this deduction. It is seen that the axial strains in the taut pipe with  ${}^{1}N_{t} = 10^{7} N$  are all positive or tensile and higher than those of the slack pipe with  ${}^{1}N_{t} = 6.4 \times 10^{6} N$ . The axial strains of such a slack pipe are found to possess negative values at the bottom portion of the pipe.
- 4.4.1.6 Axial deformation augments the static stability of marine pipes. As previously found, with reductions of the top tension, the axial strain is reduced and can be negative at the bottom portion of the slack pipe. Following the constitutive equation, a negative axial strain signifies a negative apparent tension. The author found that when the top tension is decreased until  ${}^{I}N_{I} < 6.4 \times 10^{6} N$  such a negative apparent tension will become large enough to embark the local buckling at the bottom portion of the pipe. It will be shown later that for  ${}^{I}N_{I} < 6.4 \times 10^{6} N$  the natural frequency of the pipe converges to zero, and the pitchfork bifurcation thus occurs.
- 4.4.1.7 Axial deformation magnifies the true-wall and the apparent tensions in the marine pipe, as shown in Figure 4.5 (c). It should be note that for marine structures, the apparent tension is more important than the true-wall tension, because it is the total virtual tension appearing in marine structures.

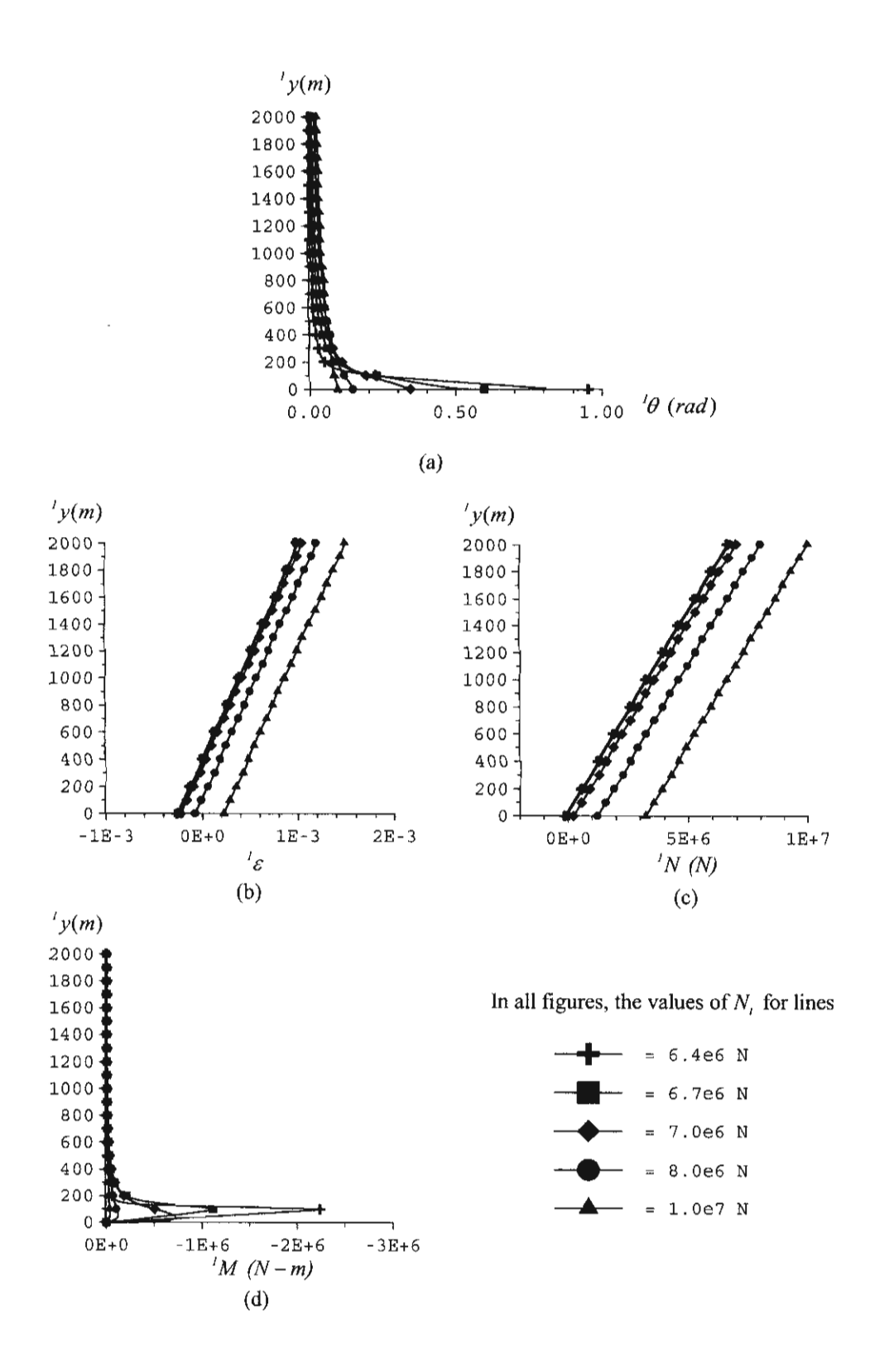


Figure 4.5 Effects of Axial Deformation on

(a) Rotations (b) Axial Strains

(c) True-Wall Axial Forces (d) Bending Moments

4.4.1.8 Axial deformation decreases the bending moments in the marine pipe especially at the large sag portion. This result is due to the effects of axial deformation on a reduction of the pipe's rotations as shown in Figure 4.5 (b). When the rotation  $\theta$  decreases, the bending moment M will also diminish corresponding to the relationship

$$\kappa = \frac{1}{\Re} = \frac{d\theta}{ds} = \frac{M}{EI_P},\tag{4.8}$$

respectively. Figure 4.5 (d) asserts these results. It is found that the bending moment diagrams of the pipe that is taut due to high axial deformation ( ${}^{\prime}N_t = 10^{7} N$ ) are almost vertically straight, whereas those of the pipe that is slack due to low axial deformation ( ${}^{\prime}N_t = 6.4 \times 10^6 N$ ) have the curve parts magnificently growing at  ${}^{\prime}y = 0$  - 200 m, where the slack pipe possesses large curvatures and large rotations. Therefore, in the design of the slack pipe, the bending stress and the shear stress should be carefully examined especially at the bottom part of the pipe. Sometimes the bending and shear stiffeners may be desired at that portion to eliminate the excessive conditions of large curvatures and bending moments, which may cause poor serviceability and localized damage to the pipe.

#### 4.4.2 Effects of Axial Deformation on Natural Frequencies

The effects of axial deformation on the natural frequencies and the stability of the linearized system of the marine pipes are illustrated in Figures 4.6 - 4.8, and are summarized as follows:

4.4.2.1 Axial deformation raises the natural frequencies of the marine pipe. To display this effect, the eigencurves are plotted in the stiffness-frequency space as shown in Figure 4.6. It is revealed that the natural frequencies of the pipe are increased with an escalation of the top tension. The natural frequencies of the slack pipe with  ${}^{\prime}N_{t} = 6.4 \times 10^{6} \, N$  are significantly lower than those of the taut pipe with  ${}^{\prime}N_{t} = 10^{7} \, N$ . As the top tension is reduced continuously, the eigencurves tend to intersect the top tension axis at the point, where the top tension possesses the critical values and the natural frequencies are zero. This implies that buckling of the pipe due to the effect of axial deformation is of static nature, and may be referred to as the divergence buckling.

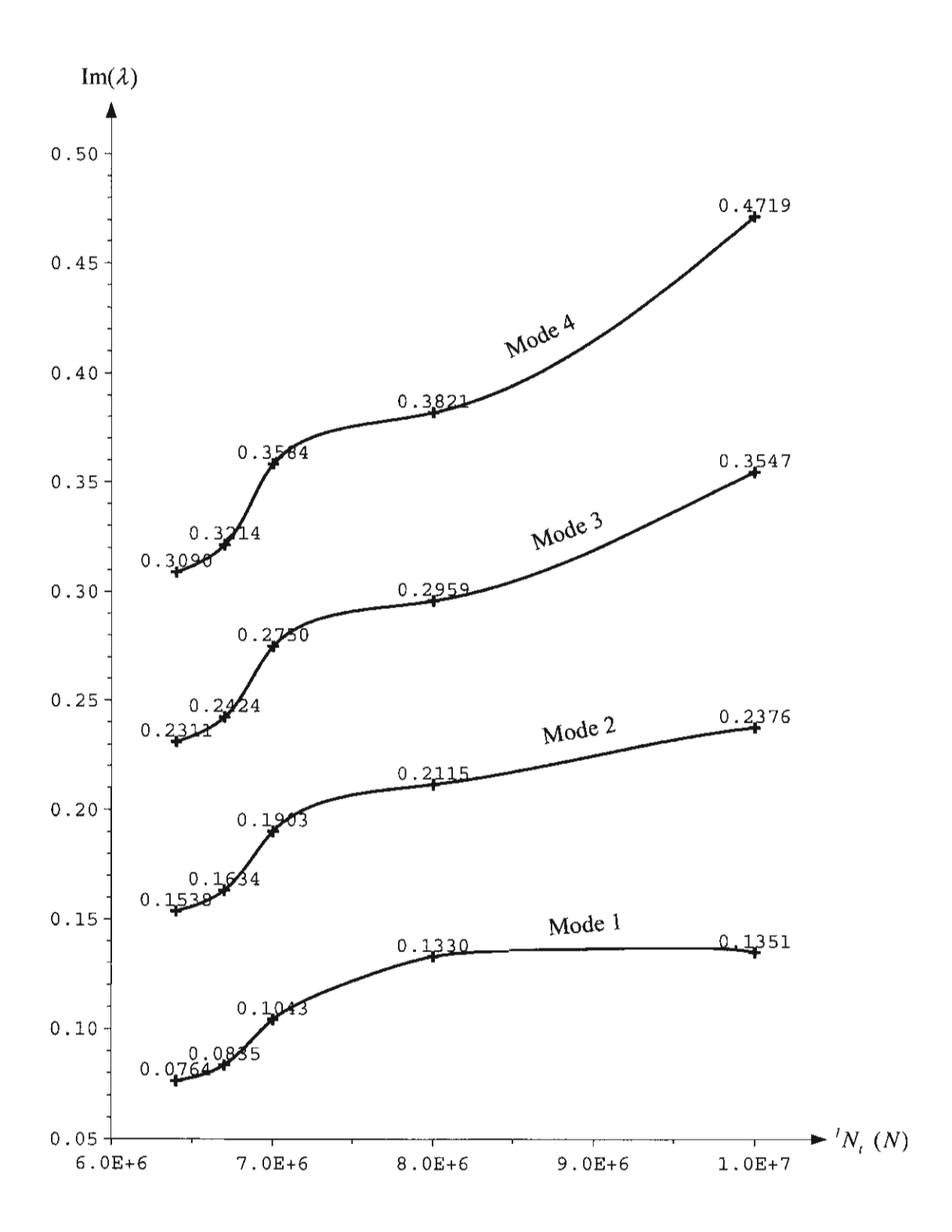


Figure 4.6 Effect of Axial Deformation on Natural Frequencies

4.4.2.2 Axial deformation boosts the dynamic stability of the linearized system of the marine pipe. To explain this effect, the complex plane of the Argand diagram is displayed in Figure 4.7. A continuous reduction of the axial deformation by incessantly diminishing the top tension motivates the pipe into experiencing 'static buckling' or 'divergence instability' at the Pitchfork bifurcation point, where the top tension has reached the critical value (Chucheepsakul and Monprapussorn, 2001). This behavior is explained as follows.

Before buckling, the complex eigenvalues  $\lambda$  have zero real part, no matter how much the top tension is varied. The constant reduction of the top tension yields a decrease in the natural frequencies of the pipe, which is imaginary part of the eigenvalues, along the vertical line  $\text{Re}(\lambda) = 0$  to converge to zero. This type of the Argand diagram deals with the divergence instability via Pitchfork bifurcation. After buckling, pitchfork bifurcation would change the eigenvalues from wholly imaginary to become wholly real along the horizontal line  $\text{Im}(\lambda) = 0$  as shown in Figure 4.7.

Based on the Liapunov indirect method, the stability of motion of the linearized system may be tested by examining the solutions of the linearized equations of motion with respect to the Liapunov stability definitions (Meirovitch, 1997). Such stability definitions can be interpreted into the complex eigenvalue analysis as follows.

For the complex eigenvalues  $\lambda_j = \alpha_j + i\omega_j$ , in which j = 1, 2, ..., 2 (numdfd), and numdfd is the dynamic degrees of freedom,

- (a) if  $\forall \alpha_j = 0$ , the system has stable motion, which is pure oscillation, and neither tends away nor moves to the equilibrium point as  $t \to \infty$ ,
- (b) if  $\forall \alpha_j < 0$ , the system oscillates by asymptotically stable motion, which tends to the equilibrium point as  $t \to \infty$ ,
- (c) if  $\exists \alpha_j > 0$ , the system exhibits unstable motion, which departs away from the equilibrium point as  $t \to \infty$ .

Note that the universal quantifier ' $\forall$ ' means 'all of', and the existential quantifier ' $\exists$ ' abbreviates 'some of'.

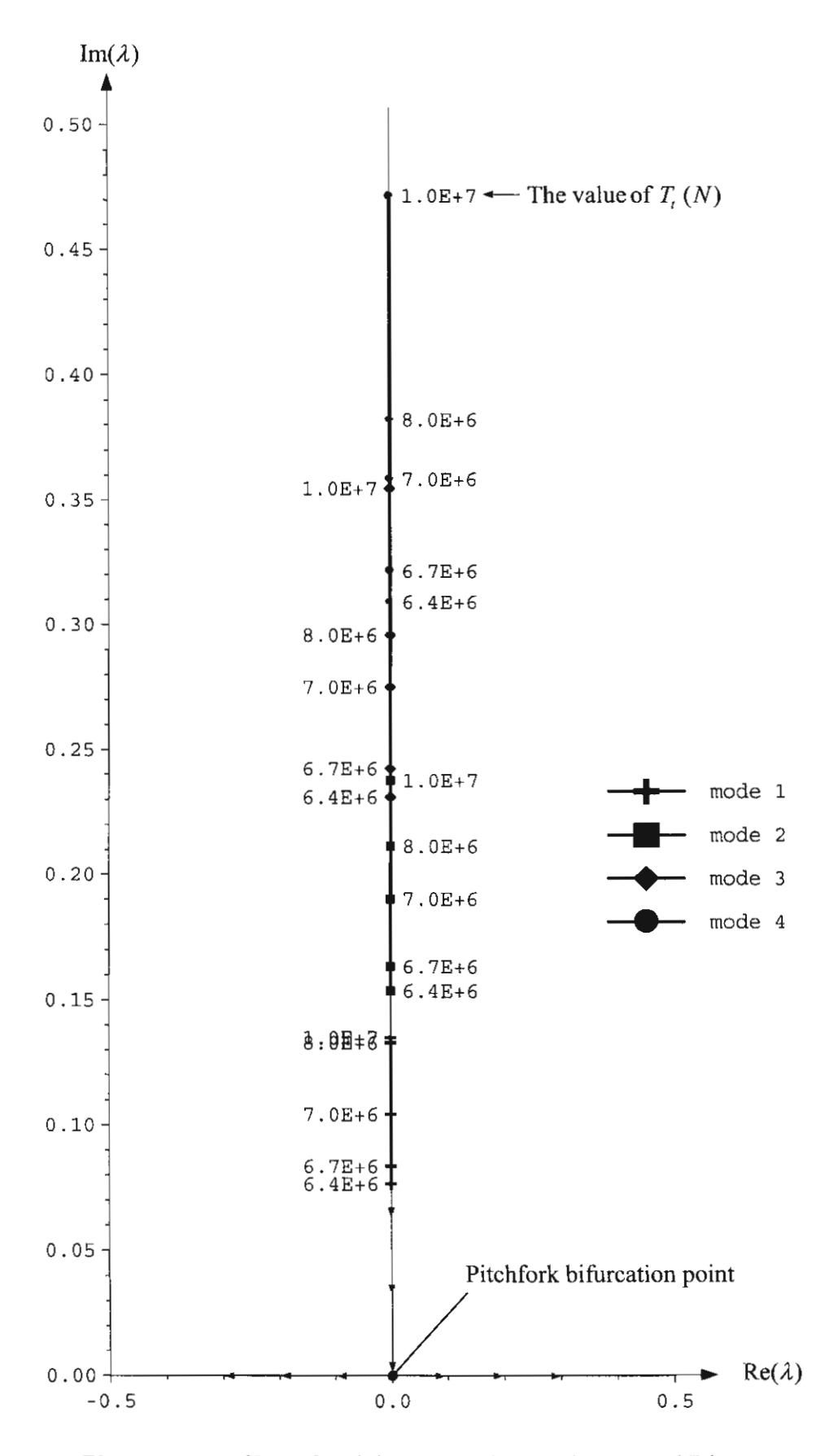


Figure 4.7 Effect of Axial Deformation on the Argand Diagrams

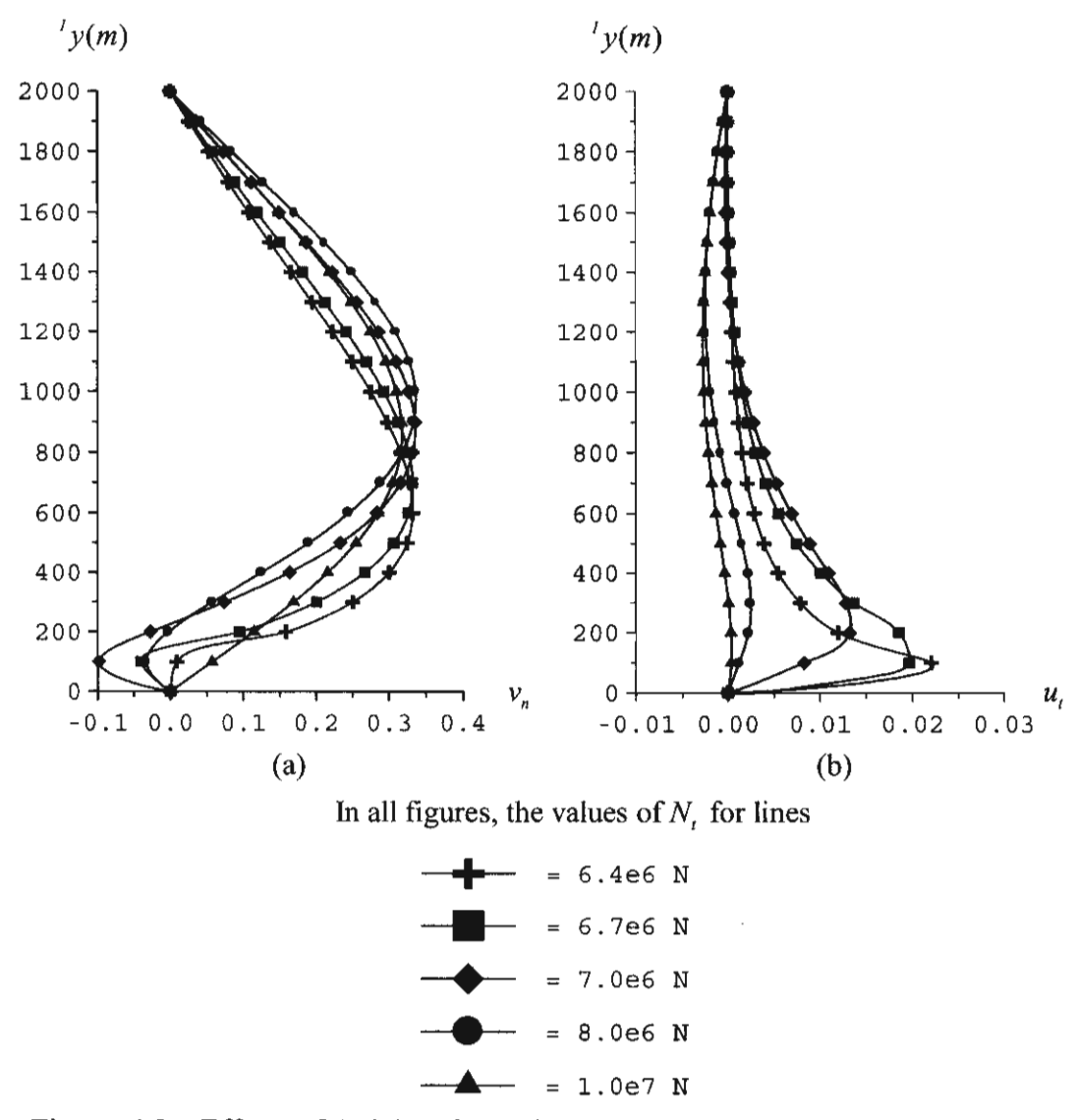


Figure 4.8 Effects of Axial Deformation on the Fundamental Mode Shapes of

#### (a) Normal Vibrations (b) Tangential Vibrations

The system is said to possess 'significant behavior' if its motion is either asymptotic stable or unstable, and is said to have 'critical behavior' if its motion is stable. The Russian mathematician and mechanician Liapunov (Meirovitch, 1997) indicated that if the linearized system exhibits significant behavior, the above stability criteria could be extended to the nonlinear system. However, if the linearized system displays critical behavior, then conclusions about the stability of the nonlinear system cannot be made accurately from the above stability criteria.

Adopting the stability criteria in the sense of Liapunov, the complex eigenvalues of the marine pipe as shown in Figure 4.7 agree with the condition (a), therefore free vibrations of the linearized system of the marine pipe possess stable oscillations and critical behavior. As a result, the stability of the linearized system cannot be guaranteed for the nonlinear system of the marine pipe. Instead, the stability of nonlinear vibrations of the marine pipe should be probed by the phase plane analysis based on the solutions of the nonlinear equations of motion, including the fully nonlinear hydrodynamic forces, as will be shown later.

4.4.2.3 Axial deformation affects the mode shapes of free vibrations of the marine pipe. Figures 4.8 (a), and 4.8 (b) demonstrate the effect on fundamental modes of free vibrations in the normal, and tangential directions, respectively. It is seen that the axial deformation has a significant effect on changing the mode shapes of normal and tangential free vibrations.

In Figure 4.8 (a), the fundamental mode shape of normal vibration of the pipe that is slack due to low axial deformation ( ${}^{1}N_{t} = 6.4 \times 10^{6} N$ ), has one more curvature than that of the pipe that is taut due to high axial deformation ( ${}^{1}N_{t} = 10^{7} N$ ) at the bottom portion ( ${}^{1}y = 0\text{-}200 \text{ m}$ ), where the pipe possesses a large sag. In Figure 4.8 (b), the slack pipe has maximum amplitudes of the tangential vibrations at the large sag portion of the pipe.

#### 4.4.4 Effects of Axial Deformation on Nonlinear Vibration Behavior

The effects of axial deformation on the nonlinear forced vibrations of marine pipes are illustrated in Figures 4.9 - 4.11, and are summarized as follows:

4.4.4.1 Axial deformation decreases nonlinear responses of forced vibrations of the marine pipe. The nonlinear responses in a time period of 0-60 seconds of forced vibrations of the taut pipe with  ${}^{I}N_{I} = 10^{7} N$  are plotted on the left-hand side of Figure 4.9, while those of the slack pipe with  ${}^{I}N_{I} = 6.4 \times 10^{6} N$  are displayed on the right-hand side of the same figure. By comparing the left- and the right-hand side figures, it is evident that the slack pipe possesses much larger amplitudes of the normal, and tangential vibrations than the taut pipe.

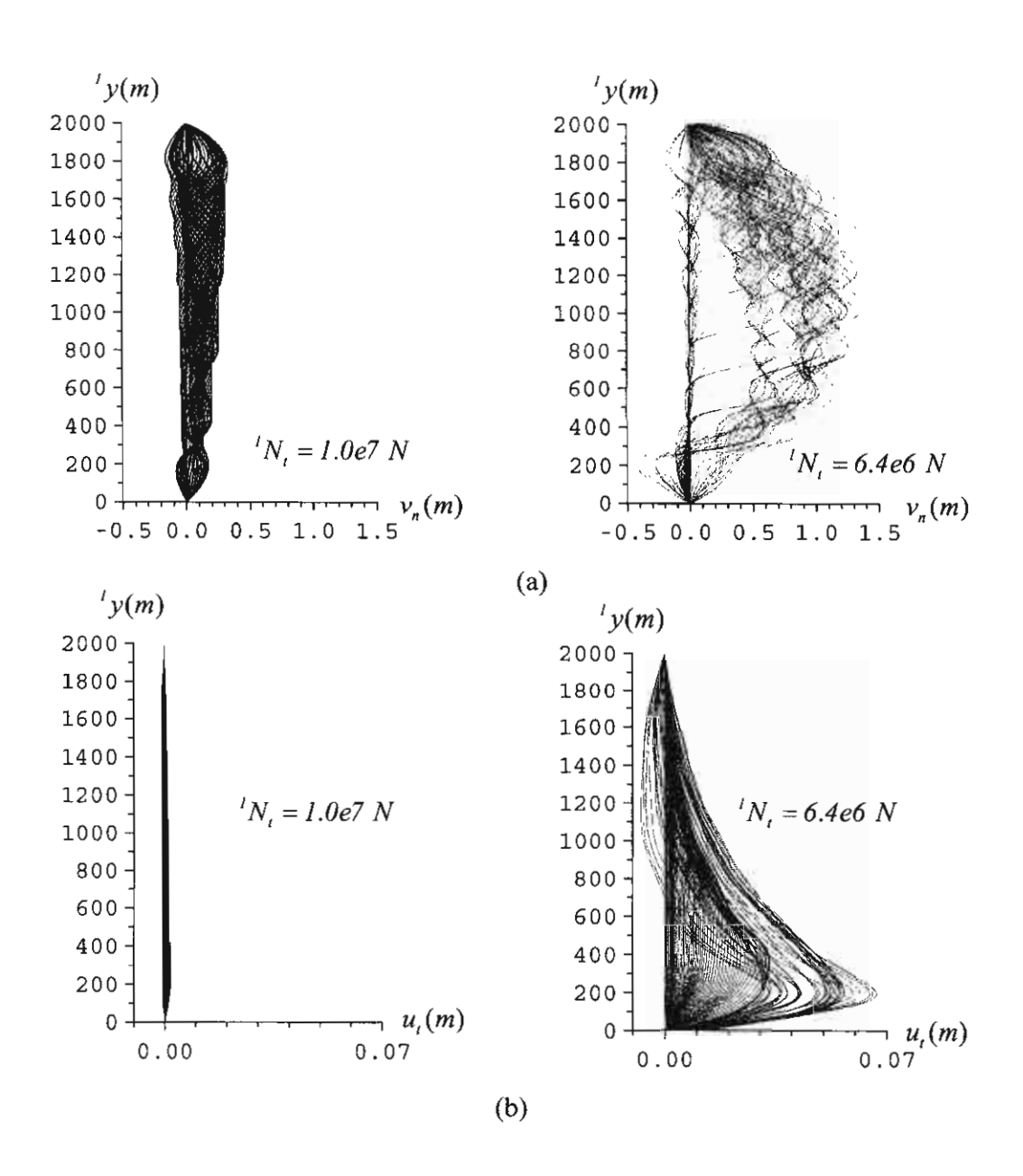


Figure 4.9 Nonlinear Responses in Time 0-60 Seconds of

(a) Normal Vibrations (b) Tangential Vibrations

4.4.4.2 Axial deformation affects the time histories of nonlinear vibrations of the marine pipe. Figures 4.10 (a), 4.10 (b) and 4.10 (c) demonstrate the time histories of the normal vibrations of the top part ( $^{I}y = 1800$  m), of the middle part ( $^{I}y = 1000$  m), and of the bottom part ( $^{I}y = 400$  m) of the pipes, respectively. It is seen that the slack pipe possesses much larger amplitudes of the normal vibrations than the taut pipe.

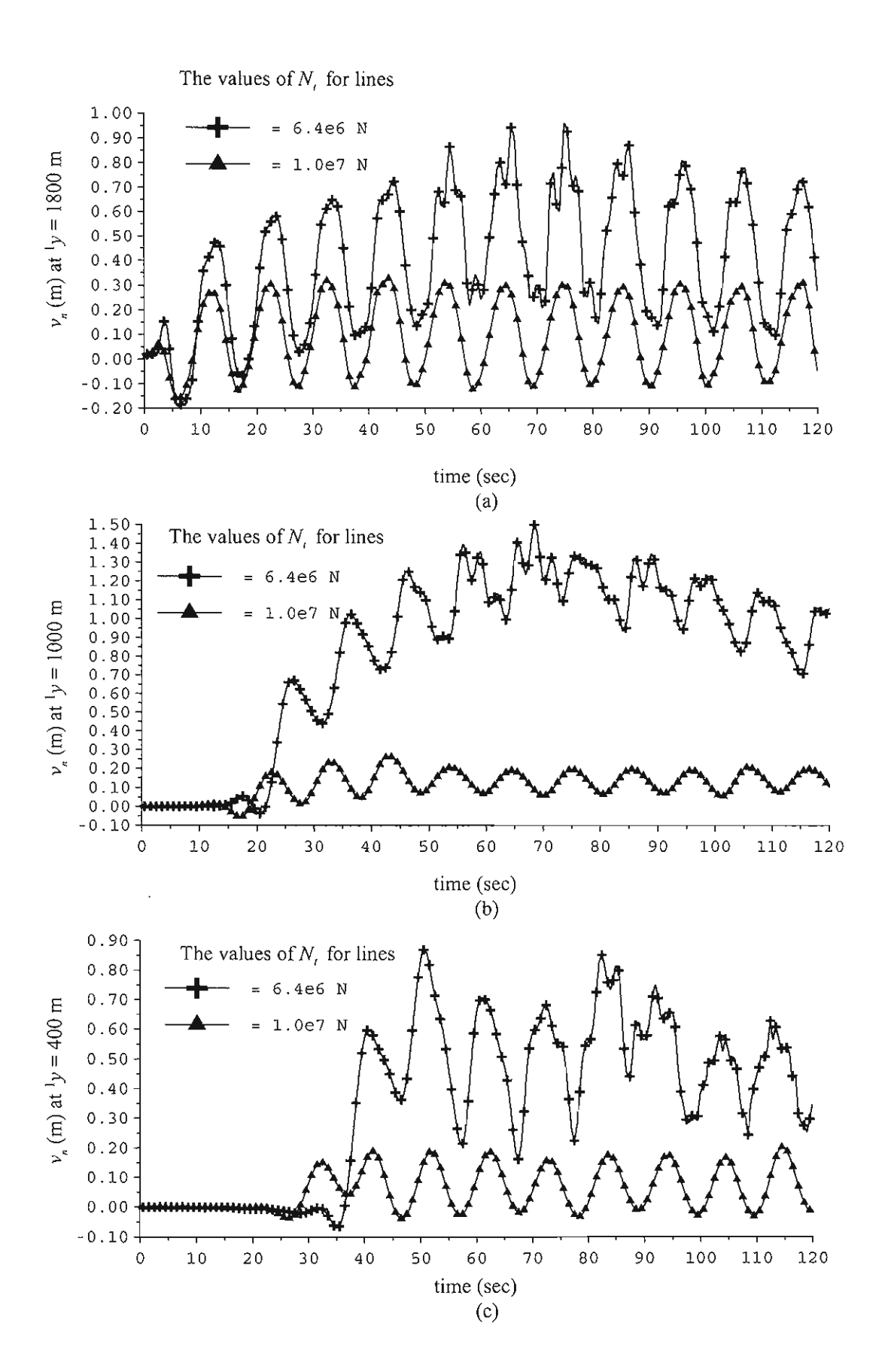


Figure 4.10 Effect of Axial Deformation on Time Histories of Normal Vibrations

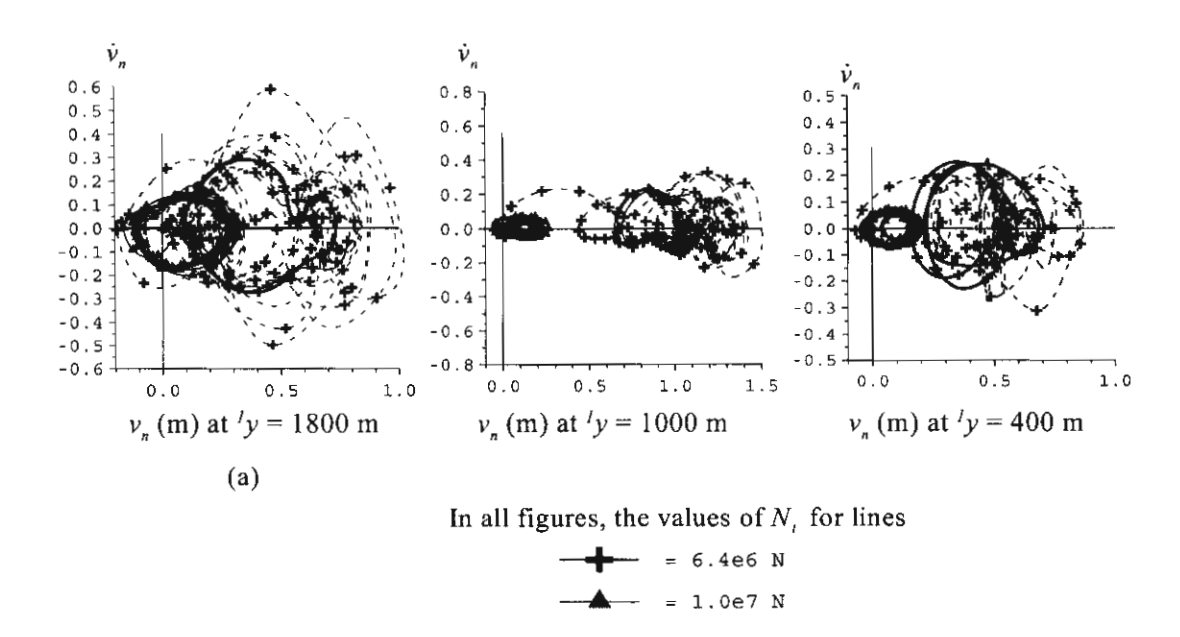


Figure 4.8 Effect of Axial Deformation on Trajectories of Normal Vibrations

Over a long-term period, the normal oscillations of all parts of the taut pipe are developed to steady motions, while all parts of the slack pipe exhibit unsteady normal vibrations. Unsteadiness of the normal vibrations of the slack pipe is remarkably great at the bottom part, where the slack pipe has a large curvature. It is noticed that the response frequencies of normal vibrations of all parts of the pipes  $\approx 2\pi/10$  are close to the wave frequency 0.6. Therefore, the normal oscillations of the pipes are ordinary harmonic.

4.4.4.3 Axial deformation increases the stability of motion of the marine pipe. The trajectories of the normal vibrations of the top part ( $^{I}y = 1800 \text{ m}$ ), of the middle part ( $^{I}y = 1000 \text{ m}$ ) and of the bottom part ( $^{I}y = 400 \text{ m}$ ) of the pipes are plotted in the phase planes as shown in Figures 4.11 (a), and 4.11 (b), respectively. The figures revealed that as a time period passes all trajectories, which start at the initial condition of the zero normal state speed and the zero normal displacement, tend to the closed curves (bold lines), which may be referred to as 'the limit cycle' (Meirovitch, 1997).

The stability of a limit cycle can be evaluated through the definitions of 'the orbital stability' or 'the stability in sense of Poincaré' (Meirovitch, 1997) as follows. Denoting the distance of a point  $\mathbf{x}_1$  to a periodic orbit  $\mathbf{C}$  by

$$\operatorname{dist}(\mathbf{x}_{1}, \mathbf{C}) = \min\{\|\mathbf{x}_{1} - \mathbf{x}\|, \text{ for all } \mathbf{x} \in \mathbf{C}\}, \tag{4.9}$$

(a) if dist( $\mathbf{x}(t_a)$ ,  $\mathbf{C}$ ) <  $\delta$  for  $\delta > 0$  implicates an existence of any  $\varepsilon > 0$  such that

$$\operatorname{dist}(\mathbf{x}(t), \mathbb{C}) < \varepsilon \text{ for all } t > t_{o},$$
 (4.10)

then the periodic orbit C is orbitally stable,

(b) if  $\operatorname{dist}(\mathbf{x}(t_o), \mathbf{C}) < \delta$  for  $\delta > 0$  implicates an existence of the condition

$$\operatorname{dist}(\mathbf{x}(t), \mathbf{C}) \to 0 \text{ as } t \to \infty,$$
 (4.11)

then the periodic orbit C is orbitally asymptotically stable,

(c) The periodic orbit C is orbitally unstable if it is not stable.

The physical meaning of the above definitions may be illuminated as follows. For a given closed trajectory  $\mathbb{C}$ , if every trajectory in the neighborhood of  $\mathbb{C}$  remains in the neighborhood of  $\mathbb{C}$ , the motion of the system is orbitally stable. If the trajectories approach  $\mathbb{C}$  as  $t \to \infty$ , the motion of the system is orbitally asymptotically stable. If the trajectories tend to leave the neighborhood of  $\mathbb{C}$  or approach  $\mathbb{C}$  as  $t \to -\infty$ , the motion of the system is orbitally unstable.

The concept of orbital stability can be extended to the nonclosed orbits of nonperiodic solutions as follows. For the two orbits  $C_1$  and  $C_2$  corresponding to the solutions  $x_1$  and  $x_2$ , which are close to each other at time  $t_o$ ,

- (a) if the orbits  $C_1$  and  $C_2$  remain close at all subsequent times  $t > t_o$ , the orbits  $C_1$  and  $C_2$  are orbitally stable,
- (b) if the orbits  $C_1$  and  $C_2$  converge to each other as  $t \to \infty$ , the orbits  $C_1$  and  $C_2$  are orbitally asymptotically stable,
- (c) if the orbits  $C_1$  and  $C_2$  tend away from each other or converge to each other as  $t \to -\infty$ , the orbits  $C_1$  and  $C_2$  are orbitally unstable.

Adopting the aforementioned concept of orbital stability, from Figures 4.11 (a), 4.11 (b) and 4.11 (c) it is found that the motions of all parts of the taut pipe are orbitally stable, because all the closed trajectories remain in the neighborhood of one another for all  $t > t_o$ , while those of the slack pipe are orbitally unstable on the grounds that the closed trajectories tend to leave the neighborhood of the others. This result indicates that the axial deformation augments the stability of motion of the pipe.

# 4.5 EFFECTS OF FLUID TRANSPORTATION ON BEHAVIORS OF THE MARINE PIPES

#### 4.5.1 Effects of Fluid Transportation on Nonlinear Static Behavior

From the parametric study of the fluid transportation effects designated in section 4.3, the results are obtained as depicted in Figures 4.12 - 4.19. The effects of fluid transportation on the nonlinear static behavior of the marine pipes are illustrated in Figures 4.12 and 4.13, and are summarized as follows:

- 4.5.1.1 Fluid transportation increases large deflections of the marine pipe. As seen in Figure 4.12, when the transportation rate is raised by an increase of internal flow velocity, the sag of the marine pipe is enlarged.
- 4.5.1.2 Fluid transportation enlarges the rotations of the marine pipe, particularly in the large sag portion of the pipe. As shown in Figure 4.13(a), the pipe without fluid transportation has a lesser rotation of the bottom support than the pipe with internal flow velocity 20 m/s.
- 4.5.1.3 Fluid transportation has an insignificant effect on reducing axial strain in the marine pipe as shown in Figure 4.13(b), and thus slightly decreases the static stability of the pipe.
- 4.5.1.4 Fluid transportation has an insignificant effect on reducing the true-wall and the apparent tensions in the marine pipe as shown in Figure 4.18(d).
- 4.5.1.5 Fluid transportation amplifies bending moments in the marine pipe, especially at the large sag portion. Figure 4.13(c) illustrates this result. It is found that the bending moments of the pipe without fluid transportation are less than those of the pipe with a transportation rate of 20 m/s, especially at the bottom part of the pipe, where the pipe possesses large curvatures and large rotations.

## 4.5.2 Effects of Fluid Transportation on Natural Frequencies

The effects of fluid transportation on natural frequencies and the dynamic stability of the linearized system of the marine pipes are illustrated in Figures 4.14 - 4.16, and are summarized as follows:

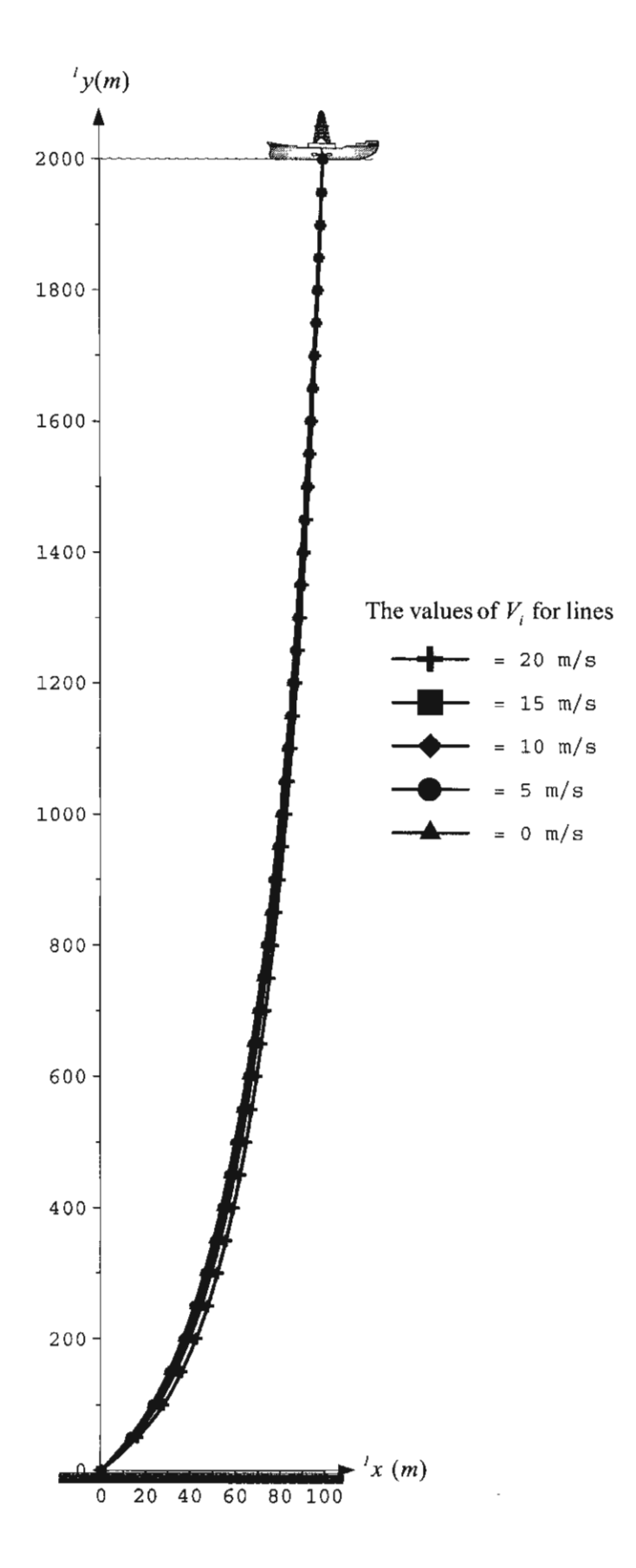


Figure 4.12 Effect of Fluid Transportation on Equilibrium Configurations of the Pipe

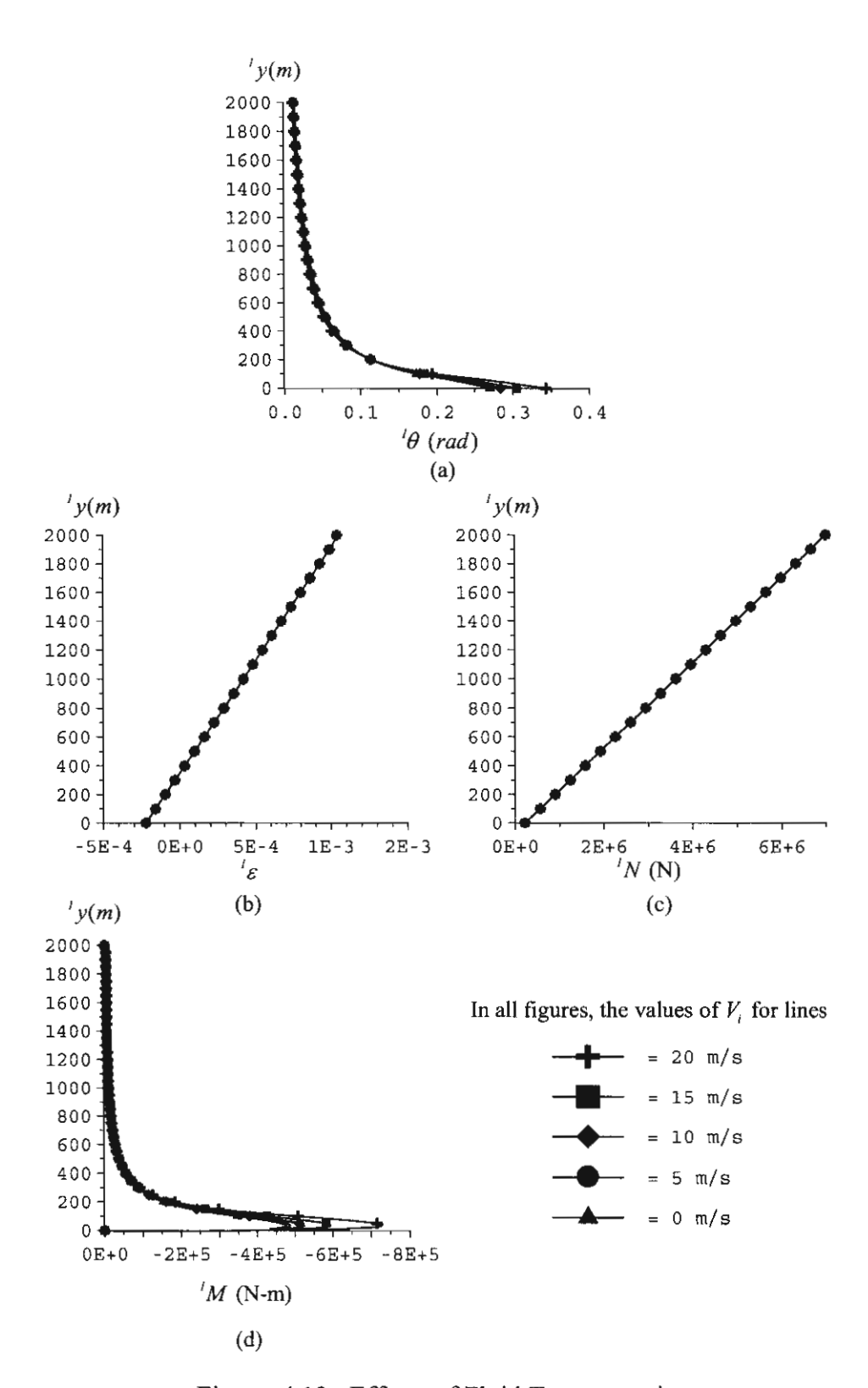


Figure 4.13 Effects of Fluid Transportation on

- (a) Rotations (b) Axial Strains
- (c) True-Wall Axial Forces (d) Bending Moments

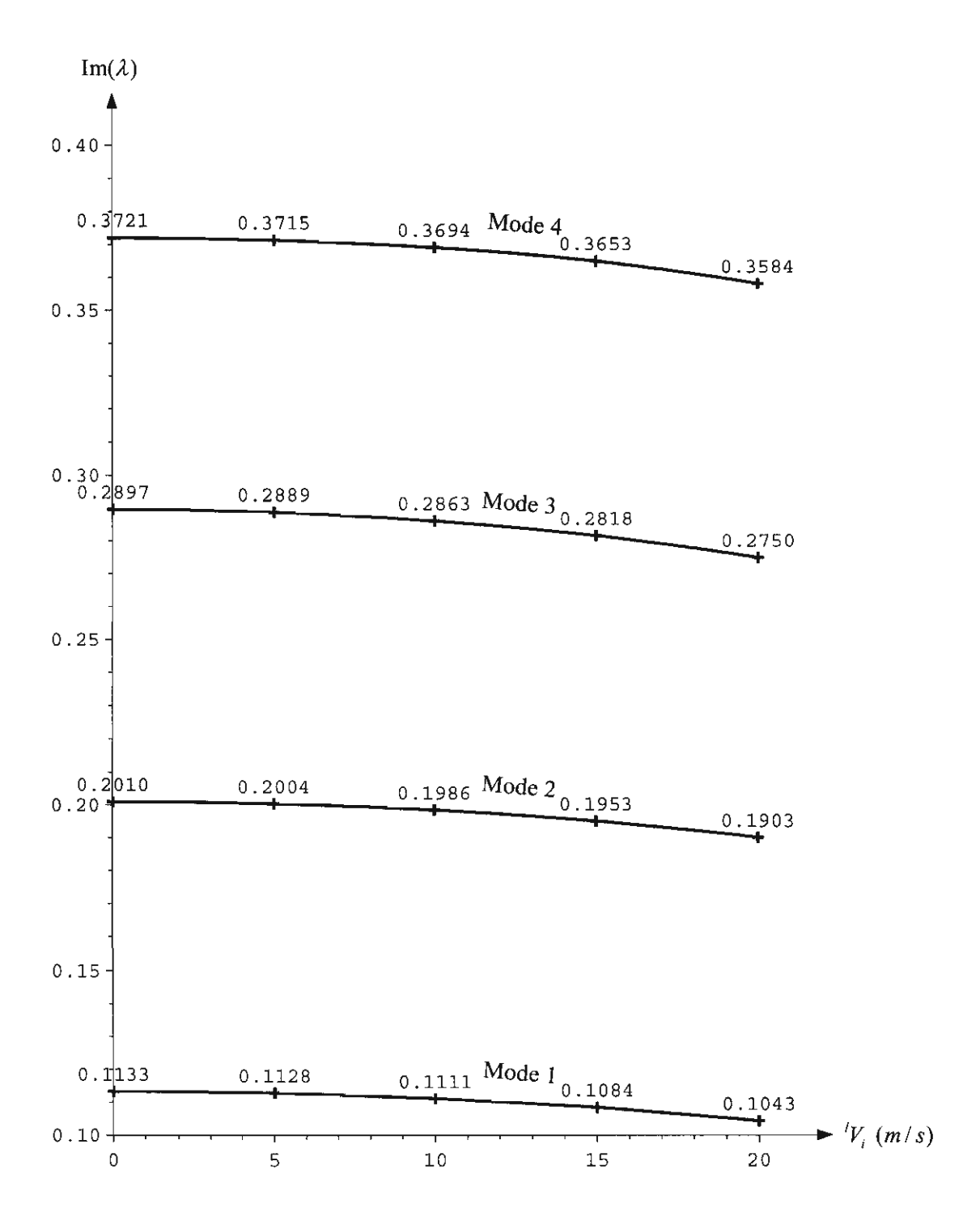


Figure 4.14 Effect of Fluid Transportation on Natural Frequencies

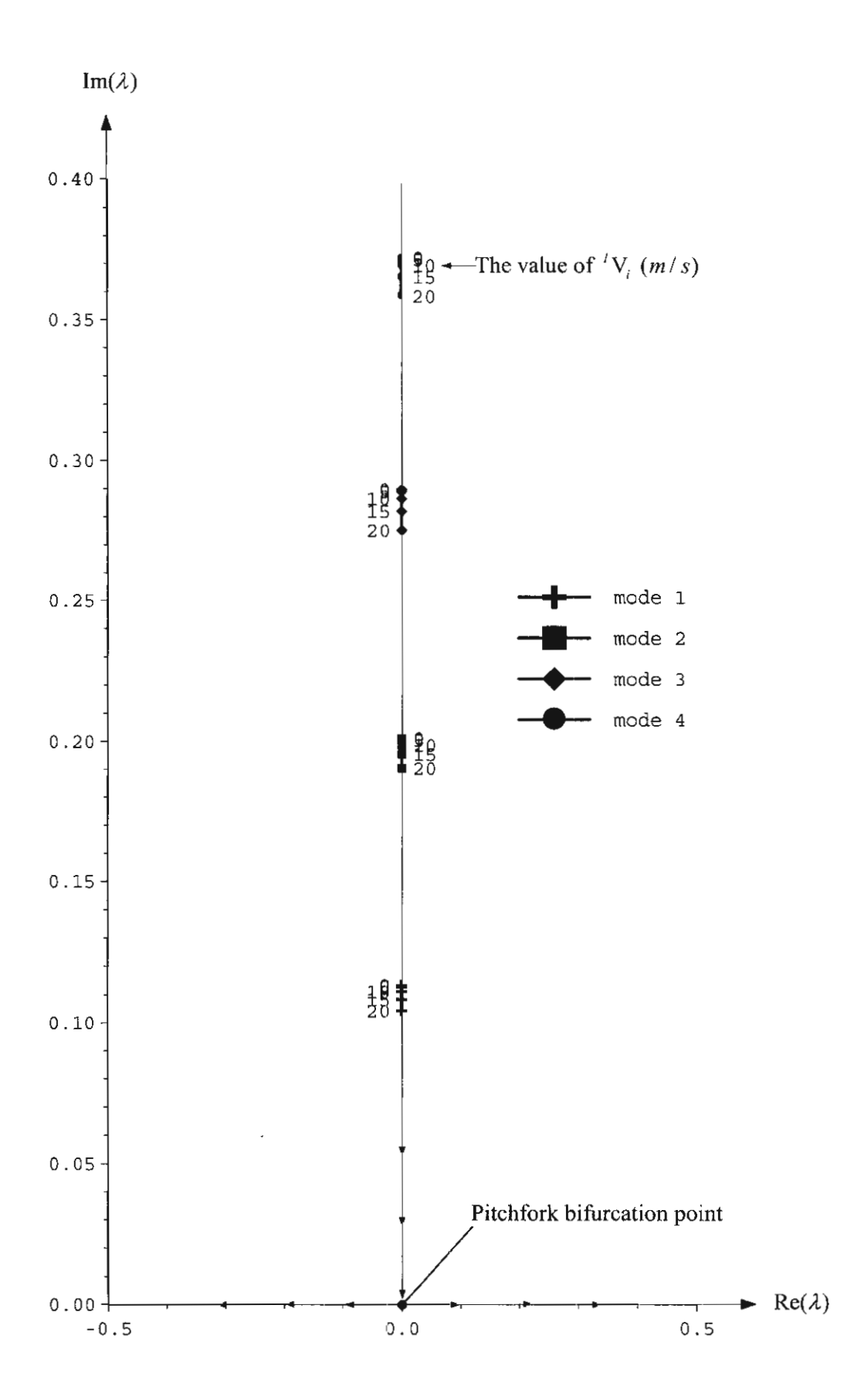


Figure 4.15 Effect of Fluid Transportation on the Argand Diagrams

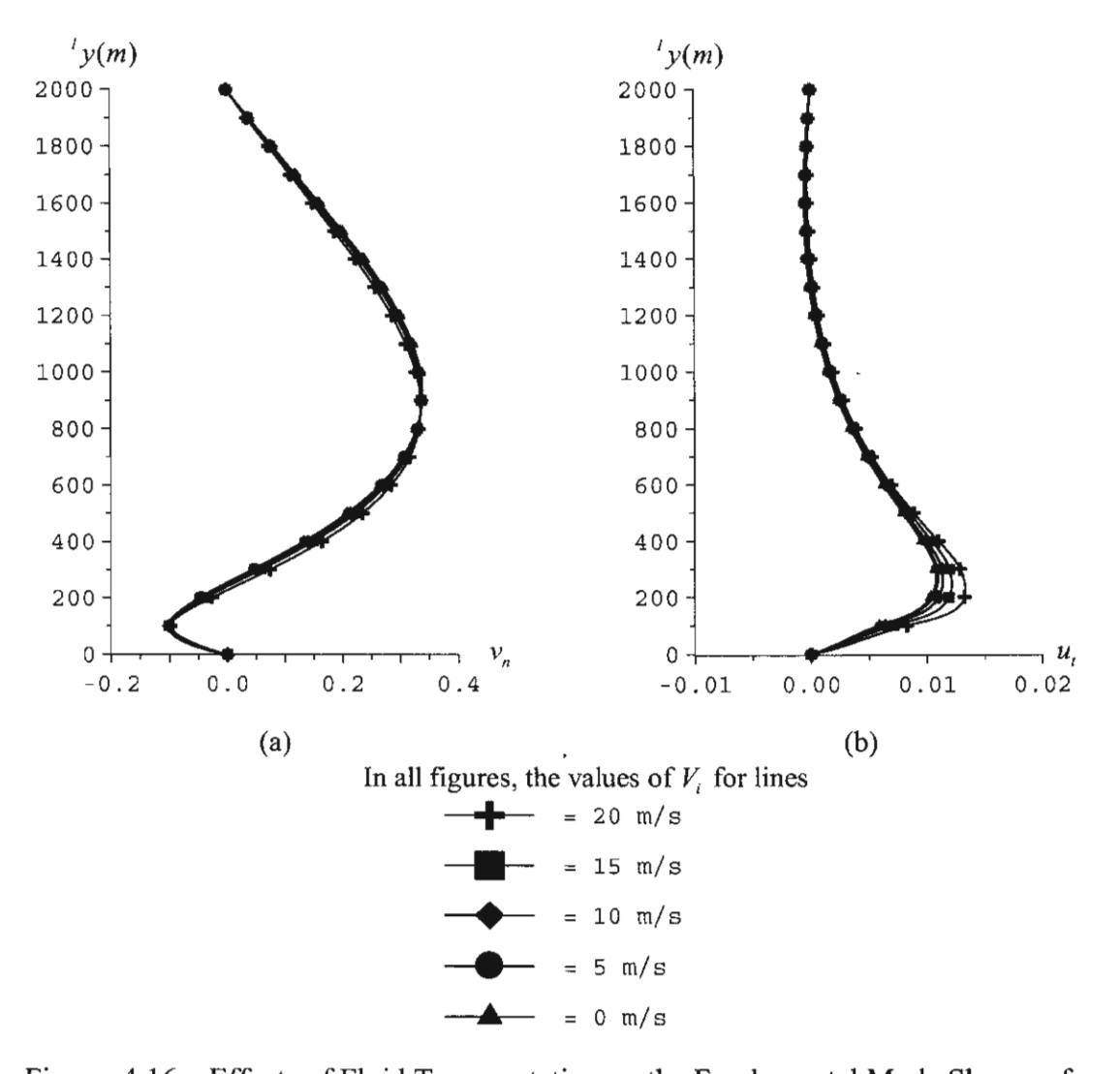


Figure 4.16 Effects of Fluid Transportation on the Fundamental Mode Shapes of

(a) Normal Vibrations (b) Tangential Vibrations

4.5.2.1 Fluid transportation diminishes natural frequencies of the marine pipe. As shown in Figure 4.14, the natural frequencies of the pipe decrease with an escalation of the internal flow velocity. When the internal flow velocity is increased continuously, the eigencurves tend to intersect the internal flow velocity axis at the point where the internal flow velocity possesses the critical values and the natural frequencies are zero. This implies that buckling of the pipe due to the effect of fluid transportation is of static nature, and may be referred to as divergence buckling.

4.5.2.2 Fluid transportation reduces the dynamic stability of the linearized system of the marine pipe. The complex plane of the Argand diagram is

displayed in Figure 4.15. It is found that a continuous augmentation of the internal flow velocity causes the pipe to experience 'the static buckling' or 'the divergence instability' at the Pitchfork bifurcation point, where the internal flow velocity possesses the critical value. Based on the Liapunov indirect method, the complex eigenvalues of the marine pipe as shown in Figure 4.15 have all zero real part, therefore free vibrations of the linearized system of the marine pipe possess stable oscillations and critical behavior.

4.5.2.3 Fluid transportation slightly affects the mode shapes of the free vibrations of the marine pipe in the normal, and tangential, directions as shown in Figures 4.16 (a), and 4.16 (b), respectively.

#### 4.5.3 Effects of Fluid Transportation on Nonlinear Vibration Behavior

The effects of fluid transportation on nonlinear forced vibrations of the marine pipes are illustrated in Figures 4.17 - 4.19, and are summarized as follows:

- 4.5.3.1 Fluid transportation increases nonlinear responses of the forced vibrations of the marine pipe. The nonlinear responses in the time period 0-60 seconds of the forced vibrations of the pipe without fluid transportation are plotted on the left-hand side of Figure 4.17, while those of the pipe with a transportation rate of 20 m/s are displayed on the right-hand side of the same figure. By comparing the left- and the right-hand side figures, it is evident that the pipe with a transportation rate of 20 m/s possesses significantly larger amplitudes of the normal, tangential, and radial vibrations, than the pipe without fluid transportation.
- 4.5.3.2 Fluid transportation affects time histories of nonlinear vibrations of the marine pipe. Figures 4.18 (a), 4.18 (b) and 4.18 (c) demonstrate the time histories of the normal vibrations of the top part ( $^{\prime}y = 1800$  m), of the middle part ( $^{\prime}y = 1000$  m), and of the bottom part ( $^{\prime}y = 400$  m) of the pipes, respectively. It is seen that the pipe with a transportation rate of 20 m/s possesses significantly larger amplitudes of the normal vibrations than the taut pipe without fluid transportation.
- 4.5.3.3 Fluid transportation reduces the stability of motion of the marine pipe. The trajectories of the normal vibrations of the top part ( $^{1}y = 1800 \text{ m}$ ),

of the middle part ( $^{1}y = 1000$  m), and of the bottom part ( $^{1}y = 400$  m) of the pipes are plotted in the phase planes as shown in Figures 4.24(a), 4.24(b) and 4.24(c), respectively. In all the figures, the orbital motion of the trajectory of the pipe with a transportation rate of 20 m/s is more complex and unsteadier than that of the pipe without fluid transportation. This result indicates that the orbital stability of the pipe is reduced by the effect of fluid transportation.

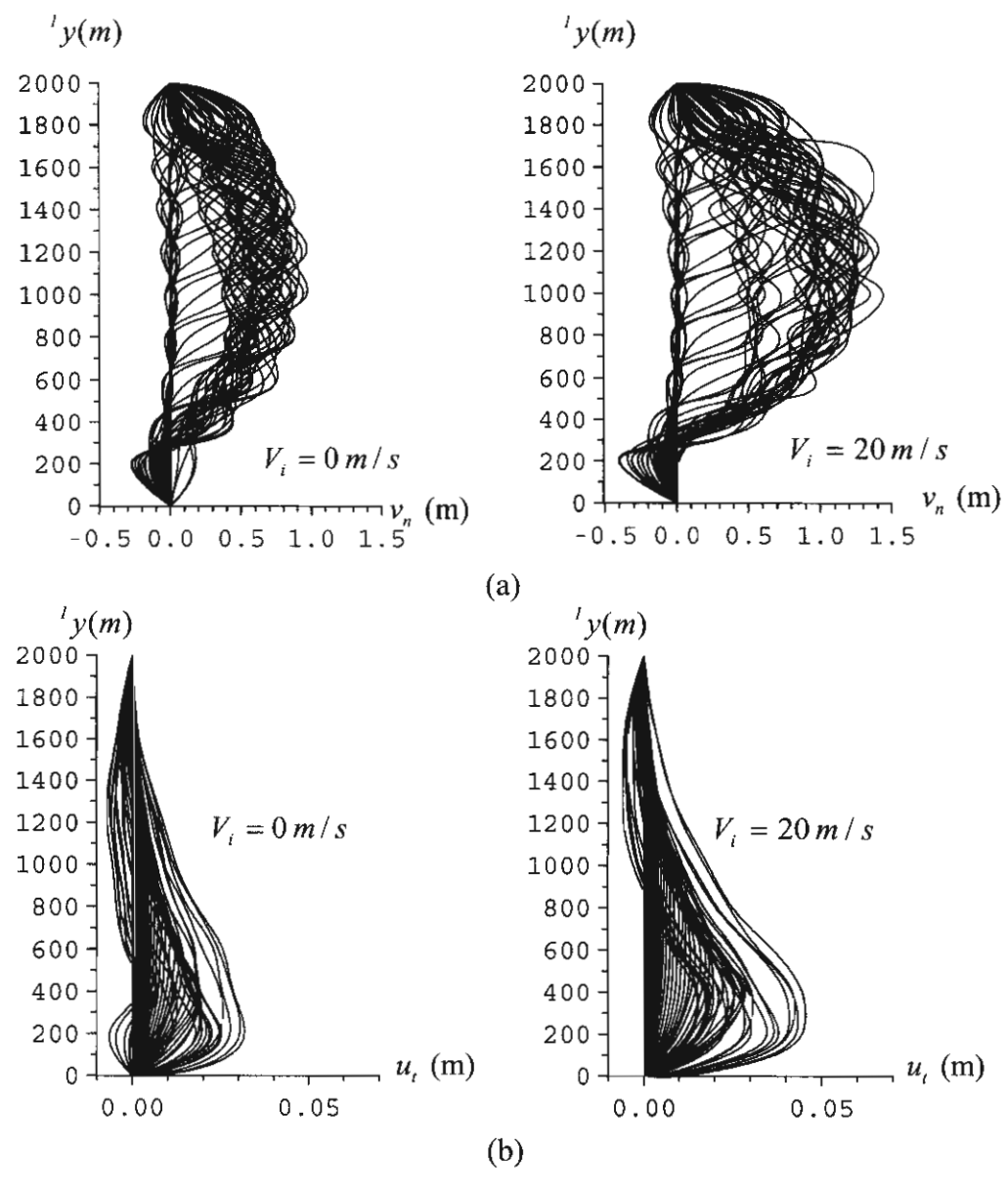


Figure 4.17 Nonlinear Responses in Time 0-60 Seconds of

(a) Normal Vibrations (b) Tangential Vibrations

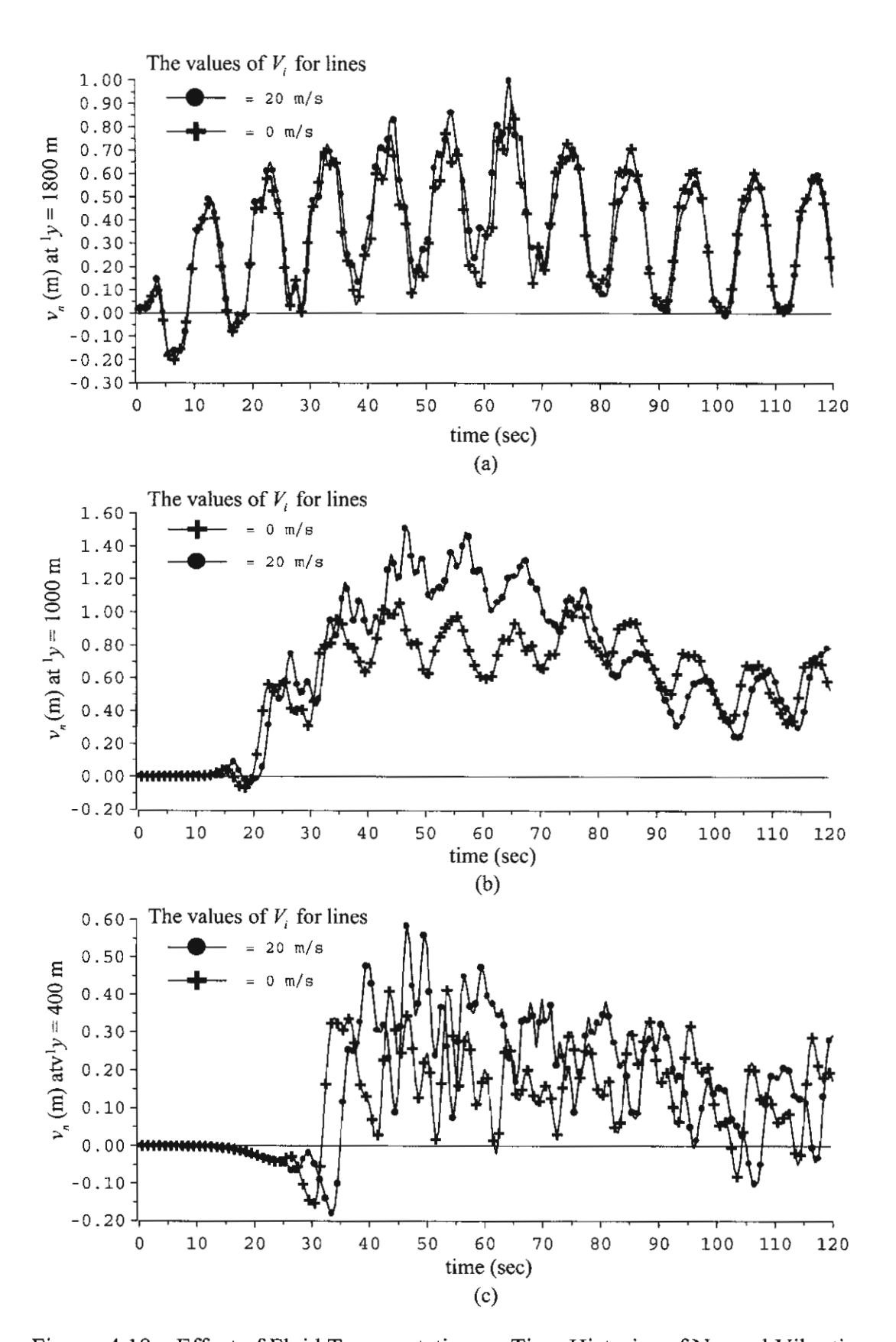


Figure 4.18 Effect of Fluid Transportation on Time Histories of Normal Vibrations

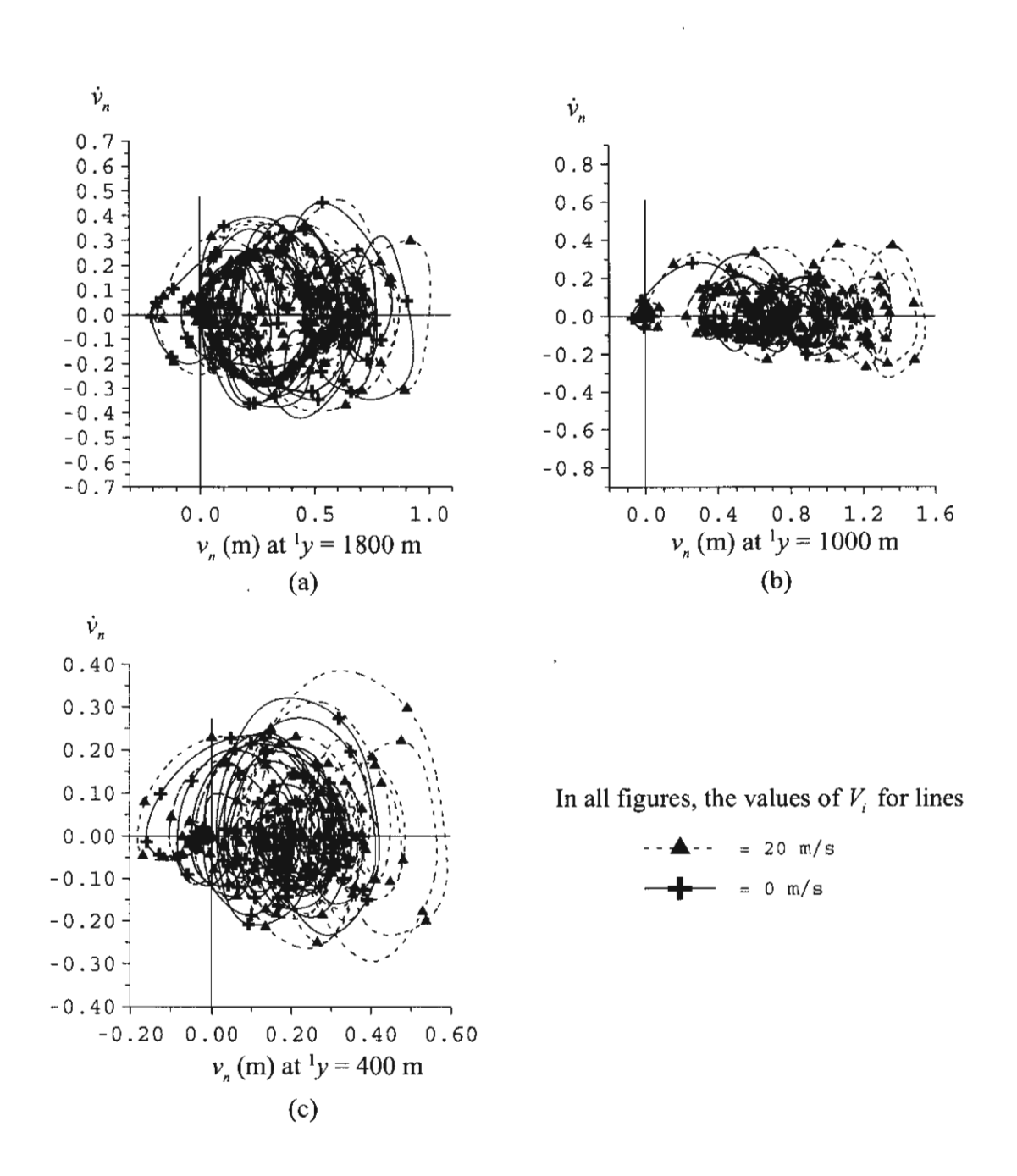


Figure 4.19 Effect of Fluid Transportation on Trajectories of Normal Vibrations

#### 5. CONCLUSIONS

This research proposes the three-dimensional model formulation of an extensible marine risers/pipes transporting fluid. The combined action of the large axial deformation bending, torsion, and the internal flow are taken into account in the formulation. A number of original theories of extensible elastica and new formulation of riser/pipe transporting fluid have been developed in this research.

The original theories compose of the extensible elastica theorems and the apparent tension concept. The extensible elastica theorems are developed in three viewpoints; namely, the total Lagrangian, the updated Lagrangian, and the Eulerian descriptions. The apparent tension concept is introduced in order to cover the effect of the Poisson's ratio.

The three-dimensional model formulation of an extensible marine risers/pipes is developed via a variational approach based on the extensible elastica theory, the work-energy principle, and the kinematics theory of mass transported on the moving frame. The total virtual internal work of the risers/pipes consists of virtual strain energies due to large axial deformation, bending rigidity, and torsional deformations. The total virtual external work consists of virtual work done by effective weight of the risers/pipes, hydrodynamic loading, inertial forces of the risers/pipes and transported fluid. The vectorial summation of forces and moments is used to validate the variational formulation. The advantages of the present models relate to the flexibility offered in choice of the independent variable, and the possibility of applying them to numerous elastica problems, including some biomechanics applications.

The numerical examples of the three-dimensional static analysis and two —dimensional dynamic analysis have been presented by using the finite element method based on the updated Lagrangian formulation. The parametric studies are established and elaborated in order to explore the profound effects of axial deformation, and fluid transportation on behaviors of the pipe. It is found that the effects of axial deformations are very important to nonlinear static, nonlinear vibration behaviors, and static and dynamic stabilities of marine pipes. The effects of fluid transportation in present practice are found to be significant to nonlinear

nonlinear vibration behavior, but insignificant to nonlinear static behavior and natural frequencies of the pipe.

From the results of parametric studies, it can be concluded that axial deformation reduces large deflections and nonlinear responses of the pipe, and increases static and dynamic stabilities of the pipe. At the same time, fluid transportation yields the contrary effects. Consequently, if axial deformation of the pipe is designed too low, the pipe may be subjected to either poor serviceability or buckling due to insufficient stiffness. On the other hand, if fluid transportation is designed too high, the pipe may experience either poor serviceability or buckling due to overloading. Therefore, the designers are encouraged to examine these effects carefully in the design of the marine risers/pipes, especially for the design of the highly flexible pipes with large sag.

Finally, the mathematical models developed in this research work could be used as the basis of other research work and for the development of commercial programs for marine riser pipe analysis. It is hoped that this study will be of some value in the analysis and the design not only of marine risers/pipes, but also of any kind of long slender rods and pipes that pursue rigorous treatments of extensibility, and transported mass.

#### REFERENCES

- Ahmad, S. and Datta, T.K., 1989, "Dynamic Response of Marine Risers,"
   Engineering Structures, Vol. 11, pp. 179-188.
- Antman, S.S., 1991, "Nonlinear Problems of Elasticity," Applied Mathematical Sciences 107, Springer Verlag.
- 3. Atadan, A.S., Calisal, S.M., Modi, V.J. and Guo, Y., 1997, "Analytical and Numerical Analysis of the Dynamics of a Marine Riser Connected to a Floating Platform," Ocean Engineering, Vol. 24, No. 2, pp. 111-131.
- 4. Atanackovic, T.M., 1997, "Stability Theory of Elastic Rods," Series on Stability, Vibration and Control of Systems, World Scientific, Vol. 1.
- 5. Bar-Avi, P., 2000, "Dynamic Response of Risers Conveying Fluid," Journal of Offshore Mechanics and Arctic Engineering, Vol. 122, pp. 188-193.
- Bathe, K.J., Ozdemir, H. and Wilson, E.L., 1974, Static and Dynamic Geometric and Material Nonlinear Analysis, Report No. UCSESM 74-4, California, University of California, Berkeley.
- 7. Bathe, K.J., 1996, Finite Element Procedures, New Jersey, Prentice Hall.
- 8. Bennett, B.E. and Metcalf, M.E., 1977, "Nonlinear Dynamic Analysis of Coupled Axis and Lateral Motions of Marine Risers," **Offshore Technology Conference**, Vol. 1, pp. 2776-2782.
- Bernitsas, M.M., 1980, "Riser Top Tension and Riser Buckling Loads,"
   Computational Methods for Offshore Structures ASME, Vol. 1, pp. 101-109.
- Bernitsas, M.M., 1982, "A Three-Dimensional Nonlinear Large-Deflection Model for Dynamic Behavior of Risers, Pipelines, and Cables," Journal of Ship Research, Vol. 26, No. 1, pp. 59-64.
- Bernitsas, M.M., Kokarakis, J.E. and Imron, A., 1985, "Large Deformation Three-Dimensional Static Analysis of Deep Water Marine Risers," Applied Ocean Research, Vol. 7, No. 4, pp. 178-187.
- 12. Bernitsas, M.M. and Kokarakis, J.E., 1988, "Importance of Nonlinearities in Static Riser Analysis," **Applied Ocean Research**, Vol. 10, No. 1, pp. 2-9.
- 13. Bernitsas, M.M. and Vlahopoulous, N., 1989, "Three Dimensional Analysis of A Riser Bundle by A Substructuring and Incremental Finite Element

- Algorithm," International Journal for Numerical Methods in Engineering, Vol. 28, pp. 2517-2540.
- Burgess, J.J. and Triantafyllou, M.S., 1988, "The Elastic Frequencies of Cables,"
   Journal of Sound and Vibration, Vol. 120, pp. 153-165.
- 15. Burke, B.G., 1974, "An Analysis of Marine Risers for Deep Water," **Journal of etroleum Technology**, Vol. 14, pp. 455-465.
- Butler, H.L., Delfosse, C., Galef, A. and Thorn, B.J., 1967, "Numerical Analysis of a Beam Under Tension," Journal of Structural Division, Proceeding of ASCE, Vol. 76, No. 8, pp. 165-173.
- 17. Chakrabarti, S.K. and Frampton, R.E., 1982, "Review of Riser Analysis Techniques," **Applied Ocean Research**, Vol. 4, No. 2, pp. 73-90.
- Chen, Y.H. and Lin, F.M., 1989, "Drag-Force Linearization for Nonlinear Analysis of Marine Risers," Ocean Engineering, Vol. 16, No. 3, pp. 265-280.
- Chou, D.Y., Minner, W.F., Ragusa, L. and Ho, R.T., 1978, "Dynamic Analysis of Coupled OTEC Platform Cold Water Pipe System," Offshore Technology Conference, Vol. 1, pp. 3338-3345.
- 20. Chucheepsakul, S., 1983, "Large Displacement Analysis of a Marine Riser,"
  Doctor of Philosophy Dissertation, Civil Engineering Program, The
  University of Texas at Arlington.
- Chucheepsakul, S. and Huang, T., 1994, "Influence of Transported Mass on the Equilibrium Configuration of Risers," Proceeding of 4th International Offshore and Polar Engineering Conference, Vol. 2, pp. 246-249.
- 22. Chucheepsakul, S., Huang, T. and Laohaporjanat, P., 1995, "Effects of Axial Deformation on the Equilibrium Configurations of Marine Cables," Proceedings of 5th International Offshore and Polar Engineering Conference, Vol. 2, pp. 244-248.
- 23. Chucheepsakul, S. and Huang, T., 1997, "Effect of Axial Deformation on Natural Frequencies of Marine Cables," Proceedings of 7th International Offshore and Polar Engineering Conference, Vol. 2, pp. 131-136.
- 24. Chucheepsakul, S., Huang, T. and Monprapussorn, T., 1999, "Influence of Transported Fluid on Behavior of an Extensible Flexible Riser/Pipe,"

- Proceedings of 9th International Offshore and Polar Engineering Conference, Vol. 2, pp. 286-293.
- Chucheepsakul, S. and Monprapussorn, T., 2001, "Nonlinear Buckling of Marine Elastica Pipes Transporting Fluid," International Journal of Structural Stability and Dynamics, Vol. 1, No. 3, pp. 333-365.
- Chucheepsakul, S., Monprapussorn, T. and Huang, T., 2002, "Large Strain Formulations of Extensible Flexible Marine Pipes Transporting Fluid," to be published in Journal of Fluids and Structures.
- Chung, J.S. and Whitney, A.K., 1983, "Dynamic Vertical Stretching Oscillation of a Deep-Ocean Mining Pipe," Journal of Energy Resources Technology, ASME, Vol. 105, pp. 195-200.
- 28. Chung, J.S., Cheng, B.R. and Huttelmaier, H.P., 1994a, "Three-Dimensional Coupled Responses of a Vertical Deep-Ocean Pipe: Part I. Excitation at Pipe Ends and External Torsion," International Journal of Offshore and Polar Engineering, Vol. 4, No. 4, pp. 320-330.
- 29. Chung, J.S., Cheng, B.R. and Huttelmaier, H.P., 1994b, "Three-Dimensional Coupled Responses of a Vertical Deep-Ocean Pipe: Part II. Excitation at Pipe Top and External Torsion," International Journal of Offshore and Polar Engineering, Vol. 4, No. 4, pp. 331-339.
- Chung, J.S. and Cheng, B.R., 1996, "Effects of Elastic Joints on 3-D Nonlinear Responses of a Deep-Ocean Pipe," International Journal of Offshore and Polar Engineering, Vol. 6, No. 3, pp. 203-211.
- 31. Dareing, D.W. and Huang, T., 1979, "Marine Riser Vibration Response Determined by Modal Analysis," **Journal of Energy Resources Technology**, Vol. 101, No. 3, pp. 159-166.
- Doll, R.W. and Mote, C.D., 1976, "On the Dynamic Analysis of Curved and Twisted Cylinders Transporting Fluids," Journal of Pressure Vessel Technology, ASME, Vol. 98, pp. 143-150.
- 33. Ertas, A. and Kozik, T.J., 1987, "A Review of Approaches to Riser Modeling," **Journal of Energy Resources Technology**, Vol. 109, No. 3, pp. 155-160.

- 34. Etok, E.U. and Kirk, C.L., 1981, "Random Dynamic Response of a Tethered Buoyant Platform Production Riser," **Applied Ocean Research**, Vol. 3, No. 2, pp. 73-86.
- 35. Felippa, C.A. and Chung, J.S., 1981, "Nonlinear Static Analysis of Deep Ocean Mining Pipe Part 1: Modeling and Formulation," Journal of Energy Resources Technology, Vol. 103, No. 1, pp. 11-15.
- 36. Fischer, W. and Ludwig, M. 1966, "Design of Floating Vessel Drilling Risers,"

  Journal of Petroleum Technology, Vol. 3, No. 1, pp. 272-283.
- 37. Fung, Y.C., 1965, Foundations of Solid Mechanics, New Jersey, Prentice-Hall.
- 38. Gambhir, M.L., Barrington, D.E. and Batchelor, V., 1978, "Parametric Study of Free Vibration of Sagged Cables," **Computers & Structures**, Vol. 8, No. 5, pp. 641-648.
- Gardner, T.N. and Kotch, M.A., 1976, "Dynamic Analysis of Risers and Caissons by the Element Method," Offshore Technology Conference, Vol. 1, pp. 2650-2655.
- 40. Gear, C.W., 1971, Numerical Initial Value Problems in Ordinary Differential Equations, New Jersey, Prentice Hall.
- 41. Gnone, E., Signorelli, P. and Giuliano, V., 1975, "Three-Dimensional Static and Dynamic Analysis of Deep-Water Sealines and Risers," **Offshore**Technology Conference, Vol. 1, pp. 2326-2331.
- 42. Goodman, T.R. and Breslin, J.P., 1976, "Static and Dynamics of Anchoring Cable in Waves," **Journal of Hydronautics**, Vol. 10, pp. 113-120.
- 43. Gosse, C.G. and Barksdale, G.L., 1969, "The Marine Riser a Procedure for Analysis," Offshore Technology Conference, Vol. 1, pp. 1080-1085.
- 44. Graham, R.D., Frost, M.A. and Wilhoit, J.C., 1965, "Analysis of the Motion of Deep-Water Drill Strings – Part 1: Forced Lateral Motion – and Part 2: Forced Rolling Motion," Journal of Engineering for Industry, Transaction of ASME, Vol. 10, No. 2, pp.137-147.
- 45. Gregory, R.W. and Païdoussis, M.P., 1966, "Unstable Oscillation of Tubular Cantilevers Conveying Fluid. I. Theory," **Proceedings of the Royal Society** (London) A, Vol. 293, pp. 512-537.

- 46. Hahn, G.D., She, M. and Carney, J.F., 1992, "Buckle Propagation in Submarine Pipelines," **ASCE Journal of Engineering Mechanics**, Vol. 118, No. 11, pp. 2191-2206.
- 47. Henghold, W.M. and Russell, J.J., 1977, "Free Vibrations of Cables in Three Dimensions," **Journal of Structural Division**, **ASCE**, Vol. 103, No. ST5, pp. 1127-1136.
- 48. Heuze, L.A.A., 1975, "A 4000 Ft Riser," **Offshore Technology Conference**, Vol. 1, pp. 2325-2329.
- 49. Holmes, P.J., 1978, "Pipes Supported at Both Ends Cannot Flutter," **Journal of Applied Mechanics**, **ASME**, Vol. 45, pp. 619-622.
- 50. Housner, G.W., 1952, "Bending Vibrations of a Pipe Line Containing Flowing Fluid," Journal of Applied Mechanics, ASME, Vol. 19, pp. 205-208.
- Huang, T. and Chucheepsakul, S., 1985, "Large Displacement Analysis of a Marine Riser," Journal of Energy Resources Technology, Vol. 107, No. 2, pp. 54-59.
- 52. Huang, T.S. and Leonard, J.W., 1990, "Lateral Stability of a Submarine Flexible Hoseline," **Ocean Engineering**, Vol. 17, No. 1, pp. 35-52.
- 53. Huang, T. and Kang, Q.L., 1991, "Three Dimensional Analysis of a Marine Riser with Large Displacements," International Journal of Offshore and Polar Engineering, Vol. 1, No. 4, pp. 300-306.
- 54. Huang, T., 1992, "A Static Equilibrium Formulation Including Axial Deformation for Marine Cables," Proceedings of 2nd International Offshore and Polar Engineering Conference, Vol. 2, pp. 252-255.
- 55. Huang, T., 1993, "Kinematics of Transported Mass Inside Risers and Pipes," Proceeding of 3rd International Offshore and Polar Engineering Conference, Vol. 2, pp. 331-336.
- Huddleston, J.V., 1981, "Computer Analysis of Extensible Cables," Journal of Engineering Mechanics Division, ASCE, Vol. 107, pp. 27-37.
- 57. Huyse, L., Singh, M.C. and Maes, M.A., 1997, "A Static Drilling Riser Model Using Free Boundary Conditions," **Ocean Engineering**, Vol. 24, No. 5, pp. 431-444.

- 58. Irani, M.B., Modi, V.J. and Weit, F., 1987, "Riser Dynamics with Internal Flow and Nutation Damping," Proceedings 6th International Offshore Mechanics and Arctic Engineering Symposium, Vol. 3, pp. 119-125.
- 59. Jain, A.K., 1994, "Review of Flexible Risers and Articulated Storage Systems," Ocean Engineering, Vol. 21, No. 8, pp. 733-750.
- 60. Jones, M.R., 1975, Problem Affecting the Design of Drilling Risers, SPE paper 5268, London, Society of Petroleum Engineering.
- 61. Karamanos, S.A. and Tassoulas, J.L., 1991, "Stability of Inelastic Tubes Under External Pressure and Bending," **ASCE Journal of Engineering Mechanics**, Vol. 117, No. 12, pp. 2845-2861.
- 62. Kirk, C.L., Etok, E.U. and Cooper, M.T., 1979, "Dynamic and Static Analysis of a Marine Riser," **Applied Ocean Research**, Vol. 1, No. 3, pp. 95-105.
- 63. Kirk, C.L., 1985, "Dynamic Response of Marine Risers by Single Wave and Spectral Analysis Methods," **Applied Ocean Research**, Vol. 7, No. 1, pp. 2-13.
- 64. Kokarakis, J.E. and Bernitsas, M.M., 1987, "Nonlinear Three-Dimensional Dynamic Analysis of Marine Risers," **Journal of Energy Resources Technology**, Vol. 109, No. 5, pp. 105-111.
- 65. Kopecky, J.A., 1971, "Drilling Riser Stress Measurements," **Petroleum Engineering and Technology**, Vol. 14, No. 71, pp. 879-890.
- 66. Krolikowski, L.P. and Gray, T.A., 1980, "An Improved Linearization Technique for Frequency Domain Riser Analysis," **Offshore Technology Conference**, Vol. 1, pp. 3777-3783.
- 67. Larsen, C.M., 1976, "Marine Riser Analysis," Norwegian Maritime Research, Vol. 4, pp. 15-26.
- 68. Lin, H.P. and Perkins, N.C., 1995, "Free Vibration of Complex Cable/Mass System: Theory and Experiment," **Journal of Sound and Vibration**, Vol. 179, pp. 131-149.
- 69. Love, A.E.H., 1944, A Treatise on the Mathematical Theory of Elasticity, London, Cambridge University Press.
- 70. Maison, J.R. and Lea, J.F., 1977, "Sensitivity Analysis of Parameters Affecting Riser Performance," **Offshore Technology Conference**, Vol. 1, pp. 2918-2923.

- 71. Marine Computation Services International, 1989, FLEXCOM-3D Program Manuals, Galway, MCSI.
- 72. Meirovitch, L., 1997, Principles and Techniques of Vibrations, New Jersey, Prentice Hall.
- 73. Moe, G. and Chucheepsakul, S., 1988, "The Effect of Internal Flow on Marine Risers," Proceedings 7th International Offshore Mechanics and Arctic Engineering Symposium, Vol. 1, pp. 375-382
- 74. Moe, G., Stromsem, K.C. and Fylling, I., 1994, "Behavior of Risers with Internal Flow Under Various Boundary Conditions," **Proceeding of 4th International Offshore and Polar Engineering Conference**, Vol. 2, pp. 258-262.
- 75. More, J., Garbow, B.S. and Hillstrom, H., 1980, User guide for MINPACK-1, Illinois, Argonne National Laboratories.
- Morgan, G.W., 1972, Riser dynamic Analysis, Texas, Sun Oil Production Research Laboratory.
- 77. Morison, J.R., O'Brian, M.P., Johnson, J.W. and Schaaf, S.A., 1950, "The Force Exerted by Surface Waves on Piles," **Transaction of American Institute of Mining Metallic Engineering**, Vol. 189, pp. 149-154.
- 78. Munson, B.R., Young, D.F. and Okiishi, T.H., 1994, Fundamentals of Fluid Mechanics, Toronto, John Wiley.
- 79. National Engineering and Science Company, 1965, Structural Dynamic Analysis of the Riser and Drill String for Project Mohole, New York, NESCO, pp. 1-2.
- Natvig, B.J., 1980, "A Large Angle Large Displacement Analysis Method for Marine Risers," Computational Methods for Offshore Structures, ASME, Vol. 1, pp. 111-125.
- Ngiam, P.C.A., 1997, "Intrinsic Coordinate Elements for Large Deflection of Offshore Pipelines," Proceeding of 7th International Offshore and Polar Engineering Conference, Vol. 2, pp. 313-320.
- 82. O'Brien, P.J., McNamara, J.F. and Dunne, F.P.E., 1988, "Three Dimensional Nonlinear Motions of Risers and Offshore Loading Towers," Journal of Offshore Mechanic and Arctic Engineering, Vol. 110, pp. 232-237.
- 83. O'Brien, P.J. and McNamara, J.F., 1989, "Significant Characteristics of Three-Dimensional Riser Analysis," **Engineering Structures**, Vol. 11, pp. 223-233.

- 84. Oran, C., 1992, "Effect of Static Offset on TLP Modeling," **ASCE Journal of Engineering Mechanics**, Vol. 118, No. 1, pp. 74-91.
- 85. Owen, D.J. and Qin, J.J., 1987, "Nonlinear Dynamics of Flexible Risers by the Finite Element Method," **Proceedings 6th International Offshore Mechanics and Arctic Engineering Symposium**, Vol. 1, pp. 163-170.
- Païdoussis, M.P., 1970, "Dynamics of Tubular Cantilevers Conveying Fluid,"
   Journal of Mechanical Engineering Science, Vol. 12, pp. 85-103.
- 87. Païdoussis, M.P., 1998, Fluid-Structure Interactions, Slender Structures and Axial Flow, Vol. 1, New York, Academic Press.
- 88. Patel, H.M. and Seyed, F.B., 1989, "Internal Flow-Induced Behaviour of Flexible Risers," **Engineering Structures**, Vol. 11, No. 3, pp. 266-280.
- 89. Patel, M.H. and Seyed, F.B., 1995, "Review of Flexible Riser Modelling and Analysis Techniques," **Engineering Structures**, Vol. 17, No. 4, pp. 293-304.
- Patrikarakis, N.M. and Kriezis, G.A., 1987, "Linear Dynamics of Flexible Risers," Journal of Offshore Mechanics and Arctic Engineering, OMAE, vol. 109, pp. 254-262.
- Paulling, J.R., 1977, A Linearized Dynamic Analysis of the Coupled OTEC Cold-Water Pipe and HMB-1 Barge System, New York, Morris Guralnick Associates.
- 92. Pesce, C.P., Fujarra, A.L.C., Simos, A.N. and Tannuri, E.A., 1999, "Analytical and Closed Form Solutions for Deep Water Riser-Like Eigenvalue Problem,"
  Proceedings of 9th International Offshore and Polar Engineering
  Conference, Vol. 2, pp. 255-264.
- Press, W.H., Teukolsky, S.A., Vettering, W.T. and Flannery, B.P., 1992,
   Numerical Recipes in Fortran, 2nd ed., New York, Cambridge University Press.
- 94. Safai, V.H., 1983, "Nonlinear Dynamic Analysis of Deep Water Risers,"

  Applied Ocean Research, Vol. 5, No. 4, pp. 215-225.
- Sexton, R.M. and Agbezuge, L.K., 1976, "Random Wave and Vessel Motion Effects on Drilling Riser Dynamics," Offshore Technology Conference, Vol. 1, pp. 2650-2658.
- Seyed, F.B. and Patel, H.M., 1992, "Mathematics of Flexible Risers Including Pressure and Internal Flow Effects," Marine Structures, Vol. 5, pp. 121-150.

- 97. Shames, I.H., 1992, Mechanics of Fluids, Singapore, McGraw-Hill.
- 98. Shih, B. and Tadjbakhsh, I.G., 1984, "Small-Amplitude Vibrations of Extensible Cables," **ASCE Journal of Engineering Mechanics**, Vol. 110, pp. 569-576.
- 99. Smith, B.T., Boyle, J.M., Dongarra, J.J., Garbow, B.S., Ikebe, Y., Klema, V.C. and Moler, C.B., 1976, Matrix Eigensystem Routines EISPACK Guide, New York, Springer-Verlag.
- 100. Spanos, P.D., Tein, W.Y. and Ghanem, R., 1990, "Frequency Domain Analysis of Marine Risers with Time Dependent Tension," **Applied Ocean Research**, Vol. 12, No. 4, pp. 200-210.
- 101. Sparks, C.P., 1984, "The Influence of Tension, Pressure and Weight on Pipe and Riser Deformations and Stresses," Journal of Energy Resources Technology, ASME, Vol. 106, pp. 46-54.
- 102. St. Denis, M. and Armijo, L., 1955, "On Dynamic Analysis of the Mohole Riser," Proceeding of Ocean Science and Ocean Engineering Conference, Vol. 1, pp. 325-330.
- 103. Thampi, S.K. and Niedzwecki, J.M., 1992, "Parametric and External Excitation of Marine Risers," ASCE Journal of Engineering Mechanics, Vol. 118, No. 5, pp. 942-960.
- 104. Thompson, J.M.T. and Lunn, T.S., 1981, "Static Elastica Formulations of a Pipe Conveying Fluid," **Journal of Sound and Vibration**, Vol. 77, pp. 127-132.
- 105. Tidwell, D.R. and Ilfrey, W.T., 1971, "Developments in Marine Drilling Riser Technology," Petroleum Engineering and Technology, Vol. 14, No. 69, pp. 272-283.
- 106. Tikhonov, V.S., Safronov, A., Kamyshev, M.A. and Figarov, N.G., 1996, "Numerical Analysis of Pipeline Dynamics in Seabed Laying," International Journal of Offshore and Polar Engineering, Vol. 6, No. 3, pp. 212-218.
- Timoshenko, S.P. and Goodier, J.N., 1982, Theory of Elasticity, Singapore, McGraw-Hill.
- 108. Tjavaras, A.A. and Triantafyllou, M.S., 1996, "Shock Waves in Curved Synthetic Cables," ASCE Journal of Engineering Mechanics, Vol. 122, pp. 308-315.

- 109. Tjavaras, A.A., Zhu, Q., Liu, Y. and Triantafyllou, M.S., 1998, "The Mechanics of Highly Extensible Cables," Journal of Sound and Vibration, Vol. 213, pp. 709-737.
- 110. Triantafyllou, M.S. and Yue, D.K.P., 1994, "Damping Amplification in Highly Extensible Hysteretic Cables," Journal of Sound and Vibration, Vol. 186, pp. 355-368.
- 111. Trim, A.D., 1990, "Time-Domain Random Dynamic Analysis of Marine Risers and Estimation of Non-Gaussian Bending Stress Statistics," Applied Ocean Research, Vol. 12, No. 4, pp. 162-174.
- 112. Tucker, T.C. and Murtha, J.P., 1973, "Nondeterministic Analysis of a Marine Riser," **Offshore Technology Conference**, Vol. 1, pp. 1770-1789.
- 113. West, H.H. and Caramanico, D.L., 1973, "Initial-Value Discrete Suspension Bridge Analysis," International Journal of Solids and Structures, Vol. 9, pp. 1087-1105.
- 114. West, H.H., Geschwindner, L.F. and Suhoski, J.E., 1975, "Natural Vibrations of Suspension Cables," Journal of Structural Division, ASCE, Vol. 101, No. ST11, pp. 2277-2291.
- 115. Wu, M.C. and Lou, J.Y.K., 1991, "Effects of Rigidity and Internal Flow on Marine Riser Dynamics," Applied Ocean Research, Vol. 13, No. 5, pp. 235-244.
- Yang, Y.B. and Kuo, S.R., 1994, Nonlinear Framed Structures, Singapore, Prentice-Hall.
- 117. Young, R.D., Fowler, J.R., Fisher, E.A. and Luke, R.R., 1978, "Dynamic Analysis as an Aid to the Design of Marine Risers," ASME Journal of Pressure Vessel Technology, Vol. 100, pp. 200-205.

# ผลงานที่ได้จากโครงการ

ตลอดระยะเวลาสามปีที่ผ่านมาศูนย์วิจัยด้านกลศาสตร์และวัสดุ (Center for Mechanics and Materials) ได้ก่อตั้งขึ้นเพื่อสร้างนักวิจัยที่มีคุณภาพสูงให้แก่ประเทศประกอบกับการผลิตผลงาน วิจัยที่มีคุณภาพเป็นที่ยอมรับในระดับนานาชาติ ศูนย์วิจัยนี้ได้รับการสนับสนุนทางด้านเงินทุนจาก ทุนเมธีวิจัยอาวุโสโดยสำนักงานกองทุนสนับสนุนการวิจัย และได้รับการสนับสนุนค้านสถานที่ และอุปกรณ์จากภาควิชาวิศวกรรมโยธา มหาวิทยาลัยเทคโนโลยีพระจอมเกล้าธนบุรี ภายใต้หัวข้อ โครงการกลศาสตร์ของท่อลำเลียงของใหลที่ยืดหคตัวได้ในสามมิติ โดยมี ศ.คร. สมชาย ชูชีพสกุล เป็นหัวหน้าโครงการ จากการสนับสนุนดังกล่าวทำให้ศูนย์วิจัยสามารถผลิตผลงานได้อย่างต่อเนื่อง ทั้งในด้านบุคลากรที่มีความสามารถในงานวิจัยและด้านผลงานวิจัยที่ได้รับการตีพิมพ์ในวารสาร วิชาการนานาชาติตรงตามเป้าหมายที่วางไว้ โดยผลงานที่ได้ทั้งหมดสามารถสรุปได้ดังนี้

### 1.) บุคลากร

บุคลากรที่ผลิตได้จากโครงการนี้แบ่งได้เป็น นักวิจัยรุ่นใหม่ ผู้สำเร็จการศึกษาใน ระดับปริญญาเอก และผู้สำเร็จการศึกษาในระดับปริญญาโทดังต่อไปนี้

- 1.1) นักวิจัยรุ่นใหม่จำนวน 5 ท่าน ได้แก่
  - 1.) รศ. คร. นคร ภู่วโรคม จากมหาวิทยาลัยธรรมศาสตร์
  - 2.) คร. จุลพจน์ จิรวัชรเคช จากมหาวิทยาลัยเทคโนโลยีพระจอมเกล้าชนบุรี
  - 3.) คร. ชูชัย สุจิวรกุล จากมหาวิทยาลัยเทค โนโลยีพระจอมเกล้าชนบุรี
  - 4.) คร. ทินกร มนต์ประภัสสร จากมหาวิทยาลัยเอเชียอาคเนย์
  - 5.) นาย บุญชัย ผึ้งใผ่งาม จากศูนย์กลางสถาบันเทคโนโลยีราชมงคล
- 1.2) ผู้สำเร็จการศึกษาในระดับปริญญาเอกจำนวน 1 ท่าน ได้แก่
  - 1.) คร. ทินกร มนต์ประภัสสร
- 1.3) ผู้สำเร็จการศึกษาในระดับปริญญาโทจำนวน 8 ท่าน ได้แก่
  - 1.) นายไพโรจน์ วรรณสวัสดิ์กุล
  - 2.) นายนรากร ศรีนิล
  - 3.) นายบุญมี ชินนาบุญ
  - 4.) นายบุญชัย ผึ้งใผ่งาม
  - 5.) นายปริญญา แซ่อุ๋ย

- 6.) นายสุวิทย์ รัตนศรีกูล
- 7.) นายศักดิรัตน์ แก้วอุ่นเรือน
- 8.) นาย อรุณ สุวรรณชีวะศิริ

# 2) ผลงานตีพิมพ์

ผลงานตีพิมพ์ที่ได้จากโครงการในรอบ 3 ปีที่ผ่านมาสรุปโดยรวมได้คังนี้ ผลงานตีพิมพ์ในวารสารวิชาการนานาชาติจำนวนทั้งสิ้น 13 เรื่อง ผลงานที่เสนอตีพิมพ์ในวารสารวิชาการ นานาชาติซึ่งอยู่ในระหว่างการตรวจสอบต้นฉบับจำนวนทั้งสิ้น 4 เรื่อง ผลงานตีพิมพ์ในที่ประชุม วิชาการนานาชาติจำนวน 11 เรื่อง ผลงานที่ตีพิมพ์ในหนังสือวิชาการต่างประเทศ (Monograph) จำนวน 1 เรื่อง และผลงานตีพิมพ์ในที่ประชุมวิชาการในประเทศจำนวน 6 เรื่อง ผลงานทั้งหมด สามารถแจกแจงได้ตามรายละเอียดต่อไปนี้

# 2.1) ผลงานตีพิมพ์ในวารสารวิชาการนานาชาติ

- Chucheepsakul, S., and Monprapussorn, T. (2000). "Divergence Instability of Variable-Arc-Length Elastica Pipes Transporting Fluid," *Journal of Fluids and Structures*, Vol. 14, No. 6, pp. 895-916. (IF 0.735/2002)
- Chucheepsakul, S., and Wongsa, S. (2001). "Effect of Axial Stretching on Large Amplitude Free Vibration of a Suspended Cable," Structural Engineering and Mechanics, An International Journal, Vol.11, No. 2, pp. 185-197. (IF 0.162/2002)
- 3. Chucheepsakul, S. and Monprapussorn, T. (2001). "Nonlinear Buckling of Marine Elastica Pipes Transporting Fluid," *International Journal of Structural Stability and Dynamics*, Vol.1, No.3, pp. 1-33.
- Chucheepsakul, S. and Srinil, N., (2002). "Free Vibrations of Three-dimensional Extensible Cables with Specified Top Tension via a Variational Method," Ocean Engineering, An International Journal of Research and Development, Vol. 29, pp. 1067-1096. (IF 0.307/2002)
- Chucheepsakul, S. and Chinnaboon, B., (2002). "An Alternative Domain/Boundary Element Technique for Analyzing Plates on Two-parameter Elastic Foundations," Engineering Analysis with Boundary Elements, Vol. 26, No. 6, pp. 547-555. (IF 0.783/2002)

- 6. Chucheepsakul, S. and Saetiew, W., (2002), "Free Vibrations of Inclined Arches using Finite Elements," *Structural Engineering and Mechanics*, *An International Journal*, Vol. 13, No. 6, pp. 713-730. (IF 0.162/2002)
- 7. Chucheepsakul, S., Monprapussorn, T., and Huang, T., (2003), "Large Strain Formulations of Extensible Flexible Marine Pipes Transporting Fluid," *Journal of Fluids and Structutres*, Vol. 17, No. 2, pp. 185-224. (IF 0.735/2002)
- Chucheepsakul, S., Srinil, N. and Petchpart, P. (2003). "A Variational Approach for Three-dimensional Model of Extensible Marine Cables with Specified Top Tension," *Applied Mathematical Modelling*, Vol. 27, pp. 781-803. (IF 0.406/2002)
- Chucheepsakul, S. and Phungpaigram, B., (2003). "Elliptic Integral Solutions of Variable-Arc-Length Elastica under an Inclined Follower Force," *Journal of Applied Mathematics and Mechanics*, (ZAMM), Vol. 83, No. 11. (IF 0.400/2000)
- Srinil, N., Rega, G., and Chucheepsakul, S. (2003). "Large Amplitude Three-dimensional Free Vibrations of Inclined Sagged Elastic Cables," *Nonlinear Dynamics*, Vol. 33, pp. 129-154. (IF 0.565/2002)
- Srinil, N., Rega, G., and Chucheepsakul, S. (2003). "Three-dimensional Nonlinear Coupling and Dynamic Tension in the Large Amplitude Free Vibrations of an Arbitrarily Sagged Cables," *Journal of Sound and Vibration*, (Inpress). (IF 0.821/2002)
- Chucheepsakul, S. and Chinaboon, B.(2003). "Plates on Two-parameters Elastic Foundations with Nonlinear Boundary Conditions by the Boundary Element Method," Computers and Structures, An International Journal, (Inpress). (IF 0.418/2002)
- 13. Monprapussorn, T., Chucheepsakul, S., and Huang, T. (2003). "The Coupled Radial-Axial Deformation Analysis of Flexible Pipes Conveying Fluid," *International Journal of Numerical Methods in Engineering*, (Inpress). (IF 1.239/2002)

# 2.2) ผลงานที่เสนอตีพิมพ์ในวารสารวิชาการนานาชาติซึ่งอยู่ในระหว่างการตรวจสอบค้น ฉบับ

Chiravachradej, J., Luxmoore, A.R. (2003). "Cleavage Fracture Toughness
 Assessment using Numerical Cleavage Model," Engineering Fracture Mechanics.
 (Submitted). (IF 0.629/2002)

- Pulngern, T., Halling, M.W., Chucheepsakul, S., and Poovarodom, N. (2003). "On Free Vibrations of Variable-Arc-Length Beams: Analytical and Experimental," *Journal of Structural Engineering*, (ASCE), (Submitted). (IF 0.732/2002)
- Chucheepsakul, S., Phungpaigram, B., and Wang, C.M., (2003). "Post-Buckling of a Simple Beam Subjected to an Intermediate Tangential Follower Force," International Journal of Nonlinear Mechanics, (Submitted).
- Chucheepsakul, S., and Saeauy P. (2003). "Nonlinear In-plane Free Vibration of Inclined Arches via Finite Elements", *Journal of Sound and Vibration*, (Second review). (IF 0.821/2002)

# 2.3) ผลงานตีพิมพ์ในที่ประชุมวิชาการนานาชาติ

- Chucheepsakul, S., Huang, T., and Monprapussorn, T. (2001). "Stability Analysis of Extensible Flexible Marine Pipes Transporting Fluid," Proc 11th Int Offshore and Polar Engineering Conference, Vol. 2, pp.722-729.
- Chucheepsakul, S., Kiattikomol K., and Sompornjaroensuk, Y., (2001). "Static and Dynamic Analysis of Symmetrical Multi-Story Plane Frame Structures Using Equivalent Beam Theories," The Eighth East Asia-Pacific Conference on Structural Engineering & Construction 5-7 December 2001, Singapore.
- Athisakul, C., Huang, T., and Chucheepsakul, S., (2002). "Large Strain Static Analysis of Marine Risers via a Variational Approach," Proc 12th Int Offshore and Polar Eng, ISOPE, Vol 2, pp. 164-170.
- Pulngern, T., and Chucheepsakul, S., (2002). "Small Amplitude Free Vibrations of Variable-Arc-Length Beams," Proc 2nd Int Advance in Structural Engineering and Mechanics, ASEM'02, August 21-23, Busan, Korea.
- Srinil, N., Chucheepsakul, S. and Rega, G. (2002). "On Large Amplitude Free Vibrations of an Inclined Cable in a Three-dimensional Space," Proc 2nd Int Structural Stability and Dynamics, December 16-18, Singapore.
- Athisakul, C., Huang, T., and Chucheepsakul, S., (2003). "A Variational Formulation for a Three-dimensional Extensible Marine Pipe Transporting Fluid," Proc 13th Int Offshore and Polar Eng. ISOPE, Vol 2., pp. 83-90.

- Sujivorakuls, C., and Naaman, A.E., (2003). "Modeling Bond Components of Deformed Steel Fibers in FRC Composites" Proceeding of the Fourth International RILEM Workshop, HPFRCC4, pp. 35-48.
- 8. Sujivorakul, C. and Naaman, A. E. (2003), "Effect of Bond Characteristics in Fiber Reinforced Cement Composites," Forth Regional Symposium on Infrastructure Development in Civil Engineering, (RSID4), April, Bangkok, Thailand.
- Srinil, N., Rega, G., and Chucheepsakul, S., (2003). "Nonlinear Interactions in the 3D Free Vibrations of Horizontal and Inclined Sagged Cables" *The5th International Symposium on Cable Dynamics*, September 15-18, Santa Margherita, Italy.
- Pulngern, T., Halling, M.W., and Chucheepsakul, S., (2004). "Vibrations of Inclined Variable-Arc-Length Beams: Analytical and Experimental" *Proc IMAC-XXII* Conference&Exposition on Structural Dynamics, January 26-29, Dearborn, Michigan.
- Pulngern, T., Halling, M.W., and Chucheepsakul, S., (2004). "Analytical and Experimental Studies on Free Vibrations of Variable Arc-Length Beams" Proc the 2th International Conference on Structural Engineering, Mechanics, and Computation, SEMC2004, July 5-7, South Africa.

# 2.4) ผลงานตีพิมพ์ในหนังสือวิชาการต่างประเทศ (Monograph)

 Sujivorakul, C. and Naaman, A. E. (2003). "Tensile Response of HPFRC Composites Using Twisted Polygonal Steel Fibers," ACI-Special Publication on Innovations in FRC for Value (in print).

# 2.5) ผลงานตีพิมพ์ในที่ประชุมวิชาการภายในประเทศ

- Wannasawaskul, P., and Chucheepsakul, S., (2001). "Effect of Prebuckling Rotation on Buckling Load of Arches," Proceedings of the 7th National Conference on Civil Engineering, EIT, STR, pp. 67-73.
- Chucheepsakul, S., and Monprapussorn, T., (2001). "Stability of Marine Elastica Pipes Transporting Fluid," Proceedings of the 7th National Conference on Civil Engineering, EIT, INV, pp. 51-60.

- 3. Kaewunruen, S., and Chucheepsakul, S., (2002), "Free Vibrations of Marine Risers Conveying Fluid," *Proceedings of the 8th National Convention on Civil Engineering, EIT*, STR, pp. 136-141.
- Phungpaigram, B., and Chucheepsakul, S., (2002), "Large Deflections af a Variable-Arc-Length Beam Subjected to An Inclined Follower Force," *Proceedings of the 8th National Convention on Civil Engineering, EIT*, STR, pp. 370-375.
- Saeauy, P., and Chucheepsakul, S., (2002), "Non-linear Buckling Analysis of Inclined Circular Arches," Proceedings of the 8th National Convention on Civil Engineering, EIT, STR, pp. 422-427.
- 6. Rattanasrikul, S., Poovarodom, N., and Chucheepsakul, S., (2002) "Dynamic Responses of Marine Cable due to Top End Excitation," *Proceedings of the 8th National Convention on Civil Engineering, EIT*, STR, pp. 428-433.

# Appendix Reprints and Manuscripts

# DIVERGENCE INSTABILITY OF VARIABLE-ARC-LENGTH ELASTICA PIPES TRANSPORTING FLUID

S. CHUCHEEPSAKUL AND T. MONPRAPUSSORN

Department of Civil Engineering, King Mongkut's University of Technology Thonburi
Bangkok 10140. Thailand

(Received 28 June 1999, and in final form 5 April 2000)

A flexible elastic pipe transporting fluid is held by an elastic rotational spring at one end, while at the other end, a portion of the pipe may slide on a frictional support. Regardless of the gravity loads, when the internal flow velocity is higher than the critical velocity, large displacements of static equilibrium and divergence instability can be induced. This problem is highly nonlinear. Based on the inextensible elastica theory, it is solved herein via the use of elliptic integrals and the shooting method. Unlike buckling with stable branching of a simply supported elastica pipe with constant length, the variable arc-length elastica pipe buckles with unstable branching. The friction at the support has an influence in shifting the critical locus over the branching point. Alteration of the flow history causes jumping between equilibrium paths due to abrupt changes of direction of the support friction. The elastic rotational restraint brings about unsymmetrical bending configurations; consequently, snap-throughs and snap-backs can occur on odd and even buckling modes, respectively. From the theoretical point of view, the equilibrium configurations could be formed like soliton loops due to snapping instability.

# 1. INTRODUCTION

A CONSIDERABLE AMOUNT OF RESEARCH WORK was done concerning the problems of a pipe conveying fluid as mentioned in the papers by Chen (1974), Païdoussis and Issid (1974), and in the textbooks by Thompson (1982), Blevins (1990), and more recently by Païdoussis (1998). Most of researchers determined stability criteria based on the small displacement theory. This conventional approach, however, does not take into consideration the post-buckling information, which supplements the lucid understanding of the mechanisms of large deflection of pipes transporting fluid, and are indispensable to the design of nonlinear system operation control. After publication of the paper by Thompson & Lunn (1981), the static elastica theory is an alternative approach for nonlinear analysis of pipes conveying fluid in the case where the pipe is dominated by divergence instability. In that study, the elastica pipe was considered to have a constant arc-length.

Nevertheless, in some applications, the arc-length of pipe is not constant and it could vary during operations. One may call such a pipe a variable-arc-length (VAL) pipe. Marine risers employed in deep-ocean mining (Huang & Chucheepsakul 1985) are examples of the variable-arc-length pipe. The riser is a flexible conductor pipe, which extends from the ball joint of the wellhead at seabed to the slip joint beneath the vessel. The slip joint allows the riser to change its length as the vessel heaves and moves laterally; consequently, the longitudinal strain is small and the effects of extensibility are negligible. Because of large deflection behaviour under offshore environment, the initial (equilibrium)

configuration of the riser may be defined as a VAL elastica and the riser behaves as a VAL elastica pipe.

To the authors' knowledge, the problem of VAL elastica pipes transporting fluid has not yet been considered in the past, thus it is the purpose of this study to explore the post-buckling behaviour and to investigate the possible equilibrium configurations of VAL elastica pipes transporting fluid. Figure 1(a) illustrates the VAL pipe studied herein. The pipe is installed on two stationary supports with a span length L and an overhang length  $\ell$ . One end is held by the pinned support A of elastic rotational spring constant K, whereas the other end-portion is propped by the support B with a static friction coefficient  $\mu$ . After buckling, it can slide over support B.

The literature review on various cases of the VAL pipe may be summarized as follows.

- (i) For K = 0 and  $\ell/L = 0$  the VAL pipe becomes a simply supported pipe, which cannot flutter, as reported by Holmes (1978).
- (ii) For K=0 and  $\ell/L=0.582$  the VAL pipe is an overhung pipe. Following the equivalent force analogy given by Thompson & Lunn (1981), the results of Elishakoff & Lottati (1988) show that if  $\ell/L < 0.582$  the pipe is dominated by divergence, if  $\ell/L > 0.582$  the pipe is dominated by flutter, and if  $\ell/L = 0.582$  the pipe is in transition between divergence and flutter instability.
- (iii) For  $K = \infty$  and  $\ell/L = 0$  the VAL pipe is a propped cantilever pipe. The experimental and theoretical results given by Yoshizawa et al. (1985) show that the pipe does lose stability by divergence.
- (iv) For  $K=\infty$  and  $\ell/L\approx 0.686$ . The experimental results given by Jendrzejczyk & Chen (1983) show that if  $\ell/L<0.686$  the pipe is dominated by divergence, if  $\ell/L>0.686$  the pipe is dominated by flutter, and if  $\ell/L=0.686$  the pipe is at a transition point between divergence and flutter instability. The finite element solutions excluding the effects of gravity forces and fluid pressures given by Escobar & Ting (1986) arrived at the same deduction, but for the transition condition  $\ell/L=0.643$ .
- (v) For  $K = \infty$  and  $\ell/L = \infty$  the VAL pipe becomes a cantilevered pipe, which behaves as Beck's problem (Beck 1952) and thus flutter instability dominates, as shown by Gregory & Païdoussis (1966).

It is inferred from the above review that the condition that the VAL pipe could be dominated by divergence is  $\ell/L < 0.582-0.686$  for K=0 to  $\infty$ . From a practical point of view, this condition is sufficient but not necessary; it is speculated that the VAL pipe with any value of  $\ell/L$  behaves as an elastica pipe if the transported fluid is suddenly jetted over the divergence velocity by a high-pressure pump. This situation, that the divergence instability always dominates, is used as the main assumption of this study.

The static elastica formulation can be achieved by consideration of equilibrium conditions between interacting fluid and pipe elements. The governing nonlinear differential equation obtained for elasticas, together with the boundary conditions, is solved analytically using elliptic integrals. As an independent check, the shooting method is also used to obtain numerical solutions. The effects of spring stiffness and friction at the supports on the stability criteria and post-buckling behaviour are studied and described in detail. Extensive bending results are presented graphically and snap-bending incidents are highlighted.

# 2. ELASTICA FORMULATION

Figure 1(b) shows diagrams of the interacting fluid and pipe infinitesimal elements. The transported fluid element is of density  $\rho_i$ , steady flow speed U, pressure  $p_i$ , and frictional drag force  $\tau$ , whereas an infinitesimal arc-length ds of the elastica pipe is of inner

cross-sectional area  $A_i$  and flexural rigidity EI. The positive directions of bending moment M, vertical and normal shear forces V and Q, and horizontal and tangential forces H and T, in the intrinsic coordinate  $(s, \theta)$ , are assigned in accordance with bending of a radius of gyration r and positive curvature  $\kappa$  as shown in Figure 1(b). Elastic buckling occurs after the critical flow velocity as shown in Figure 1(c). It should be noted that despite sliding of the pipe end-portion, the pipe tip E is assumed not to fall off the support B in the mathematical treatment herein, because such a case is irrelevant to the VAL elastica pipe.

Figure 1(d) shows a free-body diagram of forces acting on an elastica pipe segment. When the equilibrium of forces in the  $\hat{n}$  and  $\hat{t}$  directions of the diagrams of Figure 1(b) are considered, and the equilibrium of moments is taken about the centre point O of the pipe element (the derivation is given in Appendix A), the internal force equations are obtained as

$$\frac{\mathrm{d}N}{\mathrm{d}\theta} - Q = 0, \quad \frac{\mathrm{d}Q}{\mathrm{d}\theta} + N = 0, \quad \frac{\mathrm{d}M}{\mathrm{d}s} - Q = 0, \tag{1a-c}$$

where  $N = T - p_i A_i - \rho_i A_i U^2$  is the combined tension (Moe & Chucheepsakul 1988). Based on the constitutive equation of elastica theory,

$$M = -EI\frac{\mathrm{d}\theta}{\mathrm{d}s}\tag{2}$$

with some manipulation of equation (1), the second-order differential equations are

$$\frac{d^2N}{d\theta^2} + N = 0, \quad \frac{d^2Q}{d\theta^2} + Q = 0, \quad EI\frac{d^2\theta}{ds^2} + Q = 0.$$
 (3a-c)

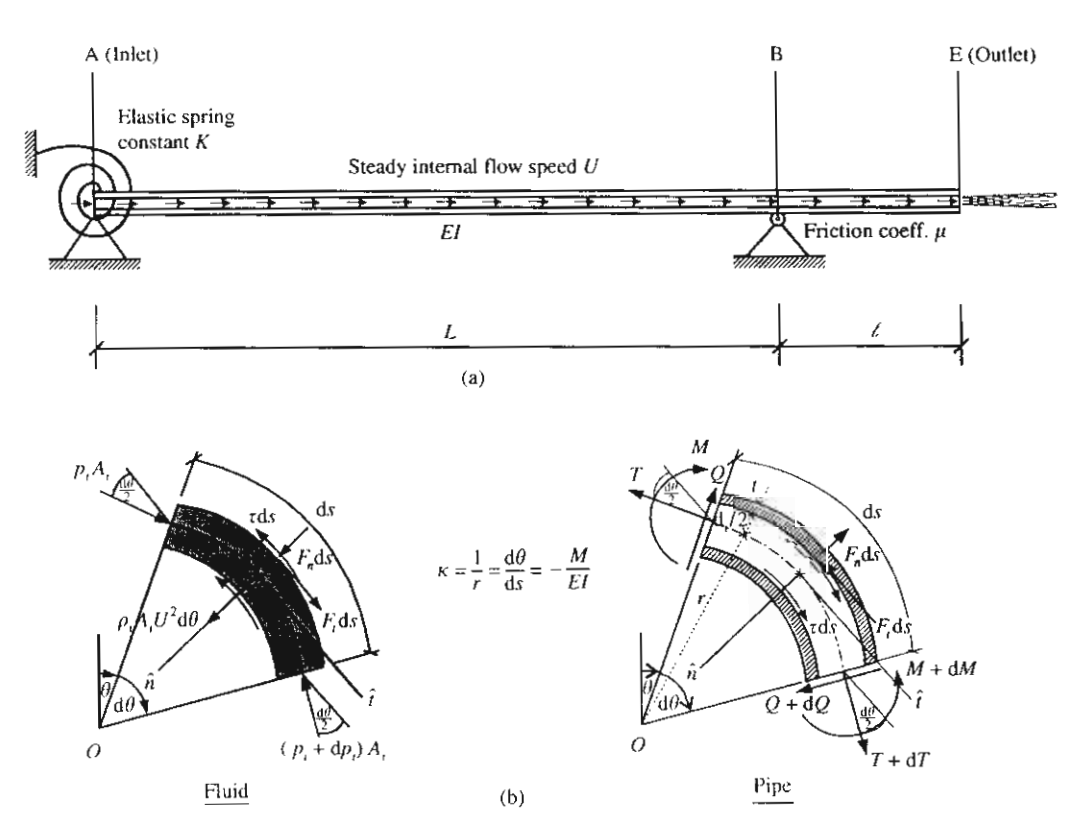


Figure 1. The variable-arc-length (VAL) elastica pipe transporting fluid: (a) undeformed configuration; (b) interaction diagrams of an elastica segment.

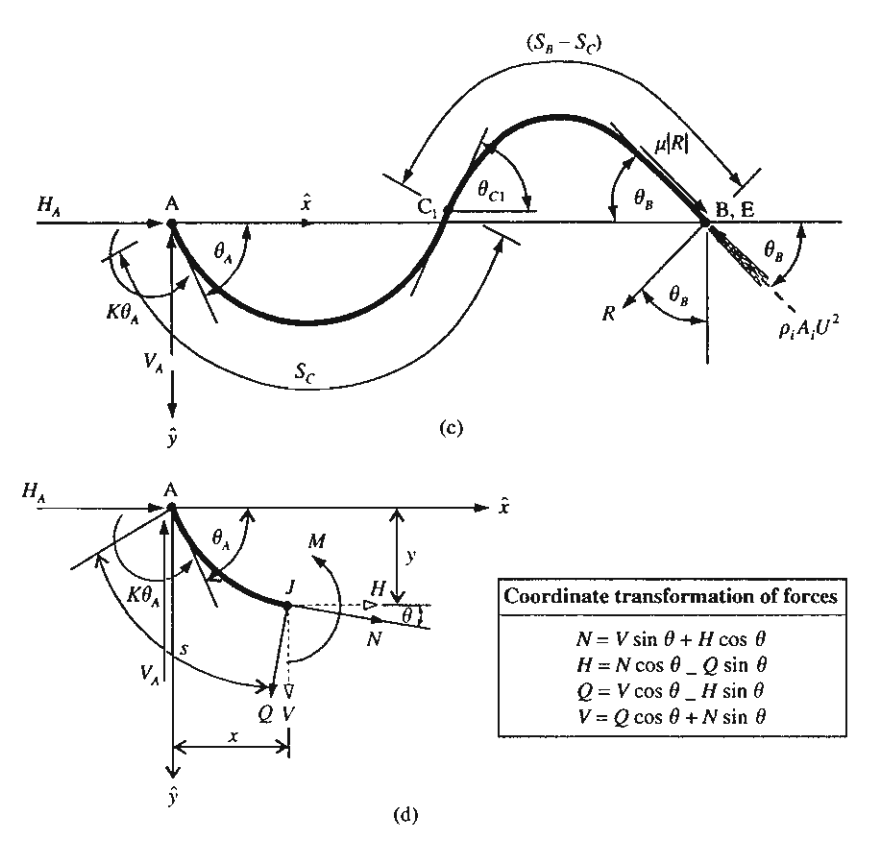


Figure 1. (continued) (c) a post-buckling configuration;(d) a free-body diagram of an elastica segment.

The general solution of equations (3) together with geometric relations and transformation of forces as shown in Figure 1(d) yield the set of equations describing plane deformations of elasticas transporting fluid, namely

$$N = -C_1 \cos \theta + C_2 \sin \theta, \quad H = -C_1, \quad \frac{\mathrm{d}x}{\mathrm{d}s} = \cos \theta,$$

$$Q = C_1 \sin \theta + C_2 \cos \theta, \quad V = C_2, \quad \frac{\mathrm{d}y}{\mathrm{d}s} = \sin \theta,$$

$$M = C_1 y + C_2 x + C_3, \quad EI \frac{\mathrm{d}^2 \theta}{\mathrm{d}s^2} + C_1 \sin \theta + C_2 \cos \theta = 0,$$

$$(4a-h)$$

where  $C_1$ ,  $C_2$  and  $C_3$  are arbitrary constants.

The boundary conditions (BCs) of the VAL elastica shown in Figure 1(c) are as follows:

Geometric BCs 
$$Natural\ BCs$$
  $M = -K\theta_A;$  (5a-c) Support B:  $(x, y) = (0, 0), (s, \theta) = (s_B, \theta_B),$   $M = 0, Q = R, T = \mu |R|;$  (5d-h) Outlet end E:  $p_i = 0,$   $N = \mu |R| - \rho_i A_i U^2.$  (5i,j)

Once the boundary conditions (5) are applied to equations (4), the constants  $C_1-C_3$  and the support reaction R are determined and written as

$$C_{1} = \rho_{i}A_{i}U^{2}(\cos\theta_{B} + \Lambda\sin\theta_{B}) + \Lambda\frac{K\theta_{A}}{L}, \quad C_{2} = \frac{K\theta_{A}}{L}, \quad C_{3} = -K\theta_{A},$$

$$R = \frac{\rho_{i}A_{i}U^{2}L\sin\theta_{B} + K\theta_{A}}{L(\cos\theta_{B} \pm \mu\sin\theta_{B})}, \quad \Lambda = \tan(\theta_{B} \mp \omega),$$
(6a-e)

where  $\omega = \tan^{-1}\mu$  is the friction angle. The signs  $\pm$  and  $\mp$  in equations (6d,e) take care of the value of |R|. Substituting equations (6) into (4) yields the governing equations of this problem:

$$N = -\left[\rho_{i}A_{i}U^{2}(\cos\theta_{B} + A\sin\theta_{B}) + \frac{AK\theta_{A}}{L}\right]\cos\theta + \frac{K\theta_{A}}{L}\sin\theta,$$

$$H = -\rho_{i}A_{i}U^{2}(\cos\theta_{B} + A\sin\theta_{B}) + \frac{AK\theta_{A}}{L}; \quad \frac{dx}{ds} = \cos\theta,$$

$$Q = \left[\rho_{i}A_{i}U^{2}(\cos\theta_{B} + A\sin\theta_{B}) + \frac{AK\theta_{A}}{L}\right]\sin\theta + \frac{K\theta_{A}}{L}\cos\theta,$$

$$V = \frac{K\theta_{A}}{L}; \quad \frac{dy}{ds} = \sin\theta,$$

$$M = \left[\rho_{i}A_{i}U^{2}(\cos\theta_{B} + A\sin\theta_{B}) + \frac{AK\theta_{A}}{L}\right]y + \frac{K\theta_{A}}{L}x - K\theta_{A},$$

$$EI\frac{d^{2}\theta}{ds^{2}} + \left[\rho_{i}A_{i}U^{2}(\cos\theta_{B} + A\sin\theta_{B}) + \frac{AK\theta_{A}}{L}\right]\sin\theta + \frac{K\theta_{A}}{L}\cos\theta = 0.$$

Thompson & Lunn (1981) showed that equations (7) can also be obtained from analysis of the empty pipe subjected to the end follower force  $\rho_i A_i U^2$  shown in Figure 1(c).

# 3. ELLIPTIC INTEGRAL SOLUTION

The following dimensionless quantities are introduced for the sake of generality:

$$\bar{x} = \frac{x}{L}, \quad \bar{y} = \frac{y}{L}, \quad \bar{s} = \frac{s}{L}, \quad s^* = \frac{s}{s_B}, \quad \bar{s}_B = \frac{s_B}{L}, \quad \bar{K} = \frac{KL}{EI}, \quad \bar{U} = \frac{\rho_i A_i U^2 L^2}{EI}, \quad (8a-g)$$

where  $s_B$  is the total arc-length of an elastica pipe. Then, equations (7h), (5c,f) and the *n* inflection conditions corresponding to the *n* unknowns  $\theta_{c1}$ ,  $\theta_{c2}$ , ...,  $\theta_{cn}$  (which are used in the integration to determine the elastica solutions), can be written in a nondimensional form

$$\frac{\mathrm{d}^2 \theta}{\mathrm{d}\bar{s}^2} + \left[ \bar{U}(\cos \theta_B + \Lambda \sin \theta_B) + \Lambda \bar{K} \theta_A \right] \sin \theta + \bar{K} \theta_A \cos \theta = 0, \tag{9a}$$

$$\frac{\mathrm{d}\theta}{\mathrm{d}\bar{s}}\Big|_{\theta=\theta_{A}} = \bar{K}\theta_{A}, \quad \frac{\mathrm{d}\theta}{\mathrm{d}\bar{s}}\Big|_{\theta=\theta_{B}} = 0, \tag{9b,c}$$

$$\frac{\mathrm{d}\theta}{\mathrm{d}\bar{s}}\Big|_{\theta=\theta_{c_1}} = \frac{\mathrm{d}\theta}{\mathrm{d}\bar{s}}\Big|_{\theta=\theta_{c_2}} = \cdots = \frac{\mathrm{d}\theta}{\mathrm{d}\bar{s}}\Big|_{\theta=\theta_{c_2}} = 0 \quad \text{in which } n=m+n_s-1. \tag{9d}$$

Let m be the order of the buckling mode and  $n_s$  the number of rotational springs, here  $n_s = 0$  for K = 0 and  $n_s = 1$  for  $K \neq 0$ . The subscripts A, B,  $C_1$ ,  $C_2$ , ...,  $C_n$  denote quantities evaluated at the support points A, B and at the inflection points  $C_1$ ,  $C_2$ , ...,  $C_n$ , respectively.

Upon integrating equation (9a) with respect to  $\theta$  and applying equations (9b-d), the following set of first-order differential equations and the n+1 constraint equations are obtained:

$$\bar{\kappa} = \frac{\mathrm{d}\theta}{\mathrm{d}\bar{s}} = \pm \sqrt{a + b\sin\theta + c\cos\theta}, \quad \frac{\mathrm{d}\bar{x}}{\mathrm{d}\bar{s}} = \cos\theta, \quad \frac{\mathrm{d}\bar{y}}{\mathrm{d}\bar{s}} = \sin\theta, \tag{10a-c}$$

$$b(\sin\theta_B - \sin\theta_A) + c(\cos\theta_B - \cos\theta_A) + \bar{K}^2\theta_A^2 = 0,$$

$$b(\sin\theta_B - \sin\theta_{C_1}) + c(\cos\theta_B - \cos\theta_{C_2}) = 0,$$

$$b(\sin\theta_B - \sin\theta_{C_2}) + c(\cos\theta_B - \cos\theta_{C_2}) = 0,$$

$$\vdots \qquad \vdots \qquad \vdots$$

$$b(\sin\theta_B - \sin\theta_{C_n}) + c(\cos\theta_B - \cos\theta_{C_n}) = 0,$$

where

$$a = -b\sin\theta_B - c\cos\theta_B$$
,  $b = -2\bar{K}\theta_A$ ,  $c = 2[\bar{U}(\cos\theta_B + \Lambda\sin\theta_B) + \Lambda\bar{K}\theta_A]$ . (12a-c)

The minus sign (+) of the dimensionless curvature  $\bar{\kappa}$  is for the concave curve, whereas the plus sign (+) is for the convex curve of elastica portions.

The integration and mapping of equations (10) by elliptic integrals (Byrd and Friedman 1971) yield the closed-form solutions of equilibrium configurations as follows in tabular form:

Coordinates refer from the point A to any Z	The interval containing a point Z is from					
	A to C <sub>1</sub>	C <sub>1</sub> to C <sub>2</sub>	•••	C <sub>n</sub> to B		
$\tilde{s}_z =$	\$ <sub>AZ</sub>	$\bar{s}_{AC_1} + \bar{s}_{C_1Z}$		$\bar{s}_{AC_1} + \bar{s}_{C_1C_2} + \cdots + \bar{s}_{C_{n-1}C_n} + \bar{s}_{C_nZ}$ (13)		
$\bar{x}_z = \bar{y}_z =$	$\bar{x}_{AZ}$ $\bar{y}_{AZ}$	$\bar{x}_{AC_1} + \bar{x}_{C_1Z}$ $\bar{y}_{AC_1} + \bar{y}_{C_1Z}$		$\bar{x}_{AC_1} + \bar{x}_{C_1C_2} + \cdots + \bar{x}_{C_{n-1}C_n} + \bar{x}_{C_nZ}(14)$ $\bar{y}_{AC_1} + \bar{y}_{C_1C_2} + \cdots + \bar{y}_{C_{n-1}C_n} + \bar{y}_{C_nZ}(15)$		

In equations (13)-(15),

$$\bar{s}_{ij} = \int_{\theta_i}^{\theta_j} \frac{\mathrm{d}\theta}{\bar{\kappa}} = \begin{cases} \frac{\sqrt{2}}{(b^2 + c^2)^{1/4}} [F(\Phi_j, k) - F(\Phi_i, k)] & \text{for } \theta_j \ge \theta_i \text{ of positive } \bar{\kappa}, \\ \frac{\sqrt{2}}{(b^2 + c^2)^{1/4}} [F(\Phi_i, k) - F(\Phi_j, k)] & \text{for } \theta_j < \theta_i \text{ of negative } \bar{\kappa}, \end{cases}$$
(16)

$$\bar{x}_{ij} = \int_{\theta_{i}}^{\theta_{i}} \frac{\cos\theta \, d\theta}{\bar{\kappa}} = \begin{cases} \frac{\sqrt{2}c}{(b^{2} + c^{2})^{3/4}} \left[ \eta(\Phi_{j}, k) - \eta(\Phi_{i}, k) + \frac{2kb}{c} (\cos\Phi_{j} - \cos\Phi_{i}) \right] & \text{for } \theta_{j} \geq \theta_{i}, \\ \frac{\sqrt{2}c}{(b^{2} + c^{2})^{3/4}} \left[ \eta(\Phi_{i}, k) - \eta(\Phi_{j}, k) + \frac{2kb}{c} (\cos\Phi_{i} - \cos\Phi_{j}) \right] & \text{for } \theta_{j} < \theta_{i}, \end{cases}$$

$$(17)$$

$$\bar{y}_{ij} = \int_{\theta_i}^{\theta_j} \frac{\sin\theta \, \mathrm{d}\theta}{\bar{\kappa}} = \begin{cases} \frac{\sqrt{2}b}{(b^2 + c^2)^{3/4}} \left[ \eta(\Phi_j, k) - \eta(\Phi_i, k) - \frac{2kc}{b} (\cos\Phi_j - \cos\Phi_i) \right] & \text{for } \theta_j \ge \theta_i, \\ \frac{\sqrt{2}b}{(b^2 + c^2)^{3/4}} \left[ \eta(\Phi_i, k) - \eta(\Phi_j, k) - \frac{2kc}{b} (\cos\Phi_i - \cos\Phi_j) \right] & \text{for } \theta_j < \theta_i, \end{cases}$$

$$(18)$$

in which the following parameters are prescribed in mapping:

$$\eta \left( \Phi_i, k \right) = 2E(\Phi_i, k) - F(\Phi_i, k), \quad \varphi = \sin^{-1} \left( \frac{b}{p} \right) = \cos^{-1} \left( \frac{c}{p} \right),$$

$$\Phi_i = \sin^{-1} \left( \sqrt{\frac{p - b \sin \theta_i - c \cos \theta_i}{a + p}} \right), \quad k = \sqrt{\frac{a + p}{2p}}, \quad p = \sqrt{b^2 + c^2}.$$
(19a-e)

The functions  $F(\Phi, k)$  and  $E(\Phi, k)$  are the adjustable elliptic integrals of the first and second kind, respectively, defined as

$$F(\Phi, k) = sgn(\theta) \times \{Jacobi's standard elliptic integrals of the first kind\},$$
 (19f)

$$E(\Phi, k) = \operatorname{sgn}(\theta) \times \{\text{Jacobi's standard elliptic integrals of the second kind}\}, (19g)$$

where

$$\operatorname{sgn}(\theta) = \begin{cases} 1 & \text{if } \sin(\varphi - \theta) \le 0, \\ -1 & \text{if } \sin(\varphi - \theta) > 0. \end{cases}$$
 (19h)

There are n+2 unknowns in the foregoing elliptic integral formulation, namely either  $(\theta_A, \theta_B, \theta_{C_1}, \theta_{C_2}, \dots, \theta_{C_n})$  under displacement control or  $(\theta_A, \theta_{C_1}, \theta_{C_2}, \dots, \theta_{C_n}, \overline{U})$  under internal flow control of the stability of the pipe. Therefore, n+2 equations are required for solution, for instance equations (5d) and (11). Equation (5d) with the assistance of equations (15) and (18) can be expressed in elliptic integrals form as

$$\bar{y}_B = \bar{y}_{AC} + \bar{y}_{C,C} + \bar{y}_{C,C} + \cdots + \bar{y}_{C,C} + \bar{y}_{C,B} = 0,$$
 (20a)

where for n being an even number,

$$\tilde{y}_{B} = \frac{\sqrt{2}}{(b^{2} + c^{2})^{3/4}} \begin{bmatrix} \eta(\Phi_{A}, k) - 2\eta(\Phi_{C_{1}}, k) + 2\eta(\Phi_{C_{2}}, k) \\ - \dots - 2\eta(\Phi_{C_{n-1}}, k) + 2\eta(\Phi_{C_{n}}, k) - \eta(\Phi_{B}, k) \\ - \frac{2kc}{b} \begin{pmatrix} \cos \Phi_{A} - 2\cos \Phi_{C_{1}} + 2\cos \Phi_{C_{2}} \\ - \dots - 2\cos \Phi_{C_{n-1}} + 2\cos \Phi_{C_{n}} - \cos \Phi_{B} \end{pmatrix}$$
(20b)

and when n is an odd number.

$$\bar{y}_{B} = \frac{\sqrt{2}}{(b^{2} + c^{2})^{3/4}} \begin{bmatrix} -\eta(\Phi_{A}, k) + 2\eta(\Phi_{C_{1}}, k) - 2\eta(\Phi_{C_{2}}, k) \\ + \dots - 2\eta(\Phi_{C_{n-1}}, k) + 2\eta(\Phi_{C_{n}}, k) - \eta(\Phi_{B}, k) \\ -\frac{2kc}{b} \begin{pmatrix} -\cos\Phi_{A} + 2\cos\Phi_{C_{1}} - 2\cos\Phi_{C_{2}} \\ + \dots - 2\cos\Phi_{C_{n-1}} + 2\cos\Phi_{C_{n}} - \cos\Phi_{B} \end{pmatrix} \end{bmatrix}.$$
(20c)

The system of nonlinear algebraic equations (11) and (20) is solved using the quasi-Newton method of minimization for the sake of global convergence (Press et al. 1992). The details of the iterative procedure are given in Chucheepsakul et al. (1999).

#### 4. SHOOTING METHOD

In view of equations (2), (5), (7) and (8), another nondimensional form of the governing differential equations and the boundary conditions can be written as

$$\frac{\mathrm{d}\theta}{\mathrm{d}s^*} = \bar{s}_B \left[ -\bar{K}\theta_A(\bar{x} + \Lambda\bar{y} - 1) - \bar{U}\bar{y}(\cos\theta_B - A\sin\theta_B) \right],\tag{21}$$

$$\frac{d\bar{x}}{ds^*} = \bar{s}_B \cos \theta, \quad \frac{d\bar{y}}{ds^*} = \bar{s}_B \sin \theta, \tag{22a,b}$$

$$\bar{x}(0) = 0$$
,  $\bar{y}(0) = 0$ ,  $\theta(0) = \theta_A$ ,  $\bar{x}(1) = 1$ ,  $\bar{y}(1) = 0$ ,  $\theta(1) = \theta_B$ . (23a-f)

There are five unknowns in the above equations, namely either  $(\theta, \bar{x}, \bar{y}, \bar{s}_B, \theta_A)$  under displacement control or  $(\bar{U}, \bar{x}, \bar{y}, \bar{s}_B, \theta_A)$  under internal flow control of the stability of the pipe. By employing the five end conditions of equations (23a-e), this boundary value problem under internal flow control could be solved by the following procedure.

Firstly, the shooting angle is prescribed by the initial values of equations (23d-f) and the guessed values of  $\bar{s}_B$ ,  $\bar{U}$  and  $\theta_A$ . Secondly, the integration is carried out from  $s^* = 1$  to 0 using the fifth-order Cash-Karp Runge-Kutta Fehlberg method (Press *et al.* 1992). Thirdly, the error norms are evaluated relative to the targets of equations (23a-c) and the following objective function  $\Pi$  is minimized using the downhill simplex method (Nelder & Mead 1965):

Minimize 
$$\Pi = |\bar{x}(0)| + |\bar{y}(0)| + |\theta(0) - \theta_A|$$
. (24)

Finally, the foregoing steps are iterated until the allowable error is achieved.

# 5. STABILITY CRITERIA

The conventional approach for determining bifurcation criteria of the VAL elastica pipe is based on linear theory, which uses the small displacement assumption,  $ds \approx dx, \theta \approx dy/dx$  and  $\cos \theta \approx 1$ ,  $\sin \theta \approx 0$ . Thereby, equations (6) yield  $C_1 = \rho_i A_i U^2$ ,  $C_2 = C_3 = 0$ , R = 0 and  $A = \mp \mu$ . By manipulating equations (2) and (4g), one obtains the boundary value problem of linear system,

$$y_{\text{xxxx}} + \beta^2 y_{\text{xx}} = 0 \tag{25a}$$

with the boundary conditions

$$y(0) = 0,$$
  $y(L) = 0,$  (25b,c)

$$y_{,xx}(0) = \hat{K}y_{,x}(0), \qquad y_{,xx}(L) = 0,$$
 (25d,e)

where a subscript ( ),<sub>x</sub> = d( )/dx,  $\beta^2 = \rho_i A_i U^2 / EI$  and  $\hat{K} = K / EI$ . Equation (25a) has the general solution

$$y = A_1 \sin \beta x + A_2 \cos \beta x + A_3 x + A_4, \tag{26}$$

in which  $A_1$ ,  $A_2$ ,  $A_3$  and  $A_4$  are constants depending on the boundary conditions.

Applying equation (26) to equations (25b-e) yields the characteristic equation

$$\begin{vmatrix}
0 & 1 & 0 & 1 \\
\sin \beta L & \cos \beta L & L & 1 \\
\hat{K}\beta & \beta^2 & \hat{K} & 0 \\
\beta^2 \sin \beta L & \beta^2 \cos \beta L & 0 & 0
\end{vmatrix} = 0.$$
(27)

Expansion of this determinant along with some manipulations yield

$$\tan u = \frac{\bar{K}u}{u^2 + \bar{K}},\tag{28}$$

where  $u = \beta L$ , and  $u^2$  is the dimensionless bifurcation velocity  $\overline{U}_b$ . For the case of simply supported VAL elastica pipes,  $\overline{K} = 0$ , thus equation (28) is simplified to  $\tan u = 0$  or  $\overline{U}_b = m^2 \pi^2$ , which is the well-known Euler buckling solution. For the case of fixed supported VAL elastica pipes, the limit of equation (28) when  $\overline{K} \to \infty$  yields the characteristic equation  $\tan u = u$ .

On switching to the elastica theory, the same stability limits are derived from the condition

$$\tilde{s}_B = \bar{s}_{AC_1} + \bar{s}_{C_1C_2} + \bar{s}_{C_2C_3} + \dots + \bar{s}_{C_{n-1}C_n} + \bar{s}_{C_nB} = 1.$$
(29a)

Substituting equation (16) into equation (29a) yields the characteristic equations of stability limits as follows. For n being an even number,

$$\bar{s}_B = \frac{\sqrt{2}}{(b^2 + c^2)^{1/4}} \begin{bmatrix} F(\Phi_A, k) - 2F(\Phi_{C_1}, k) + 2F(\Phi_{C_2}, k) \\ - \cdots - 2F(\Phi_{C_{n-1}}, k) + 2F(\Phi_{C_n}, k) - F(\Phi_B, k) \end{bmatrix} = 1$$
 (29b)

and for n being an odd number.

$$\bar{s}_B = \frac{\sqrt{2}}{(b^2 + c^2)^{1/4}} \begin{bmatrix} -F(\Phi_A, k) + 2F(\Phi_{C_1}, k) - 2F(\Phi_{C_2}, k) \\ + \cdots - 2F(\Phi_{C_{n-1}}, k) + 2F(\Phi_{C_n}, k) - F(\Phi_B, k) \end{bmatrix} = 1.$$
 (29c)

Equations (29) are easily examined by hand in the case of  $\bar{K} = 0$  under the parameters simplified from equations (19) as follows:

$$\theta_i \to 0$$
,  $i = A, C_1, C_2, ..., C_n, B$ ,  $a = -2\bar{U}_b$ ,  $b = 0$ ,  $c = 2\bar{U}_b$ , (30a-c)

$$\varphi = 0, p = 2\bar{U}_b, \Phi_i = \frac{\pi}{2}, k = 0,$$
 (30d-g)

$$F(\Phi_i, k) = F\left(\frac{\pi}{2}, 0\right) = \begin{cases} \frac{\pi}{2} & \text{if } \theta_i \to 0^+, \\ -\frac{\pi}{2} & \text{if } \theta_i \to 0^-, \end{cases} \frac{\sqrt{2}}{(b^2 + c^2)^{1/4}} = \frac{1}{\sqrt{\overline{U}_b}}.$$
 (30h,i)

Substituting equations (30) into equations (29) yields the stability limit as

$$\bar{U}_b = (n+1)^2 \pi^2 = m^2 \pi^2, \tag{31}$$

which is the Euler buckling solution as well. The numerical results of bifurcation velocity determined from equations (28) and (29) are found identical and are shown in Figure 5(b).

The numerical results of flow velocity-displacement curves shown in Figures (2) and 5(a) indicate that the bifurcation velocities  $\bar{U}_b$  at the branching point are also the critical velocities. Nevertheless, when the support friction is taken into account, the critical

velocities are set apart from the bifurcation velocities as shown in Figure 4(a). In such a case, the critical velocities are determined using the dichotomous search method (Rao 1996).

# 6. RESULTS AND DISCUSSION

The elliptic integral method and the shooting method have been cross-checked for validating almost all of the postbuckling results presented in this study. An example to show validity of the solution is given in Table 1 in which numerical results are compared for the VAL elastica pipes with  $\bar{K}=0$  and  $\mu=0$ . It is seen that the two methods yield almost identical results. However, the shooting method has advantage over the elliptic integral method in view of the unknown number, complexity of formulation, and independence of inflection points. To demonstrate the effects of arc-length variableness, of support friction, and of elastic rotational restraint on postbuckling behaviour of the VAL elastica pipe, the following three numerical examples with different boundary conditions are studied.

# 6.1. SIMPLY SUPPORTED VAL ELASTICA PIPES

Figure 2 illustrates the relationship between the internal flow velocity  $\bar{U}$  and the support rotations  $\theta_A$ ,  $\theta_B$  of the constant-arc-length elastica pipe and the VAL elastica pipe. The equilibrium paths of the systems are along the vertical axis, the horizontal branching lines, and the ascendent and descendent branching curves. On the equilibrium paths overlying on the vertical axis, the three states of possible behaviour of the pipes may be explained as follows.

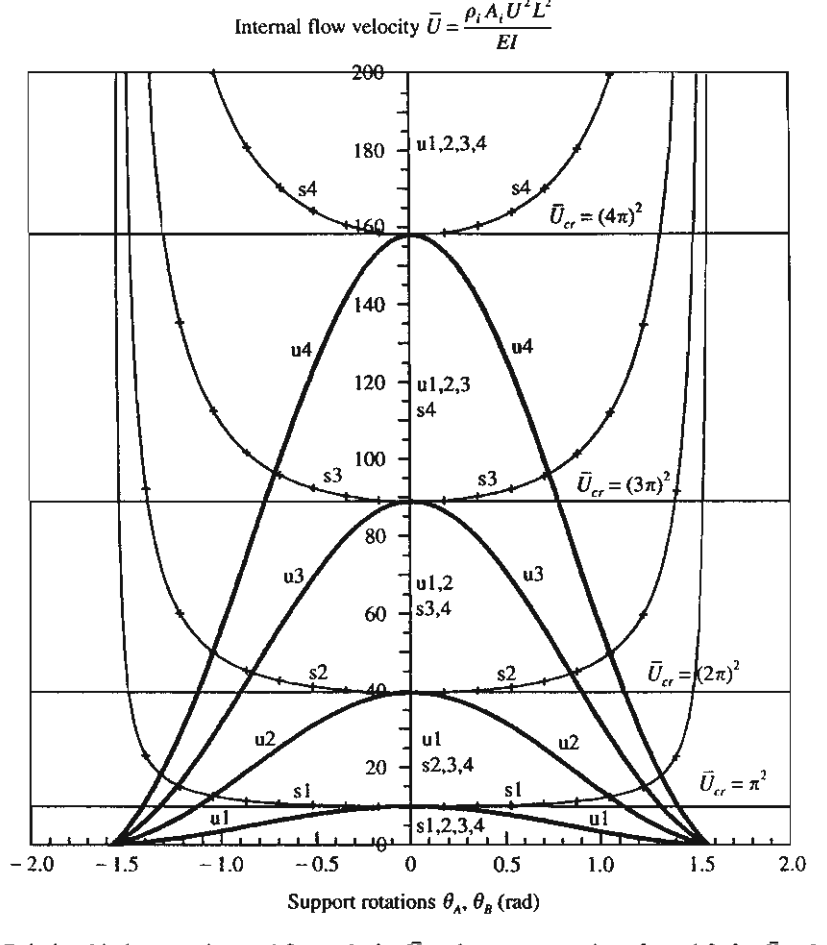
- (a) Stable state (before a branching point). This state occurs when the pipes convey fluid with internal flow velocity less than the critical flow velocity  $\overline{U}_{cr}$ . In this state the VAL elastica pipe does not have both bending and sliding ( $\theta_A = \theta_B = 0$ ) because no buckling has occurred. Consequently, there is no difference of behaviour between linear problems and elastica problems.
- (b) Critical state (at a branching point). This state occurs when the pipes convey fluid with internal flow velocity equal to the critical flow velocity  $\overline{U}_{cr}$ . In this state the VAL elastica pipe still does not have both bending and sliding ( $\theta_A = \theta_B = 0$ ) because of being in a transition state. This implies that the stability criteria of both linear problems and elastica problems are the same.
- (c) Unstable state (over a branching point). This state occurs when the pipes convey fluid with internal flow velocity higher than the critical flow velocity  $\overline{U}_{cr}$ . All the points that belong to the flow velocity axis and are located above  $\overline{U}_{cr}$  belong to this state. These equilibrium states are unstable and cannot be maintained if a disturbance, however small, is applied to the pipe. Practically, equilibrium paths will bifurcate along branching curves rather than going on this state.

On the equilibrium paths along the horizontal branching lines, and the ascendent and descendent branching curves, the three post-buckling states of the pipes may be explained as follows.

(i) Stable post-buckling state (along the ascendent branching curves) is the state that when  $\bar{U}$  increases, the end rotations  $\theta_A$  and  $\theta_B$  will increase as well, and the elastica will be bent stably, namely a small disturbance does not affect to the equilibrium of the system. The constant-arc-length elastica pipe is on this state after buckling, as shown in Figure 2.

<u> </u>	Q	9.8 <b>69604</b> 5 0	478418	88.826440 60 40 20 110 0	57.91367 20 80 40 0
		900	6,68350	88.000000000000000000000000000000000000	157. 120 80 40 0
$\frac{s_{\mathbf{B}}}{L}$	SM <sup>‡</sup>	1-000000 1-202689 2-188422	1.00000 1.079957 1.202689 1.418856 2.188424	1-000000 1-115105 1-239108 1-455474 1-662348 2-188432	1-000000 1-079957 1-202690 1-418857 2-188441
	EIM⁺	1.202689 2.188420	1.00000 1.079957 1.202689 1.418854 2.188420	1.00000 1.115105 1.239108 1.455472 1.662342 2.188420	1.000000 1.079957 1.202689 1.418854 2.188420
$\frac{y_{max}}{L}$	SMt	0-000000 0-297307 0-834614	0.000000 0.091347 0.148653 0.221600 0.417310	0.000000 0.073533 0.108319 0.154968 0.192975 0.278207	0.000000 0.047685 0.074348 0.110838 0.208665
	EIM <sup>†</sup>	0-000000 0-297307 0-834613	0.00000 0.091347 0.148653 0.221600 0.417309	0.00000 0.073533 0.108319 0.154968 0.192974 0.278206	0.000000 0.045673 0.074327 0.110800 0.208655
(p	SM <sup>‡</sup>	0-000000 -0-836104 -1-570795	$\begin{array}{c} 0.000000 \\ -0.548471 \\ -0.836104 \\ -1.122792 \\ -1.570795 \end{array}$	0.000000 -0.649662 -0.897130 -1.158452 -1.320794 -1.570795	0.000000 -0.548471 -0.836104 -1.122791 -1.570794
$\theta_B(\mathrm{rad})$	EIM <sup>†</sup>	0.000000 -0.836105 -1.570796	$\begin{array}{c} 0.000000 \\ -0.548471 \\ -0.836105 \\ -1.122793 \\ -1.570796 \end{array}$	0.000000 -0.649662 -0.897131 -1.158453 -1.320796 -1.570796	$\begin{array}{c} 0.000000 \\ -0.548471 \\ -0.836105 \\ -1.122793 \\ -1.570796 \end{array}$
$\theta_{A}(rad)$	SM <sup>‡</sup>	0-000000 0-836105 1-570799	0.000000 -0.548472 -0.836106 -1:122796 -1:570799	0.00000 0.649664 0.897134 1.158460 1.320806 1.570799	$\begin{array}{c} 0.000000 \\ -0.548473 \\ -0.836108 \\ -1.122800 \\ -1.570799 \end{array}$
	EIM†	0-000000 0-836105 1-570796	0-000000 -0-548471 -0-836105 -1-122793 -1-570796	0-00000 0-649662 0-897131 1-158453 1-320796 1-570796	0-000000 -0-548471 -0-836105 -1-122793 -1-570796
	Mode		7	٣	4

† Elliptic integral method; † Shooting Method.



- (ii) Neutral post-buckling state (along the horizontal branching lines) is the state that the pipe may undergo small lateral deflections with no change of the critical flow velocity  $\bar{U}_{cr}$ . This state occurs only with the ideal pipe based on the linear analysis, as shown in Figure 2.
- (iii) Unstable post-buckling state (along the descendent branching curves) is the state that when  $\overline{U}$  decreases, the end rotations  $\theta_A$  and  $\theta_B$  increase instead of decreasing. This implies that after buckling, the pipe will be bent unstably, namely a small disturbance will initiate continuous pipe motion. The VAL elastica pipe is on this state after buckling, as shown in Figure 2.

The possible unstable equilibrium configurations of VAL elasticas transporting fluid with the steady flow velocity  $\bar{U}=6$  are displayed in Figure 3 for the 1st-4th buckling modes. It is found that for an equal  $\bar{U}$ , the elastica length  $\bar{s}_B$  of higher-order modes is longer than that of lower-order modes. However, when the unstable equilibrium of all buckling modes of the VAL elastica pipe reaches the final state  $\theta_A=\theta_B=\pi/2$ , the arc-length of all the modes will become equal, and has the maximum value  $\bar{s}_{B(\max)}=2.1884$  as shown in Table 1.

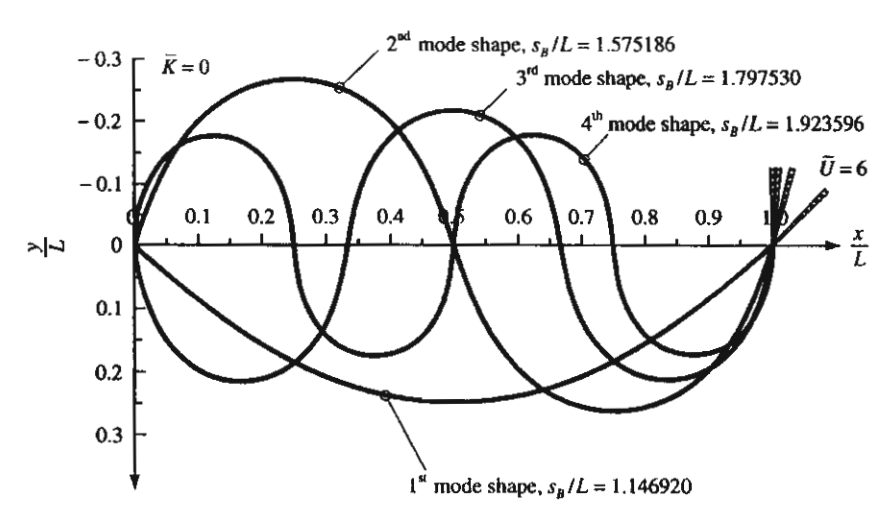


Figure 3. Unstable equilibrium configurations for  $\bar{K} = 0$ ,  $\mu = 0$ , and  $\bar{U} = 6$ .

Chucheepsakul et al. (1995,1996,1997) were aware that this value is an invariant property of the single curvature bending of VAL elasticas under moment gradient, end moment, and point load.

# 6.2. FRICTIONALLY SUPPORTED VAL ELASTICA PIPES

The effect of friction at the support B is studied on the fundamental buckling mode by fixing  $\bar{K}=0$  and varying  $\mu=0$  to 1. Figure 4(a) shows the effect on flow velocity-displacement relationships in the case of  $\mu=0.25$  and 0.5 for flow-loading condition (history of steady flow increase) and  $\mu=-0.25$  and -0.5 for flow-unloading condition (history of steady flow decrease).

Under flow-loading conditions the equilibrium paths of the frictionally supported VAL elastica pipe are somewhat different from those of the simply supported VAL elastica pipe. Though their stable states are the same on the vertical axis, after bifurcation the branching

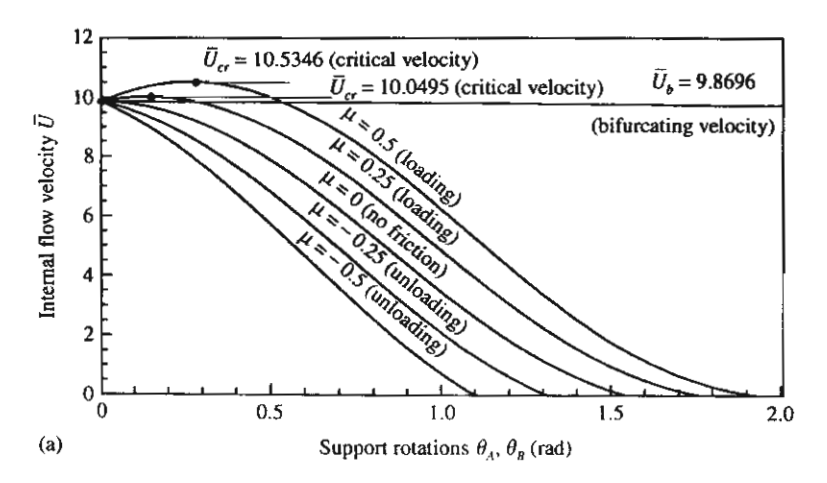


Figure 4. (a) Effect of friction coefficient  $\mu$  on the relationship between internal flow velocity  $\overline{U}$  and support rotations  $\theta_A$  and  $\theta_B$ .

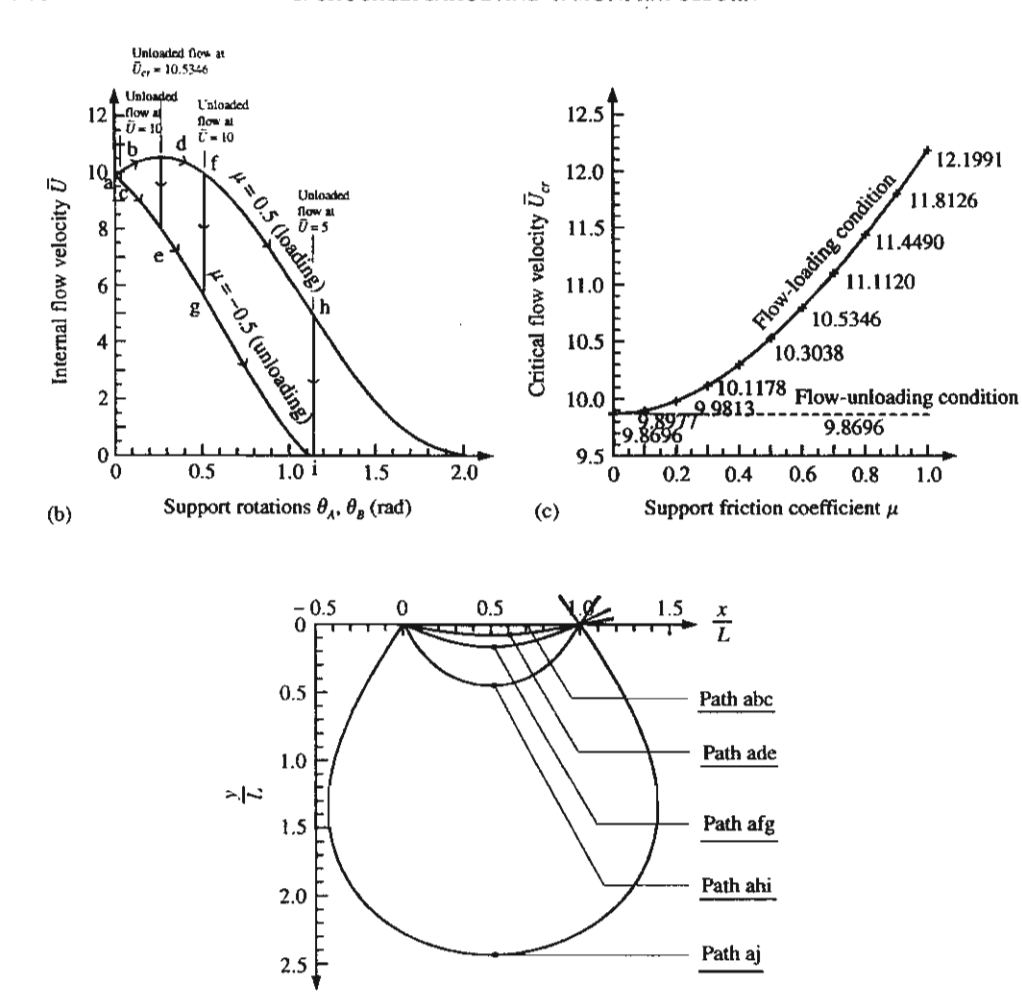


Figure 4. (continued) (b) Equilibrium path changes; (c) critical flow velocities  $\overline{U}_{cr}$  (d) equilibrium configurations: path 'abc' is stable for  $\overline{U}=10$  (loading), and unstable for  $\overline{U}=10-9.7259$  (unloading); path 'ade' is critical for  $\overline{U}=10-5346$  (loading), and unstable for  $\overline{U}=10-5346-8.0452$  (unloading); path 'afg' is unstable for both  $\overline{U}=10$  (loading) and  $\overline{U}=10-5.5703$  (unloading); path 'ahi' is unstable for  $\overline{U}=5$  (unloading), and no equilibrium for  $\overline{U}=5$  (unloading); path 'aj' is unstable for  $\overline{U}=0$  (loading), and no equilibrium for  $\overline{U}=0$  (unloading).

(d)

Table 2

Parameters of equilibrium path change corresponding to Figure 4(b)

Path $s_B/L$		$\mu = 0.5$		$\mu = -0.5$		Stability status change
	$\theta_B(rad)$	$ar{ar{U}}$	$\theta_B(rad)$	$ar{ar{U}}$	Loading → Unloading	
abc	1.0002	-0.0277	10	-0.0277	9.7259	Stable → unstable
ade	1.0174	-0.2618	10.5346	-0.2618	8.0452	Critical → unstable
afg	1.0696	-0.5136	10	-0.5136	5.5703	Unstable → unstable
afg ahi	1-4368	<b>−1·1406</b>	5	_	_	Unstable → no equilibrium exists

curves of the frictionally supported VAL pipe grow, corresponding to an increase of support rotations before reaching the critical point and their descent as shown in Figure 4(a). This means that, after buckling, the pipe will be in the stable post-buckling state, the critical post-buckling state, and the unstable post-buckling states, respectively. This behaviour could be explained as follows.

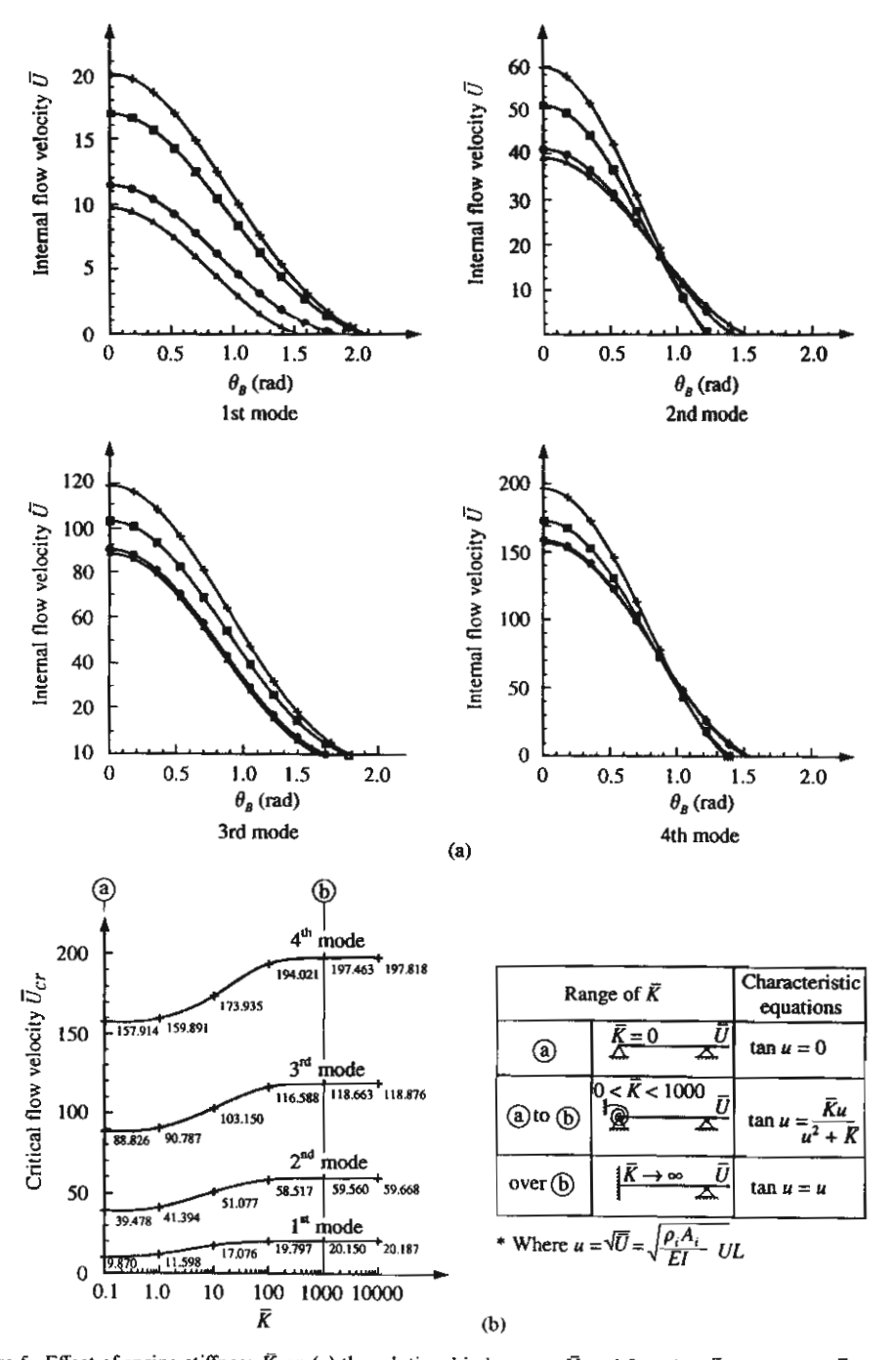


Figure 5. Effect of spring stiffness  $\vec{K}$  on (a) the relationship between  $\vec{U}$  and  $\theta_B$ :  $-\Delta$ ,  $\vec{K}=0$ ;  $-\bar{K}=1$ ;  $-\bar{K}=10000$ ; (b) critical flow velocity  $\vec{U}_{cr}$ .

Before branching, support friction has no effect on the bifurcation velocity, because it is still a nonworking force as long as the VAL pipes are motionless. Referring to equation (6d),  $R(\theta_A = 0, \theta_B = 0) = 0$ , and thus the friction force  $\mu |R| = 0$ . After branching, the friction force becomes a working force, to resist large displacements, and thus stabilizes the elastica. That yields an increase in the branching curves, which expresses the stable buckling state as explained in the previous topic. However, when the larger end-rotations are induced due to the higher internal flow velocity, it is seen that the branching curves tend to reach the peak value of  $\bar{U}$ , which is known as the maximum or critical value of  $\bar{U}$  or  $\bar{U}_{cr}$ . There, the effect of support friction is no longer enough to stabilize the elastica; thus the system turns back to be dominated by the internal flow, and after that, it undergoes the unstable post-buckling state along the descending curves as shown in Figure 4(a).

Under flow-unloading conditions as shown in Figure 4(a), the equilibrium paths of the frictionally supported VAL elastica pipe are along the vertical axis, and the descendent branching curves as well as those of the simply supported VAL elastica pipes in the previous topic. The effect of support friction destabilizes the elastica owing to the opposite change of friction direction. Also, in Figure 4(a), it is seen that the locus of critical state is raised as the friction coefficient increases.

The direction of the support friction is nonconservative. If a flow-unloading condition happens due to any reduction of flow velocity such as partially closing the valve at inlet, the friction direction will be suddenly changed to the opposite direction. Consequently, the equilibrium path is abruptly altered, and then induced jumping between the equilibrium paths of flow-loading and flow-unloading conditions as shown in Figure 4(b). As a result, changes of stability status may occur as shown in Figure 4(b), paths abc, ade, afg, and ahi. The parameters of these paths are listed in Table 2, and the equilibrium configurations are shown in Figure 4(d). The effect of the support friction on critical velocity shown in Figure 4(c) is to increase the critical velocity under the flow-loading conditions, but have no influence under the flow-unloading conditions.

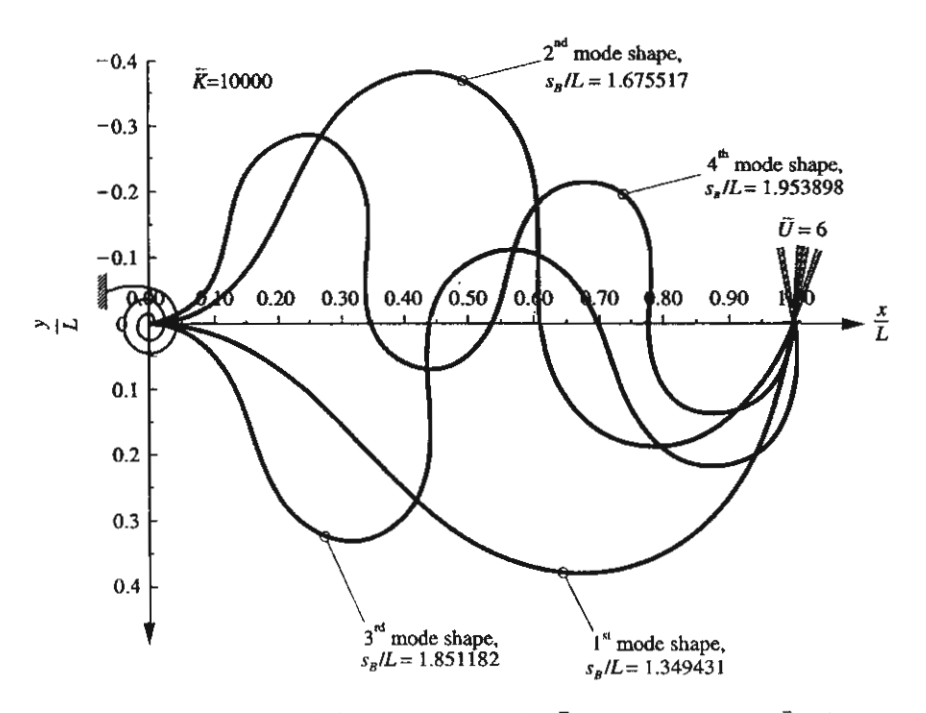


Figure 6. Unstable equilibrium configurations for  $\bar{K} = 10\,000$ ,  $\mu = 0$ , and  $\bar{U} = 6$ .

# 6.3. ELASTICALLY RESTRAINED VAL ELASTICA PIPES

The effect of elastic rotational restraint at the support A is studied in the 1st-4th buckling modes by fixing  $\mu=0$  and varying  $\bar{K}=0$ -10000. Figure 5(a) shows the effect on the relationship between the flow velocity  $\bar{U}$  and the support rotation  $\theta_B$  for  $\bar{K}=0$ , 1, 10, and 10000. Figure 5(b) shows the effect on augmentation of the bifurcation and critical velocities in semi-log scale. It is observed that the critical velocities are almost constant for  $\bar{K} \geq 1000$ . For such a condition, support A may be considered as a fixed boundary condition.

The unstable equilibrium configurations of the VAL elasticas transporting fluid for  $\bar{K}=10\,000$ ,  $\mu=0$ , and  $\bar{U}=6$  are displayed for the 1st-4th buckling modes in Figure 6. It is clearly seen that the elasticas are bent skew-forward in the odd buckling modes and skew-backward in the even buckling modes. As a thorough investigation towards these aspects, the authors detected the snap-throughs in the odd modes and the snap-backs in the even modes of instability whenever  $\bar{K}>0$ . For example, in the case of  $\bar{K}=10\,000$  and  $\mu=0$ , the complete flow velocity-displacement curves are shown and encircled with dashed line boxes on the ranges of snap-bending appearance in Figure 7.

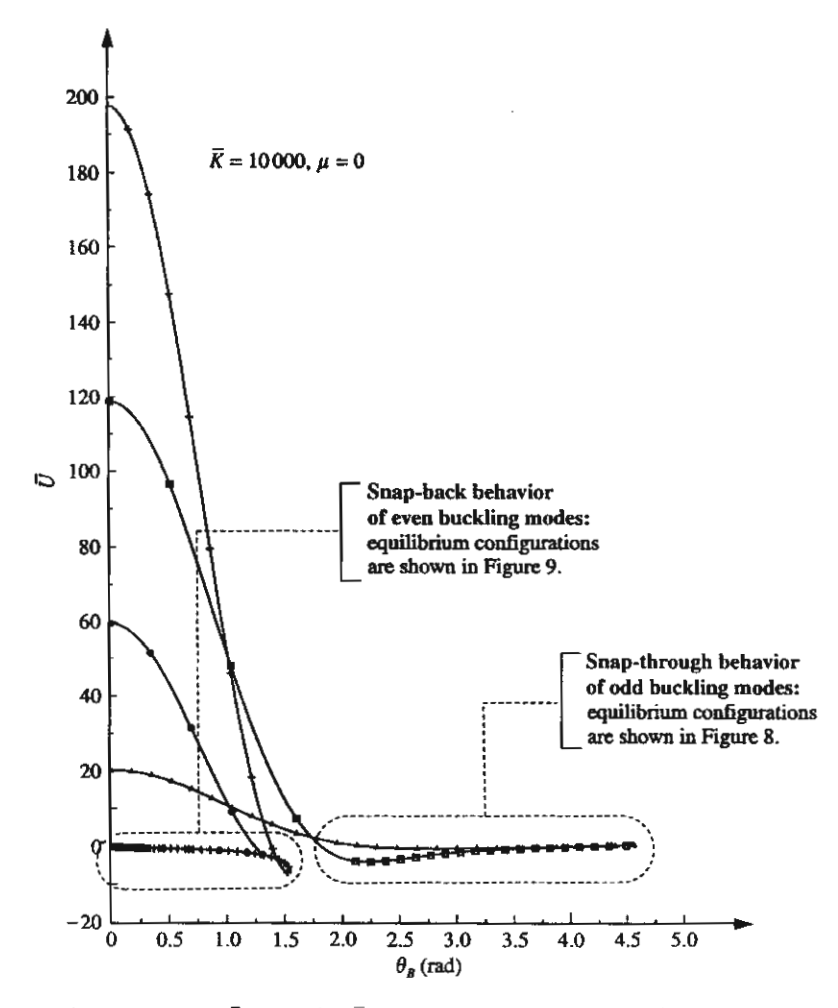


Figure 7. Relationship between  $\overline{U}$  and  $\theta_B$  for  $\overline{K} = 10\,000$  and  $\mu = 0$ .  $-\Delta$ -, First instability mode:  $-\Phi$ -, second mode;  $-\Phi$ -, fourth mode.

The snapping phenomena may be explained physically by comparing with the snapbending behaviour of a shallow arch. As the arch is subjected to transversal load until a critical state, the snapping will occur suddenly to change the curvature of the arch from convex to concave. Likewise, after buckling, the unsymmetrical large deflection of the VAL elastica pipe enhances rolling the elasticas to the complex closed loops, as shown in the gradual formation process in Figures 8 and 9. Such behaviour brings about switching of every curvature of the elasticas either from concave to convex or from convex to concave.

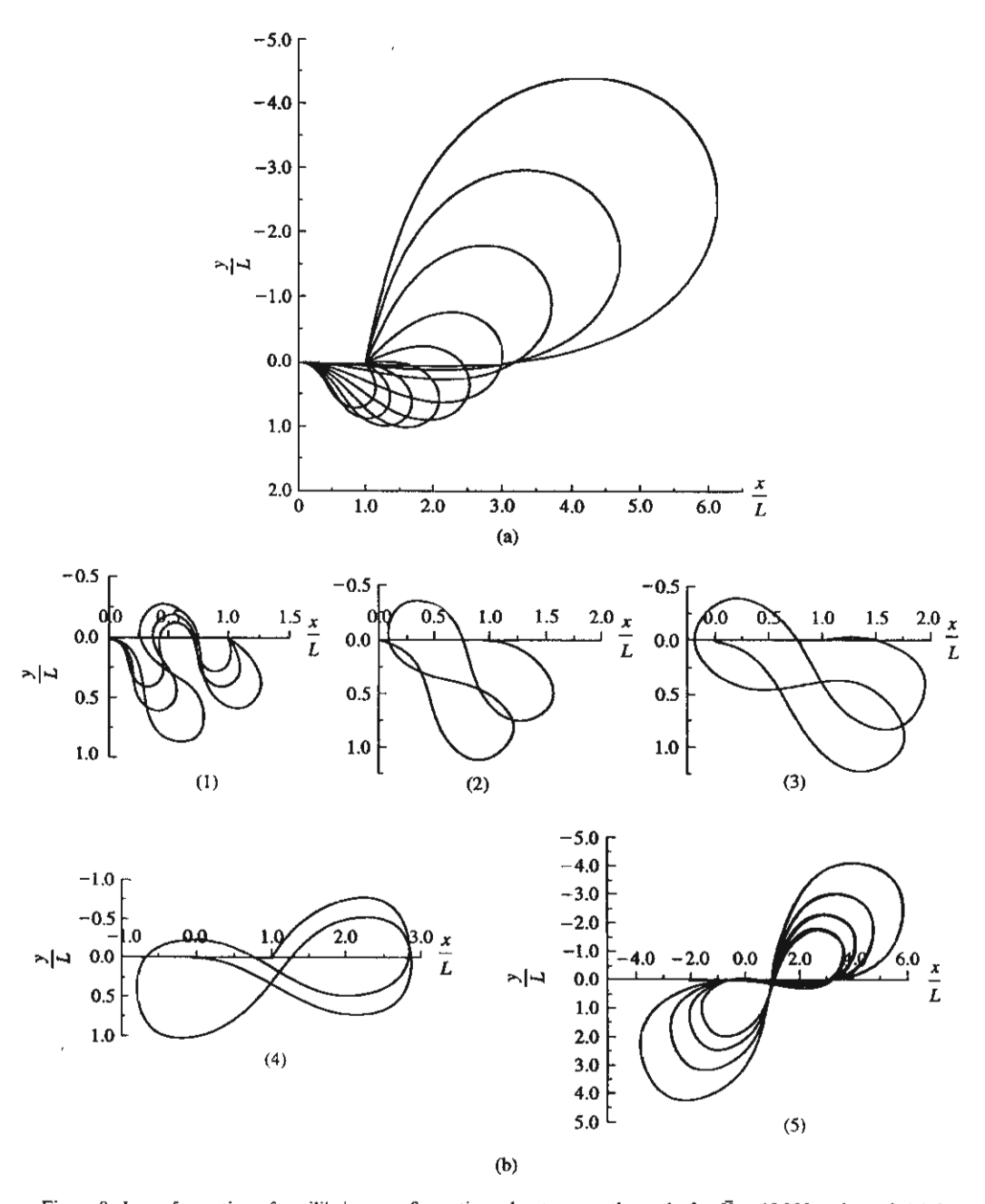


Figure 8. Loop formation of equilibrium configurations due to snap-throughs for  $\vec{K} = 10\,000$  and  $\mu = 0$ : (a) the first instability mode; (b) the third instability mode.

With the same incentive as in the case of the shallow arch, the changes of all curvatures of the elastica pipe induce snapping phenomena as well.

The skew-forward bending of the elasticas in odd buckling modes induces snapping by the counterclockwise rotation of curvatures as shown in Figures 8, which is called snapthrough. Conversely, the skew-backward bending of the elasticas in even buckling modes induces snapping by the clockwise rotation of curvatures as shown in Figures 9, which is

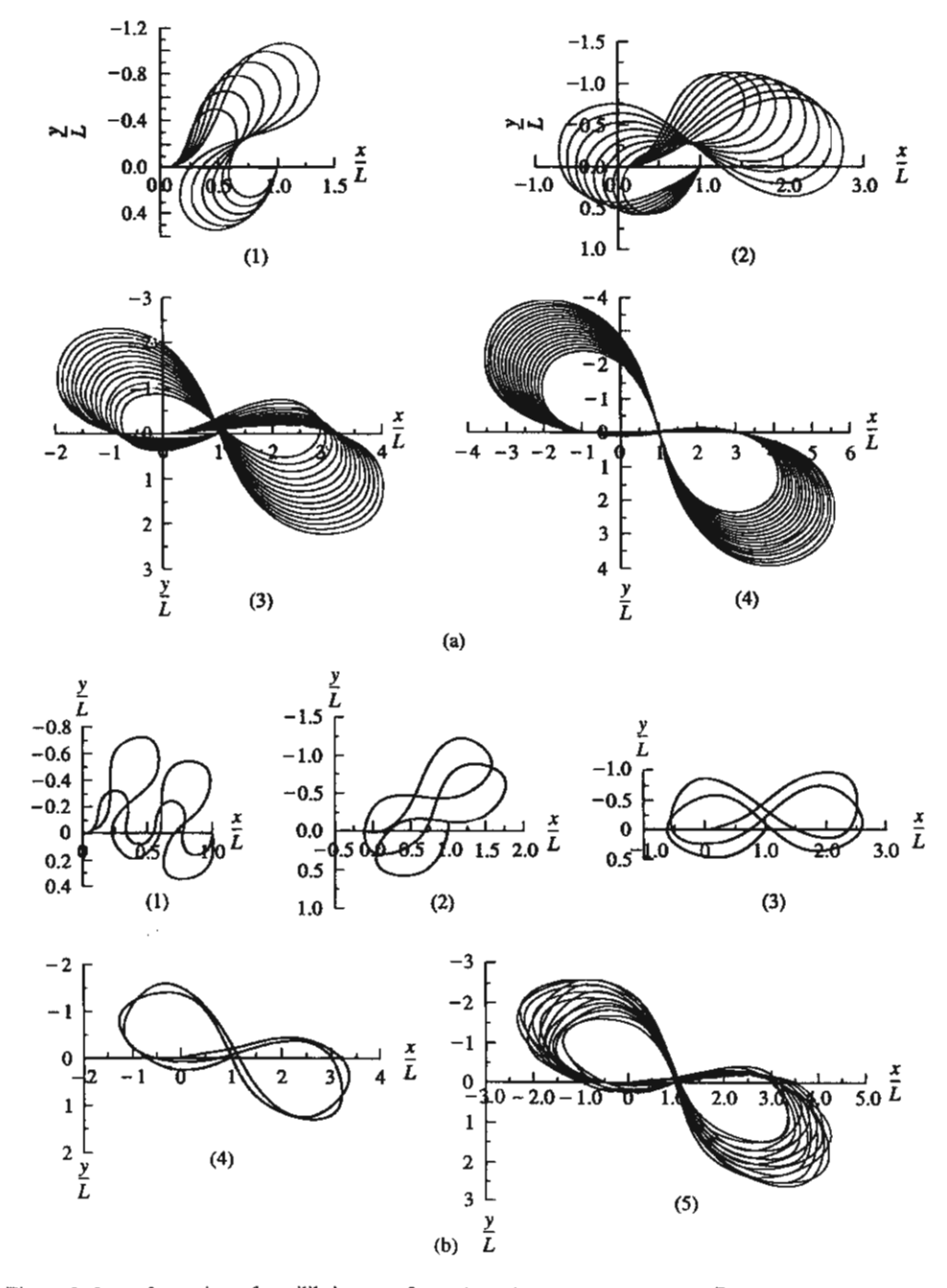


Figure 9. Loop formation of equilibrium configurations due to snap-backs for  $\bar{K} = 10\,000$  and  $\mu = 0$ : (a) the second instability mode;

called snap-back. The complex closed-loop configurations of the elasticas are found akin to the loop soliton formation of a very long flexible elastic structure such as elastic metal band, rubber band or ribbon under chaotic motion, as shown by the experiments done by El Naschie (1990).

#### 7. CONCLUDING REMARKS

The governing equations and post-buckling solutions for variable-arc-length elastica pipes transporting fluid with steady flow velocity are presented. The two approaches used to solve the problem, namely the elliptic integral method and shooting method, yield almost the same results. The branching limits obtained from the linear theory and the elastica theory are the same. After bifurcation, a simply supported elastica pipe with constant length buckles with stable bending, while the variable arc-length elastica pipe buckles with unstable bending.

Under flow-loading conditions, the support friction stabilizes the elasticas and increases the critical velocities. Under flow-unloading conditions, friction destabilizes the elasticas, but has no influence on branching states. The reduction of flow velocity may change the stability status of the elasticas due to a sudden change of friction direction. The effect of elastic rotational restraint is to stabilize the elasticas and to increase critical velocities. This effect leads to the unsymmetrical bending of at least two curvatures and eventually results in snap-bending behaviour.

#### **ACKNOWLEDGEMENTS**

The work reported in this paper is supported by the Thailand Research Fund (TRF) under Grant No. PHD/00132/2541. The authors would like to thank the anonymous reviewers for their valuable comments and suggestions.

### REFERENCES

- Beck, M. 1952 Die knicklast des einseitig eingespannten, tangential gedrückten stabes. Zeitschrift für angewandte Mathematik and Physik 3, 225-228.
- Blevins, R. D. 1990 Flow-Induced Vibration, 2nd edition, pp. 384-399. New York: Van Nostrand Reinhold.
- Byrd, P. F. & Friedman, M. D. 1971 Handbook of Elliptic Integrals for Engineers and Scientists, 2nd edition. Berlin: Springer-Verlag.
- CHEN, S. S. 1974 Flow-induced instability of an elastic tube. ASME paper No. 71-Vibr.-39.
- Chucheepsakul, S., Bunchareon, S. & Huang, T. 1995 Elastica of simple variable arc-length beam subjected to an end moment. ASCE Journal of Engineering Mechanics 121, 767-772.
- Chucheepsakul, S., Theppitak, G. & Wang, C. M. 1996 Large deflection of simple variable-arc-length beam subjected to a point load. Structural Engineering and Mechanics 4, 49-59.
- Chucheepsakul, S., Theppitak, G. & Wang, C. M. 1997 Exact solutions of variable-arc-length elasticas under moment gradient. Structural Engineering and Mechanics 5, 529-539.
- Chucheepsakul, S., Wang, C. M., He, X. Q. & Monprapussorn T. 1999 Double curvature bending of variable-arc-length elasticas. *Journal of Applied Mechanics* 66, 87-94.
- El Naschie, M. S. 1990 Stress, Stability and Chaos in Structural Engineering: an Energy Approach, pp. 645-678. London: McGraw-Hill.
- ELISHAKOFF, I. & LOTTATI, I. 1988 Divergence and flutter of nonconservative system with intermediate support. Computer Methods in Applied Mechanics and Engineering 66, 241-250.
- ESCOBAR, G. A. & TING, A. E. 1986 A finite element computational procedure for the transient and stability behaviors of fluid conveying structures. In PVP-Vol. 101, pp. 61-72. New York: ASME.
- Gregory, R. W. & Paidoussis, M. P. 1966 Unstable oscillation of tubular cantilevers conveying fluid. I. Theory. *Proceedings of the Royal Society (London)* A 293, 512-527.

HOLMES, P. J. 1978 Pipes supported at both ends cannot flutter. Journal of Applied Mechanics 45, 619-622.

Huang, T. & Chucheepsakul, S. 1985 Large displacement analysis of a marine riser. ASME Journal of Energy Resources Technology 107, 54-59.

JENDRZEJCZYK, J. A. & CHEN, S. S. 1983 Experiments on tubes conveying fluid. Argonne National Laboratory Report ANL-83-18, Argonne, Illinois, U.S.A.

Moe, G. & Chucheepsakul, S. 1988 The effect of internal flow on marine risers. Proceedings of seventh International Offshore Mechanics and Arctic Engineering Symposium, Vol. 1, pp. 375-382. New York: ASME.

Nelder, J. A. & Mead, R. 1965 A simplex method for function minimization. Computer Journal 7, 308-313.

PAIDOUSSIS, M. P. 1998 Fluid-Structure Interactions: Slender Structures and Axial Flow, Vol. 1. New York: Academic Press.

PAIDOUSSIS, M. P. & ISSID, N. T. 1974 Dynamic stability of pipes conveying fluid. Journal of Sound and Vibration 33, 267-294.

Press, W. H., Teukolsky, S. A., Vettering, W. T. & Flannery, B. P. 1992 Numerical Recipes in FORTRAN, 2nd edition, pp. 372-381, 708-716. Cambridge: Cambridge University Press.

RAO, S. S. 1996 Engineering Optimization: Theory and Practice, 3rd edition, pp. 283-286. New York: Wiley-Interscience.

THOMPSON, J. M. T. 1982 Instabilities and Catastrophes in Science and Engineering, pp. 165-178. New York: Wiley-Interscience.

THOMPSON, J. M. T. & LUNN, T. S. 1981 Static elastica formulations of a pipe conveying fluid. Journal of Sound and Vibration 77, 127-132.

Yoshizawa, M., Nao, H., Hasegawa, E. & Tsujioka, Y. 1985 Buckling and post-buckling behaviour of a flexible pipe conveying fluid. Bulletin of JSME 28, 1218-1225.

# APPENDIX A: EQUILIBRIUM EQUATIONS

### A.1. Forces Acting on a Fluid Element

From Figure 1(b), the forces acting on a fluid element are

(i) the centrifugal force = 
$$(\rho_i A_i ds)a_n = \rho_i A_i U^2 \frac{ds}{r} = \rho_i A_i U^2 d\theta$$
; (A.1)

(ii) the radial pressure force =  $(p_i + dp_i)A_i\sin(d\theta/2) + p_iA_i\sin(d\theta/2)$ , but  $\sin(d\theta/2) \approx d\theta/2$  and neglecting the higher-order term gives

the radial pressure force = 
$$\left(p_i d\theta + \frac{dp_i d\theta}{2}\right) A_i = p_i A_i d\theta;$$
 (A.2)

(iii) the normal reaction between the fluid and pipe  $F_n$  ds; from the Newton's second law  $(\sum F_n = \text{the centrifugal force})$ ,

$$F_n ds - p_i A_i d\theta = \rho_i A_i U^2 d\theta,$$
  

$$F_n ds = (\rho_i A_i U^2 + p_i A_i) d\theta;$$
(A.3)

(iv) the tangential reaction between the fluid and pipe  $F_t$  ds; because of U is constant  $(a_t = 0)$ , therefore  $\sum F_t = 0$ ,

$$F_t ds - (p_i + dp_i)A_i \cos\left(\frac{d\theta}{2}\right) + p_i A_i \cos\left(\frac{d\theta}{2}\right) - \tau ds = 0,$$

but

$$\cos\left(\frac{\mathrm{d}\theta}{2}\right) \approx 1, \qquad F_t \, \mathrm{d}s - A_t \, \mathrm{d}p_t - \tau \, \mathrm{d}s = 0,$$

$$F_t \, \mathrm{d}s = A \, \mathrm{d}p + \tau \, \mathrm{d}s. \tag{A.4}$$

# A.2. Forces Acting on a Pipe Element

From Figure 1(b), the forces acting on a pipe element are

(i) the normal reaction between the fluid and pipe  $F_n$  ds;

$$F_n ds - \left[ (Q + dQ) \cos\left(\frac{d\theta}{2}\right) - Q \cos\left(\frac{d\theta}{2}\right) \right] - \left[ (T + dT) \sin\left(\frac{d\theta}{2}\right) + T \sin\left(\frac{d\theta}{2}\right) \right] = 0,$$

$$F_n ds = dQ \cos\left(\frac{d\theta}{2}\right) + (2T + dT) \sin\left(\frac{d\theta}{2}\right),$$

$$F_n ds = dQ + T d\theta;$$
(A.5)

(ii) the tangential reaction between the fluid and the pipe  $F_t$  ds;

$$F_{t} ds + \left[ (Q + dQ) \sin\left(\frac{d\theta}{2}\right) + Q \sin\left(\frac{d\theta}{2}\right) \right] - \left[ (T + dT) \cos\left(\frac{d\theta}{2}\right) - T \cos\left(\frac{d\theta}{2}\right) \right] - \tau ds = 0,$$

$$F_{t} ds = dT \cos\left(\frac{d\theta}{2}\right) - (2Q + dQ) \sin\left(\frac{d\theta}{2}\right) + \tau ds,$$

$$F_{t} ds = dT - Q d\theta + \tau ds. \tag{A.6}$$

# A.3. Internal Force Equations

Combining equations (A.3) and (A.5) yields

$$dQ + (T - \rho_i A_i U^2 - p_i A_i) d\theta = 0. \tag{A.7}$$

Define now the combined tension (Moe & Chucheepsakul 1988)

$$N = T - p_i A_i - \rho_i A_i U^2. \tag{A.8}$$

Therefore, equation (A.7) becomes

$$\frac{\mathrm{d}Q}{\mathrm{d}\theta} + N = 0. \tag{A.9}$$

Likewise, by equality of equations (A.4) and (A.6), one obtains

$$dT - Q d\theta - A_i dp_i = d(T - p_i A_i - \rho_i A_i U^2) - Q d\theta = 0,$$

$$\frac{dN}{d\theta} - Q = 0.$$
(A.10)

Taking a moment summation about the centre of curvature of the pipe element (point O),

$$-(M+dM)+M-F_t ds\left(r+\frac{d_i}{2}\right)+(T+dT)r-Tr+\tau ds r=0.$$

Since  $r + d_i/2 \approx r$ ,  $F_t ds = dT - Q d\theta + \tau ds$  (equation (A.6)) and  $r d\theta = ds$ ,

$$-dM - (dT - Q d\theta)r + r dT = -dM + Q ds = 0,$$

$$\frac{dM}{ds} - Q = 0.$$
(A.11)

Equations (A.9)-(A.11) are the general equilibrium differential equations of internal forces for 2-D inextensible analysis of the elastica pipe, neglecting its own weight.

# Reprinted from

ISSN: 1225-4568

# **Structural Engineering**

# and Mechanics

An International Journal

Vol. 11, No. 2(2001) 185~197

# Effect of axial stretching on large amplitude free vibration of a suspended cable

Somchai Chucheepsakul†

Department of Civil Engineering, King Mongkut's University of Technology Thonburi, Bangkok 10140, Thailand

Sanit Wongsa‡

Department of Civil Technology Education, King Mongkut's University of Technology Thonburi, Bangkok 10140, Thailand

Techno - Press

# Structural Engineering & Mechanics, An International Journal

# Editors-in-chief

Professor Chang-Koon Choi

Department of Civil Engineering Korea Advanced Institute of Science & Technology Taejon 305-701, Korea

Tel: +82-42 869-3611, Fax: +82-42 869-3610

E-mail: cck@kaist.ac.kr

Professor William C. Schnobrich

Department of Civil Engineering University of Illinois at Urbana-Champaign Urbana, IL 61801, U.S.A.

Tel: (217) 333-0154, Fax: (217) 333-9464

E-mail: schnobri@uiuc.edu

### International Editorial Board

Professor D. L. Anderson University of British Columbia Vancouver, BC V6T 1W5, Canada

Professor A. H-S. Ang University of California at Irvine Irvine, CA 92717, U.S.A.

Professor E. R. de Arantes e Oliveira National Lab. of Civil Engineering 1799 Lisbon, Portugal

Professor K. J. Bathe Massachusetts Institute of Technology Cambridge, MA 02139-4307, U.S.A.

Professor P. Birkemoe University of Toronto Toronto, Ontario M5S 1A4, Canada

Professor R. de Borst Delft University of Technology NL-2600 GA Delft, The Netherlands

Professor L. Cedolin Politecnico di Milano Milano 20133, Italy

Professor H. C. Chan University of Hong Kong Hong Kong

Professor F. Y. Cheng University of Missouri Rolla Rolla, MO 65401, U.S.A.

Professor L. Esteva National University of Mexico Ciudad Universitaria, 04510 DF, Mexico

Professor Filip C. Filippou University of California Berkeley, CA 94720, U.S.A.

Professor Y. Fujino University of Tokyo Tokyo 113, Japan

Professor A. K. Gupta North Carolina State University Raleigh, NC 27695-7908, U.S.A. Professor N. M. Hawkins

University of Illinois at Urbana-Champaign Urbana, IL 61801, U.S.A.

Professor T. T. C. Hsu University of Houston Houston, TX 77204-4791, U.S.A.

Professor J. J. Jiang Tsinghua University Beijing 10084. China

Professor W. Kanok-Nukulchai Asian Institute of Technology Bangkok 10501, Thailand

Professor T. Kant Indian Institute of Technology-Powai Bombay 400076, India

Professor M. Kleiber Polish Academy of Science Swietokyska 21, 00-49 Warsaw. Poland

Professor M. B. Krackovsky Research Institute for Concrete and RC 1009428 Moscow, Russia

Professor B. M. Kwak Korea Adv. Inst. of Sci. & Tech. Taejon 305-701, Korea

Professor D. G. Lee Sung Kyun Gwan University Suwon 440-746, Korea

Professor S. L. Lee National University of Singapore Kent Ridge, Singapore 0511

Dr. S. C. Liu National Science Foundation Washington, D.C. 20550, U.S.A.

Professor Y. C. Loo Griffith University QLD 4217, Australia

Professor H. A. Mang Technical University of Vienna A-1040 Wien, Austria Professor C. Meyer

Columbia University New York, N.Y. 10027-6699, U.S.A.

Professor S. Otani University of Tokyo Tokyo 113, Japan

Professor E. Oñate

Universidad Politécnica de Cataluña 08034 Barcelona, Spain

Professor J. N. Reddy Texas A&M University College Station, Texas 77843-3123, U.S.A.

Professor R. Sampaio Pontificia Universidade Catolica Gavera, Rio de Janeiro 22.453, Brazil

Professor N. Shiraishi Maizuru Nat'l College of Techno. Kyoto 625, Japan

Professor S. Valliappan University of New South Wales Kensington, NSW 2033, Australia Professor E. Watanabe

Kyoto University Kyoto 606, Japan Professor Z. Xu

Tongji University Sanghai 200092, China

Professor Y. B. Yang National Taiwan University Taipei, Taiwan 10764, China

Professor J. Zarka Ecole Polytechnique F-91128, Palaiseau, France

Professor W. Zhong Dalian University of Technology Dalian 116023, China

# Subscription information

The Structural Engineering and Mechanics is published 12 times a year. The subscription price for 2001 including postage by surface mail is US\$427.0 for institutional subscription and US\$180.0 for personal subscription. For delivery by air mail, add US\$45.0. Subscription orders and/or enquiries should be sent to Techno-Press. P.O. Box 33 Yusong, Taejon 305-600, Korea. Fax: +82-42 869-8450, e-mail: technop@chollian.net

#### Advertisement information

For details, contact: Techno-Press, P.O. Box 33 Yusong, Tacjon 305-600, Korea. Fax: +82-42 869-8450

copyright © 2001 Techno-Press. Ltd. published monthly (12 issues a year) in 2001

# Effect of axial stretching on large amplitude free vibration of a suspended cable

# Somchai Chucheepsakul†

Department of Civil Engineering, King Mongkut's University of Technology Thonburi, Bangkok 10140, Thailand

# Sanit Wongsa‡

Department of Civil Technology Education, King Mongkut's University of Technology Thonburi, Bangkok 10140, Thailand

Abstract. This paper presents the effect of axial stretching on large amplitude free vibration of an extensible suspended cable supported at the same level. The model formulation developed in this study is based on the virtual work-energy functional of cables which involves strain energy due to axial stretching and work done by external forces. The difference in the Euler equations between equilibrium and motion states is considered. The resulting equations govern the horizontal and vertical motion of the cables, and are coupled and highly nonlinear. The solution for the nonlinear static equilibrium configuration is determined by the shooting method while the solution for the large amplitude free vibration is obtained by using the second-order central finite difference scheme with time integration. Numerical examples are given to demonstrate the vibration behaviour of extensible suspended cables.

Key words: cables; axial stretching; free vibration; large amplitude vibration; nonlinear vibration.

# Introduction

Cable structures have been used extensively in many civil and ocean engineering applications. Practical considerations of cable behaviour may be limited to the case of small sag or small amplitude of vibration such as finding the natural frequencies and mode shapes. However, in some engineering applications such as cables in offshore engineering operations, large amplitudes of vibration are encountered. The large amplitude refers to the amplitude of vibration measured from the cable's equilibrium position which may be the same as or larger than the order of magnitude of the sag. The subject of large amplitude vibration of cables has been investigated by many researchers over the past several years. Early papers on the subject include those by Keller (1959) and Anand (1969). Rega *et al.* (1984) used a simple model to investigate non-linear free vibration of a suspended cable. Forced vibration of elastic suspended cables was investigated by Al-Noury and Ali (1985), and Benedettini and Rega (1987). Ali (1986) investigated the nonlinear response of sagged cables with movable supports. Cai and Chen (1994) investigated the nonlinear dynamic

<sup>†</sup> Professor

<sup>‡</sup> Lecturer

response of an inclined elastic cable under parametric and external resonances. Leissa and Saad (1994) studied the large amplitude free vibration of elastic strings in which the effects of longitudinal and transverse displacements are coupled.

In almost all of the aforementioned papers, the static equilibrium configuration of the cables is assumed to be straight line or having a small sag and the effect of axial stretching is not considered seriously. The present paper aims to develop a rigorous formulation of the cable problem that includes the effect of axial stretching on the large amplitude free vibration of a suspended cable with a large sag. Equations of motion in the horizontal and vertical directions are obtained by considering the difference in the virtual work-energy functional of the cable between two states, namely the equilibrium state and the motion state. A finite difference scheme with time integration is used to solve these equations. The effect of axial stretching on the large amplitude free vibration behaviour of cables is investigated by considering some numerical examples for the case of specified total unstrained arc-length of cable and the case of specified applied tension.

# 2. Development of equations of motion

Fig. 1 shows a typical cable problem considered in this study. The cable with a span length L is supported at the same level, with one end of the cable fixed and the other end free to slide over the support where the specified tension is applied to maintain the cable in equilibrium position. Three distinct states of the cable configuration are to be noted. The first state is the unstretched state, the second the equilibrium state, and the third the displaced state. In the unstretched state, the cable suspends by its own weight and its configuration takes on the catenary form. Due to axial stretching, the cable moves to the equilibrium position which is considered as an initial configuration for the cable. Owing to disturbances in loading, the cable is in the vibration or displaced state. The coordinate parameters in the three states are represented as follows:

i) Unstretched state: X, Y, S ii) Equilibrium state:  $x_0$ ,  $y_0$ ,  $s_0$  iii) Displaced state: x, y, s.

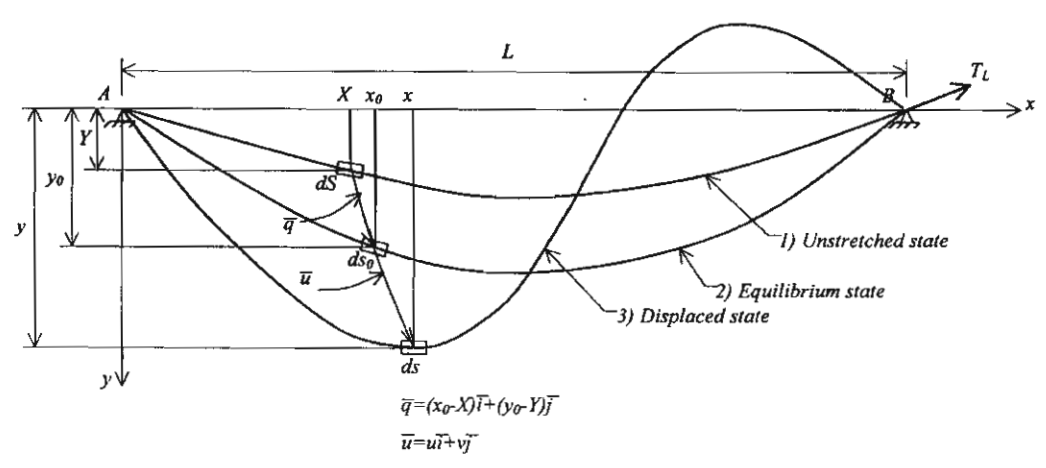


Fig. 1 Cable configurations at various states

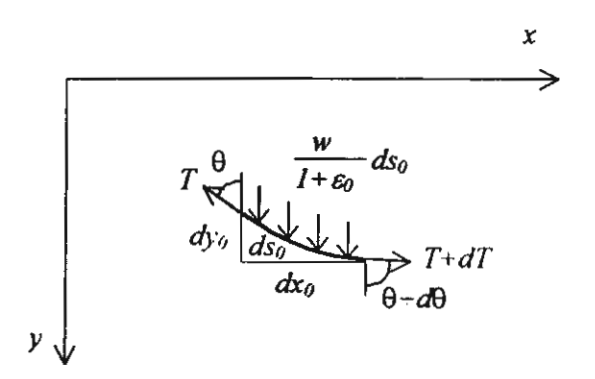


Fig. 2 Free body of infinitesimal cable segment

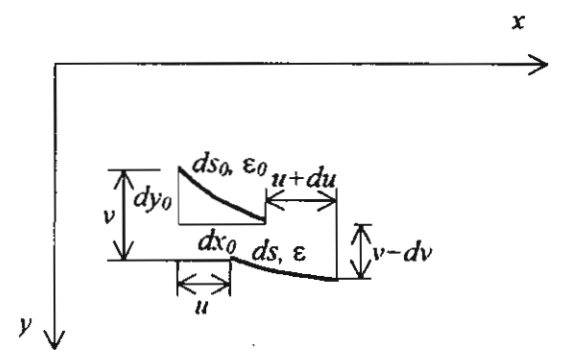


Fig. 3 Equilibrium and displaced positions of cable segment

Fig. 2 shows the components of the forces acting on an infinitesimal segment in the equilibrium position. Fig. 3 shows the same segment at the displaced position in which u and v are the displacement components in the x and y directions, respectively, and their magnitudes can be large. Consider an element having an unstretched length dS. At the equilibrium position, its length  $ds_0$  is given by

$$ds_0 = \sqrt{1 + y_0'^2} dx_0 \tag{1}$$

in which a prime denotes differentiation with respect to  $x_0$ .

The strain  $\varepsilon_0$  at the equilibrium position is

$$\varepsilon_0 = \frac{ds_0 - dS}{dS}$$
 and  $ds_0 = (1 + \varepsilon_0)dS$  (2a, b)

Using Eqs. (1) and (2b), one gets

$$dS = \frac{\sqrt{1 + y_0'^2}}{(1 + \varepsilon_0)} dx_0 \tag{3}$$

The arc length ds in the displaced position (see Fig. 3) is given by

$$ds = \sqrt{(1 + u')^2 + (y_0' + v')^2} dx_0 \tag{4}$$

The strain at the displaced position is

$$\varepsilon = \frac{ds - dS}{dS} \tag{5}$$

In view of Eqs. (3) and (4), Eq. (5) can be written as

$$\varepsilon = \frac{1 + \varepsilon_0}{\sqrt{1 + y_0'^2}} \sqrt{(1 + u')^2 + (y_0' + v')^2} - 1 \tag{6}$$

The variation of strain  $\varepsilon$  furnishes

$$\delta \varepsilon = \frac{1 + \varepsilon_0}{\sqrt{1 + y_0'^2}} \frac{(1 + u')\delta u' + (y_0' + v')\delta v'}{\sqrt{(1 + u')^2 + (y_0' + v')^2}}$$
(7)

# 3. Virtual strain energy due to axial stretching

The virtual strain energy of the cable at the displaced position is given by

$$\delta U = \int E A \varepsilon \delta \varepsilon dS \tag{8}$$

where E is the elastic modulus of the cable, and A the undeformed cross-sectional area of the cable. Using Eqs. (3), (6), and (7), Eq. (8) becomes

$$\delta U = \int \left\{ \frac{EA(1+\varepsilon_0)}{\sqrt{1+y_0'^2}} (1+u') - \frac{EA(1+u')}{\sqrt{(1+u')^2 + (y_0' + v_0')^2}} \right] \delta u' + \left[ \frac{EA(1+\varepsilon_0)}{\sqrt{1+y_0'^2}} (y_0' + v') - \frac{EA(y_0' + v')}{\sqrt{(1+u')^2 + (y_0' + v')^2}} \right] \delta v' \right\} dx_0$$
 (9)

# 4. Virtual work due to self-weight and inertia force

For free vibration, the virtual work due to the self-weight and the inertia force are given by

$$\delta W = \int \left\{ \left[ -\frac{w\sqrt{1 + y_0'^2}}{g(1 + \varepsilon_0)} \ddot{u} \right] \delta u + \left[ \frac{w\sqrt{1 + y_0'^2}}{(1 + \varepsilon_0)} - \frac{w\sqrt{1 + y_0'^2}}{g(1 + \varepsilon_0)} \ddot{v} \right] \delta v \right\} dx_0$$
 (10)

in which w is the weight of the cable per unit unstretched length, and the dot denotes differentiation with respect to time.

# 5. Euler equations

The virtual work of the cable is written as

$$\delta \pi = \delta U - \delta W \tag{11}$$

Using Eqs. (9) and (10), Eq. (11) becomes

$$\delta\pi = \int \left\{ \left[ \frac{EA\sqrt{1+\varepsilon_0}}{\sqrt{1+{y'}_0^2}} (1+u') - \frac{EA(1+u')}{\sqrt{(1+u')^2 + (y_0' + v')^2}} \right] \delta u' + \frac{w\sqrt{1+{y_0'}^2}}{g(1+\varepsilon_0)} \ddot{u} \delta u \right\} dx_0 + \int \left\{ \left[ \frac{EA(1+\varepsilon_0)}{\sqrt{1+{y'}_0^2}} (y_0' + v') - \frac{EA(y_0' + v')}{\sqrt{(1+u')^2 + (y_0' + v')^2}} \right] \delta v' + \left[ -\frac{w\sqrt{1+{y_0'}^2}}{(1+\varepsilon_0)} + \frac{w\sqrt{1+{y_0'}^2}}{g(1+\varepsilon_0)} \ddot{v} \right] \delta v \right\} dx_0$$
(12)

For static equilibrium,  $\delta \pi = 0$  and  $u = v = u' = v' = \bar{u} = \bar{v} = 0$ . Thus, the integration of Eq. (12) by parts yields two Euler equations with respect to the virtual displacements  $\delta u$  and  $\delta v$ .

$$\left[\frac{EA\varepsilon_0}{\sqrt{1+y'_0^2}}\right]' = 0 , \qquad (13)$$

$$\left[\frac{EA\varepsilon_{0}y_{0}'}{\sqrt{1+y_{0}'^{2}}}\right]' + \frac{w\sqrt{1+y_{0}'^{2}}}{(1+\varepsilon_{0})} = 0$$
 (14)

These two equations can also be obtained by considering the equilibrium of forces on the cable segment in the x and y directions, respectively.

For the cable in motion,  $u \neq v \neq u' \neq v' \neq \bar{u} \neq \bar{v} \neq 0$ , and the integration by parts gives two Euler equations associated with the virtual cable motion  $\delta u$  and  $\delta v$ .

$$\left[\frac{EA(1+\varepsilon_0)}{\sqrt{1+y'_0^2}}(1+u')\right]' - \left[\frac{EA(1+u')}{\sqrt{(1+u'^2)+(y_0'+v'^2)}}\right]' - \frac{w\sqrt{1+y'_0^2}}{g(1+\varepsilon_0)}\ddot{u} = 0$$
 (15)

$$\left[\frac{EA(1+\varepsilon_0)}{\sqrt{1+y'_0^2}}(y_0'+v')\right]' - \left[\frac{EA(y_0'+v')}{\sqrt{(1+u')^2+(y_0'+v')^2}}\right]' + \frac{w\sqrt{1+y'_0^2}}{(1+\varepsilon_0)} - \frac{w\sqrt{1+y'_0^2}}{g(1+\varepsilon_0)}\ddot{v} = 0 \quad (16)$$

By subtracting Eq. (13) from Eq. (15), and Eq. (14) from Eq. (16), one obtains the equations of motion in the u and v directions, respectively, as

$$\frac{EA\left[(1+\varepsilon_{0})(1+y'_{0}^{2})u''-(1+u'+\varepsilon_{0}u'')y_{0}'y_{0}''\right]}{(1+y'_{0}^{2})^{3/2}} \frac{EA(y_{0}'+v')\left[(y_{0}'+v')u''-(1+u')v''\right]}{\left[(1+u')^{2}+(y_{0}'+v')^{2}\right]^{3/2}} \\
= \frac{w\sqrt{1+y'_{0}^{2}}}{g(1+\varepsilon_{0})}\ddot{u} \qquad (17)$$

$$\frac{EA\left[(1+\varepsilon_{0})(1+y'_{0}^{2})v''+(1-y_{0}'u'-\varepsilon_{0}y_{0}'u')y_{0}''\right]}{(1+y'_{0}^{2})^{3/2}} \frac{EA(1+u')\left[(1+u')(y_{0}''+v'')-(y_{0}'+v')u''\right]}{\left[(1+u')^{2}+(y_{0}'+v')^{2}\right]^{3/2}} \\
= \frac{w\sqrt{1+y'_{0}^{2}}}{g(1+\varepsilon_{0})}\ddot{v} \qquad (18)$$

Eqs. (17) and (18) are the equations of motion for large amplitude free vibration of extensible suspended cables. If the terms  $y_0$ ,  $y_0'$ , and  $y_0''$  are set to zero (implying the equilibrium configuration of the cable is a straight line), then Eqs. (17) and (18) are reduced to the same form given by Leissa and Saad (1994).

#### 6. Method of solution

The shooting method is used to solve the nonlinear equilibrium Eqs. (13) and (14). The results of the static solution are the strain at the equilibrium state  $\varepsilon_o$  at any position and the equilibrium position  $y_0$  at any position  $x_0$  along the span length. For the case of specified end tension, it is more convenient to use an expression for the tension at any position in the calculations. This expression can be obtained by considering the equilibrium equation in the tangential direction which is

$$dT = \frac{w}{1 + \varepsilon_0} dy_0 \tag{19}$$

Integrating from  $x_0$  to L and replacing  $T(x_0)$  by  $EA\varepsilon_0$ , one obtains

$$T(x_0) = EA \varepsilon_0 = T_L - \frac{w}{1 + \varepsilon_0} y(x_0)$$
 (20)

Eqs. (13) and (20) are used for solving the case of specified end tension.

For free vibration analysis, Eqs. (17) and (18) are solved using the finite difference approach. The derivatives of u and v appearing in the equations of motion are replaced by the following finite difference approximations:

$$u' = \frac{u'_{i+1} - u'_{i-1}}{2h}, v' = \frac{v'_{i+1} - v'_{i-1}}{2h}$$
 (21a, b)

$$u'' = \frac{u'_{i+1} - 2u'_i + u'_{i-1}}{h^2}, v'' = \frac{v'_{i+1} - 2v'_i + v'_{i-1}}{h^2}$$
 (22a, b)

$$\bar{u} = \frac{u_i^{t+1} - 2u_i^t + u_i^{t-1}}{k^2}, \ \bar{v} = \frac{v_i^{t+1} - 2v_i^t + v_i^{t-1}}{k^2}$$
 (23a, b)

in which h is the grid size and k is the time step.

# 7. Numerical examples and results

Numerical examples involving two practical cases are given to demonstrate the vibration behaviour of u and v. The first case deals with a cable with a fixed value of unstrained total arclength and the elastic modulus is varied. The input data for this case are as follows: S=800 m, L=854 m, w=9.478 kN/m, A=0.1159 m<sup>2</sup>, and the values of the elastic modulus E are  $1.294\times10^6$  kN/m<sup>2</sup>,  $1.794\times10^6$  kN/m<sup>2</sup>, and  $2.294\times10^6$  kN/m<sup>2</sup>. The second case deals with a cable with a fixed value of applied tension and the elastic modulus is varied. The input parameters, other than A, E and E0 are E1 and E2 given in the first case, are taken as: E1 are E2 to E3 kN/m<sup>2</sup>, E3 kN/m<sup>2</sup>, and E4 kN/m<sup>2</sup>, and E5 kN/m<sup>2</sup>.

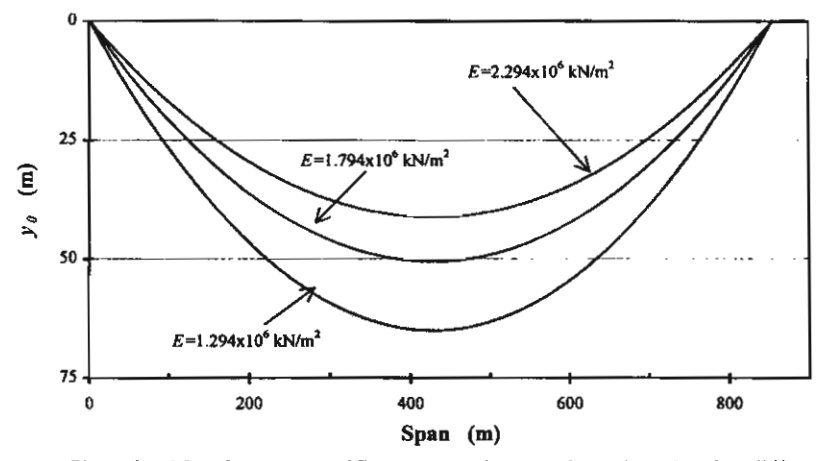


Fig. 4 Equilibrium profiles of cables for the specified unstretched total arc-length with different values of elastic modulus

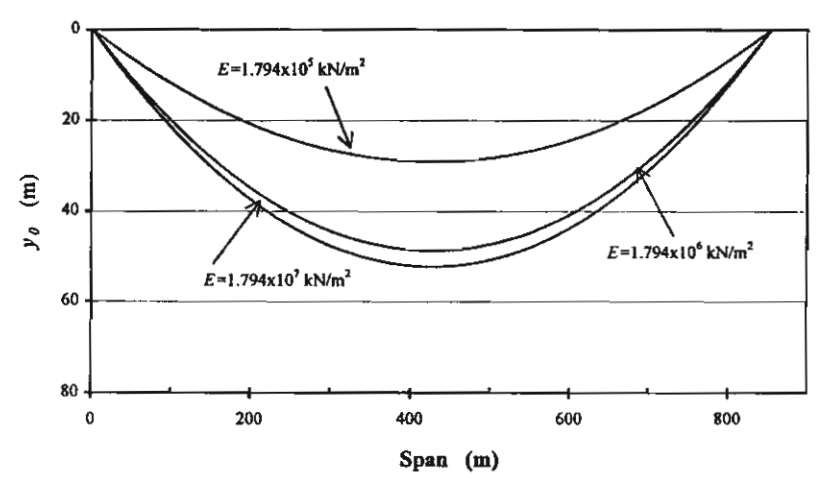


Fig. 5 Equilibrium profiles of cables for the specified end tension with different values of elastic modulus

Fig. 4 shows the static equilibrium positions of cables with a fixed value of unstrained total arc-length but different values of the elastic modulus. It is seen that the sag of the cable decreases when the elastic modulus is increased. The result is expected as the cable experiences a greater sag as EA decreases while  $T_L$  remains the same. On the other hand, if EA remains unchanged but  $T_L$  increases, the sag decreases. Fig. 5 shows the equilibrium positions for cables with a fixed value of the applied tension. Unlike the first case, it is seen that the sag increases with an increase in the elastic modulus. Figs. 6 to 11 show the motion of u and v plotted at the quarter and midspan length for the first case. The computed values of the maximum strain at the equilibrium position are also given. It can be seen from these figures that the motion of v is more periodic and has a much larger amplitude than the motion of u. The amplitude of v at midspan is slightly higher than the one at quarter span while the amplitude of u at quarter span has a much larger amplitude than the one at the midspan where it shows no oscillation. Fig. 12 shows the combined amplitude of vibration of u and v for the different values of E. The results show that

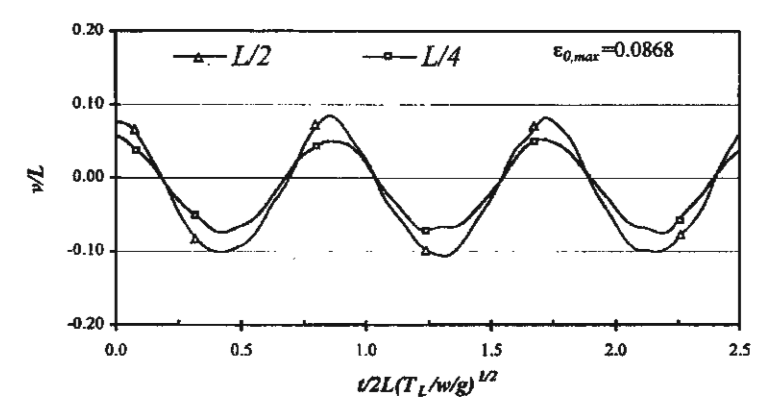


Fig. 6 Vibration amplitude of  $\nu$  at mid span and quarter span for S=800 m and E=1.294×10<sup>6</sup> kN/m<sup>2</sup>

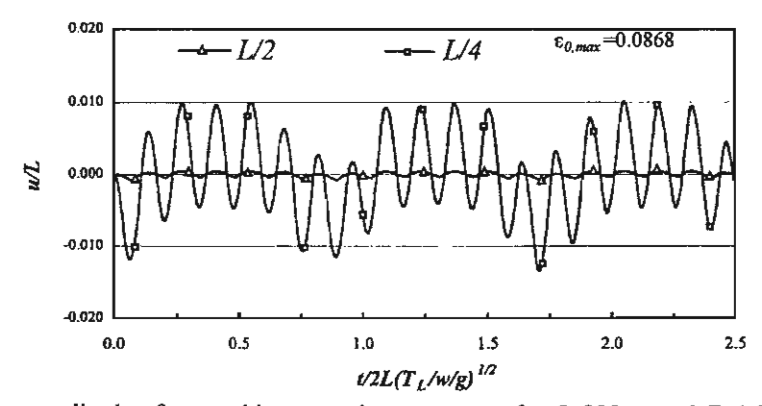


Fig. 7 Vibration amplitude of u at mid span and quarter span for S=800 m and  $E=1.294\times10^6$  kN/m<sup>2</sup>

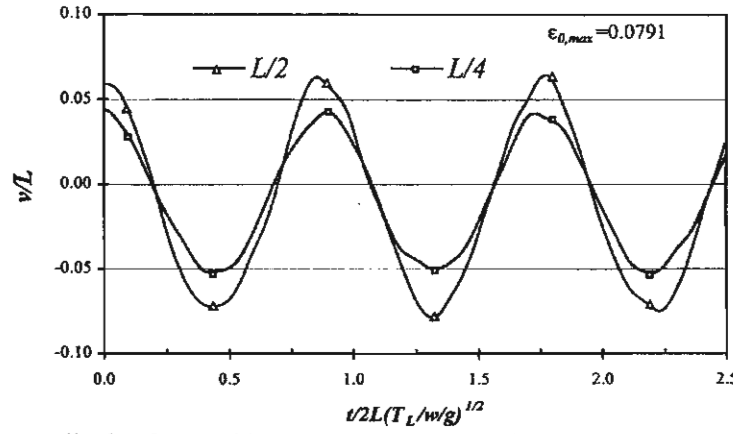


Fig. 8 Vibration amplitude of v at mid span and quarter span for S=800 m and  $E=1.794\times10^6$  kN/m<sup>2</sup>

the amplitude of vibration decreases as the elastic modulus increases. These results have the same trends as those found in the static case.

Figs. 13 to 18 demonstrate the effect of stretching on the amplitude of vibration for cables with a specified value of applied tension. The motion of u and v show the same vibration behaviour as in

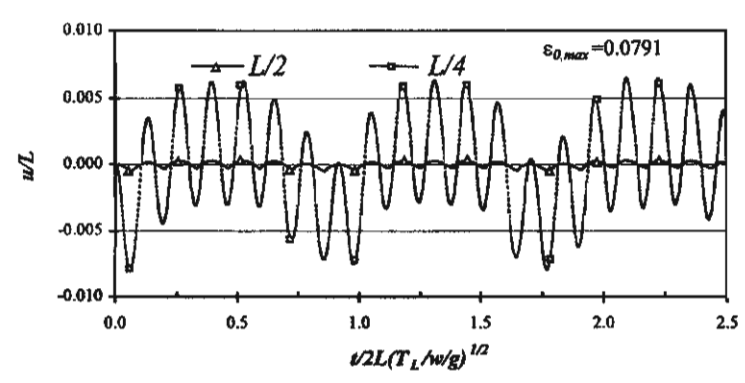


Fig. 9 Vibration amplitude of u at mid span and quarter span for S=800 m and E=1.794×10<sup>6</sup> kN/m<sup>2</sup>

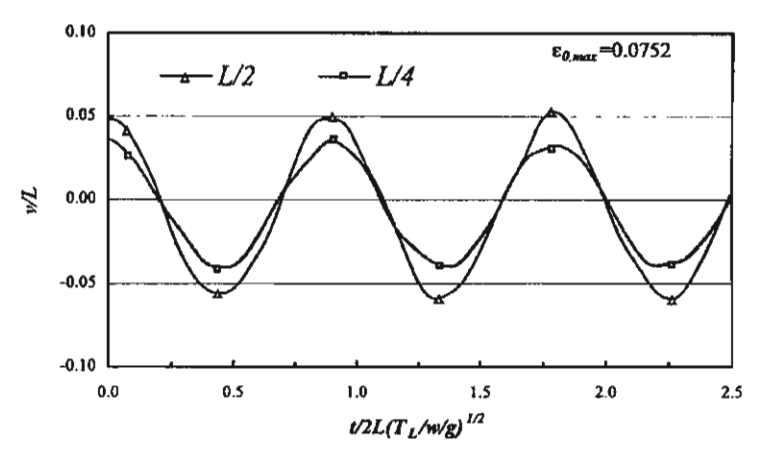


Fig. 10 Vibration amplitude of v at mid span and quarter span for S=800 m and  $E=2.294\times10^6$  kN/m<sup>2</sup>

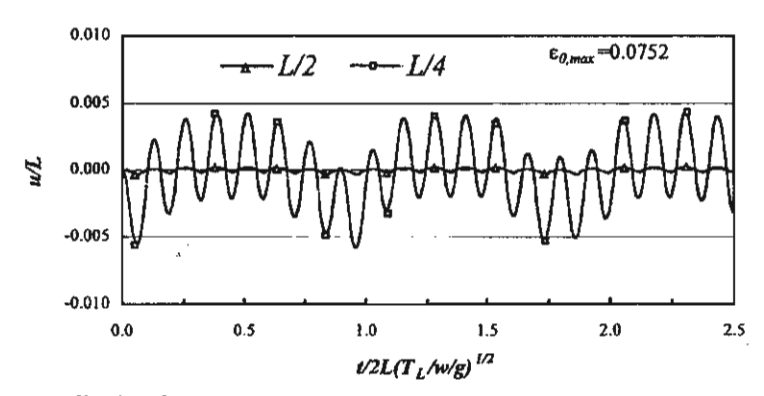


Fig. 11 Vibration amplitude of u at mid span and quarter span for S=800 m and  $E=2.294\times10^6$  kN/m<sup>2</sup>

the first case. However, it is found that the amplitudes of u and v increase as the elastic modulus increases. The maximum combined amplitude of vibration of u and v versus elastic modulus is plotted in Fig. 19. It is noted that as the elastic modulus is increased beyond the values used earlier, the resulting cable motion is unstable and the amplitude of vibration cannot be determined.

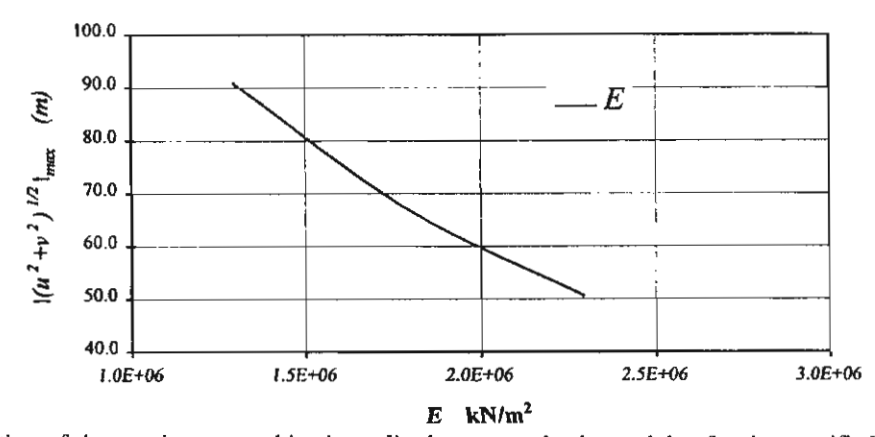


Fig. 12 Variation of the maximum combined amplitude versus elastic modulus for the specified total unstrained arc-length of 800 m

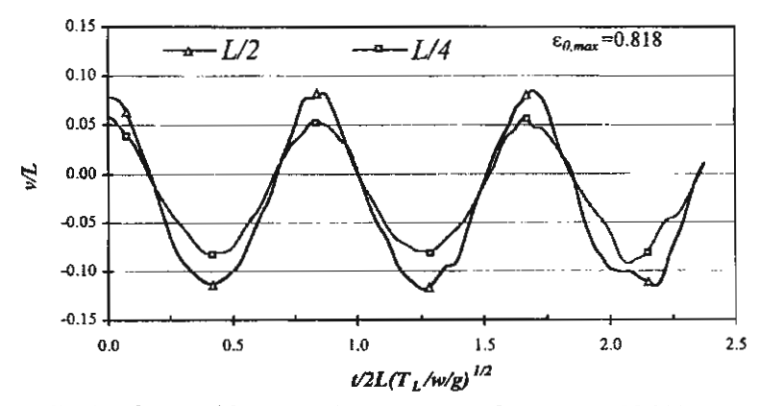


Fig. 13 Vibration amplitude of v at mid span and quarter span for  $T_L$ =17,000 kN and E=1.794×10<sup>5</sup> kN/m<sup>2</sup>

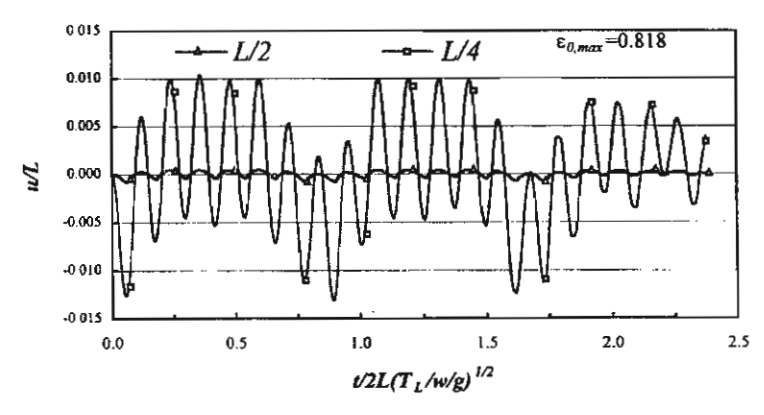


Fig. 14 Vibration amplitude of u at mid span and quarter span for  $T_L$ =17,000 kN and E=1.794×10<sup>5</sup> kN/m<sup>2</sup>

# 8. Conclusions

The equations of motion of in-plane large amplitude free vibration of a suspended cable have

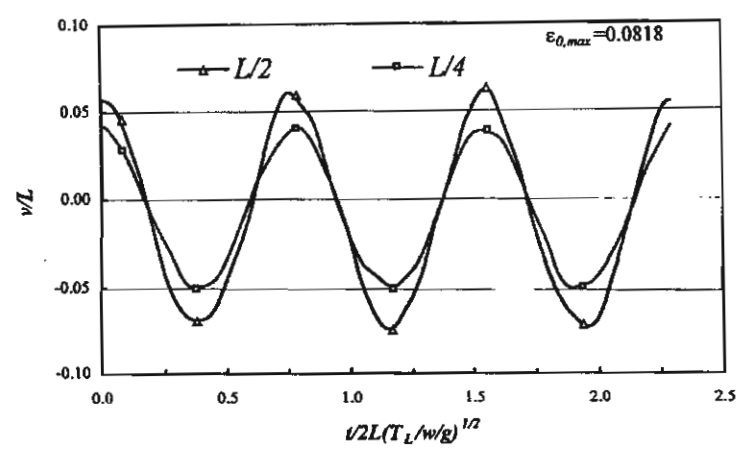


Fig. 15 Vibration amplitude of v at mid span and quarter span for  $T_L$ =17,000 kN and E=1.794×10<sup>6</sup> kN/m<sup>2</sup>

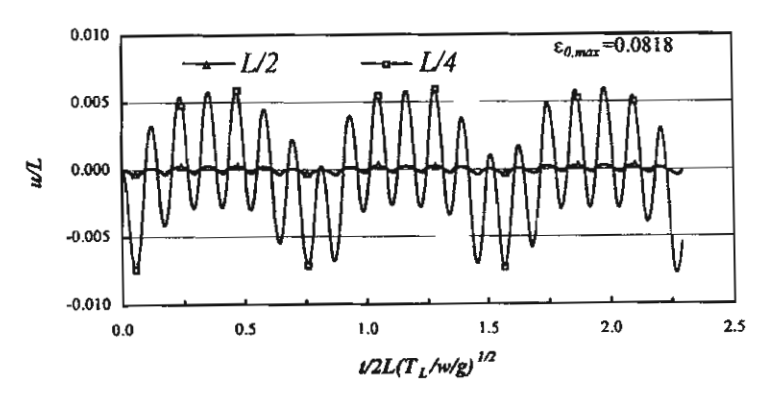


Fig. 16 Vibration amplitude of u at mid span and quarter span for  $T_L$ =17,000 kN and E=1.794×10<sup>6</sup> kN/m<sup>2</sup>

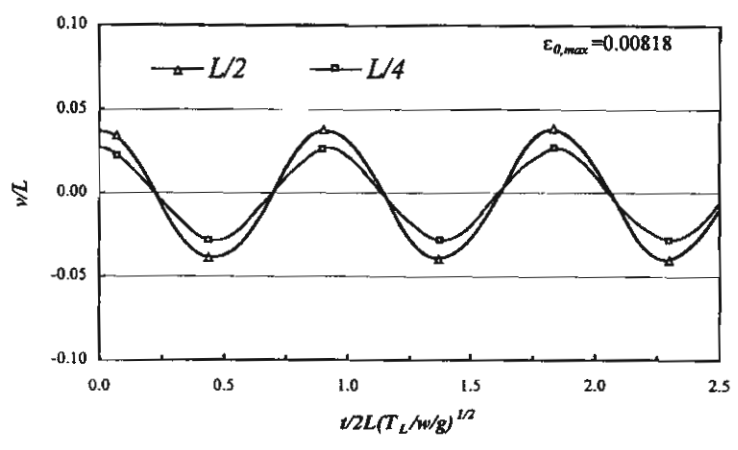


Fig. 17 Vibration amplitude of  $\nu$  at mid span and quarter span for  $T_L$ =17,000 kN and E=1.794×10<sup>7</sup> kN/m<sup>2</sup>

been developed. The formulation is applicable to cables with large sag and large axial deformation as well as a variable tension force. The method can also be conveniently applied to cables with a specified end tension. Numerical examples for the cases of fixed unstrained total arc-length and

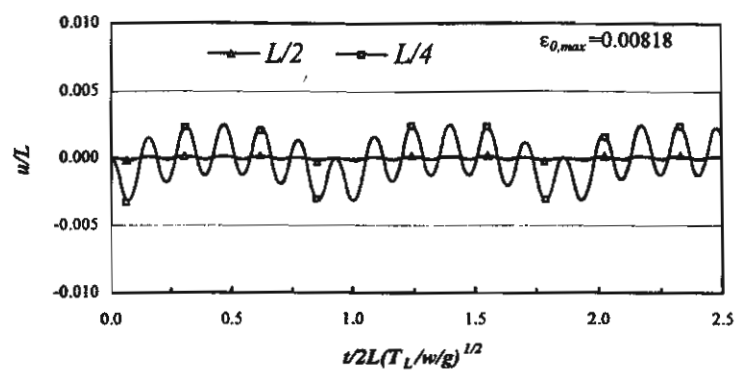


Fig. 18 Vibration amplitude of u at mid span and quarter span for  $T_L$ =17,000 kN and E=1.794×10<sup>7</sup> kN/m<sup>2</sup>

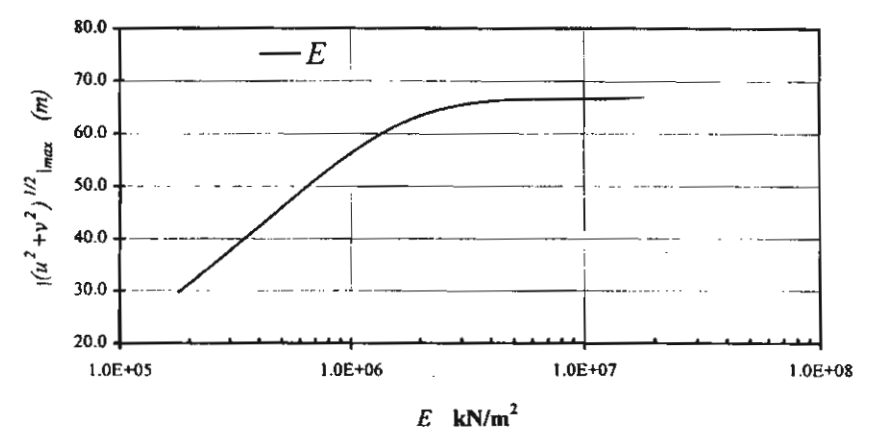


Fig. 19 Variation of the maximum combined amplitude versus elastic modulus for the specified end tension 17,000 kN

specified applied tension have been demonstrated. It can be concluded that for cables with a given total arc-length, the amplitude of vibration decreases when the elastic modulus is increased. However, for cables with a specified value of the applied tension, the results show that the amplitude of vibration increases with increasing values of elastic modulus.

# **Acknowledgements**

This work was sponsored by the Thailand Research Fund (TRF) under Grant No. RTA/03/2543.

## References

Ali, S.A. (1986), "Dynamic response of sagged cables", Computers and Structures, 23(1), 51-57.

Al-Noury, S.I. and Ali, S.A. (1985). "Large-amplitude vibrations of parabolic cables", *Journal of Sound and Vibration*, 101(4), 451-462.

Anand, G.V. (1969), "Large amplitude damped free vibration of a stretched string", Journal of the Acoustical

Society of America, 45, 1089-1096.

Benedettini, F. and Rega G. (1987), "Non-linear dynamic of an elastic cable under planar excitation", *International Journal of Non-linear Mechanics*, 22(6), 497-509.

Cai, Y. and Chen S.S. (1994), "Dynamics of elastic cable under parametric and external resonances", ASCE Journal of Engineering Mechanics, 120(8), 1786-1802.

Keller, J.B. (1959), "Large amplitude motion of a string," American Journal of Physics, 27, 584-586.

Leissa, A.W. and Saad, A.M. (1994), "Large amplitude vibrations of strings", ASME Journal of Applied Mechanics, 61(2), 296-301.

Rega, G., Vestroni, F. and Benedettini, F. (1984), "Parametric analysis of large amplitude free vibrations of a suspended cable", *International Journal of Solids and Structures*, **20**, 95-105.

ISSN: 1225-4568

# STRUCTURAL ENGINEERING AND MECHANICS

## An International Journal

#### Aims and Scope

The STRUCTURAL ENGINEERING AND MECHANICS, An International Journal, aims at:   providing a major
publication channel for structural engineering, [ wider distribution at more affordable subscription rates; [ faster reviewing
and publication for manuscripts submitted; and [] a broad scope for wider participation.
The main subject of the Journal is structural engineering concerned with aspects of mechanics. Areas covered by the Journal
include: Structural Mechanics; Design of Civil, Building and Mechanical Structures; Structural Optimization and
Controls; Structural Safety and Reliability; New Structural Materials and Applications; Effects of Wind, Earthquake
and Wave Loadings on Structures; [ Fluid-Structure and Soil-Structure Interactions; [ AI Application and Expert Systems
in Structural Engineering. Submission of papers from practising engineers is particularly encouraged.

#### Instruction to Authors

#### 1. Submission of the paper

Manuscripts should be submitted in triplicate either to:

Professor Chang-Koon Choi Department of Civil Engineering

Korea Advanced Institute of Science & Technology Taeion 305-701, Korea

Tel: +82-42 869-3611, Fax: +82-42 869-3610

E-mail: cck@kaist.ac.kr

# or to: Professor William C. Schnobrich

Department of Civil Engineering University of Illinois at Urbana-Champaign Urbana, IL 61801. U.S.A.

Tel: (217)333-0154, FAX: (217)333-9464

E-mail: schnobri@uiuc.edu

Authors will be requested to submit manuscripts on diskettes after the acceptance of paper (partial manuscript on diskettes will also be acceptable).

## 2. Preparation of the manuscript

General: The manuscripts should be in English and typed with double line spacing on single side of A4 paper. The first page of an article should contain; (1) a short title (reflecting the content of the paper), (2) all the name(s) and address(es) of author(s), (3) name and address of the author to whom correspondence and proofs should be sent, and (4) an abstract of 100-200 words. The paper should be concluded by proper conclusions which reflect the findings in the paper. The length of paper should not exceed 16 journal pages (approx. 9000-words equivalent). There will be no page charges if the length of paper is within the limit. A separate list of key words should be provided at the end of the manuscript.

Tables and figures: Tables and figures should be consecutively numbered and headed with short titles. They should be referred to in the text as Fig. 1, Table 2, etc. Originally drawn figures and glossy prints of photographs should be provided in a form suitable for photographic reproduction and reduction in the journal. A separate list of captions for illustrations should be provided at the end of the manuscript.

Units and mathematical expressions: It is desirable that units of measurements and abbreviations should follow the Systeme Internationalé (SI). The numbers identifying the displayed mathematical expression should be placed in parentheses and referred to in the text as Eq. (1), Eq. (2) ...

References: References to published literature should be referred in the text by the last name(s) of author(s) and the year of publication of the reference (e.g., Choi and Schnobrich 1975) and listed in the alphabetical order of the last name of the first author in an appendix at the end of the paper. Journal titles should be abbreviated in the style of the World List of Scientific Periodicals. References should be cited in the following style.

Journal:

Proceedings:

Choi, C.K., and Kim, S.H. (1989), "Coupled use of reduced integration and nonconforming modes in

improving quadratic plate element", Int. J. Num. Meth. Eng., 28(4), 1909-1928.

Salvadori, M.G., and Baron, M.L. (1961), Numerical Methods in Engineering, Prentice-Hall, Englewood Cliffs, N.J.

Choi, C.K., and Kwak, H.G. (1989), "Optimum RC member design with discrete sections", *Proceedings of '89 ASCE Structures Congress*, San Francisco, May.

#### 3. Proofs

Proofs will be sent to the corresponding author to correct any typesetting errors. Alterations to the original manuscript at this stage will not be accepted. Proofs should be returned within 48 hours of receipt by Express Mail.

#### 4. Copyright

Submission of an article to "Structural Engineering and Mechanics" implies that it presents the original and unpublished work, and not under consideration for publication elsewhere. On acceptance of a manuscirpt submitted, the copyright thereof is transferred to the publisher by the Transfer of Copyright Agreement.

#### 5. Reprints

A total of 50 reprints of each paper will be supplied free of charge to the corresponding author.

International Journal of Structural Stability and Dynamics Vol. 1, No. 3 (2001) 333–365 © World Scientific Publishing Company

## NONLINEAR BUCKLING OF MARINE ELASTICA PIPES TRANSPORTING FLUID

S. CHUCHEEPSAKUL\* and T. MONPRAPUSSORN†

Department of Civil Engineering,
King Mongkut's University of Technology Thonburi,
Bangkok, 10140, Thailand
\*E-mail: somchai.chu@kmutt.ac.th
†E-mail: mtinakorn@hotmail.com

Received 26 April 2001 Accepted Revised Version 7 August 2001

This paper addresses the nonlinear buckling and post-buckling behavior of an extensible marine elastica pipe conveying fluid. The mathematical model employed in the nonlinear buckling analysis is developed based on the extensible elastica theory and the large strain formulation, so that the high extensibility of the pipe due to large axial strains is tackled thoroughly. The boundary value problem of the model is solved by the shooting method, and the numerical elastica solutions are obtained. For stability examination, the method of adjacent nonlinear equilibrium is exploited. It is revealed that the fundamental mode of nonlinear buckling of the pipe is reached when the pipe experiences either the critical top tension or the critical weight. Postbuckling behavior of the pipe is recognized to be unstable. The investigation is extended to studying various parameters that impinge on the limit states of the pipe. These parameters are the dimensionless quantities that relate to density of pipe material, densities of external and internal fluids, applied top tension, Poisson's ratio, slenderness ratio, vessel offset, seawater depth, current-drag coefficients, current velocity, and internal flow velocity.

Keywords: Marine risers, elastica pipes, nonlinear buckling, large strains, internal flow, Poisson's effect, heavy imperfection columns.

#### 1. Introduction

The marine elastica pipe stated herein refers to a pipe experiencing large displacements under offshore environment. Application of the marine elastica pipe can be found extensively in deep-ocean mining industry such as the deployment of marine risers, flexible pipes, and hoses. Even though nonlinear behavior is absolutely pertinent to the marine elastica pipes, hitherto buckling analyses for most of them have not been carried out based on the elastica theory. Examples of the related work are found in Huang and Dareing, <sup>1,2</sup> Bernitsas, <sup>3</sup> Bernitsas and Kokkinis, <sup>4-6</sup> and Vaz and Patel, <sup>7</sup> who studied the buckling problems of drilled string, marine risers, and submerged slender tubular columns based on the linear small displacement

theory. Although, the linear theory can yield the bifurcation criteria, it gives no information on the nonlinear buckling behavior and post-buckling stability of the structures, which are indispensable for nonlinear system operation control. Furthermore, the linear theory cannot capture the effect of imperfection or initial curvature of the marine elastica pipes induced by large deformation behavior.

In this paper, the extensible elastica formulation involving large strains and large displacements based on the authors' work<sup>8</sup> is applied for the analyses of nonlinear buckling and post-buckling of marine pipes. For generating the mathematical model of the marine elastica pipe transporting fluid, the following three steps are obligatory. First, the real systems of the pipe and transported fluid are transformed into the apparent systems for ease of taking the hydrostatic pressure effects into consideration. Second, the equilibrium equations of the apparent systems of the pipe and transported fluid are obtained from the Newtonian derivation in the normal-tangential coordinate. Finally, the combination between the equilibrium equations of the pipe and of transported fluid yields the governing differential equations describing the nonlinear behavior of the pipe.

For the sake of generality, these equations are rendered dimensionless through the use of a set of designated dimensionless parameters. The resultant dimensionless model considers the dimensionless expressions of the following parameters that affect the structural buckling behavior of the pipe: (1) density of pipe material, (2) applied top tension, (3) density of external fluid, (4) density of internal fluid, (5) Poisson's ratio, (6) slenderness ratio, (7) vessel offset, (8) seawater depth, (9) normal current-drag coefficient, (10) tangential current-drag coefficient, (11) external flow velocity of ocean current, and (12) internal flow velocity of transported fluid. By performing parametric studies, the influences of these parameters on the limit states of the pipe are elucidated, and their significances are assessed for use in practical stability design consideration.

Since the equilibrium method is dealt with both in the formulation and in the solution of the elastica problem, it is thus suitable to apply the method of adjacent nonlinear equilibrium for nonlinear buckling analysis. This technique employs a nonlinear static analysis with gradually increasing either loads or displacements to seek the equilibrium paths. The stability condition at any point on the equilibrium paths is evaluated based upon the definitions of stability. It should be noted that buckling behaviors of a pipe-like shell such as wrinkling collapse of thin shell, and cross-section ovalization of thick shell are not treated in the present study; only the global Euler buckling problem is considered.

## 2. Large Strain Formulation

As mentioned earlier, the large strain formulation based on the previous authors' work<sup>8</sup> requests the three steps for creating the mathematical model of the marine elastica pipe transporting fluid as follows:

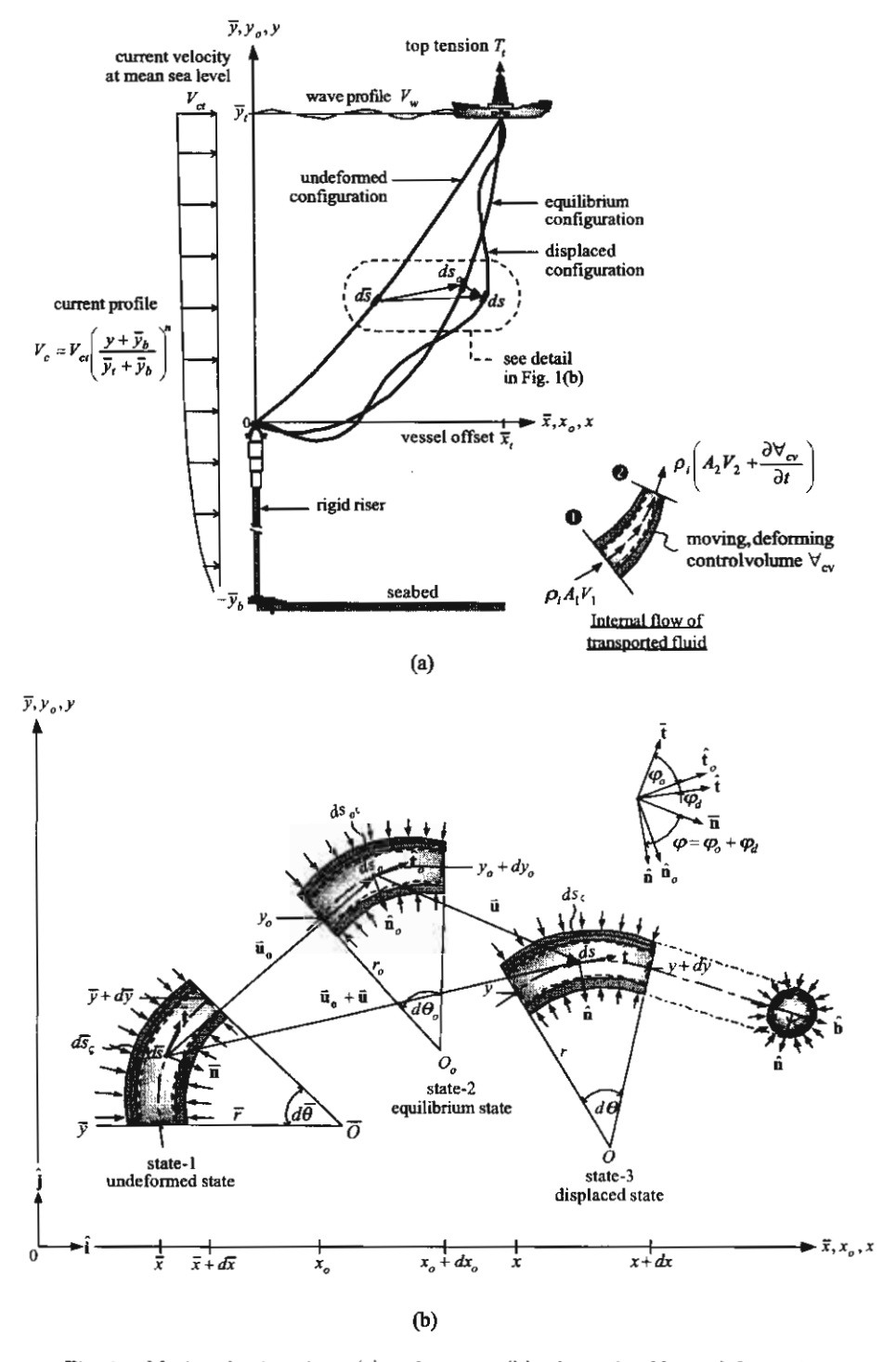


Fig. 1. Marine elastica pipes: (a) real system, (b) schematic of large deformation.

#### 2.1. Step 1: Converting the real systems into the apparent systems

The real system of the marine elastica pipe transporting fluid is portrayed in Fig. 1. The undeformed configuration of the pipe is changed into the equilibrium one when the pipe is subjected to the static loads such as gravitation, and steady flows of wind, current and transported fluid. The equilibrium configuration is transfigured into the displaced one when the pipe is subjected to the dynamic loads such as ocean wave, and unsteady flows of wind, current and transported fluid. The present study concerns the former change.

Figure 2 depict transforming the real system of the pipe into the apparent system. The total forces acting on the real system of the pipe column (the pipe plus transported fluid) as shown in Fig. 2(a) are distributed to summation of the forces acting on the pipe and transported fluid as shown in Figs. 2(g) to 2(n) by using the superposition technique, the Archimedes' law, and the elasticity theory (see Ref. (8) for more details). The apparent system of the elastica pipe as shown in Fig. 2(o) is achieved by summing up Figs. 2(g), 2(i), 2(k) and 2(m), whereas the apparent system of transported fluid as shown in Fig. 2(p) is attained by summing up Figs. 2(h), 2(j), 2(l) and 2(n). Finally, the overall apparent system as shown in Fig. 2(q) is accomplished by merging Figs. 2(o) and 2(p) together.

# 2.2. Step 2: Executing the Newtonian derivation on the apparent systems

Consider the apparent system of Fig. 2(p), the transported fluid element with the length  $s'd\alpha$  is subjected to (i) the internal pressure  $p_i$ ; (ii) its own weight  $m_i g$ ; (iii) the inertial forces  $m_i a_{Fn}$  and  $m_i a_{Ft}$ ; and (iv) the normal reaction  $f_m$  and the wall-shear friction  $\tau$ . Note that  $\alpha$  is the parameter defining an elastic curve, and ()' =  $\partial$ ()/ $\partial \alpha$ . Applying the Newton's second law in the normal and tangential directions yields

$$\sum F_n = 0: f_{rn}s' = (p_i A_i)\theta' - (m_i g \sin \theta - m_i a_{Fn})s'$$
(1)

$$\sum F_t = 0 : \tau s' = (p_i A_i)' + (m_i g \cos \theta + m_i a_{Ft}) s'$$
 (2)

in which  $(s, \theta)$  are the coordinates of arc length and rotation. Similarly, for the apparent system of the pipe element of Fig. 2(o) one obtains

$$\sum F_n = 0: f_m s' = -Q' + (T + T_{tri} + p_e A_e)\theta' + [f_{Hn} + (m_P - m_e)g \sin \theta - m_P a_{Pn}]s'$$
(3)

$$\sum F_t = \tau s' = Q\theta' + (T + T_{tri} + p_e A_e)'$$

$$+\left[f_{Ht}-(m_P-m_e)g\,\cos\theta-m_Pa_{Pt}\right]s'\tag{4}$$

$$\sum M_O = 0: M' = Qs' \tag{5}$$

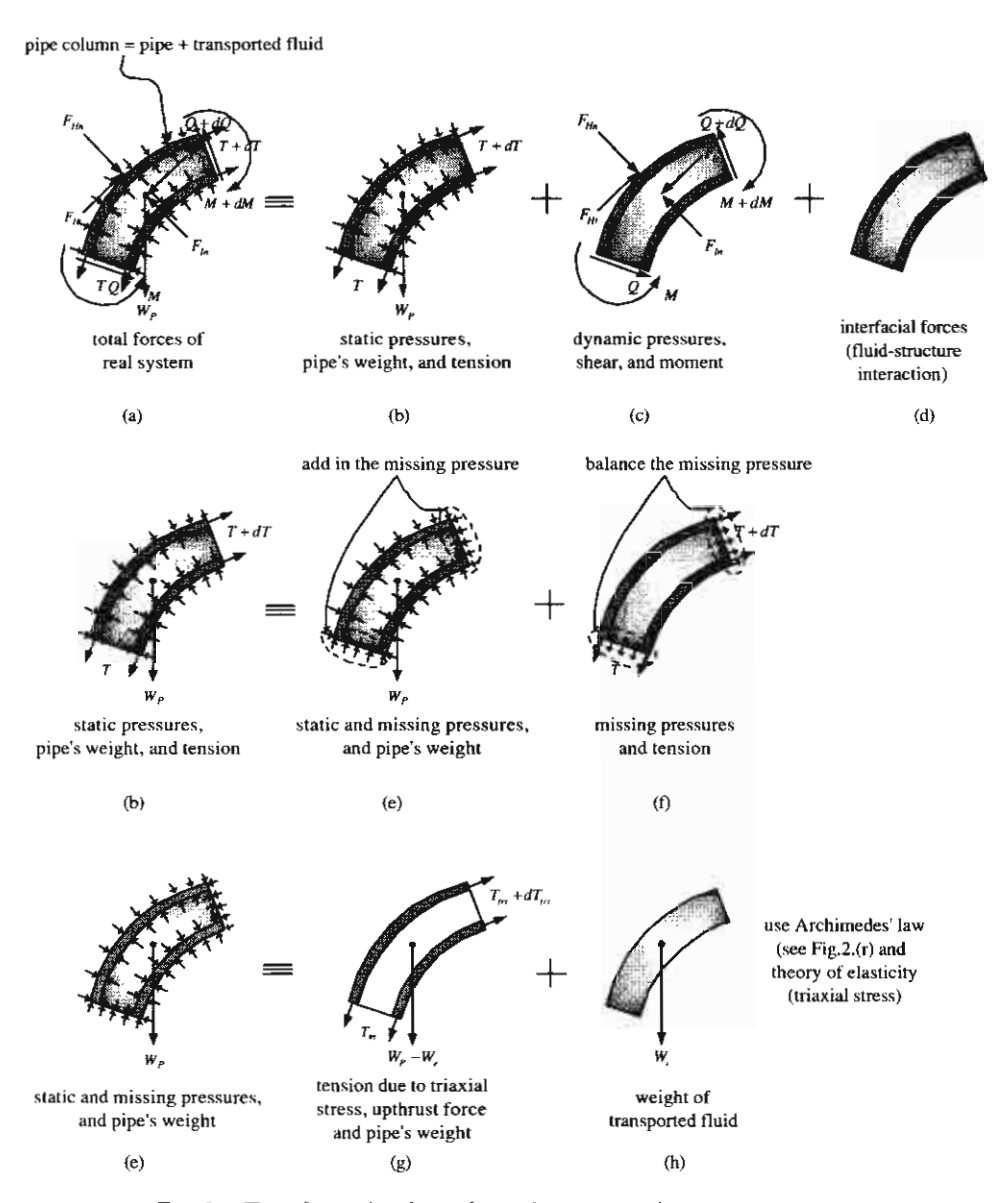
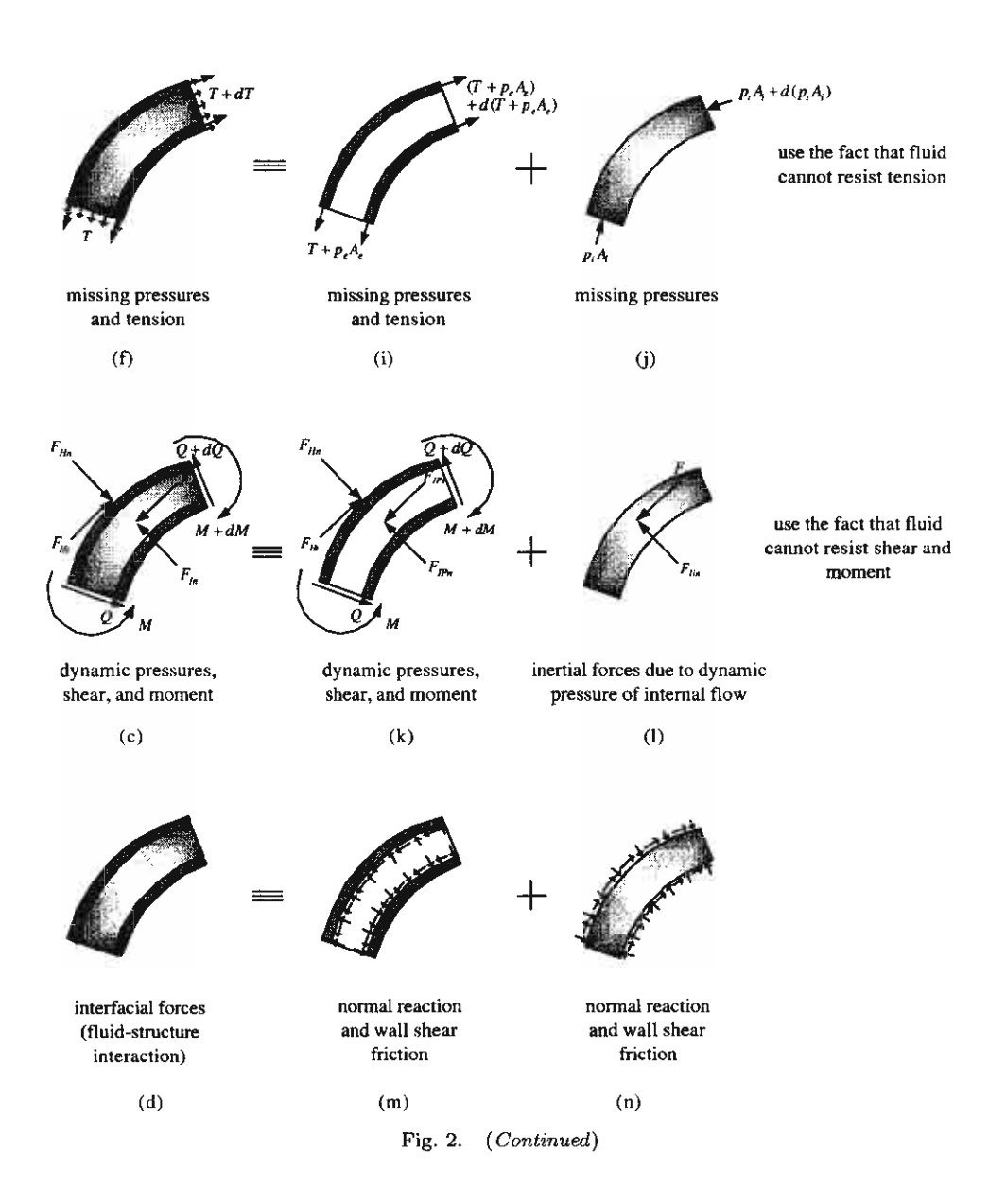
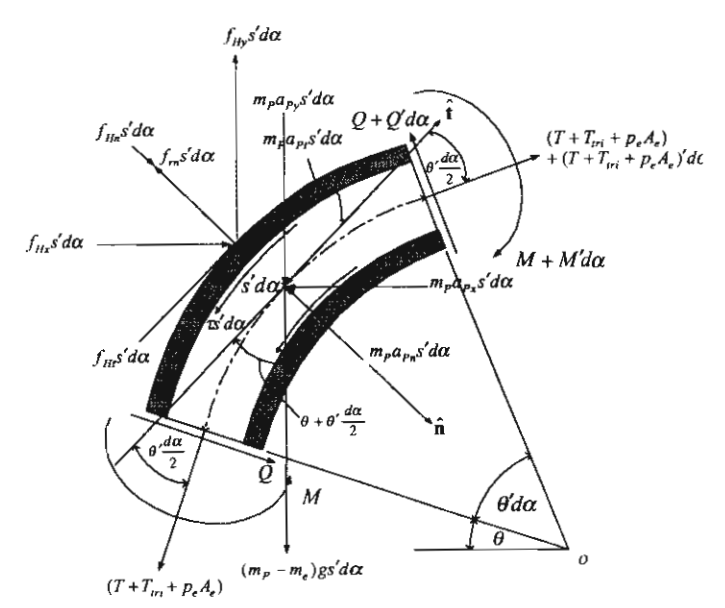


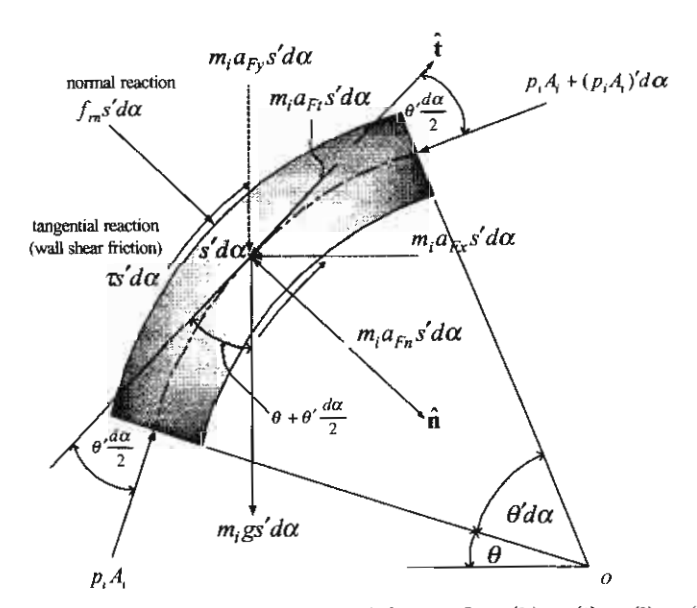
Fig. 2. Transformation from the real system to the apparent system.



-



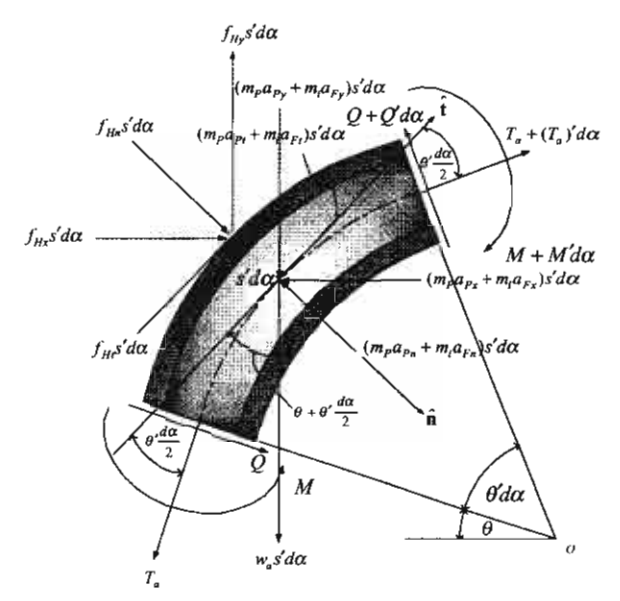
The apparent system of the pipe = figs. (g) + (i) + (k) + (m). (o)



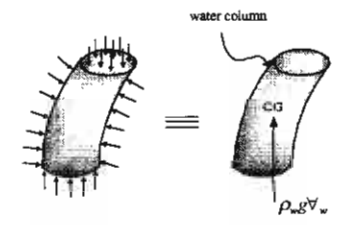
The apparent system of the transported fluid = figs. (h) + (j) + (l) + (n).

(p)

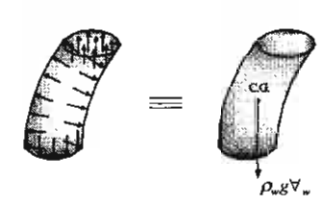
Fig. 2. (Continued)



The overall apparent system = figs. (o) + (p). (q)



external pressure induces the upthrust (buoy) force



Archimedes' Principles

(r)

Fig. 2. (Continued)

where T, Q and M are the true-wall tension, shear and bending moment, respectively,  $p_e$ , the external pressure,  $f_{Hn}$  and  $f_{Ht}$  the hydrodynamic forces of ocean current and wave,  $m_p g$  the pipe's weight,  $-m_e g$  the buoyancy force, and  $m_p a_{Pn}$ and  $m_p a_{Pt}$  the inertial forces of the pipe. From the theory of elasticity, the tension induced by triaxial pressures  $T_{\rm tri}$  can be expressed as

$$T_{\text{tri}} = (2v - 1)(p_e A_e - p_i A_i) \tag{6}$$

in which v is the Poisson's ratio, and  $A_e$  and  $A_i$  are the cross-sectional areas of the pipe column, and internal fluid, respectively.

## 2.3. Step 3: Integrating the individual systems of the pipe and transported fluid into the overall apparent sustem

Substituting Eq. (1) into (3), and (2) into (4) together with some manipulation, one obtains

$$Q' = T_a \theta' + s' [f_{Hn} + w_a \sin \theta - (m_p a_{Pn} + m_i a_{Fn})]$$
 (7)

$$T_a' = -Q\theta' - s'[f_{Ht} - w_a \cos\theta - (m_p a_{Pt} + m_i a_{Ft})]$$
 (8)

where

$$T_a = T + 2v(p_e A_e - p_i A_i), w_a = (m_p - m_e + m_i)g,$$
 (9a, b)

are referred to as the apparent tension and the apparent weight, respectively. Note that  $T_a = T_e + T_{tri}$ , where  $T_e = T + p_e A_e - p_i A_i$  is referred to as the effective tension. It is seen that  $T_a = T_e$  if, and only if v = 0.5. This signifies that the effective tension concept<sup>9</sup> is a subset of the apparent tension concept.<sup>8</sup> Equations (5), (7), and (8) are the governing differential equations describing the nonlinear behavior of the overall apparent system of the pipe. The reader should not be amazed why the transported fluid-frictional effects play no role in the overall system equations. Indeed, they do, but not explicitly seen. Physically, the reaction  $f_m$  and the friction  $\tau$  perform the tasks on transmitting the static and dynamic pressures of transported fluid (the right-hand side terms in Eqs. (1) and (2)) into the pipe wall (through the left-hand side terms in Eqs. (3) and (4)).

In this study, the deformed arc-length is used as the independent variable  $(\alpha = s)$ , the updated Lagrangian formulation is adopted, and the conservation of pipe's volume<sup>10</sup> is presumed. Therefore,

$$\varepsilon = (ds - d\bar{s})/ds, D_k = \bar{D}_k/\sqrt{1+\varepsilon}, A_k = \bar{A}_k/(1+\varepsilon)$$
 (10a-c)

$$I_k + \bar{I}_k/(1+\varepsilon)^2$$
,  $m_i + \rho_i A_i = \tilde{m}_i/(1+\varepsilon)$  (10d, e)

in which  $k \in \{e, i, P\}$ . The subscripts (e), (i), and (P) denote the properties of the pipe column, of the internal fluid, and of the pipe, respectively. The upper bar sign ( $\bar{}$ ) denotes the property at the undeformed state. For example  $\bar{A}_e$  is the cross-sectional area of the pipe column at the undeformed state, while  $A_e$  is the pipe-column's area at the equilibrium state. Note that  $\varepsilon$  is the axial strain at the neutral axis, s the arc length,  $D_k$  the diameter,  $A_k$  the cross-sectional area,  $I_k$  the moment of inertia,  $\rho_i$  the internal fluid density, and  $m_i$  the mass per unit length of transported fluid.

For static analysis, the acceleration of the pipe  $\bar{\mathbf{a}}_P = a_{Pn}\hat{\mathbf{n}} + a_{Pt}\hat{\mathbf{t}}$  is a nil vector, and the acceleration of transported fluid is derived<sup>8</sup> as

$$\mathbf{\bar{a}}_F = a_{Fn}\mathbf{\hat{n}} + a_{Ft}\mathbf{\hat{t}} = (\kappa V_i^2)\mathbf{\hat{n}} + (V_i dV_i/ds)\mathbf{\hat{t}}$$
(11)

where  $\kappa$  is the curvature, and  $V_i$  the internal flow velocity at the equilibrium state. The velocity  $V_i$  is determined from the continuity conditions<sup>8</sup> as follows:

$$V_i = \bar{V}_i \bar{A}_i / A_i = \bar{V}_i (1 + \varepsilon), \ dV_i / ds = \bar{V}_i d\varepsilon / ds$$
 (12a, b)

in which  $\bar{V}_i$  is the constant pump discharge. The current loading along the pipe is due to the drag forces

$$f_{Hn} = 0.5\rho_e D_e C_{Dn} | V_c \cos \theta | V_c \cos \theta$$
 (13a)

$$f_{Ht} = 0.5\rho_e D_e \pi C_{Dt} | V_c \sin \theta | V_c \sin \theta \tag{13b}$$

where  $\rho_e$  is the external fluid density,  $D_e$  the diameter of the pipe column,  $C_{Dn}$  and  $C_{Dt}$  the normal and tangential drag coefficients, and  $V_c$  the current velocity. The profile of current velocity may be expressed in the form

$$V_c = V_{ct} \left( \frac{y + \bar{y}_b}{\bar{y}_t + \bar{y}_b} \right)^n \tag{14}$$

where  $V_{ct}$  is the current velocity at mean sea level,  $\bar{y}_b$  and  $\bar{y}_t$  are defined in Fig. 1(a). The index n can be varied from 0 to 1 depending upon the current profile. In this study, n = 1/7 is employed for a tidal current profile.<sup>11</sup>

Based on all the above derivations along with the geometric relations and the constitutive equations of the extensible elastica theory,<sup>8</sup> the governing equations obtained from the large strain formulation are summarized as follows:

(a) Geometric Relations:

$$\frac{dx}{ds} = \sin \theta, \ \frac{dy}{ds} = \cos \theta, \ \kappa = \frac{d\theta}{ds}.$$
 (15a-c)

(b) Constitutive Equations:

$$T_a = EA_P \varepsilon, M = EI_P \kappa.$$
 (16a, b)

(c) Equilibrium Equations:

$$\frac{dM}{ds} = Q \tag{17}$$

$$\frac{dQ}{ds} = (T_a - m_i V_i^2) \frac{d\theta}{ds} + f_{Hn} + w_a \sin \theta \tag{18}$$

$$\frac{dT_a}{ds} = -Q\frac{d\theta}{ds} - f_{Ht} + w_a \cos\theta + m_i V_i \frac{dV_i}{ds}.$$
 (19)

Differentiating Eq. (16a) with respect to s, the expression of  $d\varepsilon/ds$  can be obtained

$$\frac{d\varepsilon}{ds} = \left[ \frac{(1+\varepsilon)}{EA_P(1+2\varepsilon)} \right] \frac{dT_a}{ds}.$$
 (20)

Utilizing Eqs. (12a), (12b), and (20), we have

$$m_i V_i \frac{dV_i}{ds} = \left[ \frac{m_i V_i^2}{EA_P (1 + 2\varepsilon)} \right] \frac{dT_a}{ds}.$$
 (21)

Note that  $m_i V_i^2 = \bar{m} \bar{V}_i^2 (1 + \varepsilon)$ . Substituting Eqs. (21) into (19) together with some manipulation, Eq. (19) can be cast in the form

$$\frac{dT_a}{ds} = \frac{-Q\frac{d\theta}{ds} - f_{Ht} + w_a \cos \theta}{\left[1 - \frac{m_i V_i^2}{EA_P(1 + 2\varepsilon)}\right]}.$$
 (22)

#### 3. Dimensionless Model and Solution Method

The following non-dimensional quantities are introduced:

$$s^* = s/s_t, \ \hat{x} = x/L, \ \hat{y} = y/L, \ \hat{s} = s/L, \ \eta = L/\sqrt{\hat{I}_P/\bar{A}_P}$$
 (23a-e)

$$\hat{M} = M : /E\bar{I}_P, \, \hat{Q} = QL^2/E\bar{I}_P, \, \hat{T}_a = T_aL^2/E\bar{I}_P$$
 (23f-h)

$$\hat{\rho}_P = \rho_P \bar{A}_P q L^3 / E \bar{I}_P, \, \hat{\rho}_e = \rho_e \bar{A}_e q L^3 / E \bar{I}_P, \, \hat{\rho}_i = \rho_i \bar{A}_i q L^3 / E \bar{I}_P \tag{23i-k}$$

$$\hat{V}_{ct} = V_{ct} \sqrt{\rho_e \bar{D}_e L^3 / E \tilde{I}_P}, \, \bar{V}_i = \bar{V}_i L \sqrt{\rho_i \bar{A}_i / E \bar{I}_P}$$
(23l, m)

where  $s_t$  is the total arc-length,  $L = \sqrt{\bar{x}_t^2 + \bar{y}_t^2}$  the span length, and  $\eta$  the slenderness ratio. Manipulating Eqs. (15)-(18) and (22) with application of Eqs. (23), the governing equations in the non-dimensional form are obtained as

$$\frac{d\hat{x}}{ds^*} = \hat{s}_t \sin \theta, \frac{d\hat{y}}{ds^*} = \hat{s}_t \cos \theta, \frac{d\theta}{ds^*} = \hat{s}_t \hat{M} (1 + \varepsilon)^2, \frac{d\hat{M}}{ds^*} = \hat{s}_t \hat{Q}$$
 (24a-d)

$$\frac{d\hat{Q}}{ds^*} = [\hat{T}_a - \hat{V}_i^2 (1+\varepsilon)] \frac{d\theta}{ds^*} + \hat{s}_t \hat{f}_{Hn} + \hat{s}_t \hat{w}_a \sin\theta$$
 (24e)

$$\frac{d\hat{T}_a}{ds^*} = \frac{-\hat{Q}\frac{d\theta}{ds^*} - \hat{s}_t \hat{f}_{Ht} + \hat{s}_t \hat{w}_a \cos \theta}{\left[1 - \frac{\hat{V}_i^2 (1+\varepsilon)^2}{\eta^2 (1+2\varepsilon)}\right]}.$$
 (24f)

The dimensionless quantities  $\hat{w}_a$ ,  $\hat{f}_{Hn}$ ,  $\hat{f}_{Ht}$  and  $\varepsilon$  are determined from Eqs. (9b), (13a), (13b) and (16a), respectively, as follows:

$$\hat{w}_a = \frac{w_a L^3}{E\bar{I}_P} = \frac{\hat{\rho}_P - \hat{\rho}_e + \hat{\rho}_i}{1 + \varepsilon}$$
 (25a)

$$\hat{f}_{Hn} = \frac{f_{Hn}L^3}{E\bar{I}_P} = \frac{0.5C_{Dn}}{\sqrt{1+\varepsilon}}|\hat{V}_c\cos\theta|\hat{V}_c\cos\theta$$
 (25b)

$$\hat{f}_{Ht} = \frac{f_{Ht}L^3}{E\bar{I}_P} = \frac{0.5\pi C_{Dt}}{\sqrt{1+\varepsilon}} |\hat{V}_c \sin\theta| \hat{V}_c \sin\theta$$
 (25c)

$$\varepsilon = \frac{\hat{T}_a(1+\varepsilon)}{\eta^2} = \frac{\hat{T}_a}{(\eta^2 - \hat{T}_a)}$$
 (25d)

in which

$$\hat{V}_{c} = V_{c} \sqrt{\frac{\rho_{e} \bar{D}_{e} L^{3}}{E \bar{I}_{P}}} = \hat{V}_{ct} \left[ \frac{\hat{y} + \hat{y}_{b}}{\hat{y}_{t} + \hat{y}_{b}} \right]^{1/7}.$$
 (25e)

The boundary conditions of a simply supported pipe are at  $s^* = 0$ :

$$\hat{x} = 0, \, \hat{y} = 0, \, \theta = \theta_0, \, \hat{M} = 0, \, \hat{Q} = \hat{Q}_0, \, \hat{T} = \hat{T}_0$$
 (26a-f)

at  $s^* = 1$ :

$$\hat{x} = \hat{x}_t, \, \hat{y} = \hat{y}_t, \, \theta = \theta_t, \, \hat{M} = 0, \, \hat{Q} = \hat{Q}_t, \, \hat{T} = \hat{T}_t$$
 (27a-f)

in which the dimensionless tension  $\hat{T}$  is determined from Eq. (9a) as

$$\hat{T} = \frac{TL^2}{E\bar{I}_P} = \hat{T}_a - \frac{2v(\hat{\rho}_e - \hat{\rho}_i)(\hat{y}_t - \hat{y})}{1 + \varepsilon}.$$
 (28)

Note that  $\hat{x}_t^2 + \hat{y}_t^2 = 1$ ,  $\hat{x}_t/\hat{y}_t = \tan \phi$ , where  $\phi$  denotes the angle of inclination.

The system of Eqs. (24), (26) and (27) describes the boundary value problem with nine variables. In the case where the pipe buckles because of experiencing the critical top tension, the nine variables are  $\hat{x}$ ,  $\hat{y}$ ,  $\theta$ ,  $\hat{M}$ ,  $\hat{T}_a$ ,  $\hat{s}_t$ ,  $\hat{Q}_t$  and  $\hat{T}_t$ . Whereas if the buckling occurs because the pipe is subjected to the critical weight, the nine variables are  $\hat{x}$ ,  $\hat{y}$ ,  $\theta$ ,  $\hat{M}$ ,  $\hat{Q}$ ,  $\hat{T}_a$ ,  $\hat{s}_t$ ,  $\hat{Q}_t$  and  $\hat{\rho}_P$ . In the former case, the nine equations corresponding to the nine variables are given by Eqs. 26(a), 26(b), 26(d) and 27(a)–(f). The problem is solved by the shooting method of which the solution steps<sup>12</sup> are as follows:

- Step 1. Set the initial step size of integration and the initial values of  $\hat{x}(s^*)$ ,  $\hat{y}(s^*)$ ,  $\theta(s^*)$ ,  $\hat{M}(s^*)$ ,  $\hat{Q}(s^*)$  and  $\hat{T}(s^*)$  at  $s^* = 1$ , according to Eqs. 27(a)-(f).
- Step 2. Given  $\theta_t$ , one guesses  $\hat{s}_t$ ,  $\hat{Q}_t$  and  $\hat{T}_t$  at the first iteration from the linear small displacement theory.
- Step 3. Integrate Eqs. 24(a)-(f) from  $s^* = 1$  to 0 using the fifth order Cash-Karp Runge-Kutta with adaptive step size control following Fehlberg method.<sup>13</sup>

Step 4. Minimize the error norm using the Nelder and Mead simplex method<sup>14</sup> with respect to  $\hat{s}_t$ ,  $\hat{Q}_t$  and  $\hat{T}_t$ . The objective function  $\Phi$  for the minimization process is

$$\min_{\hat{x}_t, \hat{Q}_t, \hat{T}_t} \Phi = |\hat{x}(0)| + |\hat{y}(0)| + \hat{M}(0)|.$$
 (29)

Step 5. Add an incremental  $\Delta\theta_t$  to  $\theta_t$  and repeat steps 3-4 to construct the curves of  $\hat{T}_t$  versus  $\theta_0$  and  $\theta_t$ .

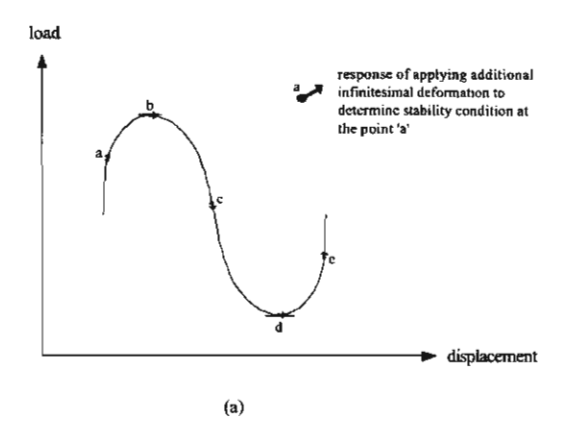
Validation of the numerical results dealing with the problem of a simple variablearc-length elastica pipe conveying fluid is given in Appendix A. It is shown that the numerical results obtained from the numerical procedure employed in this paper are in excellent agreement with the exact solutions obtained from the analytical elliptic integral method. 15 Thus the validity of the method in yielding accurate answers is confirmed.

# 4. Stabilty Analysis Based on the Method of Adjacent Nonlinear **Equilibrium**

Based on the method of adjacent nonlinear equilibrium, the stability of an equilibrium state is defined by introducing a physical perturbation, and investigating the subsequent nonlinear responses. The perturbation should provoke additional infinitesimal deformations, which make the system move to the adjacent equilibrium state. The criteria of stability are as follows:

- 1. Definition for a stable state. The state of nonlinear equilibrium is stable, if the system at that state does oppose the additional displacement due to a perturbation, and when the perturbation is eliminated the system returns to the previous equilibrium state.
- 2. Definition for a critical state. The state of nonlinear equilibrium is critical or neutral, if the system at that state is idle to the additional displacement due to a perturbation, and when the perturbation is eliminated, the system stays in the perturbation configuration, neither returns to the previous equilibrium state nor goes to a different state.
- 3. Definition for an unstable state. The state of nonlinear equilibrium is unstable, if after subjected to the additional displacement due to a perturbation, the system at that state moves continuously to a very different state, and cannot go back to the previous equilibrium state even if the perturbation would be eliminated.

To use these definitions in exploring the overall stability of the elastica, either the load-displacement diagram or the stiffness-displacement diagram needs to be constructed. For the load-displacement diagram and the stiffness-displacement diagram exemplified in Figs. 3(a) and 3(b), the stability conditions at points "a", "b", "c", "d" and "e" can be interpreted from the aforementioned definitions as follows:



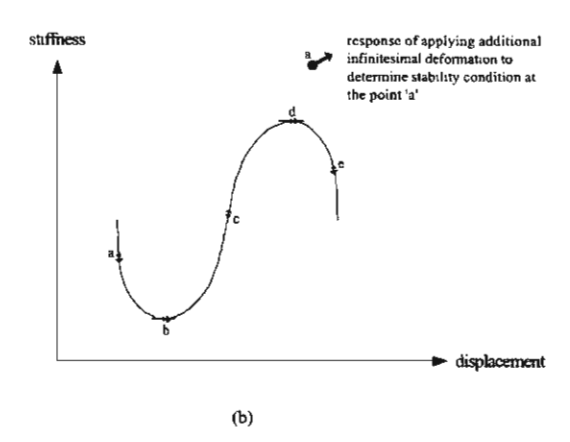


Fig. 3. The method of adjacent nonlinear equilibrium: (a) load-displacement diagram, (b) stiffness-displacement diagram.

As an additional infinitesimal displacement due to a perturbation is applied to the elasticas at the states at the points "a" and "e" as shown in Figs. 3(a) and 3(b), it is seen that the loads acting on the elasticas are increased, while the stiffness values of the elasticas are decreased. These results signify that the elasticas are against the additional displacements due to the perturbation according to definition 1. Thus, the equilibrium states at the points "a" and "e" are considered stable states.

As an additional infinitesimal displacement due to a perturbation is applied to the elasticas at the states at the points "b" and "d" as shown in Figs. 3(a) and 3(b), it is seen that no response occurs. The values of stiffness and loads acting on the elasticas have no change. These results imply that the elasticas are idle to the additional displacements due to the perturbation according to definition 2. Therefore, the equilibrium states at the points "b" and "d" are recognized as critical states.

As an additional infinitesimal displacement due to a perturbation is applied to the elastica at the state at the point "c" as shown in Figs. 3(a) and 3(b), it is seen that the load acting on the elastica is decreased, while the stiffness of the elastica is increased. These results signify that the elastica is in favor of the additional displacements due to the perturbation according to definition 3. Hence, the state at the point "c" is an unstable state.

The values of critical load and critical stiffness at the limit states can be determined numerically by using the search techniques of minimization methods. In this study, the dichotomous search algorithm<sup>16</sup> is employed.

#### 5. Parametric Studies and Discussion

As stated in the previous section, investigating the overall stability of the pipe by the adjacent nonlinear equilibrium method needs the plots of either the load-displacement or the stiffness-displacement curves. The question is what are parameters of the load and the stiffness to be plotted. From Eqs. (24)–(28), it is observed that there exist twelve parameters that affect the behavior of the pipe. These parameters are the dimensionless quantities of (1) density of pipe material  $\hat{\rho}_P$ , (2) applied top tension  $\hat{T}_t$ , (3) density of external fluid  $\hat{\rho}_e$ , (4) density of internal fluid  $\hat{\rho}_i$ , (5) Poisson's ratio v, (6) slenderness ratio  $\eta$ , (7) vessel offset  $\hat{x}_t$ , (8) seawater depth  $\hat{y}_t$ , (9) normal current-drag coefficient  $C_{Dn}$ , (10) tangential current-drag coefficient  $C_{Dt}$ , (11) current velocity at mean sea level  $\hat{V}_{ct}$ , and (12) internal flow velocity of transported fluid  $\hat{V}_i$ . Mathematically speaking, several of these parameters can have their own critical values.

In the literature, it is well known that a heavy column may buckle by its own critical weight. 17,18 The marine elastica pipe, which behaves as a heavy imperfection column, hence, is supposed to buckle by the critical weight as well. So in this case, the load is referred to as the pipe's weight parameter  $\hat{\rho}_{P}$ . On the other hand, the bending rigidity has very little influence on the behavior of the pipe. 19 The axial stiffness performed by pretension at the top end of the pipe becomes the main structural stiffness in preventing the buckling of the pipe. Therefore, in this case the stiffness is referred to as the applied top tension parameter  $\hat{T}_t$ .

Adopting the rotational angles at the bottom and top supports  $\theta_o$  and  $\theta_t$  as the interested displacements, the stiffness-displacement curves are the plots of  $\hat{T}_t - \theta_o$ and  $\hat{T}_t - \theta_t$ , while the load-displacement curves are the plots of  $\hat{\rho}_P - \theta_o$  and  $\hat{\rho}_P - \theta_t$ . The stiffness-displacement curves are used in analyzing the nonlinear buckling of the pipe due to insufficient stiffness in Sec. 5.1, while the load-displacement curves are utilized in studying the nonlinear buckling of the pipe due to overloading in Sec. 5.2. Finally, the parametric studies of the parameters  $\hat{\rho}_e$ ,  $\hat{\rho}_i$ , v,  $\eta$ ,  $\hat{x}_t$ ,  $\hat{y}_t$ ,  $C_{Dn}$ ,  $C_{Dt}$ ,  $\hat{V}_{ct}$  and  $\hat{V}_{i}$ , which are considered to provide secondary effects to the nonlinear buckling behavior of the pipe, are carried out in Sec. 5.3. The input data of the parameters used in parametric studies are given in Table 1. The parametric study

Table 1. Input data used in parametric studies.

The typical value of the	The parametric study is carried out in		
parameter	Figs.	by varying	
$\hat{ ho}_P=100.57$	4(a)	$\hat{\rho}_P = 100, 200, 400, 700, 1000, 1300, 1600$	
$\hat{T}_t = 235.13$	5(a)	$\hat{T}_t = 100, 500, 1000, 2000, 3000, 4000$	
$\hat{\rho}_{\boldsymbol{e}} = 32.16$	6	$\hat{\rho}_e = 10, 30, 50, 70, 90$	
$\hat{\rho}_i = 18.53$	7	$\hat{\rho}_i = 10, 30, 50, 70, 90$	
v=0.5	8	v = 0, 0.1, 0.3, 0.5, 0.7, 1.0	
$\eta=1488.49$	9	$\eta = 1000, 1500, 2000, 2500, 3000, 4000, 5000$	
$\hat{x}_t = 0.57$ which yields	10	$\hat{x}_t = 0, 0.2195, 0.4730, 0.8192, 1.4189, 3.0574$ , which yield	
$\phi=35^{ m o}$		$\phi = 15^{\circ}, 30^{\circ}, 45^{\circ}, 60^{\circ}, 75^{\circ}, \text{ respectively}$	
$\hat{y}_t = 0.82$ which yields	11	$\hat{y}_t = 2.1402,  0.9933,  0.5735,  0.3311,  0.1537,  0,  \text{which yield}$	
$\phi = 35^{\circ}$		$\phi = 15^{\circ}, 30^{\circ}, 45^{\circ}, 60^{\circ}, 75^{\circ}, 90^{\circ}, $ respectively	
$\hat{y}_b = 0.41$		_	
$C_{Dn} = 0.7$	12	$C_{Dn} = 0, 0.3, 0.5, 0.7, 0.9$	
$C_{Dt} = 0.03$	13	$C_{Dt} = 0,  0.03,  0.05,  0.07,  0.1$	
$\hat{V}_{ct} = 6.01$	14	$\hat{V}_{ct} = 0, 5, 10, 15, 20, 30$	
$\hat{V}_i=2.49$	15	$\hat{V}_i = 0, 5, 10, 15$	

is performed by varying the value of the studied parameter, while the typical values of other parameters are retained.

## 5.1. Nonlinear buckling of the pipe due to insufficient stiffness

Figures 4(a)–4(c) demonstrate influence of the applied top tension  $\hat{T}_t$  on the nonlinear buckling of the pipe. Based on the method of adjacent nonlinear equilibrium, it is found from the stiffness-displacement diagram as shown in Fig. 4(a) that continuous reduction of the applied top tension can change stability status of the pipe from the stable state in the stable zone to the critical state on the critical tension path, and change from the critical state to the unstable state in the unstable zone, respectively. The nonlinear buckling of the pipe takes place at the lowest points of the stiffness-displacement curves, where  $\hat{T}_t$  holds the limit value  $\hat{T}_{t(cr)}$ .

Therefore, the safety design values of the applied top tension  $\hat{T}_t$  should not be less than or equal to the critical tension  $\hat{T}_{t(cr)}$ . Because if  $\hat{T}_t < \hat{T}_{t(cr)}$ , meaning that axial stiffness is designed insufficiently; consequently, no equilibrium state of the pipe exists. In other words, the pipe is subjected to buckling suddenly. If  $\hat{T}_t \to \hat{T}_{t(cr)}$  is designed, the pipe will be in the transition state. A small perturbation will lead the pipe into an unstable state, and divergence instability will occur suddenly. Variations of the critical top tension  $\hat{T}_{t(cr)}$ , when the pipe's weight parameter  $\hat{\rho}_P$  is varied, are also shown in Fig. 4(a). It is evident that the value of the critical top tension is raised linearly by increasing the pipe's weight parameter.

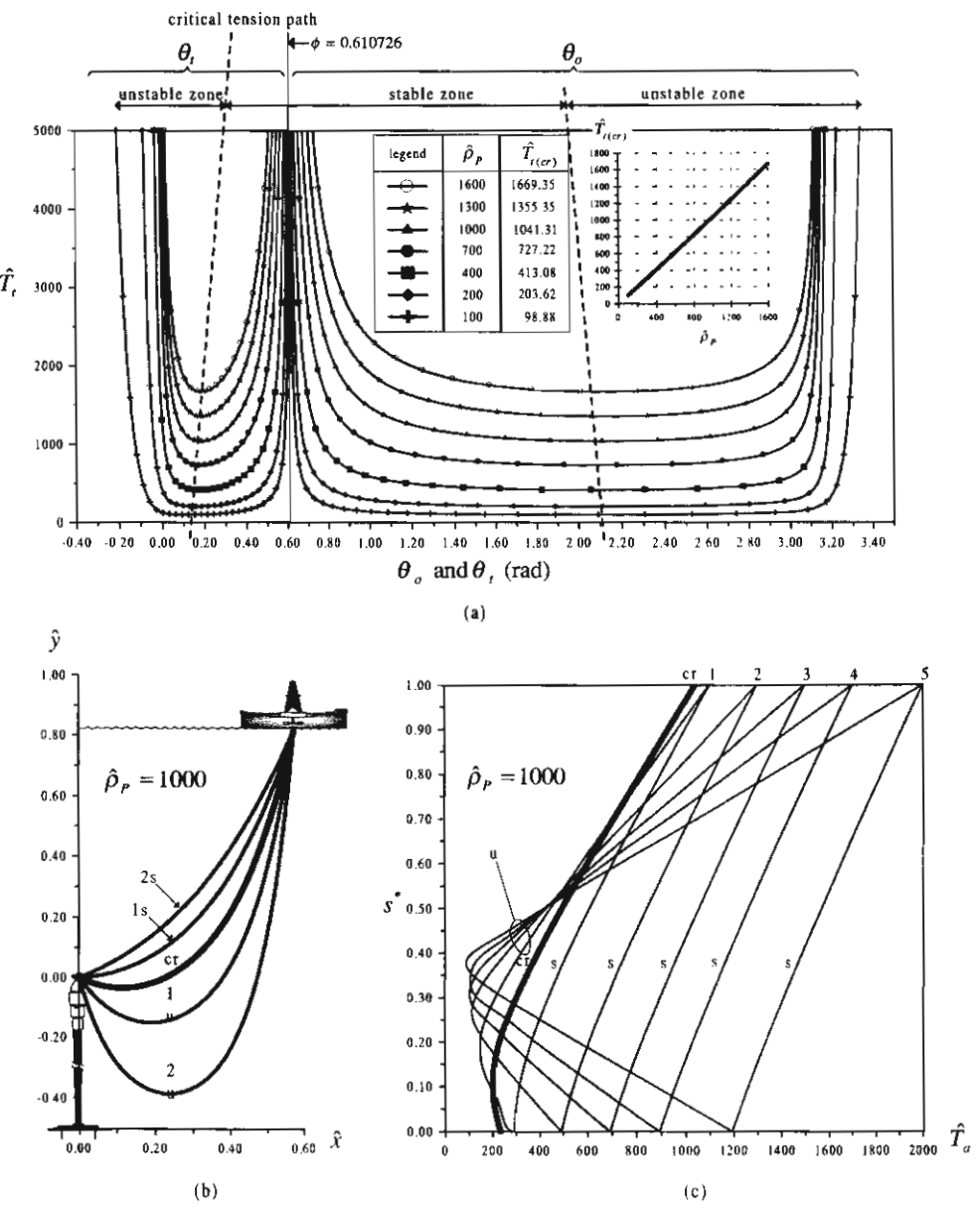


Fig. 4. Nonlinear buckling by critical top tension: (a) stiffness-displacement curves, (b) equilibrium configurations of the pipe, (c) distribution of the apparent tension along arc-length; the characters "s", "u", "cr" represent the stable, unstable, and critical states, respectively; the consecutive numbers 1–5 represent  $\hat{T}_t = 1100$ , 1300, 1500, 1700, 2000, respectively.

Nonlinear behavior of the pipe before and after buckling by the critical top tension is depicted in Figs. 4(b) and 4(c). Before buckling, the pipe is subjected to a small sag, and the stable equilibrium configuration of the pipe has a moderate curvature as shown in Fig. 4(b). Most of the positions of the lowest tension are at the bottom support of the pipe and the gradient of distribution of the apparent tension along arc length is almost linear with one slope as shown in Fig. 4(c). After buckling, the pipe experiences a large sag and a large curvature as shown in Fig. 4(b). As the large sag increases, the positions of the lowest tension move from the bottom support of the pipe to the bottom points of sagging, where the apparent tension approaches to zero, and the gradient of distribution of the apparent tension along arc length turns into another slope as shown in Fig. 4(c).

From Fig. 4(c), it is important to note that the pipe may buckle, even if every part has not yet been subjected to the compressive force. This is due to the fact that the apparent tension is not enough to maintain equilibrium of the pipe. It is not a familiar phenomenon under which structural buckling mostly occurs because of compressive force.

#### 5.2. Nonlinear buckling of the pipe due to overloading

Figures 5(a)-5(c) expose influence of the pipe's weight parameter on the nonlinear buckling of the pipe. Based on the method of adjacent nonlinear equilibrium, it is found from the load-displacement diagram as shown in Fig. 5(a) that under a constant applied top tension, a continuous increase of pipe's weight can change stability status of the pipe from the stable state in the stable zone to the critical state on the critical weight path, and change from the critical state to the unstable state in the unstable zone, respectively. The nonlinear buckling of the pipe takes place at the peaks of the stiffness-displacement curves, where  $\hat{\rho}_P$  holds the limit value  $\hat{\rho}_{P(cr)}$ .

Therefore, to be under a certain limit of the maximum safety tension of the tensioning system, the desired pipe's weight should not be greater than or equal to the critical weight parameter  $\hat{\rho}_{P(cr)}$ . In the case that  $\hat{\rho}_{P} > \hat{\rho}_{P(cr)}$ , the pipe will be overloaded, and no equilibrium state of the pipe exists. In other words, the pipe is subjected to buckling suddenly. In another case if  $\hat{\rho}_{P} \to \hat{\rho}_{P(cr)}$ , the pipe will be in the transition state. A small perturbation will cause the pipe stepping into an unstable state, and divergence instability will occur suddenly. Variations of the critical pipe's weight parameter  $\hat{\rho}_{P(cr)}$ , when the applied top tension  $\hat{T}_{t}$  is varied, are shown in Fig. 5(a). It is evident that the value of the critical pipe's weight parameter is raised linearly by increasing the applied top tension.

Nonlinear behavior of the pipe before and after buckling by the critical weight is depicted in Figs. 5(b) and 5(c). It can be explained in the same manner as in the case of nonlinear buckling by critical top tension. In fact, it is proper to state that the nonlinear buckling of the pipe due to overloading is the reverse problem of the nonlinear buckling due to insufficient stiffness.

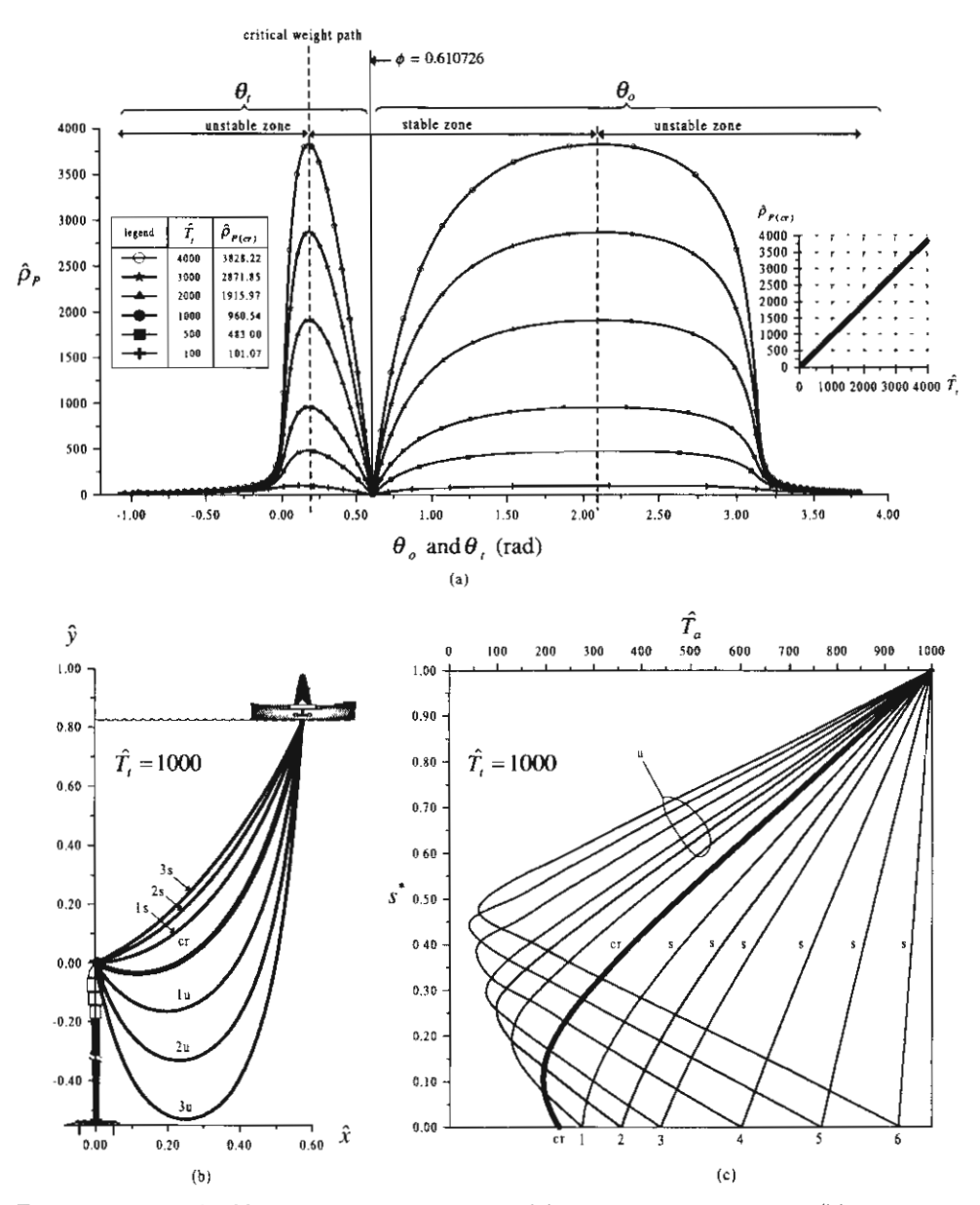


Fig. 5. Nonlinear buckling by critical pipe's weight: (a) load-displacement curves, (b) equilibrium configurations of the pipe, (c) distribution of the apparent tension along arc-length; the characters "s", "u", "cr" represent the stable, unstable, and critical states, respectively; the consecutive numbers 1–6 represent  $\hat{\rho}_P = 900, 800, 700, 500, 300, 100$ , respectively.

Table 2. Summary of results of parametric studies.

		Actions of the parameter	induces internal compression and bucking behavior of heavy column (see Eq. (25a))	increases stiffness of the pipe by pre-tensioning (see Eq. (27f))	increases the apparent tension by adding the internal tension due to Poisson's effect (see Eq. (28)), and reduces the apparent weight by producing buoyancy force (see Eq. (25a))	reduces the apparent tension by adding the internal compression due to Poisson effect (see Eq. (28)), and increases the apparent weight by adding weight of transported mass (see Eq. (25a))	contributes lateral actions of external and internal fluid pressures (see Eq. (28))	reduces axial stiffness of the pipe (see Eq. 25d))
		Significance	vital	vital	medium	medium	very small	very small
no .		Stability	<b>→</b>	<b>←</b>	←	<b>→</b>	<b>←</b>	→
Effects of increasing values of the parameter on	Critical Pipe's	weight	1	see Fig. 5(a) $\rightarrow$	see Fig. 6(b)	see Fig. 7(b)	see Fig. 8	see Fig. 9
increasing values	Critical Top	tensions	see Fig. 4(a)	1 -	see Fig. 6(a)	see Fig. 7(a)	ç see Fig. 8	see Fig. 9
Effects of	Large	displacement	see Fig. 4(a)	↓ see Fig. 5(a)	see Figs. 6(a) and 6(b)	↑ see Figs. 7(a) and 7(b)	$\rightarrow$	<b>←</b>
		Parametric studies of	1. Pipe's weight	2. Applied top tension	3. External fluid pressure	4. Internal fluid pressure	5. Poisson's ratio	6. Slenderness ratio

Symbols: ↑ = increase, ↓ = decrease

Table 2. (Continued)

	Effects of	Effects of increasing values of the parameter on	of the parameter	uo		
	Large	Critical Top	Critical Pipe's			
Parametric studies of	displacement	tensions	weight	Stability	Significance	Actions of the parameter
7. Vessel offset	see Figs. 10(a) and 10(b)	see Fig. 10(c)	see Fig. 10(c)	<b>→</b>	important	increases effects of structural imperfection and structural inclination of the pipe (see Eq. (27a))
8. Seawater depth	see Figs. $11(a)$ and $11(b)$	see Fig. 11(c)	see Fig. 11(c)	$\rightarrow$	vital	increases current loading (see Eq. (25e)), but reduces structural inclination of the pipe (see Eq. (27b))
9. Normal current-drag coefficient	←	see Fig. 12	↓ see Fig. 12	$\rightarrow$	small	increases a normal drag force and structural imperfection of the pipe (see Eq. (25b))
<ol> <li>Tangential current- drag coefficient</li> </ol>	$\rightarrow$	↓ see Fig. 13	ee Fig. 13	←	very small	increases tension in the pipe by amplifying a tangential drag force (see Eq. 25c))
11. Current flow velocity	† see Figs. 14(a) and 14(b)	see Fig. 14(c)	↓ see Fig. 14(b)	$\rightarrow$	medium	increases current loading and structural imperfection of the pipe (see Eqs. (25b), (25c) and (25e))
12. Internal flow velocity	† see Figs. 15(a) and 15(b)	see Fig. 15(a) see Fig. 15(b)	↓ see Fig. 15(b)	$\rightarrow$	important	reduces tension in the pipe (see Eqs. (24e) and (24f))

Symbols:  $\uparrow$  = increase,  $\downarrow$  = decrease

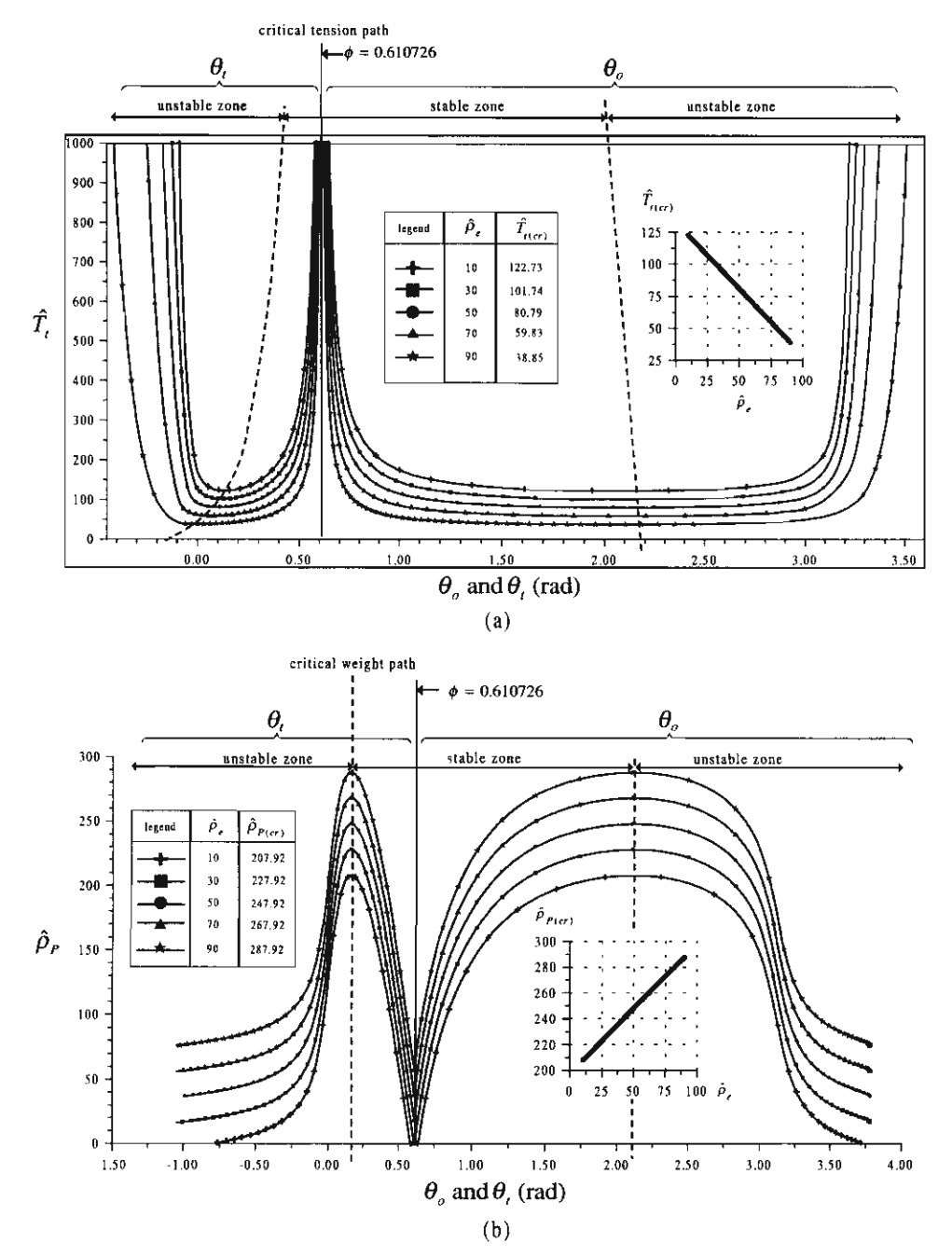


Fig. 6. Effects of external fluid pressure on (a) stiffness-displacement curves, (b) load-displacement curves.

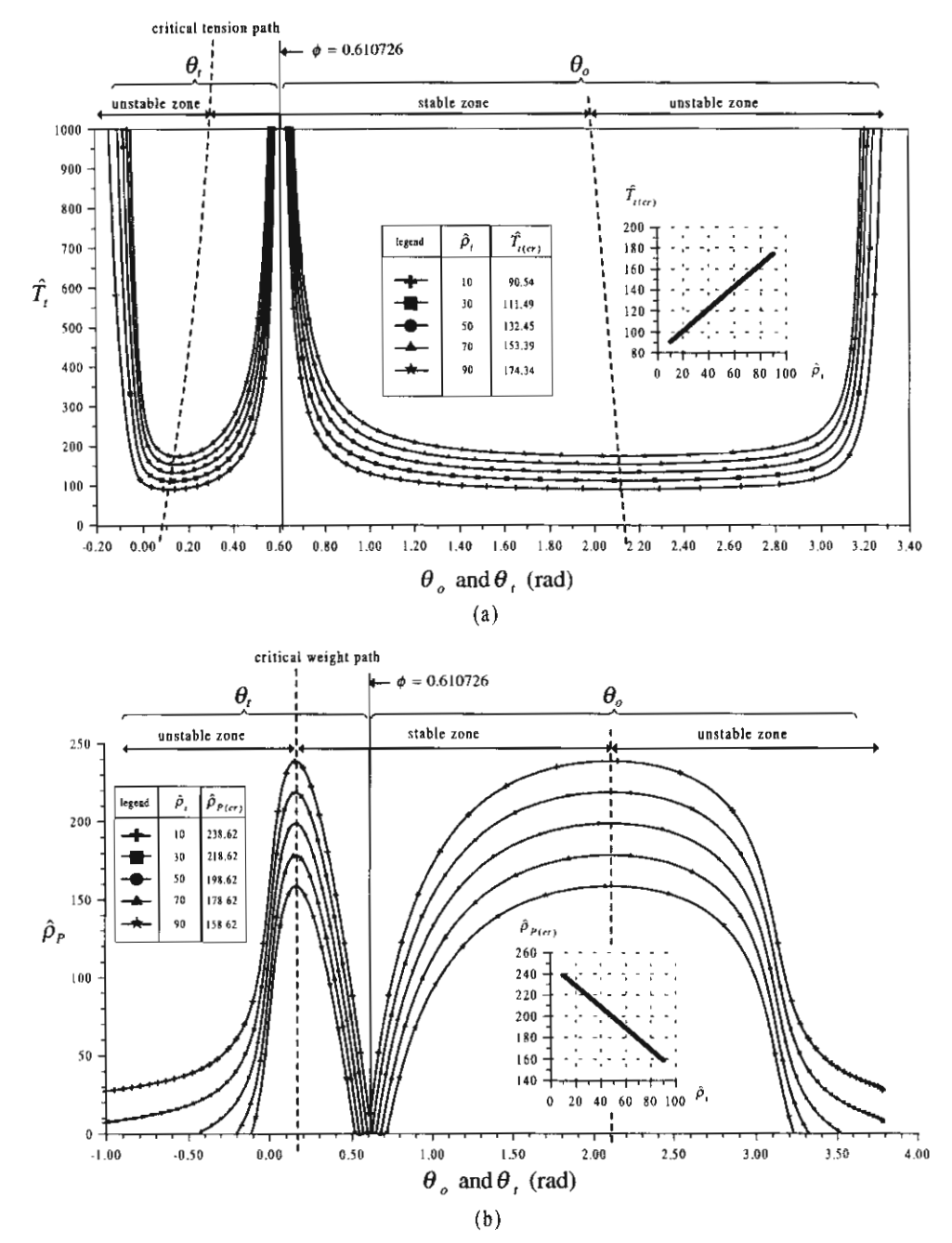
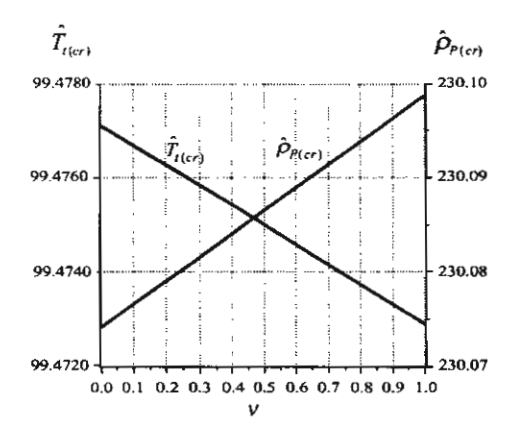
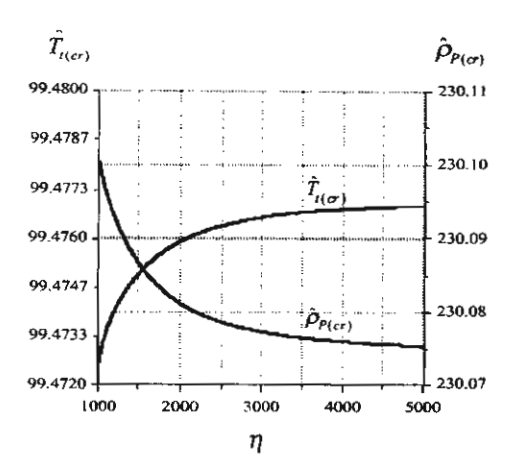


Fig. 7. Effects of internal fluid pressure on (a) stiffness-displacement curves, (b) loaddisplacement curves.



ν	$\hat{T}_{\iota(cr)}$	$\hat{ ho}_{\!\scriptscriptstyle P(cr)}$
0	99.4771	230.0743
0.1	99.4766	230.0767
0.3	99.4758	230.0816
0.5	99.4750	230.0865
0.7	99.4741	230.0913
1.0	99.4729	230.0986

Fig. 8. Effects of Poisson's ratio on limit states of the pipe.

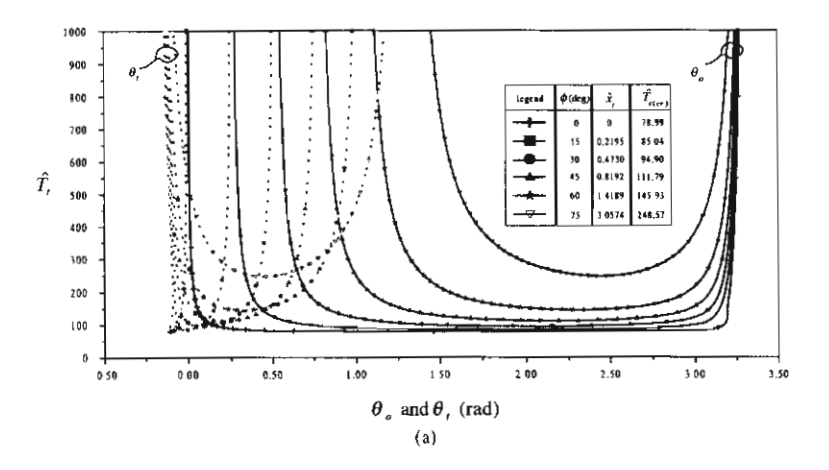


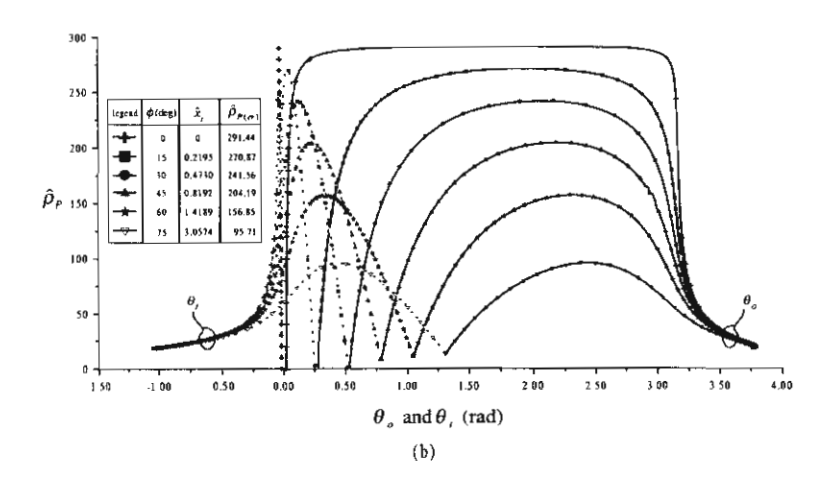
η	$\hat{T}_{i(cr)}$	$\hat{ ho}_{_{P(cr)}}$
1000	99.47245	230.1013
1500	99.47505	230.0863
2000	99.47594	230.0811
2500	99.47636	230.0786
3000	99.47659	230.0773
4000	99.47681	230.0760
5000	99.47691	230.0754

Fig. 9. Effects of slenderness ratio on limit states of the pipe.

## 5.3. Other parametric studies

In Secs. 5.1 and 5.2, the parameters  $\hat{T}_t$  and  $\hat{\rho}_P$  are studied, and found to be the major factors in causing the nonlinear buckling of the pipe due to insufficient stiffness and overloading, respectively. In this section, influences of the parameters  $\hat{\rho}_e$ ,  $\hat{\rho}_i$ , v,  $\eta$ ,  $\hat{x}_t$ ,  $\hat{y}_t$ ,  $C_{Dn}$ ,  $C_{Dt}$ ,  $\hat{V}_{ct}$  and  $\hat{V}_i$  on the nonlinear buckling behavior of the pipe are scrutinized.





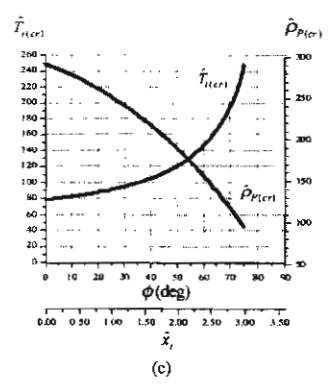
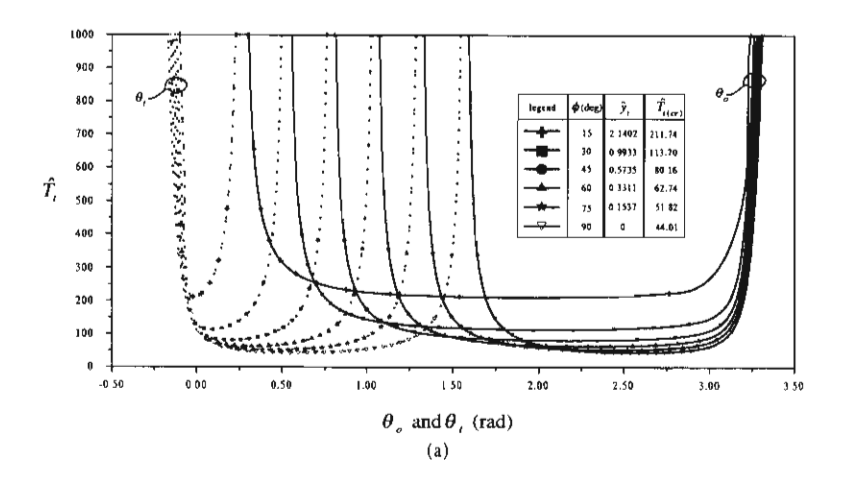
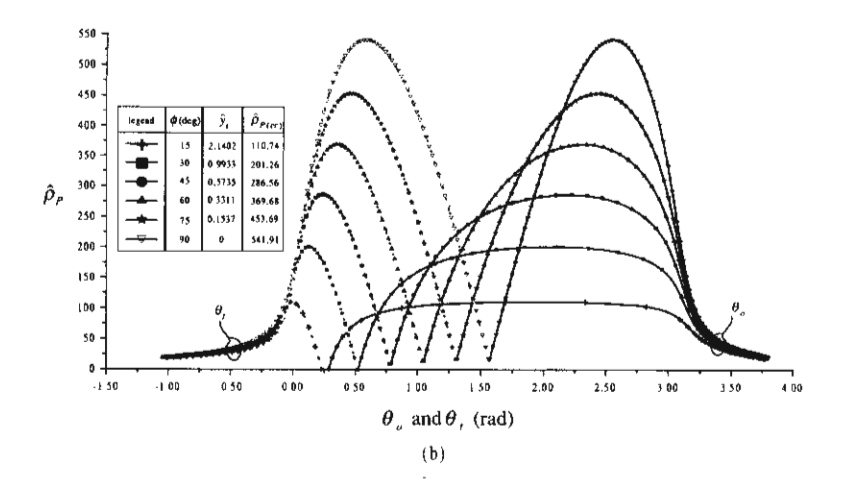


Fig. 10. Effects of static offset on (a) stiffness-displacement curves, (b) load-displacement curves, (c) limit states.





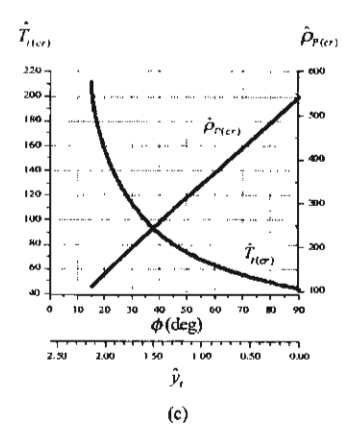
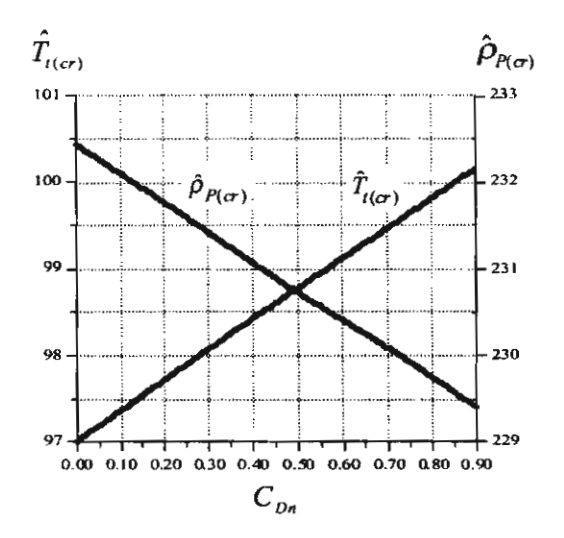
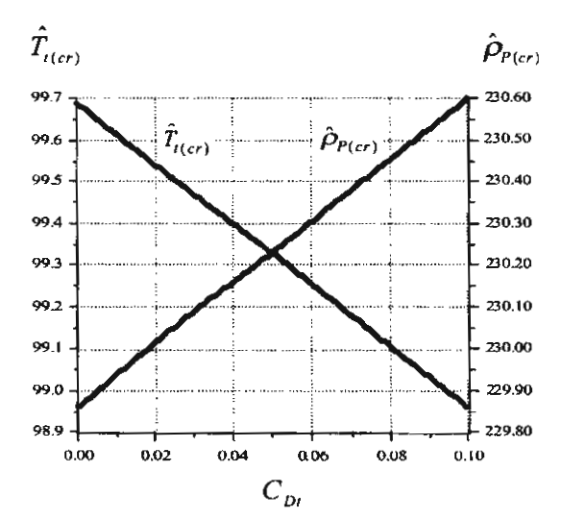


Fig. 11. Effects of water depth on (a) stiffness-displacement curves, (b) load-displacement curves, (c) limit states.



$C_{Dn}$	$\hat{T}_{\iota(cr)}$	$\hat{oldsymbol{ ho}}_{\!\scriptscriptstyle P(cr)}$
0	97.01	232.44
0.3	98.08	231.43
0.5	98.78	230.74
0.7	99.47	230.09
0.9	100.16	229.41

Fig. 12. Effects of normal current-drag coefficient on limit states of the pipe.



$C_{Di}$	$\hat{T}_{\iota(cr)}$	$\hat{ ho}_{\!\scriptscriptstyle P(cr)}$
0	99.69	229.86
0.03	99.47	230.09
0.05	99.33	230.23
0.07	99.18	230.38
0.10	98.96	230.60

Fig. 13. Effects of tangential current-drag coefficient on limit states of the pipe.

The results of parametric studies are summarized in Table 2. The effects are deliberated on the large displacements, the critical top tension, the critical pipe's weight, and the stability of the pipe. Significance of each parameter is assessed by comparing with significances of the parameters  $\hat{T}_t$  and  $\hat{\rho}_P$ , which are stipulated to be vital. The brief explanations on the action of the parameters are given in Table 2. It should be realized that the significance evaluation in Table 2 is done for the individual parameter. Although, some parameters are considered to have not much influence on the behavior of the pipe, it is not inferred that they should be

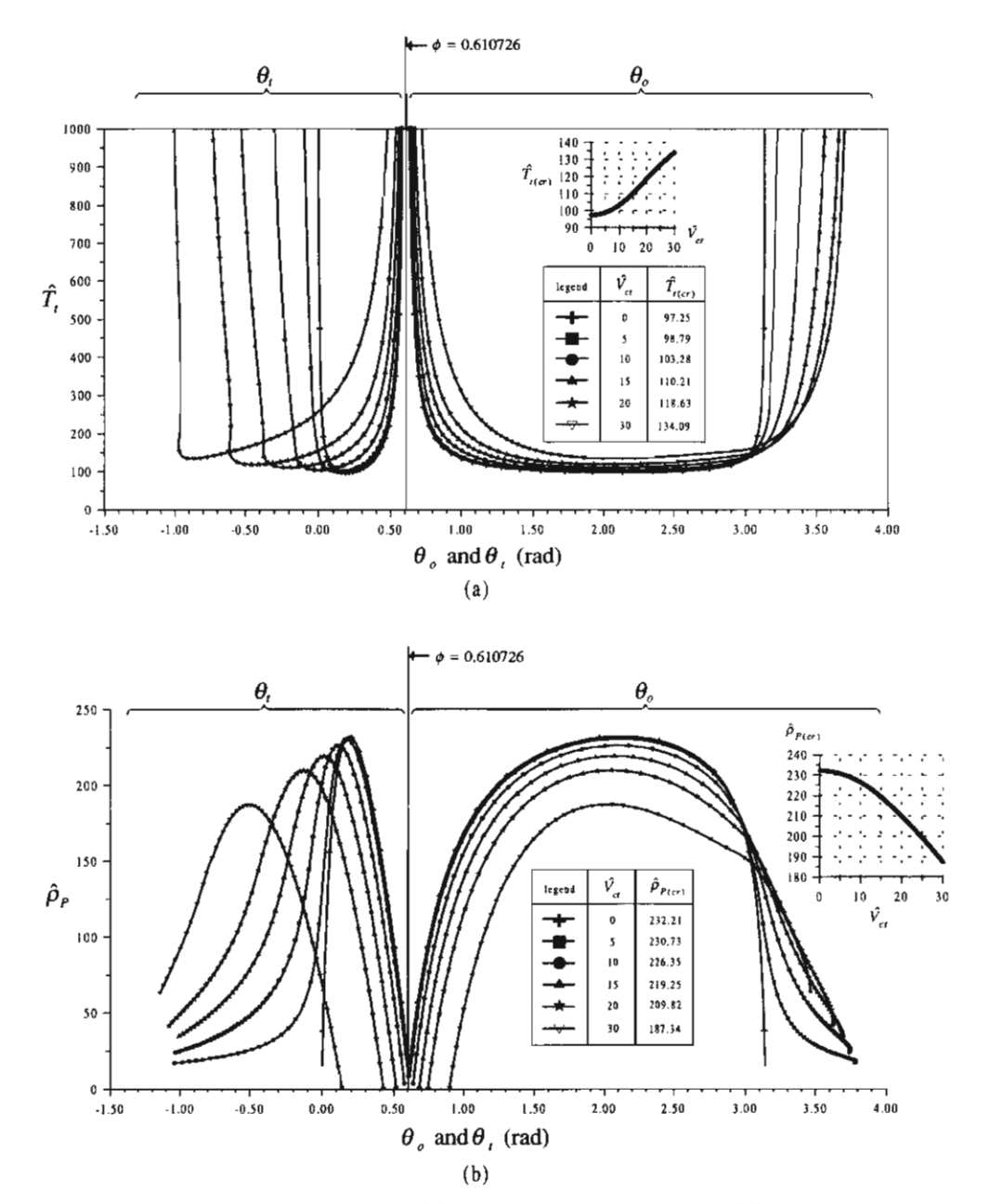
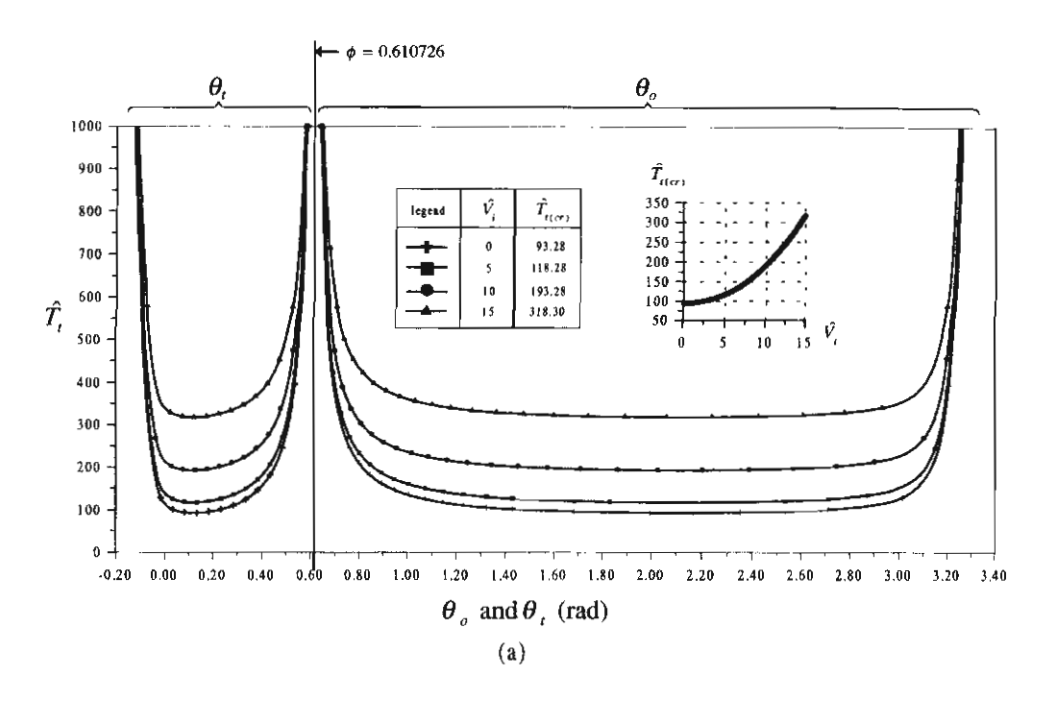


Fig. 14. Effects of current velocity on (a) stiffness-displacement curves, (b) load-displacement curves.



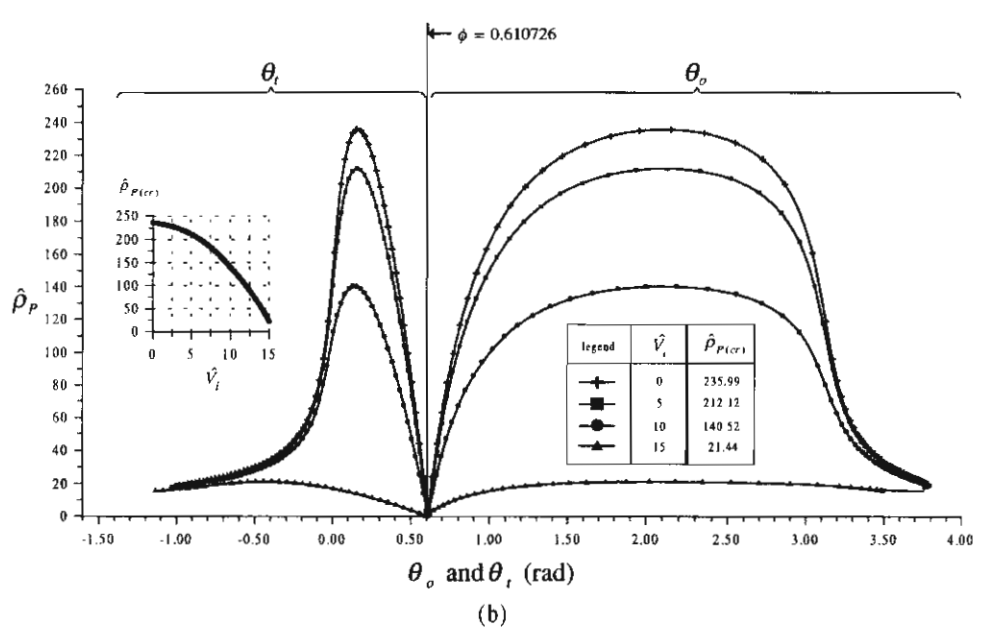


Fig. 15. Effect of internal flow velocity on (a) stiffness-displacement curves, (b) load-displacement curves.

of absolute negligence in the stability design of the pipe. The combined action with other parameters may raise further importance of them on the behavior of the pipe.

#### 6. Conclusions

Based on the numerical elastica solutions and stability examination by the method of adjacent nonlinear equilibrium, it can be concluded that the nonlinear buckling of the marine elastica pipe can occur due to insufficient stiffness and overloading, which are referred to as buckling by the critical top tension, and buckling by the critical pipe's weight, respectively. The marine elastica pipe may buckle even if every part has not yet been subjected to the compressive force. This is because the apparent tension may be deficient to hold the pipe in equilibrium position. Furthermore, the nonlinear equilibrium state of the pipe after buckling is found to be unstable.

The influences of all the parameters that affect the large displacement, the critical top tension, the critical pipe's weight, and the stability of the marine elastica pipe transporting fluid, are studied and summarized in Table 2. The results indicate that the effects of applied top tension, external fluid pressure, Poisson's ratio, and tangential current-drag coefficient are to reduce the large displacement and the critical top tension, and to increase the critical pipe's weight and the structural stability of the pipe. On the contrary, the effects of pipe's weight, internal fluid pressure, slenderness ratio, vessel offset, water depth, normal current-drag coefficient, current velocity, and internal flow velocity are to increase the large displacement and the critical top tension, and to decrease the critical pipe's weight and the structural stability of the pipe.

## 7. Acknowledgments

The work reported in this paper is financially supported by the Thailand Research Fund (TRF) through Contract No. RTA/03/2543.

#### Appendix A: Validation of Numerical Results

The problem of a simple variable-arc-length elastica pipe conveying fluid as shown in Fig. 16(a) is exploited in verification of the numerical solution procedure employed in this paper. Validation of the numerical results is given in Table 3. It is clearly seen that the numerical solutions obtained from the numerical method used in this paper are in excellent agreement with the exact solutions that are obtained from the elliptic integral method.<sup>15</sup> The post-buckling configuration of the variable-arc-length elastica pipe transporting fluid with internal flow velocity  $\hat{V}_i = \sqrt{5}$  is shown in Fig. 16(a). The bending moment  $\hat{M}$ , the shear force  $\hat{Q}$ , and the axial force  $\hat{T}_a$  are plotted along the normalized dimensionless arc-length  $s^*$  as shown in Fig. 16(b).

Table 3. Validation of numerical results.

Û2	$\theta_A \text{ (rad.)}$	rad.)	$\theta_B$ (rad.)	rad.)	$\hat{y}_{(\mathrm{max})}$	ax)	‡§	43
11	EIMª	$_{ m qMS}$	EIMa	$SM^b$	EIMa	$\mathrm{SM}^\mathrm{b}$	$\mathrm{EIM}^{\mathrm{a}}$	$\mathrm{SM}^\mathrm{b}$
9.869604	0.000000	0.000000	0.000000	0.000000	0.000000	0.00000.0	1.000000	1.000000
6	0.322394	0.322394	-0.322394	-0.322393	0.104207	0.104207	1.026530	1.026530
œ	0.482097	0.482097	-0.482097	-0.482097	0.158891	0.158891	1.060902	1.060902
1-	0.610245	0.610245	-0.610245	-0.610245	0.205576	0.205576	1.100489	1.100489
9	0.725693	0.725693	-0.725693	-0.725692	0.250650	0.250650	1.146920	1.146920
5	0.836105	0.836105	-0.836105	-0.836104	0.297307	0.297307	1.202689	1.202689
4	0.946461	0.946462	-0.946461	-0.946461	0.348461	0.348461	1.271881	1.271881
က	1.061549	1.061551	-1.061549	-1.061549	0.408121	0.408121	1.361862	1.361862
21	1.188058	1.188060	-1.188058	-1.188058	0.483723	0.483723	1.488003	1.488004
	1.339744	1.339747	-1.339744	-1.339743	0.594239	0.594240	1.691736	1.691738
0	1.570796	1.570799	-1.570796	-1.570795	0.834613	0.834614	2.188420	2.188422

<sup>a</sup>Elliptic Integral Method, <sup>b</sup>Shooting Method used in this paper.

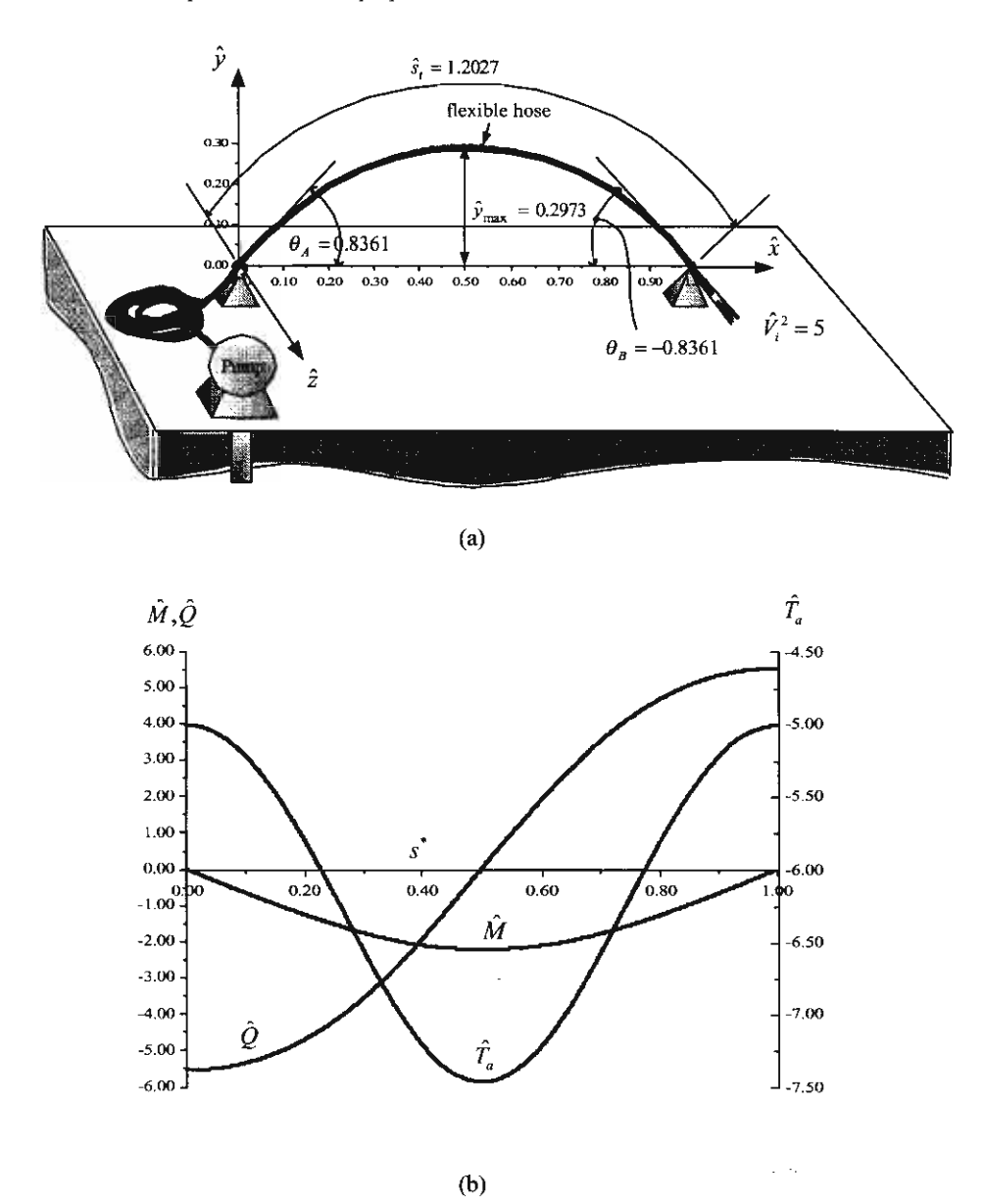


Fig. 16. Variable-arc-length pipes conveying fluid: (a) postbuckling configuration for  $\hat{V}_i = \sqrt{5}$ , (b) diagrams of bending moment, shear force, and axial force.

#### References

- T. Huang and D. W. Dareing, "Buckling and frequencies of long vertical pipes," J. Eng. Mech. Div. ACSE 99(1), pp. 167–181, 1967.
- T. Huang and D. W. Dareing, "Buckling and lateral vibration of drill pipe," J. Eng. Ind. 90, pp. 613-619, 1968.

- 3. M. M. Bernitsas, "Riser top tension and riser buckling loads," in Computer Methods for Offshore Structures, ASME, New York, pp. 101-109, 1980.
- 4. M. M. Bernitsas and T. Kokkinis, "Buckling of columns with nonmovable boundaries," J. Struct. Eng. ASCE 105(9), pp. 2113-2128, 1983.
- 5. M. M. Bernitsas and T. Kokkinis, "Buckling of columns with movable boundaries," J. Struct. Mech. 11(3), pp. 351-370, 1983.
- 6. M. M. Bernitsas and T. Kokkinis, "Asymptotic behavior of heavy column and riser stability boundaries," J. Appl. Mech. ASME 51(3), pp. 560-565, 1984.
- 7. M. A. Vaz and M. H. Patel, "Analysis of drill strings in vertical and deviated holes using the Galerkin technique," Eng. Struct. 17(6), pp. 437-442, 1995.
- 8. S. Chucheepsakul, T. Huang and T. Monprapussorn, "Large strain formulations of extensible flexible marine pipes transporting fluid," to be published in J. Fluids Struct.
- C. P. Spark, "The influence of tension, pressure and weight on pipe and riser deformations and stresses," J. Energy Resources Tech. ASME 106, 46-54, 1984.
- T. R. Goodman and J. P. Breslin, "Statics and dynamics of anchoring cables in waves," J. Hydronautic 10, 113–120, 1976.
- 11. C. M. Larsen, "Marine riser analysis," Norwegian Maritime Res. 4, pp. 15-26, 1976.
- 12. S Chucheepsakul, C. M. Wang, X. Q. He and T. Monprapussorn. "Double curvature bending of variable-arc-length elasticas," J. Appl. Mech. ASME 66(1), pp. 87-94, 1999.
- 13. W. H. Press, S. A. Teukolsky, W. T. Vettering and B. P. Flannery, Numerical Recipes in Fortran, 2nd edn., Cambridge University Press, 1992.
- 14. J. A. Nelder and R. Mead, "A simplex method for function minimization," Comp. J. 7, 308-313, 1965.
- 15. S. Chucheepsakul and T. Monprapussorn. "Divergence instability of variable-arclength elastica pipes transporting fluid," J. Fluids Struct. 14(6), pp. 895-916, 2000.
- 16. S. S. Rao, Engineering Optimization: Theory and Practice, 3rd edn., Wiley-Interscience, New York, pp. 283-286, 1996.
- 17. C. Y. Wang, "Buckling and postbuckling of heavy columns," J. Eng. Mech. ASCE 113(8), pp. 1229-1233, 1987.
- 18. C. M. Wang, "Elastic stability of heavy rotating columns," J. Eng. Mech. ASCE 116(1), pp. 234-239, 1990.
- 19. C. P. Spark, "Mechanical behavior of marine risers mode of influence of principal parameters," Deepwater Mooring and Drilling ASME, OED-7, pp. 59-81, 1979.





Ocean Engineering 29 (2002) 1067-1096

www.elsevier.com/locate/oceaneng

# Free vibrations of three-dimensional extensible marine cables with specified top tension via a variational method

Somchai Chucheepsakul \*, Narakorn Srinil

Department of Civil Engineering, King Mongkut's University of Technology Thonburi, Bangkok 10140, Thailand

Received 8 February 2001; accepted 9 May 2001

#### Abstract

This paper presents a model formulation that can be used for analyzing the three-dimensional vibration behaviours of an inclined extensible marine cable. The virtual work-energy functional, which involves strain energy due to axial stretching of the cable and virtual work done by external hydrostatic forces is formulated. The coupled equations of motion in the Cartesian coordinates of global systems are obtained by taking into account the difference between Euler's equations and equilibrium equations. The method of Galerkin finite element is used to obtain the mass and stiffness matrices which are transformed into the local coordinate systems. Then the eigenvalue problem is solved to determine its natural frequencies and corresponding mode shapes. The model formulation developed herein is conveniently applied for the cases of specified top tension. The numerical investigations are carried out to demonstrate the validity of the model and to explore in details the influence of various parameters on the behaviours of marine cables. Results for the frequency avoidance phenomenon, maximum dynamic tension and coupled transverse mode shapes are presented and discussed. © 2002 Elsevier Science Ltd. All rights reserved.

Keywords: Marine cables; Free vibrations; Coupled transverse modes; Variational method; Dynamic tension; Frequency avoidance phenomenon

<sup>\*</sup> Corresponding author. Tel.: +662-470-9146; fax: +662-427-9063. E-mail address: somchai.chu@kmutt.ac.th (S. Chucheepsakul).

#### 1. Introduction

Analysis of marine cables has been of interest due to their wide range of applications in deep-ocean engineering. Normally, marine cables deployed in undersea environments are particularly susceptible to vibration since their shapes attract fluctuating forces when situated in a current field. For this reason, most marine cable systems must be operating in a three-dimensional space, while one or two-dimensional cases are rare in practical problems. All applications require the ability to accurately predict their static and dynamic behaviour of cables.

The three-dimensional steady-state of cables has been investigated by various researchers. De Zoysa (1978), Chucheepsakul and Subwonglee (1991), Wang et al. (1993) and Friswell (1995) presented numerous hydrodynamic force models acting on the cables by using an identical model of the resulting two-point boundary value problem. The axial extensibility of the cable was not considered in their studies. Vaz and Patel (2000) have studied the three-dimensional behaviour of elastic cables subjected to arbitrary sheared currents. The results displayed the importance of current profiles on static equilibrium positions. However, all of the aforementioned studies are only limited to general steady-state cable problems and the ongoing analyses about dynamic phenomena were not accomplished continuously.

Investigations into the dynamic analysis of marine cables have also received much attention in the research literature with development of different algorithms to solve the problem. Ramberg and Griffin (1977) measured the natural frequencies of horizontal cables in air and in water and obtained good agreement with the linear theory of Irvine and Caughey (1974) for extensible cables having small sag. Griffin and Rosenthal (1988) extended the studies into inclined slack cables with and without arrays of attached discrete masses by using cable properties from Triantafyllou (1984). Due to hydrodynamic drag forces, the dynamics of marine cables are quite different from the cable in air, as proposed by Vassalos and Huang (1996). All the numerical solutions for three-dimensional vibrations, which are mentioned above begin with the derivation of a theoretical model about a planar and sagged equilibrium configuration leading to the associated eigenvalue problems governing free inplane and out-of-plane motions, referring to the case of submerged cables. The outof-plane motions are well described by using the taut string approximation but the in-plane motions induce mainly longitudinal and transverse cable deflections. These motions have been investigated analytically by Perkins and Mote (1987), Behbahani-Nejad and Perkins (1996). Nevertheless, they do not take into consideration marine cables having three-dimensional equilibrium profiles resulting from the action of hydrodynamic drag forces.

There are some efforts to extend the numerical analysis into three-dimensional dynamics of elastic marine cables, such as Huang (1994), Sun and Leonard (1998), but no comprehensive studies concerning the free vibration behaviours rigorously. Especially on the natural frequencies and corresponding mode shapes, these research works are very limited. Moreover, the analyses in most studies based on the specified unstrained arc-length are rare in practical problems when the cable is limited to the physical condition such as the given allowable tensile strength of cable material.

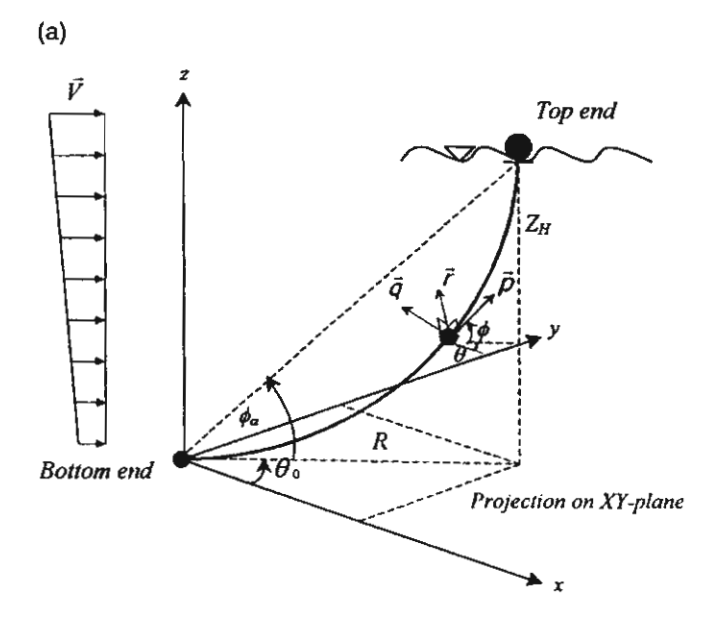
According to this restriction, the numerical technique in which the top-point tension specified first as the constant input parameter is recommended herein. Consequently, this is the first time that the natural frequencies corresponding to the coupled transverse modes, which are necessary for predicting the dynamic behaviours of elastic marine cables, is presented.

The main objective of this study is to present the cable model formulation for analyzing the three-dimensional motions of an inclined extensible marine cable based on the work-energy variational principle. The hydrodynamic damping vanishes but added mass is still considered to obtain three linearized undamped free vibration equations of motion. These equations can be readily applied through the case of submerged cables. Numerical results for two case studies are conveniently shown in the form of non-dimensionalized quantities tabularly and graphically. The first case is to investigate more details for out-of-plane motion and to explain the dynamic behaviour of a submerged cable by comparing it to a cable in air. The second case is to present new numerical results of marine cables in ocean studies. The natural frequencies and corresponding mode shapes for various configurations are demonstrated, in order to show the effect of current direction on the cable behaviour and to show how cables vibrate in the form of coupled motion. The effects of axial extensibility on the natural frequencies for both cases are also presented herein. Finally, the effect of sag or curvature on the natural frequencies associated with the lateral deflections are investigated for predicting dynamic tensions that can be induced during the motion of the cables.

#### 2. Derivation of equations of motion

Fig. 1a shows the reference configuration systems of the marine cables between the Cartesian coordinate system represented by unit vectors  $\vec{i}, \vec{j}, \vec{k}$  and the local system represented by three orthogonal unit vectors  $\vec{p}, \vec{q}, \vec{r}$ , i.e. tangential, bi-normal and normal vectors, respectively. The geometric compatibility relation of both systems can be written in the form of a matrix as

where  $\phi$  is the vertical angle between the XY plane and vector  $\vec{p}$ ,  $\theta$  is the horizontal angle between the XZ plane and projection line of vector  $\vec{p}$ , when vector  $\vec{q}$  lies on the XY plane. A cable is installed by two unmovable pinned-supports at the top and bottom ends. The top end is tied to the floating structure whereas the bottom end is anchored on the seabed. With regards to Fig. 1b, it can be seen the circular plan view of cable configuration (De Zoysa, 1978) in which  $\theta_0$  is the horizontal angle



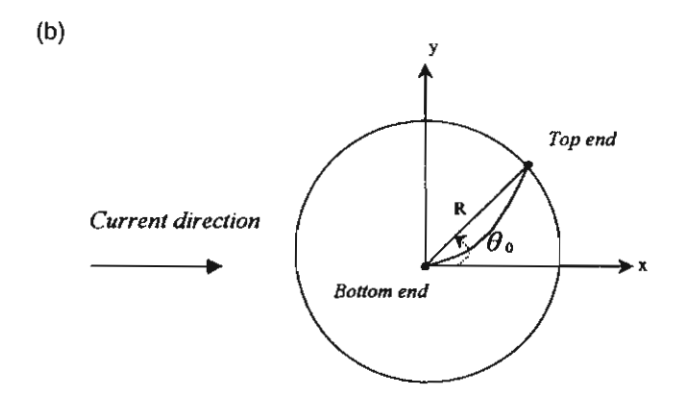


Fig. 1. (a) Reference configurations and coordinate systems of marine cables. (b) Plan view of cable configurations.

between the X-axis direction and the projection line of cable chord length onto XY plane, R is the horizontal distance projected onto the seabed between the top and bottom ends. The X-axis is also the current direction. Fig. 2 displays the infinitesimal element of cable in which u,v and w are the components of displacement from the equilibrium position in the direction of unit vectors  $\vec{i}, \vec{j}, \vec{k}$ , respectively.

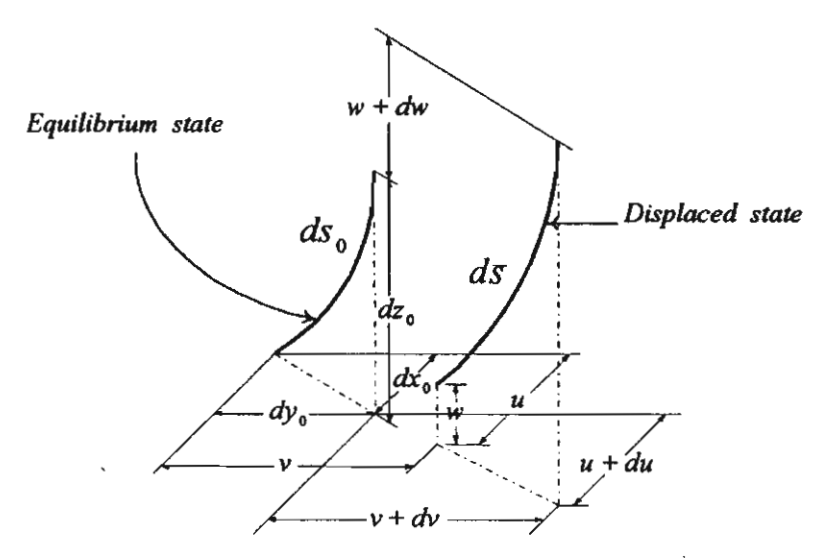


Fig. 2. Two different states of cables.

#### 2.1. Governing equations

Considering an element having an unstretched arc-length ds, its length at an equilibrium state is

$$ds_0 = \sqrt{1 + x_0^2 + y_0^2} \cdot dz_0 \tag{2}$$

in which a superscript prime denotes a differentiation with respect to  $z_0$ . Let  $\sqrt{1+x_0'^2+y_0'^2}$  be  $s_0'$ , another form of  $ds_0$  using Lagrangian strain definition is

$$ds_0 = (1 + \varepsilon_0) ds ag{3a}$$

Thus

$$ds = \frac{s'_0}{1 + \varepsilon_0} \cdot dz_0 \tag{3b}$$

Likewise, the arc length  $d\bar{s}$ , the strain  $\bar{\varepsilon}$  and the displacements u, v and w at the displaced state are given by

$$d\bar{s} = \sqrt{(x_0' + u')^2 + (y_0' + v')^2 + (1 + w')^2} \cdot dz_0 \tag{4}$$

$$d\bar{s} = (1 + \bar{\epsilon}) ds \tag{5}$$

From Eqs. (2) to (5) one can write the strain at the displaced state as

$$\bar{\varepsilon} = \frac{d\bar{s} - ds}{ds} = \frac{1 + \varepsilon_0}{s_0'} \sqrt{(\dot{x_0} + u')^2 + (\dot{y_0} + v')^2 + (1 + w')^2} - 1 \tag{6}$$

and its variation can be written as

$$\delta \bar{\varepsilon} = \frac{1 + \varepsilon_0}{s_0'} \left[ \frac{(x_0' + u')\delta u' + (y_0' + v')\delta v' + (1 + w')\delta w'}{\sqrt{(x_0' + u')^2 + (y_0' + v')^2 + (1 + w')^2}} \right]$$
(7)

#### 2.2. Strain energy due to axial deformation

The strain energy due to axial deformation is caused by two actions: pulling on the cable due to axial tension and squeezing of cable due to hydrodynamic pressure (Sparks, 1984). The strain energy expression is written as

$$U = \int_{0}^{s_{t}} \frac{1}{2} E A \bar{\varepsilon}^{2} ds + \int_{0}^{s_{t}} 2 \nu \rho_{w} g A_{0}(Z_{H} - z_{0}) d\bar{s}$$
 (8)

where  $S_t$  is the total undeformed arc-length,  $\bar{S}_t$  is the total deformed arc-length, E is Young's modulus, A and  $A_0$  is the undeformed and deformed cable cross sectional areas, respectively. Using Eqs. (3), (6) and (7), the variation of Eq. (8) becomes

$$\delta U = \int_{0}^{z_{H}} \left\{ \left[ T_{a} + T_{b} \left( 1 - \frac{1}{\sqrt{1 + 2\lambda}} \right) \right] \left[ \frac{(x_{0}' + u')\delta u' + (y_{0}' + v')\delta v' + (1 + w')\delta w'}{s_{0}'} \right] \right\} dz_{0}$$
(9)

in which

$$\lambda = \frac{x_0^{'}u^{\prime} + y_0^{'}v^{\prime} + w^{\prime} + \frac{1}{2}(u^{\prime 2} + v^{\prime 2} + w^{\prime 2})}{s_0^{\prime 2}}$$
(10)

 $T_a = EA \varepsilon_0 + 2v \rho_w g A_0 (Z_H - z_0)$  and  $T_b = EA - 2v \rho_w g A_0 (Z_H - z_0)$ , when  $Z_H$  is the total sea depth. If Poisson's ratio v is set to zero it states that there is no reduction in cable diameter, then  $T_a$  is equal to the actual cable tension and axial strain is proportional to this tension (Burgess, 1993). By neglecting small quantities of higher order term and using the binomial approximation, Eq. (10) reduces to

$$\lambda \cong \frac{x'_{0}u' + y'_{0}v' + w'}{s'_{0}^{2}}$$
 (11a)

and

$$\frac{1}{\sqrt{1+2\lambda}} \cong 1 - \lambda \tag{11b}$$

Substituting Eq. (11) into Eq. (9) yields

$$\delta U = \int_{0}^{Z_{H}} \left\{ \frac{T_{a}}{s_{0}'} (x_{0}' + u') + \frac{T_{b}}{s_{0}'^{3}} (x_{0}'^{2}u' + x_{0}'y_{0}'v' + x_{0}'w') \right] \delta u'$$

$$\delta U = \int_{0}^{Z_{H}} \left\{ \frac{T_{a}}{s_{0}'} (y_{0}' + v') + \frac{T_{b}}{s_{0}'^{3}} (x_{0}'y_{0}'u' + y_{0}'^{2}v' + y_{0}'w') \right] \delta v'$$

$$\left\{ \frac{T_{a}}{s_{0}'} (1 + w') + \frac{T_{b}}{s_{0}'^{3}} (x_{0}'u' + y_{0}'v' + w') \right\} \delta w'$$

$$\left\{ \frac{T_{a}}{s_{0}'} (1 + w') + \frac{T_{b}}{s_{0}'^{3}} (x_{0}'u' + y_{0}'v' + w') \right\} \delta w'$$

$$\left\{ \frac{T_{a}}{s_{0}'} (1 + w') + \frac{T_{b}}{s_{0}'^{3}} (x_{0}'u' + y_{0}'v' + w') \right\} \delta w'$$

At equilibrium state, Eq. (12) may be expressed by evaluating at u, v, w, u', v', w' and  $\lambda = 0$  as

$$\delta U = \int_{0}^{Z_H} \frac{T_a}{\dot{s_0}} (\dot{x_0} \delta u' + \dot{y_0} \delta v' + \delta w') dz_0$$
 (13)

#### 2.3. Virtual work done by external forces

The virtual work done by effective weight of submerged cable is expressed as

$$\delta W_{\epsilon} = -\int_{0}^{Z_{H}} \frac{w_{\epsilon} s_{0}'}{1 + \varepsilon_{0}} \delta w \cdot dz_{0}$$
 (14)

where  $w_e$  is the effective weight of the cable.

The virtual work done by inertia force is

$$\delta W_i = -\int_0^{z_H} (\bar{m}\ddot{u}\delta u + \bar{m}\ddot{v}\delta v + \bar{m}\ddot{w}\delta w) \cdot dz_0$$
 (15)

where  $\bar{m} = [w_C/g(1 + \varepsilon_0)]s_0'$  is the cable mass per unit stretched length at the equilibrium state, and  $w_C$  is the cable's weight per unit unstretched length.

The virtual work done by hydrodynamic forces is written as

$$\delta W_{H} = \int_{0}^{z_{H}} (F_{u}\delta u + F_{v}\delta v + F_{w}\delta w) s_{0}^{\prime} dz_{0}$$
 (16)

in which the subscripts u, v and w are the components of forces per unit arc-length in the Cartesian system corresponding to these following expressions

$$\vec{i}$$
 direction:  $F_u = D_{pu} + D_{qu} + D_{ru}$  (17a)

$$\vec{j}$$
 direction:  $F_v = D_{pv} + D_{qv} + D_{rv}$  (17b)

$$\vec{k}$$
 direction:  $F_w = D_{pw} + D_{qw} + D_{rw}$  (17c)

where  $D_p$ ,  $D_q$  and  $D_r$  are the tangential and normal components of the Morison's drags and inertia forces due to added mass per unit arc length that can be simply expressed as

$$D_{p} = \frac{1}{2} \rho_{\mathsf{u}} \pi D_{0} C_{DT} \dot{\bar{\rho}} |\dot{\bar{\rho}}| + \rho_{\mathsf{u}} A_{0} C_{A} \ddot{\bar{\rho}}$$
(18a)

$$D_{q} = \frac{1}{2} \rho_{\text{w}} D_{0} C_{DN} \dot{q} \dot{q} + \rho_{\text{w}} A_{0} C_{A} \ddot{q}$$
 (18b)

$$D_{r} = \frac{1}{2} \rho_{v} D_{0} C_{DN} \dot{\vec{n}} \dot{\vec{n}} + \rho_{v} A_{0} C_{A} \ddot{\vec{r}}$$
 (18c)

The tangential and normal drag forces are proportional to the square of tangential and normal relative fluid velocities (Friswell, 1995), in which  $\dot{p}(\dot{q},\dot{r})$ ,  $\ddot{p}(\ddot{q},\dot{r})$  are the relative velocity and acceleration of the cable and fluid particle in unit vectors  $\vec{p}$ ,  $\vec{q}$  and  $\vec{r}$ ,  $C_A$  is equal to  $C_{M^-}1$  and  $C_{DT}$ ,  $C_{DN}$ ,  $C_A$ ,  $C_M$  are the tangential drag, normal drag, added mass and inertia coefficients, respectively. The model of current profile chosen here is defined in Appendix A.

#### 2.4. Euler's equations

The virtual work-energy of the marine cable system is written as

$$\delta\Pi = \delta U - \delta W_e - \delta W_i - \delta W_H \tag{19}$$

Substitution of Eqs. (12), (14), (15) and (16) into Eq. (19), then integration by parts of Eq. (19) is performed by evaluating  $\delta u = \delta v = \delta w = 0$  at boundary conditions  $(z_0 = 0 \text{ and } z_0 = Z_H)$ . Then, Euler's equations associated with the virtual displacement  $\delta u$ ,  $\delta v$  and  $\delta w$  are obtained respectively as

$$\left[\frac{T_a}{s_0'}(x_0+u')+\frac{T_b}{s_0'^3}(x_0'^2u'+x_0'y_0'v'+x_0'w')\right]-m\ddot{u}=-(D_{pu}+D_{qu}+D_{ru})s_0'$$
(20)

$$\left[\frac{T_a}{s_0'}(\dot{y_0} + v') + \frac{T_b}{s_0'^3}(\dot{x_0}\dot{y_0}u' + \dot{y_0'^2}v' + \dot{y_0}w')\right] - \bar{m}\ddot{v} = -(D_{\rho v} + D_{qv} + D_{rv})s_0'$$
 (21)

$$\left[\frac{T_{a}}{s_{0}^{'}}(1+w')+\frac{T_{b}}{s_{0}^{''}}(x_{0}u'+y_{0}v'+w')\right]-\bar{m}\bar{w}=-\left(D_{pw}+D_{qw}+D_{rw}-\frac{w_{e}}{1+\varepsilon_{0}}\right)s_{0}^{'}$$
(22)

#### 2.5. Equilibrium equations

By substituting the equilibrium conditions u = v = w = u' = v' = w' = u'' = v'' = w'' = u'' =

$$\left(\frac{T_{a}x_{0}'}{\dot{s_{0}}}\right)' + (\tilde{D}_{pu} + \tilde{D}_{qu} + \tilde{D}_{ru})\,\dot{s_{0}} = 0 \tag{23}$$

$$\left(\frac{T_{a}y_{0}^{'}}{s_{0}^{'}}\right)' + (\tilde{D}_{pv} + \tilde{D}_{qv} + \tilde{D}_{rv}) s_{0}^{'} = 0$$
(24)

$$\left(\frac{T_a}{s_0'}\right)' + \left(\tilde{D}_{pw} + \tilde{D}_{qw} + \tilde{D}_{rw} - \frac{w_e}{1 + \varepsilon_0}\right) s_0' = 0 \tag{25}$$

A superscript (~) represents for the components of drag force derived from Eq. (18) when the latter terms of them vanish. It is seen that the equilibrium profile of a marine cable is formed in three-dimensional space before vibrating.

#### 2.6. Coupled equations of motion

Subtracting Eq. (20) with Eq. (23), Eq. (21) with Eq. (24), and Eq. (22) with Eq. (25) yields the equation of motion in the directions of u, v and w, respectively. Three equations are consequently written as

$$\frac{T_a u''}{s_0'} + \frac{T_b}{s_0'^3} (x_0'^2 u'' + x_0' y_0' v'' + x_0' w'') - m\ddot{u} = \rho_w A_0 C_A s_0' \ddot{u}$$
 (26)

$$\frac{T_a v''}{\dot{s_0}} + \frac{T_b}{\dot{s_0'}^3} (\dot{x_0} \dot{y_0'} u'' + \dot{y_0'}^2 v'' + \dot{y_0'} w'') - \bar{m} \ddot{v} = \rho_w A_0 C_A \dot{s_0} \ddot{v}$$
 (27)

$$\frac{T_a w''}{s_0'} + \frac{T_b}{s_0'^3} (x_0' u'' + y_0' v'' + w'') - \bar{m} \ddot{w} = \rho_w A_0 C_A s_0' \ddot{w}$$
 (28)

For undamped free vibration analysis, only the added mass terms are considered, Eqs. (26), (27) and (28) can be rearranged in the form of matrix notation as

$$[A]\{\ddot{u}\} + [B]\{u''\} = \{F\} \tag{29}$$

where

$$\{u\} = \begin{cases} u \\ v \\ w \end{cases}, \tag{30a}$$

$$[A] = \begin{bmatrix} \bar{m} & 0 & 0 \\ 0 & \bar{m} & 0 \\ 0 & 0 & \bar{m} \end{bmatrix}, \tag{30b}$$

$$\{F\} = -\rho_{w}A_{0}C_{A}s_{0}\left\{\begin{array}{c} \ddot{u} \\ \ddot{v} \\ \ddot{w} \end{array}\right\}$$
(30c)

$$[B] = -\begin{bmatrix} \frac{T_a}{s_0'} + \frac{T_b x_0'^2}{s_0'^3} & \frac{T_b x_0' y_0}{s_0'^3} & \frac{T_b x_0'}{s_0'^3} \\ \frac{T_b x_0' y_0'}{s_0'^3} & \frac{T_a}{s_0'} + \frac{T_b y_0'^2}{s_0'^3} & \frac{T_b y_0'}{s_0'^3} \\ \frac{T_b x_0'}{s_0'^3} & \frac{T_b y_0'}{s_0'^3} & \frac{T_a}{s_0'} + \frac{T_b}{s_0'^3} \end{bmatrix}$$

$$(31)$$

For problems of submerged cables lying on the XZ plane, equilibrium configurations are obtained from Eqs. (23) and (25) by neglecting the components of drag force, i.e. the cable suspended only by its own effective weight. These lead to the associated problems governing the in-plane motions, which decouple from the out-of-plane motion in the Cartesian coordinates. The coupled in-plane motions are described by the in-plane components, u and w, and the out-of-plane motion is described by the out-of-plane component, v. By evaluating y' = 0, Eq. (31) becomes

$$[B] = -\begin{bmatrix} \frac{T_a}{s_0'} + \frac{T_b x_0'^2}{s_0'^3} & 0 & \frac{T_b x_0'}{s_0'^3} \\ 0 & \frac{T_a}{s_0'} & 0 \\ \frac{T_b x_0'}{s_0'^3} & 0 & \frac{T_a}{s_0'} + \frac{T_b}{s_0'^3} \end{bmatrix}$$
(32)

Assembling Eqs. (30b) and (30c) together yields

$$[\bar{A}]\{\bar{u}\} + [B]\{u''\} = \{0\} \tag{33}$$

in which

and  $\bar{m} = \bar{m} + \rho_w A_0 C_A s_0$ 

#### 3. Static solution

Since the closed form solution of nonlinear equilibrium equations ((23)–(25)) is generally unavailable. A numerical scheme recommended herein for solving the three-dimensional equilibrium configuration is the finite element discretization applied with the specified top-point tension. Under an independent variable  $z_0$ , only the variation of horizontal displacements is considered,  $\delta w = 0$ . The reference cable configuration is determined by substitution of Eqs. (12), (14), (15) and (16) into (19) once again, and then the form of a hybrid formulation is modified by rearrangement of Eq. (19) as

$$\delta \Pi = \delta \int_{0}^{Z_{H}} [T_{a}\sqrt{1 + (x'_{0} + u')^{2} + (y'_{0} + v')^{2}} - \bar{F}_{u}s'_{0}u - \bar{F}_{v}s'_{0}v]dz_{0} = 0$$
 (35)

where  $\bar{F}_u = \tilde{D}_{pu} + \tilde{D}_{qu} + \tilde{D}_{ru}$  and  $\bar{F}_v = \tilde{D}_{pv} + \tilde{D}_{qv} + \tilde{D}_{rv}$ . At the displaced state,  $x = x_0 + u$ ,  $y = y_0 + v$ , hence  $x' = x_0' + u'$ ,  $\delta x = \delta u$ ,  $\delta x' = \delta u'$ ,  $y' = y_0' + v'$ ,  $\delta y = \delta v$  and  $\delta y' = \delta v'$ . At the equilibrium state,  $x = x_0$  and  $y = y_0$ , then Eq. (34) can be conveniently simplified to

$$\delta\Pi = \delta \int_{0}^{z_{H}} (T_{a}\sqrt{1 + x_{0}^{'2} + y_{0}^{'2}} - \bar{F}_{u}s_{0}^{'}x_{0} - \bar{F}_{v}s_{0}^{'}y_{0})dz_{0} = 0$$
 (36)

Three unknowns to be involved substantially in the algorithm consist of  $x_0(z_0)$ ,  $y_0(z_0)$  and  $\varepsilon_0(z_0)$ . The relevant equilibrium equation corresponding to the tangential direction of a cable segment, representing the cable tension at any point, is considered and converted to the integral expression as follows,

$$T_a(z_0) = T_H - \int_{z_0}^{z_H} \left[ \frac{w_e}{(1 + \varepsilon_0)} - \tilde{D}_p \sqrt{1 + x_0^2 + y_0^2} \right] dz_0$$
 (37)

Using the combination of Eqs. (36) and (37), these algorithm technique is appropriate and efficient for solving the cable problem of which the top-point tension  $T_H$  is specified.

A set of vertical discrete elements of ocean depth is depicted in Fig. 3. The horizontal projection of element coordinates  $x_0(z_0)$  and  $y_0(z_0)$  on the XZ and YZ planes consist of two components which are linear  $(x_L, y_L)$  and non-linear  $(x_{NL}, y_{NL})$ . The linear parts  $(x_L, y_L)$  are directly obtained from the specified cable positions while the non-linear parts  $(x_{NL}, y_{NL})$  are approximated by a cubic polynomials shape function in  $z_0$ , hence

$$[N_s] = \begin{bmatrix} N_1 & N_2 & 0 & 0 & N_3 & N_4 & 0 & 0 \\ 0 & 0 & N_1 & N_2 & 0 & 0 & N_3 & N_4 \end{bmatrix}$$
(39)

$$\{q\} = \left[ x_{NL}(0) \ x_{NL}(0) \ y_{NL}(0) \ y_{NL}(0) \ x_{NL}(h) \ x_{NL}(h) \ y_{NL}(h) \ y_{NL}(h) \right]^{T}$$
(40)

in which  $[N_s]$  is the matrix of the shape function in which each component is defined in Appendix B, and  $\{q\}$  is the degree of freedom of nodal displacements and rotation. For the kinematic relations of strain, the matrix notations can be written as

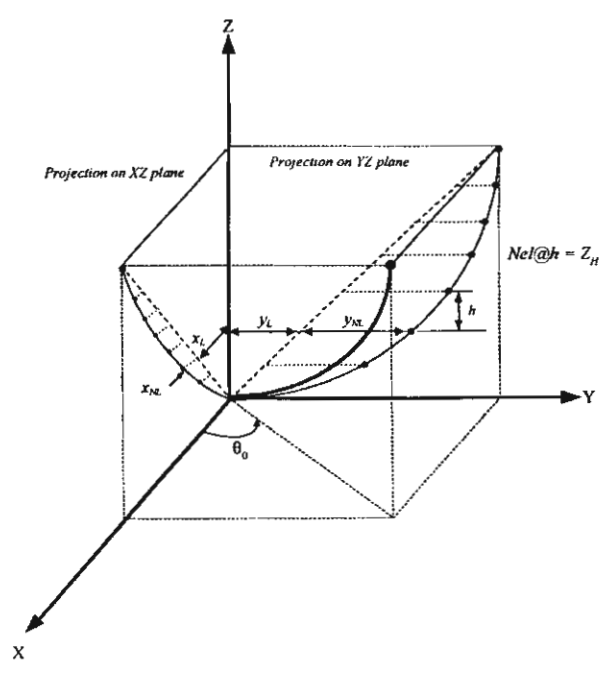


Fig. 3. Horizontal projection of the finite element coordinates on XZ and YZ planes.

$$\varepsilon_0 = \lfloor L \rfloor \{e\} \tag{41}$$

$$\lfloor L \rfloor = \lfloor 1 - z_0 / h \ z_0 / h \rfloor \tag{42}$$

$$\{e\} = \lfloor \varepsilon_0(0) \ \varepsilon_0(h) \rfloor^T \tag{43}$$

where  $\lfloor L \rfloor$  is the matrix of the strain shape function and  $\{e\}$  is the nodal strain. The global equilibrium condition  $\delta \Pi = (\partial \pi/\partial q_i)\delta \ q_i = 0$  yields a system of non-linear equations. Consequently, by the Newton-Raphson iterative algorithm, one can write the incremental process as follows

$$[K_s]\{\Delta Q\} = -\{R\} \tag{44}$$

Consider the  $k^{th}$  element, the contribution to the square matrix  $[K_s]_k$  and to the column vector  $\{R\}_k$  are as follows,

$$[K_s]_k = \left[\frac{\partial^2 \pi_k}{\partial q_i \partial q_j}\right] = \int_0^h \frac{[N_s]^T T_a[N_s]}{(1 + x_0^2 + y_0^2)^{3/2}} \, dz_0 \tag{45}$$

$$\{R\}_{k} = \left\{\frac{\partial \pi_{k}}{\partial q_{i}}\right\} = \int_{0}^{h} \left[\frac{[N_{s}]T_{a}}{(1 + x_{0}^{'2} + y_{0}^{'2})^{1/2}} \begin{cases} x_{0}^{'} \\ y_{0}^{'} \end{cases} - [N_{s}]^{T} \begin{cases} \bar{F}_{u} \\ \bar{F}_{v} \end{cases} \right] dz_{0}$$

$$(46)$$

in which h is an element height, Q and q are the global and local degrees of freedom, respectively. Eqs. (45) and (46) are evaluated by using Gaussian quadrature numerical integration. The boundary conditions are the zero value of non-linear parts of coordinates at  $z_0 = 0$  and  $Z_H$ . The detailed procedure and numerical examples for the static case are given comprehensively by Petchpeart (1999).

#### 4. Dynamic solution

Continuing from the static analysis in discretization of domain, the assumed displacement fields for a single element in the Cartesian systems u, v and w are approximated by

$$\{\tilde{u}\}\cong[N]\{d\}\tag{47}$$

where

$$\{d\} = \begin{bmatrix} u_1 & u'_1 & v_1 & v'_1 & w_1 & w'_1 & u_2 & u'_2 & v_2 & v'_2 & w_2 & w'_2 \end{bmatrix}^T \tag{48}$$

$$[N] = \begin{bmatrix} N_1 & N_2 & 0 & 0 & 0 & 0 & N_3 & N_4 & 0 & 0 & 0 & 0 \\ 0 & 0 & N_1 & N_2 & 0 & 0 & 0 & N_3 & N_4 & 0 & 0 \\ 0 & 0 & 0 & N_1 & N_2 & 0 & 0 & 0 & 0 & N_3 & N_4 \end{bmatrix}$$
(49)

Here  $N_i$ , i=1,2,3,4 represent the weight functions and are the same cubic polynomial shape functions as those used in static analysis. Following the standard procedure of Galerkin finite element method proposed by Cook et al. (1989), and if the displacements in the rectangular coordinates are transformed to the local displacement fields in the  $\vec{p} - \vec{q} - \vec{r}$  vector systems, the structural equation of motion (Eq. 33) in the matrix form is obtained

$$[M]\{\ddot{D}\} + [K]\{D\} = \{0\} \tag{50}$$

where  $\{\vec{D}\}$  and  $\{D\}$  are the acceleration and displacement vectors, respectively, in the coordinate systems of  $\vec{p} - \vec{q} - \vec{r}$  vectors, [M] is the total mass matrix defined as

$$[M] = \sum_{j=1}^{Net} \int_{0}^{h} [T]^{T} [N]^{T} [\bar{A}] [N] [T] dz_{0}$$
 (51)

and [K] is the total stiffness matrix defined as

$$[K] = \sum_{j=1}^{Nel} \int_{0}^{h} [T]^{T} [N']^{T} [\bar{B}] [N'] [T] dz_{0}$$
 (52)

in which Nel is the total number of used elements and [T] is the transformation matrix expressed by the following notation,

where subscripts j and j+1 denote the first and second node of the individual cable segment, and  $T(i) = T(\theta, \phi, \theta', \phi')$  is defined in Appendix C. It can be noted that

$$\theta = \tan^{-1}(y_0/x_0) \tag{54a}$$

S. Chucheepsakul, N. Srinil / Ocean Engineering 29 (2002) 1067-1096 1081

$$\phi = \tan^{-1} \left( \frac{1}{\sqrt{x_0^{'2} + y_0^{'2}}} \right) \tag{54b}$$

$$\theta' = \left(\frac{x_0'y_0' - y_0'x_0'}{x_0'^2 + y_0'^2}\right)$$
 (54c)

and

$$\phi' = \frac{-(x_0'x_0'' + y_0'y_0'')}{(1 + x_0'^2 + y_0'^2)\sqrt{x_0'^2 + y_0'^2}}$$
(54d)

Under this coordinate transformation treatment, the physical meaning of cable behaviour can be clearly seen and the mode shapes of cable vibrations can be described explicitly. For harmonic undamped free vibration, Eq. (50) leads to the following eigenvalue problem

$$([K] - \omega^2[M])\{\bar{D}\} = \{0\}$$
 (55)

where  $\omega_i$  is the natural frequency of vibration and  $\{\vec{D}\}$  is the corresponding mode shapes in the  $\vec{p} - \vec{q} - \vec{r}$  coordinates. The boundary conditions are the zero values of cable displacements at the top and bottom ends. Finally, the eigenvalue problem is solved using the method of inverse iteration.

#### 5. Numerical results and discussions

Certain checks must be made first to test the validity of the model formulation and the procedure presented herein. The finite element model used in the analysis also calculates the out of plane and in-plane frequencies for a cable starting from the 2D equilibrium configuration, in addition to the frequencies of three dimensional coupled motions. After transforming coordinates, the out-of-plane motion is specified by the  $\vec{q}$  (bi-normal) direction and the in-plane motions are specified by the  $\vec{p}$  (tangential) and  $\vec{r}$  (normal) directions.

A simple case of an inclined extensible cable in air suspended by its own weight is considered. The distributed external load can be expressed as  $w_c\sqrt{1+x_0^2}/(1+\varepsilon_0)$ , representing the uniform weight of cable per unit stretched length associated with the actual cable tension. This tension is modified in order to handle the corresponding static configurations. The in-plane and out-of-plane dimensionless frequencies for the first for modes are favorably compared with Henghold et al. (1977) in Table 1 for a value of cable stiffness to weight ratio EA/mgL=5000, and dimensionless frequencies formed as  $\bar{\omega} = \omega/\sqrt{g/L}$ , in which L is the unstretched cable length. Considering these results, the authors believed that the model formulation developed herein would yield sufficient accuracy in applications. In the next examples, the numerical results for predicting the three-dimensional vibration behaviour of a cable are considered.

Table 1 Comparisons of the first four dimensionless frequencies for an inclined extensible cable in air for a value of  $AE/mgL=5000^{\circ}$ 

Mode	Dimensionless frequencies, &						
	Inclined cable 30°		Inclined cable 60°				
	This study (40 elements)	Henghold et al. (1977)	This study (40 elements)	Henghold et al. (1977)			
0	2.84	2.83	2.24	2.24			
I	5.28	5.17	3.57	3.65			
0	5.63	5.67	4.45	4.53			
I	8.34	8.17	6.01	6.30			

<sup>&</sup>lt;sup>a</sup> O: out-of-plane modes; I: in-plane modes.

#### 5.1. Out-of-plane motions

Since Griffin and Rosenthal (1988) have illustrated the hybrid behaviour of the frequency plots for an inclined cable in air, the following results will confirm the same behaviours with sag to length ratio for an inclined submerged cable as shown in Fig. 4. The only difference is that the natural frequencies in each mode decrease when the cable in air moves to under water. For in-plane motion, the frequency of the first mode approaches that of the second mode with an increase of cable sag-to-length ratio and so on. The mode shapes become hybrid (not symmetry or anti-

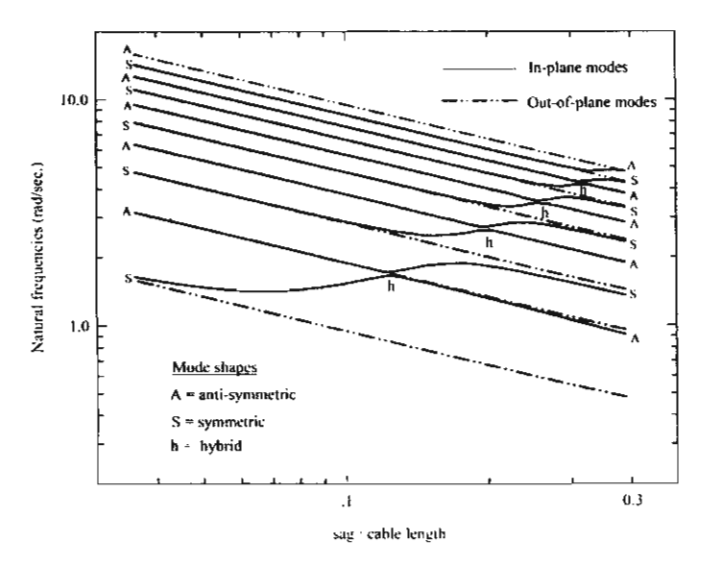


Fig. 4. The first ten in-plane and out-of-plane frequencies for an inclined extensible submerged cable as a function of cable sag to cable length ratio.

symmetry) and the modal crossover is not found. On the other hand, the frequency is remarkably linear with sag for the out-of-plane motion. These appearances are well-known and were discussed intensively by Triantafyllou (1984).

It was known from Burgess and Triantafyllou (1988) that the in-plane frequencies corresponding to elastic mode shapes depend significantly on the elastic modulus of the cable material. A further result is to demonstrate the effect of extensibility on the out-of-plane frequencies of inclined submerged cables. To facilitate the numerical results, a value of top-point tension to cable stiffness ratio is formed from the following dimensionless quantity  $T_H/EA$ . Fig. 5a and b shows the first five out-of-plane frequencies for an inclined extensible submerged cable, versus the different values of  $T_H/EA$ , which are fixed in value of specified top-point tension and cable cross-sectional area for cable having a value of vertical chord inclination angle  $\phi_{\alpha}$  equal to 60 and 36 degrees, respectively. For every nonzero chord inclination, the out-of-plane frequencies decrease with the increase in value of elastic modulus and stand constantly for high value of elastic modulus or very low extensible cable. Furthermore, by comparing Fig. 5a and b, the out-of-plane frequencies increase with the increase of chord inclination angle.

#### 5.2. Coupled transverse motions

The focus of this study is to demonstrate the coupling of three-dimensional motion considered with the small amplitude assumptions for marine cables, which are not reported elsewhere. At the static equilibrium state, the time-independent drag forces resulted from the steady current velocity in the X-axis direction are included in the calculations. It is quite difficult to explain the vibration behaviours because of the coupled motion, however it can be properly described by the natural frequencies. Hence, in order to show the preliminary numerical investigation, the effect of changes in the horizontal chord inclination angle to the X-axis, i.e.  $\theta_0$ , and the extensibility on the natural frequencies were carried out to be the numerical example using the cable properties defined in Table 2.

Numerical results as given in Table 3 show the first four natural frequencies of marine cable under the variations in values of  $\theta_0$  from 0 to 180 degrees in each value of the extensibility index  $T_H/EA$ . A value of  $\theta_0$  is varied considerably from 0 to 180 degrees so that the significance of current direction can be clearly seen when maintaining the uniform current profile in the X-axis direction. An interesting result from this study is that there are virtually no differences in the natural frequencies in each mode with the different angles of  $\theta_0$ . In odd modes, the natural frequencies form like a taut string, since the frequencies of the next odd modes and the higher ones (not shown herein) are found to be multiples of the first mode. Moreover, the frequencies tend to decrease with the increasing value of elastic modulus and to be unchanged for a high value of elastic modulus, as well as out-of-plane motion. By contrast, the natural frequencies for the even modes increase with an increase in value of elastic modulus, as well as the in-plane motion in the case of submerged cable (Chucheepsakul and Huang, 1997)

However, when the value of  $\theta_0$  increases, these appears to be a modal transition

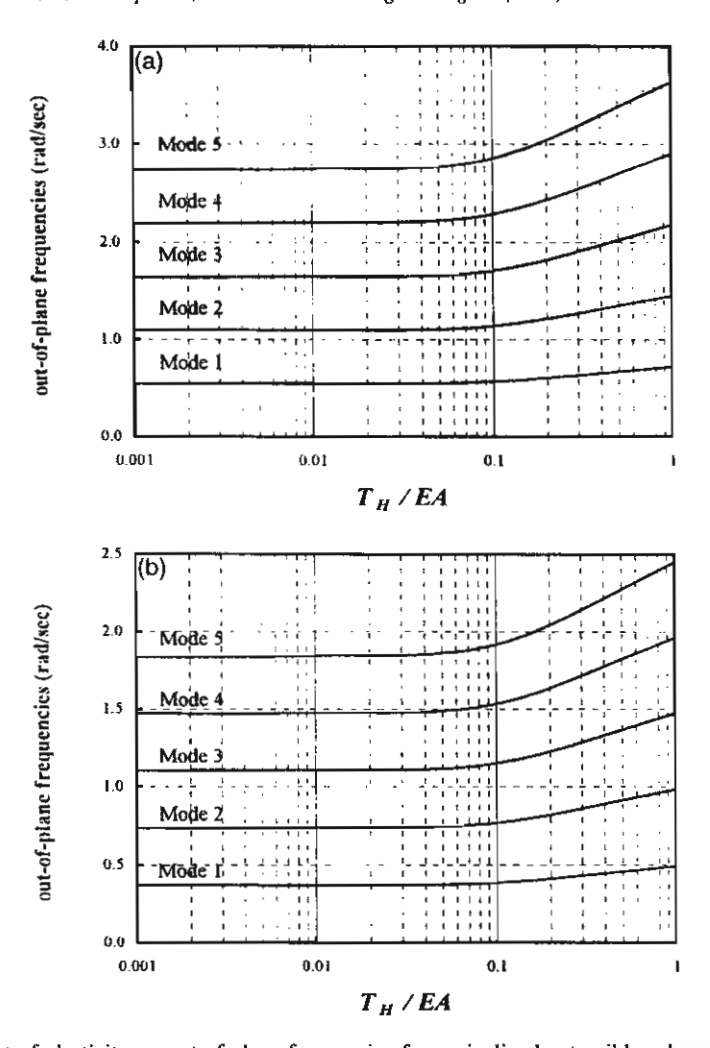


Fig. 5. Effect of elasticity on out-of-plane frequencies for an inclined extensible submerged cable, for the different values of  $T_H/EA$ , (a)  $\phi_{\alpha}$ = 60 degrees and (b)  $\phi_{\alpha}$ = 36 degrees.

of cable shapes developing from value of  $\theta_0$  from 0 to 180 degrees as shown in Fig. 6, which plots the first two normalized mode shapes  $(\eta)$  as the non-dimensionalized are-length  $(\xi)$ . Considering these local standing modes, two distinct physical mechanisms of vibration are identified. These correspond to the longitudinal or elastic modes and the coupled transverse modes, which are dominated substantially and simultaneously by the bi-normal and normal amplitudes.

As reported by Burgess and Triantafyllou (1988), the elastic modes, which can occur in much higher order modes, do not appear to be also presented here in the low mode. Only in angles,  $\theta_0$ =0 and 180 degrees, the frequencies of the odd modes and even modes corresponding to the out-of-plane and in-plane motions, respectively. Because the current direction is parallel to the X-axis line, therefore the force compo-

Table 2
Cable properties for program input parameters

Cable properties	Symbols	Values	Unit	
Specified top-point tension	$T_H$	25	kN.	
Water depth	$Z_H$	500	m.	
Top-to-bottom point distance	R	300	m.	
Outside diameter	$D_0$	0.023	m.	
Density of cable	$\rho_s$	4039.8	kg/m³	
Density of water	$\rho_{w}$	1021	kg/m³	
Effective weight	W <sub>e</sub>	12.3	N/m.	
Uniform current velocity in X-axis direction	<i>V</i> <sub>3</sub>	3.7	km./hr.	
Elastic modulus	E	0.601×10°	kN/m <sup>2</sup>	
Normal drag coefficient	$C_{DN}$	1.00		
Tangential drag coefficient	$C_{DT}$	0.05		
Inertial coefficient	$C_{M}$	2		

nent in the bi-normal direction is not generated. This makes a cable lie only in the vertical plane, and the mode shapes of vibrations for the first and second modes correspond to the bi-normal and normal directions, respectively.

Moreover, the further observation is the switch of the local amplitude directions between two ranges of angle  $\theta_0$ . For instance, the amplitude corresponding to the bi-normal direction in the first quadrant ( $0 < \theta_0 < 90$  deg.) switches to be the normal direction in the second one ( $90 < \theta_0 < 180$  deg.) for the first mode of vibration. These changes are amenable to the specified vectors and start approximately from a value of  $\theta_0$  equal to 90 degrees.

Figs. 7 and 8 display graphically the overall configurations (global systems) for the first three mode shapes for an inclined extensible marine cable using the forgoing cable properties in Table 2, with the projection on three planes that are XZ, YZ and XY planes. These plots are used to represent two crucial aspects. The first is to show initially the cable equilibrium configuration in three dimensions (solid line) for two different angles of  $\theta_0$  that are 60 and 150 degrees, and the second is to demonstrate typically how the cable vibrates in the Cartesian coordinate systems. Due to the difference in the establishment of the cable equilibrium profiles in any prescribed angle  $\theta_0$ , the modal transition or the changes in the mode of vibration is formed substantially over these regions. It should be remarked that these examples would become to be the other form, if the value of the prescribed angle  $\theta_0$  and the profile of current, both in terms of magnitudes and directions, are separate from this situation.

#### 5.3. Dynamic tension for coupled transverse motions

To gain further insight into the dynamic behaviours of the coupled transverse motions, it is necessary to examine the characteristics of frequency spectra and

Table 3
The first four natural frequencies of marine cable and corresponding mode shapes for different values of  $\theta_0$  and  $T_H/EA$ , for cable properties defined in Table 2<sup>a</sup>

T <sub>H</sub> /EA	Mode	Natural frequencies (rad./sec.) $\theta_0$ (degree)							
		0	30	60	90	120	150	180	
0.0001	$\omega_1$	0.545	0.545	0.544	0.545	0.546	0.549	0.547	
	$\omega_2$	1.078	1.076	1.073	1.074	1.076	1.076	1.057	
	$\omega_3$	1.090	1.089	1.088	1.090	1.092	1.094	1.094	
	ω4	1.552	1.551	1.550	1.551	1.550	1.532	1.531	
0.001	$\omega_{\scriptscriptstyle 1}$	0.546	0.545	0.544	0.545	0.546	0.547	0.547	
	$\omega_2$	1.078	1.076	1.073	1.072	1.070	1.069	1.060	
	$\omega_{3}$	1.090	1.090	1.088	1.090	1.093	1.094	1.094	
	ω,	1.509	1.509	1.508	1.494	1.493	1.475	1.474	
0.01	ω,	0.548	0.547	0.547	0.547	0.548	0.549	0.549	
	$\omega_2$	0.875	0.880	0.876	0.826	0.827	0.815	0.814	
	$\omega_3$	1.084	1.083	1.084	1.089	1.094	1.097	1.098	
	$\omega_{\scriptscriptstyle 4}$	1.095	1.094	1.093	1.094	1.097	1.098	1.098	
T <sub>H</sub> /EA	Mode	Corresponding mode shapes							
		$\theta_0$ (degree)							
		0	30	60	90	120	150	180	
0.0001	$\omega_1$	0	С	С	С	С	С	o	
0.001	$\omega_2$	í	Č	Ċ	č	Č	Č	ī	
0.01	$\omega_3$	O	C	C	C	C	C	O	
-	$\omega_{4}$	I	C	C	C	C	C	I	

<sup>&</sup>lt;sup>a</sup> O: out-of-plane modes; I: in-plane modes; C: coupled transverse modes.

dynamic tension plots for a cable having significance in sag and curvature in each mode. For cables of engineering interest  $EA >> T_H$ , by setting cable stiffness to be invariant and applying consecutively a value of specified top tension as the foregoing input parameters from values of 15 kN. to 150 kN, this modification leads to the additional numerical results for a cable having a difference in sags. Employing the following dimensionless quantities for the sake of convenience and simplicity:

$$\Omega = \frac{\omega L_0}{\pi} \sqrt{\frac{M}{T_\alpha}},\tag{56a}$$

$$\tau = \frac{EA\varepsilon_D}{T_H} \tag{56b}$$

\_

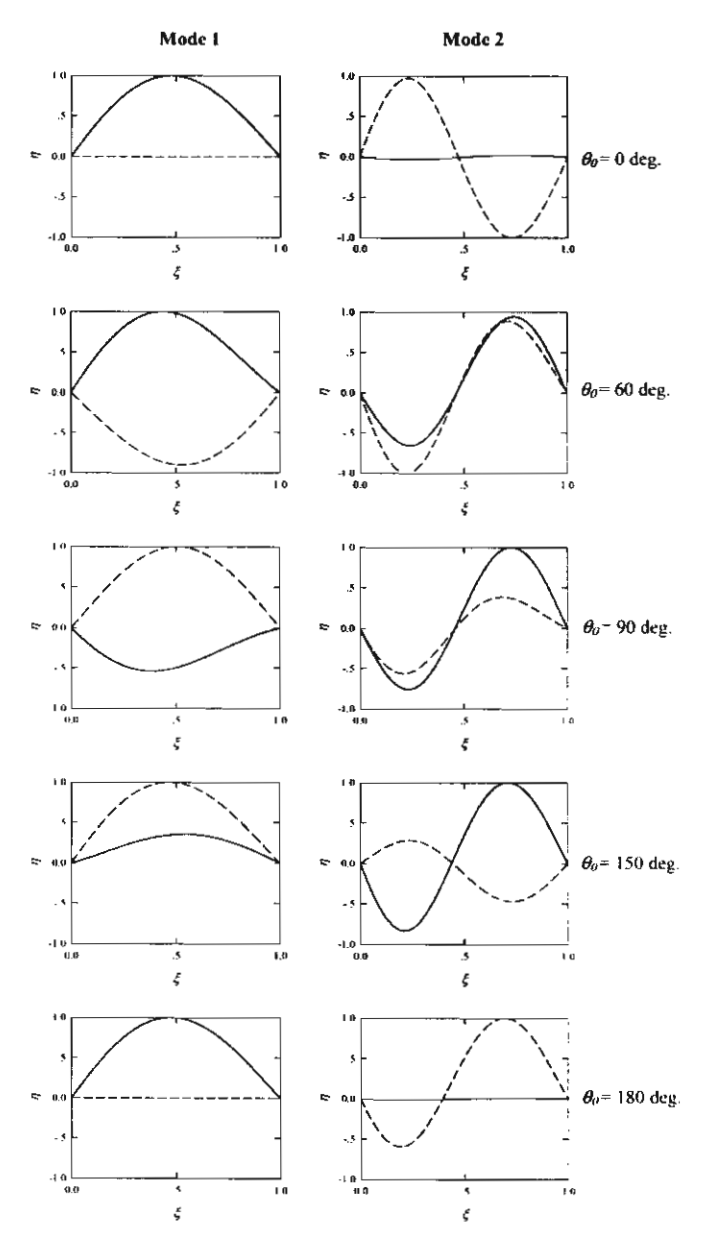


Fig. 6. The first two normalized mode shapes  $(\eta)$  plotted versus the dimensionless arc-length  $(\xi)$  for the different values of  $\theta_0$ , for cable properties defined in Table 2, solid line (dash line) denotes bi-normal (normal) direction.

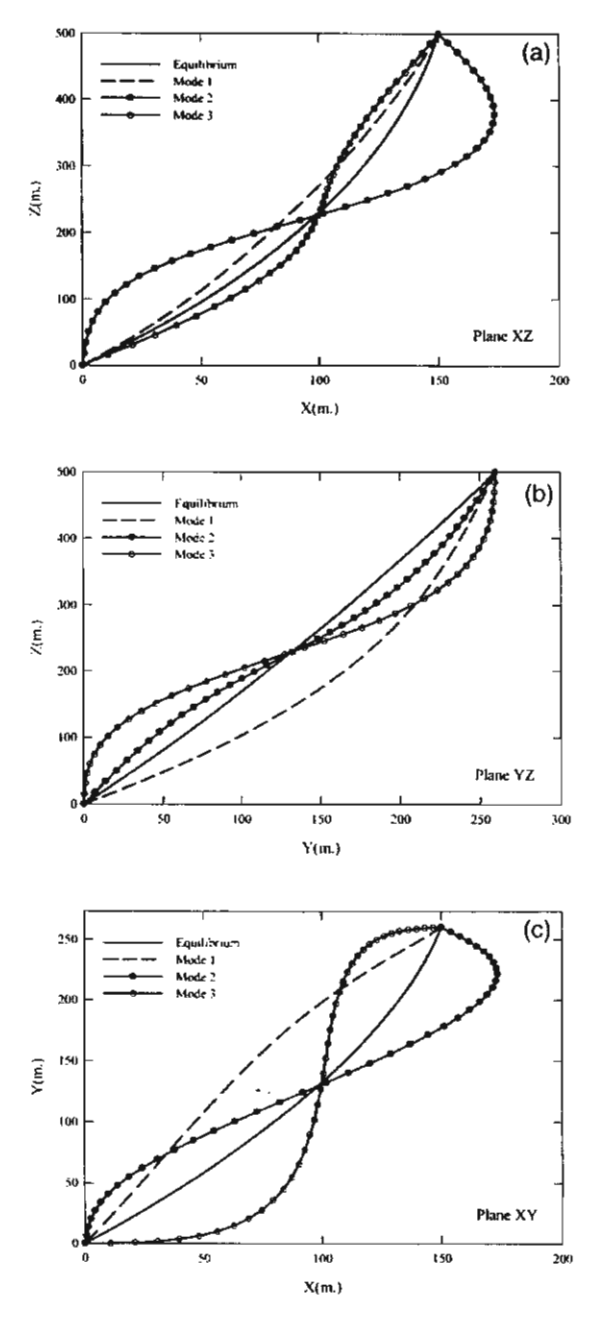


Fig. 7. The first three mode shapes corresponding to the global system, representing for a value of  $\theta_0$  = 60 degrees and  $T_H$  = 25 kN., projection on (a) XZ plane, (b) YZ plane and (c) XY plane.

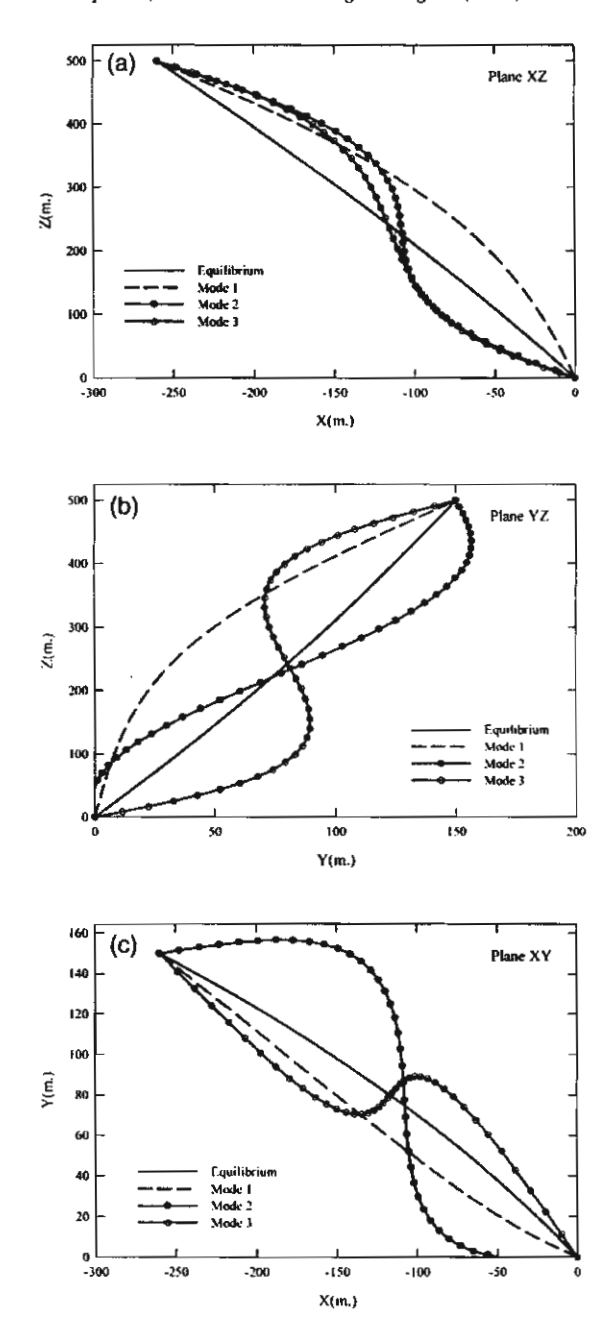


Fig. 8. The first three mode shapes corresponding to the global system, representing for a value of  $\theta_0$  = 150 degrees and  $T_H$  = 25 kN., projection on (a) XZ plane, (b) YZ plane and (c) XY plane.

and

$$\lambda^2 = \frac{EA}{T_{\alpha}^3} (w_e L_0)^2 \cos^2 \phi_{\alpha} \tag{56c}$$

in which M is the total mass of the submerged cable plus added mass per unit length,  $T_{\alpha}$  represents the static cable tension at  $\phi = \phi_{\alpha}$  when  $\phi_{\alpha}$  is the vertical angle of the chord inclination measured from the XY plane,  $L_0$  is the stretched cable length. These parameters are the well-known frequency, the dynamic tension factor and cable parameter accounting for the cable equilibrium geometry and material properties (Irvine and Caughey, 1974). The parameter  $\Omega$  is non-dimensionalized by dividing it with the first transverse natural frequency of taut string while a variable  $\varepsilon_D$  is the maximum dynamic strain obtained from the following expression,

$$\varepsilon_D = MAX_i \left[ (1 + \varepsilon_0) \left( 1 + \frac{x'_0 u' + y'_0 v' + w'}{1 + x'_0^2 + y'_0^2} \right) - 1 \right]$$
 (57)

$$i = 1,2,...,Nel$$

The natural frequency spectrum represented for cable having a value of  $\theta_0 = 60$  degrees is manifested in Fig. 9a as a function of the parameter  $\lambda/\pi$ . The plots for the odd modes, which are drawn perfectly straight in the horizontal line, will not be shown herein because the parameters  $\Omega$  are independent of  $\lambda/\pi$ , as well as the case of taut string. On the other hand, the phenomenon of frequency avoidance exists for each pair of even mode and the gaps of avoidance region are very close. The mode shapes in the veering region corresponding to the coupled transverse amplitudes, become hybrids (h) in certain value of  $\lambda/\pi$  within this range ( $\lambda/\pi = 0.792$  for mode 2 and  $\lambda/\pi = 0.859$  for mode 4), and are extremely sensitive to small changes in the cable parameter  $\lambda/\pi$ . Consequently, the dynamic tension in the cable increases substantially over the modal transition range as displayed in Fig. 9b.

Once again, by alternating the value of  $\theta_0$  to be 150 degrees, the characteristics of the frequency spectrum (frequency avoidance phenomenon) and dynamic tension plots are still the same as the first angle range but the gaps of avoidance are increased substantially, as shown in Fig. 10a and b. In addition to the distinction of cable equilibrium profile between two angle ranges, the qualitative differences are the shifts of the avoidance region from the left to the right in the frequency spectrum following a value of  $\lambda/\pi$ . For example, a value of  $\lambda/\pi$  over the first avoidance region in Fig. 10a ( $\theta_0 = 150$  degrees) is approximated as 2.186 whereas it is approximated as 0.829 in Fig. 9a ( $\theta_0 = 60$  degrees). From these values, it can be stated that the sag condition (following the cable parameter) of cable placing in the first quadrant for the occurrence of frequency avoidance is slack more than a cable placing in the first one.

Fig. 11 illustrates the modal transition of the even modes corresponding to the coupled transverse amplitudes in the first veering phenomenon for a cable having value of  $\theta_0$  equals to 150 degrees. In order to display how the coupled transverse

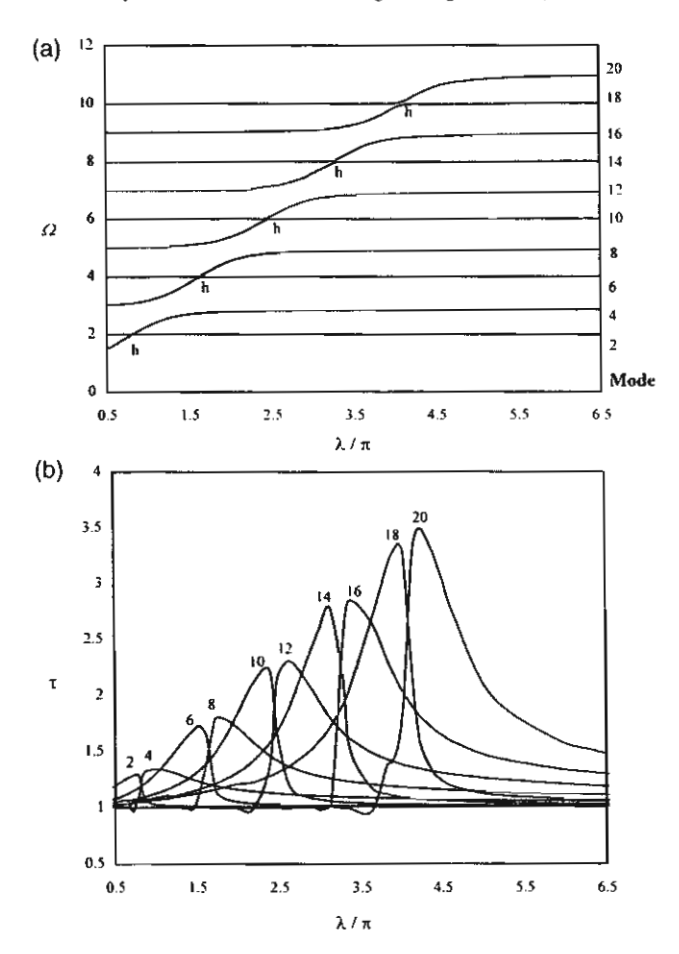


Fig. 9. (a) Natural frequency spectrum of marine cable corresponding to the first ten even modes, represented for a value of  $\theta_0 = 60$  degrees, h: coupled transverse hybrid modes. (b) Dynamic tension factor  $\rho$ f marine cable corresponding to the first ten even modes, represented for a value of  $\theta_0 = 60$  degrees.

modes become hybrids ( $\lambda/\pi=2.022$  for mode 2 and  $\lambda/\pi=2.186$  for mode 4) even for cable vibrating from the three-dimensional static configuration. It should be remarked that mode shapes corresponding to the odd modes (not shown herein) do not change to be the hybrid form for the variation of the parameter  $\lambda/\pi$ , as well as the taut string case.

The present numerical examinations reveal that the features in the frequency spectrum and dynamic tension plots of a marine cable resemble those of a cable in air and a submerged cable (comparing the odd modes with out-of-plane modes, and the even modes with in-plane modes). The difference in the free vibration characteristic is the local standing mode shapes, which now have been identified herein as the coupled transverse mode, and can occur whenever a marine cable vibrates from the three-dimensional static configuration.

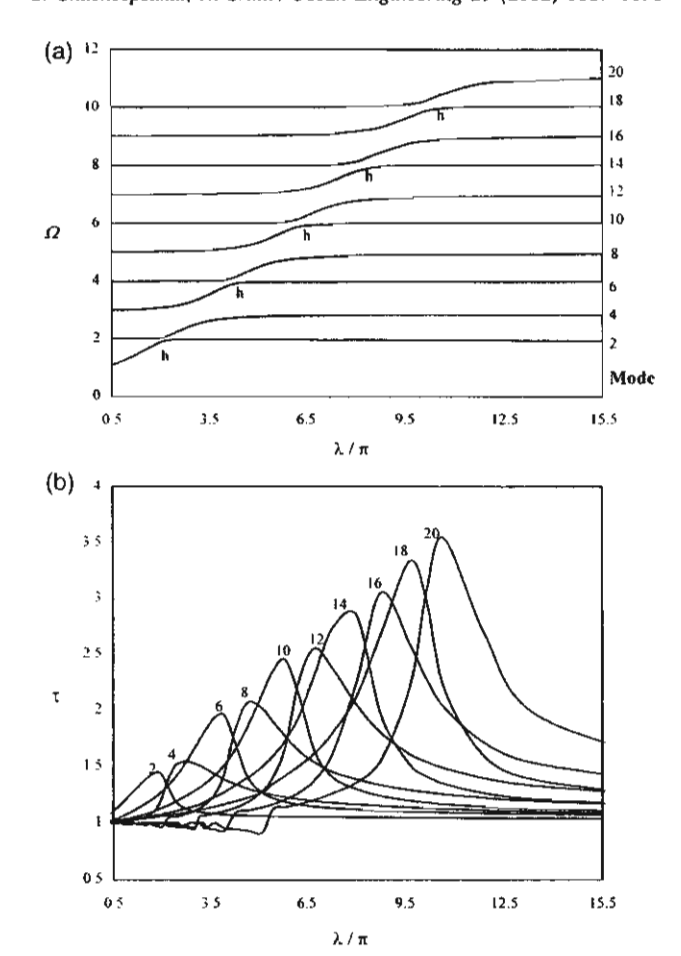


Fig. 10. (a) Natural frequency spectrum of marine cable corresponding to the first ten even modes, represented for a value of  $\theta_0 = 150$  degrees, h: coupled transverse hybrid modes. (b) Dynamic tension factor of marine cable corresponding to the first ten even modes, represented for a value of  $\theta_0 = 150$  degrees.

#### 6. Conclusions

The model formulation for analyzing the three-dimensional vibration behaviours of an inclined extensible marine cable is presented. This model is efficient and conveniently applied for solving the cable problem with the specified top tension. The coupled equations of motion derived in a global coordinate system are transformed into a local coordinate system by a matrix transformation technique. Based on the Galerkin finite element solution, numerical studies have shown that the axial extensibility of the cable has an effect on the natural frequencies for both of out-of-plane motions and three-dimensional coupled motions.

An interesting result of this paper is that of the two modal transitions of marine

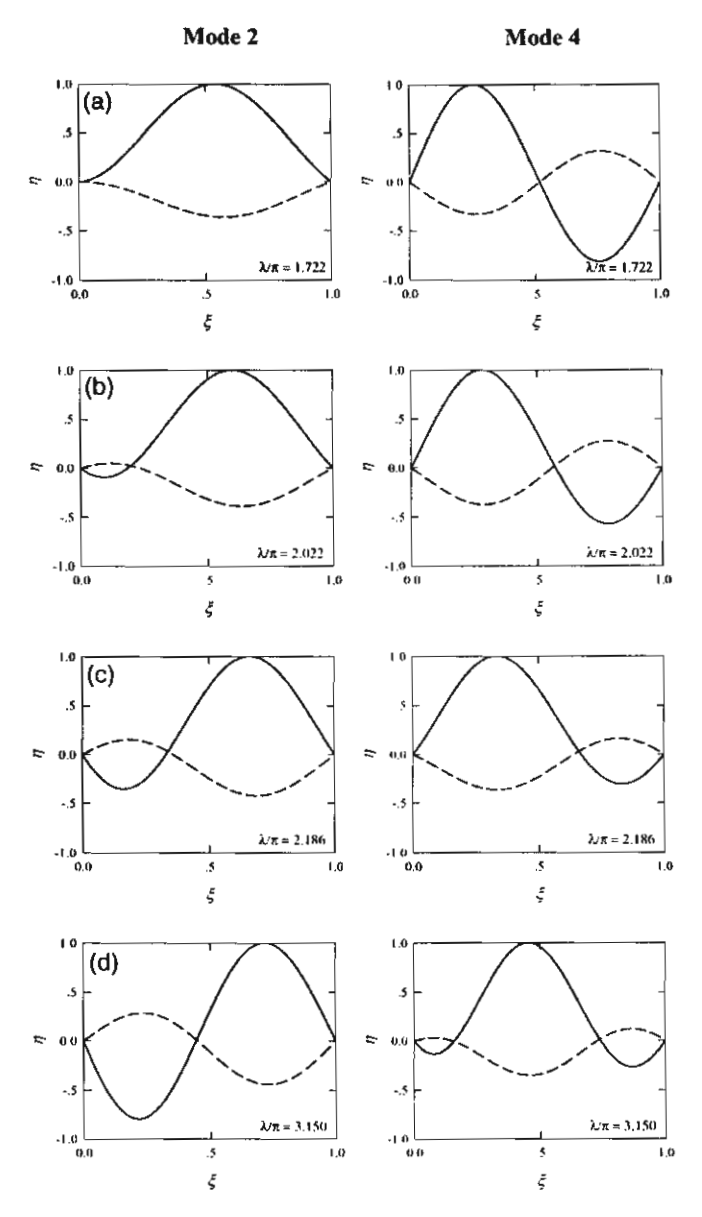


Fig. 11. Modal transition of the even modes for the first avoidance region, for marine cable having a value of  $\theta_0 = 150$  degrees, solid line (dash line) denotes bi-normal (normal) direction.

cables subjected to the current fields. The first modal transition is caused by the variation of the angle between ocean current direction and the projection of the top-to-bottom point distance line onto the horizontal plane, which slightly affects the natural frequencies. The second one is formed over the avoidance region in the frequency spectrum plots for a cable vibrating in the even modes. In that region, the

dynamic tension in the cable is increased substantially and the corresponding mode shape becomes hybrid. By contrast, the frequencies in the odd modes are independent of the cable parameter and form like a taut string motion. Nevertheless, the odd and even mode shapes are coupled in the transverse directions. The coupled transverse modes are dominated by the bi-normal and normal amplitudes simultaneously.

#### Acknowledgements

This work was financially supported by the Thailand Research Fund (TRF) under Grant No. RTA/03/2543.

#### Appendix A

Current profile

The current velocity is a function of depth only and is given by

$$\vec{V} = v_x(z_0)\vec{i} + v_y(z_0)\vec{j} \tag{A1}$$

In terms of local coordinate system, the current profile is

$$\vec{V} = \begin{cases}
[v_x(z_0)\cos\phi\cos\theta + v_y(z_0)\cos\phi\sin\theta]\vec{p} + \\
[-v_x(z_0)\sin\theta + v_y(z_0)\cos\theta]\vec{q} + \\
[-v_x(z_0)\sin\phi\cos\theta - v_y(z_0)\sin\phi\sin\theta]\vec{r}
\end{cases}$$
(A2)

#### Appendix B

Components of cubic shape functions matrices  $[N_s]$  and [N]

$$N_1 = 1 - 3(z_0^2/h^2) + 2(z_0^3/h^3)$$
 (B1)

$$N_2 = z_0 - 2(z_0^2/h) + (z_0^3/h^2)$$
 (B2)

$$N_3 = 3(z_0^2/h^2) - 2(z_0^3/h^3)$$
 (B3)

$$N_4 = -(z_0^2/h) + (z_0^3/h^2)$$
 (B4)

#### Appendix C

#### Components of transformation matrix [T]

$T1 = \cos\phi\cos\theta$	(C1)
$T2 = -\sin\theta$	(C2)
$T3 = -\sin\phi\cos\theta$	(C3)
$T4 = (-\cos\phi\sin\theta\cdot\theta' - \sin\phi\cos\theta\cdot\phi')$	(C4)
$T5 = -\cos\theta \cdot \theta'$	(C5)
$T6 = (\sin\phi\sin\theta \cdot \theta' - \cos\phi\cos\theta \cdot \phi')$	(C6)
$T7 = \cos\phi\sin\theta$	(C7)
$T8 = \cos\theta$	(C8)
$T9 = -\sin\phi\sin\theta$	(C9)
$T10 = (\cos\phi\cos\theta\cdot\theta' - \sin\phi\sin\theta\cdot\phi')$	(C10)
$T11 = -\sin\theta \cdot \theta'$	(C11)
$T12 = (-\sin\phi\cos\theta\cdot\theta' - \cos\phi\sin\theta\cdot\phi')$	(C12)
$T13 = \sin\phi$	(C13)
$T14 = \cos\phi$	(C14)
$T15 = \cos\phi \cdot \phi'$	(C15)
$T16 = -\sin\phi \cdot \phi'$	(C16)

#### References

Behbahani-Nejad, M., Perkins, N.C., 1996. Freely propagating waves in elastic cables. Journal of Sound and Vibration 196 (2), 189-202.

Burgess, J.J., 1993. Bending stiffness in a simulation of undersea cable deployment. International Journal of Offshore and Polar Engineering 3 (3), 197-204.

Burgess, J.J., Triantafyllou, M.S., 1988. The elastic frequencies of cables. Journal of Sound and Vibration 120 (1), 153-165.

Chucheepsakul, S., Subwonglee, S., 1991. Three-dimensional analysis of marine cables. In: Cheung, Lee, Leung (Eds.), Computational Mechanics. Balkema, Rotterdam, Netherlands, pp. 389-394.

Chucheepsakul, S., Huang, T., 1997. Effect of axial deformation on the natural frequencies of marine cables. In: Proceedings of the 7th International Journal of Offshore and Polar Engineering Conference, 2., pp. 131-136.

- Cook, R.D., Malkus, D.S., Plesha, M.E., 1989. Concepts and Applications of Finite Element Analysis, 3rd ed. John Wiley & Sons,
- De Zoysa, A.P.K., 1978. Steady-state analysis of undersea cables. Ocean Engineering 5 (3), 209-223.
- Friswell, M.I., 1995. Steady-state analysis of underwater cables. Journal of Waterway, Port, Coastal and Ocean Engineering, ASCE 121 (2), 98-104.
- Griffin, O.M., Rosenthal, F., 1988. The dynamics of slack marine cables. In: Proceedings of the 7th International Conference on Offshore Mechanics and Arctic Engineering, 1, pp. 481-488.
- Henghold, W.M., Russell, J.J., Morgan, J.D., 1977. Free vibrations of cable in three dimensions. Journal of Structural Division, ASCE 103 (ST5), 1127-1136.
- Huang, S., 1994. Dynamic analysis of three-dimensional marine cables. Ocean Engineering 21 (6), 587-605.
- Irvine, H.M., Caughey, T.K., 1974. The linear theory of free vibrations of a suspended cable. Proceedings of the Royal Society of London, A 341, 229-315.
- Perkins, N.C., Mote, C.D., 1987. Three-dimensional vibration of travelling elastic cables. Journal of Sound and Vibration 1142, 325-340.
- Petchpeart, P., 1999. Effect of deformation on static equilibrium configurations of marine cables in three dimensions. Master Engineering Thesis, King Mongkut's University of Technology Thonburi, Bangkok, Thailand.
- Ramberg, S.E., Griffin, O.M., 1977. Free vibrations of taut and slack marine cables. Journal of Structural Division, ASCE 103 (ST11), 2079–2092.
- Sparks, C.P., 1984. The influence of tension, pressure and weight on pipe and riser deformations and stresses. Journal of Energy Resource and Technology, ASME 106, 46-54.
- Sun, Y., Leonard, J.W., 1998. Dynamics of ocean cables with local low tension regions. Ocean Engineering 25 (6), 443-463.
- Triantafyllou, M.S., 1984. The dynamic of taut inclined cables. Quarterly Journal of Mechanics and Applied Mathematics 37, 421-440.
- Vassalos, D., Huang, S., 1996. Dynamics of small-sagged taut-slack marine cables. Computers and Structures 58 (3), 557-562.
- Vaz, M.A., Patel, M.H., 2000. Three-dimensional behaviour of elastic marine cables in sheared currents. Applied Ocean Research 22, 45-53.
- Wang, C.M., Cheong, H.F., Chucheepsakul, S., 1993. Static analysis of marine cables via shooting-optimization technique. Journal of Waterway, Port, Coastal and Ocean Engineering, ASCE 119 (4), 450–457.



Engineering Analysis with Boundary Elements 26 (2002) 547-555



www.elsevier.com/locate/enganabound

## An alternative domain/boundary element technique for analyzing plates on two-parameter elastic foundations

### Somchai Chucheepsakul\*, Boonme Chinnaboon

Department of Civil Engineering, King Mongkut's University of Technology Thonburi, 91 Suksawat Road 48, Bangmod, Toongkru, Bangkok 10140, Thailand

Received 7 December 2000; revised 2 January 2002; accepted 4 January 2002

#### Abstract

This paper presents an alternative domain/boundary element technique for analyzing plates on two-parameter elastic foundations, in which the fundamental solution for the linear plate theory is used in the formulation. The main advantages of using this technique are that the kernels of the boundary integral equations are conveniently established and can be used for solving plate problems with various boundary conditions as well as mixed boundary conditions. The surface integration of the kernels for the foundation pressure is evaluated using a numerical procedure presented herein instead of the conventional Gauss-Legendre method, resulting in the reduction of computing time. The application of higher-order elements, i.e. cubic elements, for improving the solution is adopted. Numerical results of several problems with various boundary conditions are given to demonstrate the accuracy and validity of the method. © 2002 Elsevier Science Ltd. All rights reserved.

Keywords: Boundary element method; Plates; Two-parameter elastic foundations; Domain integrals; Cubic elements

#### 1. Introduction

Two-parameter elastic foundation models have been developed to overcome the inadequacy of Winkler's model in describing the real soil response and the mathematical complexity of the three-dimensional continuum. They are characterized by two independent elastic constants and they are derived either as an extension of the Winkler's model by assuming the interaction between the spring elements or by simplifying the three-dimensional continuum. The two-parameter foundations can be modeled to include the Filonenko-Borodich, Pasternak Vlasov and Winkler models. Although these foundation models can adequately approximate the soil-structure interaction, an analytical solution to the governing boundary value problem is obtained only when the plate has a simple geometry and loading.

Boundary integral equation formulation is a powerful method for solving this problem. Many researchers have extensively studied the problem of plates on Winkler foundation. Katsikadelis and Armenakas [1,2] introduced this method for simply supported and clamped boundary conditions. Costa and Brebbia [3,4] generalized the analysis

to plates with arbitrary shapes and boundary conditions. Puttonen and Varpasuo [5] employed direct and indirect boundary element formulations for plates on one- or twoparameter foundations, but their analysis was limited to plates with smooth boundaries and the accuracy of results depends on the location of an auxiliary boundary. Benzine [6] proposed a new method by using an original boundary integral equation involving the fundamental solution for plate flexure problems. El-Zafrany et al. [7] introduced a new fundamental solution based upon newly defined modified Kelvin functions. For plates on two-parameter foundations, a limited number of publications have been found. Balas et al. [8] have presented a boundary integral formulation for plates of any shape and they employed Fourier integral transform for the derivation of fundamental solutions. Katsikadelis and Kallivokas [9] have used the boundary element method for plates on Pasternak-type elastic foundation with clamped boundary, and the same authors [10] have presented a boundary differential integral equation method for the analysis of plates with free boundaries of any shape resting on biparametric elastic foundations.

In the present paper, an alternative method of boundary element analysis is developed for analyzing plates on twoparameter elastic foundations. The proposed method uses the fundamental solution of linear plate theory and treats the subgrade reactions as unknown domain forces. Thus,

<sup>\*</sup> Corresponding author. Tel.: +662-470-9146; fax: +662-427-9063. E-mail address: somehai.chu@kmutt.ac.th (S. Chucheepsakul).

the kernels of the boundary integral equations are conveniently established and evaluated and they can be used for solving the plate problems with various boundary conditions including mixed boundary conditions. The emphasis of this study is placed on evaluating an integration representation for foundation pressure. In integrating over the boundaries, cubic elements are employed for improving the solution. Numerical results of several problems with various boundary conditions are provided to demonstrate the accuracy and the validity of this method.

#### 2. Formulation of the boundary value problem

Consider a plate with bending rigidity D as shown in Fig. 1 resting on two-parameter elastic foundation (Pasternak model) subjected to a transverse loading intensity q. Let S be the interior of the plate and  $\Gamma$  its boundary. Assuming that the plate maintains contact with the subgrade and that there are no friction forces at the interface, its transverse deflection w(P) at any point  $P \in S$  satisfies the following differential equation:

$$\nabla^4 w + \frac{p_s}{D} = \frac{q}{D} \tag{1}$$

where  $p_s$  is the interaction pressure between plate and subgrade and is defined as

$$p_s = kw - G\nabla^2 w \tag{2}$$

Eq. (1) can be considered in a more general form as

$$Lw = \frac{q}{D} \tag{3}$$

where L is an operator defined as

$$L = \nabla^4 - \frac{G}{D}\nabla^2 + \frac{k}{D} \tag{4}$$

where  $\nabla^2 = \frac{\partial^2}{\partial x^2} + \frac{\partial^2}{\partial y^2}$ ,  $\nabla^4 = (\nabla^2)^2$ ,  $D = Eh^3/12(1 - \nu^2)$  is the flexural rigidity of the plate, G the shear modulus, and k the modulus of subgrade reaction.

In this paper, plates with free boundaries are not treated here. In this case, it is necessary to consider the interaction of the plate on its boundary with the foundation. Detailed

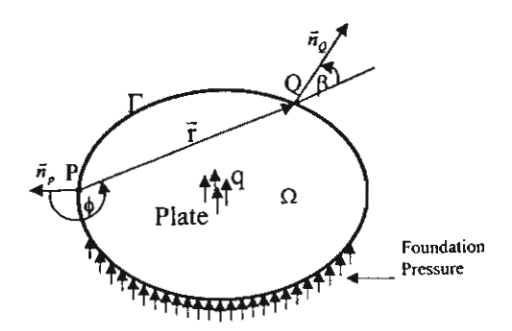


Fig. 1. Plate on two-parameter elastic foundation and notation.

information related to this case can be found in the work of Balas et al. [8] and Katsikadelis and Kallivokas [10].

#### 3. Boundary element method

The integral representation of the solution can be obtained by combining the Rayleigh-Green identity for the biharmonic equation with classical Green identity for the harmonic equation. This identity can be written as

$$\iint_{\Omega} (uLw - wLu) dS$$

$$= \frac{1}{D} \int_{\Gamma} \left[ wV_{n}(u) - \frac{\partial w}{\partial n} M_{n}(u) + \frac{\partial u}{\partial n} M_{n}(w) - uV_{n}(w) - Gu \frac{\partial w}{\partial n} + Gw \frac{\partial u}{\partial n} \right] d\Gamma$$
(5)

where u, w,  $V_n$ ,  $M_n$  are deflections, equivalent shear force, normal bending moment and  $\partial/\partial n$  denotes the outward normal derivative.

Eq. (5) is valid for any two functions w and u, which are four times continuously differentiable inside the region S and three times continuously differentiable on its boundary  $\Gamma$ . However, the identity of Eq. (5) ignores the corner force term, which will not affect the results by using discontinuous elements at all corners as discussed by Venturini and Paiva [11].

Normally, the problem of plates on two-parameter elastic foundations consists of taking the suitable fundamental solution to Eq. (1) that is a singular particular solution of the following differential equation:

$$Lu = \delta(Q - P)/D \tag{6}$$

in which  $\delta(Q-P)$  is the Dirac delta function, Q is the field point and P is the source point. The nature of the solution to Eq. (6) involves the zero-order Hankel function of the first kind that cannot be evaluated easily because of its mathematical complexity. This formulation has been used by many authors [5,8-10] who have treated this problem with the boundary integral equation method.

The formulation proposed herein uses the classical fundamental solution for plate flexure problem:

$$\nabla^4 u = \delta(Q - P)/D \tag{7}$$

and represents the pressure distribution in the foundation interface by the load applied at each node of a mesh used to discretize the plate domain.

The fundamental solution of Eq. (7) is given as

$$u_{\rm F}(P,Q) = w_{\rm F}(r) = \frac{1}{8\pi D} r^2 \ln r$$
 (8)

where  $r = |\overrightarrow{PQ}|$  and the subscript F denotes the fundamental solution corresponding to a concentrated unit force. Substituting Eqs. (7) and (8) into Eq. (5) one gets the deflection

for any point P inside the domain as follows:

$$w_{P \in S} = -\int_{\Gamma} \left[ w(V_{F} + GN_{F}) - \frac{\partial w}{\partial n} (M_{F} + Gu_{F}) + M_{n}N_{F} - V_{n}u_{F} \right] d\Gamma - \int_{\Omega} (ku_{F} - G\nabla^{2}u_{F})w dS + \int_{\Omega} qu_{F}dS$$

$$(9)$$

where the equivalent shear force  $V_F$ , normal bending moment  $M_F$ , normal slope  $N_F$  and  $\nabla^2 u_F$  resulting from the fundamental solution of Eq. (8) are expressed as follows [12]:

$$V_{\rm F} = -\frac{\cos \beta}{4\pi r} [2 + (1 - \nu)\cos 2\beta] + \frac{(1 - \nu)}{4\pi R} \cos 2\beta$$

$$M_{\rm F} = -\frac{(1 + \nu)}{4\pi} (1 + \ln r) - \frac{(1 - \nu)}{8\pi} \cos 2\beta$$

$$N_{\rm F} = \frac{1}{8\pi D} (1 + 2\ln r)r \cos \beta$$

$$\nabla^2 u_{\rm F} = \frac{1}{2\pi D} (1 + \ln r)$$
(10)

where  $\beta$  is an angle between direction r and outer normal vector  $\bar{n}$ .

Letting point P tend to Q on the boundary and taking the limit value of the integral, the following equation for a regular point P on the boundary is obtained as

$$0.5w_{P \in \Gamma} = -\int_{\Gamma} \left[ w(V_{F} + GN_{F}) - \frac{\partial w}{\partial n} (M_{F} + Gu_{F}) + M_{n}N_{F} - V_{n}u_{F} \right] d\Gamma - \iint_{\Omega} (ku_{F} - G\nabla^{2}u_{F})w \, dS + \iint_{\Omega} qu_{F}dS$$
(11)

In addition to the solution in Eq. (8), a second fundamental solution is required. This solution corresponds to a concentrated unit moment applied at P that is

$$\nabla^4 u = \frac{\partial}{\partial n} \delta(Q - P)/D \tag{12}$$

The solution of Eq. (12) is

$$u_{\rm m} = w_{\rm m}(r) = \frac{1}{2\pi D} r \ln r \cos \phi \tag{13}$$

where  $\phi$  is the angle of rotation of r with respect to a local coordinate  $\eta \xi$  applied at point P. By substituting Eqs. (12) and (13) into Eq. (5) and taking  $\xi$  in the direction of the normal, the normal derivative of w at point P along the

boundary is obtained:

$$-\frac{\partial w}{\partial n_{P \in I}} = -\int_{I} \left[ (w - w|_{P})(V_{m} + GN_{m}) - \frac{\partial w}{\partial n} (M_{m} + Gu_{m}) + M_{n}N_{m} - V_{n}u_{m} \right] d\Gamma$$
$$-\int_{\Omega} (ku_{m} - G\nabla^{2}u_{m})w \, dS + \int_{\Omega} qu_{m}dS$$
(14)

where

$$N_{\rm m} = \frac{1}{2\pi D} \left[ \cos \phi \cos \beta + \ln r \cos(\phi + \beta) \right]$$

$$M_{\rm m} = \frac{1}{2\pi r} \left[ -(1 + \nu)\cos \phi + (1 - \nu)\sin \phi \sin 2\beta \right]$$

$$V_{\rm m} = \frac{1}{2\pi r^2} \left\{ \cos(\beta - \phi) \left[ 2 + (1 - \nu)\cos 2\beta \right] + 2(1 - \nu)\sin \phi \cos \beta \sin 2\beta \right\}$$

$$-\frac{1 - \nu}{\pi R r} \sin \phi \sin 2\beta$$

$$\nabla^2 u_{\rm m} = \frac{1}{\pi D} \frac{\cos \phi}{r}$$
(15)

The subscript m denotes the fundamental solution corresponding to a concentrated unit moment [12]. Using Eqs. (9), (11) and (14) and the boundary conditions, one can solve for the unknowns along the boundary and the unknown deflections inside the domain.

#### 3.1. Evaluation of domain integrals for foundation pressure

In view of Eqs. (9), (11) and (14), to solve the problem by the present method it is necessary to evaluate the domain integrals:

$$\int\int_{\Omega} (ku - G\nabla^2 u) w \, \mathrm{d}S$$

The steps to solve these domain integrals are as follows:

Step 1: discretize the plate domain into m finite panels. Step 2: assume the value of the deflection w of each panel is constant and is defined at the center point of each panel (Fig. 2).

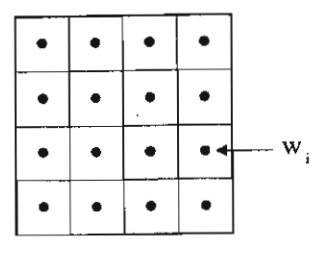


Fig. 2. Domain discretization for unknown deflections.

Step 3: use the following property of Dirac delta function:

$$\int f(t)\delta(t-t_0)dt = f(t_0)$$
(16)

ther

$$\iint_{\Omega} (ku - G\nabla^{2}u)wdS$$

$$= \sum_{i=1}^{m} \{kA_{si}u(p, Q_{i}) - GA_{si}\nabla^{2}u(p, Q_{i})\}w_{i}$$
(17)

where P is the source point,  $Q_i$  the center point of each panel,  $A_{si}$  the area of each panel, and  $w_i$  is the unknown deflection inside the domain.

When the source point P and the field point  $Q_i$  are at the same point then the domain integrals:

$$\iint_{\Omega} (ku - G\nabla^{2}u)wdS$$

$$= w_{i} \frac{G}{4\pi D} \left[ A_{si} \left( \ln\left(\frac{a^{2} + b^{2}}{4}\right) - 1 \right) + a^{2} \tan^{-1}\left(\frac{b}{a}\right) + b^{2} \tan^{-1}\left(\frac{a}{b}\right) \right]$$
(18)

where a and b are the width and length of each panel, respectively.

Obviously, by using this method the integral representation for the foundation pressure need not perform the surface integration of the kernels by Gauss-Legendre method, so computer time is considerably reduced.

# 4. Numerical procedure

In order to solve the boundary integral Eqs. (9), (11) and (14) by means of the boundary element method, discretization of the boundary needs to be done. The boundary is partitioned into a number of boundary elements and the associated boundary functions are interpolated by piecewise polynomials. The problem, thus, is reduced to the task of determining the nodal values of the unknown functions by a point collocation procedure.

In order to improve the numerical solution the high-order elements such as isoparametric cubic elements are adopted in the calculation of the unknown functions along the boundary. These functions can be expressed as

$$\phi(\xi) = \sum_{i=1}^{4} F^{i}(\xi)\phi_{i} \tag{19}$$

where  $\xi$  varies between -1 and +1,  $F^{i}(\xi)$  are the interpolation functions defined later.

## 4.1. Continuous cubic elements

These elements assume a cubic variation of the values  $\phi(\xi)$ . The interpolation functions are (Fig. 3(a))

$$F^{1}(\xi) = \frac{1}{16}(-9\xi^{3} + 9\xi^{2} + \xi - 1)$$

$$F^{2}(\xi) = \frac{1}{16}(27\xi^{3} - 9\xi^{2} - 27\xi + 9)$$

$$F^{3}(\xi) = \frac{1}{16}(-27\xi^{3} - 9\xi^{2} + 27\xi + 9)$$

$$F^{4}(\xi) = \frac{1}{16}(9\xi^{3} + 9\xi^{2} - \xi - 1)$$
(20)

# 4.2. Discontinuous cubic elements

The interpolation functions are (Fig. 3(b))

$$F^{1}(\xi) = -\frac{9}{4}\xi^{3} + \frac{3}{2}\xi^{2} + \frac{1}{4}\xi - \frac{1}{6}$$

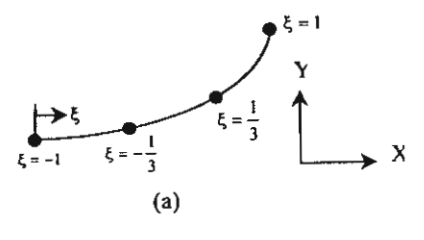
$$F^{2}(\xi) = \frac{9}{2}\xi^{3} - \frac{3}{2}\xi^{2} - 2\xi + \frac{2}{3}$$

$$F^{3}(\xi) = -\frac{9}{2}\xi^{3} - \frac{3}{2}\xi^{2} + 2\xi + \frac{2}{3}$$

$$F^{4}(\xi) = \frac{9}{4}\xi^{3} + \frac{3}{2}\xi^{2} - \frac{1}{4}\xi - \frac{1}{6}$$
(21)

The interpolation functions of cubic elements both continuous and discontinuous elements can be derived according to the procedure suggested by Kane [13].

Gaussian quadrature formula is used in the integration procedure to calculate the coefficients of the nodal variables. However, in integrating over boundary elements adjacent to the source point, some terms of the integrand become



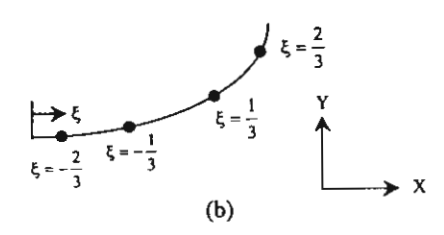


Fig. 3. Cubic elements: (a) continuous elements; (b) discontinuous elements.

singular and the integrals are generally evaluated in the Cauchy principal value sense.

# 5. Matrix formulation

# 5.1. Matrix formulation of boundary integral equation

A matrix formulation for Eqs. (11) and (14) can be obtained by:

- 1. discretization of the boundary into a number of elements with total n nodes of which the value of deflection w, normal slope  $\partial w/\partial n$ , normal bending moment  $M_n(w)$ , equivalent shear force  $V_n(w)$  are defined;
- discretization of the domain S in m rectangular panels at the middle (nodal points) of which the value of deflections w are defined.

For Eq. (11) one obtains

$$\frac{1}{2}\{w\} = \left[A_{\Gamma}^{0}\right]\{w\} + \left[B_{\Gamma}^{0}\right]\left\{\frac{\partial w}{\partial n}\right\} + \left[C_{\Gamma}^{0}\right]\{M_{n}\} + \left[D_{\Gamma}^{0}\right]\{V_{n}\} + \left[E_{\Gamma}^{0}\right]\{w_{s}\} + \{\bar{q}_{0}\} \tag{22}$$

and for Eq. (14):

$$-\left\{\frac{\partial w}{\partial n}\right\} = \left[A_{\Gamma}^{1}\right]\left\{w\right\} + \left[B_{\Gamma}^{1}\right]\left\{\frac{\partial w}{\partial n}\right\} + \left[C_{\Gamma}^{1}\right]\left\{M_{n}\right\} + \left[D_{\Gamma}^{1}\right]\left\{V_{n}\right\} + \left[E_{\Gamma}^{1}\right]\left\{w_{s}\right\} + \left\{\bar{q}_{1}\right\}$$
 (23)

With Eqs. (22) and (23) and boundary conditions the following formulation is performed:

$$[G_{\Gamma}]\{I\} + [J_{\Gamma}]\{w_s\} = \{\bar{q}_{\Gamma}\}$$
 (24)

where  $[G_{\Gamma}]$  is a 2n by 2n matrix,  $[I_{\Gamma}]$  a 2n by m matrix, [I] the vector with 2n components of which are the 2n boundary unknowns among w,  $\partial w/\partial n$ ,  $M_n(w)$  and  $V_n(w)$ ,  $\{W_s\}$  the vector with m components of which are the m unknown domain deflections and  $\{\bar{q}_{\Gamma}\}$  the load vector with 2n components. Subscript  $\Gamma$  shows that the matrices are obtained in the case of point P belonging to the boundary.

# 5.2. Matrix formulation of deflection inside domain S

For the point P inside the domain S, Eq. (9) can be written in the matrix form similar to Eq. (24) as

$$[G_S]{I} + {J_S}{w_s} = {\bar{q}_S}$$
 (25)

where  $[G_S]$  is an m by 2n matrix and  $[J_S]$  an m by m matrix. The plate bending on two-parameter elastic foundation problem consists of solving simultaneously Eqs. (24) and (25), which have (2n + m) equations with (2n + m) unknowns. Nevertheless, it is more useful to modify the

formulation by the elimination of the boundary unknowns  $\{I\}$  using a procedure according to Benzine  $\{6\}$ .

# 6. Evaluation of stress resultants inside the plate domain

When Eqs. (24) and (25) are solved, all the boundary values  $(w, \partial w/\partial n, M_n, V_n)$  and the deflections inside the domain are obtained. Then, the deflection w(P) at any point inside the domain can be obtained from Eq. (9).

The bending moments  $M_x$ ,  $M_y$ , the twisting moment  $M_{xy}$  and the shear force  $Q_x$ ,  $Q_y$  at any point of the plate are expressed as

$$M_{x} = -D \left( \frac{\partial^{2} w}{\partial x^{2}} + \nu \frac{\partial^{2} w}{\partial y^{2}} \right)$$
 (26a)

$$M_{y} = -D \left( \frac{\partial^{2} w}{\partial y^{2}} + \nu \frac{\partial^{2} w}{\partial x^{2}} \right)$$
 (26b)

$$Q_x = -D\frac{\partial}{\partial x}\nabla^2 w \tag{26c}$$

$$Q_{y} = -D\frac{\partial}{\partial y}\nabla^{2}w \tag{26d}$$

$$M_{xy} = -M_{yx} = D(1 - \nu) \frac{\partial^2 w}{\partial x \, \partial y}$$
 (26e)

The second and third order derivatives of the deflections in Eqs. (26a)–(26e) can be evaluated from the computed values of the deflections with sufficient accuracy using numerical differentiation in which the hyper-singular domain integrals do not occur. However, the stress resultants become more accurate when they are evaluated by direct differentiation of Eq. (9) which yields the singular domain integrals. The technique to convert the singular domain integrals with kernel derivatives of the fundamental solution to regular boundary integrals can be found in Refs. [14,15].

# 7. Numerical examples and results

A computer program based upon some modifications from a plate flexure program with cubic boundary elements has been developed. Examples aiming at validating the formulations of this method presented in this work are analyzed. Numerical results of examples are compared with those obtained from analytical or other numerical solutions. In all the cases, the boundary has been divided into 16

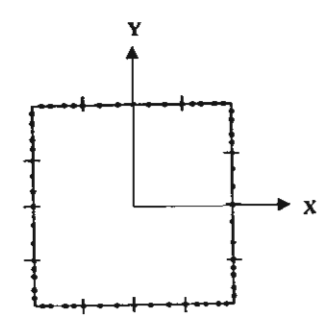


Fig. 4. Boundary discretization with 16 cubic elements.

Table 1 Influence coefficients for  $\tilde{w} = wl(Pa^2/D)$  at x = 0, y = 0 in a clamped rectangular  $(2a \times 2b)$  plate

Load position		xla						
			0	0.2	0.4	0.6	0.8	
ylb	0	Present work Katsikadelis and Kallivokas [9]	$3.2504 \times 10^{-3}$ $3.1970 \times 10^{-3}$	$1.9324 \times 10^{-3}$ $1.9200 \times 10^{-3}$	8.7404 × 10 <sup>-4</sup> 8.7650 × 10 <sup>-4</sup>	$3.4393 \times 10^{-4}$ $3.4650 \times 10^{-4}$	9.2576×10 <sup>-5</sup> 9.3300×10 <sup>-5</sup>	
	0.2	Present work Katsikadelis and Kallivokas [9]	$1.6679 \times 10^{-3}$ $1.6640 \times 10^{-3}$	$1.2595 \times 10^{-3}$ $1.2610 \times 10^{-3}$	$6.5810 \times 10^{-4}$ $6.6200 \times 10^{-4}$	$2.7732 \times 10^{-4}$ $2.7960 \times 10^{-4}$	$7.7405 \times 10^{-5}$ $7.7350 \times 10^{-5}$	
	0.4	Present work Katsikadelis and Kallivokas [9]	$6.2807 \times 10^{-4}$ $6.3310 \times 10^{-4}$	$5.2671 \times 10^{-4}$ $5.3140 \times 10^{-4}$	$3.2531 \times 10^{-4}$ $3.2870 \times 10^{-4}$	$1.5429 \times 10^{-4}$ $1.5580 \times 10^{-4}$	$4.4870 \times 10^{-5}$ $4.5470 \times 10^{-5}$	
	0.6	Present work Katsikadelis and Kallivokas [9]	$2.0953 \times 10^{-4}$ $2.1210 \times 10^{-4}$	$1.8365 \times 10^{-4}$ $1.8580 \times 10^{-4}$	$1.2475 \times 10^{-4}$ $1.2610 \times 10^{-4}$	$6.4484 \times 10^{-5}$ $6.5040 \times 10^{-5}$	$1.9528 \times 10^{-5}$ $1.9700 \times 10^{-5}$	
	8.0	Present work Katsikadelis and Kallivokas [9]	$5.1148 \times 10^{-5}$ $5.1620 \times 10^{-5}$	$4.5760 \times 10^{-5}$ $4.6020 \times 10^{-5}$	$3.2274 \times 10^{-5}$ $3.2480 \times 10^{-5}$	$1.7294 \times 10^{-5}$ $1.7270 \times 10^{-5}$	$5.5783 \times 10^{-6}$ $5.1260 \times 10^{-6}$	

Table 2
Central deflections in simply supported plate subjected to uniform load

Thickness	1-Parameter		2-Parameter	
	This work	Analytical [16]	This work	FEM [17]
10	0.772910	0.771390	0.732820	0.731427
20	0.218810	0.218070	0.215250	0.214917
50	0.016742	0.016680	0.016720	0.016850

cubic elements as shown in Fig. 4 and the domain has been divided into  $15 \times 15$  rectangular panels. This model uses discontinuous elements at all corners as mentioned in Section 3. In the following examples, the results obtained by this model are shown to be in good agreement with those from well-recognized methods.

# 7.1. Clamped plate subjected to a point load

For this example, the present results are compared with those of Katsikadelis and Kallivokas [9] for  $2a \times 2b$  rectangular plate with b/a = 1.2. In Table 1 the influence coefficients for the central deflection  $\bar{w} = w/(Pa^2/D)$  are given for various positions of the concentrated load P with the subgrade reaction modulus  $k = 625D/a^4$  and the shear modulus  $G = 49D/a^2$ .

As can be seen, it is clear that the present results agree very well for every position of load location except for that near a corner of plate (x = 0.8a, y = 0.8b) which show

some discrepancies. This may be due to strong singularity near that position.

# 7.2. Simply supported plate subjected to a uniform load

A simply supported plate with the following properties is considered:

plate dimension: 1000 × 1000 mm<sup>2</sup> load intensity: 0.01 N/mm<sup>2</sup> Young's modulus: 210,000 N/mm<sup>2</sup>

Poisson's ratio: 0.3

For this example, the present results are compared with those obtained from the finite element method (FEM) [17]. To demonstrate the accuracy of the proposed method, numerical results of the central deflection are compared in Table 2. Two cases are considered: (a) a plate on Winkler foundation with  $k = 0.0123 \text{ N/mm}^3$  and (b) a plate on Pasternak foundation with  $k = 0.0123 \text{ N/mm}^3$  and G = 60 N/mm. It is obvious that the results obtained from this proposed method are in very good agreement with the FEM and analytical solution [16], thus confirming the validity of the formulations. Moreover, for the plate thickness h = 10, the deflections, bending moments and shear forces at the plate center with variation of k and k are given in Tables 3 and 4, respectively. One can see the insignificant difference between the proposed approach and the FEM.

Table 3 Deflections, bending moments and shear forces at center in simply supported plate subjected to uniform load with variation of k

k	G	Deflection		Bending moment		Shear force	
		This work	FEM [17]	This work	FEM [17]	This work	FEM [17]
0.0123	60	0.732820	0.731427	144.18	142.61	1.49	1.41
0.0247	60	0.446620	0.446139	75.80	75.51	1.12	1.05
).0329	60	0.351800	0.351389	53.91	53.88	0.99	0.93
0.0657	60	0.184170	0.183949	17.80	17.91	0.74	0.69
0.0822	60	0.146630	0.146462	10.71	10.76	0.68	0.63

Table 4
Deflections, bending moments and shear forces at center in simply supported plate subjected to uniform load with variation of *G* 

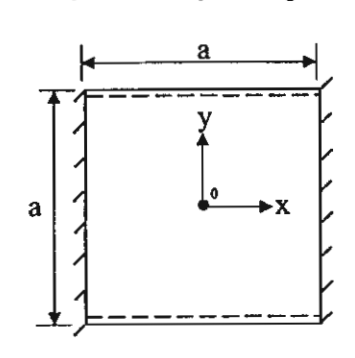
k	G	Deflection		Bending momen	nt	Shear force	
		This work	FEM [17]	This work	FEM [17]	This work	PEM [17]
0.0123	60	0.732820	0.731427	144.18	142.61	1.49	1.41
0.0123	120	0.689060	0.691051	133.80	133.93	1.44	1.35
0.0123	200	0.642750	0.642922	124.14	123.53	1.37	1.28
0.0123	400	0.550510	0.549367	105.16	103.50	1.22	1.14
0.0123	800	0.428450	0.424273	80.73	78.11	1.03	0.95

Table 5 Influence coefficients for  $\dot{w} = wl(Pa^2/D)$  of a quarter of square plate subjected to concentrated load at center (x = 0, y = 0)

Position		xla	xla									
		0	0.1	0.2	0.3	0.4						
ylb	0	2.0366 × 10 <sup>-3</sup>	1.5653 × 10 <sup>-3</sup>	$1.0085 \times 10^{-3}$	5.8153 × 10 <sup>-4</sup>	2.6294 × 10 <sup>-4</sup>						
	0.1	$1.5531 \times 10^{-3}$	$1.3110 \times 10^{-3}$	$8.8915 \times 10^{-4}$	$5.2412 \times 10^{-4}$	$2.3925 \times 10^{-4}$						
	0.2	$9.6218 \times 10^{-4}$	$8.5507 \times 10^{-4}$	$6.2208 \times 10^{-4}$	$3.8288 \times 10^{-4}$	$1.7855 \times 10^{-4}$						
	0.3	$4.8999 \times 10^{-4}$	$4.4512 \times 10^{-4}$	$3.3776 \times 10^{-4}$	$2.1505 \times 10^{-4}$	$1.0222 \times 10^{-4}$						
	0.4	$1.5111 \times 10^{-4}$	$1.3839 \times 10^{-4}$	$1.0675 \times 10^{-4}$	$6.8958 \times 10^{-5}$	$3.3043 \times 10^{-5}$						

# 7.3. Plate with opposite edges simply supported and the other two edges clamped

This example demonstrates an application of the proposed method for a combination of various boundary conditions. A square  $(a \times a)$  plate subjected to a concentrated load at its center is considered with  $k = 1000D/a^4$  and  $G = 100D/a^2$  (Fig. 5(a)). The influence coefficients for the deflection  $\bar{w} = w/(Pa^2/D)$  of a quarter of the plate are given in Table 5 and the



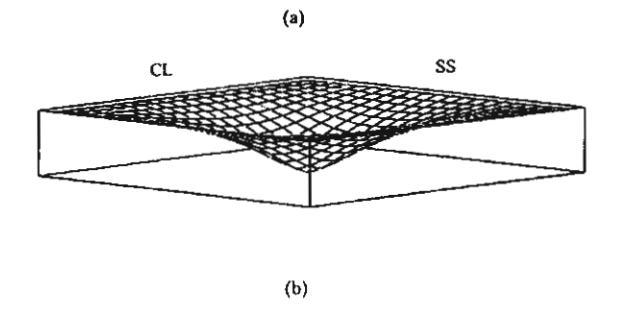


Fig. 5. (a) Plate with a combination of simply supported and clamped edges; (b) the perspective of the deflection surface of a square plate.

perspective of the deflection surface is shown in Fig. 5(b). Finally, the equivalent shear forces along clamped and simply supported edges are plotted and shown in Figs. 6 and 7, respectively. Because of using cubic elements (higher-order elements), it can be seen that there are no oscillations in the equivalent shear force values along the boundaries.

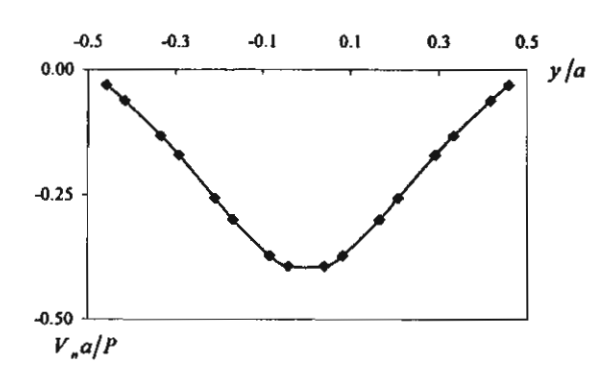


Fig. 6. Equivalent shear force along clamped edge.

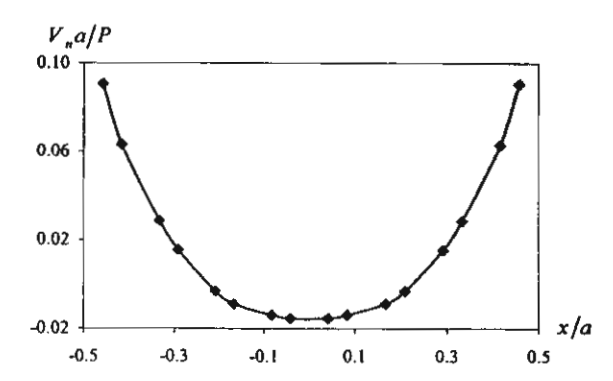


Fig. 7. Equivalent shear force along simply supported edge.

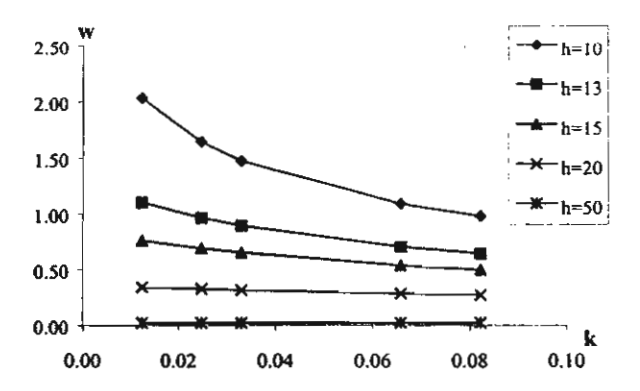


Fig. 8. Clamped plate: variation of central deflection with k by constant G = 60.

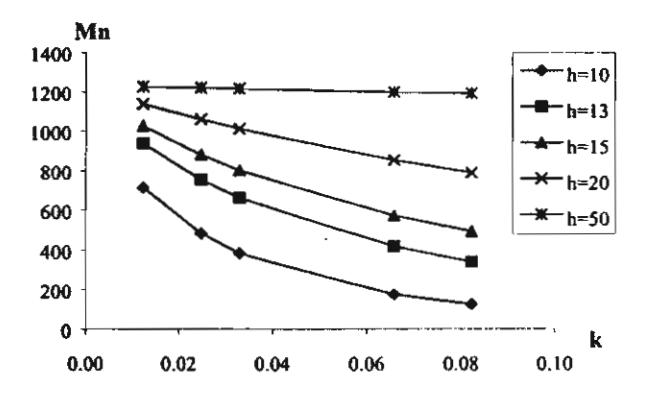


Fig. 9. Clamped plate: variation of normal bending moment at a middle side with k by constant G = 60.

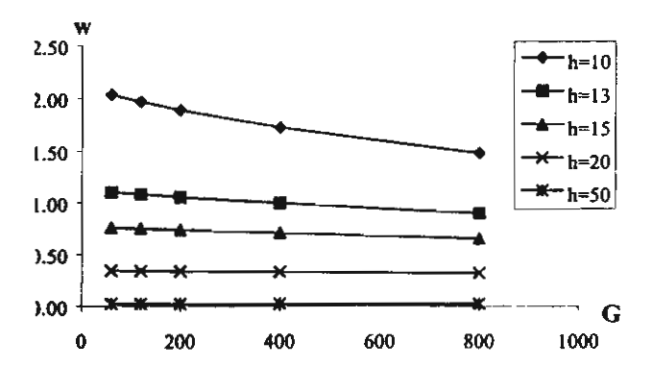


Fig. 10. Clamped plate: variation of central deflection with G by constant k = 0.0123.

The above examples provide confirmation to the validity and accuracy of the proposed method. In Section 7.4, a parametric study is conducted to determine the influence of various parameters on bending of plates on two-parameter elastic foundations.

# 7.4. Parametric study

The parameters concerned in this study are plate thickness (h), subgrade reaction modulus (k), and shear modulus

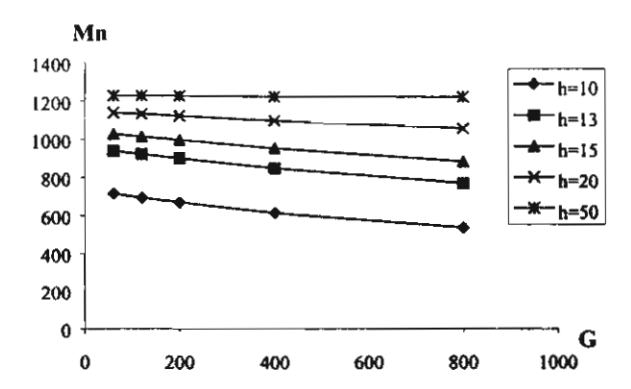


Fig. 11. Clamped plate: variation of normal bending moment at a middle side with G by constant k = 0.0123.

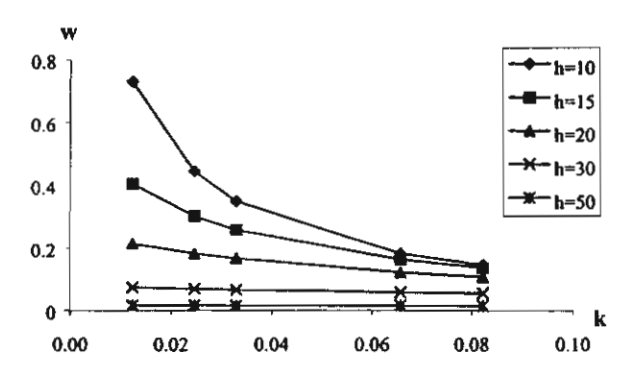


Fig. 12. Simply supported plate: variation of central deflection with k by constant G = 60.

(G). Two cases are considered: (a) a clamped plate subjected to a point load (P = 10,000 N) at the center and (b) a simply supported plate subjected to a uniform load ( $q = 0.01 \text{ N/mm}^2$ ). All plates have the following properties:

plate dimension: 1000 × 1000 mm<sup>2</sup> Young's modulus: 210,000 N/mm<sup>2</sup> Poisson's ratio: 0.3

by varying  $10 \le h \le 50$ ,  $0.0123 \le k \le 0.822$  and  $60 \le G \le 800$ .

For clamped plates the central deflection and normal bending moment at mid-side with variation of k and G are plotted in Figs. 8–11. It is obvious that the central reflection and normal bending moment at mid-side decrease as the foundation parameter (k or G) increases. The present results tend to be unvaried for the plates which have the higher value of thickness. For simply supported plates the central deflection and central bending moment with variation of k and G are shown in Figs. 12–15. It can be concluded in the same way as the first case that the present results decrease as the foundation parameter increases and tend to be unvaried when plate thickness increases.

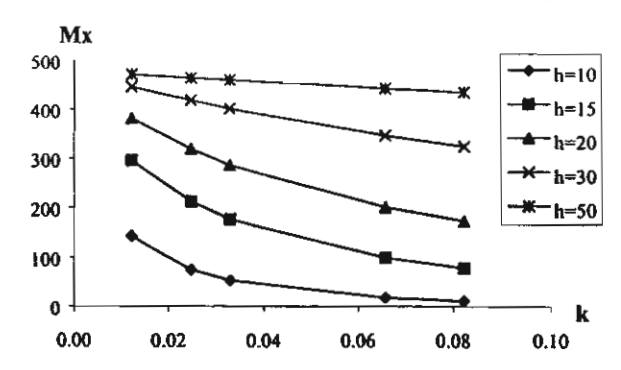


Fig. 13. Simply supported plate: variation of central bending moment  $(M_s)$  with k by constant G = 60.

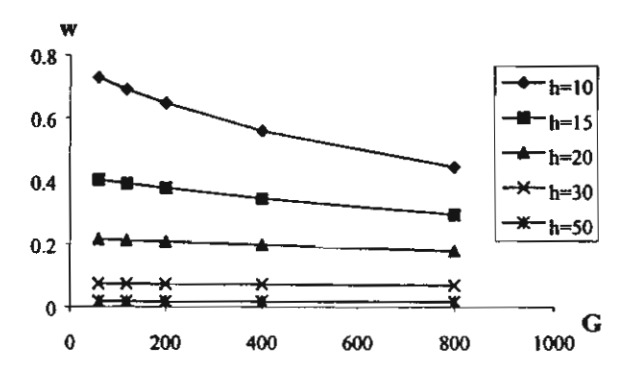


Fig. 14. Simply supported plate: variation of central deflection with G by constant k = 0.0123.

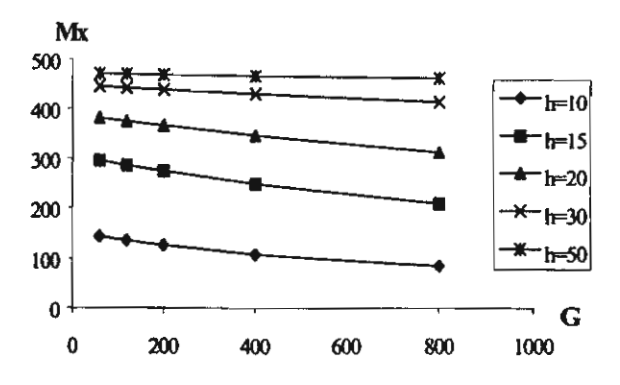


Fig. 15. Simply supported plate: variation of central bending moment  $(M_x)$  with G by constant k = 0.0123.

# 8. Conclusions

The following conclusions can be drawn from this study:

 In the proposed formulation the classical fundamental solution is used to solve plates bending on two-parameter elastic foundations. Thus, the difficulty in the evaluation of the integrals is alleviated. The application of higherorder elements, i.e. cubic elements is adopted for improving the solution.

- The domain integral representation for the foundation pressure along with the proposed method is easily evaluated without necessity to perform the surface integration by Gauss-Legendre method.
- The kernels of the boundary integral equations are conveniently established, thus plates with various boundary conditions including mixed boundary conditions can be solved.
- 4. The proposed method can be applied conveniently to solve for the nonhomogeneous two-parameter elastic foundations by specifying the foundation parameters (k and G) in each subdomain.

## Acknowledgement

The authors are grateful for support from the Thailand Research Fund (TRF) under grant RTA/03/2543.

### References

- Katsikadelis JT, Armenakas AE. Plates on elastic foundation by BIE method. J Engng Mech 1984;110(7):1086-105.
- [2] Katsikadelis JT, Armenakas AE. Analysis of clamped plates on elastic foundation by the boundary integral equation method. J Appl Mech ASME 1984;51:574-80.
- [3] Costa JA, Brebbia CA. The boundary element method applied to plates on elastic foundations. Engng Anal 1985;2:174-82.
- [4] Costa JA, Brebbia CA. On the reduction of domain integrals to the boundary for the BEM formulation of plates on elastic foundations. Engng Anal 1986;3:123-6.
- [5] Puttonen J, Varpasuo P. Boundary element analysis of a plate on elastic foundations. Int J Num Meth Engng 1986;23:287-303.
- [6] Benzine G. A new boundary element method for bending of plates on elastic foundations. Int J Solids Struct 1988;24(6):557-65.
- [7] El-Zafrany A, Fadhil S, Al-Hosani K. A new fundamental solution for boundary element analysis of thin plates on Winkler foundation. Int J Num Meth Engng 1995;38:887-903.
- [8] Balas J, Sładek V, Sładek J. The boundary integral equation method for plates resting on a two parameter foundation. ZAMM 1984;64:137-46.
- [9] Katsikadelis JT, Kallivokas LF. Clamped plates on Pasternak-type elastic foundation by the boundary element method. J Appl Mech ASME 1986;53:909-17.
- [10] Katsikadelis JT, Kallivokas LF. Plates on biparametric elastic foundation by BDIE method. J Engng Mech 1988;114(5):847-75.
- [11] Venturini WS, Paiva JB. Boundary element for plate bending analysis. Engng Anal 1993;11:1-8.
- [12] Stern M. A general boundary integral formulation for the numerical solution of plate bending problems. Int J Solids Struct 1979;15:769-82.
- [13] Kane JH. Boundary element analysis in engineering continuum mechanics. Engelwood Cliffs, NJ: Prentice Hall, 1994.
- [14] Nerantzaki MS, Katsikadelis JT. A Green's function method for large deflection analysis of plates. Acta Mech 1988;75:211-25.
- [15] Katsikadelis JT, Nerantzaki MS. Non-linear analysis of plates by the analog equation method. Comput Mech 1994;14(2):154-64.
- [16] Timoshenko S, Woinowsky-Krieger S. Theory of plates and shells. 2nd ed. New York: McGraw-Hill, 1959.
- [17] Narin N. Thick plates on 2-parameters elastic foundation via finite element method. Master of Engineering Thesis. King Mongkut's University of Technology Thonburi, Thailand, 1996.

# Reprinted from

ISSN: 1225-4568

# Structural Engineering

# and Mechanics

An International Journal

Vol. 13, No. 6(2002) 713~730

# Free vibrations of inclined arches using finite elements

Somchai Chucheepsakul† and Wasuroot Saetiew‡

Department of Civil Engineering, King Mongkut's University of Technology Thonburi, Bangkok 10140, Thailand

(Received June 20, 2001, Accepted April 8, 2002)

Techno - Press

# Structural Engineering & Mechanics, An International Journal

# Editors-in-chief

**Professor Chang-Koon Chol** 

Department of Civil Engineering Korea Advanced Institute of Science & Technology Daejeon 305-701, Korea

Tel: +82-42 869-3611, Fax: +82-42 869-3610

E-mail: cck@kaist.ac.kr

Professor William C. Schnobrich

Department of Civil Engineering University of Illinois at Urbana-Champaign Urbana, IL 61801, U.S.A.

Tel: (217) 333-0154, Fax: (217) 333-9464

E-mail: schnobri@uiuc.edu

# International Editorial Board

Professor D. L. Anderson University of British Columbia

Vancouver, BC V6T 1W5, Canada

Professor E. R. de Arantes e Oliveira National Lab. of Civil Engineering

1799 Lisbon, Portugal Professor K. J. Bathe

Massachusetts Institute of Technology Cambridge, MA 02139-4307, U.S.A.

Professor P. Birkernoe University of Toronto Toronto, Ontario M5S 1A4, Canada

Professor R. de Borst Delft University of Technology NL-2600 GA Delft, The Netherlands

Professor L. Cedolin Politecnico di Milano Milano 20133, Italy

Professor F. Y. Cheng University of Missouri Rolla Rolla, MO 65401, U.S.A.

Professor L. Esteva National University of Mexico Ciudad Universitaria, 04510 DF, Mexico

Professor Filip C. Filippou University of California Berkeley, CA 94720, U.S.A.

Professor Y. Fujino University of Tokyo Tokyo 113, Japan

Professor A. K. Gupta North Carolina State University Raleigh, NC 27695-7908, U.S.A.

Professor T. T. C. Hsu University of Houston Houston, TX 77204-4791, U.S.A. Professor J. J. Jiang Tsinghua University Beijing 10084, China

Professor W. Kanok-Nukulchai Asian Institute of Technology Bangkok 10501, Thailand

Professor T. Kant Indian Institute of Technology-Powai Bombay 400076, India

Professor M. K. Kim Yonsei University Seoul 120-749, Korea

Professor M. Kleiber Polish Academy of Science Swietokyska 21, 00-49 Warsaw, Poland

Professor M. B. Krackovsky Research Institute for Concrete and RC 1009428 Moscow, Russia

Professor H. G. Kwak Korea Adv. Inst. of Sci. & Tech. Taejon 305-701, Korea

Or. S. C. Llu National Science Foundation Washington, D.C. 20550, U.S.A. Professor Y. C. Loo

Griffith University QLD 4217, Australia

Professor H. A. Mang Technical University of Vienna A-1040 Wien, Austria

Professor C. Meyer Columbia University New York, N.Y. 10027-6699, U.S.A.

Professor S. Otani University of Tokyo Tokyo 113, Japan Professor E. Oñate Universidad Politécnica de Catalufia 08034 Barcelona, Spain

Professor J. N. Reddy Texas A&M University College Station, Texas 77843-3123, U.S.A.

Professor R. Sampalo Pontificia Universidade Catolica Gavera, Rio de Janeiro 22.453, Brazil

Professor N. Shiraishl Maizuru Nat'l College of Techno. Kyoto 625, Japan

Professor S. Swaddiwudhlpong National University of Singapore Kent Ridge, Singapore 0511

Professor I. Takewaki Kyoto University Kyoto 606-8501, Japan Professor S. Valliappan

University of New South Wales Kensington, NSW 2033, Australia Professor Z. Xu

Tongji University Sanghai 200092, China Professor Y. B. Yang

National Taiwan University Taipei, Taiwan 10764, China

Professor J. Zarka Ecole Polytechnique F-91128, Palaiscau, France

Professor W. Zhong Dalian University of Technology Dalian 116023, China

Professor A.H. Zureick Georgia Institute of Technology Atlanta, Georgia 30332, U.S.A.

# Subscription information

The Structural Engineering and Mechanics is published 12 times a year. The subscription price for 2002 including postage by surface mail is US\$439.0 for institutional subscription and US\$190.0 for personal subscription. For delivery by air mail, add US\$45.0. Subscription orders and/or enquiries should be sent to Techno-Press. P.O. Box 33 Yuseong, Daejeon 305-600, Korea. Fax: +82-42 869-8450, e-mail: technop@chollian.net

# Advertisement information

For details, contact: Techno-Press, P.O. Box 33 Yuseong, Daejeon 305-600, Korea. Fax: +82-42 869-8450 copyright © 2002 Techno-Press. Ltd. published monthly (12 issues a year) in 2002

# Free vibrations of inclined arches using finite elements

Somchai Chucheepsakul† and Wasuroot Saetiew‡

Department of Civil Engineering, King Mongkut's University of Technology Thonburi, Bangkok 10140, Thailand

(Received June 20, 2001, Accepted April 8, 2002)

Abstract. This paper presents a finite element approach for determining the natural frequencies for planar inclined arches of various shapes vibrating in three-dimensional space. The profile of inclined arches, represented by undeformed centriodal axis of cross-section, is defined by the equation of plane curves expressed in the rectangular coordinates which are: circular, parabolic, sine, elliptic, and catenary shapes. In free vibration state, the arch is slightly displaced from its undeformed position. The linear relationship between curvature-torsion and axial strain is expressed in terms of the displacements in three-dimensional space. The finite element discretization along the span length is used rather than the total arc length. Numerical results for arches of various shapes are given and they are in good agreement with those reported in literature. The natural frequency parameters and mode shapes are reported as functions of two nondimensional parameters: the span to cord length ratio (e) and the rise to cord length ratio (f).

**Key words:** finite elements; free vibrations; inclined elastic arches; mode shapes.

# 1. Introduction

A considerable amount of research work has been done on the problem of free vibrations of arches and curved beams over the past several decades. In the literature, most of the research work is limited to arches supported at same level, and the analyses have been done only in a single plane: either in-plane or out-of-plane motion. Analytical solution for free vibrations can be found in cases where arches have simple geometry. For more complex configurations, a numerical method such as finite element method may be used. In-plane vibration analysis of circular arches were reported by Den Hartog (1928), Wolf (1971), Veletsos et al. (1972), Austin and Veletsos (1973), Irie et al. (1983) and Wilson et al. (1994). Arches with variable curvature (non-circular geometries) had been studied by many researchers, including, Volterra and Morell (1960, 1961a), Wang (1972), Romanelli and Laura (1972), Lee and Wilson (1989) and Oh et al. (1999). Free vibration of planar catenary arch with unsymmetric axes was reported by Wilson and Lee (1995). Circular arches and curved beams vibrating out-of-plane were reported by Culver (1967), Shore and Chaudhuri (1972), Volterra and Morell (1961b), and Irie et al. (1980, 1982a, 1982b).

Although the analysis of arches and curved structures using the finite element method has been well established, it does not take advantage of arch geometry. In many practical cases, arch

<sup>†</sup> Professor

<sup>:</sup> Graduate Student

geometry can be defined by the equation of plane curves in rectangular coordinates. With this information, it is more convenient to use the present procedure to solve the problem of planar inclined arch vibrating in three-dimensional space. In the procedure, geometry of the arch is represented by the undeformed centroidal axis of cross section and defined by equation of plane curves expressed in rectangular coordinates. In the vibration state, where the arch is slightly displaced from its undeformed position, the linear relationship between curvature-torsion and axial strain is expressed in terms of displacements in three-dimensional space. In the finite element formulation, the displacements causing bending, torsion and axial deformations along its curved axis are approximated by cubic polynomials in terms of the arc length parameters. The effects of shear deformation, rotatory inertia and warping are not considered in the present paper. In the discretizing process, the span length of the arch rather than total arc length is subdivided into a number of elements since, from the architectural point of view, span length is usually known or given, but the total arc length may not. Together with the arch geometry information, input data can be reduced and alleviated. The stiffness and mass matrices are formulated to obtain the natural frequencies and corresponding mode shapes of free vibrations. Numerical results of the test problems are presented and compared favorably with those found in the literature. The natural frequency parameters and the corresponding in-plane and out-of-plane modes are demonstrated as functions of two geometrical parameters: the span to cord length ratio (e) and the rise to cord length ratio (f).

# 2. Method of analysis

The geometry of an inclined arch with a uniform cross-section is shown in Fig. 1(a). It can be represented by the equation of plane curves expressed in rectangular coordinates. For a given shape of the plane curve, span length, cord length and arch rise, every location along the curve can be determined. The equations of plane curves for various shapes of arches are as follows

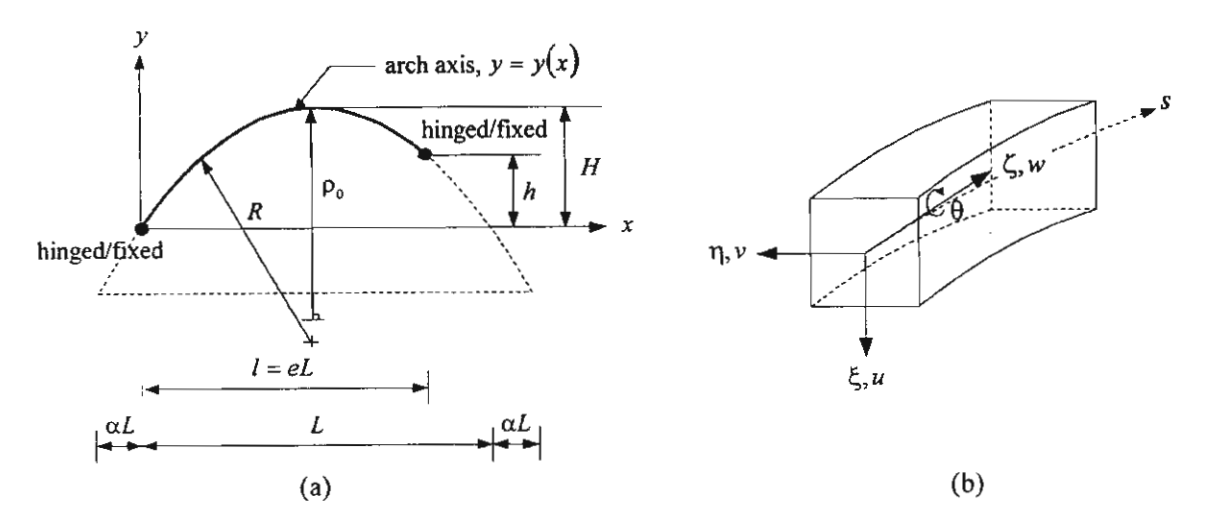


Fig. 1 (a) Arch geometry and geometric parameters; (b) coordinates at centroidal axis

# 2.1 Circular arch

$$y(x) = -(R - H) + \sqrt{R^2 - \left(x - \frac{L}{2}\right)^2}, \quad 0 \le x \le l$$
 (1a)

where

$$R = \left(\frac{L^2 + 4H^2}{8H}\right), \quad H = (R+h) + \sqrt{R^2 - \left(l - \frac{L}{2}\right)^2}$$
 (1b, c)

# 2.2 Parabolic arch

$$y(x) = \frac{4H}{L^2}(Lx - x^2), \quad 0 \le x \le l$$
 (2a)

where

$$H = \frac{hL^2}{4l(L-l)} \tag{2b}$$

# 2.3 Sinusoidal arch

$$y(x) = H - a + a\sin(bx + b\alpha L), \quad 0 \le x \le l$$
 (3a)

where

$$a = \frac{H}{1 - \sin(b\alpha L)}, \quad b = \frac{\pi}{L(1 + 2\alpha)}$$
 (3b, c)

$$H = h + a - a\sin(bl + b\alpha l) \tag{3d}$$

# 2.4 Elliptic arch

$$y(x) = -(c-H) + \frac{c}{d}\sqrt{d^2 - \left(x - \frac{L}{2}\right)^2}, \quad 0 \le x \le l$$
 (4a)

where

$$c = \frac{dH}{d - L\sqrt{\alpha + \alpha^2}}, \quad d = \frac{L}{2} + \alpha L$$
 (4b, c)

$$H = (h+c) - \frac{c}{d} \sqrt{d^2 - \left(l - \frac{L}{2}\right)^2}$$
 (4d)

# 2.5 Catenary arch

$$y(x) = H + \rho_0 - \rho_0 \cosh\left(\frac{x - 0.5L}{\rho_0}\right), \quad 0 \le x \le l$$
 (5a)

where

$$H = h - \rho_0 + \rho_0 \cosh\left(\frac{l - 0.5L}{\rho_0}\right) \tag{5b}$$

The geometric parameters in Eqs. (1)-(5) are defined as follows, l is the span length; L is the cord length; h is the different distance of both ends supported; H is the arch rise; R is the radius of the curvature of the circular arch;  $\alpha$  is the parameter used for identifying sinusoidal and elliptic arches only; and  $\rho_0$  is the radius of curvature at the crown of the catenary arch which is determined by normalizing Eq. 5(a) by the catenary cord length. The non-dimensional equation of the catenary arch is defined by the shape parameters (f) and (g) as

$$\overline{y}(\overline{x}) = f + g^{-1} - g^{-1} \cosh[g(\overline{x} - 0.5)]$$
 (6)

where

$$\overline{x} = x/L, \quad \overline{y} = y/L$$
 (7a, b)

$$f = H/L$$
,  $g = L/\rho_0$  (shape factors) (8a, b)

Substituting  $\bar{x} = 1$  and  $\bar{y} = 0$  into Eq. (6) leads to

$$fg - \cosh(0.5g) + 1 = 0 (9)$$

For a given catenary shape factor f, the corresponding g value can be obtained from Eq. (9) using the Newton-Raphson method.

In this study it is assumed that the undeformed centroidal axis of cross-section has a shape resembling that of plane curves. Finite element discretization along the arch length, which is not yet known, may be inconvenient for the input data process, therefore, it is preferable to discretize along the span length. In the vibration state, the undeformed centroidal axis is assumed to be slightly displaced from its initial position. The  $\xi$ ,  $\eta$ , and  $\zeta$  axes form a right-handed coordinate system in normal, binomial and tangential directions, and the displacements u, v, and w at the centroidal axis corresponding to the coordinate system are shown in Fig. 1(b). The relations between curvature-torsion, strain and displacements at the deformed state for any section s along the curved centroidal axis, are obtained and given here as follows (Chucheepsakul 1989):

$$\kappa_{\xi} = -\frac{d^2v}{ds^2} + \kappa\theta \tag{10a}$$

$$\kappa_{\eta} = \kappa + \frac{d^2 u}{ds^2} + \kappa^2 u + w \frac{d\kappa}{ds}$$
 (10b)

$$\tau_{\zeta} = \frac{d\theta}{ds} + \kappa \frac{dv}{ds} \tag{10c}$$

$$\varepsilon_{\zeta} = \frac{dw}{ds} - \kappa u \tag{10d}$$

where  $\kappa_{\xi}$ ,  $\kappa_{\eta}$ , and  $\tau_{\zeta}$  are the final curvatures and torsion about the  $\xi$ ,  $\eta$ ,  $\zeta$  axes, respectively.  $\theta$  is the rotation about the  $\zeta$ -axis,  $\varepsilon_{\zeta}$  is the axial strain and  $\kappa$  is the in-plane curvature of the undeformed centroidal axis and is defined as

$$\kappa = \frac{y''}{(1 + {y'}^2)^{3/2}} \tag{11}$$

# 2.6 Element strain energy and kinetic energy

Considering the  $e^{th}$  element along the curved axis, the element strain energy,  $U_e$ , and the element kinetic energy,  $T_e$ , can be expressed as

$$U_{\epsilon} = \int_{0}^{t} \left[ EA \varepsilon_{\zeta}^{2} + EI_{\xi} \kappa_{\xi}^{2} + EI_{\eta} (\kappa_{\eta} - \kappa)^{2} + GJ \tau_{\zeta}^{2} \right] ds \tag{12}$$

$$T_{e} = \frac{1}{2} \int_{0}^{t} \left\{ \rho \left[ \left( \frac{\partial u}{\partial t} \right)^{2} + \left( \frac{\partial v}{\partial t} \right)^{2} + \left( \frac{\partial w}{\partial t} \right)^{2} \right] + I_{\rho} \left( \frac{\partial \theta}{\partial t} \right)^{2} \right\} ds \tag{13}$$

where  $EI_{\xi}$  and  $EI_{\eta}$  are the bending rigidities about  $\xi$  and  $\eta$  axes, GJ and EA are the torsional and axial rigidities,  $\rho$  is the mass density of arch per unit length,  $I_{\rho}$  is the mass polar of inertia per unit length about  $\zeta$  and I is an element length measured along the curve. Eqs. (12) and (13) can be written in the following form as

$$U_{\epsilon} = \frac{1}{2} \int_{0}^{t} \left[ \left\{ \kappa^{*} \right\}^{T} \left\{ E \right\} \left\{ \kappa^{*} \right\} + \left\{ \varepsilon \right\}^{T} E A \left\{ \varepsilon \right\} \right] ds \tag{14}$$

$$T_{e} = \frac{1}{2} \int_{0}^{t} \{\dot{u}\}^{T} [\rho] \{\dot{u}\} ds$$
 (15)

where

$$\{\kappa^*\} = \begin{Bmatrix} \kappa_{\zeta} \\ \kappa_{\eta} - \kappa \\ \kappa_{\zeta} \end{Bmatrix}, \quad [E] = \begin{bmatrix} EI_{\zeta} & 0 & 0 \\ 0 & EI_{\eta} & 0 \\ 0 & 0 & GJ \end{bmatrix}, \quad \{\varepsilon\} = \varepsilon_{\zeta}$$
 (16-18)

$$\{\dot{u}\} = \begin{bmatrix} \frac{\partial u}{\partial t} & \frac{\partial v}{\partial t} & \frac{\partial w}{\partial t} & \frac{\partial \theta}{\partial t} \end{bmatrix}^{T}, \quad [\rho] = \begin{bmatrix} \rho & 0 & 0 & 0 \\ 0 & \rho & 0 & 0 \\ 0 & 0 & \rho & 0 \\ 0 & 0 & 0 & I_{\rho} \end{bmatrix}$$
(19, 20)

# 3. Finite element formulation

The displacement components u, v, w and  $\theta$  of the  $e^{th}$  element can be expressed by cubic polynomials in term of the arc length parameter s. Hence, the displacement vector  $\{u\}$  can be simply expressed in terms of a nodal displacement vector  $\{d\}$  through the matrix of shape functions [F] as:

$$\{u\} = [F]\{d\} \tag{21}$$

in which

$$\{u\} = \begin{bmatrix} u & v & w & \theta \end{bmatrix}^T \tag{22}$$

The elements of  $4 \times 16$  matrix [F] are

$$[F] = \begin{bmatrix} f_1 & f_2 & 0 & 0 & 0 & 0 & 0 & f_3 & f_4 & 0 & 0 & 0 & 0 & 0 & 0 \\ 0 & 0 & f_1 & f_2 & 0 & 0 & 0 & 0 & 0 & f_3 & f_4 & 0 & 0 & 0 & 0 \\ 0 & 0 & 0 & 0 & f_1 & f_2 & 0 & 0 & 0 & 0 & 0 & f_3 & f_4 & 0 & 0 \\ 0 & 0 & 0 & 0 & 0 & f_1 & f_2 & 0 & 0 & 0 & 0 & 0 & f_3 & f_4 \end{bmatrix}$$
 (23)

where the components  $f_1$ ,  $f_2$ ,  $f_3$ , and  $f_4$  are the standard shape functions for a beam element (Cook 1981), and

$$\{d\} = \begin{bmatrix} u_1 & u_1' & v_1 & v_1' & w_1 & w_1' & \theta_1 & \theta_1' & u_2 & u_2' & v_2 & v_2' & w_2 & w_2' & \theta_2 & \theta_2' \end{bmatrix}^T$$
(24)

Substitution of Eq. (21) into Eqs. (14) and (15), the strain energy and kinetic energy can be written as:

$$U_e = \frac{1}{2} \{d\}^T [k_e] \{d\}$$
 (25)

$$T_e = \frac{1}{2} \{\dot{d}\}^T [m_e] \{\dot{d}\}$$
 (26)

in which  $\{\dot{d}\}$  is the nodal velocity vector, and  $[k_e]$  and  $[m_e]$  are the element stiffness and element mass matrices, written respectively as:

$$[k_e] = \int_0^t [G]^T [[A]^T [E][A] + [P]^T E A[P]][G] ds$$
 (27)

$$[m_e] = \int_0^t [F]^T [\rho] [F] ds \tag{28}$$

where matrices [G], [A] and row matrix [P] are as follows:

$$[G] = \begin{bmatrix} f_1 & f_2 & 0 & 0 & 0 & 0 & 0 & f_3 & f_4 & 0 & 0 & 0 & 0 & 0 & 0 \\ f'_1 & f'_2 & 0 & 0 & 0 & 0 & 0 & 0 & f'_3 & f'_4 & 0 & 0 & 0 & 0 & 0 & 0 \\ f''_1 & f''_2 & 0 & 0 & 0 & 0 & 0 & 0 & 0 & f''_3 & f''_4 & 0 & 0 & 0 & 0 & 0 \\ 0 & 0 & f'_1 & f'_2 & 0 & 0 & 0 & 0 & 0 & 0 & f'_3 & f'_4 & 0 & 0 & 0 & 0 \\ 0 & 0 & f''_1 & f''_2 & 0 & 0 & 0 & 0 & 0 & 0 & f''_3 & f''_4 & 0 & 0 & 0 & 0 \\ 0 & 0 & 0 & 0 & f_1 & f_2 & 0 & 0 & 0 & 0 & 0 & f_3 & f_4 & 0 & 0 \\ 0 & 0 & 0 & 0 & 0 & f'_1 & f'_2 & 0 & 0 & 0 & 0 & 0 & 0 & f_1 & f_2 \\ 0 & 0 & 0 & 0 & 0 & 0 & f'_1 & f'_2 & 0 & 0 & 0 & 0 & 0 & 0 & f'_3 & f'_4 \end{bmatrix}$$

$$(29)$$

$$[A] = \begin{bmatrix} 0 & 0 & 0 & 0 & -1 & 0 & 0 & \kappa & 0 \\ \kappa^2 & 0 & 1 & 0 & 0 & \kappa' & 0 & 0 & 0 \\ 0 & 0 & 0 & \kappa & 0 & 0 & 0 & 0 & 1 \end{bmatrix}$$
(30)

$$[P] = [-\kappa \ 0 \ 0 \ 0 \ 0 \ 1 \ 0 \ 0] \tag{31}$$

Here 'prime' denotes the derivative with respect to s.

Because of discretizing along the x coordinate, before the element matrices are evaluated, the variables in term of s are required to be expressed in term of x by the following relation:

$$ds = \sqrt{1 + {y'}^2} dx \tag{32}$$

Therefore, the derivative terms with respect to s can be changed to x by the relation:

$$\frac{d(\ )}{ds} = \frac{1}{\sqrt{1 + {v'}^2}} \frac{d(\ )}{dx} \tag{33}$$

After the element stiffness and mass matrices are evaluated they are assembled to the global system. Hence, the global equations of motion for free vibration are:

$$[K]\{D\} = \omega^2[M]\{D\} \tag{34}$$

where [K] and [M] are global stiffness and mass matrices,  $\{D\}$  is a mode shape vector, and  $\omega$  is the natural frequencies of vibrations. The boundary conditions are as follows:

(a) hinged-hinged arches:

$$u = v = w = \theta = 0$$
, at the left end  $(x = 0)$  and the right end  $(x = l)$  (35)

(b) hinged-fixed arches:

$$u = v = w = \theta = 0$$
, at the left end  $(x = 0)$  (36a)

$$u = u' = v = v' = w = w' = \theta = \theta' = 0$$
, at the right end  $(x = l)$  (36b)

(c) fixed-hinged arches:

$$u = u' = v = v' = w = w' = \theta = \theta' = 0$$
, at the left end  $(x = 0)$  (37a)

$$u = v = w = \theta = 0$$
, at the right end  $(x = l)$  (37b)

(d) fixed-fixed arches:

$$u = u' = v = v' = w = w' = \theta = \theta' = 0$$
, at the left end  $(x = 0)$  and the right end  $(x = 1)$  (38)

Gaussian quadrature numerical integration with four points is used to calculate the stiffness and mass matrices, and a standard inverse vector iteration (Bathe and Wilson 1976) is used to solve Eq. (34).

# 4. Numerical results and comments

A Fortran computer program based on the procedure described above was developed for determining the natural frequencies and the corresponding mode shapes. Test examples of arch problems are used to demonstrate the validity of the model formulation. The total number of span elements used throughout this analysis is twenty elements. For ease of calculation, the arches having uniform prismatic cross section and two axes of symmetry are used. The material properties of arches are as follows: cross-section area  $A = 1.2 \times 10^{-3}$  m<sup>2</sup>, mass per unit length  $\rho = 9.42$  kg/m, moment of inertia  $I_{\xi} = I_{\eta} = 1.2 \times 10^{-7}$  m<sup>4</sup>, torsional constant  $J = 2.02464 \times 10^{-7}$  m<sup>4</sup>, elastic modulus  $E = 210 \times 10^{9}$  N/m<sup>2</sup>, shear modulus  $G = 81 \times 10^{9}$  N/m<sup>2</sup>. Table 1 shows the numerical comparison of frequency parameter  $C_{ni}$  for the in-plane mode of various arch shapes whereas Table 2 shows the

Table 1 Comparison of frequency parameter  $C_{ni}$  for in-plane mode

		Frequency parameter, $C_{ni}$					
Geometry of arch	(ni)	This study	Veletsos et al. (1972)	Lee and Wilson (1989)	Wilson and Lee (1995)	Mode shape*	
Circular	1	27.50	27.51	-	-	A	
hinged-hinged,	2	63.79	63.80	-	-	S	
l = L = 1.0606 m,	3	123.07	123.12	-	-	A	
H = 0.2197  m	4	141.56	141.52	-	-	S	
Parabolic	1	36.11	-	36.52	-	Α	
hinged-hinged,	2	64.95	-	64.83	-	S	
l = L = 1.0  m,	3	88.92	_	89.38	-	S	
H = 0.1  m	4	148.64	-	-	-	A	
Sinusoidal	1	28.52	-	29.35	÷	N	
hinged-fixed, $\alpha = 0.5$ ,	2	67.45	-	68.44	-	N	
l = L = 1.0  m,	3	119.31	-	119.86	-	N	
H = 0.3  m	4	149.65	-	-	-	N	
Elliptic	1	20.77	-	20.88	•	Α	
fixed-fixed, $\alpha = 0.5$ ,	2	49.15	_	49.95	-	S	
l = L = 1.0  m,	3	85.68	-	85.79	-	Α	
H = 0.5  m	4	128.28	-	-	-	S	
Catenary	1	45.02	-	-	46.32	A*	
hinged-hinged,	2	107.44	-	-	107.79	S*	
l = 0.75  m, $L=1.0  m$ ,	3	166.83	-	-	166.51	$\mathcal{S}^*$	
H = 0.3  m	4	203.69	-	-	204.21	$A^*$	
Catenary	1	73.18	-	-	72.21	A*	
fixed-fixed,	2	130.99	-	-	129.23	S*	
l = 0.75  m, L = 1.0  m,	3	182.39	-	-	180.57	S*	
H = 0.3  m	4	256.94	-	-	254.69	$A^*$	

#A = antisymmetric; S = symmetric; N = neither antisymmetric nor symmetric;  $A^*$  = close fit to antisymmetric;  $S^*$  = close fit to symmetric.

Coometer of each	(= a)	Frequency parameter, $C_{no}$			
Geometry of arch	(no) –	This study	Shore and Chaudhuri (1972)	shape#	
Circular	1	5.10	5.10	S	
hinged-hinged,	2	28.63	28.65	Α	
l = L = 1.0606 m,	3	68.48	68.55	S	
H = 0.2197  m	4	124.39	124.51	Α	

#A = antisymmetric; S = symmetric.

out-of-plane frequency parameter  $C_{no}$  of a circular arch. The values of frequency parameters  $C_{ni}$  and  $C_{no}$  are defined as follows:

$$C_{ni} = \omega_{ni} L^2 / \sqrt{E I_{\eta} / \rho} \tag{39}$$

$$C_{no} = \omega_{no} L^2 / \sqrt{EI_{\xi}/\rho} \tag{40}$$

It can be seen that the results are in good agreement for all cases. Thus, the authors believe that the model formulation presented herein can be used for determining the natural frequencies of arches of various shapes having geometry defined by the equation plane curves expressed in the rectangular coordinates.

The results shown in Figs. 2-17 depict the values of the first four frequency parameters ( $C_{ni}$  and  $C_{no}$ )

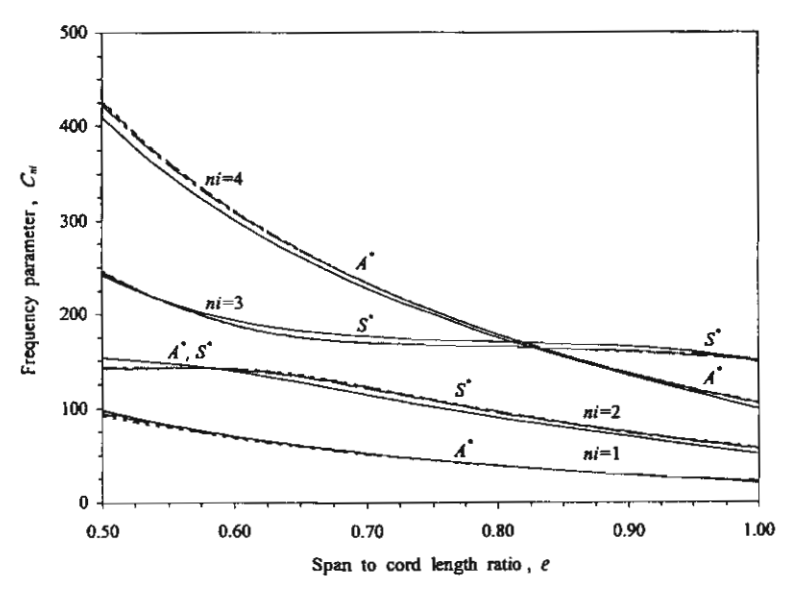


Fig. 2 Hinged-hinged arches: effect of e with f = 0.3 on frequency for in-plane vibration; ——, circular; ——, parabolic; ——, sinusoidal( $\alpha = 0.5$ ); ——, elliptic( $\alpha = 0.5$ ); ——, catenary

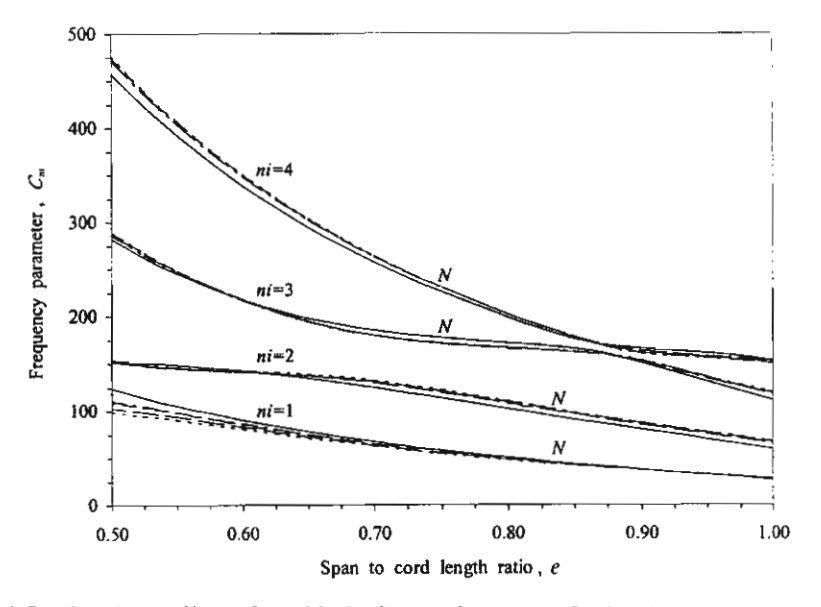


Fig. 3 Hinged-fixed arches: effect of e with f = 0.3 on frequency for in-plane vibration. Key as Fig. 2

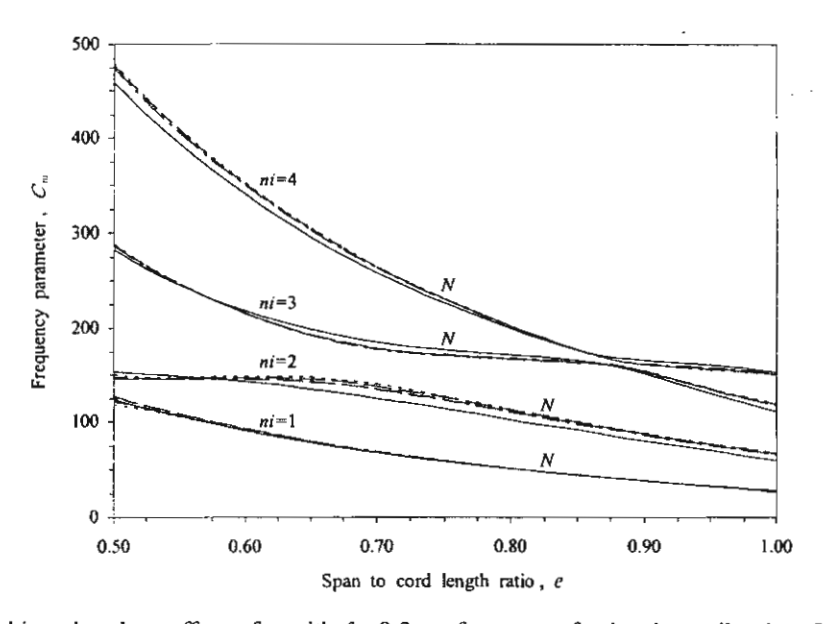


Fig. 4 Fixed-hinged arches: effect of e with f = 0.3 on frequency for in-plane vibration. Key as Fig. 2

corresponding to the first four free vibration modes of the five arch shapes. The hinged-hinged, hinged-fixed, fixed-hinged, and fixed-fixed end constraints were considered for each of the arch geometry with the given parameters of the span to cord length ratio (e), and the rise to cord length ratio (f) and  $\alpha$  (it is noted here that  $\alpha$  is used for sinusoidal and elliptic geometries only).

Figs. 2-9 show the variation of  $C_{ni}$  and  $C_{no}$  due to effect of the span to cord length ratio e with

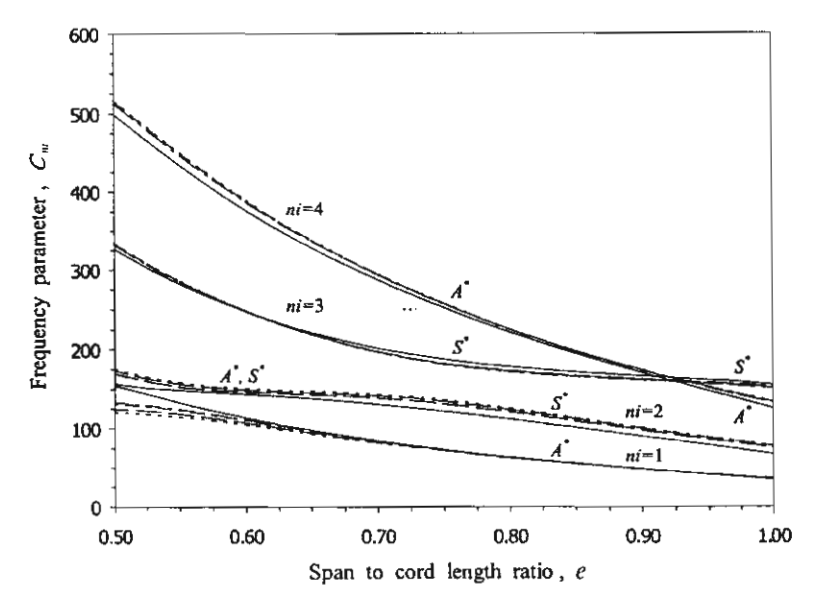


Fig. 5 Fixed-fixed arches: effect of e with f = 0.3 on frequency for in-plane vibration. Key as Fig. 2

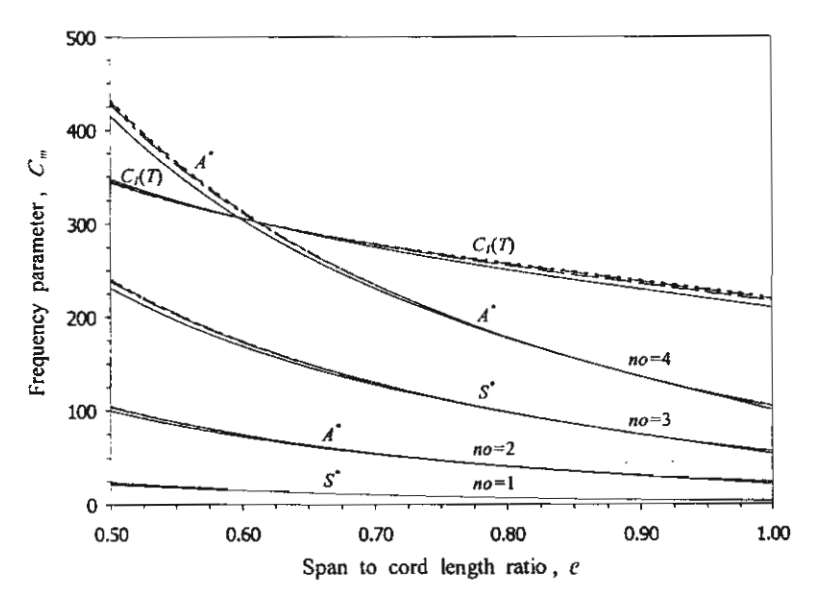


Fig. 6 Hinged-hinged arches: effect of e with f = 0.3 on frequency for out-of-plane vibration. Key as Fig. 2

fixed value of f = 0.3 and  $\alpha = 0.5$ . The end constraint of all five arches are varied consecutively from hinged-hinged, to hinged-fixed, to fixed-hinged, and to fixed-fixed conditions. It can be seen that each value of frequency parameter increases with the increase of constraint condition, while the other parameters remain constant. It is also observed that the frequency parameters decrease with the increase in span to cord length ratio. For in-plane vibration (Figs. 2 and 5), it appears that frequency crossover as well as modal transition occur between two mode shapes ni = 3 and ni = 4,

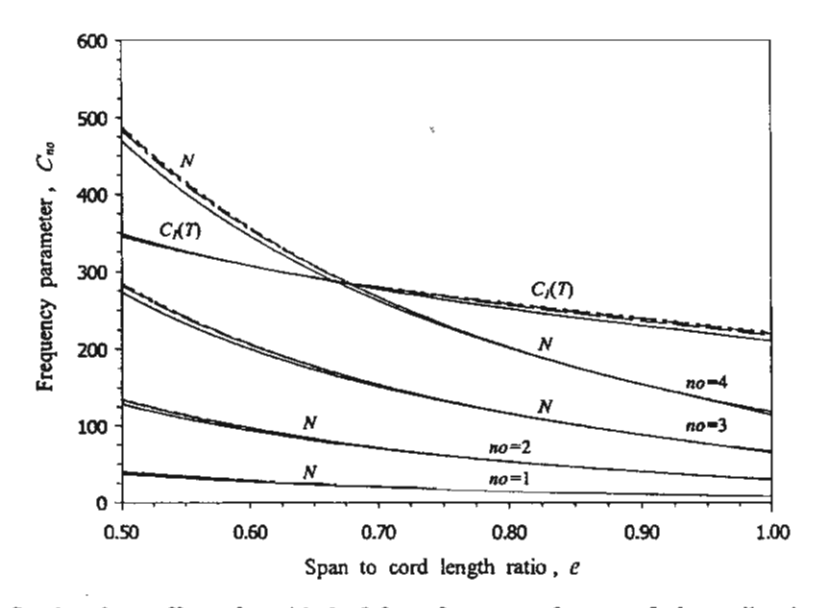


Fig. 7 Hinged-fixed arches: effect of e with f = 0.3 on frequency for out-of-plane vibration. Key as Fig. 2

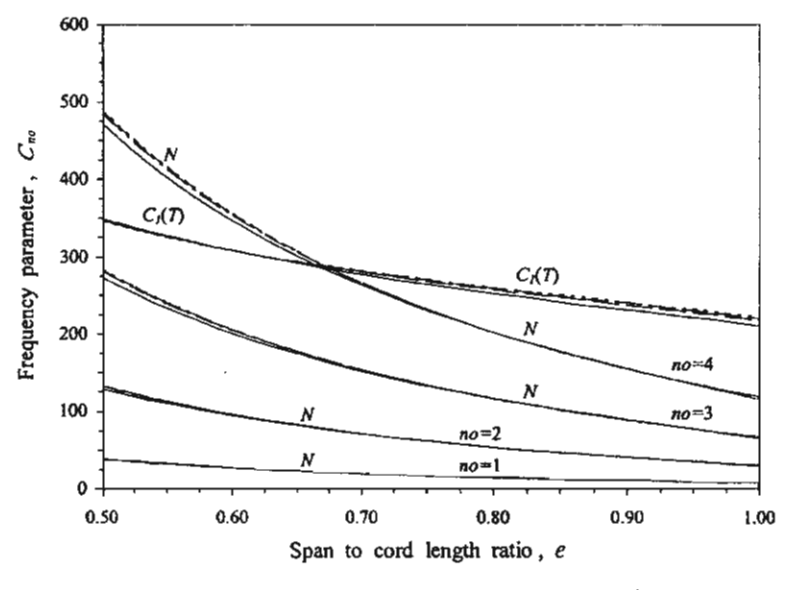


Fig. 8 Fixed-hinged arches: effect of e with f = 0.3 on frequency for out-of-plane vibration. Key as Fig. 2

except for hinged-fixed and fixed-hinged conditions in Figs. 3 and 4. The circular arch is nearly fit to symmetric mode shape at where ni = 2, where as the arches with variable curvature (parabolic, sinusoidal, elliptic and catenary) are nearly fit to antisymmetric and changed to symmetric mode shapes when the span to cord length ratio is increased, as shown in Figs. 2 and 5 respectively. For out-of-plane vibration (Figs. 6-9), the values of  $C_{no}$  for all arch geometries are slightly different and have the same trend. The lowest torsional frequency parameter  $C_1(T)$  represented by the torsional

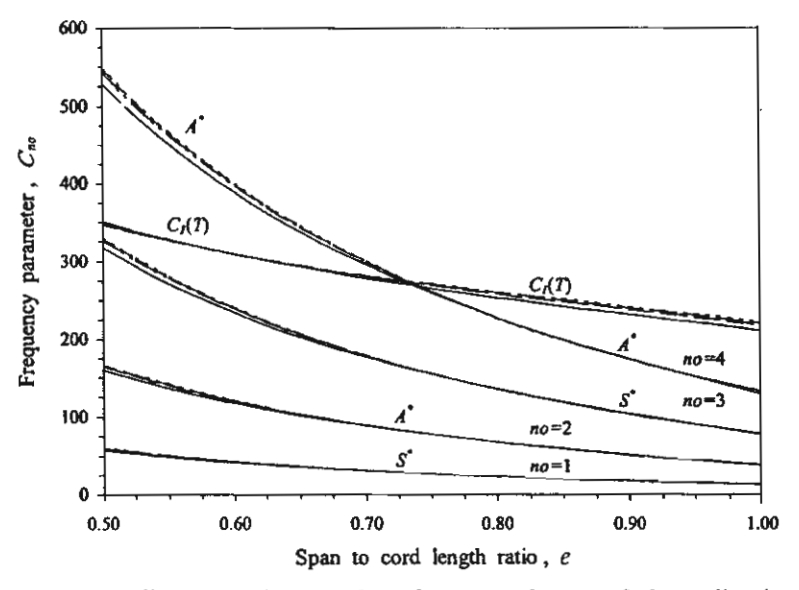


Fig. 9 Fixed-fixed arches: effect of e with f = 0.3 on frequency for out-of-plane vibration. Key as Fig. 2

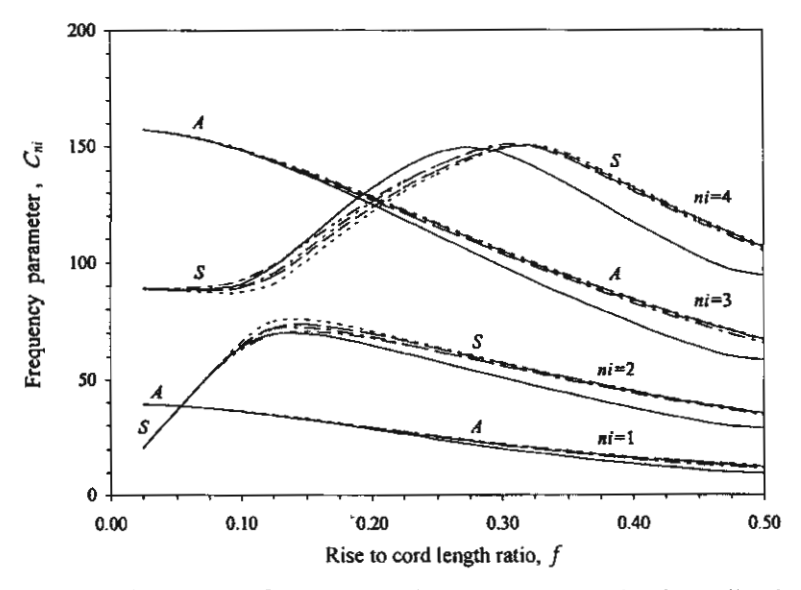


Fig. 10 Hinged-hinged arches: effect of f with e = 1.0 on frequency for in-plane vibration. Key as Fig. 2

angle is found and at e = 0.5 this value belongs to the fourth mode of vibration.

Figs. 10-17 show the variation of  $C_{ni}$  and  $C_{no}$  due to the effect of the rise to cord length ratio f with fixed value of e = 1.0 and  $\alpha = 0.5$ . The end constraint conditions are varied from hinged-hinged to hinged-fixed (or fixed-hinged) to fixed-fixed conditions for all geometry of arches. It can be seen that each value of frequency parameter increases, while other parameters remain constant (for hinged-fixed and fixed-hinged arches, the frequency parameters are equivalent due to the same end

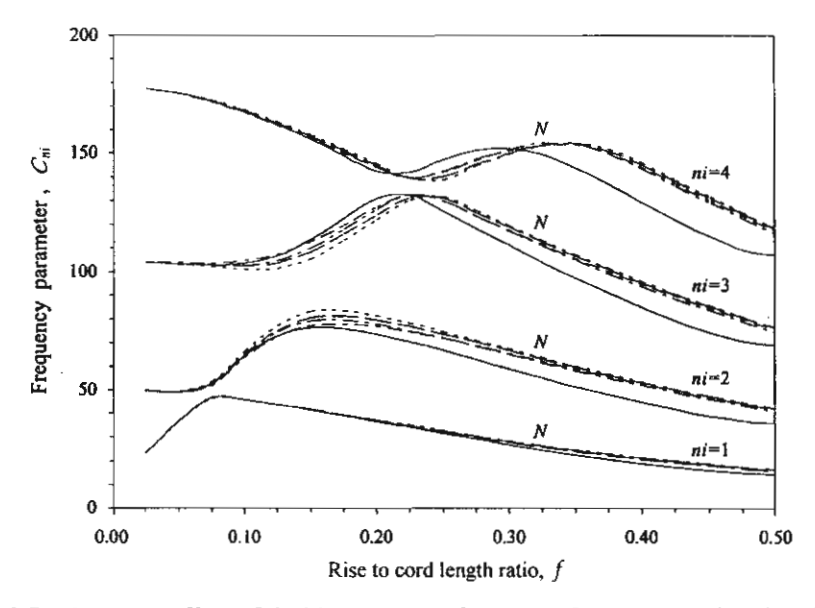


Fig. 11 Hinged-fixed arches: effect of f with e = 1.0 on frequency for in-plane vibration. Key as Fig. 2

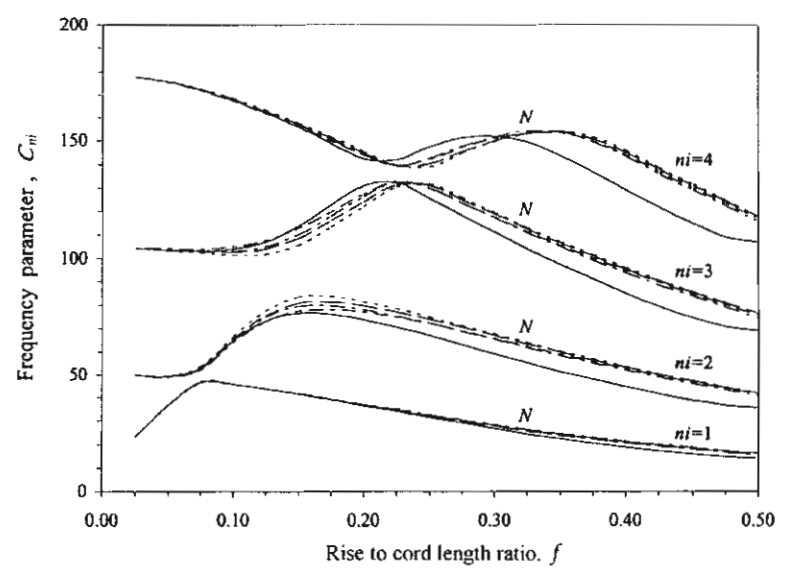


Fig. 12 Fixed-hinged arches: effect of f with e = 1.0 on frequency for in-plane vibration. Key as Fig. 2

constraint condition). For in-plane vibration (Figs. 10 and 13), it is observed that frequency crossover as well as modal transitions can occur between two mode shapes ni = 1 and ni = 2, ni = 3 and ni = 4, however, the frequency crossover does not occur in hinged-fixed and fixed-hinged arches as found in Figs. 11, 12. For out-of-plane vibration (Figs. 14-17), it is found typically that the frequency parameters decrease with the increasing value of rise to cord length ratio, and the mode shapes of arches with same end conditions can be identified. The mode shapes for arches with

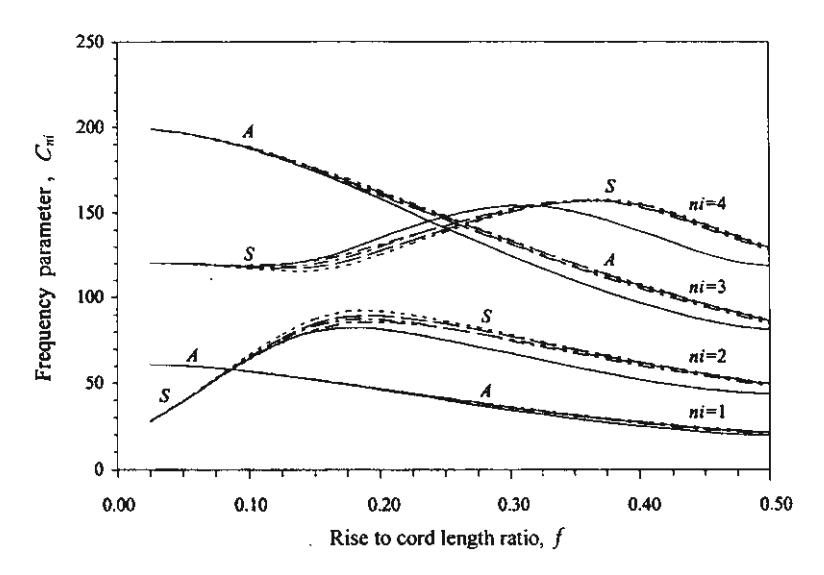


Fig. 13 Fixed-fixed arches: effect of f with e = 1.0 on frequency for in-plane vibration. Key as Fig. 2

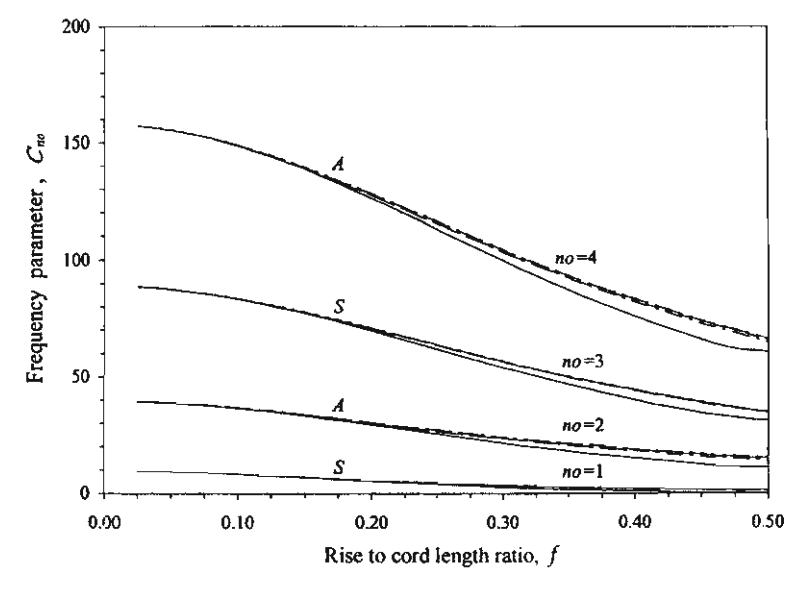


Fig. 14 Hinged-hinged arches: effect of f with e = 1.0 on frequency for out-of-plane vibration. Key as Fig. 2

mixed end conditions can be neither symmetric nor anti-symmetric.

# 5. Conclusions

A finite element procedure for free vibration analysis of the planar arches with support at the same or different level, and vibrating in three-dimensional space has been presented. The geometry

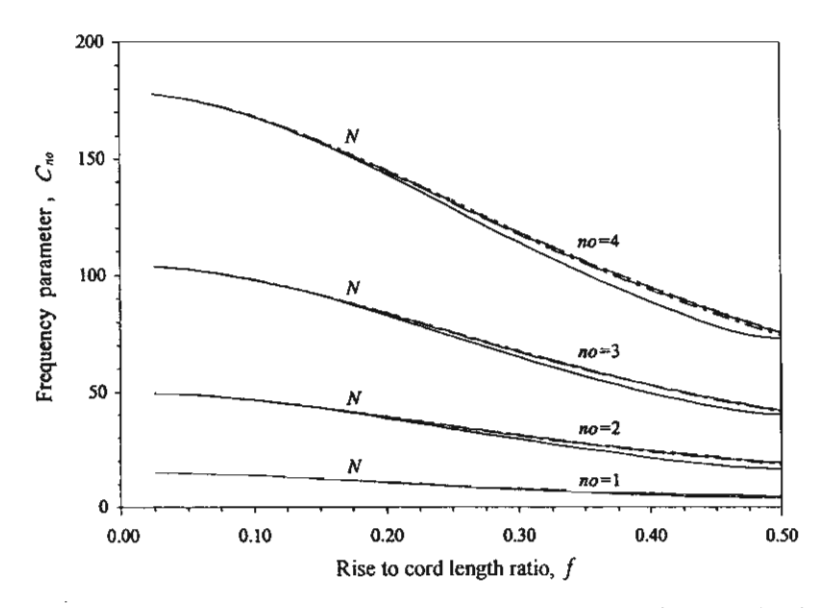


Fig. 15 Hinged-fixed arches: effect of f with e = 1.0 on frequency for out-of-plane vibration. Key as Fig. 2

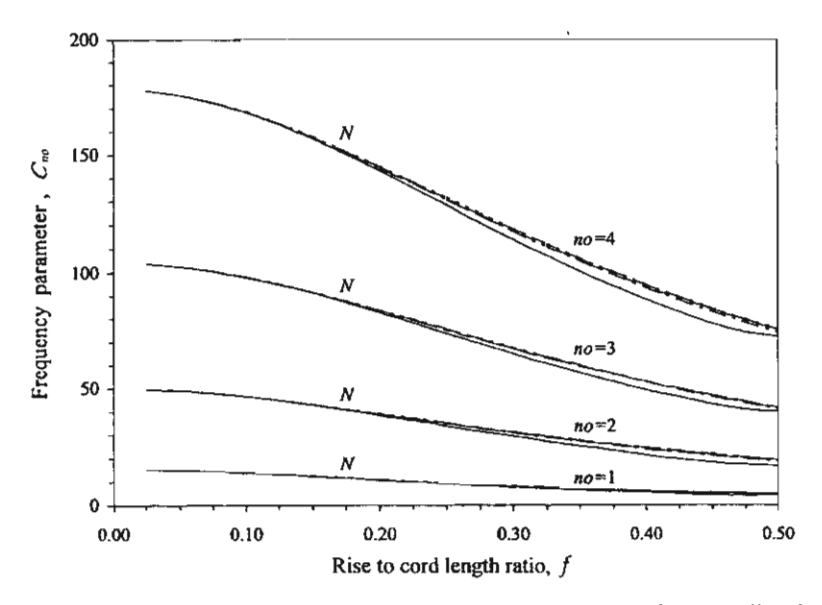


Fig. 16 Fixed-hinged arches: effect of f with e = 1.0 on frequency for out-of-plane vibration. Key as Fig. 2

of arches is represented by an equation of a plane curve in rectangular coordinates. The model formulation has been verified by the favorable comparisons the values of the frequency parameters with those reported in the literature. For a given set of arch parameters (e and f) and matching end constrains, numerical results have shown that the frequency parameters for arches with variable curvature (parabolic, sinusoidal, elliptic and catenary arches) change only slightly in these groups; but show somewhat larger differences for the circular arch due to its constant curvature. As

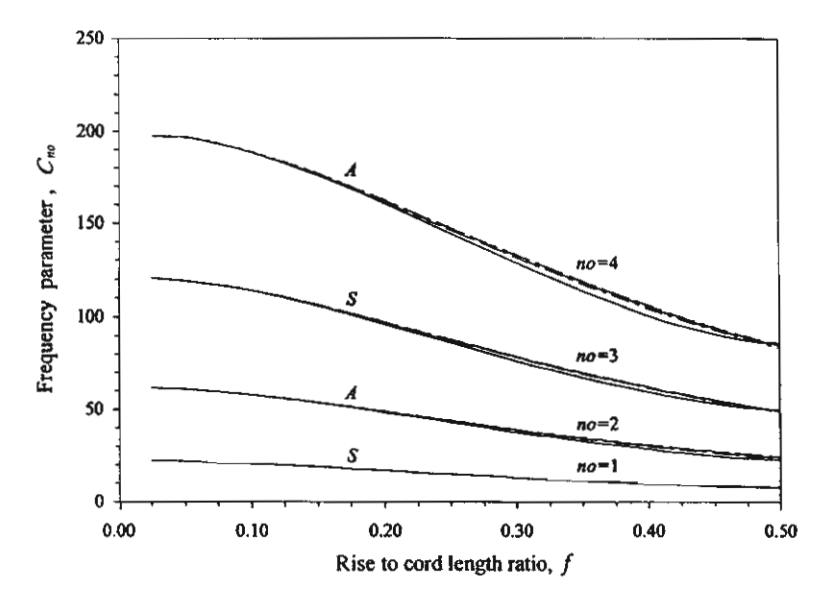


Fig. 17 Fixed-fixed arches: effect of f with e = 1.0 on frequency for out-of-plane vibration. Key as Fig. 2

expected, the mode shapes for the hinged-fixed and fixed-hinged cases are neither symmetric nor antisymmetric because of the difference in end conditions. For the hinged-hinged and the fixed-fixed types of arches supporting at the same level the mode shapes are found to be the alternating pattern between anti-symmetric and symmetric modes. For the hinged-hinged and the fixed-fixed end conditions of arches supporting at different levels, the numerical results have shown that neither pure symmetric nor pure antisymmetric mode shapes exist.

# Acknowledgements

The authors are grateful for financial support from the Thailand Research Fund (TRF) under grant RTA/03/2543.

# References

Austin, W.J. and Veletsos, A.S. (1973), "Free vibration of arches flexible in shear", J. Eng. Mech. Div., ASCE, 99(EM4), 735-753.

Bathe, K.J. and Wilson, E.L. (1976), Numerical Methods in Finite Element Analysis, Prentice-Hall, Inc., Englewood Cliffs, N.J.

Chucheepsakul, S. (1989), "Free vibration of elastic arches", Proc. the Second East Asia-Pacific Conf. on Struct. Engrg. and Const., Chiang Mai, Thailand, 1610-1616.

Cook, R.D. (1981), Concepts and Applications of Finite Element Analysis, Third Edition, John Wiley & Sons, Singapore.

Culver, C.G. (1967), "Natural frequencies of horizonatally curved beams", J. Struct. Div., ASCE, 93(ST2), 189-203.

Den Hartog, J.P. (1928), "The lowest natural frequency of circular arcs", Philosophical Magazine, Series 7,

- 5(28), 400-408.
- Irie, T., Yamada, G. and Takahashi, I. (1980), "Out-of-plane vibration of arc bar of variable cross-section", Bulletin of the JSME, 23(181), 1200-1205.
- Irie, T., Yamada, G. and Tanaka, K. (1982a), "Free out-of-plane vibration of arcs", J. Appl. Mech., ASME, 49, 439-441.
- Irie, T., Yamada, G. and Tanaka, K. (1982b), "Natural frequencies of out-of-plane vibration of arcs", J. Appl. Mech., ASME, 49, 910-913.
- Irie, T., Yamada, G. and Tanaka, K. (1983c), "Natural frequencies of in-plane vibration of arcs", J. Appl. Mech., ASME, 50, 449-452.
- Lee, B.K. and Wilson, J.F. (1989), "Free vibration of arches with variable curvature", J. Sound and Vib., 136(1), 75-89.
- Oh, S.J., Lee, B.K. and Lee, I.W. (1999), "Natural frequencies of non-circular arches with rotatory inertia and shear deformation", J. Sound and Vib., 219(1), 23-33.
- Romanelli, E. and Laura, P.A.A. (1972), "Fundamental frequencies of non-circular, elastic, hinged arch", J. Sound and Vib., 24(1), 17-22.
- Shore, S. and Chauduri, S. (1972), "Free vibration of horizontally curved beams", J. Struct. Div., ASCE, 98(ST3), 793-796.
- Veletsos, A.S., Austin, W.J., Pereira, C.A.L. and Wung, S.J. (1972), "Free in-plane vibration of circular arches", J. Eng. Mech. Div., ASCE, 98(EM2), 311-329.
- Volterra, E. and Morell, J.D. (1960), "A note on the lowest natural frequency of elastic arcs", J. Appl. Mech., ASME, Series E, 27(4), 744-746.
- Volterra, E. and Morell, J.D. (1961a), "Lowest natural frequencies of elastic hinged arcs", J. Acoust. Soc. Am., 33(12), 1787-1790.
- Volterra, E. and Morell, J.D. (1961b), "Lowest natural frequency of elastic arcs for vibrations outside the plane of initial curvature", *J. Appl. Mech.*, ASME, Series E, 28(4), 624-627.
- Wang, T.M. (1972), "Lowest natural frequency of clamped parabolic arch", J. Struct. Div., ASCE, 98(ST1), 407-411.
- Wilson, J.F., Lee, B.K. and Oh, S.J. (1994), "Free vibrations of circular arches with variable cross-section", Struct. Eng. Mech., 2(4), 345-357.
- Wilson, J.F. and Lee, B.K. (1995), "In-plane free vibrations of catenary arches with unsymmetric axes", Struct. Eng. Mech., 3(5), 511-525.
- Wolf, J.A., Jr. (1971), "Natural frequencies of circular arches", J. Struct. Div., ASCE, 97(ST9), 2337-2350.

ISSN: 1225-4568

# STRUCTURAL ENGINEERING AND MECHANICS

# An International Journal

# Aims and Scope

The STRUCTURAL ENGINEERING AND MECHANICS, An International Journal, aims at: providing a major publication channel for structural engineering, wider distribution at more affordable subscription rates; faster reviewing and publication for manuscripts submitted; and a broad scope for wider participation.	
The main subject of the Journal is structural engineering concerned with aspects of mechanics. Areas covered by the Journal include:   Structural Mechanics;   Design of Civil, Building and Mechanical Structures;   Structural Optimization and Controls;   Structural Safety and Reliability;   New Structural Materials and Applications;   Effects of Wind, Earthquake and Wave Loadings on Structures;   Fluid-Structure and Soil-Structure Interactions;   Al Application and Expert Systems	
in Structural Engineering. Submission of papers from practising engineers is particularly encouraged.	

## Instruction to Authors

# 1. Submission of the paper

Manuscripts should be submitted in triplicate either to:

Professor Chang-Koon Choi

Department of Civil Engineering

Korea Advanced Institute of Science & Technology

Taejon 305-701, Korea

Tel: +82-42 869-3611, Fax: +82-42 869-3610

E-mail: cck@kaist.ac.kr

# or to: Professor William C. Schnobrich

Department of Civil Engineering

University of Illinois at Urbana-Champaign

Urbana, IL 61801. U.S.A.

Tel: (217)333-0154, FAX: (217)333-9464

E-mail: schnobri@uiuc.edu

Authors will be requested to submit manuscripts on diskettes after the acceptance of paper (partial manuscript on diskettes will also be acceptable).

# 2. Preparation of the manuscript

General: The manuscripts should be in English and typed with double line spacing on single side of A4 paper. The first page of an article should contain; (1) a short title (reflecting the content of the paper), (2) all the name(s) and address(es) of author(s), (3) name and address of the author to whom correspondence and proofs should be sent, and (4) an abstract of 100-200 words. The paper should be concluded by proper conclusions which reflect the findings in the paper. The length of paper should not exceed 16 journal pages (approx. 9000-words equivalent). There will be no page charges if the length of paper is within the limit. A separate list of key words should be provided at the end of the manuscript.

Tables and figures: Tables and figures should be consecutively numbered and headed with short titles. They should be referred to in the text as Fig. 1, Table 2, etc. Originally drawn figures and glossy prints of photographs should be provided in a form suitable for photographic reproduction and reduction in the journal. A separate list of captions for illustrations should be provided at the end of the manuscript.

Units and mathematical expressions: It is desirable that units of measurements and abbreviations should follow the Systeme Internationalé (SI). The numbers identifying the displayed mathematical expression should be placed in parentheses and referred to in the text as Eq. (1), Eq. (2) ...

References: References to published literature should be referred in the text by the last name(s) of author(s) and the year of publication of the reference (e.g., Choi and Schnobrich 1975) and listed in the alphabetical order of the last name of the first author in an appendix at the end of the paper. Journal titles should be abbreviated in the style of the World List of Scientific Periodicals. References should be cited in the following style.

Journal: Choi, C.K., and Kim, S.H. (1989), "Coupled use of reduced integration and nonconforming modes in

improving quadratic plate element", Int. J. Num. Meth. Eng., 28(4), 1909-1928.

Salvadori, M.G., and Baron, M.L. (1961), Numerical Methods in Engineering, Prentice-Hall, Englewood Book:

Cliffs, N.J.

Proceedings: Choi, C.K., and Kwak, H.G. (1989), "Optimum RC member design with discrete sections", Proceedings of '89 ASCE Structures Congress, San Francisco, May.

Proofs will be sent to the corresponding author to correct any typesetting errors. Alterations to the original manuscript at this stage will not be accepted. Proofs should be returned within 48 hours of receipt by Express Mail.

Submission of an article to "Structural Engineering and Mechanics" implies that it presents the original and unpublished work, and not under consideration for publication elsewhere. On acceptance of a manuscirpt submitted, the copyright thereof is transferred to the publisher by the Transfer of Copyright Agreement.

A total of 50 reprints of each paper will be supplied free of charge to the corresponding author.



Journal of Fluids and Structures 17 (2003) 185-224

JOURNAL OF FLUIDS AND STRUCTURES

www.elsevier.nl/locate/jnlabr/yjfls

# Large strain formulations of extensible flexible marine pipes transporting fluid

S. Chucheepsakul<sup>a,\*</sup>, T. Monprapussorn<sup>a</sup>, T. Huang<sup>b</sup>

<sup>a</sup> Department of Civil Engineering, King Mongkut's University of Technology Thonburi, Bangmod, Toongkru, Bangkok 10140, Thailand
<sup>b</sup> Department of Civil and Environmental Engineering, University of Texas at Arlington, Arlington, TX 76019-0167, USA

Received 15 August 2000; accepted 8 August 2002

## Abstract

This paper develops mathematical formulations for large strain analysis of extensible flexible marine pipes transporting fluid in two different coordinates: Cartesian and natural coordinates. Both the virtual work method and the vectorial method are applied to generate the large strain formulations, in which deformation descriptions based upon the total Lagrangian, the updated Lagrangian, and the Eulerian mechanics are taken into consideration. The new ideas used in the model formulations deal with applications of the extensible elastica theory and the apparent tension concept to handle combined action of the effect of axial deformation with large strain and behaviour of flow of transported fluid inside the pipe including the effect of Poisson's ratio. The present models cover nonlinear statics and nonlinear dynamics, and provide flexibility in the choice of the independent variables used to define the elastic curves. © 2002 Elsevier Science Ltd. All rights reserved.

# 1. Introduction

In the past five decades, flexible pipes have been employed extensively in numerous offshore engineering applications. The most vital function of them is to transport fluids drilled from underneath ocean floor such as oil, gas, hydrocarbon, and other crude resources, up to the production platform or drilling ship. In the deep-ocean mining industry, flexible pipes play the role of the main module of the production system as shown in Fig. 1(a). In moderate sea-depth applications, they are often used as the secondary part, linked to rigid risers as shown in Fig. 1b and c.

In the literature, there are many papers related to flexible pipe analysis as reviewed by Chakrabarti and Frampton (1982), Ertas and Kozik (1987), Jain (1994) and Patel and Seyed (1995). It is remarkable that most of them omit the effect of axial deformation of the pipe, and the influence of internal flow. Furthermore, all of them overlook the Poisson's ratio effect. As will be reviewed and discussed later, the individual effect of axial deformation, internal flow, and Poisson's ratio can be significant for behaviour of low flexibility pipes. It is therefore conceivable that combined actions of all the effects become more important for behaviour of highly flexible pipes. In such cases, those effects should be carefully examined, and large strain analysis is essential.

However, hitherto a mathematical treatment for the large strain analysis that takes into consideration the combined actions of those effects has not been elucidated. Hence it is the objective of this paper: first to introduce and explain the mathematical principles for large strain analysis of extensible flexible marine pipes conveying fluid from viewpoints of the total Lagrangian, the updated Lagrangian, and the Eulerian mechanics; second to show how to formulate large strain models of marine pipes in Cartesian and natural coordinates by relying upon the extensible elastica theory and

<sup>\*</sup>Corresponding author. Tel.: +662-470-9134-36; fax: +662-427-9063. E-mail address: somchai.chu@kmutt.ac.th (S. Chucheepsakul).

# 186 S. Chucheepsakul et al. I Journal of Fluids and Structures 17 (2003) 185-224 Nomenclature $\bar{A}_e$ , $A_{eo}$ , $A_e$ sectional areas of the external fluid column at the three states $\bar{A}_i, A_{ia}, A_i$ sectional areas of the internal fluid column at the three states $\bar{A}_P$ , $A_{Po}$ , $A_P$ sectional areas of a pipe at the three states a<sub>F</sub>, a<sub>FP</sub> acceleration vectors of transported fluid relative to a fixed frame and a pipe $a_{Fh}, a_{Fl}, a_{F\chi}, a_{F\chi}$ accelerations of transported fluid relative to a fixed frame in normal, tangential, horizontal, and vertical directions, respectively acceleration vector of a pipe relative to a fixed frame $a_{Pn}, a_{Pt}, a_{Px}, a_{Pv}$ accelerations of a pipe relative to a fixed frame in normal, tangential, horizontal, and vertical directions, respectively $\bar{B}$ , $B_o$ , B bending rigidities at the three states C<sub>Dn</sub>, C<sub>Dt</sub>, C<sub>a</sub>, C<sub>M</sub> coefficients of normal drag, tangential drag, added mass, and inertia $\bar{D}_e, D_{ea}, D_e$ diameters of the external fluid column at the three states $\bar{D}_P, D_{Po}, D_P$ diameters of a pipe at the three states elastic modulus $\tilde{\mathbf{f}}, \mathbf{f}_o, \mathbf{f}$ external load vectors at the three states $\mathbf{f}_H, \mathbf{f}_{Ho}, \mathbf{f}_H$ hydrodynamic force vectors at the three states $F_{Hn}, F_{Hi}, F_{Hx}, F_{Hy}$ hydrodynamic forces in normal, tangential, horizontal, and vertical directions, respectively $f_{Hn}, f_{Hx}, f_{Hx}$ , hydrodynamic forces per unit length in normal, tangential, horizontal, and vertical directions, respectively $F_{IPn}$ , $F_{lin}$ , $F_{lin}$ normal inertial forces of a pipe, transported fluid, and overall system $F_{IPI}$ , $F_{III}$ , $F_{II}$ tangential inertial forces of a pipe, transported fluid, and overall system normal reaction between pipe wall and transported fluid per unit length $f_n, f_t, f_x, f_y$ external load components in Eqs. (123c) and (129g) gravitational acceleration $\vec{H}$ , $H_o$ , H horizontal internal forces at the three states horizontal and vertical unit vectors in Cartesian system $\bar{I}_P$ , $I_{Po}$ , $I_P$ moments of inertia of a pipe at the three states $\bar{M}, M_o, M$ bending moments at the three states $\bar{N}, N_o, N$ axial forces at the three states $\bar{m}_e, m_{eo}, m_e$ masses of the external fluid column per unit length at the three states $\bar{m}_i, m_{io}, m_i$ masses of the internal fluid column per unit length at the three states $\bar{m}_P, m_{Po}, m_P$ masses of a pipe per unit length at the three states $\bar{n}$ , $\hat{n}_o$ , $\hat{n}$ normal unit vectors in natural system at the three states pressures of external and internal fluids $p_e, p_i$ $\bar{Q}, Q_o, Q$ shear forces at the three states radii of curvatures at the three states $\bar{r}, r_o, r$ position vectors of transported fluid relative to a fixed frame and a pipe $\Gamma_F, \Gamma_{FP}$ position vector of a pipe relative to a fixed frame $\Gamma_P$ arc-length coordinates at the three states $\bar{s}, s_o, s$ $\bar{T}$ , $T_o$ , T true wall tensions at the three states $\bar{T}_a, T_{ao}, T_a$ apparent tensions at the three states $\bar{T}_e, T_{eo}, T_e$ effective tensions at the three states

apparent tension due to triaxial stress

 $\bar{V}, V_o, V$  vertical internal forces at the three states

time (time derivative denoted by overdot such as  $\partial x/\partial t = \dot{x}$ )

tangential unit vectors in natural system at the three states displacement vectors from state 1 to 2 and state 2 to 3

horizontal displacements from state 1 to 2 and state 2 to 3

 $V_F, V_{FP}$  velocity vectors of transported fluid relative to a fixed frame and a pipe  $V_{Hn}$ ,  $V_{Ht}$  external hydrodynamic velocities in normal and tangential directions

normal displacements from state 1 to 2 and state 2 to 3

 $V_{ct}$ ,  $V_c$  current velocities at mean sea level and at any sea depth

 $T_{tri}$ 

 $\bar{t}, \hat{t}_o, \hat{t}$ 

u,, u

 $u_o, u$ 

```
V_{H_Y}, V_{H_Y} external hydrodynamic velocities in horizontal and vertical directions
\bar{V}_i, V_{io}, V_i internal flow velocities at the three states
           velocity vector of a pipe relative to a fixed frame
\mathbf{V}_{P}
V_{Px}, V_{Py}, V_{P\theta} horizontal, vertical, and rotational velocities of a pipe
V_{ii}
           wave velocity
           vertical displacements from state 1 to 2 and state 2 to 3
v_o, v
           tangential displacements from state 1 to 2 and state 2 to 3
v_{no}, v_n
W_P, W_e, W_i weights of a pipe, the external fluid column, and the internal fluid column
\bar{w}_a, w_{ao}, w_a apparent weights per unit length at the three states
           Cartesian vectors of displacements from state 1 to 2 and state 2 to 3
\mathbf{X}_{o}, \mathbf{X}
\bar{x}, x_o, x horizontal Cartesian coordinates at the three states
            static offset
\bar{x}_t
           vertical Cartesian coordinates at the three states
\bar{y}, y_o, y
            vertical distances from bottom support to seabed and to sea surface
\bar{y}_b, \bar{y}_t
Greek symbols
            independent variable (its derivative \partial/\partial\alpha denoted by ('))
α
            Almansi's and Green's strains
7A.76
\gamma, \gamma_v, \gamma_d total, static, and dynamic updated Green strains
            relative velocities of external fluid in normal and tangential directions
70271
            axial strains at the three states
\bar{\epsilon}, \epsilon_o, \epsilon
\varepsilon, \varepsilon_o, \varepsilon_d total, static, and dynamic axial strains (\varepsilon_d = \varepsilon - \varepsilon_o)
            axial strain due to the tension T_{tri}
\varepsilon_{tri}
\bar{\epsilon}_r, \epsilon_{ro}, \epsilon_r volumetric strains of a pipe at the three states
            axial strain at a fibre radius coordinate ç
\boldsymbol{\epsilon}_{z}
            a fibre radius coordinate
\bar{\theta}, \theta_o, \theta rotational angles at the three states
\bar{\kappa}, \kappa_o, \kappa curvatures at the three states
            Poisson's ratio
\pi_{an}, \pi_{at}, \pi_{ax}, \pi_{ay} total virtual works of apparent system in normal, tangential, horizontal, and vertical directions,
            respectively
\rho_P, \rho_e, \rho_i densities of a pipe, external fluid, and internal fluid
            end effect stress
\sigma_P
\sigma_t, \sigma_\theta, \sigma_r triaxial stress in Fig. 4(f)
            shear stress in pipe wall
            wall shear friction between pipe wall and transported fluid
 \bar{\forall}_{cr}, \forall_{cr}, \forall_{cr}, \forall_{cr} control volumes of a pipe at the three states
 \bar{\forall}_e, \forall_{eo}, \forall_e volumes of the external fluid column at the three states
 \overline{\forall}_i, \forall_{ia}, \forall_i volumes of the internal fluid column at the three states
 \nabla_P, \nabla_P, \nabla_P volumes of a pipe at the three states
 Subscripts
 P
            pipe
            external fluid
            internal fluid
 i
            static quantity
 0
 d
            dynamic quantity
             natural coordinates.
 n
```

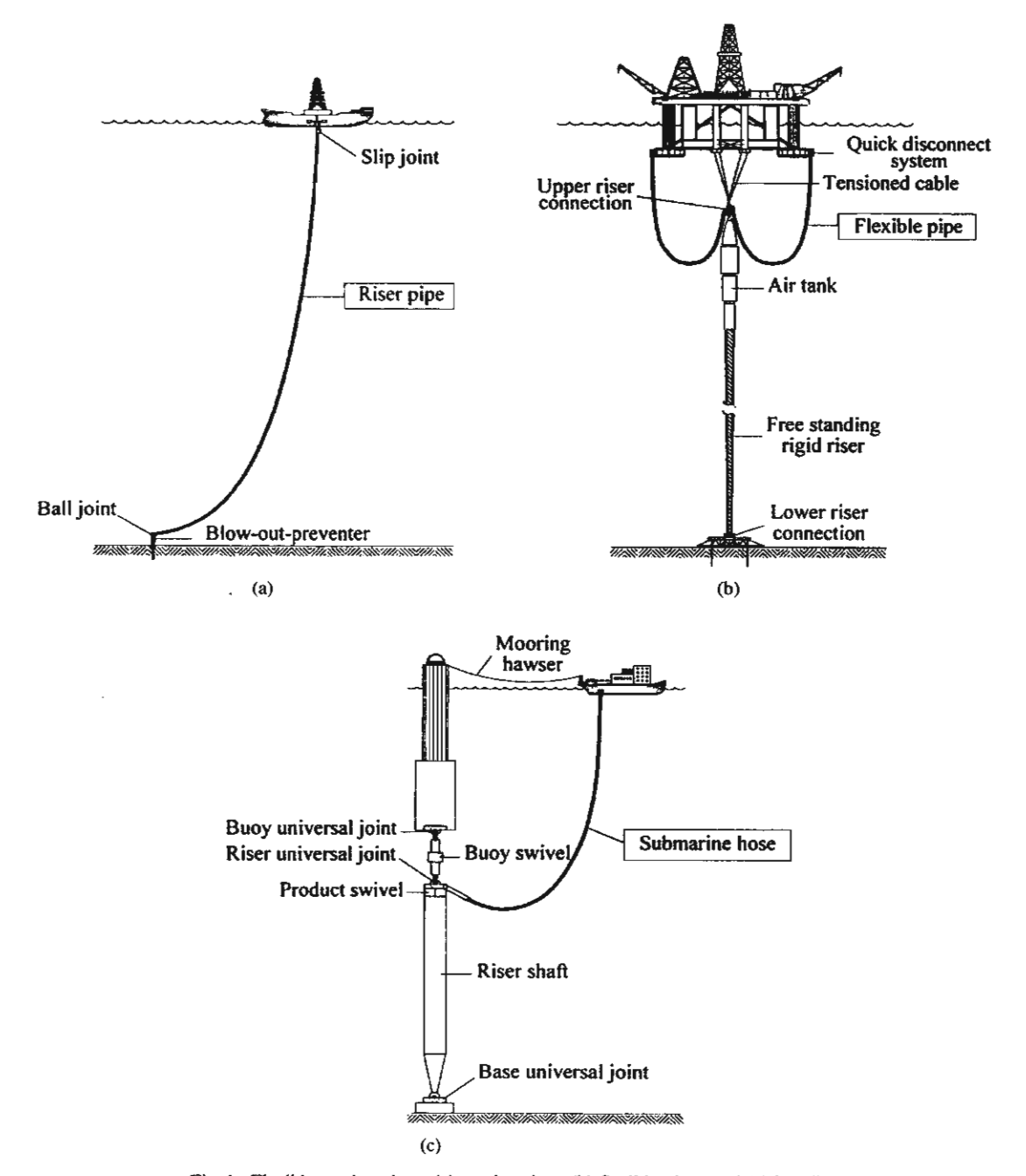


Fig. 1. Flexible marine pipes: (a) marine riser; (b) flexible pipe; and (c) hoseline.

the apparent tension concept; and finally to illustrate versatile and sophisticated models suitable for two-dimensional large strain analysis of extensible flexible marine pipes conveying fluid.

# 1.1. Significance of effect of axial deformation

From a literature review, the effect of axial deformation on behaviour of marine cables was investigated by Huang (1992), Chucheepsakul et al. (1995) and Chucheepsakul and Huang (1997). The effect on behaviour of suspended cables was studied by Huddleston (1981), Shih and Tadjbakhsh (1984), Burgess and Triantafyllou (1988), Lin and Perkins

(1995), Triantafyllou and Yue (1994) and Tjavaras et al. (1996, 1998). The effect was included in analysis of low flexibility marine risers by Chung and Whitney (1983), Chung et al. (1994), Chung and Cheng (1996) and Bernitsas and Kokarakis (1988); Bernitsas et al. (1985).

It was reported that the effect of axial deformation on static behaviour of those structures is to increase static displacements of low-tensioned cables, due to extensibility dominating; but to reduce the static displacement of high-tensioned cables, due to pre-stressing dominating (Chucheepsakul et al., 1995; Chucheepsakul and Huang, 1997). Although Bernitsas and Kokarakis (1988); Bernitsas et al. (1985) found that the effect on static behaviour of low flexibility pipes was rather small, they did not provide evidence of the same result with the highly flexible pipes.

In relation to the dynamic behaviour of these structures, the effect of axial deformation is to increase dynamic stresses (Chung and Whitney, 1983; Chung et al. (1994); Chung and Cheng, 1996), to reduce natural frequencies (Chucheepsakul and Huang, 1997), and to provoke elastic mode transition of cable vibrations (Burgess and Triantafyllou, 1988; Lin and Perkins, 1995). If the stress-strain relation is hysteretic, the effect can amplify damping of dynamic strain in the axial direction (Triantafyllou and Yue, 1994). Several papers by Chung and Whitney (1983), Chung et al. (1994), Chung and Cheng (1996) comment that the effect of axial deformation is crucial to dynamics of low flexibility pipes and should be considered in the design of the pipe.

The interesting point in all the previous research is that the effect of axial deformation has been investigated by using small-strain analysis that adopts quadratic expressions for strain definitions. This approach, however, is proper if, and only if, the axial strain is small compared to unity (Fung, 1994). For highly flexible pipes, such an assumption is no longer necessarily valid; thus, this paper proposes large strain modelling by employing the square-root expressions for large strain definitions, as will be shown later.

# 1.2. Significance of influence of internal flow

Although transporting fluid is the main function, marine riser pipe analysis from the middle of the 1950s to the end of the 1970s paid little attention to the influence of transported fluid. In the same period, research concerning mechanics of pipes conveying fluid grew rapidly. Research work related to vibrations of straight and curved pipes can be found in the papers by Housner (1952), Gregory and Païdoussis (1966), Païdoussis (1970) and Doll and Mote (1976). It was reported that the internal flow reduced stability of the pipe and acted on the pipe like an end follower force (Thompson and Lunn, 1981). As a result, it could engender divergence instability or buckling of simply supported pipes (Holmes, 1978), and could induce flutter instability or snaking behaviour of cantilever pipes (Gregory and Païdoussis, 1966).

The lack of connection between research work on marine pipes and pipes conveying fluid has led to a misconception amongst some authors. When the effect of internal flow on marine pipes was handled in the early 1980s, it was considered that internal flow induced only friction forces to act on the pipe wall. However, researchers concerned with pipes conveying fluid, such as Gregory and Païdoussis (1966), Païdoussis (1970), and Thompson and Lunn (1981), had been well aware that the internal friction forces did not act directly on the pipe, but they affected the internal pressure transmitted to the pipe wall, which yielded tensioning and pressure drop (Païdoussis, 1998). In addition, internal flow generates not only the pressure effects, but also the other fictitious forces such as Coriolis and centrifugal forces.

By the end of the 1980s, the effect of internal flow on behaviour of marine pipes began to draw specific interest from a number of researchers, and the misconception was remedied. It was reported that internal flow reduced structural stiffness, provided negative damping (Irani et al., 1987), and induced additional large displacements of the pipes (Chucheepsakul and Huang, 1994); reduction of natural frequencies of the pipes is slight at a low speed of internal flow, but significant at a high speed of internal flow (Moe and Chucheepsakul, 1988; Wu and Lou, 1991); internal slug flow can induce significant cyclic fatigue loading in deep water (Patel and Seyed, 1989); and simply supported marine riser pipes transporting fluid lost stability by divergence (Chucheepsakul et al., 1999).

However, mathematical models used in most of those works do not consider the effects of geometric nonlinearity, extensibility, and the Poisson's ratio effect on the pipes, despite the fact that flexible marine pipes are inclined, initially curved, significantly deflected and deformed. This shortcoming motivates the aim of this work to exhibit how to take into account these effects in large strain formulations of flexible marine pipes conveying fluid. Revealing the interaction between the transported fluid and the pipe subjected to these effects provides new understanding of the behaviour of such systems.

# 1.3. Significance of Poisson's ratio effect and fluid pressures

It will be shown later that the Poisson's ratio effect and lateral actions of fluid pressures disturb the behaviour of flexible marine pipes in three ways: first, altering structural stiffness; second, modifying internal flow characteristics; and third, varying the apparent tension in the pipe.

A review of the literature shows that while the first two effects have not been examined in marine pipe analysis, the first effect has been included in marine cable analysis by Goodman and Breslin (1976). Even if the third effect on the flexible marine pipes has been treated through the effective tension concept proposed by Sparks (1984), the Poisson's ratio effect is not fully taken into account.

As will be shown later, using the effective tension concept creates an error in evaluating the apparent tension arising in the cross-section of the pipe, whenever the Poisson's ratio is not equal to 0.5. The greater the difference of Poisson's ratio from 0.5, the higher the error grows, especially under a condition of severe fluid pressures. In order to avoid such an error, this paper establishes the apparent tension concept instead of the effective tension concept. The detailed treatments of the first two effects on mathematical models for large strain analysis of flexible marine pipes are also included.

## 1.4. Assumptions

The following assumptions are stipulated in the present mathematical modelling:

- (a) The pipe materials are linearly elastic. Therefore, the Kelvin-Voigt internal dissipation or the dissipative recovery is not relevant.
- (b) At the undeformed state, the pipes are initially straight, and have no residual stresses.
- (c) The pipes are sufficiently thick-walled to suppose that, ideally, their cross-sections remain circular after change of cross-sectional size due to the Poisson's ratio effect, so that the elastic rod theories are usable, and Brazier's effect or flattening of bent tubes is negligible.
- (d) Longitudinal strain is large, but shear strain is insignificant for elastic rods with high slenderness ratio.
- (e) Plane sections of the pipes remain plane at all states.
- (f) The internal and external fluids are inviscid, incompressible, and irrotational. Their densities are uniform along arc lengths of the pipes.
- (g) The internal flow is the one-dimensional plug laminar flow.
- (h) The general form of Morison's equation is adopted for evaluating external hydrodynamic forces of external fluid. The distributed couple induced by a flow asymmetry due to vortex shedding is neglected.
- (i) The effect of rotary inertia is negligible.

# 2. Fundamentals of large strain modelling of flexible marine pipes conveying fluid

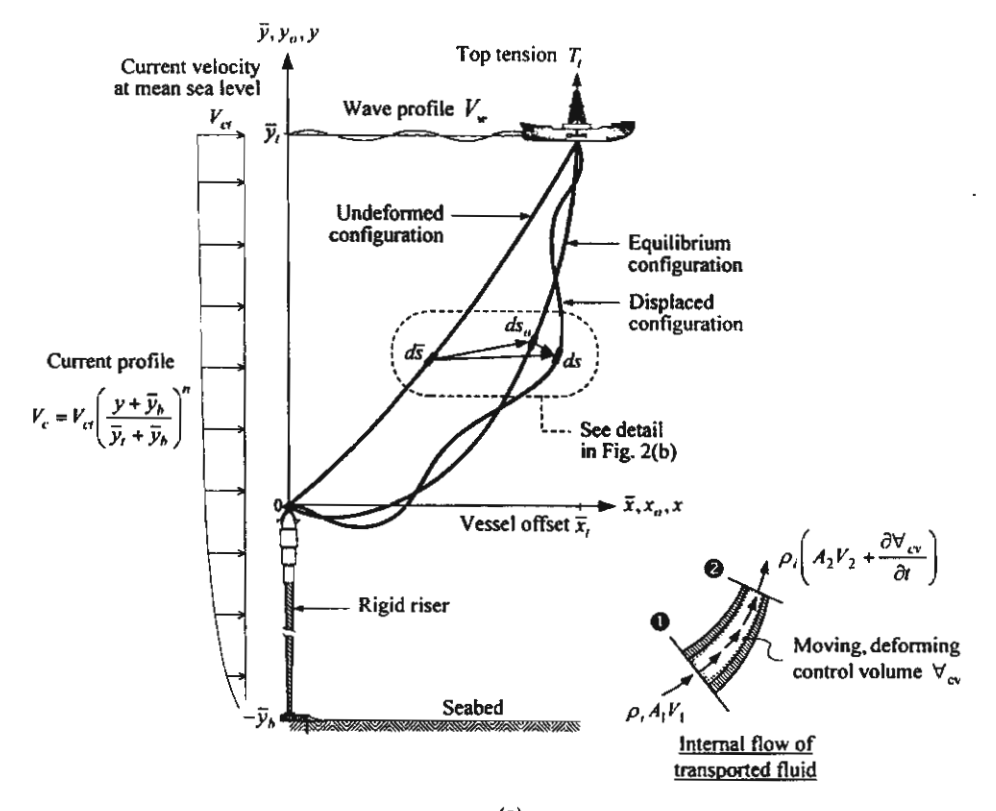
Large displacement behaviour of an extensible flexible marine pipe is depicted in Fig. 2. Firstly, the pipe is at rest and unstretched at state 1: the undeformed state. Subsequently, as the pipe is subjected to time-independent loads due to gravitation, steady current flow, and steady internal flow, the pipe experiences large displacement and forms the initial condition of the pipe at state 2: the equilibrium state. Finally, under dynamic actions of disturbances such as waves, unsteady current, and unsteady internal flow, the pipe sustains vibration about the equilibrium configuration at state 3: the displaced state.

Corresponding to the three states, mathematical treatments of the following subjects are considered to be requisite for large strain analysis of extensible marine pipes transporting fluid: (1) physical descriptions, (2) large strain measurements, (3) the extensible elastica theory, (4) the apparent tension concept, and (5) dynamic interactions between fluids and pipes. Details of these subjects are given as follows.

# 2.1. Physical descriptions

In order to define positions, motions, and deformations of an extensible flexible pipe and transported fluid, the descriptions for geometry, kinematics, and deformation are necessary for large strain modelling.

- (a) Geometric description. Fig. 2 uses the Cartesian coordinates  $(\hat{\mathbf{i}}, \hat{\mathbf{j}})$  and the intrinsic coordinates of arc length and rotation  $(\hat{\mathbf{s}}, \hat{\boldsymbol{\theta}})$  as the global geometric descriptors, and employs the natural coordinates  $(\hat{\mathbf{n}}, \hat{\mathbf{t}})$  as the local geometric descriptor. From the two global systems, there exist a number of choices of the independent variable. For versatility of mathematical models, the symbol  $\alpha \in \{\bar{x}, x_o, x, \bar{y}, y_o, y, \bar{s}, s_o, s, \bar{\theta}, \theta_o, \theta\}$  is introduced to represent any independent variable, and the superscript (') denotes  $\partial()/\partial \alpha$ .
- (b) Kinematic and deformation descriptions. As shown in Fig. 3, there may be three ways to describe motions and deformations of a pipe and transported fluid. These involve the descriptions by total Lagrangian, updated Lagrangian, and Eulerian coordinates as follows.



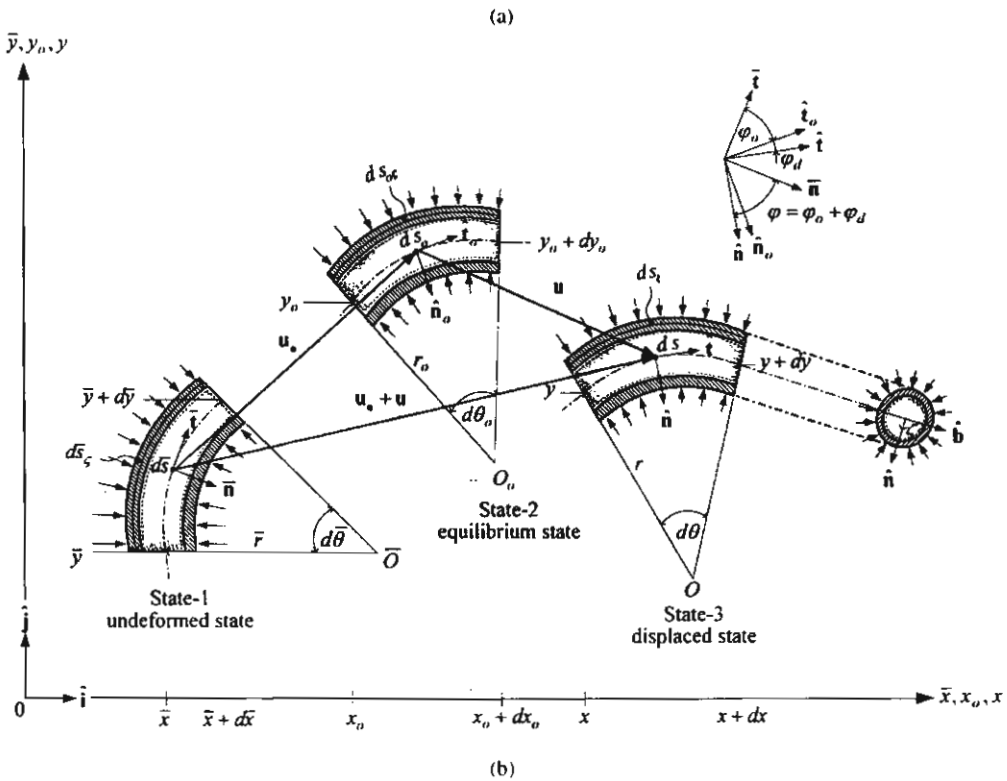
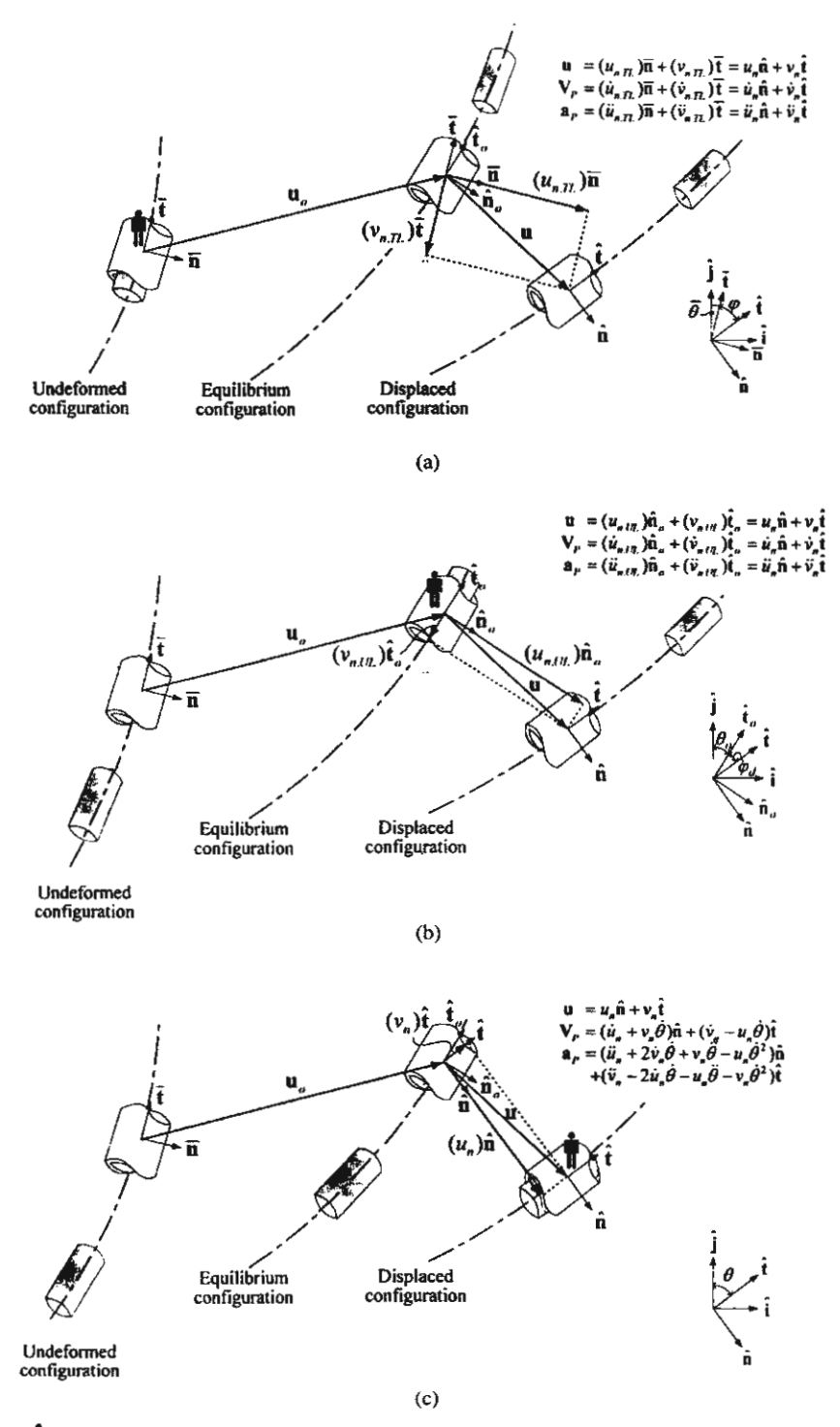


Fig. 2. Schematics of large displacements and large deformations.



The local observer, who monitors motions, deformations, and rotations of the pipe and transported fluid with respect to the positions, directions, and sizes of the pipe and transported fluid at the state he stands.

Fig. 3. Physical descriptions: (a) total Lagrangian; (b) updated Lagrangian; and (c) Eulerian approaches.

Definition 1. The coordinate that follows motion and deformation of a deformable body with respect to position, direction, and size of the body at the original state (or the undeformed state herein) is said to be the total Lagrangian descriptor (TL) as shown in Fig. 3(a).

**Definition 2.** The coordinate that follows motion and deformation of a deformable body with respect to position, direction, and size of the body at the intermediate state (or the equilibrium state herein) is said to be *the updated Lagrangian descriptor (UL)* as shown in Fig. 3(b).

**Definition 3.** The coordinate that follows motion and deformation of a deformable body with respect to position, direction, and size of the body at the final state (or the displaced state herein) is said to be *the Eulerian descriptor (EL)* as shown in Fig. 3(c).

# 2.2. Large strain measurements

Corresponding to the three deformation descriptors defined in the previous section, definitions of the total axial strain  $\varepsilon_0$ , and the dynamic strain  $\varepsilon_d$  can be provided in the following three forms.

(i) For deformation descriptor TL:

$$\varepsilon = \frac{s'}{\overline{s'}} - 1,\tag{1a}$$

$$\varepsilon_o = \frac{s_o'}{v'} - 1,\tag{1b}$$

$$\varepsilon_d = \frac{s' - s'_o}{\overline{s}'}.$$

(ii) For deformation descriptor UL:

$$\varepsilon = \frac{s' - \overline{s}'}{s'_{\alpha}},\tag{2a}$$

$$\varepsilon_{o} = 1 - \frac{\vec{s}'}{s'_{o}},\tag{2b}$$

$$\varepsilon_d = \frac{s'}{s'} - 1. \tag{2c}$$

(iii) For deformation descriptor EL:

$$\varepsilon = 1 - \frac{\vec{s}'}{\epsilon'},\tag{3a}$$

$$\varepsilon_{o} = \frac{s_{o}' - \overline{s}'}{s'},\tag{3b}$$

$$\varepsilon_d = 1 - \frac{s_o'}{s'}.\tag{3c}$$

Note that  $\varepsilon = \varepsilon_o + \varepsilon_d$ , and the differential arc lengths at the undeformed, the equilibrium, and the displaced states  $\vec{s}'$ ,  $s'_o$ , and s' may be expressed as

$$\vec{s}' = \sqrt{\vec{x}'^2 + \vec{y}'^2},$$
 (4a)

$$s'_{o} = \sqrt{(\bar{x}' + u'_{o})^{2} + (\bar{y}' + v'_{o})^{2}},$$
(4b)

in Cartesian coordinates:

$$s' = \sqrt{(\bar{x}' + u'_o + u')^2 + (\bar{y}' + v'_o + v')^2},$$
(4c)

in natural coordinates:

$$s' = \sqrt{(u'_n + v_n \theta'_o)^2 + (s'_o + v'_n - u_n \theta'_o)^2}.$$
 (4d)

The large strain expressions given by Eqs. (1)-(3) can be exhibited in classical square-root forms of axial strains as follows

Definition 4. The large axial strain for flexible pipe analysis is defined by

$$\varepsilon = \begin{cases} \frac{s'}{\overline{s'}} - 1 = \varepsilon_o + \left(\frac{s'}{s'_o} - 1\right)(1 + \varepsilon_o) = \sqrt{1 + 2\gamma_G} - 1 & \text{for TL,} \\ \frac{s' - \overline{s'}}{s'_o} = \varepsilon_o + \left(\frac{s'}{s'_o} - 1\right) = \sqrt{1 + 2\gamma_d} - \sqrt{1 - 2\gamma_o} & \text{for UL,} \\ 1 - \frac{\overline{s'}}{s'} = \varepsilon_o + \left(1 - \frac{s'_o}{s'}\right) = 1 - \sqrt{1 - 2\gamma_A} & \text{for EL.} \end{cases}$$

In other words, the large axial strains are measured by means of 'engineering strains' or 'relative elongations'. The square-root expressions in Eqs. (5) demonstrate that the large axial strains are functions of the lower-order axial strains such as the static updated Green strain  $\gamma_o$ , the dynamic updated Green strain  $\gamma_d$ , the total updated Green strain  $\gamma_d$ , the Green strain  $\gamma_d$ , and the Almansi strain  $\gamma_d$ . By substituting Eqs. (4) into Eqs. (5), and undertaking some manipulation, the expressions of these lower-order axial strains can be obtained as

$$\gamma_o = \frac{1}{s_o^2} \left[ \bar{x}' u_o' + \bar{y}' v_o' + \frac{u_o'^2}{2} + \frac{v_o'^2}{2} \right],\tag{6a}$$

in Cartesian coordinates:

$$\gamma_d = \frac{1}{s_o^2} \left( x_o' u' + y_o' v' + \frac{u'^2}{2} + \frac{v'^2}{2} \right),\tag{6b}$$

in natural coordinates

$$\gamma_d = \frac{1}{s_o'^2} \left[ s_o'(v_n' - u_n \theta_o') + \frac{(u_n' + v_n \theta_o')^2}{2} + \frac{(v_n' - u_n \theta_o')^2}{2} \right],\tag{6c}$$

$$\gamma = \gamma_o + \gamma_d, \quad \gamma_G = \gamma (s'_o/\vec{s})^2, \quad \gamma_A = \gamma (s'_o/s')^2. \tag{6d-f}$$

For lower-order large strain analysis, the dynamic axial strains in Eqs. (5) may be approximated by the two-term binomial series such that

$$\frac{s'}{s'_o} = \sqrt{1 + 2\gamma_d} \approx 1 + \gamma_d, \quad \frac{s'_o}{s'} = \frac{1}{\sqrt{1 + 2\gamma_d}} \approx 1 - \gamma_d. \tag{7a-b}$$

Inserting Eqs. (7) into Eqs. (5), the quadratic forms of axial strains are derived as Definition 5.

Definition 5. The nonlinear second-order axial strain for flexible pipe analysis is defined by

$$\varepsilon \approx \begin{cases} \varepsilon_o + \gamma_d (1 + \varepsilon_o) & \text{for } TL, \\ \varepsilon_o + \gamma_d & \text{for } UL \text{ and } EL, \end{cases}$$
 (8a, b)

to which quadratic expressions of  $\gamma_d$  as shown in Eqs. (6b) and (6c) are applied.

For linear approximation, the second-order terms of  $\gamma_d$  are negligible as higher-order terms, so that Eq. (6b) is linearized to

in Cartesian coordinates:

$$\gamma_d \simeq \frac{1}{s_o' 2} (x_o' u' + y_o' v'),$$
 (9a)

in natural coordinates:

$$\gamma_d \simeq \frac{1}{s'} (v'_n - u_n \theta'_\alpha). \tag{9b}$$

By utilizing Eq. (9), the linear forms of axial strains are derived as Definition 6.

**Definition 6.** The linear axial strain for flexible pipe analysis is defined by Eqs. (8), to which linear approximation of  $\gamma_d$  by Eqs. (9) is applied.

The large strain definition (Definition 4) is considered necessary for nonlinear dynamic analysis of flexible pipes, in which large amplitude vibrations and large strain behaviour are concerned. The nonlinear second-order strain definition (Definition 5) is desired for nonlinear dynamic analysis of flexible pipes, in which large amplitude vibrations with large static and small dynamic strains are interested. The linear strain definition (Definition 6) is sufficient for dynamic stability analysis and linear dynamic problems of flexible pipes, to which large static and infinitesimal dynamic strains are relevant.

Variations of the axial strain among the three states bring about variations of differential arc length of the pipe, cross-sectional properties of the pipe, and internal flow velocity of transported fluid as follows.

(a) Variations of differential arc length of the pipe. By solving Eqs. (1a) and (1b) for \$\vec{s}'\$, solving Eqs. (2b) and (2c) for  $s'_0$ , and solving Eqs. (3a) and (3c) for s', one obtains

$$\vec{s}' = \frac{s'_o}{1+\varepsilon_o} = \frac{s'}{1+\varepsilon}$$
 for TL, (10a)

$$\frac{\vec{s}'}{1-\varepsilon_o} = s'_o = \frac{s'}{1+\varepsilon_d} \quad \text{for UL},$$

$$\frac{s'}{1-\varepsilon} = \frac{s'_o}{1-\varepsilon_o} = s' \quad \text{for EL}. \tag{10c}$$

(b) Variations of cross-sectional properties of the pipe. The volumetric strain of the pipe is expressed as

$$\varepsilon_{r} = \begin{cases} \frac{dV_{P} - d\bar{V}_{P}}{d\bar{V}_{P}} = \frac{A_{P}S'}{\bar{A}_{P}\bar{S}'} - 1 = \frac{A_{P}}{\bar{A}_{P}}(1 + \varepsilon) - 1 & \text{for TL,} \\ \frac{dV_{P} - d\bar{V}_{P}}{dV_{Po}} = \frac{A_{P}S' - \bar{A}_{P}\bar{S}'}{A_{Po}S'_{o}} = \frac{A_{P}}{A_{Po}}(1 + \varepsilon_{d}) - \frac{\bar{A}_{P}}{A_{Po}}(1 - \varepsilon_{o}) & \text{for UL,} \\ \frac{dV_{P} - d\bar{V}_{P}}{dV_{P}} = 1 - \frac{\bar{A}_{P}\bar{S}'}{A_{P}S'} = 1 - \frac{\bar{A}_{P}}{A_{P}}(1 - \varepsilon) & \text{for EL.} \end{cases}$$

Based on the control volume approach (Goodman and Breslin, 1976), the pipe volume is conserved, and thus the volumetric strain of the pipe  $\varepsilon_r = \varepsilon_{ro} = 0$ . Once these conditions are applied to Eqs. (11), the cross-sectional areas of the pipe at the three states can be related together as

$$\bar{A}_P = A_{Pol}(1 + \varepsilon_o) = A_P(1 + \varepsilon)$$
 for TL, (12a)

$$\bar{A}_P = \frac{A_{Po}}{1 - \varepsilon_o} = \frac{(1 + \varepsilon_d)A_P}{(1 - \varepsilon_o)} \quad \text{for UL}, \tag{12b}$$

$$\bar{A}_P = \frac{A_{Po}}{1 - \varepsilon_o} = \frac{A_P}{1 - \varepsilon}$$
 for EL. (12c)

Corresponding to Eqs. (12), variations of diameter and moment of inertia of the circular pipe among the three states are determined as

$$\bar{D}_P = D_{Po}\sqrt{1+\varepsilon_o} = D_P\sqrt{1+\varepsilon} \quad \text{for TL}, \tag{13a}$$

$$\bar{D}_{P} = \frac{D_{Po}}{\sqrt{1 - \varepsilon_{o}}} = D_{P} \sqrt{\frac{1 + \varepsilon_{d}}{1 - \varepsilon_{o}}} \quad \text{for UL},$$
(13b)

$$\tilde{D}_{P} = \frac{D_{Po}}{\sqrt{1 - \varepsilon_{o}}} = \frac{D_{P}}{\sqrt{1 - \varepsilon}} \quad \text{for EL}, \tag{13c}$$

$$\bar{I}_P = I_{Po}(1 + \varepsilon_o)^2 = I_P(1 + \varepsilon)^2 \quad \text{for TL},$$

in natural coordinates:

$$s' = \sqrt{(u'_n + v_n \theta'_o)^2 + (s'_o + v'_n - u_n \theta'_o)^2}.$$
 (4d)

The large strain expressions given by Eqs. (1)-(3) can be exhibited in classical square-root forms of axial strains as follows

Definition 4. The large axial strain for flexible pipe analysis is defined by

$$\varepsilon = \begin{cases} \frac{s'}{\overline{s'}} - 1 = \varepsilon_o + \left(\frac{s'}{s'_o} - 1\right)(1 + \varepsilon_o) = \sqrt{1 + 2\gamma_G} - 1 & \text{for TL,} \\ \frac{s' - \overline{s'}}{s'_o} = \varepsilon_o + \left(\frac{s'}{s'_o} - 1\right) = \sqrt{1 + 2\gamma_d} - \sqrt{1 - 2\gamma_o} & \text{for UL,} \\ 1 - \frac{\overline{s'}}{s'} = \varepsilon_o + \left(1 - \frac{s'_o}{s'}\right) = 1 - \sqrt{1 - 2\gamma_A} & \text{for EL.} \end{cases}$$

In other words, the large axial strains are measured by means of 'engineering strains' or 'relative elongations'. The square-root expressions in Eqs. (5) demonstrate that the large axial strains are functions of the lower-order axial strains such as the static updated Green strain  $\gamma_o$ , the dynamic updated Green strain  $\gamma_d$ , the total updated Green strain  $\gamma$ , the Green strain  $\gamma_G$ , and the Almansi strain  $\gamma_A$ . By substituting Eqs. (4) into Eqs. (5), and undertaking some manipulation, the expressions of these lower-order axial strains can be obtained as

$$\gamma_o = \frac{1}{s_o^{\prime 2}} \left[ \bar{x}' u_o' + \bar{y}' v_o' + \frac{u_o'^2}{2} + \frac{v_o'^2}{2} \right],\tag{6a}$$

in Cartesian coordinates:

$$\gamma_d = \frac{1}{s_o^2} \left( x_o' u' + y_o' v' + \frac{u'^2}{2} + \frac{v'^2}{2} \right),\tag{6b}$$

in natural coordinates:

$$\gamma_d = \frac{1}{s_o^2} \left[ s_o'(v_n' - u_n \theta_o') + \frac{(u_n' + v_n \theta_o')^2}{2} + \frac{(v_n' - u_n \theta_o')^2}{2} \right],\tag{6c}$$

$$\gamma = \gamma_o + \gamma_d, \quad \gamma_G = \gamma (s'_o/\vec{s})^2, \quad \gamma_A = \gamma (s'_o/s')^2. \tag{6d-f}$$

For lower-order large strain analysis, the dynamic axial strains in Eqs. (5) may be approximated by the two-term binomial series such that

$$\frac{s'}{s'_o} = \sqrt{1 + 2\gamma_d} \approx 1 + \gamma_d, \quad \frac{s'_o}{s'} = \frac{1}{\sqrt{1 + 2\gamma_d}} \approx 1 - \gamma_d. \tag{7a-b}$$

Inserting Eqs. (7) into Eqs. (5), the quadratic forms of axial strains are derived as Definition 5.

Definition 5. The nonlinear second-order axial strain for flexible pipe analysis is defined by

$$\varepsilon \approx \begin{cases} \varepsilon_o + \gamma_d (1 + \varepsilon_o) & \text{for } TL, \\ \varepsilon_o + \gamma_d & \text{for } UL \text{ and } EL, \end{cases}$$
 (8a, b)

to which quadratic expressions of  $\gamma_d$  as shown in Eqs. (6b) and (6c) are applied.

For linear approximation, the second-order terms of  $\gamma_d$  are negligible as higher-order terms, so that Eq. (6b) is linearized to

in Cartesian coordinates:

$$\gamma_d \simeq \frac{1}{s_o' 2} (x_o' u' + y_o' v'),$$
 (9a)

in natural coordinates:

$$\gamma_d \simeq \frac{1}{s'} (v'_n - u_n \theta'_o). \tag{9b}$$

By utilizing Eq. (9), the linear forms of axial strains are derived as Definition 6.

**Definition 6.** The linear axial strain for flexible pipe analysis is defined by Eqs. (8), to which linear approximation of  $\gamma_d$  by Eqs. (9) is applied.

The large strain definition (Definition 4) is considered necessary for nonlinear dynamic analysis of flexible pipes, in which large amplitude vibrations and large strain behaviour are concerned. The nonlinear second-order strain definition (Definition 5) is desired for nonlinear dynamic analysis of flexible pipes, in which large amplitude vibrations with large static and small dynamic strains are interested. The linear strain definition (Definition 6) is sufficient for dynamic stability analysis and linear dynamic problems of flexible pipes, to which large static and infinitesimal dynamic strains are relevant.

Variations of the axial strain among the three states bring about variations of differential arc length of the pipe, cross-sectional properties of the pipe, and internal flow velocity of transported fluid as follows.

(a) Variations of differential arc length of the pipe. By solving Eqs. (1a) and (1b) for  $\vec{s}'$ , solving Eqs. (2b) and (2c) for  $s'_o$ , and solving Eqs. (3a) and (3c) for s', one obtains

$$\vec{s}' = \frac{s'_o}{1 + \varepsilon_o} = \frac{s'}{1 + \varepsilon} \quad \text{for TL}, \tag{10a}$$

$$\frac{\vec{s}'}{1-\varepsilon_o} = s'_o = \frac{s'}{1+\varepsilon_d} \quad \text{for UL}, \tag{10b}$$

$$\frac{\vec{s}'}{1-\varepsilon} = \frac{s'_o}{1-\varepsilon_d} = s' \quad \text{for EL}. \tag{10c}$$

(b) Variations of cross-sectional properties of the pipe. The volumetric strain of the pipe is expressed as

$$\varepsilon_{r} = \begin{cases} \frac{d \forall_{P} - d \bar{\forall}_{P}}{d \bar{\forall}_{P}} = \frac{A_{P} s'}{\bar{A}_{P} \bar{s}'} - 1 = \frac{A_{P}}{\bar{A}_{P}} (1 + \varepsilon) - 1 & \text{for TL,} \\ \frac{d \forall_{P} - d \bar{\forall}_{P}}{d \forall_{Po}} = \frac{A_{P} s' - \bar{A}_{P} \bar{s}'}{A_{Po} s'_{o}} = \frac{A_{P}}{A_{Po}} (1 + \varepsilon_{d}) - \frac{\bar{A}_{P}}{A_{Po}} (1 - \varepsilon_{o}) & \text{for UL,} \\ \frac{d \forall_{P} - d \bar{\forall}_{P}}{d \forall_{P}} = 1 - \frac{\bar{A}_{P} \bar{s}'}{A_{P} s'} = 1 - \frac{\bar{A}_{P}}{A_{P}} (1 - \varepsilon) & \text{for EL.} \end{cases}$$

Based on the control volume approach (Goodman and Breslin, 1976), the pipe volume is conserved, and thus the volumetric strain of the pipe  $\varepsilon_r = \varepsilon_{ro} = 0$ . Once these conditions are applied to Eqs. (11), the cross-sectional areas of the pipe at the three states can be related together as

$$\bar{A}_P = A_{Po}(1 + \varepsilon_o) = A_P(1 + \varepsilon)$$
 for TL, (12a)

$$\bar{A}_P = \frac{A_{Po}}{1 - \varepsilon_o} = \frac{(1 + \varepsilon_d)A_P}{(1 - \varepsilon_o)} \quad \text{for UL}, \tag{12b}$$

$$\bar{A}_P = \frac{A_{Po}}{1 - \varepsilon_o} = \frac{A_P}{1 - \varepsilon}$$
 for EL. (12c)

Corresponding to Eqs. (12), variations of diameter and moment of inertia of the circular pipe among the three states are determined as

$$\bar{D}_P = D_{Po}\sqrt{1+\varepsilon_o} = D_P\sqrt{1+\varepsilon}$$
 for TL, (13a)

$$\bar{D}_{P} = \frac{D_{Po}}{\sqrt{1 - \varepsilon_{o}}} = D_{P} \sqrt{\frac{1 + \varepsilon_{d}}{1 - \varepsilon_{o}}} \quad \text{for UL},$$
 (13b)

$$\tilde{D}_P = \frac{D_{Po}}{\sqrt{1 - \varepsilon_o}} = \frac{D_P}{\sqrt{1 - \varepsilon}} \quad \text{for EL},$$
(13c)

$$\bar{I}_P = I_{Po}(1 + \varepsilon_o)^2 = I_P(1 + \varepsilon)^2 \quad \text{for TL}, \tag{14a}$$

$$\bar{I}_{P} = \frac{I_{Po}}{\left(1 - \varepsilon_{o}\right)^{2}} = I_{P} \frac{\left(1 + \varepsilon_{d}\right)^{2}}{\left(1 - \varepsilon_{o}\right)^{2}} \quad \text{for UL}, \tag{14b}$$

$$\bar{I}_P = \frac{I_{Po}}{(1 - \varepsilon_o)^2} = \frac{I_P}{(1 - \varepsilon)^2} \quad \text{for EL}. \tag{14c}$$

(c) Variations of internal flow velocity of transported fluid. From the fluid mechanics (Munson et al., 1994), the continuity equation for transitions of a transportation rate among the three states can be displayed in the form

$$\bar{A}_i \bar{V}_i = A_{io}(s_o) V_{io}(s_o) = A_i(s,t) V_i(s,t) + \frac{\partial \forall_{cv}(s,t)}{\partial t}. \tag{15}$$

Nevertheless, because the pipe volume is conserved, time rate of control volume of the pipe  $\partial V_{cv}/\partial t$  is zero. With application of Eqs. (12), Eq. (15) yields the relationships of internal flow velocities at the three states as follows:

$$\tilde{V}_i = \frac{V_{io}}{1 + \varepsilon_o} = \frac{V_i}{1 + \varepsilon} \quad \text{for TL},$$
(16a)

$$\bar{V}_i = V_{io}(1 - \varepsilon_o) = \frac{(1 - \varepsilon_o)V_i}{(1 + \varepsilon_d)}$$
 for UL, (16b)

$$\bar{V}_i = V_{io}(1 - \varepsilon_o) = V_i(1 - \varepsilon)$$
 for EL. (16c)

Physical interpretation of Eqs. (16) substantiates Propositions 1 and 2.

**Proposition 1.** The plug flow of incompressible fluid inside largely deformable pipes that is the steady uniform flow  $(\partial \bar{V}_i/\partial \alpha = \partial \bar{V}_i/\partial t = 0)$  at the undeformed state, would become the steady nonuniform flow  $(\partial V_{io}/\partial \alpha \neq 0, \partial V_{io}/\partial t = 0)$  at the equilibrium state, and then the unsteady nonuniform flow  $(\partial V_i/\partial \alpha \neq 0, \partial V_i/\partial t \neq 0)$  at the displaced state.

Proposition 2. Extensibility of the pipes causes an increase of internal flow velocity of transported fluid.

# 2.3. The extensible elastica theory

A sophisticated strategy highlighted in this work is to adopt the extensible elastica theory for large strain formulations of extensible flexible pipes. In Appendix A, the following extensible elastica theorems corresponding to the three deformation descriptors are developed.

**Theorem 1.** For the Hookean material pipe, if the TL is employed to describe deformation of the pipe, then the constitutive relations are

$$\varepsilon_{\varsigma} = \varepsilon + \varsigma [\kappa(1+\varepsilon) - \vec{\kappa}],$$
 (17a)

$$N = E\bar{A}_{P}\varepsilon, \tag{17b}$$

$$M = E\bar{I}_{P}[\kappa(1+\varepsilon) - \bar{\kappa}], \tag{17c}$$

$$\delta U = \int_{\bar{s}} \{ N \delta \varepsilon + M \delta [\kappa (1 + \varepsilon) - \bar{\kappa}] \} d\bar{s} = \int_{z} [N \delta s' + M \delta (\theta' - \bar{\theta}')] d\alpha, \tag{17d}$$

in which  $\varepsilon_{\gamma}$  is the axial strain at any fibre radius  $\zeta$ , E the elastic modulus, N the axial force, M the bending moment, and U the strain energy of the pipe.

**Theorem 2.** For the Hookean material pipe, if the UL is employed to describe deformation of the pipe, then the constitutive relations are

$$\varepsilon_z = \varepsilon + \zeta [\kappa (1 + \varepsilon_d) - \bar{\kappa} (1 - \varepsilon_o)],$$
 (18a)

$$N = \mathcal{E}A_{Po}\varepsilon,\tag{18b}$$

$$M = EI_{Po}[\kappa(1 + \varepsilon_d) - \bar{\kappa}(1 - \varepsilon_o)], \tag{18c}$$

$$\delta U = \int_{\bar{s}} \{ N \delta \varepsilon + M \delta [\kappa (1 + \varepsilon_d) - \bar{\kappa} (1 - \varepsilon_o)] \} ds_o = \int_{\gamma} [N \delta s' + M \delta (\theta' - \bar{\theta}')] d\alpha.$$
 (18d)

**Theorem 3.** For the Hookean material pipe, if the EL is employed to describe deformation of the pipe, then the constitutive relations are

$$\varepsilon_{\varepsilon} = \varepsilon + \zeta[\kappa - \tilde{\kappa}(1 - \varepsilon)],$$
 (19a)

$$N = EA_{P}\varepsilon, \tag{19b}$$

$$M = EI_{P}[\kappa - \bar{\kappa}(1 - \varepsilon)], \tag{19c}$$

$$\delta U = \int_{\delta} \{ N \delta \varepsilon + M \delta [\kappa - \bar{\kappa} (1 - \varepsilon)] \} \, \mathrm{d}s = \int_{\beta} [N \delta s' + M \delta (\theta' - \bar{\theta}')] \, \mathrm{d}\alpha. \tag{19d}$$

#### 2.4. The apparent tension concept

Externally and internally flowing fluids interact with a pipe through hydrostatic and hydrodynamic pressures. The apparent tension concept is proposed herein to represent the effect of hydrostatic pressures, while the effect of dynamic pressures will be considered in the next section.

The apparent tension concept for handling the hydrostatic pressure effect of external and internal fluids is illustrated in Fig. 4. First of all, Archimedes' law, which will be used in the apparent tension concept, is recalled. As shown in Fig. 4(a), equilibrium of an external fluid column in an external pressure field proves physically that the enclosing external pressure field induces a vertical buoyancy force equal to the weight of the external fluid column  $\rho_e g \forall_e$ . This tenet is commonly referred to as the first law of Archimedes. A reverse viewpoint of the first law of Archimedes yields the corollary that the enclosing internal pressure field generates the apparent weight of the internal fluid column  $\rho_i g \forall_i$ .

It is remarkable that Archimedes' principle is usable with the enclosing pressure fields. However, for marine pipes, the pressure fields of external and internal fluids surround only external and internal side surfaces of the pipe segment, as seen in Fig. 4(b). Both cut ends of the pipe segment are not subjected to the pressure fields, which are called *the missing pressures*. Archimedes' principle cannot therefore be used straightforwardly for marine pipe analysis. Fortunately, this problem can be solved by the superposition technique to transform the real system into the apparent system of marine pipes as follows.

Step 1: The total forces acting on the real system of the pipe column (the pipe plus transported fluid) as shown in Fig. 4(b) are equal to the summation of the forces acting on the pipe columns in Figs. 4(c-e):

Fig. 
$$4(b) = \text{Fig. } 4(c) + \text{Fig. } 4(d) + \text{Fig. } 4(e).$$
 (20)

Step 2: The forces acting on the pipe column in Fig. 4(c) are equal to the summation of the forces acting on the pipe columns in Figs. 4(f) and (g):

Fig. 
$$4(c) = Fig. 4(f) + Fig. 4(g)$$
. (21)

Step 3: The static pressures exerted on the pipe column in Fig. 4(f) are made enclosing the pipe column by adding in the missing pressures at both cut ends of the pipe segment. However, the added pressures are nonexistent, so they must be removed for balance by applying the opposite pressure fields at the both ends of the pipe in Fig. 4(g).

Step 4: After the pressure fields enclose the pipe segment, Archimedes's principle is now applicable. Therefore, the enclosing external and internal pressure fields induce the buoyancy force  $W_e$  and the internal fluid weight  $W_i$ :

$$W_e = \rho_e \forall_e g, \quad W_i = \rho_i \forall_i g.$$
 (22a, b)

In addition, the enclosing pressure fields in Fig. 4(f) induce triaxial stresses, which in polar coordinates are: the radial stress  $\sigma_r$ , the circumferential stress  $\sigma_\theta$ , and the tensile stress due to the missing pressures  $\sigma_t$ . These triaxial stresses provoke the axial force

$$T_{\text{tri}} = EA_P \varepsilon_{tri} = (2\nu - 1)(p_e A_e - p_i A_i). \tag{22c}$$

Note that from the theory of elasticity (Timoshenko and Goodier, 1984):

$$\varepsilon_{trt} = [\sigma_t - v(\sigma_r + \sigma_\theta)]/E,$$
 (22d)

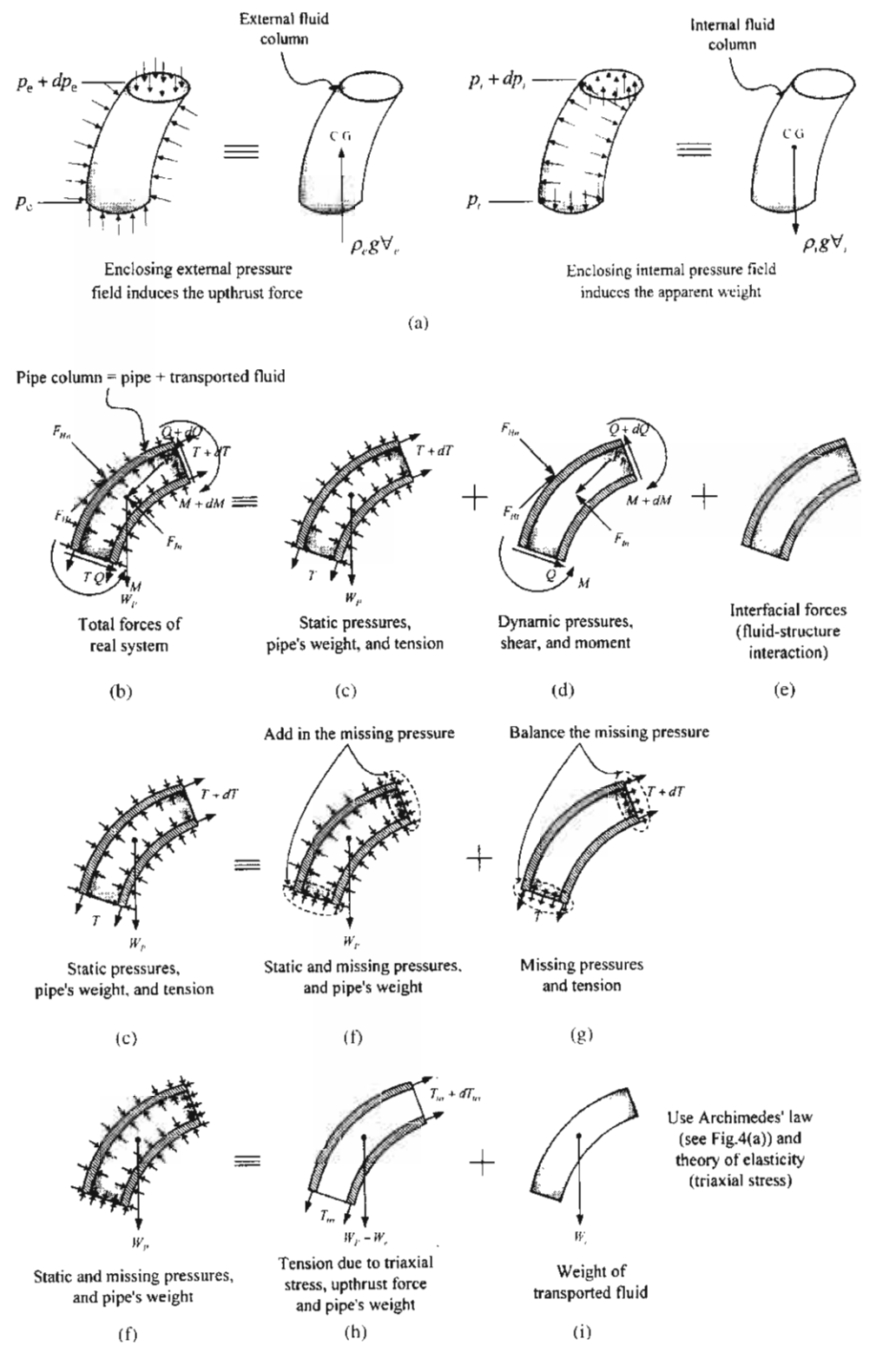
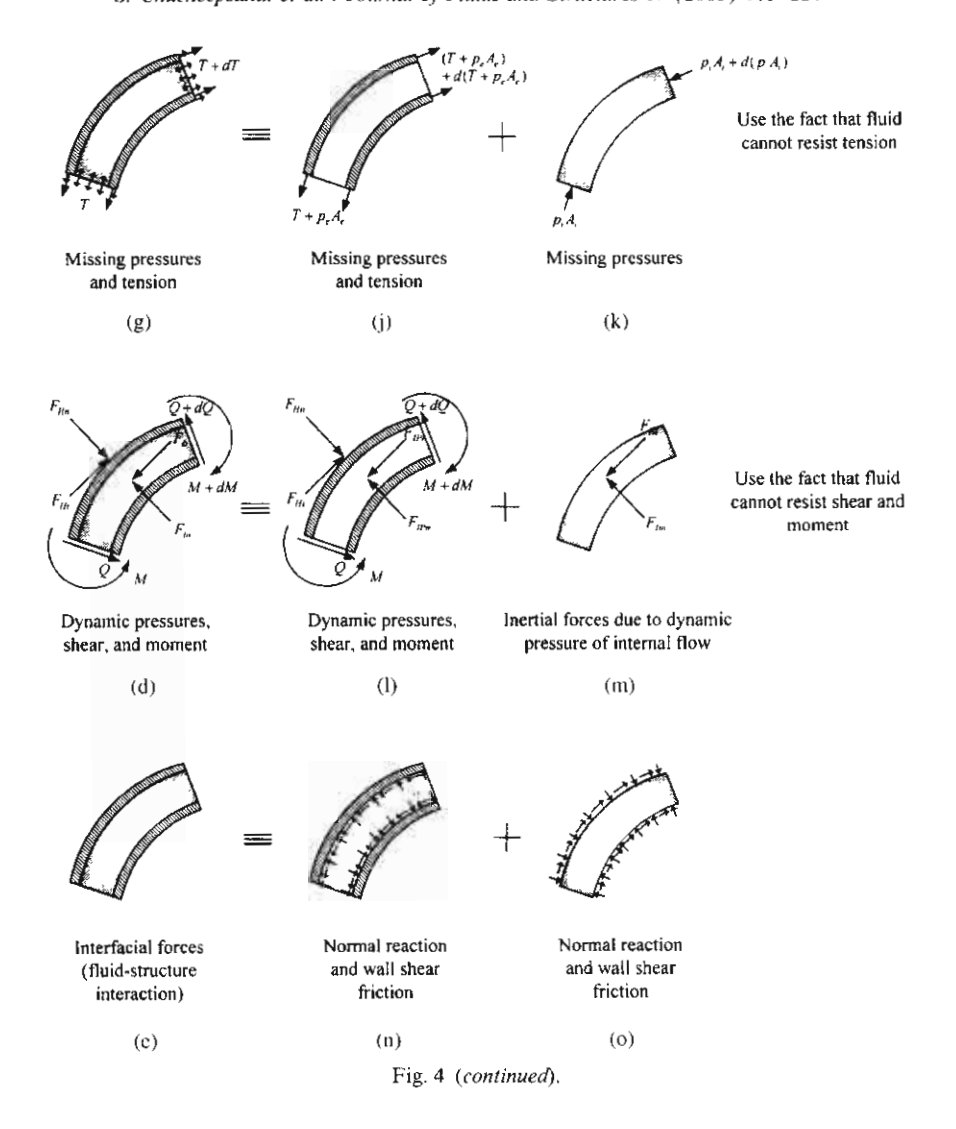


Fig. 4. Transformation from the real system to the apparent system.



and the enclosing pressure fields in Fig. 4(f) yield

$$\sigma_{\theta} = \sigma_P + \tau, \quad \sigma_r = \sigma_P - \tau, \quad \sigma_{\theta} + \sigma_r = 2\sigma_P,$$
 (22e-g)

$$\sigma_P = (p_1 A_1 - p_e A_e)/A_P, \tag{22h}$$

where  $\tau$  is the shear stress in pipe wall, and  $\sigma_P$  the end effect stress (Sparks, 1984).

Step 5: The pipe column in Fig. 4(f) is decomposed into a combination of the pipe element in Fig. 4(h) and the transported fluid element in Fig. 4(i):

Fig. 
$$4(f) = Fig. 4(h) + Fig. 4(i)$$
. (23)

The effect of the enclosing pressure fields is replaced by  $W_e$  and  $T_{tri}$  in Fig. 4(h), and by  $W_i$  in Fig. 4(i).

Step 6: The pipe column in Fig. 4(g) is decomposed into a combination of the pipe element in Fig. 4(j) and the transported fluid element in Fig. 4(k):

Fig. 
$$4(g) = \text{Fig. } 4(j) + \text{Fig. } 4(k)$$
. (24)

The missing pressure  $p_v A_v$  is entirely transmitted to the pipe element, because the transported fluid element cannot resist tension.

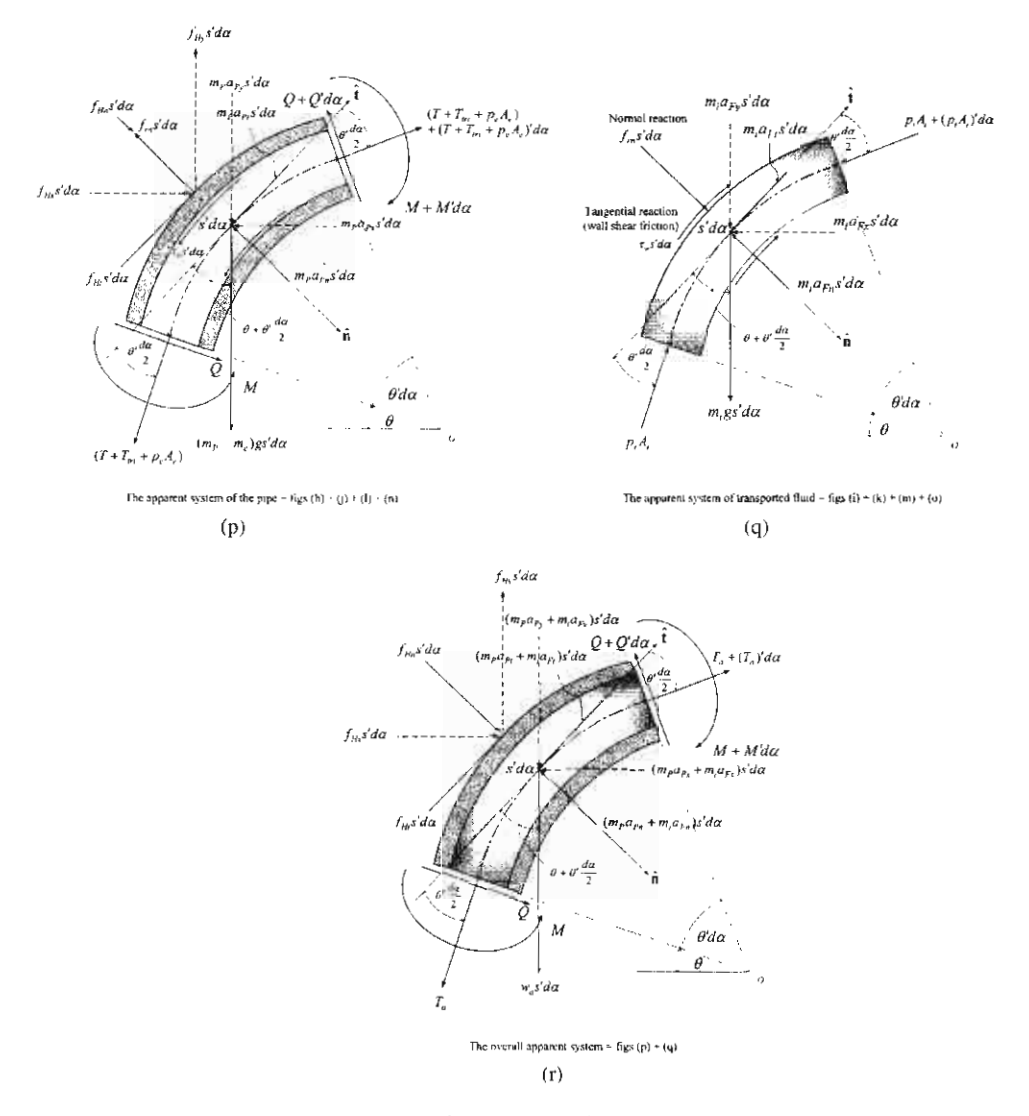


Fig. 4 (continued).

Step 7: The pipe column in Fig. 4(d) is decomposed into a combination of the pipe element in Fig. 4(l) and the transported fluid element in Fig. 4(m):

Fig. 
$$4(d) = \text{Fig. } 4(l) + \text{Fig. } 4(m)$$
. (25)

Shear forces and bending moments are entirely transmitted to the pipe element, because the transported fluid element cannot resist them.

Step 8: The pipe column in Fig. 4(e) is decomposed into a combination of the pipe element in Fig. 4(n) and the transported fluid element in Fig. 4(o):

Fig. 
$$4(e) = Fig. 4(n) + Fig. 4(o)$$
. (26)

Step 9: Substituting Eqs. (21), (23)–(26) into Eq. (20) together with some manipulation, one can obtain the expression

$$Fig. \ 4(b) = [Fig. \ 4(h) + Fig. \ 4(j) + Fig. \ 4(l) + Fig. \ 4(n)] + [Fig. \ 4(i) + Fig. \ 4(k) \\ Fig. \ 4(m) + Fig. \ 4(o)]. \tag{27}$$

\_

The first bracket on the right-hand side of Eq. (27) represents the apparent system of the pipe as portrayed in Fig. 4(p), while the second bracket expresses the apparent system of transported fluid as displayed in Fig. 4(q). Combination of the apparent systems of the pipe and transported fluid in Eq. (27) yields the overall apparent system of the pipe column that is subjected to the apparent weight  $w_a$  and the apparent tension  $T_a$  as shown in Fig. 4(r).

Writing expressions for the apparent weight and the apparent tension generally for the three deformation descriptors, one obtains

$$w_{a} = (\rho_{P}\tilde{A}_{P} - \rho_{e}\tilde{A}_{e} + \rho_{i}\tilde{A}_{i})g, \tag{28}$$

$$T_{a} = E\tilde{A}_{P}\varepsilon = T + 2\nu(p_{e}\tilde{A}_{e} - p_{i}\tilde{A}_{i}), \tag{29}$$

in which  $\tilde{A}_x = \tilde{A}_x$  for TL,  $\tilde{A}_x = A_{x0}$  for UL,  $\tilde{A}_x = A_x$  for EL, and the subscript  $\alpha \in \{P, e, i\}$ .

Ability to transform the real system into the apparent system of the pipe column establishes Proposition 3 that describes the apparent tension concept.

**Proposition 3.** The real system of the pipe column that is subjected to static external and internal pressures as shown in Fig. 4(b) is equivalent to the overall apparent system of the pipe column that is subjected to the apparent weight and the apparent tension as shown in Fig. 4(r).

On the other hand, the apparent tension may be expressed as

$$T_a = T_c + T_{tri}, (30)$$

where '

$$T_{c} = T + p_{c}\tilde{A}_{c} - p_{i}\tilde{A}_{i} \tag{31}$$

is referred to as the effective tension (Sparks, 1984). From Eqs. (29), it is seen that the condition  $T_a = T_e$  is achieved if, and only if, v = 0.5. This signifies that the effective tension concept is a subset of the apparent tension concept, and can be evidently inaccurate, whenever realistic Poisson's ratio of the pipe is significantly different from 0.5.

#### 2.5. Dynamic interactions between fluids and pipes

For flexible marine pipes transporting fluid, dynamic interactions between fluid and pipe occur due to steady and unsteady flows of external and internal fluids through the displaced pipe. Steady flows will cause quasi-static forces, and unsteady flows will engender dynamic forces to act on the pipe wall. The flow outside the pipe is normally associated with cross flows of ocean currents and waves, whereas the flow inside the pipe relates to the tangential flow of transported fluid.

#### 2.5.1. Hydrodynamic forces due to cross-flows of currents and waves

Based on the coupled Morison equation (Chakrabarti, 1990), the hydrodynamic forces exerted on flexible marine pipes with large displacements in natural coordinates can be expressed as

$$\mathbf{f}_{H} = \begin{cases} f_{Hn} \\ f_{Ht} \end{cases} = \underbrace{0.5\rho_{e}D_{e} \begin{cases} C_{Dn}\gamma_{n} | \dot{\gamma}_{n} | \\ \pi C_{Dt}\gamma_{t} | \gamma_{t} | \end{cases}}_{\text{Viscous drag force}} + \underbrace{\rho_{e}A_{e}C_{a} \begin{cases} \dot{\gamma}_{n} \\ \dot{\gamma}_{t} \end{cases}}_{\text{Hydrodynamic mass force}} + \underbrace{\rho_{e}A_{e} \begin{cases} \dot{V}_{Hn} \\ \dot{V}_{Ht} \end{cases}}_{\text{Froude-Krylov force}}, \tag{32}$$

where overdot denotes  $\partial()/\partial t$ ,  $C_{Dn}$  and  $C_{Dt}$  are the normal and tangential drag coefficients,  $C_a$  the added mass coefficient,  $V_{Hn}$  and  $V_{Ht}$  the normal and tangential velocities of currents and waves; and  $\gamma_n = V_{Hn} - \dot{u}_n$  and  $\gamma_t = V_{Ht} - \dot{v}_n$  are the velocities of currents and waves relative to pipe velocities  $\dot{u}_n$  and  $\dot{v}_n$  in normal and tangential directions, respectively. For large strain consideration, the effect of cross-sectional changes of the pipe according to Eqs. (12) and (13) has to be applied to Eq. (32).

In order to eliminate the difficulty of operating with absolute functions in Eq. (32), the signum function is introduced:

$$\operatorname{sgn}(\gamma) = \begin{cases} 1 & \text{if } \gamma \ge 0, \\ -1 & \text{if } \gamma < 0. \end{cases}$$
 (33)

Using the signum function, Eq. (32) can be manipulated into the form

$$\mathbf{f}_{H} = \begin{cases} f_{Hn} \\ f_{Ht} \end{cases} = - \underbrace{\begin{bmatrix} C_{a}^{*} & 0 \\ 0 & C_{a}^{*} \end{bmatrix} \begin{Bmatrix} \ddot{u}_{n} \\ \ddot{v}_{n} \end{Bmatrix}}_{\text{Added mass force}} - \underbrace{\begin{bmatrix} C_{eqn}^{*} & 0 \\ 0 & C_{eqt}^{*} \end{bmatrix} \begin{Bmatrix} \dot{u}_{n} \\ \dot{v}_{n} \end{Bmatrix}}_{\text{Added mass force}} + \underbrace{\begin{bmatrix} C_{cqn}^{*} & 0 \\ 0 & C_{eqt}^{*} \end{bmatrix} \begin{Bmatrix} \dot{u}_{n} \\ \dot{v}_{n} \end{Bmatrix}}_{\text{Added mass force}} + \underbrace{\begin{bmatrix} C_{cqn}^{*} & 0 \\ 0 & C_{eqt}^{*} \end{bmatrix} \begin{Bmatrix} \dot{u}_{n} \\ \dot{v}_{n} \end{Bmatrix}}_{\text{Added mass force}} + \underbrace{\begin{bmatrix} C_{cqn}^{*} & 0 \\ 0 & C_{eqt}^{*} \end{bmatrix} \begin{Bmatrix} \dot{u}_{n} \\ \dot{v}_{n} \end{Bmatrix}}_{\text{Added mass force}} + \underbrace{\begin{bmatrix} C_{cqn}^{*} & 0 \\ 0 & C_{eqt}^{*} \end{bmatrix} \begin{Bmatrix} \dot{u}_{n} \\ \dot{v}_{n} \end{Bmatrix}}_{\text{Added mass force}} + \underbrace{\begin{bmatrix} C_{cqn}^{*} & 0 \\ 0 & C_{eqt}^{*} \end{bmatrix} \begin{Bmatrix} \dot{u}_{n} \\ \dot{v}_{n} \end{Bmatrix}}_{\text{Added mass force}} + \underbrace{\begin{bmatrix} C_{cqn}^{*} & 0 \\ 0 & C_{eqt}^{*} \end{bmatrix} \begin{Bmatrix} \dot{u}_{n} \\ \dot{v}_{n} \end{Bmatrix}}_{\text{Added mass force}} + \underbrace{\begin{bmatrix} C_{cqn}^{*} & 0 \\ 0 & C_{eqt}^{*} \end{bmatrix} \begin{Bmatrix} \dot{v}_{n} \\ \dot{v}_{n} \end{Bmatrix}}_{\text{Added mass force}} + \underbrace{\begin{bmatrix} C_{cqn}^{*} & 0 \\ 0 & C_{eqt}^{*} \end{bmatrix} \begin{Bmatrix} \dot{v}_{n} \\ \dot{v}_{n} \end{Bmatrix}}_{\text{Added mass force}} + \underbrace{\begin{bmatrix} C_{cqn}^{*} & 0 \\ 0 & C_{eqt}^{*} \end{Bmatrix}}_{\text{Added mass force}} + \underbrace{\begin{bmatrix} C_{cqn}^{*} & 0 \\ 0 & C_{eqt}^{*} \end{bmatrix} \begin{Bmatrix} \dot{v}_{n} \\ \dot{v}_{n} \end{Bmatrix}}_{\text{Added mass force}} + \underbrace{\begin{bmatrix} C_{cqn}^{*} & 0 \\ 0 & C_{eqt}^{*} \end{bmatrix} \begin{Bmatrix} \dot{v}_{n} \\ \dot{v}_{n} \end{Bmatrix}}_{\text{Added mass force}} + \underbrace{\begin{bmatrix} C_{cqn}^{*} & 0 \\ 0 & C_{eqt}^{*} \end{bmatrix} \begin{Bmatrix} \dot{v}_{n} \\ \dot{v}_{n} \end{Bmatrix}}_{\text{Added mass force}} + \underbrace{\begin{bmatrix} C_{cqn}^{*} & 0 \\ 0 & C_{eqt}^{*} \end{Bmatrix}}_{\text{Added mass force}} + \underbrace{\begin{bmatrix} C_{cqn}^{*} & 0 \\ 0 & C_{eqt}^{*} \end{bmatrix} \begin{Bmatrix} \dot{v}_{n} \\ \dot{v}_{n} \end{Bmatrix}}_{\text{Added mass force}} + \underbrace{\begin{bmatrix} C_{cqn}^{*} & 0 \\ 0 & C_{eqt}^{*} \end{Bmatrix}}_{\text{Added mass force}} + \underbrace{\begin{bmatrix} C_{cqn}^{*} & 0 \\ 0 & C_{eqt}^{*} \end{Bmatrix}}_{\text{Added mass force}} + \underbrace{\begin{bmatrix} C_{cqn}^{*} & 0 \\ 0 & C_{eqt}^{*} \end{Bmatrix}}_{\text{Added mass force}} + \underbrace{\begin{bmatrix} C_{cqn}^{*} & 0 \\ 0 & C_{eqt}^{*} \end{Bmatrix}}_{\text{Added mass force}} + \underbrace{\begin{bmatrix} C_{cqn}^{*} & 0 \\ 0 & C_{eqt}^{*} \end{Bmatrix}}_{\text{Added mass force}} + \underbrace{\begin{bmatrix} C_{cqn}^{*} & 0 \\ 0 & C_{eqt}^{*} \end{Bmatrix}}_{\text{Added mass force}} + \underbrace{\begin{bmatrix} C_{cqn}^{*} & 0 \\ 0 & C_{eqt}^{*} \end{Bmatrix}}_{\text{Added mass force}} + \underbrace{\begin{bmatrix} C_{cqn}^{*} & 0 \\ 0 & C_{eqt}^{*} \end{Bmatrix}}_{\text{Added mass force}} + \underbrace{\begin{bmatrix} C_{cqn}^{*} & 0 \\ 0 & C_{eqt}^{*} \end{Bmatrix}}_{\text{Added mass force}} + \underbrace{\begin{bmatrix} C_{cqn}^{*} & 0 \\ 0 & C_{eqt}^{*} \end{Bmatrix}}_{\text{Added ma$$

where the c oefficients of equivalent damping and drag forces in the normal direction are

$$C_{eun}^* = C_{Dn}^* [2V_{Hn} - \dot{u}_n], \ C_{Dn}^* = 0.5\rho_e D_e C_{Dn} \, sgn(\gamma_n); \tag{35a, b}$$

the coefficients of equivalent damping and drag forces in the tangential direction are

$$C_{eqt}^* = C_{Dt}^* [2V_{Ht} - \dot{v}_n], \quad C_{Dt}^* = 0.5\rho_e D_e \pi C_{Dt} \operatorname{sgn}(\gamma_t);$$
 (35c, d)

and the coefficients of added mass and inertia forces are

$$C_a^* = \rho_e A_e C_a, \quad C_M^* = \rho_e A_e C_M, \tag{35e, f}$$

in which  $C_M = 1 + C_a$  is the inertia coefficient.

In Cartesian coordinates, Eq. (34) can be transformed to

$$\mathbf{f}_{H} = \begin{cases} f_{Hx} \\ f_{Hy} \end{cases} = -\underbrace{\begin{bmatrix} C_{a}^{*} \ 0 \\ 0 \ C_{u}^{*} \end{bmatrix} \begin{Bmatrix} \ddot{x} \\ \ddot{y} \end{Bmatrix}}_{\text{Added mass force}} - \underbrace{\begin{bmatrix} C_{eqx}^{*} C_{eqxy}^{*} \\ C_{eqxy}^{*} C_{eqyy}^{*} \end{bmatrix} \begin{Bmatrix} \dot{x} \\ \dot{y} \end{Bmatrix}}_{\text{Added mass force}} + \underbrace{\begin{cases} C_{Dx}^{*} V_{Hx}^{2} + 2 C_{Dxy1}^{*} V_{Hx} V_{Hy} + C_{Dxy2}^{*} V_{Hy}^{2} + C_{M}^{*} \dot{V}_{Hx} \\ C_{Dy}^{*} V_{Hy}^{2} + 2 C_{Dxy2}^{*} V_{Hx} V_{Hy} + C_{Dxy1}^{*} V_{Hx}^{2} + C_{M}^{*} \dot{V}_{Hy} \end{Bmatrix}}_{\text{Hydrodynamic excitation}},$$
(36)

where  $V_{Hx}$  and  $V_{Hy}$  are the horizontal and vertical velocities of external fluid; the coefficients of equivalent damping and drag forces in the horizontal direction are

$$C_{eqx}^* = C_{equ}^* \cos^2 \theta + C_{eqt}^* \sin^2 \theta, \quad C_{Dx}^* = C_{Dq}^* \cos^3 \theta + C_{Dt}^* \sin^3 \theta;$$
 (37a, b)

the coefficients of equivalent damping and drag forces in the vertical direction are

$$C_{eqy}^* = C_{eqn}^* \sin^2 \theta + C_{eqt}^* \cos^2 \theta, \quad C_{Dy}^* = -C_{Dn}^* \sin^3 \theta + C_{Dt}^* \cos^3 \theta;$$
 (37c, d)

the coupling coefficient of equivalent hydrodynamic damping in the x - y plane is

$$C_{eux}^* = (-C_{eux}^* + C_{eal}^*)\sin\theta\cos\theta; \tag{37e}$$

and the coupling coefficients of drag forces in the x - y plane are

$$C_{Dxy1}^* = -C_{Dn}^* \sin \theta \cos^2 \theta + C_{Dt}^* \sin^2 \theta \cos \theta, \tag{37f}$$

$$C_{Dyr2}^{\bullet} = C_{Du}^{\bullet} \sin^2 \theta \cos \theta + C_{Dt}^{\bullet} \sin \theta \cos^2 \theta. \tag{37g}$$

At the equilibrium state, static loading is due only to the steady flow of external fluid. Therefore, the hydrodynamic forces from Eqs. (34) and (36) are reduced to

$$\mathbf{f}_{Ho} = \begin{cases} f_{Hno} \\ f_{Hto} \end{cases} = \begin{cases} C_{Dno}^* V_{Hno}^2 \\ C_{Dto}^* V_{Hto}^2 \end{cases}, \tag{38}$$

$$\mathbf{f}_{Ho} = \begin{cases} f_{Hxo} \\ f_{Hyo} \end{cases} = \begin{cases} C_{Dxo}^{*} V_{Hxo}^{2} + 2C_{Dxylo}^{*} V_{Hxo} V_{Hyo} + C_{Dxy2o}^{*} V_{Hyo}^{2} \\ C_{Dyo}^{*} V_{Hyo}^{2} + 2C_{Dxy2o}^{*} V_{Hxo} V_{Hyo} + C_{Dxylo}^{*} V_{Hxo}^{2} \end{cases},$$
(39)

respectively. Note that the additional subscripts 'o' on all variables designate the equilibrium-state parameters. For example,  $C_{Dno}^*$  implies the equilibrium state of  $C_{Dn}^*$ ; hence, Eq. (35b) uses equilibrium-state parameters to obtain  $C_{Dno}^* = 0.5\rho_c D_{eo} C_{Dn} \operatorname{sgn}(\gamma_{no})$ .

#### 2.5.2. Hydrodynamic forces due to internal flow of transported fluid

Based on the control volume approach of Computational Fluid Dynamics, hydrodynamic forces due to flow of transported fluid inside extensible flexible pipes with large deformation can be derived as follows. Let  $V_F$  and  $V_P$  represent the velocity vectors of transported fluid and the pipe with respect to the fixed frame of reference, then the

velocity vector of transported fluid relative to the pipe velocity is given by

$$\mathbf{V}_{FP} = V_{FP}\hat{\mathbf{t}} = V_{FP}\,\partial\mathbf{r}_P/\partial s = \mathbf{V}_F - \mathbf{V}_P,\tag{40}$$

where  $V_{FP}$  is the internal flow velocity function:  $V_{FP} = \bar{V}_i$ ,  $V_{FP} = V_{io}$ , and  $V_{FP} = V_i$  at states 1, 2, and 3, respectively. From Newton's law of momentum conservation, hydrodynamic pressures due to internal flow induces the inertial force on the transported mass:

$$\int_{\forall_i} \mathbf{B}_i \, d\forall_i = \int_{\forall_i} \frac{D(\rho_i \mathbf{V}_F)}{Dt} \, d\forall_i = \int_{\forall_i} \left[ \frac{D\rho_i}{Dt} \mathbf{V}_F + \rho_i \mathbf{a}_F \right] \, d\forall_i, \tag{41}$$

where  $B_i$  is the inertial force per unit control volume  $\forall_i$ ,  $a_F$  the acceleration vector of transported fluid with respect to the fixed frame of reference, and

$$\frac{D()}{Dt} = \frac{\partial()}{\partial t} + (V_{FP} \cdot \nabla)() = \frac{\partial()}{\partial t} + \frac{V_{FP}}{s'} \frac{\partial()}{\partial \alpha}.$$
 (42)

Note that

$$\mathbf{V}_{FP}.\nabla = \mathbf{V}_{FP} \left[ \frac{\partial x}{\partial s} \hat{\mathbf{i}} + \frac{\partial y}{\partial s} \hat{\mathbf{j}} + \frac{\partial z}{\partial s} \hat{\mathbf{k}} \right] \left[ \frac{\partial}{\partial x} \hat{\mathbf{i}} + \frac{\partial}{\partial y} \hat{\mathbf{j}} + \frac{\partial}{\partial z} \hat{\mathbf{k}} \right] = \mathbf{V}_{FP} \frac{\partial}{\partial s} = \frac{\mathbf{V}_{FP}}{s'} \frac{\partial}{\partial \alpha}.$$
(43)

Lemma 1 shows that  $D\rho_i/Dt$  vanishes.

**Lemma 1.** The conservation condition of transported mass yields  $D\rho_i/Dt = 0$ .

Proof. Utilizing Eq. (40), Eq. (41) can be written as

$$\int_{\forall_i} \mathbf{B}_i \, d\forall_i = \int_{\forall_i} \left[ \frac{\mathbf{D}(\rho_i \mathbf{V}_P)}{\mathbf{D}t} \right] \, d\forall_i + \int_{\forall_i} \left[ \frac{\mathbf{D}(\rho_i \mathbf{V}_{FP})}{\mathbf{D}t} \right] \, d\forall_i. \tag{44}$$

From the Reynolds transport theorem (Shames, 1992), the last integral is given by

$$\int_{\forall_{i}} \frac{D(\rho_{i} V_{FP})}{Dt} dV_{i} = \frac{\partial}{\partial t} \left[ \int_{\forall_{i}} (\rho_{i} V_{FP}) dV_{i} \right] + \iint_{\hat{A}_{si}} V_{FP} (\rho_{i} V_{FP}) dA_{si}, \tag{45}$$

where  $A_{si}$  is the vector of internal control surface of the pipe  $\tilde{A}_{si}$ .

Employing the Gauss divergence theorem, one can demonstrate that

$$\iint_{\mathbb{R}} \mathbf{V}_{FP}(\rho_i \mathbf{V}_{FP} \cdot \mathbf{d} \mathbf{A}_{si}) = \int_{\mathbb{V}} \left[ (\rho_i \mathbf{V}_{FP} \cdot \nabla) \mathbf{V}_{FP} + \nabla \cdot (\rho_i \mathbf{V}_{FP}) \mathbf{V}_{FP} \right] dV_i.$$
(46)

· Substituting Eqs. (46) into Eq. (45) together with some manipulation, one obtains

$$\int_{\forall_{i}} \frac{D(\rho_{i} \mathbf{V}_{FP})}{Dt} d\forall_{i} = \int_{\forall_{i}} \left\{ \rho_{i} \underbrace{\left[ \frac{\partial \mathbf{V}_{FP}}{\partial t} + (\mathbf{V}_{FP} \cdot \nabla) \mathbf{V}_{FP} \right]}_{(1)} + \underbrace{\left[ \frac{\partial \rho_{i}}{\partial t} + \nabla \cdot (\rho_{i} \mathbf{V}_{FP}) \right]}_{(2)} \mathbf{V}_{FP} \right\} d\forall_{i}. \tag{47}$$

Referring to Eq. (42), the bracketed term (1) is known as the acceleration of transported fluid  $a_{FP}$ , whereas term (2) is zero due to the continuity condition of conservation of mass. Thereby, Eq. (47) yields

$$\frac{D(\rho_i V_{FP})}{Dt} = \rho_i \mathbf{a}_{FP}. \tag{48}$$

Since

$$\frac{D(\rho_i V_{FP})}{Dt} = \frac{D\rho_i}{Dt} V_{FP} + \rho_i \mathbf{a}_{FP},$$

and  $V_{FP} \neq 0$ , Eq. (48) is valid if, and only if,

$$D_{\theta}/D_{t} = 0$$
.  $\Box$ 

Using Lemma 1 in Eq. (41), one can constitute Proposition 4.

**Proposition 4.** Internal flow of transported fluid through the moving, deforming internal control volume of the pipe induces the inertial force exerted on the pipe wall:

$$\mathbf{B}_i = \rho_i \mathbf{a}_F \quad or \quad \mathbf{F}_i = m_i \mathbf{a}_F, \tag{50a, b}$$

where  $\mathbf{F}_i$  and  $m_i$  are the inertial force and the transported mass per unit length of the pipe.

From Eqs. (50), it is seen that determining the inertial force on the transported fluid needs the expression of transported mass acceleration  $a_F$ . Based on Eulerian mechanics (Huang, 1993), the velocity and acceleration of transported fluid can be derived as

$$\mathbf{V}_{F} = \mathbf{V}_{P} + \mathbf{V}_{FP} = \frac{\partial \mathbf{r}_{P}}{\partial t} + \frac{V_{FP}}{c'} \frac{\partial \mathbf{r}_{P}}{\partial \alpha},\tag{51}$$

$$\mathbf{a}_{F} = \mathbf{a}_{P} + \mathbf{a}_{FP} = \frac{\mathbf{D}V_{P}}{\mathbf{D}t} + \frac{\mathbf{D}V_{FP}}{\mathbf{D}t} = \frac{\mathbf{D}}{\mathbf{D}t} \left( \frac{\partial \mathbf{r}_{P}}{\partial t} \right) + \frac{\mathbf{D}}{\mathbf{D}t} \left( \frac{V_{FP}}{s'} \frac{\partial \mathbf{r}_{P}}{\partial \alpha} \right)$$

$$= \underbrace{\left[ \frac{\partial^{2}\mathbf{r}_{P}}{\partial t^{2}} + \frac{V_{FP}}{s'} \frac{\partial^{2}\mathbf{r}_{P}}{\partial \alpha} \frac{\partial^{2}\mathbf{r}_{P}}{\partial t} \right] + \underbrace{\left[ \frac{\partial}{\partial t} \left( \frac{V_{FP}}{s'} \right) + \frac{V_{FP}}{s'} \frac{\partial}{\partial \alpha} \left( \frac{V_{FP}}{s'} \right) \right] \frac{\partial \mathbf{r}_{P}}{\partial \alpha}}_{\mathbf{a}_{P}}. \tag{52}$$

Eq. (52) can be rearranged to obtain

$$\mathbf{a}_{F} = \underbrace{\frac{\partial^{2} \mathbf{r}_{P}}{\partial t^{2}}}_{(1)} + \underbrace{\left(\frac{2V_{FP}}{s'}\right) \frac{\partial^{2} \mathbf{r}_{P}}{\partial \alpha \partial t}}_{(2)} + \underbrace{\left(\frac{V_{FP}}{s'}\right)^{2} \frac{\partial^{2} \mathbf{r}_{P}}{\partial \alpha^{2}}}_{(3)} + \underbrace{\left(\frac{\dot{V}_{FP}}{s'}\right)^{2} \frac{\partial^{2} \mathbf{r}_{P}}{\partial \alpha^{2}}}_{(4)} + \underbrace{\left(\frac{\dot{V}_{FP}}{s'}\right)^{2} \frac{\partial^{2} \mathbf{r}_{P}}{\partial \alpha^{2}}}_{(5)} - \underbrace{\left(\frac{\dot{V}_{FP}}{s'}\right)^{2} \frac{\partial^{2} \mathbf{r}_{P}}{\partial \alpha^{2}}}_{(6)} + \underbrace{\left(\frac{\dot{V}_{FP}}{s'}\right)^{2} \frac{\partial^{2} \mathbf{r}_{P}}{\partial \alpha^{2}}}_{(5)} + \underbrace{\left(\frac{\dot{V}_{FP}}{s'}\right)^{2} \frac{\partial^{2} \mathbf{r}_{P}}{\partial \alpha^{2}}}_{(6)} + \underbrace{\left(\frac{\dot{V}_{FP}}{s'}\right)^{2} \frac{\partial^{2} \mathbf{r}_{P}}{\partial \alpha^{2}}_{(6)}}_{(6)} + \underbrace{\left(\frac{\dot{V$$

in which term (1) is the transported mass acceleration, (2) the coriolis acceleration, (3) the centripetal acceleration, (4) the local acceleration due to unsteady flow, (5) the convective acceleration due to nonuniform flow, and (6) the relative accelerations due to local coordinate rotation and displacement.

In 2-D Cartesian coordinates, at the displaced state:

$$V_{FP} = V_i, \quad \mathbf{r}_P = x\hat{\mathbf{i}} + y\hat{\mathbf{j}}, \quad s' = \sqrt{x'^2 + y'^2}, \quad s's'' = x'x'' + y'y'', \quad s'\dot{s}' = x'\dot{x}' + y'\dot{y}'. \tag{54a-e}$$

Inserting Eqs. (54) into Eqs. (51) and (53), one obtains

$$\mathbf{V}_{F} = [\dot{x} + V_{i}x'/s']\hat{\mathbf{i}} + [\dot{y} + V_{i}y'/s']\hat{\mathbf{j}}, \tag{55}$$

$$\mathbf{a}_{F} = \left\{ \ddot{x} + \left[ \left( \frac{2}{s'} - \frac{x'^{2}}{s'^{3}} \right) \dot{x}' - \left( \frac{x'y'}{s'^{3}} \right) \dot{y}' \right] V_{i} + \left( \frac{\kappa y'}{s'} \right) V_{i}^{2} + \left( \frac{DV_{i}}{Dt} \right) \frac{x'}{s'} \right\} \hat{\mathbf{i}}$$

$$+ \left\{ \ddot{y} + \left[ -\left( \frac{x'y'}{s'^{3}} \right) \dot{x}' + \left( \frac{2}{s'} - \frac{y'^{2}}{s'^{3}} \right) \dot{y}' \right] V_{i} - \left( \frac{\kappa x'}{s'} \right) V_{i}^{2} + \left( \frac{DV_{i}}{Dt} \right) \frac{y'}{s'} \right\} \hat{\mathbf{j}}.$$

$$(56)$$

Note that

$$\frac{\kappa y'}{s'} = \left(\frac{y'^2}{s'^4}\right) x'' - \left(\frac{x'y'}{s'^4}\right) y'', \quad -\frac{\kappa x'}{s'} = -\left(\frac{x'y'}{s'^4}\right) x'' + \left(\frac{x'^2}{s'^4}\right) y''. \tag{57a,b}$$

In 2-D natural coordinates, at the displaced state:

$$V_{FP} = V_i, (58a)$$

$$\frac{\partial \mathbf{r}_P}{\partial \alpha} = s' \hat{\mathbf{t}},\tag{58b}$$

$$\frac{\partial^2 \mathbf{r}_P}{\partial \alpha^2} = s' \theta' \,\hat{\mathbf{n}} + s'' \hat{\mathbf{t}},\tag{58c}$$

$$\frac{\partial^2 \mathbf{r}_P}{\partial t^2} = \ddot{u}_n \hat{\mathbf{n}} + \ddot{v}_n \hat{\mathbf{t}}. \tag{58d}$$

$$\frac{\partial^2 \mathbf{r}_P}{\partial \mathbf{x} \, \partial t} = s' \dot{\theta} \hat{\mathbf{n}} + \dot{s}' \hat{\mathbf{t}}. \tag{58e}$$

Exploiting Eqs. (58), Eqs. (51) and (53) yield

$$\mathbf{V}_F = \dot{u}_n \hat{\mathbf{n}} + (\dot{v}_n + V_i) \hat{\mathbf{t}},\tag{59}$$

$$\mathbf{a}_F = \left[\ddot{u}_n + 2V_i\dot{\theta} + \kappa V_i^2\right]\hat{\mathbf{n}} + \left[\ddot{v}_n + \frac{V_i\dot{s}'}{s'} + \frac{DV_i}{Dt}\right]\hat{\mathbf{t}}.$$
(60)

It is evident that the relative accelerations due to local coordinate rotation and displacement vanish in the natural system.

At the equilibrium state,  $V_{FP} = V_{io}$ ,  $(x, y) = (x_o, y_o)$ ,  $u_n = v_n = 0$ ,  $(s, \theta) = (s_o, \theta_o)$ , and the time-dependent terms vanish. Thereby, Eqs. (55), (56), (59), and (60) are reduced to

$$\mathbf{V}_{F_o} = (V_{io} x'_o / s'_o) \hat{\mathbf{i}} + (V_{io} y'_o / s'_o) \hat{\mathbf{j}} = V_{io} \hat{\mathbf{t}}, \tag{61}$$

$$\mathbf{a}_{Fo} = \left\{ \left( \frac{\kappa_o y_o'}{s_o'} \right) V_{io}^2 + \frac{V_{io} V_{io}' x_o'}{s_o'} \mathbf{\hat{s}}_o^2 \mathbf{\hat{i}} + \left\{ -\left( \frac{\kappa_o x_o'}{s_o'} \right) V_{io}^2 + \frac{V_{io} V_{io}'}{s_o'} \frac{y_o'}{s_o'} \mathbf{\hat{j}} \mathbf{\hat{i}} \right\} \mathbf{\hat{i}} = \left[ \kappa_o V_{io}^2 \right] \mathbf{\hat{n}} + \left[ \frac{V_{io} V_{io}'}{s_o'} \mathbf{\hat{j}} \mathbf{\hat{i}} \right] \mathbf{\hat{t}}.$$
 (62)

#### 3. Virtual work formulations

Based on the method of virtual work, the fundamentals of large strain modelling proposed in Section 2 are employed to develop large strain formulations of extensible flexible marine pipes transporting fluid as follows.

Step 1: Converting the real system into the apparent system of the marine pipe by the apparent tension concept (Section 2.4).

Step 2: Applying the extensible elastica theory (Section 2.3) on the apparent system to obtain the stiffness or internal virtual work equation.

Step 3: Expressing the equation of external virtual work induced by the apparent weight (Section 2.4), hydrodynamic forces due to external and internal flows (Section 2.5), and inertial forces of the pipe.

Step 4: Applying the principle of virtual work to generate weak and strong forms of the large strain formulations of the apparent system.

#### 3.1. Step 2: Applying the extensible elastica theory on the apparent system

In Fig. 4(r), the overall apparent system is subjected to the apparent tension  $T_a$  in place of the axial force N of the real system. Therefore, applying Eqs. (17d), (18d), and (19d) of the extensible elastica theory on the apparent system yields the stiffness equation:

$$\delta U_a = \int_{\mathbf{z}} [T_a \delta s' + M \delta (\theta' - \bar{\theta}')] \, \mathrm{d}\alpha, \tag{63}$$

where  $U_a$  is the strain energy of the apparent system,

$$T_a = E\tilde{A}_P \varepsilon,$$
 (64a)

$$M = \begin{cases} E\bar{I}_{P}[\kappa(1+\varepsilon) - \vec{\kappa}] & \text{for TL,} \\ EI_{Po}[\kappa(1+\varepsilon_{d}) - \vec{\kappa}(1-\varepsilon_{o})] & \text{for UL,} \\ EI_{P}[\kappa - \vec{\kappa}(1-\varepsilon)] & \text{for EL.} \end{cases}$$
(64b)

From the assumption that the pipe is straight in the undeformed state, and the basic formulas of differential geometry, one has

$$\bar{\kappa} = \bar{\theta}' = 0,\tag{65a}$$

$$s' = x' + v', \tag{65b}$$

$$\theta' = (x''y' - x'y'')/s^2. \tag{65c}$$

Substituting Eq. (65a) into Eq. (64b), and taking the first variation of Eqs. (65b) and (65c) in association with the coordinate transformations of the displacement vectors, one obtains

$$M = B\kappa, \quad B = \begin{cases} E\overline{I}_{P}(1+\varepsilon) & \text{for } TL, \\ EI_{Po}(1+\varepsilon_{d}) & \text{for } UL, \\ EI_{P} & \text{for } EL, \end{cases}$$
(66a, b)

in Cartesian coordinates

$$\delta s' = \left(\frac{x'}{s'}\right)\delta u' + \left(\frac{y'}{s'}\right)\delta v',\tag{67a}$$

$$\delta\theta' = \frac{1}{s'} \left( \frac{y'}{s'} \right) \delta u'' - \left[ \kappa \left( \frac{x'}{s'} \right) + \frac{s''}{s'^2} \left( \frac{y'}{s'} \right) \right] \delta u' - \frac{1}{s'} \left( \frac{x'}{s'} \right) \delta v'' - \left[ \kappa \left( \frac{y'}{s'} \right) - \frac{s''}{s'^2} \left( \frac{x'}{s'} \right) \right] \delta v', \tag{67b}$$

in natural coordinates:

$$\delta s' = \delta v'_n - \theta' \delta u_n, \tag{68a}$$

$$\delta\theta' = \frac{\partial}{\partial\alpha} \left[ \frac{\delta u'_n + \theta' \delta v_n}{s'} \right]. \tag{68b}$$

By substituting Eqs. (66)–(68) into Eq. (63), and then taking integrations by parts twice, the three forms of the internal virtual work can be expressed as follows:

Form 1: In Cartesian coordinates:

$$\delta U_{a} = \int_{\alpha} \left\{ \begin{array}{l} \frac{B\kappa}{s'} \left( \frac{y'}{s'} \right) \delta u'' + \left[ (T_{a} - B\kappa^{2}) \left( \frac{x'}{s'} \right) - B\kappa \frac{s''}{s'^{2}} \left( \frac{y'}{s'} \right) \right] \delta u' \\ - \frac{B\kappa}{s'} \left( \frac{x'}{s'} \right) \delta v'' + \left[ (T_{a} - B\kappa^{2}) \left( \frac{y'}{s'} \right) + B\kappa \frac{s''}{s'^{2}} \left( \frac{x'}{s'} \right) \right] \delta v' \end{array} \right\} d\alpha, \tag{69a}$$

and in natural coordinates:

$$\delta U_{a} = \int_{\Gamma} \left\{ \left[ -T_{a}\theta' \right] \delta u_{n} + \left[ T_{a} \right] \delta v_{n}' + \left[ M \right] \delta \theta' \right\} d\alpha. \tag{69b}$$

Form 2 (after a first integration by parts): In Cartesian coordinates:

$$\delta U_{\alpha} = [M \,\delta\theta]_{\mathbf{z}_{\alpha}}^{\mathbf{z}_{i}} + \int_{\mathbf{z}} \{H \,\delta u' + V \,\delta v'\} \,\mathrm{d}\alpha,\tag{70a}$$

and in natural coordinates:

$$\delta U_a = [M \, \delta \theta]_{\alpha_o}^{\alpha_i} + \int_{\gamma} \{ -[Q] \, \delta u_n' - [T_a \theta'] \, \delta u_n + [T_a] \, \delta v_n' + [Q \theta'] \, \delta v_n \} \, \mathrm{d}\alpha, \tag{70b}$$

where

$$H = T_a \left( \frac{x'}{s'} \right) - Q \left( \frac{y'}{s'} \right), \tag{71a}$$

$$V = T_u \left(\frac{y'}{s'}\right) + Q\left(\frac{x'}{s'}\right),\tag{71b}$$

$$Q = \frac{M'}{s'} = \frac{(B\kappa)'}{s'}.$$

Form 3 (after a second integration by parts): In Cartesian coordinates:

$$\delta U_a = [H \, \delta u + V \, \delta v + M \, \delta \theta]_x^2 + \int_z \{ [-H'] \delta u + [-V'] \delta v \} \, \mathrm{d}\alpha, \tag{72a}$$

and in natural coordinates:

$$\delta U_a = [T_a \, \delta v_n - Q \, \delta u_n + M \, \delta \theta]_2^z + \int_{\Sigma} \{ [Q' - T_a \theta'] \, \delta u_n + [-T_a' - Q \theta'] \, \delta v_n \} \, \mathrm{d}\alpha. \tag{72b}$$

Note that

$$x'/s' = \sin \theta$$
,  $y'/s' = \cos \theta$ ,  $\kappa = \theta'/s' = (x''y' - x'y'')/s'^3$ .

# 3.2. Step 3: Expressing the equation of external virtual work

The equation of external virtual work is given by

$$\delta W_a = \delta W_w + \delta W_H + \delta W_I, \tag{73}$$

where  $W_w$ ,  $W_H$ , and  $W_I$  are the virtual works done by the apparent weight, hydrodynamic pressures, and inertial forces of the pipe and transported fluid. In Cartesian coordinates:

$$\delta W_{w} = -\int_{\alpha} w_{a} s' \, \delta v \, \mathrm{d}\alpha, \tag{74a}$$

$$\delta W_H = \int_{\alpha} \left[ (f_{H_X} s') \, \delta u + (f_{H_Y} s') \delta v \right] \, \mathrm{d}\alpha, \tag{75a}$$

$$\delta W_I = -\int_{a} \left[ (m_P a_{Px} + m_i a_{Fx}) s' \, \delta u + (m_P a_{Py} + m_i a_{Fy}) s' \, \delta v \right] \, \mathrm{d}\alpha. \tag{76a}$$

In natural coordinates:

$$\delta W_w = -\int_{z} \left[ \left( -w_a s' \sin \theta \right) \delta u_n + \left( w_a s' \cos \theta \right) \delta v_n \right] d\alpha, \tag{74b}$$

$$\delta W_H = \int_{\sigma} \left[ (f_{Hn}s') \, \delta u_n + (f_{Ht}s') \, \delta v_n \right] \, \mathrm{d}\alpha, \tag{75b}$$

$$\delta W_I = -\int_{a} \left[ (m_P a_{Pn} + m_i a_{Fn}) s' \, \delta u_n + (m_P a_{Pt} + m_i a_{Ft}) s' \, \delta v_n \right] \, \mathrm{d}\alpha. \tag{76b}$$

Note that  $\mathbf{a}_P = a_{Px}\hat{\mathbf{i}} + a_{Py}\hat{\mathbf{j}} = \ddot{\mathbf{r}}_P = x\hat{\mathbf{i}} + y\hat{\mathbf{j}} = \ddot{u}\hat{\mathbf{i}} + v\hat{\mathbf{j}}$  and  $\mathbf{a}_P = a_{Pn}\hat{\mathbf{n}} + a_{Pt}\hat{\mathbf{t}} = \ddot{u}_n\hat{\mathbf{n}} + \ddot{v}_n\hat{\mathbf{t}}$ . The expressions of  $w_a$ ,  $\mathbf{f}_H = f_{Hx}\hat{\mathbf{i}} + f_{Hy}\hat{\mathbf{j}}$ ,  $\mathbf{a}_F = a_{Fx}\hat{\mathbf{i}} + a_{Fy}\hat{\mathbf{j}}$ , and  $\mathbf{a}_F = a_{Fn}\hat{\mathbf{n}} + a_{Ft}\hat{\mathbf{t}}$  are given by Eqs. (28), (34), (36), (56), and (60), respectively

Substituting Eqs. (74)-(76) into Eq. (73), in Cartesian coordinates one obtains

$$\delta W_{a} = \int_{x} \left\{ s' [f_{Hx} - m_{P} a_{Px} - m_{i} a_{Fx}] \, \delta u \right\} d\alpha$$

$$+ \int_{x} \left\{ s' [-w_{a} + f_{Hy} - m_{P} a_{Py} - m_{i} a_{Fy}] \, \delta v \right\} d\alpha, \tag{77a}$$

and in natural coordinates:

$$\delta W_{a} = \int_{\alpha} \left\{ s' [w_{a} \sin \theta + f_{Hn} - m_{P} a_{Pn} - m_{i} a_{Fn}] \delta u_{n} \right\} d\alpha$$

$$+ \int_{\alpha} \left\{ s' [-w_{a} \cos \theta + f_{Ht} - m_{P} a_{Pt} - m_{i} a_{Ft}] \delta v_{n} \right\} d\alpha. \tag{77b}$$

# 3.3. Step 4: Applying the principle of virtual work

From the principle of virtual work, the total virtual work of the apparent system is zero:

$$\delta \pi_a = \delta U_a - \delta W_a = 0. \tag{78}$$

By substituting Eq. (69), (70), (72), and (77) into Eq. (78), the three weak forms of the total virtual work are obtained as follows:

Weak form 1: In Cartesian coordinates:

$$\delta \pi_{a} = \int_{\mathcal{I}} \left\{ \frac{B\kappa}{s'} \left( \frac{y'}{s'} \right) \delta u'' + \left[ (T_{a} - B\kappa^{2}) \left( \frac{x'}{s'} \right) - B\kappa \frac{s''}{s'^{2}} \left( \frac{y'}{s'} \right) \right] \delta u' - s' [f_{Hx} - m_{P}a_{Px} - m_{i}a_{Fx}] \delta u \right\} d\alpha$$

$$+ \int_{\mathcal{I}} \left\{ -\frac{B\kappa}{s'} \left( \frac{x'}{s'} \right) \delta v'' + \left[ (T_{a} - B\kappa^{2}) \left( \frac{y'}{s'} \right) + B\kappa \frac{s''}{s'^{2}} \left( \frac{x'}{s'} \right) \right] \delta v' - s' [-w_{a} + f_{Hy} - m_{P}a_{Py} - m_{i}a_{Fy}] \delta v \right\} d\alpha = 0.$$

$$(79a)$$

In natural coordinates:

$$\delta \pi_{a} = \int_{\alpha} \left\{ -T_{a}\theta' - s'[w_{a}\sin\theta + f_{Hn} - m_{P}a_{Pn} - m_{i}a_{Fn}] \right\} \delta u_{n} d\alpha$$

$$+ \int_{\alpha} \left\{ [T_{a}] \delta v'_{n} - s'[-w_{a}\cos\theta + f_{Ht} - m_{P}a_{Pt} - m_{i}a_{Ft}] \delta v_{n} \right\} d\alpha$$

$$+ \int_{\alpha} \left\{ [M] \delta \theta' \right\} d\alpha = 0. \tag{79b}$$

Weak form 2: In Cartesian coordinates:

$$\delta \pi_{\alpha} = [M \, \delta \theta]_{z_{\alpha}}^{z_{\alpha}} + \int_{\alpha} \{H \delta u' - s' [f_{Hx} - m_{P} a_{Px} - m_{i} a_{Fx}] \, \delta u \} \, d\alpha$$

$$+ \int_{\alpha} \{V \delta v' - s' [-w_{\alpha} + f_{Hy} - m_{P} a_{Py} - m_{i} a_{Fy}] \delta v \} \, d\alpha = 0.$$
(80a)

In natural coordinates:

$$\delta \pi_{a} = [M \, \delta \theta]_{x_{a}}^{x_{f}} + \int_{\alpha} \{-Q \, \delta u'_{n} - [T_{a}\theta' + s'(w_{a} \sin \theta + f_{Hn} - m_{P}a_{Pn} - m_{i}a_{Fn})] \, \delta u_{n}\} \, d\alpha$$

$$+ \int_{\alpha} \{T_{a}\delta v'_{n} + [Q\theta' - s'(-w_{a} \cos \theta + f_{Ht} - m_{P}a_{Pt} - m_{i}a_{Ft})] \delta v_{n}\} \, d\alpha = 0. \tag{80b}$$

Weak form 3: In Cartesian coordinates:

$$\delta \pi_{a} = [H \, \delta u + V \, \delta v + M \, \delta \theta]_{\alpha_{o}}^{\alpha_{i}} + \int_{\alpha} \{ [-H' - s'(f_{Hx} - m_{P}a_{Px} - m_{i}a_{Fx})] \, \delta u \} \, d\alpha$$

$$+ \int_{\alpha} \{ [-V' - s'(-w_{a} + f_{Hy} - m_{P}a_{Py} - m_{i}a_{Fy})] \, \delta v \} \, d\alpha = 0.$$
(81a)

In natural coordinates

$$\delta \pi_{a} = [T_{a} \delta v_{n} - Q \, \delta u_{n} + M \, \delta \theta]_{x_{a}}^{z_{t}}$$

$$+ \int_{x} \{ [Q' - T_{a} \theta' - s'(w_{a} \sin \theta + f_{Hn} - m_{P} a_{Pn} - m_{i} a_{Fn})] \, \delta u_{n} \} \, d\alpha$$

$$+ \int_{x} \{ [-T'_{a} - Q \theta' - s'(-w_{a} \cos \theta + f_{Ht} - m_{P} a_{Pt} - m_{i} a_{Ft})] \, \delta v_{n} \} \, d\alpha = 0.$$
(81b)

# 3.3.1. Governing equations by weak form 1

In view of Eqs. (79), the following conditions are necessary and sufficient for  $\delta \pi_a$  to vanish for all admissible functions of virtual displacements.

In Cartesian coordinates:

$$\delta \pi_{ax} = 0 : \int_{x} \left\{ \frac{B\kappa}{s'} \left( \frac{y'}{s'} \right) \delta u'' + \left[ (T_a - B\kappa^2) \left( \frac{x'}{s'} \right) - B\kappa \frac{s''}{s'^2} \left( \frac{y'}{s'} \right) \right] \delta u' - s' [f_{Hx} - m_P a_{Px} - m_i a_{Fx}] \delta u \right\} d\alpha = 0, \tag{82}$$

$$\delta \pi_{ay} = 0 : \int_{x} \left\{ -\frac{B\kappa}{s'} \left( \frac{x'}{s'} \right) \delta v'' + \left[ (T_a - B\kappa^2) \left( \frac{y'}{s'} \right) + B\kappa \frac{s''}{s'^2} \left( \frac{x'}{s'} \right) \right] \delta v' - s' [-w_a + f_{Hy} - m_P a_{Py} - m_i a_{Fy}] \delta v \right\} d\alpha = 0.$$

(83)

In natural coordinates:

$$\delta \pi_{an} = 0: \int_{\alpha} \left\{ \left[ \frac{B\kappa}{s'} \right] \delta u_n'' - \left[ B\kappa \frac{s''}{s'^2} \right] \delta u_n' + \left[ -T_a \theta' - s' (w_a \sin\theta + f_{Hn} - m_P a_{Pn} - m_i a_{Fn}) \right] \delta u_n \right\} d\alpha = 0, \tag{84}$$

$$\delta \pi_{at} = 0: \int_{\sigma} \left\{ \left[ T_a + B\kappa^2 \right] \delta v_n' + \left[ \frac{B\kappa}{s'} (\theta'' - \kappa s'') - s'(-w_a \cos \theta + f_{Ht} - m_P a_{Pt} - m_i a_{Ft}) \right] \delta v_n \right\} d\alpha = 0. \tag{85}$$

#### 3.3.2. Governing equations by weak form 2

Similarly, in view of Eqs. (80), the following conditions have to be valid.

In Cartesian coordinates:

$$\delta \pi_{\alpha x} = 0: \int_{\alpha} \{H \delta u' - s' [f_{Hx} - m_P a_{Px} - m_i a_{Fx}] \delta u\} d\alpha = 0, \tag{86}$$

$$\delta \pi_{ay} = 0: \int_{\alpha} \{ V \delta v' - s' [-w_a + f_{Hy} - m_P a_{Py} - m_l a_{Fy}] \, \delta v \} \, d\alpha = 0, \tag{87}$$

with the natural boundary condition of bending moment:

$$[M \delta \theta]_{\mathbf{x}_{i}}^{\mathbf{x}_{i}} = 0. \tag{88}$$

In natural coordinates:

$$\delta \pi_{ah} = 0 : \int_{z} \left\{ -Q \delta u'_{n} - \left[ T_{a} \theta' + s'(w_{a} \sin \theta + f_{Hn} - m_{P} a_{Pn} - m_{i} a_{Fn}) \right] \delta u_{n} \right\} d\alpha = 0, \tag{89}$$

$$\delta \pi_{ai} = 0: \int_{2} \{ T_{a} \delta v'_{n} + [Q\theta' - s'(-w_{a} \cos\theta + f_{Hi} - m_{P} a_{Pi} - m_{i} a_{Fi})] \, \delta v_{n} \} \, d\alpha = 0, \tag{90}$$

with the same boundary condition as Eq. (88).

#### 3.3.3. Governing equations by weak form 3

Likewise, the necessary and sufficient conditions of Eqs. (81) yield the weak form 3.

In Cartesian coordinates:

$$\delta \pi_{ax} = 0: \int_{a} \{ [-H' - s'(f_{Hx} - m_P a_{Px} - m_i a_{Fx})] \, \delta u \} \, d\alpha = 0, \tag{91}$$

$$\delta \pi_{ay} = 0: \int_{\tau} \{ [-V' - s'(-w_a + f_{Hy} - m_P a_{Py} - m_i a_{Fy})] \, \delta v \} \, d\alpha = 0, \tag{92}$$

with the natural boundary conditions of horizontal and vertical forces, and bending moment:

$$[H \delta u + V \delta v + M \delta \theta]_{x_i}^{x_i} = 0. \tag{93}$$

In natural coordinates:

$$\delta \pi_{an} = 0 : \int_{\alpha} \{ [Q' - T_a \theta' - s'(w_a \sin \theta + f_{Hn} - m_P a_{Pn} - m_i a_{Fn})] \, \delta u_n \} \, d\alpha = 0, \tag{94}$$

$$\delta \pi_{at} = 0: \int_{z} \left\{ \left[ -T'_{a} - Q\theta' - s'(-w_{a}\cos\theta + f_{Ht} - m_{P}a_{Pt} - m_{i}a_{Ft}) \right] \delta v_{n} \right\} d\alpha = 0, \tag{95}$$

with the natural boundary conditions of apparent tension, shear force, and bending moment:

$$[T_u \delta v_n - Q \delta u_n + M \delta \theta]_u^{\mathbf{z}_i} = 0. \tag{96}$$

It is important to make a decision which forms of governing equations should be used. In the governing equations by weak form 1, there is no natural boundary condition (BC). So if those equations are employed, all natural BCs may be unconstrained. Another choice is using the governing equations by weak form 2 such that all essential BCs and some natural BCs such as Eq. (88) would have to be constrained. On the other hand, if the governing equations by weak form 3 are selected, all essential BCs and all natural BCs such as Eqs. (93) and (96) need to be constrained.

#### 3.3.4. Strong formulations by weak form 3

By considering that all virtual displacements  $\delta u$ ,  $\delta v$ ,  $\delta u_n$  and  $\delta v_n$  in Eqs. (91), (92), (94) and (95) are nonzero, the following strong formulations are achieved:

(i) Force-based strong form. In Cartesian coordinates:

$$\Sigma F_{x} = 0: -H' - s'(f_{Hx} - m_{P}a_{Px} - m_{i}a_{Fx}) = 0, \tag{97}$$

$$\Sigma F_{v} = 0: -V' - s'(-w_{a} + f_{Hv} - m_{P}a_{Pv} - m_{i}a_{Fv}) = 0.$$
(98)

In natural coordinates:

$$\Sigma F_n = 0: Q' - T_a \theta' - s'(w_a \sin \theta + f_{Hn} - m_p a_{Pn} - m_i a_{Fn}) = 0, \tag{99}$$

$$\Sigma F_t = 0 : -T_a' - Q\theta' - s'(-w_a \cos \theta + f_{Ht} - m_P a_{Pt} - m_i a_{Ft}) = 0.$$
 (100)

If the right-hand sides of Eqs. (97)–(100) are considered as the residuals, one can demonstrate that based on the Galerkin method, Eqs. (91), (92), (94) and (95) yield the weighted residual forms of Eqs. (97)–(100), respectively. This fact indicates that the governing equations obtained from the weak variational method and the Galerkin residual method, are the same. As a result, if both methods used the same approximating functions, their solutions would be identical.

The vector expressions of Eqs. (97)-(100) are given by

$$-\mathbf{P}' - s'(-w_a\hat{\mathbf{j}} + \mathbf{f}_H - m_P \mathbf{a}_P - m_i \mathbf{a}_F) = 0, \tag{101}$$

where the internal force vectors P are represented by

$$\mathbf{P}'_{XY} = \begin{cases} H' \\ V' \end{cases} \quad \text{and} \quad \mathbf{P}'_{NT} = \begin{cases} T_a \theta' - Q' \\ T'_a + Q \theta' \end{cases} = \begin{bmatrix} y'/s' & -x'/s' \\ x'/s' & y'/s' \end{bmatrix} \begin{cases} H' \\ V' \end{cases}, \tag{102}$$

in Cartesian and natural coordinate systems, respectively.

(ii) Displacement-based strong form. Based on Eqs. (71a)-(71c), one can demonstrate that

$$H = \left[ (T_u - B\kappa^2) \frac{x'}{s'} - B\kappa \left( \frac{s''}{s'^2} \right) \left( \frac{y'}{s'} \right) \right] - \left[ \frac{B\kappa}{s'} \left( \frac{y'}{s'} \right) \right]', \tag{103a}$$

$$V = \left[ (T_a - B\kappa^2) \frac{y'}{s'} - B\kappa \left( \frac{s''}{s'^2} \right) \left( \frac{x'}{s'} \right) \right] + \left[ \frac{B\kappa}{s'} \left( \frac{x'}{s'} \right) \right]', \tag{103b}$$

consequently, one obtains

$$\mathbf{P}' = \left[ (T_a - B\kappa^2) \frac{\mathbf{r}_P'}{s'} - B \left( \frac{s''}{s'^3} \right) \frac{\partial}{\partial \alpha} \left( \frac{\mathbf{r}_P'}{s'} \right) \right]' - \left[ \frac{B}{s'^2} \frac{\partial}{\partial \alpha} \left( \frac{\mathbf{r}_P'}{s'} \right) \right]''. \tag{104}$$

Note that

$$\frac{\partial}{\partial \alpha} \left( \frac{\mathbf{r}'_P}{s'} \right) = \frac{\partial}{\partial \alpha} \left( \frac{x'}{s'} \right) \hat{\mathbf{i}} + \frac{\partial}{\partial \alpha} \left( \frac{y'}{s'} \right) \hat{\mathbf{j}} = (\kappa y') \hat{\mathbf{i}} + (-\kappa x') \hat{\mathbf{j}} = \hat{\mathbf{t}}' = \theta' \hat{\mathbf{n}}. \tag{105}$$

Utilizing Eqs. (53) and (104), Eq. (101) can be transformed into the displacement-based form:

$$s'(m_{P} + m_{i})\frac{\partial^{2}\mathbf{r}_{P}}{\partial t^{2}} + s'm_{i}\left(\frac{2V_{FP}}{s'}\right)\frac{\partial^{2}\mathbf{r}_{P}}{\partial\alpha\partial t} + \left[\frac{B}{s'^{2}}\frac{\partial}{\partial\alpha}\left(\frac{\mathbf{r}'_{P}}{s'}\right)\right]''$$

$$-\left[\left(T_{a} - B\kappa^{2}\right)\frac{\mathbf{r}'_{P}}{s'} - B\left(\frac{s''}{s'^{3}}\right)\frac{\partial}{\partial\alpha}\left(\frac{\mathbf{r}'_{P}}{s'}\right)\right]' + s'm_{i}\left(\frac{V_{FP}}{s'}\right)^{2}\frac{\partial^{2}\mathbf{r}_{P}}{\partial\alpha^{2}}$$

$$+ s'm_{i}\left[\frac{V_{FP}V'_{FP}}{s'^{2}} - \frac{V_{FP}s'}{s'^{2}} - \frac{V'_{FP}s''}{s'^{3}}\right]\frac{\partial\mathbf{r}_{P}}{\partial\alpha} = s'\mathbf{f}_{H} - s'w_{a}\hat{\mathbf{j}} - s'm_{i}\left[\frac{\dot{V}_{FP}}{s'}\right]\frac{\partial\mathbf{r}_{P}}{\partial\alpha}.$$
(106)

If  $\alpha = s$  is used and the internal flow effect is excluded, Eq. (106) is reduced to

$$m_P \ddot{\mathbf{r}}_P + (B\mathbf{r}_P'')'' - [(T_a - B\kappa^2)\mathbf{r}_P']' = \mathbf{f}_H - w_a \hat{\mathbf{j}}, \tag{107}$$

which is compatible with the vector equation of motion of slender rods given by Garrett (1982).

#### 4. Vectorial formulation

Based on the vectorial method, the fundamentals of large strain modelling proposed in Section 2 are employed to develop large strain formulations of extensible flexible marine pipes transporting fluid as follows.

- Step 1: Converting the real system of the pipe column into the apparent systems of the pipe and transported fluid by the apparent tension concept (Section 2.4).
  - Step 2: Using the Newtonian derivation for the apparent systems of the pipe and transported fluid.
- Step 3: Integrating the individual systems of the pipe and transported fluid into the overall apparent system, which is subjected to the apparent weight (Section 2.4), hydrodynamic forces exerted by external and internal flows (Section 2.5), and inertial forces of the pipe.
- Step 4: Applying the extensible elastica theory (Section 2.3) on the apparent system to obtain the constitutive equations.

#### 4.1. Step 2: Using the Newtonian derivation for the apparent systems

Consider Fig. 4(q). The apparent system of the transported fluid element with the length s' d $\alpha$  is subjected to (i) the internal pressure  $p_i$ ; (ii) the internal fluid weight  $m_i g$ ; (iii) the inertial forces  $m_i a_{Fn}$  and  $m_i a_{Fi}$ ; and (iv) the normal reaction  $f_m$  and the wall-shear friction  $\tau_w$ . Note again that  $\alpha$  could be any parameter used to define the elastic curve of the pipe, and ()' =  $\partial()/\partial \alpha$ . Applying Newton's second law in normal and tangential directions, one obtains

$$\sum F_n = 0 : f_{rn}s' = (p_i A_i)\theta' - (m_i g \sin \theta - m_i a_{Fn})s', \tag{108}$$

$$\sum F_{i} = 0, \ \tau_{w}s' = (p_{i}A_{i})' + (m_{i}g\cos\theta + m_{i}a_{Fi})s', \tag{109}$$

in which  $(s, \theta)$  are the coordinates of arc length and rotation. Similarly, for the apparent system of the pipe element as shown in Fig. 4(p), applying Newton's second law in normal and tangential directions yields

$$\sum F_n = 0: f_{rn}s' = -Q' + (T + T_{tri} + p_e A_e)\theta' + [f_{Hn} + (m_P - m_e)g\sin\theta - m_P a_{Pn}]s', \tag{110}$$

$$\sum F_t = 0 : \tau_w s' = Q\theta' + (T + T_{tri} + p_e A_e)' + [f_{Ht} - (m_P - m_e)g\cos\theta - m_P a_{Pt}]s', \tag{111}$$

$$\sum M_o = 0: M' = Qs', \tag{112}$$

where T, Q, and M are the true wall tension, shear, and bending moment, respectively,  $p_c$  the external pressure,  $f_{Hn}$  and  $f_{Hi}$  the hydrodynamic forces of external fluid given by Eq. (34),  $m_P g$  the pipe weight,  $-m_c g$  the buoyancy force,  $m_P a_{Pn}$  and  $m_P a_{Pi}$  the inertial forces of the pipe, and  $T_{Iri}$  the tension induced by triaxial pressures given by Eq. (22c).

# 4.2. Step 3: Integrating the individual systems of the pipe and transported fluid into the overall apparent system

The relationship between Eqs. (108) and (110), and Eqs. (109) and (111), respectively indicates that the interaction between the pipe and the transported fluid is such that physically the reaction  $f_{rn}$  and the friction  $\tau$  have the effects of:

- transmitting the effect of hydrostatic and hydrodynamic pressures of transported fluid represented by the right-hand side terms in Eqs. (108) and (109) into the pipe wall through the left-hand side terms in Eqs. (110) and (111), and
- conversely, transmitting the effect of resultant forces in pipe wall represented by the right-hand side terms in Eqs. (110) and (111) into transported fluid through the left-hand side terms in Eqs. (108) and (109).

The former effect induces deformation of the pipe, and the latter alters the characteristics of the internal flow of transported fluid as described by Proposition 1.

The interaction links together the individual systems of the pipe and transported fluid into the overall system. Using this fact, one substitutes Eq. (108) into Eq. (110), and Eq. (109) into Eq. (111) to obtain

$$\Sigma F_n = 0: \quad Q' - T_u \theta' - s'(w_u \sin \theta + f_{Hn} - m_P a_{Pn} - m_i a_{Fn}) = 0, \tag{113}$$

$$\Sigma F_t = 0: \quad -T_a' - Q\theta' - s'(-w_a \cos \theta + f_{Hi} - m_P a_{Pi} - m_i a_{Fi}) = 0, \tag{114}$$

where  $w_a$  and  $T_a$  are referred to as the apparent weight and the apparent tension, as given by Eqs. (28) and (29). The governing differential Eqs. (112)-(114) describe the nonlinear behaviour of the overall apparent system of the pipe.

Comparing Eqs. (113) and (114) with Eqs. (99) and (100), we can see that the vectorial method yields the same force-based strong formulation as that obtained from the virtual work method. Thus exact agreement between the virtual work and vectorial formulations is confirmed.

#### 4.3. Step 4: Applying the extensible elastica theory on the apparent system

On the apparent system, the axial force appears to be the apparent tension  $T_a$  rather than the true wall axial force N of the real system. Applying the extensible elastica theory on the apparent system therefore deals with replacing the axial force N in the constitutive Eqs. (17b), (18b) and (19b) by the apparent tension  $T_a$ . As a result, Eqs. (64) are obtained as the constitutive equations of the apparent system.

Based on the foregoing derivations along with the geometric relations, the governing equations for the vectorial formulation are summarized as follows:

(a) Geometric relations:

$$x'/s' = \sin \theta, \quad y'/s' = \cos \theta, \quad \kappa = \theta'/s' = (x''y' - x'y'')/s'^3.$$
 (115a-c)

(b) Constitutive equations:

$$T_a = E\tilde{A}_P \varepsilon, \quad M = B\kappa.$$
 (116a, b)

(c) Equilibrium equations:

$$M' = s'O, \tag{117}$$

$$O' = T_n \theta' + s' [f_{H_n} + w_n \sin \theta - (m_P a_{P_n} + m_i a_{F_n})], \tag{118}$$

$$T'_{a} = -Q\theta' - s'[f_{H_{I}} - w_{a}\cos\theta - (m_{P}a_{P_{I}} + m_{i}a_{F_{I}})].$$
 (119)

#### 5. Nonlinear dynamic, large amplitude vibration models

Based on the virtual work and the vectorial formulations, the governing equations describing nonlinear dynamics of the flexible marine pipe have been achieved in the three weak forms such as Eqs. (82)–(85), (86)–(90), and (91)–(96), and in the one strong form such as Eqs. (97)–(100), or Eqs. (101) and (106), or Eqs. (115)–(119). Hence, large amplitude vibration models of the pipe may be generated in four ways, namely from any of the three weak forms or the strong form. However, if the weak forms are employed, the intermediate procedure will require application of some approximate method such as the Rayleigh–Ritz method, the assumed-modes method, or the finite element method. A drawback is that these methods are applicable to self-adjoint systems alone. On the other hand, the models obtained via this approach are concerned with integral equations.

On the other hand, in the case where the strong form is exploited for creating the models, there is no need for any approximate method to be used during the process, and the obtained models deal with differential equations. This yields the possibility of using a broad range of numerical solution methods, including the weighted residuals methods, which are applicable to both self-adjoint and nonself-adjoint systems. For the sake of generality in obtaining the model solution, the strong form thus seems preferable to the weak forms. Derivation of the nonlinear dynamic models based on the strong form given by Eq. (106) is as follows.

# 5.1. Large amplitude vibration models in the Cartesian system

By utilizing Eqs. (54) and introducing the position vector in the Cartesian system

$$\mathbf{x} = \{x \mid y\}^{\mathsf{T}},\tag{120a}$$

one has the gyroscopic matrix

$$\mathbf{g} = \frac{m_i V_i}{s'^2} \begin{bmatrix} 2s'^2 - x'^2 & -x'y' \\ -x'y' & 2s'^2 - y'^2 \end{bmatrix},$$
 (120b)

the bending stiffness matrices

$$\mathbf{k}_{b1} = \frac{B}{s'^5} \begin{bmatrix} y'^2 & -x'y' \\ -x'y' & x'^2 \end{bmatrix}, \quad \mathbf{k}_{b2} = \frac{B\kappa}{s'^4} \begin{bmatrix} 2x'y' & y'^2 - x'^2 \\ y'^2 - x'^2 & -2x'y' \end{bmatrix}, \tag{120c, d}$$

and the axial stiffness matrices

$$\mathbf{k}_{i1} = \frac{(T_a - m_i V_i^2)}{s'^3} \begin{bmatrix} -y'^2 & x'y' \\ x'y' & -x'^2 \end{bmatrix}, \quad \mathbf{k}_{i2} = -\left(\frac{T_a' - m_i V_i V_i'}{s'}\right) \begin{bmatrix} 1 & 0 \\ 0 & 1 \end{bmatrix}, \tag{120e, f}$$

and one can express that

$$s'm_i\left[\left(\frac{V_{FP}}{s'}\right)^2\frac{\partial^2\mathbf{r}_P}{\partial\alpha^2} - \left(\frac{V_{FP}^2s''}{s'^3}\right)\frac{\partial\mathbf{r}_P}{\partial\alpha}\right] = m_iV_i^2\left(\frac{\mathbf{r}_P'}{s'}\right)',\tag{121a}$$

$$s'm_i \left[ \left( \frac{2V_{FP}}{s'} \right) \frac{\partial^2 \mathbf{r}_P}{\partial \alpha} - \left( \frac{V_{FP}\dot{s'}}{s'^2} \right) \frac{\partial \mathbf{r}_P}{\partial \alpha} \right] = \mathbf{g}\dot{\mathbf{x}}'$$
 (121b)

$$\frac{B}{s'^2} \frac{\partial}{\partial \alpha} \left( \frac{\mathbf{r}'_P}{s'} \right) = \mathbf{k}_{b1} \mathbf{x}'', \tag{121c}$$

$$(T_a - B\kappa^2) \frac{\mathbf{r}'_P}{s'} - B\left(\frac{s''}{s'^3}\right) \frac{\partial}{\partial \alpha} \left(\frac{\mathbf{r}'_P}{s'}\right) = T_a \frac{\mathbf{x}'}{s'} - \mathbf{k}_{b2} \mathbf{x}'', \tag{121d}$$

$$\left(T_a \frac{\mathbf{r}'_P}{s'}\right)' - m_i V_i^2 \left(\frac{\mathbf{r}'_P}{s'}\right)' = -\mathbf{k}_{i1} \mathbf{x}'' - \mathbf{k}_{i2} \mathbf{x}'. \tag{121e}$$

By substituting Eqs. (36) and (121) into Eq. (106) together with some manipulation, the nonlinear dynamic, large amplitude vibration model in the Cartesian system is obtained as

$$\mathbf{m}\ddot{\mathbf{x}} + \mathbf{c}\dot{\mathbf{x}} + \mathbf{g}\dot{\mathbf{x}}' + (\mathbf{k}_{b1}\mathbf{x}'')'' + (\mathbf{k}_{b2}\mathbf{x}'')' + \mathbf{k}_{d1}\mathbf{x}'' + \mathbf{k}_{d2}\mathbf{x}' = \mathbf{f},$$
(122)

where the total mass matrix is

$$\mathbf{m} = s'(m_P + m_i + C_a^*) \begin{bmatrix} 1 & 0 \\ 0 & 1 \end{bmatrix}, \tag{123a}$$

the hydrodynamic damping matrix is

$$\mathbf{c} = s' \begin{bmatrix} C_{eqx}^* & C_{eqxy}^* \\ C_{eqxy}^* & C_{eqy}^* \end{bmatrix}, \tag{123b}$$

and the external load vector is

$$\mathbf{f} = \begin{cases} f_x \\ f_y \end{cases} = s' \begin{cases} C_{Dx}^* V_{Hx}^2 + 2C_{Dxy1}^* V_{Hx} V_{Hy} + C_{Dxy2}^* V_{Hy}^2 + C_M^* \dot{V}_{Hx} - m_i \dot{V}_i x' / s' \\ C_{Dy}^* V_{Hy}^2 + 2C_{Dxy2}^* V_{Hx} V_{Hy} + C_{Dxy1}^* V_{Hx}^2 + C_M^* \dot{V}_{Hy} - w_a - m_i \dot{V}_i y' / s' \end{cases}.$$
(123c)

In Eq. (122), the effect of large axial strain and the Poisson's ratio effect contribute in all the coefficient matrices, especially to the terms of the combined tension  $T_a - m_i V_i^2$  and the tension gradient  $T'_a - m_i V_i V'_i$  in the axial stiffness matrices. It is also evident that the effect of transported fluid is

- to add the inertial force of transported mass into the total mass matrix,
- to provide the negative damping force in the gyroscopic matrix,
- · to reduce the internal tension and axial stiffness of the system in the axial stiffness matrices,
- to provide an excitation term in the external load vector.

5.2. Large amplitude vibration models in the natural system

Introducing the bending coefficients in the natural system

$$b_{1n} = \frac{B}{s'^3}, \quad b_{2n} = \frac{2B'}{s'^3} - \frac{3B}{s'^3} \left(\frac{s''}{s'}\right), \quad b_{3n} = \frac{B'}{s'^3} - \frac{B}{s'^3} \left(\frac{s''}{s'}\right), \tag{124a-c}$$

$$b_{4n} = \frac{B''}{s'^3} - \frac{3B'}{s'^3} \left(\frac{s''}{s'}\right) - \frac{B}{s'^3} \left(\frac{s'''}{s'}\right) + \frac{3B}{s'^3} \left(\frac{s''}{s'}\right)^2, \tag{124d}$$

one can express that

$$Q = \frac{(B\kappa)'}{s'} = \frac{1}{s'} \frac{\partial}{\partial \alpha} \left( B \frac{\theta'}{s'} \right) = b_{1n}(s'\theta'') + b_{3n}(s'\theta'), \tag{125}$$

$$Q' = \left[ \frac{(B\kappa)'}{s'} \right]' = b_{1n}(s'\theta''') + b_{2n}(s'\theta'') + b_{4n}(s'\theta'), \tag{126}$$

where the expressions for s' and  $\theta$  can be determined from the geometric relations

$$s'\sin(\theta - \theta_o) = u'_n + v_n\theta'_o, \quad s'\cos(\theta - \theta_o) = s'_o + v'_n - u_n\theta'_o, \tag{127a,b}$$

$$s'^{2} = (u'_{n} + v_{n}\theta'_{o})^{2} + (s'_{o} + v'_{n} - u_{n}\theta'_{o})^{2}, \quad \tan(\theta - \theta_{o}) = \frac{u'_{n} + v_{n}\theta'_{o}}{s'_{o} + v'_{n} - u_{n}\theta'_{o}}.$$
 (127c, d)

By substituting Eqs. (34), (58a), (60), (125), and (126) into Eq. (101) together with some manipulation, the large amplitude vibration model in the natural system is obtained as

$$\mathbf{m} \left\{ \begin{array}{c} \ddot{u}_{n} \\ \ddot{v}_{n} \end{array} \right\} + \mathbf{c}_{n} \left\{ \begin{array}{c} \dot{u}_{n} \\ \dot{v}_{n} \end{array} \right\} + \mathbf{g}_{n} \left\{ \begin{array}{c} s'\dot{\theta} \\ \dot{s}' \end{array} \right\} + \mathbf{k}_{b1n} \left\{ \begin{array}{c} s'\theta''' \\ s'\theta'\theta'' \end{array} \right\} + \mathbf{k}_{b2n} \left\{ \begin{array}{c} s'\theta'' \\ s'\theta'^{2} \end{array} \right\} + \mathbf{k}_{t1n} \left\{ \begin{array}{c} s'\theta' \\ 0 \end{array} \right\} + \mathbf{k}_{t2n} \left\{ \begin{array}{c} 0 \\ s' \end{array} \right\} = \mathbf{f}_{n}, \tag{128}$$

where the hydrodynamic damping matrix is

$$\mathbf{c}_n = s' \begin{bmatrix} C_{eqn}^* & 0\\ 0 & C_{eqt}^* \end{bmatrix},\tag{129a}$$

the gyroscopic matrix is

$$\mathbf{g}_n = m_i V_i \begin{bmatrix} 2 & 0 \\ 0 & 1 \end{bmatrix}, \tag{129b}$$

the bending stiffness matrices are

$$\mathbf{k}_{b1n} = \begin{bmatrix} b_{1n} & 0 \\ 0 & -b_{1n} \end{bmatrix}, \quad \mathbf{k}_{b2n} = \begin{bmatrix} b_{2n} & 0 \\ 0 & -b_{3n} \end{bmatrix}, \tag{129c, d}$$

the axial stiffness matrices are

$$\mathbf{k}_{l1n} = \begin{bmatrix} b_{4n} - \frac{(T_a - m_i V_i^2)}{s'} \end{bmatrix} \begin{bmatrix} 1 & 0 \\ 0 & 0 \end{bmatrix}, \quad \mathbf{k}_{l2n} = -\left(\frac{T_a' - m_i V_i V_i'}{s'}\right) \begin{bmatrix} 0 & 0 \\ 0 & 1 \end{bmatrix}, \tag{129e, f}$$

and the external load vector is

$$\mathbf{f}_{n} = \begin{cases} f_{n} \\ f_{t} \end{cases} = s' \begin{cases} C_{Dn}^{*} V_{Hn}^{2} + C_{M}^{*} \dot{V}_{Hn} + w_{a} \sin \theta \\ C_{Dt}^{*} V_{Ht}^{2} + C_{M}^{*} \dot{V}_{Ht} - w_{a} \cos \theta - m_{i} \dot{V}_{i} \end{cases}$$
(129g)

It is evident that in the natural coordinate system there is no coupling term in all the coefficient matrices. Note that for the lower order analysis, the following approximations by two-term binomial expansion may be used in Eq. (128):

$$s' \approx s'_o + v'_n - u_n \theta'_o$$
,  $\theta \approx \theta_o + (u'_n + v_n \theta'_o)/s'$ , (130a, b)

$$\dot{s}' \approx \dot{v}'_{n} - \dot{u}_{n}\theta'_{o}, \quad \dot{s}'\dot{\theta} \approx \dot{u}'_{n} + \dot{v}_{n}\theta'_{o}, \quad \dot{s}'\theta' \approx \dot{s}'_{o}\theta'_{o} + u''_{n} + 2v'_{n}\theta'_{o}, \tag{130c-e}$$

$$s'\theta'' \approx s_n'\theta_n'' + u_n''' + v_n''\theta_n', \quad s'\theta''' \approx s_n'\theta_n''' + u_n'''' + v_n'''\theta_n'. \tag{130f, g}$$

$$s'\theta'^2 \approx s_o'\theta'^2 + 2u_n''\theta_o', \quad s'\theta'\theta'' \approx s_o'\theta_o'\theta'' + u_n'''\theta_o'. \tag{130h, i}$$

#### 5.3. First-order models for large amplitude vibrations

Once Eqs. (36) and (56) are substituted into Eqs. (97) and (98), the second-order model of large amplitude vibrations of the pipe is established. To reduce the second-order system to the first-order system, the velocity expressions following Eqs. (131a)–(131c) are introduced. By adopting Eqs. (115)–(117) and (123c), the first-order model can be obtained as

$$\frac{\partial x}{\partial t} = V_{P_X},\tag{131a}$$

$$\frac{\partial y}{\partial t} = V_{Py},\tag{131b}$$

$$\frac{\partial \theta}{\partial t} = V_{P\theta},\tag{131c}$$

$$\frac{\partial x}{\partial \alpha} = s' \sin \theta, \tag{132a}$$

$$\frac{\partial y}{\partial \alpha} = s' \cos \theta,\tag{132b}$$

$$\frac{\partial \theta}{\partial \alpha} = s' \frac{M}{R},\tag{132c}$$

$$\frac{\partial M}{\partial \alpha} = s'(V\sin\theta - H\cos\theta),\tag{132d}$$

$$\frac{\partial H}{\partial \alpha} = s'(m_P + m_i + C_{\alpha}^*) \frac{\partial V_{Px}}{\partial t} + m_i V_i (2 - \sin^2 \theta) \frac{\partial V_{Px}}{\partial \alpha} - m_i V_i \sin \theta \cos \theta \frac{\partial V_{Py}}{\partial \alpha} + s' \left( C_{eqx}^* V_{Px} + C_{eqxy}^* V_{Py} + m_i V_i^2 \frac{M}{B} \cos \theta + \frac{m_i V_i V_i'}{s'} \sin \theta \right) - f_x, \tag{132e}$$

$$\frac{\partial V}{\partial \alpha} = s'(m_P + m_i + C_a^*) \frac{\partial V_{Py}}{\partial t} - m_i V_i \sin \theta \cos \theta \frac{\partial V_{Px}}{\partial \alpha} + m_i V_i (2 - \cos^2 \theta) \frac{\partial V_{Py}}{\partial \alpha} + s' \left( C_{eqxy}^* V_{Px} + C_{eqy}^* V_{Py} - m_i V_i^2 \frac{M}{B} \sin \theta + \frac{m_i V_i V_i'}{s'} \cos \theta \right) - f_y.$$
(132f)

If  $\alpha = s$  is used, and hydrodynamic effects due to external flow, and unsteady, nonuniform internal flow are excluded, Eqs. (132) become

$$\frac{\partial x}{\partial s} = \sin \theta,\tag{133a}$$

$$\frac{\partial y}{\partial s} = \cos \theta,\tag{133b}$$

$$\frac{\partial \theta}{\partial s} = \frac{M}{R},$$
 (133c)

$$\frac{\partial M}{\partial s} = V \sin \theta - H \cos \theta,\tag{133d}$$

$$\frac{\partial H}{\partial s} = (m_P + m_i) \frac{\partial V_{Px}}{\partial t} + 2m_i V_i V_{P\theta} \cos \theta + m_i V_i^2 \frac{M}{B} \cos \theta, \tag{133e}$$

$$\frac{\partial V}{\partial s} = (m_P + m_i) \frac{\partial V_{P_F}}{\partial t} - 2m_i V_i V_{P\theta} \sin \theta - m_i V_i^2 \frac{M}{B} \sin \theta + (m_P + m_i) g. \tag{133f}$$

Note that

$$\frac{\partial V_{Px}}{\partial t} = \frac{\partial^2 x}{\partial t^2}, \quad V_{P\theta} \cos \theta = \frac{\partial V_{Px}}{\partial s} = \frac{\partial^2 x}{\partial s \partial t}, \quad -V_{P\theta} \sin \theta = \frac{\partial V_{Py}}{\partial s} = \frac{\partial^2 y}{\partial s \partial t}, \tag{134a,b}$$

and

$$\frac{\partial V_{Py}}{\partial t} = \frac{\partial^2 y}{\partial t^2}, \quad \frac{M}{B} \cos \theta = \frac{\partial \theta}{\partial s} \frac{\partial y}{\partial s} = \frac{\partial^2 x}{\partial s^2}, \quad -\frac{M}{B} \sin \theta = -\frac{\partial \theta}{\partial s} \frac{\partial x}{\partial s} = \frac{\partial^2 y}{\partial s^2}. \tag{134c,d}$$

Eqs. (133) describe the nonlinear dynamics of an onshore pipe steadily conveying fluid (Atanackovic, 1997; Païdoussis, 1998).

#### 6. Nonlinear static equilibrium models

The static equilibrium models are derived by eliminating the time-dependent terms in the nonlinear dynamic equations. As a result, all parameters at the displaced state contained in the nonlinear dynamic equations will alter to the parameters at the equilibrium state for nonlinear static equilibrium models.

#### 6.1. Nonlinear static models in the Cartesian system

Eliminating the time-dependent terms in Eq. (122), and replacing the variables at the displaced state by those at the equilibrium state, one obtains the static equilibrium model as

$$(\mathbf{k}_{b1a}\mathbf{x}''_{o})'' + (\mathbf{k}_{b2a}\mathbf{x}''_{o})' + \mathbf{k}_{t1a}\mathbf{x}''_{o} + \mathbf{k}_{t2a}\mathbf{x}'_{o} = \mathbf{f}_{o}, \tag{135}$$

where the position vector is

$$\mathbf{x}_o = \left\{ x_0 \quad y_0 \right\}^\mathsf{T},\tag{136a}$$

the bending stiffness matrices are

$$\mathbf{k}_{b1o} = \frac{B_o}{s_o^{\prime 5}} \begin{bmatrix} y_o^{\prime 2} & -x_o^{\prime} y_o^{\prime} \\ -x_o^{\prime} y_o^{\prime} & x_o^{\prime 2} \end{bmatrix}, \quad \mathbf{k}_{b2} = \frac{B_o \kappa_o}{s_o^{\prime 4}} \begin{bmatrix} 2x_o^{\prime} y_o^{\prime} & y_o^{\prime 2} - x_o^{\prime 2} \\ y_o^{\prime 2} - x_o^{\prime 2} & -2x_o^{\prime} y_o^{\prime} \end{bmatrix},$$
(136b, c)

and the axial stiffness matrices are

$$\mathbf{k}_{t1o} = \frac{(T_{ao} - m_{io}V_{io}^2)}{s_o'^3} \begin{bmatrix} -y_o'^2 & x_o'y_o' \\ x_o'y_o' & -x_o'^2 \end{bmatrix}, \quad \mathbf{k}_{t2o} = -\left(\frac{T_{ao}' - m_{io}V_{io}V_{io}'}{s_o'}\right) \begin{bmatrix} 1 & 0 \\ 0 & 1 \end{bmatrix}, \tag{136d, e}$$

and the external load vector is

$$\mathbf{f}_{o} = \begin{cases} f_{xo} \\ f_{yo} \end{cases} = s'_{o} \begin{cases} C^{*}_{Dxo} V^{2}_{Hxo} + 2C^{*}_{Dxy1o} V_{Hxo} V_{Hyo} + C^{*}_{Dxy2o} V^{2}_{Hyo} \\ C^{*}_{Dyo} V^{2}_{Hyo} + 2C^{*}_{Dxy2o} V_{Hxo} V_{Hyo} + C^{*}_{Dxy1o} V^{2}_{Hxo} - w_{ao} \end{cases}.$$
(136f)

#### 6.2. Nonlinear static models in the natural system

Similarly, eliminating the time-dependent terms in Eq. (128) yields the static model

$$\mathbf{k}_{h1no} \begin{Bmatrix} s'_{o} \theta'''_{o} \\ s'_{o} \theta''_{o} \theta''_{o} \end{Bmatrix} + \mathbf{k}_{h2no} \begin{Bmatrix} s'_{o} \theta''_{o} \\ s'_{o} \theta'^{2}_{o} \end{Bmatrix} + \mathbf{k}_{t1no} \begin{Bmatrix} s'_{o} \theta''_{o} \\ 0 \end{Bmatrix} + \mathbf{k}_{t2no} \begin{Bmatrix} 0 \\ s'_{o} \end{Bmatrix} = \mathbf{f}_{no}, \tag{137}$$

where the bending stiffness matrices are

$$\mathbf{k}_{h1no} = \begin{bmatrix} b_{1no} & 0 \\ 0 & -b_{1no} \end{bmatrix}, \quad \mathbf{k}_{h2no} = \begin{bmatrix} b_{2no} & 0 \\ 0 & -b_{3no} \end{bmatrix}, \tag{138a,b}$$

in which the bending coefficients are

$$b_{1no} = \frac{B_o}{s_o^{\prime 3}}, \quad b_{2no} = \frac{2B_o'}{s_o^{\prime 3}} - \frac{3B_o}{s_o^{\prime 3}} \left(\frac{s_o''}{s_o'}\right), \quad b_{3no} = \frac{B_o'}{s_o^{\prime 3}} - \frac{B_o}{s_o^{\prime 3}} \left(\frac{s_o''}{s_o'}\right), \quad (139c-e)$$

$$b_{4no} = \frac{B_o''}{s_o'^3} - \frac{3B_o'}{s_o'^3} \left(\frac{s_o''}{s_o'}\right) - \frac{B_o}{s_o'^3} \left(\frac{s_o'''}{s_o'}\right) + \frac{3B_o}{s_o'^3} \left(\frac{s_o''}{s_o'}\right)^2, \tag{139f}$$

the axial stiffness matrices are

$$\mathbf{k}_{i1no} = \left[ b_{4no} - \frac{(T_{ao} - m_{io} V_{io}^2)}{s_o'} \right] \begin{bmatrix} 1 & 0 \\ 0 & 0 \end{bmatrix}, \quad \mathbf{k}_{i2no} = -\left( \frac{T_{ao}' - m_{io} V_{io} V_{io}'}{s_o'} \right) \begin{bmatrix} 0 & 0 \\ 0 & 1 \end{bmatrix}, \tag{139g, h}$$

and the external load vector is

$$\mathbf{f}_{no} = \begin{cases} f_{no} \\ f_{to} \end{cases} = s_o' \begin{cases} C_{Dno}^* V_{Hno}^2 + w_{oo} \sin \theta_o \\ C_{Dto}^* V_{Hto}^2 - w_{oo} \cos \theta_o \end{cases}. \tag{139i}$$

# 6.3. First-order models for nonlinear static equilibriums

Likewise, once the time-dependent terms in Eqs. (131) and (132) are eliminated, the system of the first-order differential equilibrium equations is obtained as

$$\frac{\mathrm{d}x_o}{\mathrm{d}\sigma} = s_o' \sin \theta_o,\tag{140a}$$

$$\frac{\mathrm{d}y_o}{\mathrm{d}x} = s_o' \cos \theta_o,\tag{140b}$$

$$\frac{\mathrm{d}\theta_o}{\mathrm{d}\alpha} = s_o' \frac{M_o}{B_o},\tag{140c}$$

$$\frac{\mathrm{d}M_o}{\mathrm{d}\alpha} = s_o'(V_o \sin \theta_o - H_o \cos \theta_o) = s_o'Q_o,\tag{140d}$$

$$\frac{\mathrm{d}H_o}{\mathrm{d}\alpha} = s_o' \left( m_{io} V_{io}^2 \frac{M_o}{B_o} \cos \theta_o + \frac{m_{io} V_{io} V_{io}'}{s_o'} \sin \theta_o \right) - f_{xo},\tag{140e}$$

$$\frac{\partial V_o}{\partial \alpha} = s_o' \left( -m_{io} V_{io}^2 \frac{M_o}{B_o} \sin \theta_o + \frac{m_{io} V_{io} V_{io}'}{s_o'} \cos \theta_o \right) - f_{yo}, \tag{140f}$$

$$\frac{\mathrm{d}Q_o}{\mathrm{d}\alpha} = (T_{ao} - m_{io}V_{io}^2)\frac{\mathrm{d}\theta_o}{\mathrm{d}\alpha} + f_{no},\tag{140g}$$

$$\frac{\mathrm{d}T_{oo}}{\mathrm{d}\alpha} = -Q_o \frac{\mathrm{d}\theta_o}{\mathrm{d}\alpha} + m_{io}V_{io} \frac{\mathrm{d}V_{io}}{\mathrm{d}\alpha} - f_{to}. \tag{140h}$$

The boundary-value problem of the system of the first-order ordinary differential equations (140) can be solved directly by numerical integrations. Application of the system of equations (140) to a nonlinear bucking analysis of extensible flexible marine pipes transporting fluid via the method of adjacent nonlinear equilibrium has been demonstrated by Chucheepsakul and Monprapussorn (2001).

# 7. Choices of the independent variable

One salient feature of the large strain formulations presented in this work is that the independent variable  $\alpha$  used in the formulations provides flexibility in the choice of parameters defining elastic curves. The formulations therefore allow users to select the independent variable that is most efficient for their own problem solution. For example, analysis of flexible marine pipes as shown in Fig. 1 has at least three alternatives for the independent variable  $\alpha$  such as the vertical coordinate y, the offset distance x, and the arc length s.

The advantage of using  $\alpha = y$  is that the total water depth or the boundary condition is known initially, while by using  $\alpha = x$  the boundary condition is known if the offset at the top end of the pipe can be assumed to be static, and is unknown if the offset is dynamic. If one uses  $\alpha = s$ , the boundary condition is always unknown, because the total arc

length changes after deformation. The problem for which the boundary condition is unknown becomes much more difficult, and requires specific treatment.

However, the disadvantage of using  $\alpha = y$  is that if elastic curves after large displacements form like the U-shape or the semi-U-shape as shown in Figs. 1(b) and (c), the vertical position is no longer a one-to-one function for all points on the elastic curves. Consequently,  $\alpha = y$  is not an effective choice in this case. Likewise, using  $\alpha = x$  encounters the same difficulty when the elastic curves after large displacements develop akin to the C-shape or the semi-C-shape. In these troublesome cases, using  $\alpha = s$  becomes the best way, because arc length is an intrinsic property, and thus is always a one-to-one function for all points of the elastic curves.

Therefore for flexible marine pipes which do not face the problem of elastic curves having a U-shape, such as the high-tensioned pipes as shown in Fig. 1(a), using  $\alpha = y$  is sufficient. However, if the pipes confront the problem that occurs in the case of low-tensioned pipes as shown in Figs. 1(b) and (c),  $\alpha = s$  should be employed. It should be noted that in addition to the three alternatives of  $\alpha$  as exemplified earlier, there are still other choices of  $\alpha$  such as the span length, the rotational angle, and so on, which may be employed if efficient.

#### 8. Extension to other applications

The present formulations are applicable to large strain analysis not only of flexible marine pipes, but also of any kind of elastica structures listed below.

- (a) Onshore pipes: The effect of external fluid would be excluded from the present models.
- (b) Submerged pipes: The hydrodynamic pressure effect of external fluid would be excluded.
- (c) Marine cables: Bending rigidity and influence of internal fluid would be excluded.
- (d) Submerged cables: Bending rigidity, influence of internal fluid, and hydrodynamic pressure effect of external fluid would be excluded from the present models.
- (e) Onshore cables and strings: Bending rigidity, and influences of internal and external fluids would be excluded from the present models.
- (f) Elastic rods, long columns, and long beams: Influences of external and internal fluids would be excluded from the present models.

Even though the present models are intended for elastica structures with environment-induced initial curvatures, the models can still be extended to elastica structures with man-made initial curvatures such as curved beams and arches by considering  $\vec{\kappa} \neq 0$  in application of the extensible elastica theory presented in this paper.

#### 9. Conclusions

A literature review has shown that the effects of axial deformation, internal flow, and Poisson's ratio effect can be significant in the behaviour of flexible marine pipes. To take account of the combined action of these effects in flexible marine pipe analysis, large strain formulations are needed. The essential mathematical principles for large strain modelling are developed in this paper. These include original developments of the apparent tension concept, and the extensible elastica theories from the viewpoints of total Lagrangian, updated Lagrangian, and Eulerian mechanics. Based on large strain elasticity and the apparent tension concept, it is shown that the Poisson's ratio effect influences the characteristics of internal flow, and induces the apparent tension rather than the effective tension. Therefore, the apparent tension should be used in large strain analysis for general Poisson's ratios.

Based on the proposed mathematical principles, the large strain formulations are developed by the virtual work method and the vectorial method in both Cartesian and natural coordinates. The virtual work method produces large strain models in the three weak forms of integral equations, and one strong form of differential equations, while the vectorial method yields the identical strong form. All the four forms of the models can be used for large strain analysis of the pipe, however, with different aspects of model solutions as summarized in Table 1. Relying upon the strong form, one can create large strain models of large amplitude vibrations and nonlinear static equilibrium of pipes. The advantages of the present models relate to the flexibility offered in choice of the independent variable, and the possibility of applying them to numerous elastica problems, including even some biomechanics applications such as veins conveying fluids inside the human body, and vessels rising water in the xylem of a plant.

Table 1 Alternatives of large strain modeling of flexible marine pipes

Large strain models by	Governing equations		Constraint of natural BCs	Solution methods
	Equations	Type		
Weak form 1	(82)–(85)		None	
Weak form 2	(86), (87), (89), (90)	Integral equations	Some	Limited to assumed mode methods
Weak form 3	(91), (92), (94), (95)		Ali	
Strong form	(97)–(100), or (101), (106), or (115)–(119)	Differential equations	Ali	Unlimited

#### Acknowledgements

The authors gratefully acknowledge the support of the Thailand Research Fund (TRF) under Contract No. RTA/03/2543.

#### Appendix A. Derivation of extensible elastica theory

Consider Fig. 2(b). Displacements and deformations of the pipe element from the undeformed state (state 1) to the equilibrium state (state 2), and then to the displaced state (state 3) result in changes of

- axial strain at the neutral axis  $\bar{\epsilon} \rightarrow \epsilon_o \rightarrow \epsilon$ ,
- bending moment  $\bar{M} \to M_o \to M$ ,
- radius of curvature r→r<sub>0</sub>→r,
- differential arc length ds→ds, →ds,
- differential rotation angle  $d\bar{\theta} \rightarrow d\theta_o \rightarrow d\theta$ .

Rotations of cross-section from state 1 to 2, from state 2 to 3, and from state 1 to 3 are denoted by  $d\phi_o = d\theta_o - d\bar{\theta}$ ,  $d\phi_d = d\theta - d\theta_o$ , and  $d\phi = d\theta - d\bar{\theta}$ , respectively.

In order to describe these changes, the three deformation descriptors previously defined in Section 2.1 are employed. Consequently, the extensible elastica theory can be developed by the total Lagrangian, the updated Lagrangian, and the Eulerian formulations as follows.

# A.I. Total Lagrangian formulation

The total Lagrangian formulation considers total changes from state 1 to 3 by neglecting the intermediate state 2. All changes are measured relative to the original state 1. The theoretical development starts by expressing the undeformed and deformed arc lengths of the fibre at any radius  $\varsigma$  as

$$d\bar{s}_{\zeta} = (\bar{r} + \zeta) d\bar{\theta}, \tag{A.1a}$$

$$ds_{\varsigma} = (r + \varsigma)(d\varphi + d\bar{\theta}) = r d\theta + \varsigma(d\varphi + d\bar{\theta}). \tag{A.1b}$$

Since  $d\tilde{\theta} = d\tilde{s}/\tilde{r}$  and  $d\theta = ds/r = (1 + \varepsilon) d\tilde{s}/r$ , Eqs. (A.1) may be written in the form

$$d\bar{s}_{\varsigma} = \left(1 + \frac{\varsigma}{r}\right) d\bar{s} = (1 + \varsigma \bar{\kappa}) d\bar{s}, \tag{A.2a}$$

$$ds_{\zeta} = (1+\varepsilon)d\tilde{s} + \zeta \left(d\varphi + \frac{d\bar{s}}{\tilde{r}}\right) = \left(1+\varepsilon + \zeta \frac{d\varphi}{d\bar{s}} + \zeta \bar{\kappa}\right)d\bar{s}, \tag{A.2b}$$

where  $\bar{\kappa} = 1/\bar{r}$  and  $\kappa = 1/r$  are the curvatures at the undeformed and the displaced states, and

$$\frac{d\varphi}{d\bar{s}} = \frac{d\theta}{ds}\frac{ds}{d\bar{s}} - \frac{d\bar{\theta}}{d\bar{s}} = \kappa(1+\varepsilon) - \bar{\kappa}.$$
 (A.3)

From Definition 4, the TL-strain of the fibre at any radius ç is defined by

$$\varepsilon_{\varsigma} = \frac{\mathrm{d}s_{\varsigma} - \mathrm{d}\bar{s}_{\varsigma}}{\mathrm{d}\bar{s}_{\varsigma}} = \frac{(\varepsilon + \varsigma(\mathrm{d}\varphi/\mathrm{d}\bar{s}))\,\mathrm{d}\bar{s}}{(1 + \varsigma\bar{\kappa})\,\mathrm{d}\bar{s}} = \frac{\varepsilon + \varsigma[\kappa(1 + \varepsilon) - \bar{\kappa}]}{1 + \varsigma\bar{\kappa}}.$$
(A.4)

The stress corresponding to the TL-strain  $\sigma_{\varphi} = E \varepsilon_{\varphi}$  is referred to as the Kirchhoff stress. The axial force and the bending moment due to the Kirchhoff stress can be expressed as

$$N = \int_{\tilde{A}_P} \sigma_{\zeta} \, d\bar{A}_P = E \int_{\tilde{A}_P} \left[ \frac{\varepsilon + \zeta [\kappa (1 + \varepsilon) - \bar{\kappa}]}{1 + \zeta \bar{\kappa}} \right] d\bar{A}_P, \tag{A.5a}$$

$$M = \int_{\bar{A}_P} \sigma_{\varsigma} \varsigma \, d\bar{A}_P = E \int_{\bar{A}_P} \left[ \frac{\varepsilon \varsigma + \varsigma^2 [\kappa (1 + \varepsilon) - \bar{\kappa}]}{1 + \varsigma \bar{\kappa}} \right] d\bar{A}_P, \tag{A.5b}$$

in which E is the elastic modulus and  $\bar{A}_P$  is the undeformed cross-sectional area of a pipe.

If the following geometrical properties of the cross-section

$$\tilde{A}_{P}^{*} = \int_{\tilde{A}_{P}} \frac{\mathrm{d}\tilde{A}_{P}}{1 + \varsigma \kappa'}, \quad \tilde{Q}_{P}^{*} = \int_{\tilde{A}_{P}} \frac{\varsigma \, \mathrm{d}\tilde{A}_{P}}{1 + \varsigma \kappa'}, \quad \vec{I}_{P}^{*} = \int_{\tilde{A}_{P}} \frac{\varsigma^{2} \, \mathrm{d}\tilde{A}_{P}}{1 + \varsigma \kappa'}. \tag{A.6a-c}$$

are defined, Eqs. (A.5) may be rewritten in the form

$$N = E\bar{A}_{P}^{\bullet}\varepsilon + E\bar{Q}_{P}^{\bullet}[\kappa(1+\varepsilon) - \bar{\kappa}], \quad M = E\bar{Q}_{P}^{\bullet}\varepsilon + E\bar{I}_{P}^{\bullet}[\kappa(1+\varepsilon) - \bar{\kappa}]. \tag{A.7a,b}$$

The TL-strain energy due to the TL-strain  $\varepsilon_{z}$  is measured with respect to the undeformed volume of the pipe  $\overline{V}_{P}$ . Therefore, its expression is given by

$$U = \int_{\tilde{\mathbb{Y}}_P} \frac{\sigma_{\tilde{\mathbf{y}}} \varepsilon_{\tilde{\mathbf{y}}}}{2} d\tilde{\mathbb{Y}}_P = \int_{\tilde{\mathbb{Y}}_P} \frac{\varepsilon_{\tilde{\mathbf{y}}}^2}{2} d\tilde{\mathbb{Y}}_P. \tag{A.8}$$

Taking the first variation of Eq. (A.8), one obtains

$$\delta U = \int_{\tilde{\mathbb{Y}}_P} E \varepsilon_{\tilde{\gamma}} \delta \varepsilon_{\tilde{\gamma}} \, d\tilde{\mathbb{Y}}_P = \int_{\tilde{S}} \int_{\tilde{A}_P} \sigma_{\tilde{\gamma}} \left[ \frac{\delta \varepsilon + \varsigma \delta [\kappa (1 + \varepsilon) - \tilde{\kappa}]}{1 + \varsigma \tilde{\kappa}} \right] \, d\tilde{A}_P \, d\tilde{s}. \tag{A.9}$$

For elastica problems,  $\zeta \vec{\kappa} = \zeta/\bar{r} \ll 1$ , thus  $1/(1+\zeta \bar{\kappa}) \approx 1$ . Consequently, Eqs. (A.6) yield  $\bar{A}_P^* \approx \bar{A}_P$ ,  $\bar{Q}_P^* \approx 0$ , and  $\bar{I}_P^* \approx \bar{I}_P$ . Substituting these conditions in Eqs. (A.4), (A.7), and (A.9), the constitutive equations of the extensible elastica theory can be obtained as

TL-axial strain:

$$\varepsilon_{\varsigma} = \varepsilon + \varsigma [\kappa (1 + \varepsilon) - \bar{\kappa}],$$
 (A.10)

TL-axial force:

$$N = E\bar{A}_{P}\varepsilon, \tag{A.11}$$

TL-bending moment:

$$M = E\bar{I}_{P}[\kappa(1+\varepsilon) - \bar{\kappa}], \tag{A.12}$$

TL-strain energy:

$$\delta U = \int_{\bar{s}} \{N\delta \varepsilon + M\delta [\kappa(1+\varepsilon) - \bar{\kappa}]\} \, d\bar{s} = \int_{\alpha} [N\delta s' + M\delta(\theta' - \bar{\theta}')] \, d\alpha \tag{A.13}$$

Note that

$$\delta\varepsilon = \delta\left(\frac{\mathrm{d}s - \mathrm{d}\bar{s}}{\mathrm{d}\bar{s}}\right) = \delta s'/\bar{s}', \quad \delta[\kappa(1+\varepsilon) - \bar{\kappa}] = \delta\left(\frac{\mathrm{d}\theta}{\mathrm{d}\bar{s}} - \frac{\mathrm{d}\bar{\theta}}{\mathrm{d}\bar{s}}\right) = \delta(\theta' - \bar{\theta}')/\bar{s}'.$$

#### A.2. Updated Lagrangian formulation

The updated Lagrangian formulation considers the two-step changes from state 1 to 2, and then from state 2 to 3. All changes are measured relative to the intermediate state 2. The development starts by expressing the three state are lengths of the fibre at any  $\varsigma$  as

$$d\bar{s}_{\varsigma} = (\bar{r} + \varsigma) d\bar{\theta} = \bar{r} d\bar{\theta} + \varsigma (d\theta_{o} - d\varphi_{o}), \tag{A.14a}$$

$$ds_{\theta} = (r_{\theta} + \varepsilon) d\theta_{\theta}, \tag{A.14b}$$

$$ds_{c} = (r + \varsigma)(d\varphi_{d} + d\theta_{n}) = r d\theta + \varsigma(d\varphi_{d} + d\theta_{n}). \tag{A.14c}$$

Since  $d\bar{\theta} = d\bar{s}/\bar{r} = (1 - \epsilon_o) ds_o/\bar{r}$ ,  $d\theta_o = ds_o/r_o$ , and  $d\theta = ds/r = (1 + \epsilon_d) ds_o/r$ , Eqs. (A.14) may be written in the form

$$d\bar{s}_{\varsigma} = (1 - \varepsilon_{o}) ds_{o} + \varsigma \left(\frac{ds_{o}}{r_{o}} - d\varphi_{o}\right) = \left(1 - \varepsilon_{o} + \varsigma \kappa_{o} - \varsigma \frac{d\varphi_{o}}{ds_{o}}\right) ds_{o}, \tag{A.15a}$$

$$ds_{o\varsigma} = \left(1 + \frac{\varsigma}{r_o}\right) ds_o = (1 + \varsigma \kappa_o) ds_o, \tag{A.15b}$$

$$ds_{\varsigma} = (1 + \varepsilon_d) ds_o + \varsigma \left( d\varphi_d + \frac{ds_o}{r_o} \right) = \left( 1 + \varepsilon_d + \varsigma \frac{d\varphi_d}{ds_o} + \varsigma \kappa_o \right) ds_o, \tag{A.15c}$$

where  $\bar{\kappa} = 1/\bar{r}$ ,  $\kappa_o = 1/r_o$ , and  $\kappa = 1/r$  are the curvatures at the three states, and

$$\frac{\mathrm{d}\varphi_o}{\mathrm{d}s_o} = \frac{\mathrm{d}\theta_o}{\mathrm{d}s_o} - \frac{\mathrm{d}\bar{\theta}}{\mathrm{d}\bar{s}} \frac{\mathrm{d}\bar{s}}{\mathrm{d}s_o} = \kappa_o - \bar{\kappa}(1 - \varepsilon_o),\tag{A.16a}$$

$$\frac{\mathrm{d}\varphi_d}{\mathrm{d}s_o} = \frac{\mathrm{d}\theta}{\mathrm{d}s} \frac{\mathrm{d}s}{\mathrm{d}s_o} - \frac{\mathrm{d}\theta_o}{\mathrm{d}s_o} = \kappa(1 + \varepsilon_d) - \kappa_o,\tag{A.16b}$$

$$\frac{\mathrm{d}\varphi}{\mathrm{d}s_o} = \frac{\mathrm{d}\varphi_o}{\mathrm{d}s_o} + \frac{\mathrm{d}\varphi_d}{\mathrm{d}s_o} = \kappa(1 + \varepsilon_d) - \bar{\kappa}(1 - \varepsilon_o). \tag{A.16c}$$

From Definition 4, the UL-strain of the fibre at any radius  $\varsigma$  is defined by

$$\varepsilon_{\varsigma} = \frac{\mathrm{d}s_{\varsigma} - \mathrm{d}\bar{s}_{\varsigma}}{\mathrm{d}s_{o\varsigma}} = \frac{\left[\varepsilon_{d} + \varepsilon_{o} + \varsigma(\mathrm{d}\varphi_{d}/\mathrm{d}s_{o} + \mathrm{d}\varphi_{o}/\mathrm{d}s_{o})\right]\mathrm{d}s_{o}}{\left(1 + \varsigma\kappa_{o}\right)\mathrm{d}s_{o}} = \frac{\varepsilon + \varsigma[\kappa(1 + \varepsilon_{d}) - \bar{\kappa}(1 - \varepsilon_{o})]}{1 + \varsigma\kappa_{o}}.$$
(A.17)

The stress corresponding to the UL-strain is referred to as the updated Kirchhoff stress. The axial force and the bending moment due to the updated Kirchhoff stress can be expressed as

$$N = \int_{A_{Po}} \sigma_{\varsigma} \, dA_{Po} = E \int_{A_{Po}} \left[ \frac{\varepsilon + \varsigma [\kappa (1 + \varepsilon_d) - \bar{\kappa} (1 - \varepsilon_o)]}{1 + \varsigma \kappa_o} \right] dA_{Po}, \tag{A.18a}$$

$$M = \int_{A_{Po}} \sigma_{\varsigma} \varsigma \, dA_{Po} = E \int_{A_{Po}} \left[ \frac{\varepsilon \varsigma + \varsigma^2 [\kappa (1 + \varepsilon_d) - \bar{\kappa} (1 - \varepsilon_o)]}{1 + \varsigma \kappa_o} \right] dA_{Po}, \tag{A.18b}$$

in which  $A_{Pa}$  is the deformed cross-sectional area of the pipe at the equilibrium state.

If the following geometrical properties of the cross-section

$$A_{Po}^* = \int_{A_{Po}} \frac{\mathrm{d}A_{Po}}{1 + \varsigma \kappa_o}, \quad Q_{Po}^* = \int_{A_{Po}} \frac{\varsigma \, \mathrm{d}A_{Po}}{1 + \varsigma \kappa_o}, \quad I_{Po}^* = \int_{A_{Po}} \frac{\varsigma^2 \, \mathrm{d}A_{Po}}{1 + \varsigma \kappa_o}. \tag{A.19a-c}$$

are defined, Eqs. (A.18) may be rewritten in the form

$$N = EA_{Po}^* \varepsilon + EQ_{Po}^* [\kappa(1 + \varepsilon_d) - \bar{\kappa}(1 - \varepsilon_o)], \tag{A.20a}$$

$$M = EQ_{Po}^{\bullet} \varepsilon + EI_{Po}^{\bullet} [\kappa(1 + \varepsilon_d) - \bar{\kappa}(1 - \varepsilon_o)]. \tag{A.20b}$$

The UL-strain energy due to the UL-strain  $\varepsilon_{\tau}$  is measured based on the deformed volume at the equilibrium state of the pipe  $\forall_{Po}$ . Thus, it can be expressed as

$$U = \int_{\forall p_o} \frac{\sigma_{\varsigma} \varepsilon_{\varsigma}}{2} \, d \forall_{P_o} = \int_{\forall p_o} \frac{\varepsilon_{\varsigma}^2}{2} \, d \forall_{P_o}. \tag{A.21}$$

Taking the first variation of Eq. (A.21), one obtains

$$\delta U = \int_{\forall p_o} E \varepsilon_{\varsigma} \delta \varepsilon_{\varsigma} \, d\forall p_o = \int_{s_o} \int_{A_{P_o}} \sigma_{\varsigma} \left[ \frac{\delta \varepsilon + \varsigma \delta [\kappa (1 + \varepsilon_d) - \bar{\kappa} (1 - \varepsilon_o)]}{1 + \varsigma \kappa_o} \right] dA_{P_o} \, ds_o. \tag{A.22}$$

For elastica problems,  $\varsigma \kappa_o = \varsigma/r_o \leqslant 1$ , so  $1/(1+\varsigma \kappa_o) \approx 1$ . Consequently, Eqs. (A.19) produce  $A_{Po}^* \approx A_{Po}$ ,  $Q_{Po}^* \approx 0$ , and  $I_{Po}^* \approx I_{Po}$ . Using these conditions in Eqs. (A.17), (A.20), and (A.22), the constitutive equations of the extensible elastica theory can be obtained as

UL-axial strain:

$$\varepsilon_{\varsigma} = \varepsilon + \varsigma [\kappa (1 + \varepsilon_d) - \bar{\kappa} (1 - \varepsilon_o)], \tag{A.23}$$

UL-axial force:

$$N = EA_{Po}\varepsilon, \tag{A.24}$$

UL-bending moment:

$$M = EI_{Po}[\kappa(1 + \varepsilon_d) - \bar{\kappa}(1 - \varepsilon_o)], \tag{A.25}$$

UL-strain energy:

$$\delta U = \int_{\bar{s}} \{ N \delta \varepsilon + M \delta [\kappa (1 + \varepsilon_d) - \bar{\kappa} (1 - \varepsilon_o)] \} ds_o$$

$$= \int_{\bar{s}} [N \delta s' + M \delta (\theta' - \bar{\theta}')] d\alpha. \tag{A.26}$$

Note that

$$\delta \varepsilon = \delta \left( \frac{\mathrm{d}s - \mathrm{d}\bar{s}}{\mathrm{d}s_o} \right) = \delta s'/s'_o, \quad \delta [\kappa (1 + \varepsilon_d) - \bar{\kappa} (1 - \varepsilon_o)] = \delta \left( \frac{\mathrm{d}\theta}{\mathrm{d}s_o} - \frac{\mathrm{d}\bar{\theta}}{\mathrm{d}s_o} \right) = \delta (\theta' - \bar{\theta}')/s'_o.$$

#### A.3. Eulerian Formulation

The Eulerian formulation considers total changes from state 1 to 3 by neglecting the intermediate state 2. All changes are measured relative to the final state 3. The development starts by expressing the undeformed and deformed arc lengths of the fibre at any radius  $\varsigma$  as

$$d\bar{s}_{\varsigma} = (\bar{r} + \varsigma) d\bar{\theta} = \bar{r} d\bar{\theta} + \varsigma (d\theta - d\varphi), \tag{A.27a}$$

$$ds_{\zeta} = (r + \zeta) d\theta. \tag{A.27b}$$

Since  $d\bar{\theta} = (1 - \varepsilon) ds/\bar{r}$  and  $d\theta = ds/r$ , Eq. (A.27) may be written in the form

$$d\bar{s}_{\varsigma} = (1 - \varepsilon) ds + \varsigma \left(\frac{ds}{r} - d\varphi\right) = \left(1 - \varepsilon + \varsigma \kappa - \frac{d\varphi}{ds}\right) ds, \tag{A.28a}$$

$$ds_{z} = (1 + \varsigma \kappa) ds, \tag{A.28b}$$

where  $\bar{\kappa} = 1/\bar{r}$  and  $\kappa = 1/r$  are the curvatures at the undeformed and the displaced states, and

$$\frac{\mathrm{d}\varphi}{\mathrm{d}s} = \frac{\mathrm{d}\theta}{\mathrm{d}s} - \frac{\mathrm{d}\bar{\theta}}{\mathrm{d}\bar{s}}\frac{\mathrm{d}\bar{s}}{\mathrm{d}s} = \kappa - \bar{\kappa}(1-\varepsilon). \tag{A.29}$$

From Definition 4, the EL-strain of the fibre at any radius  $\varsigma$  is defined by

$$\varepsilon_{\varsigma} = \frac{\mathrm{d}s_{\varsigma} - \mathrm{d}\bar{s}_{\varsigma}}{\mathrm{d}s_{\varsigma}} = \frac{(\varepsilon + \varsigma(\mathrm{d}\varphi/\mathrm{d}s))\,\mathrm{d}s}{(1 + \varsigma\kappa)\,\mathrm{d}s} = \frac{\varepsilon + \varsigma[\kappa - \bar{\kappa}(1 - \varepsilon)]}{1 + \varsigma\kappa}.\tag{A.30}$$

The stress corresponding to the EL-strain is referred to as the Cauchy stress. The axial force and bending moment due to the Cauchy stress can be expressed as

$$N = \int_{A_P} \sigma_{\varsigma} \, \mathrm{d}A_P = E \int_{A_P} \left[ \frac{\varepsilon + \varsigma [\kappa - \bar{\kappa} (1 - \varepsilon)]}{1 + \varsigma \kappa} \right] \, \mathrm{d}A_P, \tag{A.31a}$$

$$M = \int_{A_P} \sigma_{\zeta} \zeta \, dA_P = E \int_{A_P} \left[ \frac{\varepsilon \zeta + \zeta^2 [\kappa - \bar{\kappa} (1 - \varepsilon)]}{1 + \zeta \kappa} \right] dA_P, \tag{A.31b}$$

in which  $A_P$  is the deformed cross-sectional area of the pipe at the displaced state.

If the following geometrical properties of the cross-section

$$A_P^* = \int_{A_P} \frac{\mathrm{d}A_P}{1 + \varsigma \kappa},\tag{A.32a}$$

$$Q_P^* = \int_{A_P} \frac{\varsigma \, \mathrm{d}A_P}{1 + \varsigma \kappa},\tag{A.32b}$$

$$I_P^* = \int_{A_0} \frac{\varsigma^2 \, \mathrm{d}A_P}{1 + \varsigma \kappa}.$$
 (A.32c)

are defined, Eqs. (A.31) may be rewritten in the form

$$N = EA_P^* \varepsilon + EQ_P^* [\kappa - \bar{\kappa}(1 - \varepsilon)], \tag{A.33a}$$

$$M = EQ_p^* \varepsilon + EI_p^* [\kappa - \bar{\kappa}(1 - \varepsilon)]. \tag{A.33b}$$

The EL-strain energy due to the EL-strain  $\varepsilon_{\varsigma}$  is measured with respect to the deformed volume at the displaced state of the pipe  $\forall_{P}$ . Thus, its expression is given by

$$U = \int_{\forall_P} \frac{\sigma_{\varsigma} \varepsilon_{\varsigma}}{2} \, d\forall_P = \int_{\forall_P} \frac{\varepsilon_{\varsigma}^2}{2} \, d\forall_P. \tag{A.34}$$

Taking the first variation of Eq. (A.34), one obtains

$$\delta U = \int_{\forall_P} E \varepsilon_{\varsigma} \delta \varepsilon_{\varsigma} \, d\forall_P = \int_{s} \int_{A_P} \sigma_{\varsigma} \left[ \frac{\delta \varepsilon + \varsigma \delta [\kappa - \vec{\kappa} (1 - \varepsilon)]}{1 + \varsigma \kappa} \right] dA_P \, ds. \tag{A.35}$$

For elastica problems,  $\zeta \kappa = \zeta/r \ll 1$ , thus  $1/(1+\zeta\kappa) \approx 1$ . As a result, Eqs. (A.32) yield  $A_P^* \approx A_P$ ,  $Q_P^* \approx 0$ , and  $I_P^* \approx I_P$ . Substituting these conditions in Eqs. (A.30), (A.33), and (A.35), the constitutive equations of the extensible elastical theory are obtained as

EL-axial strain:

$$\varepsilon_{\varepsilon} = \varepsilon + \varsigma[\kappa - \bar{\kappa}(1 - \varepsilon)],$$
 (A.36)

EL-axial force:

$$N = EA_{PE}. (A.37)$$

EL-bending moment:

$$M = EI_P[\kappa - \bar{\kappa}(1 - \varepsilon)], \tag{A.38}$$

EL-strain energy:

$$\delta U = \int \{N\delta\varepsilon + M\delta[\kappa - \bar{\kappa}(1-\varepsilon)]\} ds = \int [N\delta s' + M\delta(\theta' - \bar{\theta}')] d\alpha. \tag{A.39}$$

Note that

$$\delta \varepsilon = \delta \left( \frac{\mathrm{d} s - \mathrm{d} \bar{s}}{\mathrm{d} s} \right) \approx \delta s' / s', \quad \delta [\kappa - \bar{\kappa} (1 - \varepsilon)] = \delta \left( \frac{\mathrm{d} \theta}{\mathrm{d} s} - \frac{\mathrm{d} \bar{\theta}}{\mathrm{d} s} \right) \approx \delta (\theta' - \bar{\theta}') / s'.$$

# References

Atanackovic, T.M., 1997. Stability Theory of Elastic Rods. World Scientific, Singapore.

Bernitsas, M.M., Kokarakis, J.E., 1988. Importance of nonlinearities in static riser analysis. Applied Ocean Research 10, 2-9.

Bernitsas, M.M., Kokarakis, J.E., Imron, A., 1985. Large deformation three-dimensional static analysis of deep water marine risers. Applied Ocean Research 7, 178-187.

Burgess, J.J., Triantafyllou, M.S., 1988. The elastic frequencies of cables. Journal of Sound and Vibration 120, 153-165.

Chakrabarti, S.K., 1990. Nonlinear Methods in Offshore Engineering. Elsevier, Amsterdam.

Chakrabarti, S.K., Frampton, R.E., 1982. Review of riser analysis techniques. Applied Ocean Research 4, 73-90.

Chucheepsakul, S., Huang, T., 1994. Influence of transported mass on the equilibrium configuration of risers. Proceedings of the Fourth International Offshore and Polar Engineering Conference (ISOPE), Vol. 2, pp. 246-249.

Chucheepsakul, S., Huang, T., 1997. Effect of axial deformation on natural frequencies of marine cables. Proceedings of the Seventh International Offshore and Polar Engineering Conference (ISOPE), Vol. 2, pp. 131-136.

Chucheepsakul, S., Monprapussorn, T., 2001. Nonlinear buckling of marine elastica pipes transporting fluid. International Journal of Structural Stability and Dynamics 1, 333-365.

Chucheepsakul, S., Huang, T., Laohaporjanat, P., 1995. Effects of axial deformation on the equilibrium configurations of marine cables. Proceedings of the Fifth International Offshore and Polar Engineering Conference (ISOPE), Vol. 2, pp. 244-248.

Chucheepsakul, S., Huang, T., Monprapussorn, T., 1999. Influence of transported fluid on behaviour of an extensible flexible riser/pipe. Proceedings of the Ninth International Offshore and Polar Engineering Conference (ISOPE), Vol. 2, pp. 286-293.

Chung, J.S., Cheng, B.-R.. 1996. Effects of elastic joints on 3-D nonlinear responses of a deep-ocean pipe; modeling and boundary conditions. International Journal of Offshore and Polar Engineering 6, 203-211.

Chung, J.S., Whitney, A.K., 1983. Dynamic vertical stretching oscillation of a deep-ocean mining pipe. ASME Journal of Energy Resources Technology 105, 195-200.

Chung, J.S., Cheng, B.-R., Huttelmaier, H.-P., 1994. Three-dimensional coupled responses of a vertical deep-ocean pipe: Part I. Excitation at pipe ends and external torsion. International Journal of Offshore and Polar Engineering 4, 320-330.

Doll, R.W., Mote, C.D., 1976. On the dynamic analysis of curved and twisted cylinders transporting fluids. ASME Journal of Pressure Vessel Technology 98, 143-150.

Ertas, A., Kozik, T.J., 1987. A review of current approaches to riser modeling. ASME Journal of Energy Resources Technology 109, 155-160.

Fung, Y.C., 1994. A First Course in Continuum Mechanics. Prentice-Hall, Englewood Cliffs, NJ.

Garrett, D.L., 1982. Dynamic analysis of slender rods. ASME Journal of Energy Resources Technology 104, 302-306.

Goodman, T.R., Breslin, J.P., 1976. Static and dynamics of anchoring cable in waves. Journal of Hydronautics 10, 113-120.

Gregory, R.W., Païdoussis, M.P., 1966. Unstable oscillation of tubular cantilevers conveying fluid. I. Theory. Proceedings of the Royal Society (London) A 293, 512-537.

Holmes, P.J., 1978. Pipes supported at both ends cannot flutter. ASME Journal of Applied Mechanics 45, 619-622.

Housner, G.W., 1952. Bending vibrations of a pipe line containing flowing fluid. ASME Journal of Applied Mechanics 19, 205-208. Huang, T., 1992. A static equilibrium formulation including axial deformation for marine cables. Proceedings of the Second International Offshore and Polar Engineering Conference (ISOPE), Vol. 2, pp. 252-255.

Huang, T., 1993. Kinematics of transported mass inside risers and pipes. Proceedings of the Third International Offshore and Polar Engineering Conference (ISOPE), Vol. 2, pp. 331-336.

Huddleston, J.V., 1981. Computer analysis of extensible cables. ASCE Journal of Engineering Mechanics Division 107, 27-37.

Irani, M.B., Modi, V.J., Weit, F., 1987. Risers dynamics with internal flows and nutation damping. Proceedings of Sixth International Offshore Mechanics and Arctic Engineering Symposium, Vol. 3. ASME, Houston, pp. 119-125.

Jain, A.K., 1994. Review of flexible risers and articulated storage systems. Ocean Engineering 21, 733-750.

Lin, H.P., Perkins, N.C., 1995. Free vibration of complex cable/mass system: theory and experiment. Journal of Sound and Vibration 179, 131-149.

Moe, G., Chucheepsakul, S., 1988 The effect of internal flow on marine risers. Proceedings of the Seventh International Offshore Mechanics and Arctic Engineering Symposium, Vol. 1. ASME, Houston, pp. 375-382.

Munson, B.R., Young, D.F., Okiishi, T.H., 1994. Fundamentals of Fluid Mechanics. Wiley, Toronto.

Païdoussis, M.P., 1970. Dynamics of tubular cantilevers conveying fluid. Journal of Mechanical Engineering Science 12, 85-103.

Païdoussis, M.P., 1998. Fluid-Structure Interactions: Slender Structures and Axial Flow, Vol. 1. Academic Press, New York.

Patel, H.M., Seyed, F.B., 1989. Internal flow-induced behaviour of flexible risers. Engineering Structures 11, 266-280.

Patel, H.M., Seyed, F.B., 1995. Review of flexible riser modeling and analysis techniques. Engineering Structures 17, 293-304.

Shames, I.H., 1992. Mechanics of Fluids. McGraw-Hill, Singapore.

Shih, B., Tadjbakhsh, I.G., 1984. Small-amplitude vibrations of extensible cables. ASCE Journal of Engineering Mechanics 110, 569-576.

Sparks, C.P., 1984. The influence of tension, pressure and weight on pipe and riser deformations and stresses. ASME Journal of Energy Resources Technology 106, 46-54.

Thompson, J.M.T., Lunn, T.S., 1981. Static elastica formulations of a pipe conveying fluid. Journal of Sound and Vibration 77, 127-132

Timoshenko, S.P., Goodier, J.N., 1984. Theory of Elasticity. McGraw-Hill, Singapore.

Tjavaras, A.A., Triantafyllou, M.S., 1996. Shock waves in curved synthetic cables. ASCE Journal of Engineering Mechanics 122, 308-315.

Tjavaras, A.A., Zhu, Q., Liu, Y., Triantafyllou, M.S., 1998. The mechanics of highly extensible cables. Journal of Sound and Vibration 213, 709-737.

Triantafyllou, M.S., Yue, D.K.P., 1994. Damping amplification in highly extensible hysteretic cables. Journal of Sound and Vibration 186, 355-368.

Wu, M.C., Lou, J.Y.K., 1991. Effects of rigidity and internal flow on marine riser dynamics. Applied Ocean Research 13, 235-244.



# WWW.MATHEMATICSWEB.ORG



Applied Mathematical Modelling 27 (2003) 781-803

www.elsevier.com/locate/apm

# A variational approach for three-dimensional model of extensible marine cables with specified top tension

Somchai Chucheepsakul \*, Narakorn Srinil, Pisek Petchpeart

Department of Civil Engineering, King Mongkut's University of Technology Thonburi, Bangmod, Toongkru, Bangkok 10140, Thailand

Received 8 May 2001; received in revised form 2 January 2003; accepted 13 February 2003

#### **Abstract**

This paper presents a variational model formulation that can be used for analyzing the three-dimensional steady-state behavior of an extensible marine cable. The virtual work-energy functional, which involves virtual strain energy due to a cable stretching, and virtual works done by the gravitational, inertial and external drag forces, is formulated. Euler-Lagrange's equations, obtained by considering the first variation of the functional, are identical to those obtained by equilibrating forces on a cable infinitesimal segment. Two mathematical simulations, namely, the finite element method and the shooting-optimization technique, are employed to solve and evaluate the problems. The numerical investigations are carried out for the case of a specified end tension, whereas the specified cable unstrained length case can be applied in the algorithm procedure. The validity of the present model and the influence of various geometrical parameters on the cable equilibrium configuration are demonstrated. The effects of cable extensibility and the omnidirectionality of current actions are presented and discussed.

© 2003 Elsevier Inc. All rights reserved.

Keywords: Mathematical simulation; Variational approach; Three-dimensional marine cable model; Extensible marine cables; Finite element method; Shooting-optimization method

# 1. Introduction

With the increases in deployment of cables in deep-ocean engineering, the determination of cable configurations as well as cable tensile forces has become the important parameters in the design process. As far as the hydrodynamic drag forces are concerned, the performance of marine

0307-904X/\$ - see front matter © 2003 Elsevier Inc. All rights reserved. doi:10.1016/S0307-904X(03)00089-1

<sup>\*</sup>Corresponding author. Tel.: +662-470-9146; fax: +662-427-9063. E-mail address: somchai.chu@kmutt.ac.th (S. Chucheepsakul).

cables must be considered in three-dimensional space. Hence, to accomplish a fundamental understanding of cable behaviors, accurate three-dimensional modelling of cable should be fully accounted for in the analysis.

The research work by De Zoysa [1] on the three-dimensional steady-state analysis of under cable towing a sea buggy was recognized by a number of researchers in the past. In that paper the static equilibrium equations of the problem are solved by using a shooting method. The obtained results showed the variations of tension components at the buggy end with respect to different directions made by the currents. Chucheepsakul and Subwonglee [2] solved the same problem using a variational approach. Wang et al. [3] used the shooting-optimization technique to yield more accuracy of the results. Friswell [4] corrected the hydrodynamic force model used by Wang et al. [3] and suggested approximate guidelines on choosing optimum cable length in the operating systems, in addition to the cable profile and tensile force developments. All of the aforementioned studies, however, do not take into consideration the effect of axial extensibility, which is essential for determining the cable configuration. This restriction may not yield an accurate analysis, especially in the case of cables having high extensibility.

Recently, a various of mathematical models of extensible cables has been considered by many researchers. A brief review of their work should be mentioned herein. Webster [5] presented the finite element approach to simulate the non-linear effects under hydrodynamic actions. Huyse et al. [6] modified the riser model to a three-dimensional tensioned string and used the cylindrical coordinates to obtain the admissible configuration. Drever and Van Vuuren [7] derived the numerical solutions of both continuous and discrete models through the concept of inextensible cable (elastic modulus is assumed to be large). Vassalos [8] provided detailed information on explaining the appropriate models in the design of marine structure. However, the essential parameters associated with the static behavior have not been tackled rigorously in their study [5-8]. Vaz and Patel [9] were particularly interested in investigating the cable configuration during installation in sheared current field. They demonstrated the importance of current profile for predicting of suspended line behaviors, especially when imposing a more complex three-dimensional current profile. Nevertheless, the influence of cable extensibility has not yet been thoroughly investigated. Thus, it is the main objective of this study to examine the geometrical parameters for any cable equilibrium configuration by including the extensibility effect under the omnidirectionality of the current actions. The important factors in the preliminary design stage include the cable tension distribution, elongation and geometric relations, such as cable unstrained or strained arc-length, vertical and horizontal angles of any point along a cable.

In the present paper numerical computations based on the finite element approach are used. The numerical technique presented in this study is computationally efficient to carry out for the solution in which the top tension is specified. However, the technique is not limited to the solution in which the total arc-length of cable is specified. A more detail description of this technique for two-dimensional case can be found in Chucheepsakul et al. [10]. As an alternative check, the shooting method is also used to validate the numerical solutions obtained from the variational approach.

The following assumptions are made throughout this analysis:

(1) A cable is installed with two stationary supports at the bottom and top end positions. Each end is held by the pinned support.

- (2) The effect of bending, shear and torsional rigidities is neglected.
- (3) The material of cable is assumed to be linearly elastic and the material density per unit volume remains invariant during stretching.

Numerical results are demonstrated tabularly and graphically for two case studies, namely, the practical cases of specified top tension and specified cable unstrained arc-length.

# 2. Cable model and governing equations

A typical cable model in its relationship to a fixed Cartesian reference frame called the global coordinate system is represented in Fig. 1a, which also shows the rotated system, i.e., the local coordinate system. This system is useful since it allows a simplified expression of the equations. The geometric compatibility relation of both systems can be expressed as the following matrix notation,

in which unit vectors  $\vec{i}$ ,  $\vec{j}$ ,  $\vec{k}$  and  $\vec{p}$ ,  $\vec{q}$ ,  $\vec{r}$  represent for the sets of global and local coordinate systems, respectively. The cable orientation at any point is defined by  $\phi$  and  $\theta$ , where  $\phi$  is the vertical angle between the XY plane and vector  $\vec{p}$ ,  $\theta$  is the horizontal angle between the XZ plane and projection line of vector  $\vec{p}$ , when vector  $\vec{q}$  lies on the XY plane. The bottom end of the cable is anchored at the seabed, while the top end is tied to the floating structure. With regard to Fig. 1b, it can be seen the circular plan view of the cable configuration, in which  $\theta_0$  is the horizontal angle between X-axis and the projection line of cable chord length on XY plane, R is the distance along the seabed between the top and bottom ends.

The current velocity is a function of depth only and is given by  $\vec{V} = v_x(z_0)\vec{i} + v_y(z_0)\vec{j}$ . In terms of the local coordinate system, the current profile is taken as  $\vec{V} = p_s\vec{p} + q_s\vec{q} + r_s\vec{r}$ , namely

$$p_s = v_x(z_0)\cos\phi\cos\theta + v_y(z_0)\cos\phi\sin\theta \tag{2a}$$

$$q_s = -v_x(z_0)\sin\theta + v_v(z_0)\cos\theta \tag{2b}$$

$$r_s = -v_x(z_0)\sin\phi\cos\theta - v_y(z_0)\sin\phi\sin\theta \tag{2c}$$

For stationary cable, the drag force is given by  $D_F = D_p \vec{p} + D_q \vec{q} + D_r \vec{r}$ , in which  $D_p$ ,  $D_q$  and  $D_r$  are the components of drag force along the direction of vectors  $\vec{p}$ ,  $\vec{q}$  and  $\vec{r}$ , respectively. Simple time-independent hydrodynamic loading models are chosen here, where the tangential and normal forces are proportional to the square of tangential and normal fluid velocities. Thus,  $D_F$  becomes

$$D_F = C_{\rm T} p_s |p_s| \vec{p} + C_{\rm N} (q_s \cdot \vec{q} + r_s \cdot \vec{r}) \sqrt{q_s^2 + r_s^2}$$
(3)

$$C_{\rm T} = \frac{1}{2} \rho_{\rm w} D \pi C_{\rm DT} (1 - \nu \varepsilon_0) \quad \text{and} \quad C_{\rm N} = \frac{1}{2} \rho_{\rm w} D C_{\rm DN} (1 - \nu \varepsilon_0) \tag{4a,b}$$

in which  $\rho_{\rm w}$  is the density of seawater,  $C_{\rm DT}$  and  $C_{\rm DN}$  are the tangential and normal drag coefficients,  $D(1 - \nu \varepsilon_0)$  is the deformed cable diameter, and  $\nu$  is the Poisson's ratio.

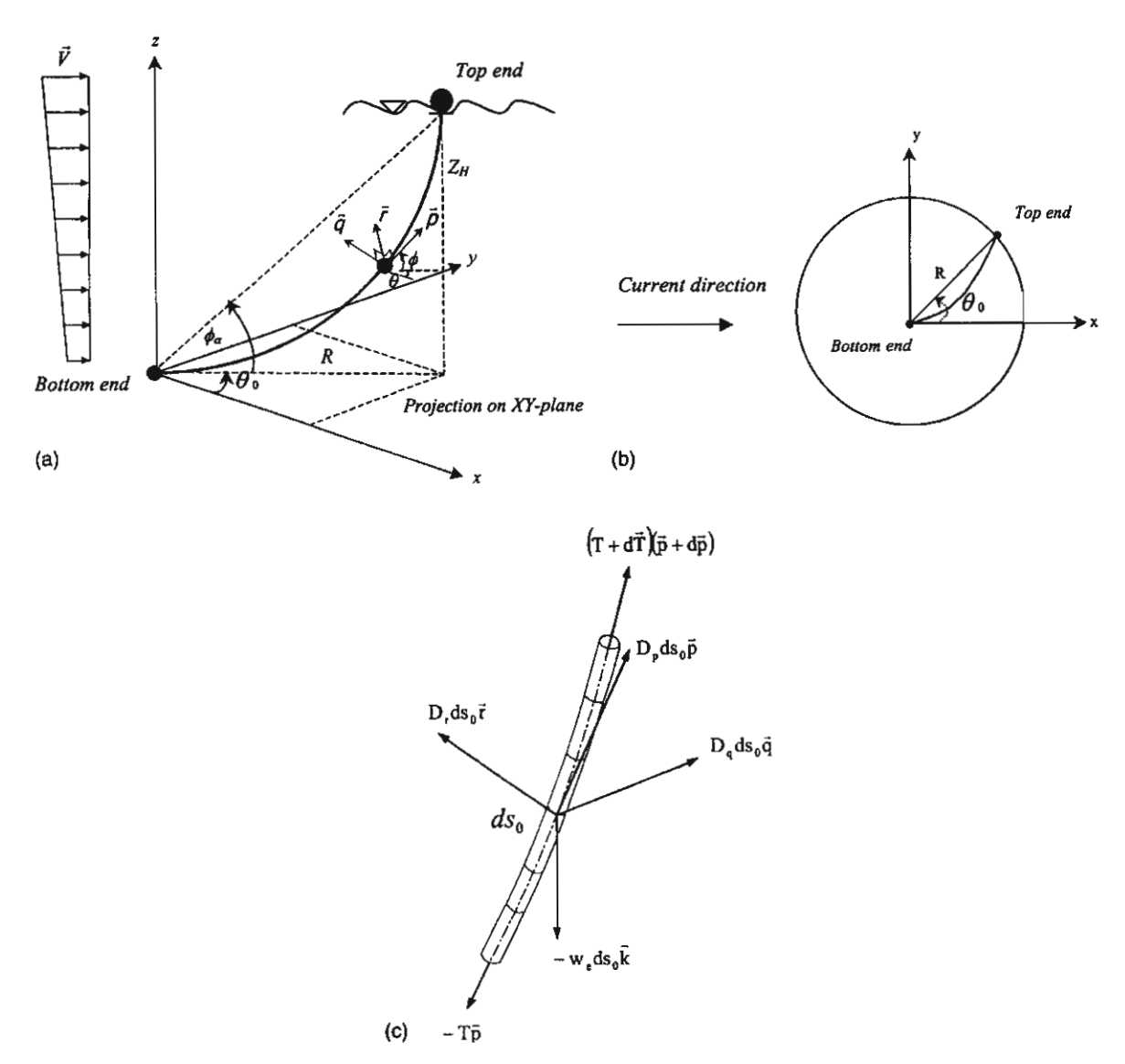


Fig. 1. (a) Reference configuration and coordinate systems of marine cables. (b) Circular plan view of cable model. (c) Forces on cable infinitesimal segment.

Referring to Fig. 1c, the equilibrium equations for an infinitesimal element of an immersed cable as given by Berteaux [11] can be written along the direction of  $\vec{p}$ ,  $\vec{q}$ ,  $\vec{r}$  as

$$\frac{dT}{ds_0} = \frac{w_e \sin \phi}{(1 + \varepsilon_0)} - D_p$$

$$\frac{d\theta}{ds_0} = -\frac{D_q}{T \cos \phi}$$

$$\frac{d\phi}{ds_0} = \left(\frac{w_e \cos \phi}{(1 + \varepsilon_0)} - D_r\right) / T$$
(5a,b,c)

where T is the cable effective tension and not the actual tension that controls the extensibility of the cable. The effective tension [12] is written as

$$T = EA\varepsilon_0 + 2\nu\rho_{\rm w}gA(1 - \nu\varepsilon_0)^2(Z_{\rm H} - z_0)$$
(6)

#### 3. Variational formulation

Fig. 2 shows an infinitesimal element of cable in which u, v and w are the components of displacement from the equilibrium position in the direction of unit vectors  $\vec{i}$ ,  $\vec{j}$ ,  $\vec{k}$ , respectively. The derivatives of its length  $ds_0$  in each direction are

$$dx_0 = \cos\phi\cos\theta ds_0$$
,  $dy_0 = \cos\phi\sin\theta ds_0$  and  $dz_0 = \sin\phi ds_0$  (7a,b,c)

Differentiation of Eq. (7) with respect to  $z_0$  (1), the cable stretched length is

$$ds_0 = \sqrt{1 + x_0'^2 + y_0'^2} dz_0 \tag{8}$$

Let  $\sqrt{1+x_0'^2+y_0'^2}$  be  $s_0'$ . Another form of  $ds_0$  using the Lagrangian strain definition is

$$ds_0 = (1 + \varepsilon_0) ds \tag{9a}$$

Thus,

$$ds = \frac{s_0'}{1 + \varepsilon_0} dz_0 \tag{9b}$$

in which ds is the unstretched cable length. Likewise, the arc-length  $d\bar{s}$ , the strain  $\bar{\epsilon}$  and the displacements u, v and w at the displaced state are given by

$$d\bar{s} = \sqrt{(x'_0 + u')^2 + (y'_0 + v')^2 + (1 + w')^2} dz_0$$
(10a)

$$d\bar{s} = (1 + \bar{\epsilon}) ds \tag{10b}$$

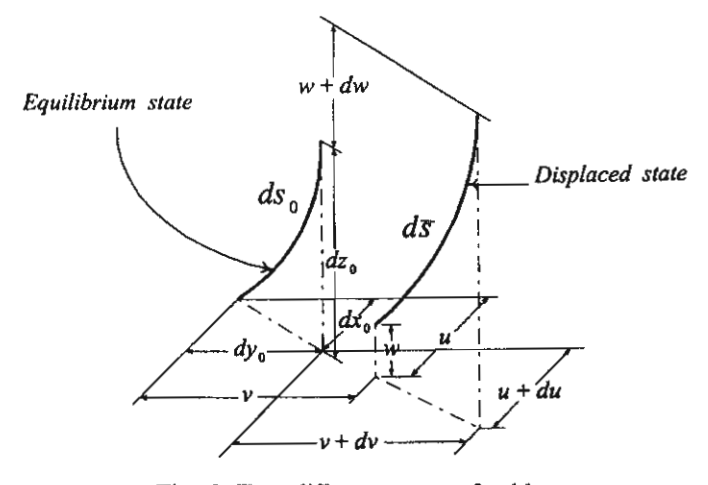


Fig. 2. Two different states of cables.

From Eqs. (8)–(10), one can write the dynamic strain as

$$\bar{\varepsilon} = \frac{d\bar{s} - ds}{ds} = \frac{1 + \varepsilon_0}{s_0'} \sqrt{(x_0' + u')^2 + (y_0' + v')^2 + (1 + w')^2} - 1$$
(11)

and its variation can be written as

$$\delta\bar{\varepsilon} = \frac{1 + \varepsilon_0}{s_0'} \left[ \frac{(x_0' + u')\delta u' + (y_0' + v')\delta v' + (1 + w')\delta w'}{\sqrt{(x_0' + u')^2 + (y_0' + v')^2 + (1 + w')^2}} \right]$$
(12)

#### 3.1. Strain energy due to axial deformation

The strain energy due to axial deformation is caused by two actions, namely, pulling on the cable due to tension and the squeezing of the cable due to hydrostatic pressure, as proposed by Sparks [13]. The strain energy expression is written as

$$U = \int_0^{S_t} \frac{1}{2} E A \bar{\epsilon}^2 \, \mathrm{d}s + \int_0^{\bar{S}_t} 2\nu \rho_w g A_0 (Z_H - z_0) \, \mathrm{d}\bar{s}$$
 (13)

where  $S_t$  is the total undeformed arc-length,  $\bar{S}_t$  is the total deformed arc-length, E is Young's modulus, A and  $A_0$  is the undeformed and deformed cable cross-sectional areas respectively. Using Eqs. (9), (11) and (12), the variation of Eq. (13) becomes

$$\delta U = \int_0^{Z_{\rm H}} \left\{ \left[ T_{\rm a} + T_{\rm b} \left( 1 - \frac{1}{\sqrt{1 + 2\lambda}} \right) \right] \left[ \frac{(x'_0 + u')\delta u' + (y'_0 + v')\delta v' + (1 + w')\delta w'}{s'_0} \right] \right\} dz_0$$
 (14)

$$\lambda = \frac{x_0'u' + y_0'v' + w' + \frac{1}{2}(u'^2 + v'^2 + w'^2)}{s_0'^2}$$
(15)

in which  $T_a = EA\varepsilon_0 + 2v\rho_w gA_0(Z_H - z_0)$  and  $T_b = EA - 2v\rho_w gA_0(Z_H - z_0)$ , when  $Z_H$  is the total sea depth. It is seen that Eq. (6) and  $T_a$  are identical to the usual form of the cable effective tension. If Poisson's ratio v is set to be zero so that there is no reduction in cable diameter, then  $T_a$  is equal to the cable actual tension and axial strain is proportional to this tension [14]. By neglecting the small quantities of higher order terms, and using the binomial approximation, Eq. (15) reduces to

$$\lambda \cong \frac{x_0'u' + y_0'v' + w'}{s_0'^2} \quad \text{and} \quad \frac{1}{\sqrt{1+2\lambda}} \cong 1 - \lambda$$
 (16a,b)

Substituting Eq. (16) into Eq. (14) yields

$$\delta U = \int_{0}^{Z_{H}} \left[ \left[ \frac{T_{a}}{s'_{0}} (x'_{0} + u') + \frac{T_{b}}{s'_{0}^{3}} (x'_{0}^{2}u' + x'_{0}y'_{0}v' + x'_{0}w') \right] \delta u' \right.$$

$$+ \left[ \frac{T_{a}}{s'_{0}} (y'_{0} + v') + \frac{T_{b}}{s'_{0}^{3}} (x'_{0}y'_{0}u' + y'_{0}^{2}v' + y'_{0}w') \right] \delta v'$$

$$+ \left[ \frac{T_{a}}{s'_{0}} (1 + w') + \frac{T_{b}}{s'_{0}^{3}} (x'_{0}u' + y'_{0}v' + w') \right] \delta w' \right] dz_{0}$$

$$(17)$$

#### 3.2. Virtual work done by external forces

The virtual work done by effective weight of a submerged cable is expressed as

$$\delta W_{\rm e} = -\int_0^{Z_{\rm H}} \frac{w_{\rm e} s_0'}{1 + \varepsilon_0} \delta w \mathrm{d}z_0 \tag{18}$$

where  $w_e$  is the effective weight of the cable.

The virtual work done by hydrodynamic forces is written as

$$\delta W_{\rm H} = \int_0^{Z_{\rm H}} s_0' [(D_{pu} + D_{qu} + D_{ru}) \delta u + (D_{pv} + D_{qv} + D_{rv}) \delta v + (D_{pw} + D_{qw} + D_{rw}) \delta w] dz_0$$
 (19)

in which the subscripts u, v and w denote the forces per unit length components corresponding to the Cartesian system.

The virtual work done by inertia force is

$$\delta W_{i} = -\int_{0}^{Z_{H}} (\bar{m}\ddot{u}\,\delta u + \bar{m}\ddot{v}\,\delta v + \bar{m}\ddot{w}\,\delta w) dz_{0}$$
(20)

where  $\bar{m} = (w_C/g(1+\epsilon_0))s'_0$  is the cable mass per unit stretched length at the equilibrium state, and  $w_C$  is the cable weight per unit unstretched length.

#### 3.3. Euler's equations

The virtual work-energy of the marine cable system is written as

$$\delta \Pi = \delta U - \delta W_{\rm e} - \delta W_{\rm H} - \delta W_{\rm i} = 0 \tag{21}$$

Substitution of Eqs. (17)-(20) into Eq. (21), then integration by part of Eq. (21) is performed by evaluating  $\delta u = \delta v = \delta w = 0$  at boundary conditions, i.e.,  $z_0 = 0$  and  $z_0 = Z_H$ . Then, Euler's equations associated with the virtual displacement  $\delta u$ ,  $\delta v$  and  $\delta w$  are obtained respectively as

$$\left[ \frac{T_{a}}{s'_{0}} (x'_{0} + u') + \frac{T_{b}}{s'_{0}^{3}} (x'_{0}^{2}u' + x'_{0}y'_{0}v' + x'_{0}w') \right]' - \bar{m}\ddot{u} = -(D_{pu} + D_{qu} + D_{ru})s'_{0}$$
(22)

$$\left[ \frac{T_{a}}{s'_{0}} (y'_{0} + v') + \frac{T_{b}}{s'_{0}^{3}} (x'_{0} y'_{0} u' + y'_{0}^{2} v' + y'_{0} w') \right]' - \bar{m} \ddot{v} = -(D_{pv} + D_{qv} + D_{rv}) s'_{0}$$
(23)

$$\left[ \frac{T_{a}}{s'_{0}} (1 + w') + \frac{T_{b}}{s'_{0}^{3}} (x'_{0}u' + y'_{0}v' + w') \right]' - \bar{m}\ddot{w} = - \left[ D_{pw} + D_{qw} + D_{rw} - \frac{w_{e}}{1 + \varepsilon_{0}} \right] s'_{0}$$
 (24)

#### 3.4. Equilibrium equations

Applying the initial conditions  $u = v = w = u' = v' = w' = u'' = v'' = w'' = \ddot{u} = \ddot{v} = \ddot{w} = 0$  on Eqs. (22)–(24), the following equilibrium equations are obtained

$$\left(\frac{T_{\rm a}x_0'}{s_0'}\right)' + (D_{pu} + D_{qu} + D_{ru})s_0' = 0 \tag{25}$$

$$\left(\frac{T_{\rm a}y_0'}{s_0'}\right)' + (D_{pv} + D_{qv} + D_{rv})s_0' = 0 \tag{26}$$

$$\left(\frac{T_{a}}{s'_{0}}\right)' + \left(D_{pw} + D_{qw} + D_{rw} - \frac{w_{e}}{1 + \varepsilon_{0}}\right) s'_{0} = 0$$
 (27)

It is noted that when assembling these equations using vector relations yields the equilibrium equation, which is identical to Eq. (5).

#### 4. Mathematical simulations

Eqs. (25)–(27) are the system of non-linear differential equations, analytical solution to these equations are not be obtainable. Numerical solutions using the finite element method or the shooting-optimization may be used for practical problems. For the purposes of comparison and validation of the results, the two numerical methods are employed in this investigation. In the finite element procedure, the variational formulation given in Eqs. (17)–(21) is involved while in the shooting-optimization method the governing differential equation given in Eqs. (5) is used. In each method, either top tension or the cable unstrained arc-length may be either known a prior or may be determined.

## 4.1. Finite element method

For independent variable  $z_0$ , only the variation of horizontal displacement is considered,  $\delta w = \delta w' = 0$ . The reference of three-dimensional equilibrium configuration is determined by substitution of Eqs. (17)–(20) into Eq. (21) again, and then Eq. (21) is rearranged in the form of a hybrid formulation as follows

$$\delta \Pi = \delta \int_0^{z_H} \left[ T_a \sqrt{1 + (x_0' + u')^2 + (y_0' + v')^2} - F_u s_0' u - F_v s_0' v \right] dz_0 = 0$$
 (28)

in which  $F_u = D_{pu} + D_{qu} + D_{ru}$  and  $F_v = D_{pv} + D_{qv} + D_{rv}$ . At the displaced state,  $x = x_0 + u$ ,  $y = y_0 + v$ , hence  $x' = x'_0 + u'$ ,  $\delta x = \delta u$ ,  $\delta x' = \delta u'$ ,  $y' = y'_0 + v'$ ,  $\delta y = \delta v$  and  $\delta y' = \delta v'$ . At the equilibrium state,  $x = x_0$  and  $y = y_0$ , then Eq. (28) can be simplified to

$$\delta \Pi = \delta \int_0^{Z_{\rm H}} \left( T_{\rm a} \sqrt{1 + x_0^2 + y_0^2} - F_{\nu} s_0' x_0 - F_{\nu} s_0' y_0 \right) dz_0 = 0$$
 (29)

This formulation is suitable and efficient for a practical cable problem of which the top tension is specified, the total cable arc-length either unstrained or strained is to be determined. Three unknowns to be involved in the algorithm are  $x_0(z_0)$ ,  $y_0(z_0)$  and  $\varepsilon_0(z_0)$ . The relevant equilibrium equation corresponding to the tangential direction of a cable segment (5a), representing the cable tension at any point, is converted to the following integral expression

$$T_{\rm a}(z_0) = T_{\rm H} - \int_{z_0}^{z_{\rm H}} \left[ \frac{w_{\rm e}}{(1 + \varepsilon_0)} - D_p \sqrt{1 + x_0^{\prime 2} + y_0^{\prime 2}} \right] \mathrm{d}z_0 \tag{30}$$

in which  $T_{\rm H}$  is the specified tension at the top end. The combination of Eqs. (29) and (30) are used to solve for the cable static problem.

Since the vertical axis is chosen as an independent variable, the total water depth is discretized into number of regions or elements, each with an equal length h as depicted in Fig. 3. In the analysis, the horizontal projection of element coordinates  $x_0(z_0)$  and  $y_0(z_0)$  on XZ and YZ planes consist of two components which are linear and non-linear. The linear parts  $(x_L, y_L)$  are directly obtained from the prescribed positions of cable while the non-linear parts  $(x_{NL}, y_{NL})$  are approximated by a cubic polynomials shape function in  $z_0$ , thus

$$\begin{cases} x_{\text{NL}} \\ y_{\text{NL}} \end{cases} = [N]\{q\}$$
 (31)

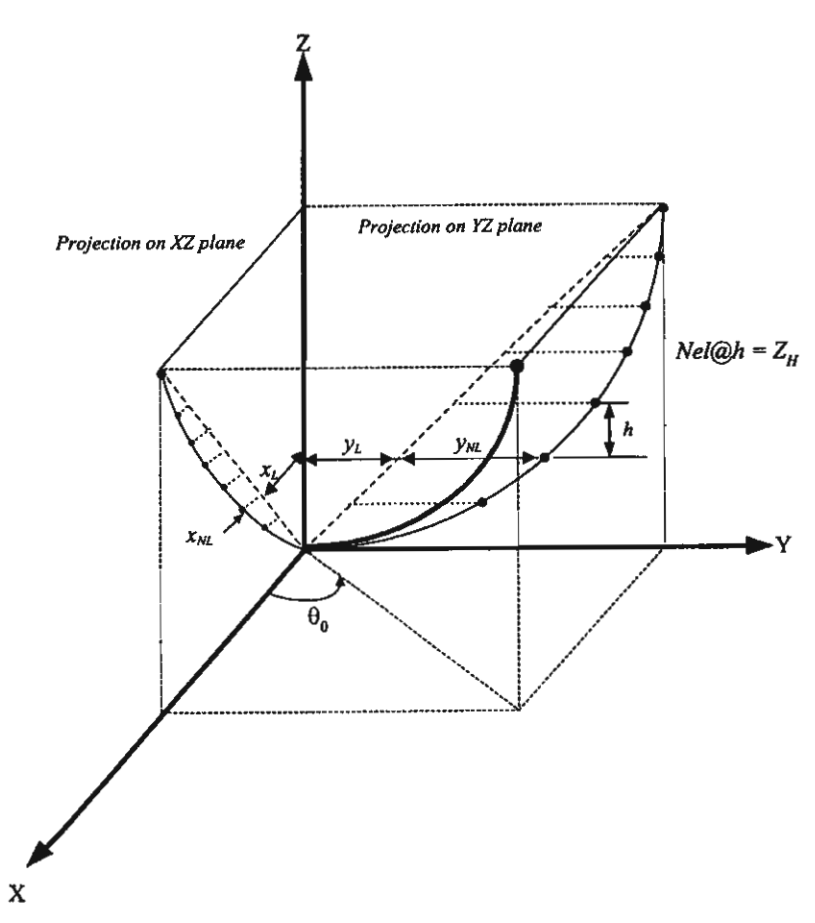


Fig. 3. Modelling for horizontal projection of the finite element coordinates on XZ and YZ planes.

where

$$[N] = \begin{bmatrix} N_1 & N_2 & 0 & 0 & N_3 & N_4 & 0 & 0 \\ 0 & 0 & N_1 & N_2 & 0 & 0 & N_3 & N_4 \end{bmatrix}$$
(32)

$$N_1 = 1 - 3(z_0^2/h^2) + 2(z_0^3/h^3), \quad N_2 = z_0 - 2(z_0^2/h) + (z_0^3/h^2)$$

$$N_3 = 3(z_0^2/h^2) - 2(z_0^3/h^3), \quad N_4 = -(z_0^2/h) + (z_0^3/h^2)$$
(33a-d)

$$\{q\} = |x_{NL}(0) \quad x'_{NL}(0) \quad y_{NL}(0) \quad y'_{NL}(0) \quad x_{NL}(h) \quad x'_{NL}(h) \quad y_{NL}(h) \quad y'_{NL}(h) \mid^{T}$$
(34)

in which [N] is the matrix of the shape function and  $\{q\}$  is the degree of freedom of nodal displacement and rotation. For the kinematic relations of strain, the matrix notations can be written as

$$\varepsilon_0 = \lfloor L \rfloor \{e\} \tag{35}$$

$$|L| = \lfloor 1 - z_0/h \quad z_0/h \, \rfloor \tag{36}$$

$$\{e\} = \begin{bmatrix} \varepsilon_0(0) & \varepsilon_0(h) \end{bmatrix}^{\mathrm{T}}$$
 (37)

where  $\lfloor L \rfloor$  is the matrix of the strain shape function and  $\{e\}$  is the nodal strain. The global equilibrium condition  $\delta \Pi = (\partial \pi/\partial q_i)\delta q_i = 0$  yields a system of non-linear equations. Consequently, by the Newton-Raphson iterative algorithm, one can write the incremental process as

$$[K]\{\Delta Q\} = -\{R\} \tag{38}$$

Consider the kth element, the contributions to the square matrix  $[K]_k$  and to the vector  $\{R\}_k$  are as follows,

$$[K]_{k} = \left\lceil \frac{\partial^{2} \pi_{k}}{\partial q_{i} \partial q_{j}} \right\rceil = \int_{0}^{h} \frac{[N']^{\mathsf{T}} T_{a}[N']}{(1 + x_{0}^{\prime 2} + y_{0}^{\prime 2})^{3/2}} dz_{0}$$
(39)

$$\{R\}_{k} = \left\{ \frac{\partial \pi_{k}}{\partial q_{i}} \right\} = \int_{0}^{h} \left[ \frac{[N']T_{a}}{(1 + x_{0}^{\prime 2} + y_{0}^{\prime 2})^{1/2}} \left\{ \frac{x_{0}'}{y_{0}'} \right\} - [N]^{T} \left\{ \frac{F_{u}}{F_{v}} \right\} \right] dz_{0}$$

$$(40)$$

in which h is an element height,  $\{Q\}$  and  $\{q\}$  are the global and local degrees of freedom, respectively. Eqs. (39) and (40) are evaluated by using Gaussian quadrature numerical integration with four points. The boundary conditions are the zero value of non-linear parts of coordinates at  $z_0 = 0$  and  $Z_H$ . The step-by-step iteration procedure can be comprehensively described as follows:

- The initial estimated value of global strain {Θ} and global degrees of freedom {Q} are assumed to be zero.
- The values of  $F_u$ ,  $F_v$  and  $T_a$  are calculated consecutively.
- After the components of  $[K]_k$  and  $\{R\}_k$  are numerically evaluated, all element matrices are assembled together to form the global systems.
- By applying boundary conditions, the solutions of  $\{\Delta Q\}$  are obtained using Eq. (38).
- The new value of nodal strain is updated by the Newton-Raphson process; that is,  $\varepsilon^{n+1} = \varepsilon^n f(\varepsilon^n)/f'(\varepsilon^n)$ , in which n = step of iteration,

$$f(\varepsilon_0^n) = EA\varepsilon_0^n + 2v\rho_{\rm w}gA(1 - v\varepsilon_0^n)^2(Z_{\rm H} - z_0) - T_{\rm H} + \int_{z_0}^{Z_{\rm H}} \left[ \frac{w_{\rm e}}{(1 + \varepsilon_0^n)} - D_p\sqrt{1 + x_0'^2 + y_0'^2} \right] dz_0$$

and  $f'(\varepsilon_0^n)$  is approximated using the forward difference formula; namely  $f'(\varepsilon_0^n) = (f(\varepsilon_0^n + \Delta) - f(\varepsilon_0^n))/\Delta$ . Since the spatial variation of the initial static strain of cable is very small compared to unity, the spatial step length used  $\Delta$  is assumed to be a constant and it is set to be equal to  $1 \times 10^{-8}$ .

- Then an incremental global strain  $\{\Delta\Theta\}$  is obtained.
- Adding an incremental global displacement  $\{\Delta Q\}$  to Q and repeating overall steps, the iterative procedures are terminated when  $\{\Delta Q\}$  and  $\{\Delta \Theta\}$  are negligible or the error tolerance is achieved.

#### 4.2. Shooting-optimization method

The following governing eight first-order differential equations, Eqs. (41)–(44), together with the eight known end conditions, Eq. (45) or (46), may be solved for T,  $\theta$ ,  $\phi$ ,  $x_0$ ,  $y_0$ ,  $s_0$ , s and  $\varepsilon_0$  as functions of  $z_0$ . Let  $\xi_i$ ,  $i=1,2,\ldots,8$  be the unknown parameters. In view of these governing equations and their associated initial conditions at the seabed,  $z_0=0$ , the preceding differential equations corresponding to the equilibrium of cable segment, Eq. (5), can be rearranged as follows

$$\frac{\mathrm{d}T}{\mathrm{d}z_0} = \left(\frac{w_e}{(1+\varepsilon_0)} - \frac{D_p}{\sin\phi}\right), \quad T(0) = \xi_1$$

$$\frac{\mathrm{d}\theta}{\mathrm{d}z_0} = \left(-\frac{D_q}{T\cos\phi\sin\phi}\right), \quad \theta(0) = \xi_2$$

$$\frac{\mathrm{d}\phi}{\mathrm{d}z_0} = \left(\frac{w_e\cos\phi}{(1+\varepsilon_0)} - D_r\right) / T\sin\phi, \quad \phi(0) = \xi_3$$
(41a,b,c)

Differentiation of Eq. (6) with respect to  $z_0$  gives

$$\frac{d\varepsilon_0}{dz_0} = \frac{dT/dz_0 + 2\nu\rho_w gA(1 - \nu\varepsilon_0)^2}{\{EA - 4\nu^2\rho_w gA(1 - \nu\varepsilon_0)(Z_H - z_0)\}}, \quad \varepsilon(0) = \xi_4$$
(42)

From the geometrical considerations, Eqs. (7a)–(7c) can be rewritten as

$$\frac{\mathrm{d}x_0}{\mathrm{d}z_0} = \left\langle \frac{\cos\phi\cos\theta}{\sin\phi} \right\rangle, \quad x_0(0) = 0$$

$$\frac{\mathrm{d}y_0}{\mathrm{d}z_0} = \left\langle \frac{\cos\phi\sin\theta}{\sin\phi} \right\rangle, \quad y_0(0) = 0$$

$$\frac{\mathrm{d}s_0}{\mathrm{d}z_0} = \left\langle \frac{1}{\sin\phi} \right\rangle, \quad s_0(0) = 0$$
(43a,b,c)

Finally, from the strain definition, Eq. (9a) can also be rewritten as

$$\frac{\mathrm{d}s}{\mathrm{d}z_0} = \left(\frac{1}{\sin\phi(1+\varepsilon_0)}\right), \quad s(0) = 0 \tag{44}$$

The terminal boundary conditions depend on whether the top tension force or the unstrained cable length is specified, namely, for the case of specified top tension,

$$\theta(z_{\rm H}) = \zeta_5, \quad \phi(z_{\rm H}) = \zeta_6, \quad s_0(z_{\rm H}) = \zeta_7, \quad s(z_{\rm H}) = \zeta_8$$

$$T(z_{\rm H}) = T_{\rm H}, \quad x_0(z_{\rm H}) = R\cos\theta_0, \quad y_0(z_{\rm H}) = R\sin\theta_0, \quad \varepsilon_0(z_{\rm H}) = \frac{T_{\rm H}}{EA}$$
(45a-h)

for the case of specified cable unstrained length,

$$\theta(z_{\rm H}) = \zeta_5, \quad \phi(z_{\rm H}) = \zeta_6, \quad s_0(z_{\rm H}) = \zeta_7, \quad s(z_{\rm H}) = S_L$$

$$T(z_{\rm H}) = \zeta_8, \quad x_0(z_{\rm H}) = R\cos\theta_0, \quad y_0(z_{\rm H}) = R\sin\theta_0, \quad \varepsilon_0(z_{\rm H}) = \frac{\zeta_8}{EA}$$
(46a-h)

Instead of solving a set of algebraic equations formed from the error between the prescribed and computed terminal boundary values, the error norms are minimized by an optimization algorithm. The numerical procedure starts from the initial estimated values of T,  $\theta$ ,  $\phi$  and  $\varepsilon$  at the bottom end. Then, the integration is carried out from  $z_0 = 0$  to  $z_0 = Z_H$  using the fifth-order Cash-Karp Runge-Kutta method as given in Press et al. [15]. An objective function  $\Psi$  for the optimization exercise is minimized using the downhill simplex method proposed by Nelder and Meade [16], depending on the specified values, namely, for the case of specified top tension,

Minimize 
$$\Psi = |\mathbf{x}_0(\mathbf{Z}_H) - \mathbf{R}\cos\theta_0| + |\mathbf{y}_0(\mathbf{Z}_H) - \mathbf{R}\sin\theta_0| + |\mathbf{T}(\mathbf{Z}_H) - \mathbf{T}_H|$$
 (47)

or for the case of specified cable unstrained length,

$$\underset{x_0, y_0, s}{\text{Minimize}} \Psi = |x_0(Z_H) - R\cos\theta_0| + |y_0(Z_H) - R\sin\theta_0| + |s(Z_H) - S_L|$$
(48)

Consequently, the overall steps are iterated until the allowable error is achieved. It should be remarked that the integration with respect to  $z_0$  coordinate (from the seabed to the surface) has an implicit constraint that cable profile must lie above the seabed.

#### 5. Computational results and discussion

Three case studies for some typical problems are presented. The first case provides confirmation of the accuracy of the variational formulation. The finite element method (FEM) and the shooting-optimization method (SOM) have been cross-checked for the validity of the cable model and mathematical examinations. The latter two cases consider the static behavior of cable, using the specified top tension or cable unstrained length to be the main type of analyses.

The cable data input parameters are as follows:  $Z_{\rm H}=500$  m; R=300 m; uniform current velocity in X-axis direction V=3.7 km/h; cable diameter D=0.023 m; weight of cable in seawater  $w_{\rm e}=12.3$  N/m;  $C_{\rm DN}=1.0$ ;  $C_{\rm DT}=0.05$ ;  $\rho_{\rm w}=1021$  kg/m³, and  $E=0.1628\times10^7$  kN/m², and v=0. The specified unstrained arc-length is 550 m and the specified top tension is 25 kN.

Numerical results given in Tables 1 and 2 show the cable tension components corresponding to the global directions at the bottom end and the cable strained length  $S_{L_0}$  versus the variations in values of  $\theta_0$  from 0° to 180°, for the case of specified top tension and cable unstrained length, respectively. The calculated length of  $S_{L_0}$  is equal to  $\sum_{k=1}^{N_{\rm el}} \int_0^h \sqrt{1 + x_0'^2 + y_0'^2} \, dz_0$ , in which  $N_{\rm el}$  is the

Table 1
Comparisons of cable tension components at the bottom end and cable strained length for the specified top tension case, FEM: finite element method, SOM: shooting-optimization method

$\theta_0$ (deg)	Cable tens	Cable tension components at the buggy end							
	$T_x$ (N)		$T_{y}$ (N)	$T_{y}$ (N)		T <sub>z</sub> (N)		$S_{L_0}$ (m)	
	FEM	SOM	FEM	SOM	FEM	SOM	FEM	SOM	
0	13 044.77	13 044.82	0.00	0.00	13 917.31	13917.26	587.18	587.18	
30	11 860.48	11860.42	5175.70	5175.96	14 004.11	14 004.06	587.26	587.26	
60	8495.60	8495.53	9168.76	9168.88	14 379.29	14 379.25	587.21	587.21	
90	3421.33	3421.33	11 057.45	11 057.49	15 122.85	15 122.82	586.44	586.44	
120	-2401.31	-2401.30	10051.88	10051.10	15 986.69	15 986.68	584.99	584.99	
150	-7179.69	-7179.69	5986.84	5986.84	16 565.44	16 565.43	583.71	583.71	
180	-9024.86	-9024.87	0.00	0.00	16735.33	16735.32	583.25	583.25	

Table 2
Comparisons of cable tension components at the bottom end and cable strained length for the specified cable unstrained arc-length case, FEM: finite element method, SOM: shooting-optimization method

$\theta_0$ (deg)	Cable tensi	on componen	ts at the but	ggy end			Strained 1	length
	$T_x$ (N)		$T_y$ (N)		$T_{z}$ (N)		$S_{L_0}$ (m)	
	FEM	SOM	FEM	SOM	FEM	SOM	FEM	SOM
0	23 641.42	23 641.38	0.00	0.00	31 267.32	31 267.22	584.16	584.16
30	21 078.43	21 078.44	10 398.89	10 398.83	31 397.11	31 397.05	584.19	584.19
60	13 875.21	13875.27	18 226.10	18 226.12	31 798.84	31 798.88	584.18	584.18
90	3525.51	3525.50	21 387.09	21 387.02	32 344.99	32 344.86	584.00	584.00
120	-7370.06	-7370.05	18 747.21	18 747.21	32 752.48	32 752.43	583.62	583.62
150	-15613.49	-15613.50	10871.71	10871.72	32 895.07	32 895.07	583.27	583.27
180	-18671.59	-18671.58	0.00	0.00	32 905.56	32 905.52	583.14	583.14

number of elements used in FEM. This study used 20 elements in the calculation. It is seen that both methods yield almost identical results. In spite of the fact that on convergence of SOM is limited by an initial estimated condition, this method is efficient and robust, especially when the initial estimate is close to the solution. The solution of FEM is based on the total number of prescribed elements, whereas the solution of SOM is based on an adaptive step-size controlled by an algorithm in the Runge-Kutta process. To gain further insights into the cable static behavior, the following examples for various cable geometrical parameters are studied. For the sake of convenience, the following dimensionless quantities are introduced as an extensibility index, namely  $T_{\rm H}/EA$  and  $w_{\rm e}S_L/EA$ .

#### 5.1. Specified top tension case

In this case, it was known that the maximum and minimum tensions occur at the cable top and bottom ends respectively, and the tension distribution is a function of ocean depth. A preliminary numerical investigation was carried out to demonstrate the effect of axial extensibility, using the forgoing input data and FEM. The parameter of  $T_H/EA$ , fixed in value of top tension and cable diameter, is assumed to be equal to 1.0, 0.1, 0.01, 0.001 and 0.0001. The value of elastic modulus was varied considerably so that the extensibility effect can be clearly seen, and a value of prescribed angle  $\theta_0$  was also varied so that the significance of omnidirectional current actions is involved by maintaining the uniform current profile in the X-axis direction.

Fig. 4a-c illustrate the distribution of cable tension components corresponding to the global directions at the bottom end in each value of  $T_{\rm H}/EA$  under the variations of  $\theta_0$  from 0° to 180°. It can be seen that the changes in a value of  $\theta_0$  and cable extensibility have effect on the tension in each direction as well as the resultant forces, namely  $T_{\rm b} = \sqrt{T_x^2 + T_y^2 + T_z^2}$ , as shown numerically in Table 3. The tension  $T_{\rm b}$  decreases with the decreasing values of  $T_{\rm H}/EA$  and with the increasing values of  $\theta_0$ . This tension is the important parameter in designing a cable and is capable of prediction to the cable sag condition [1,9].

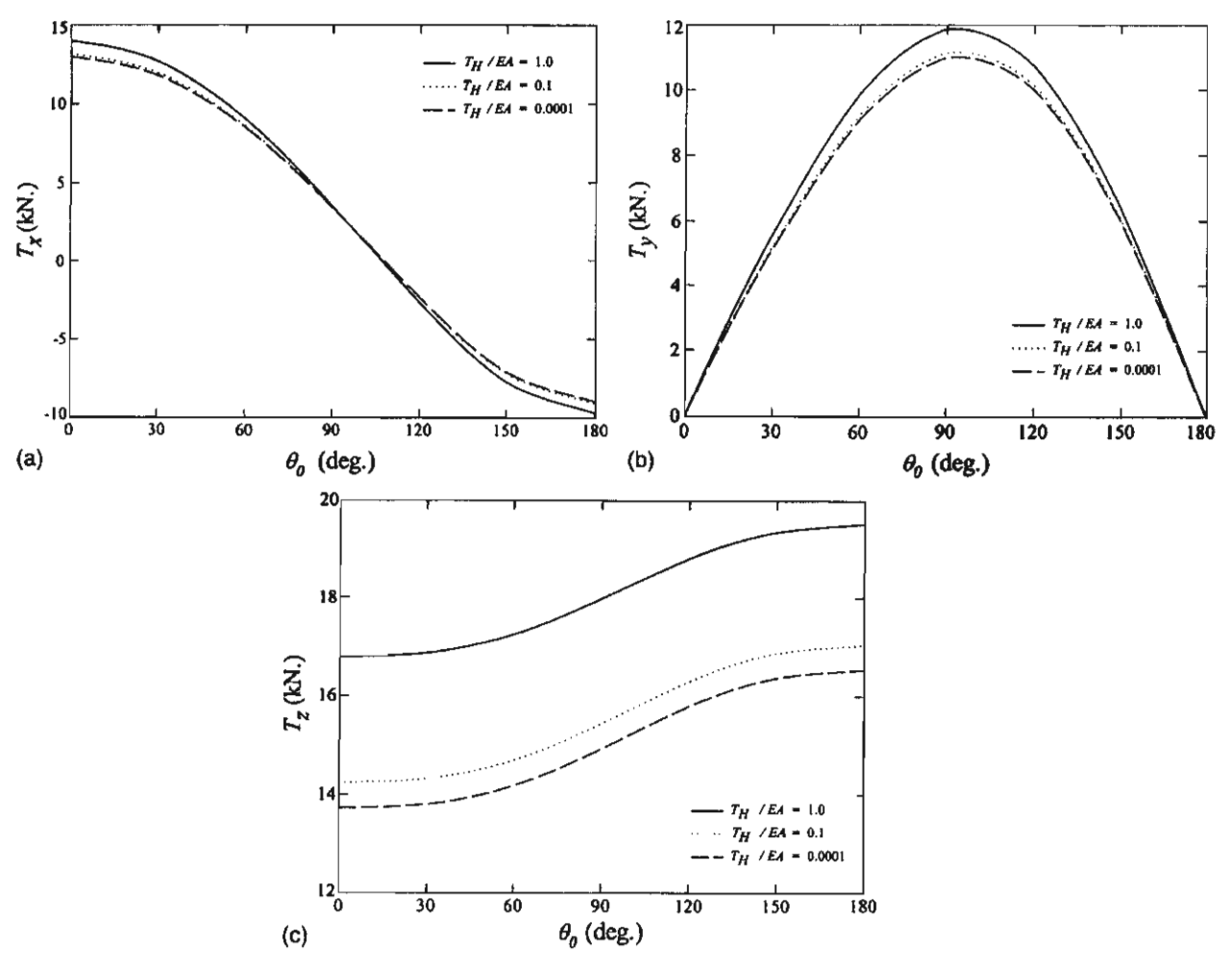


Fig. 4. Variation in tension components at the bottom end in each value of  $T_H/EA$ , for a different value of angle  $\theta_0$ , for the specified top tension case: (a) tension in X-axis direction, (b) tension in Y-axis direction and (c) tension in Z-axis direction.

Table 3 Calculated values of the resultant forces at the bottom end and cable unstrained length in each value of  $T_{\rm H}/EA$ , for the specified top tension case

$\theta_0$ (deg)	$T_{\rm H}/EA=1.0$		$T_{\rm H}/EA=0.1$		$T_{\rm H}/EA = 0.01$		$T_{\rm H}/EA=0.001$		$T_{\rm H}/EA=0.0001$	
	$T_{b}$ (N)	$S_L$ (m)	$T_{\rm b}$ (N)	$S_L$ (m)	$\overline{T_{b}(N)}$	$S_L$ (m)	<i>T</i> <sub>b</sub> (N)	$S_L$ (m)	T <sub>b</sub> (N)	$S_L$ (m)
0	21 855.66	301.77	19 382.31	539.06	18 934.62	582.13	18 886.46	586.77	18 881.61	587.23
30	21 848.02	302.06	19 374.84	539.21	18 927.20	582.23	18 879.05	586.86	18 874.20	587.33
60	21 832,78	302.54	19 359.85	539.29	18 912.32	582.19	18864.18	586.81	18 859.32	587.27
90	21 824.19	302.50	19 351.14	538.64	18 903.60	581.40	18 855.46	586.00	18 850.61	586.47
120	21 815.76	302.27	19 342.98	537.41	18 895.53	579.94	18 847.40	584.51	18 842.55	584.97
150	21 800.52	302.25	19 328.14	536.38	18 880.84	578.65	18832.73	583.20	18 827.88	583.66
180	21 792.84	302.30	19 320.62	536.03	18 873.38	578.19	18 825.27	582.73	18 820.42	583.18

In each value of  $T_{\rm H}/EA$ , the calculated unstrained length of  $S_L$  equal to  $\sum_{k=1}^{N_{\rm el}} \int_0^h \sqrt{1+x_0'^2+y_0'^2/(1+\epsilon_0)} \, \mathrm{d}z_0$  is not quite different under the variations of  $\theta_0$ . The shortest length can be found when cable having high extensible cable  $(T_{\rm H}/EA=1.0)$ , however, the length is increased under high elongation and almost equal to the lower one at the equilibrium state, as shown in Fig. 5. The effect of extensibility on the cable unstrained and strained length can be clearly seen when  $T_{\rm H}/EA$  is greater than 0.1. The shortest strained length may be approximated when  $\theta_0$  is equal to 180°.

The next investigation was to consider the cable orientation under the influence of current timeindependent forces, in terms of magnitude and direction. Three values of velocity were considered, V is taken to have value of 0, 2.0, 3.7 km/h, and  $T_{\rm H}/EA$  was taken to be 0.1. Figs. 6 and 7 present the distributions of vertical angle  $\phi$  and horizontal angle  $\theta$  against the ocean depth under the variations of  $\theta_0$  for any nodal point along the cable, where  $\phi$  is measured from XY plane and  $\theta$  is

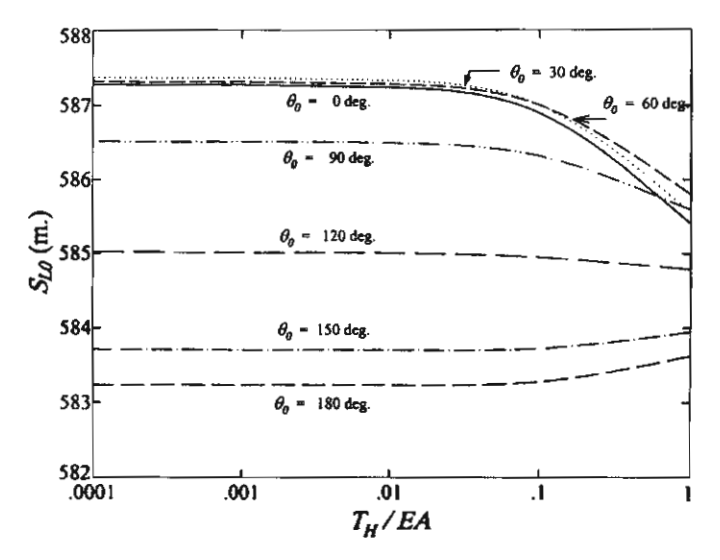


Fig. 5. Variation in total cable strained length in each value of angle  $\theta_0$ , for a different value of  $T_H/EA$ , for the specified top tension case.

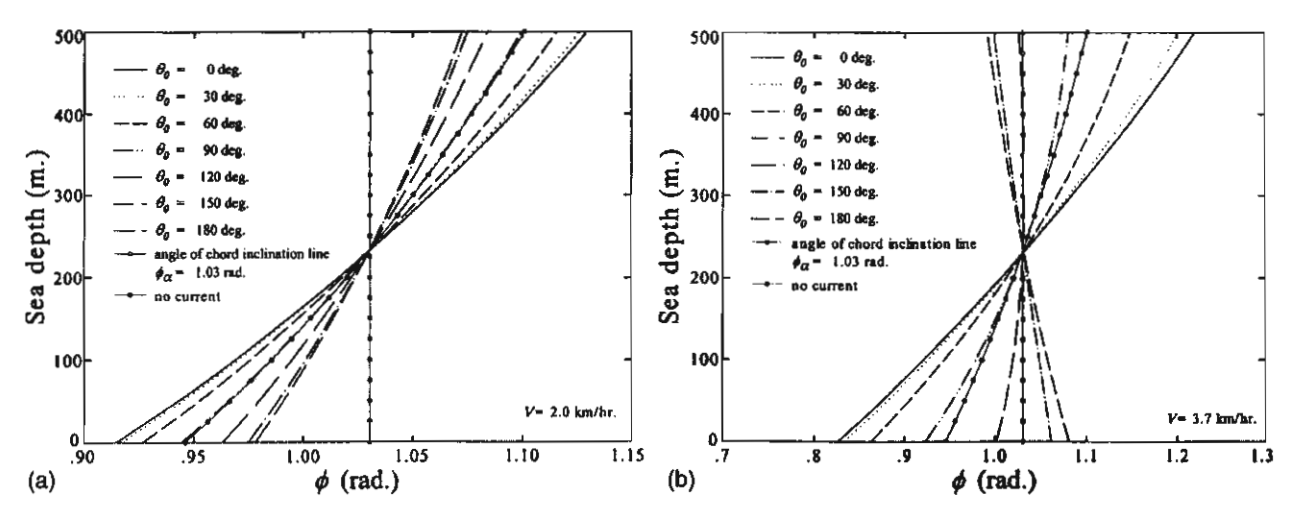


Fig. 6. Distribution of vertical angle  $\phi$  at any point along a cable against ocean depth, for a different value of angle  $\theta_0$ , for the specified top tension case and  $T_H/EA = 0.1$ : (a) V = 2.0 km/h and (b) V = 3.7 km/h.

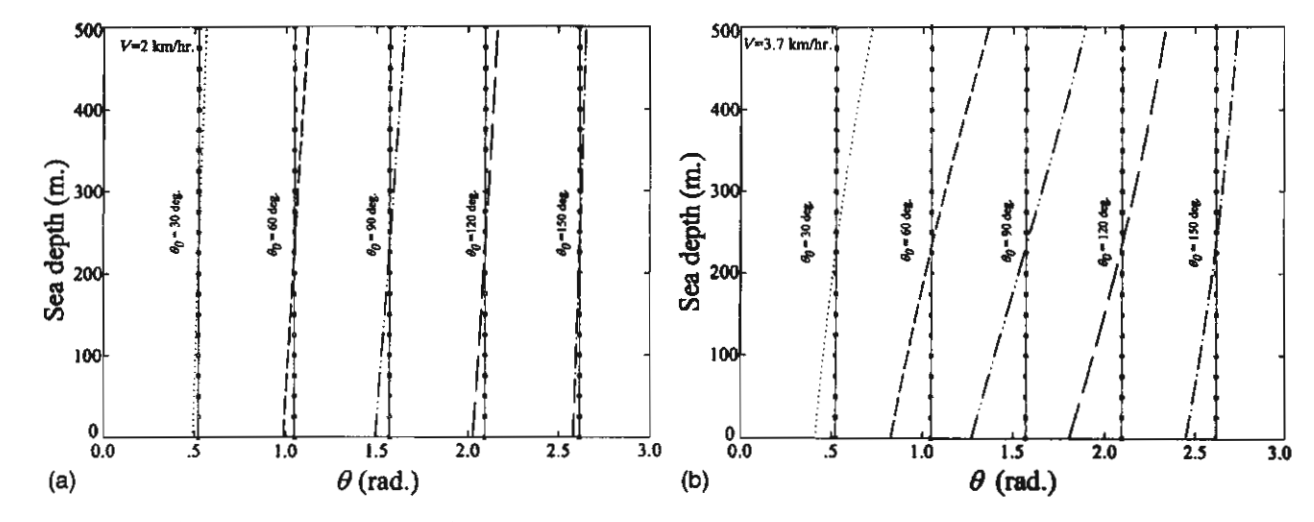


Fig. 7. Distribution of horizontal angle  $\theta$  at any point along a cable against ocean depth, for a different value of angle  $\theta_0$ , for the specified top tension case and  $T_H/EA = 0.1$ : (a) V = 2.0 km/h and (b) V = 3.7 km/h (——: no current).

measured from the  $\vec{i}$  direction. These illustrations are useful for evaluating the cable equilibrium profile in space with the different action of current forces instead of cable sag prediction.

As shown in Fig. 6a for V=2.0 km/h, the distribution of  $\phi$  is varied along the depth, and the values of  $\phi$  at the top and bottom ends are respectively greater and less than the value of  $\phi_{\alpha}$ . For  $\theta_0=0^{\circ}$ , it may be speculated that cable is more slack than the others since values of  $\phi$  are maximum and minimum at the top and bottom ends, respectively. When  $\theta_0=90^{\circ}$ , the plot is identical to the case of no current.

As shown in Fig. 6b, when the magnitude of V is increased to 3.7 km/h, the plots for  $\theta_0$  equal to 120°, 150° and 180° are different from the former case. For  $\theta_0 = 120^\circ$ , the value of  $\phi$  in the range

of 250-500 m depth aligns closely to the angle  $\phi_{\alpha}$ . Hence, the sag of cable is apparently small for this situation. For  $\theta_0 = 150^{\circ}$  and 180°, the values of  $\phi$  at the top and bottom ends are respectively less and greater than  $\phi_{\alpha}$ . Therefore, the profiles are formed in the contrary direction with respect to a normal shape of the other prescribed angles  $\theta_0$ . This feature may be explained as current forces in the lateral direction having a more significant influence on the cable configuration more than the cable effective self-weight. This effect becomes significance especially as the magnitude of V increases.

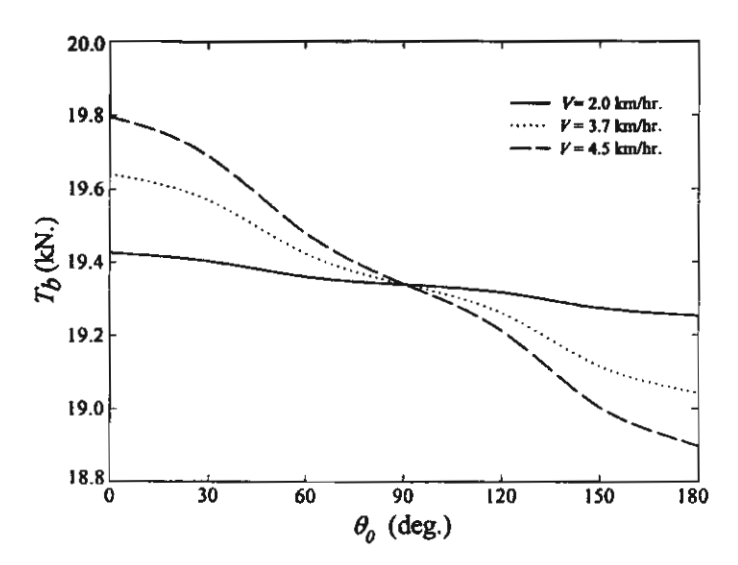


Fig. 8. Variation in the resultant forces at the bottom end in each current magnitude, for a different value of angle  $\theta_0$ , for the specified top tension case and  $T_H/EA = 0.1$ .

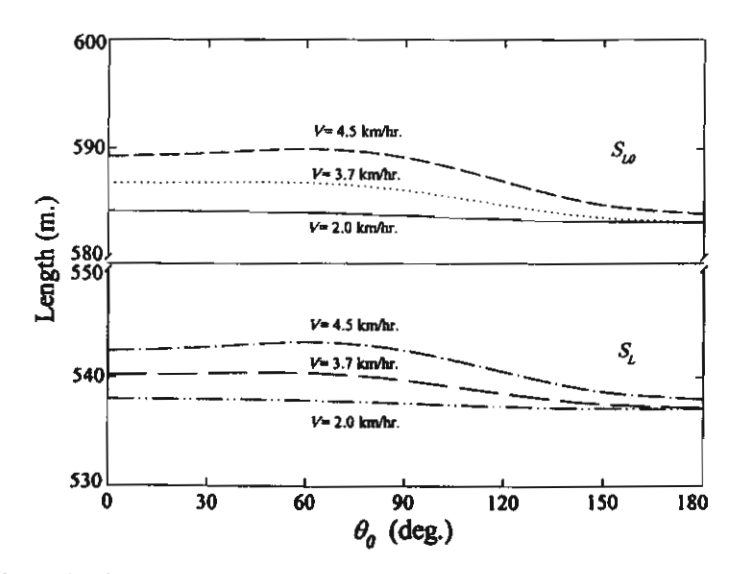


Fig. 9. Variation of cable strained and unstrained lengths in each current magnitude, for a different value of angle  $\theta_0$ , for the specified top tension case and  $T_H/EA = 0.1$ .

Fig. 7a presents how the current forces displace the cable laterally, which is more noticeable with the higher magnitude of the current velocity, as compared with Fig. 7b. The vertical lines in the plots are used to represent for the absence of currents in each specified value of  $\theta_0$ . It may be seen that cable configuration entirely lies in the vertical plane because there is no force to disturb the cable from the plane, as is well-known for the case of a submerged cable. For  $\theta_0 = 0^\circ$  and 180° (not shown herein), the current direction is parallel to the cable configuration line, therefore the force component in the bi-normal direction  $(\vec{q})$  is not generated. This makes a cable lies in the vertical plane and only in the distribution of vertical angle has been presented in Fig. 6.

Fig. 8 shows the influence of changes in the magnitude of current velocity on the resultant forces at the bottom end in each value of  $\theta_0$ . It can be seen that, for the ranges of  $0^{\circ} < \theta_0 < 90^{\circ}$  and  $90^{\circ} < \theta_0 < 180^{\circ}$ , respectively, tension  $T_b$  increases and decreases with the increasing magni-

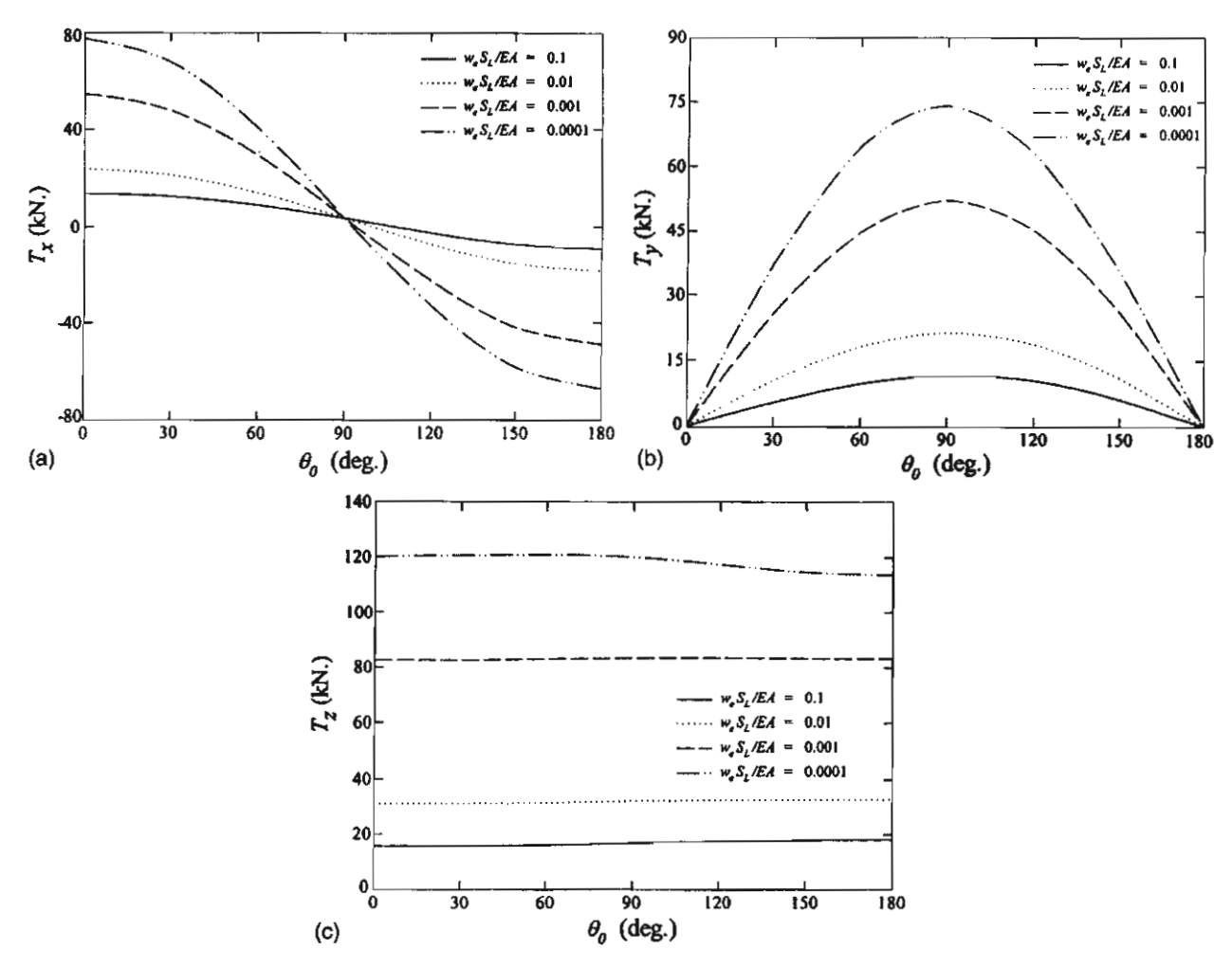


Fig. 10. Variation in tension components at the bottom end in each value of  $w_eS_L/EA$ , for a different value of angle  $\theta_0$ , for the specified cable unstrained arc-length case: (a) tension in X-axis direction, (b) tension in Y-axis direction and (c) tension in Z-axis direction.

tude of current velocity. Moreover, the cable strained and unstrained lengths increase with the increasing magnitude of current velocity, as presented in Fig. 9.

### 5.2. Specified unstrained arc-length case

Although the numerical algorithm mentioned above is efficient for solving the cable problem with the case of specified top tension, this algorithm can be treated using the concept of specified unstrained length. Firstly, the initial trial value of top tension is assigned, and then the approximated unstrained length is calculated. If the computed length is not equal to the prescribed one, then a new trial value of tension will be assumed and the procedure is repeated until the allowable error is achieved.

Table 4 Calculated values of the resultant forces at the bottom and top ends in each value of  $w_eS_L/EA$ , for the specified cable unstrained arc-length case

$\theta_0$ (deg)	$w_{\rm e}S_L/EA=0.1$		$w_{\rm e}S_L/EA=0.01$		$w_{\rm e}S_L/EA=0.001$		$W_{\rm e}S_L/EA=0.0001$	
	$T_{b}$ (N)	<i>T</i> <sub>H</sub> (N)	$T_{b}$ (N)	T <sub>H</sub> (N)	$T_b$ (N)	<i>T</i> <sub>H</sub> (N)	$T_b$ (N)	T <sub>H</sub> (N)
0	21 403.77	25 337.52	39 897.99	45 390.63	99 605.96	105 368.65	142 913.56	148 750.00
30	21 374.50	25 372.05	39 881.10	45 447.08	99 609.28	105 153.04	142 838.37	148 750.00
60	21 291.62	25 418.22	39 774.90	45 488.28	99 492.51	105 479.74	142 687.98	148 750.00
90	21 172.94	25 374.98	39 483.72	45 275.88	99 027.31	105 090.33	140 737.33	146 875.00
120	21 014.82	25 292.22	38 987.38	44 858.40	98 182.48	104 321.29	137 302.34	143 515.63
150	20 837.21	25 248.79	38 491.45	44 512.63	97 375.51	103 664.55	133 401.68	139 765.63
180	20 762.51	25 240.96	38 398.26	44 394.38	97 068.48	103 432.62	131 920.12	138 359.38

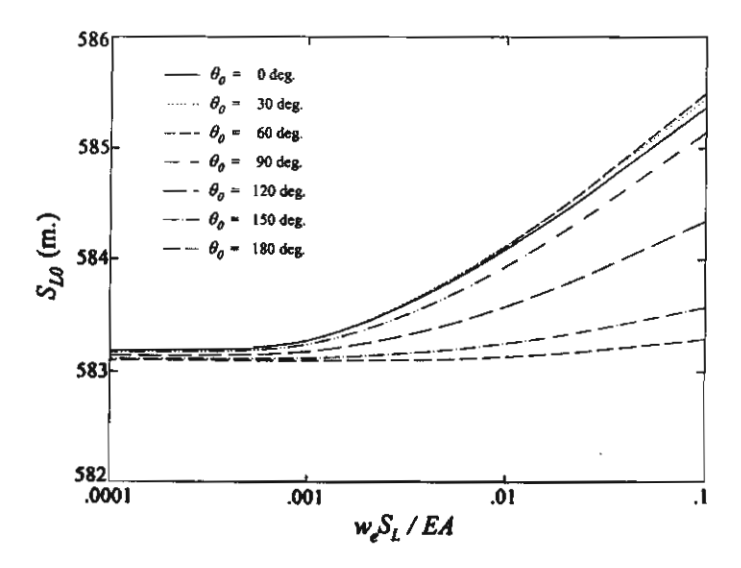


Fig. 11. Variation in total cable strained length in each value of angle  $\theta_0$ , for a different value of  $w_e S_L/EA$ , for the specified cable unstrained arc-length case.

In accordance with the representation of specified top tension case, the following results are shown to demonstrate the effect of extensibility and the omnidirectionality of current forces. By assuming a parameter of  $w_e S_L/EA = 0.1$ , 0.01, 0.001, 0.0001, the value of  $w_e/A$  is kept constant, whereas the specified cable unstrained length  $S_L$  is equal to 400, 550, 575 and 582 m, and the corresponding cable elastic modulus E is equal to  $0.118 \times 10^6$ ,  $0.163 \times 10^7$ ,  $0.170 \times 10^8$ ,  $0.172 \times 10^9$  kN/m², respectively. Once again, Fig. 10a-c illustrate the distributions of cable tension components at the bottom end in each value of  $w_e S_L/EA$  and under the variations of  $\theta_0$  from 0° to 180°. It can be clearly seen that the changes in a value of  $\theta_0$  and cable extensibility have effects on the tension in each direction and also on the resulting force  $T_b$ , which decreases consecutively from

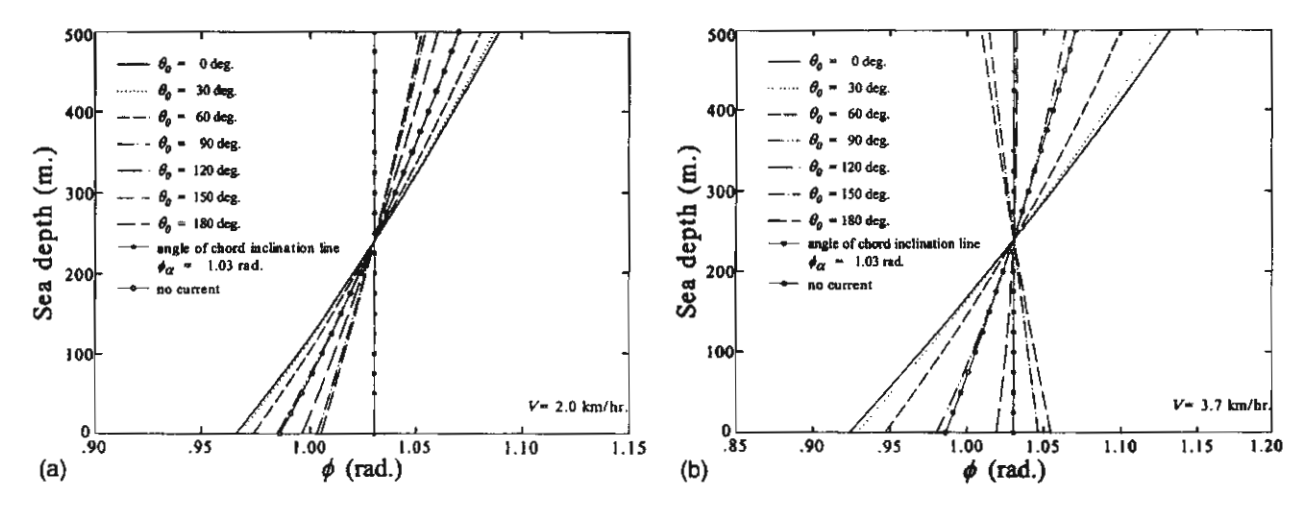


Fig. 12. Distribution of vertical angle  $\phi$  at any point along a cable against ocean depth, for a different value of angle  $\theta_0$ , for the specified cable unstrained arc-length case and  $w_e S_L/EA = 0.01$ : (a) V = 2.0 km/h and (b) V = 3.7 km/h.

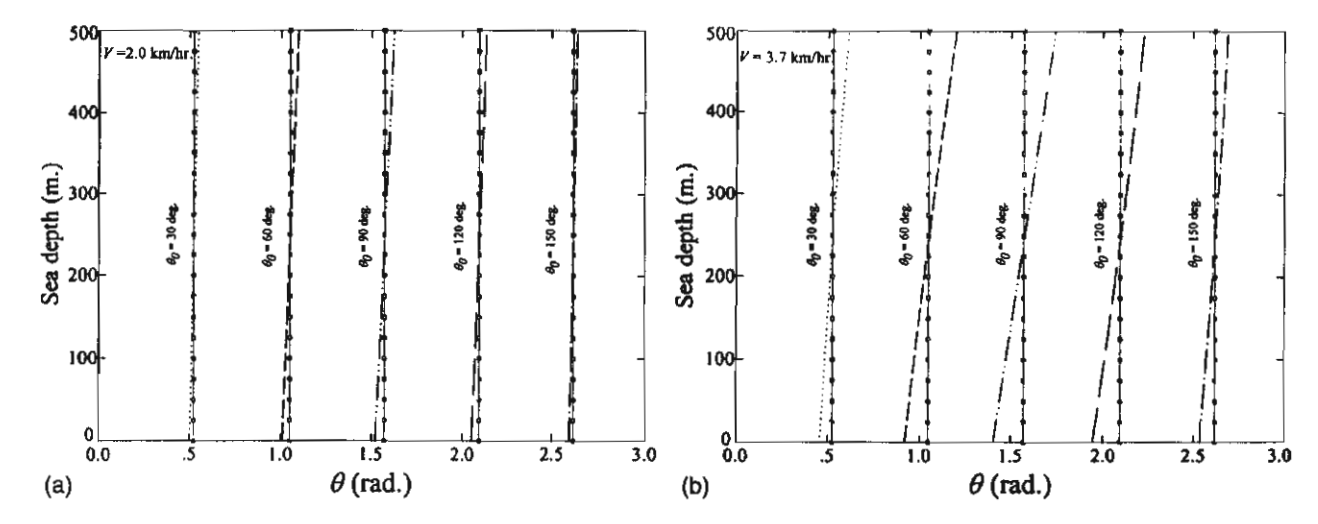


Fig. 13. Distribution of horizontal angle  $\theta$  at any point along a cable against ocean depth, for a different value of angle  $\theta_0$ , for the specified cable unstrained arc-length case and  $w_eS_L/EA = 0.01$ : (a) V = 2.0 km/h and (b) V = 3.7 km/h (——: no current).

 $\theta_0 = 0^\circ$  to 180°, as shown in Table 4. In each value of  $w_e S_L/EA$ , the maximum required top tension  $T_H$  can be found when  $\theta_0 = 60^\circ$ , approximately.

Fig. 11 shows the computed cable strained length for each angle  $\theta_0$ . It is worth noticing that these strained lengths are comparable (in the range of 583-586 m), even though the specified unstrained cable lengths are quite different (400-582 m) for each value of  $w_e S_L/EA$ . This can be explained that the highly extensible (small E) cable with shorter length can be stretched considerably more than that of the low extensible (large E) cable with longer length. Figs. 12 and 13 are

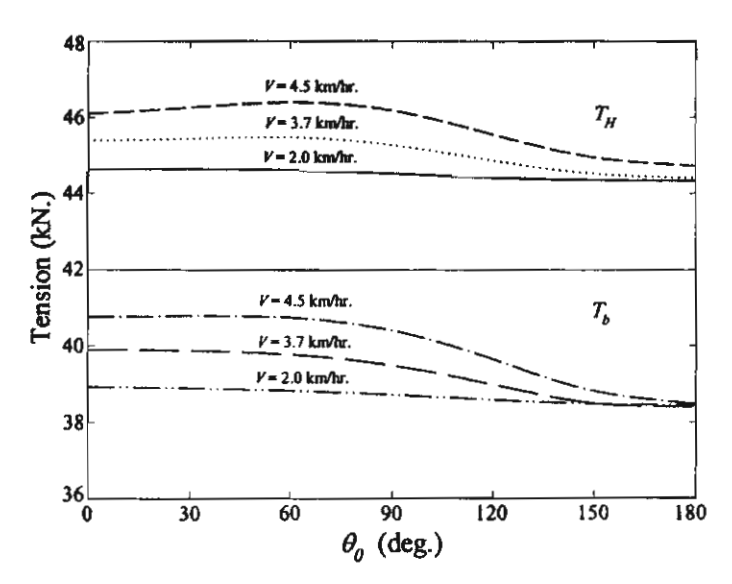


Fig. 14. Variation in the resultant forces at the top and bottom ends in each current magnitude, for a different value of angle  $\theta_0$ , for the specified cable unstrained arc-length case and  $w_e S_L/EA = 0.01$ .

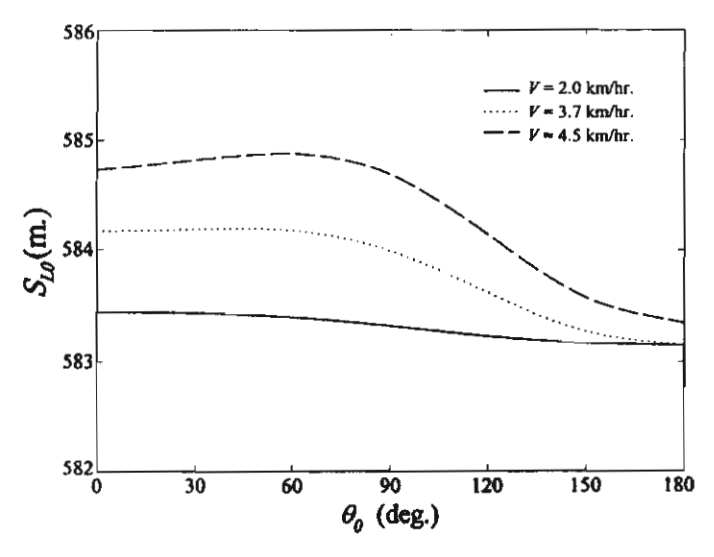


Fig. 15. Variation of cable strained length in each current magnitude, for a different value of angle  $\theta_0$ , for the specified cable unstrained arc-length case and  $w_e S_L/EA = 0.01$ .

plotted to show the distribution of  $\phi$  and  $\theta$  for  $w_eS_L/EA = 0.01$ , under the variation in magnitude and direction of current velocity. It can be seen that the results in these figures are in good agreement with those in the aforementioned case. Fig. 14 shows the effect of current on the resultant forces at the top and bottom ends under the variation in value of  $\theta_0$ . The results show that tensions  $T_H$  and  $T_b$  increase with the increasing magnitude of current velocity as well as the strained length, as shown in Fig. 15.

#### 6. Conclusions

The variational model formulation and computational results for analyzing the three-dimensional steady-state behavior of an extensible marine cable is presented. Two mathematical simulations were used to solve and evaluate the problems, namely, the finite element approach and the shooting-optimization procedure, which gave almost identical results. The cable model and algorithm technique proposed in this study is efficient and robust when the top tension is specified. Numerical investigations were carried out for the specified top tension case and specified cable unstrained arc-length case. A number of parametric studies have been presented to evaluate cable profile, the tensile force development and the cable length estimation. The combined effects of axial extensibility and the current forces, both in terms of magnitude and directions, have been shown to be significant on the static behavior of extensible marine cable.

#### Acknowledgements

The authors gratefully acknowledge the financial support of the Thailand Research Fund (TRF) under Grants PHD/0167/2543 and RTA/03/2543.

#### References

- [1] A.P.K. De Zoysa, Steady-state analysis of undersea cables, Ocean Engineering 5 (1978) 209-223.
- [2] S. Chucheepsakul, S. Subwonglee, Three-dimensional static analysis of marine cables, in: Cheung, Lee, Leung (Eds.), Computational Mechanics, Balkema, Rotterdam, Netherlands, 1991, pp. 389–394.
- [3] C.M. Wang, H.F. Cheong, S. Chucheepsakul, Static analysis of marine cables via shooting-optimization technique, Journal of Waterway, Port, Coastal and Ocean Engineering ASCE 119 (1993) 450-457.
- [4] M.I. Friswell, Steady-state analysis of underwater cables, Journal of Waterway, Port, Coastal and Ocean Engineering ASCE 121 (1995) 98-104.
- [5] R.W. Webster, Nonlinear static and dynamic response of underwater cable structures using finite element method, in: Proceeding of the 7th Offshore Technology Conference ASCE 1975, Paper OTC 2322, Houston, Texas.
- [6] L. Huyse, M.C. Singh, M.A. Maes, A static drilling riser model using free boundary conditions, Ocean Engineering 24 (1997) 431-444.
- [7] T.P. Dreyer, J.H. Van Vuuren, A comparison between continuous and discrete modelling of cables with bending stiffness, Applied Mathematical Modelling 23 (1999) 527-541.
- [8] D. Vassalos, Physical modelling and similitude of marine structures, Ocean Engineering 26 (1999) 111-123.
- [9] M.A. Vaz, M.H. Patel, Three-dimensional behaviour of elastic marine cables in sheared currents, Applied Ocean Research 22 (2000) 45-53.

- [10] S. Chucheepsakul, T. Huang, P. Laohaporjanart, Effect of axial deformation on the equilibrium configurations of marine cables, in: Proceeding of the 5th International Journal of Offshore and Polar Engineering Conference 1995, vol. 2, pp. 244–248.
- [11] H.O. Berteaux, Buoy Engineering, John Wiley and Sons, New York, 1976, pp. 97-134.
- [12] T.R. Goodman, J.P. Breslin, Statics and dynamics of anchoring cable in waves, Journal of Hydronautics 10 (1976) 113-120.
- [13] C.P. Sparks, The influence of tension, pressure and weight on pipe and riser deformations and stresses, Journal of Energy Resource Technology ASME 106 (1984) 46-54.
- [14] J.J. Burgess, Bending stiffness in a simulation of undersea cable deployment, International Journal of Offshore and Polar Engineering 3 (1993) 197–204.
- [15] W.H. Press, S.A. Teukolsky, W.T. Vettering, B.P. Flannery, Numerical Recipes in Fortran, second ed., Cambridge University Press, Cambridge, 1992, pp. 372-381, 708-716.
- [16] J.A. Nelder, R. Meade, A simplex method for function minimization, Computer Journal 7 (1965) 308-313.

# Elliptic integral solutions of variable-arc-length elastica under an inclined follower force

Somchai Chucheepsakul<sup>1,\*</sup> and Boonchai Phungpaigram<sup>2</sup>

Department of Civil Engineering, King Mongkut's University of Technology Thonburi, Bangkok 10140, Thailand

<sup>2</sup> Department of Civil Engineering, Rajamangala Institute of Technology, Patumthani 12110, Thailand

Received 17 June 2002, revised 30 December 2002, accepted 19 February 2003 Published online

**Key words** elastica, variable-arc-length beam, follower force, large deflection, elliptic integrals MSC (2000) 74K10

This paper presents exact closed-formed solutions using elliptic integrals for large deflection analysis of elastica of a beam with variable arc-length subjected to an inclined follower force. The beam is hinged at end but slides freely over the support at the other end. In the undeformed state, the inclined follower force applied at any distance from the hinged end making an angle  $\gamma$  with respect to vertical axis while in the deformed state its direction remains at an angle  $\gamma$  from the normal to the beam axis. The set of nonlinear equations is obtained from the boundary conditions, and solved iteratively for the solutions. The effect of the direction and the position of the follower force on the beam bending behaviour is demonstrated. Comparisons of equilibrium configurations of the beam under non-follower force and follower force are also given.

#### 1 Introduction

Research studies on large deflection of elastica of beam with variable arc-length have dealt mostly with the conservative force (see, for example in Chucheepsakul and Huang [1], Chucheepsakul et al. [2], and Wang et al. [3]). In the case of non-conservative force, most of the research works in this field have dealt with the problem of cantilever beam (Hartono [4], Rao and Rao [5], Shwartsman [6], Rao et al. [7]). There are a few studies dealt with the problem of variable-arc-length beam subjected to a follower (non-conservative) force (Wang et al. [8], Hartono [9], Chucheepsakul and Monprapaussorn [10]). As mentioned above, the problem of variable-arc-length beam under a follower force acting within the span length of beam has not yet been studied elsewhere before. Therefore, the purpose of this paper is to continually investigate and present the new results of this beam problem under an inclined follower force.

In the present work, the follower force is attached to the beam with initial inclined angle  $\gamma$  with respect to the vertical line of the undeformed configuration of the beam and away from the hinged support at distance  $\beta L$ . The force maintains the inclined angle  $\gamma$  when the beam deforms. The governing nonlinear differential equation together with the boundary conditions is solved analytically using elliptic integrals which give the closed-form solutions, and the results are exact and could serve as a benchmark for other numerical investigations.

#### 2 Formulation of the problem

From Fig. 1a, consider a simple flexible elastic beam of constant flexural rigidity EI and span length L. It is hinged at end A and rested on the frictionless support at end B. This beam is subjected to a follower force, which is applied at a distance  $\beta L$  away from end A and it inclines at an angle  $\gamma$  from the vertical undeformed configuration of the beam.

A deformed configuration of the simple beam is shown in Fig. 1b. The slope of the deflected beam at end A and B is  $\Theta_A$  and  $\Theta_B$ , respectively. The angle  $\Theta_C$  is the slope of deflected beam at the position of the follower force. In a deformed configuration of the beam, the original position  $(\beta L,0)$  of the follower force is changed into the new position  $(x^*,y^*)$ , where  $x^*$  and  $y^*$  are the length measured from end A in horizontal and vertical directions respectively. The follower force P maintains the inclined angle  $\gamma$  when the beam deforms, while the arc-length AC still equals to  $\beta L$ . Sign conventions are also demonstrated in Fig. 1b. Fig. 1c illustrates the free-body diagram of part of the beam from support A on the left of force P.

Referring to the free body diagram of the deflected beam as shown in Fig. 1c, the equations of bending moment M can be written as:

Case I:  $x \le x^*$ 

25

27

31

32

33

$$M = P \left\{ \left( \sin \left( \Theta_{C} + \gamma \right) - \frac{\tan \Theta_{B}}{L} \left( x^{*} \cos \left( \Theta_{C} + \gamma \right) + y^{*} \sin \left( \Theta_{C} + \gamma \right) \right) \right) y + \left( \cos \left( \Theta_{C} + \gamma \right) - \frac{1}{L} \left( x^{*} \cos \left( \Theta_{C} + \gamma \right) + y^{*} \sin \left( \Theta_{C} + \gamma \right) \right) \right) x \right\},$$
(1a)

<sup>\*</sup> Corresponding author, e-mail: somchai.chu@kmutt.ac.th

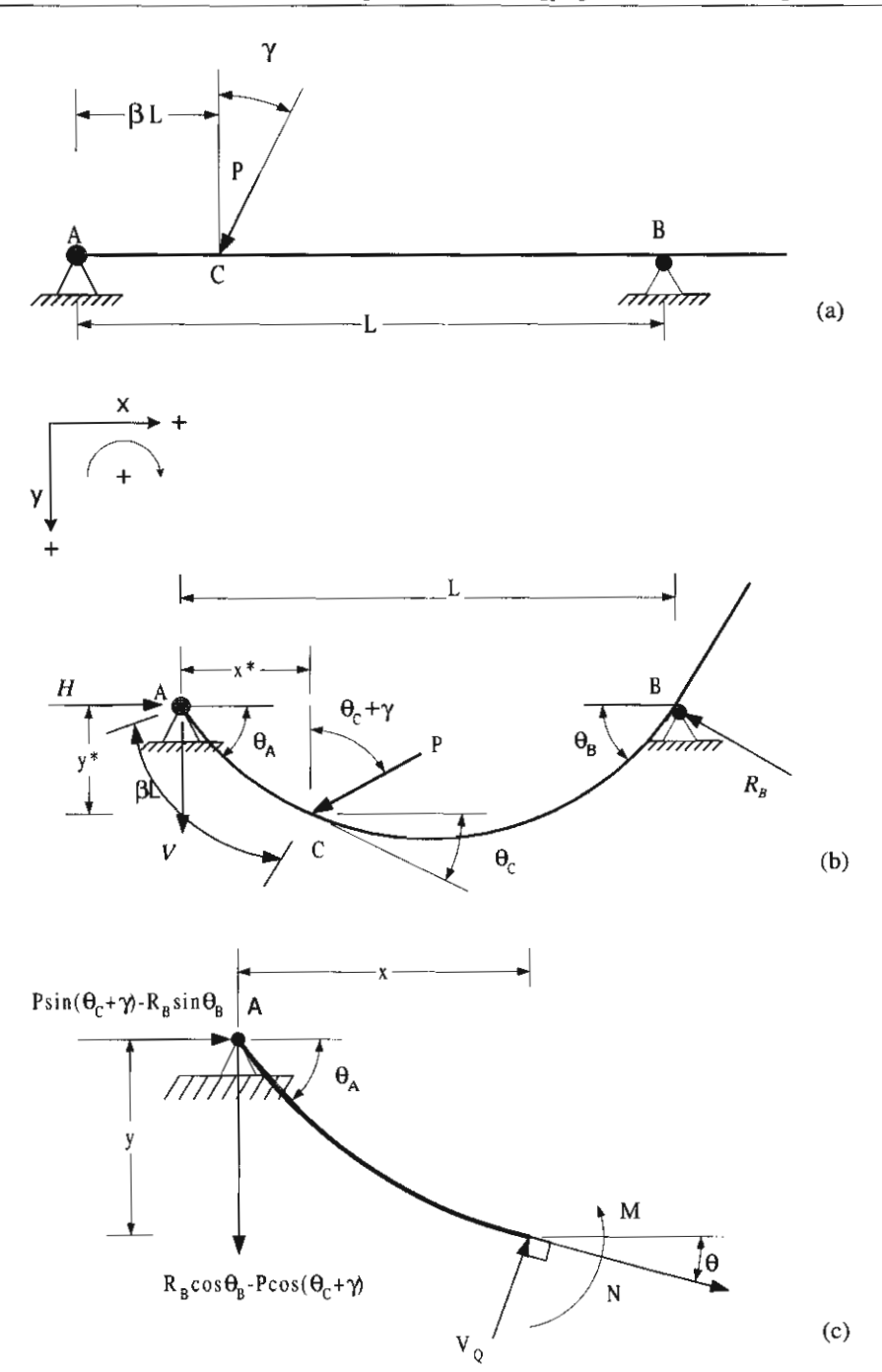


Fig. 1 (a) Undeformed configuration of elastica; (b) deformed configuration and positive direction of elastica; (c) free body of elastica segment.

Case II: $x > x^*$ 

$$M = P \left\{ \left( \sin \left( \Theta_{C} + \gamma \right) - \frac{\tan \Theta_{B}}{L} \left( x^{*} \cos \left( \Theta_{C} + \gamma \right) + y^{*} \sin \left( \Theta_{C} + \gamma \right) \right) \right) y + \left( \cos \left( \Theta_{C} + \gamma \right) - \frac{1}{L} \left( x^{*} \cos \left( \Theta_{C} + \gamma \right) + y^{*} \sin \left( \Theta_{C} + \gamma \right) \right) \right) x - \sin \left( \Theta_{C} + \gamma \right) \left( y - y^{*} \right) - \cos \left( \Theta_{C} + \gamma \right) \left( x - x^{*} \right) \right\}.$$
(1b)

From the elastica theory and geometric relations of the beam in deformed configuration, the constitutive relation and the geometric relations are given by

$$\frac{d\theta}{ds} = \frac{M}{EI}, \quad \frac{dx}{ds} = \cos\theta, \quad \frac{dy}{ds} = \sin\theta,$$
 (2a,b,c)

- where x and y are the Cartesian coordinates measured from end A,  $\theta$  is the slope of the centroidal axis of the beam with respect to the horizontal axis, and s is the arc-length of the deformed shape of the beam.
- The following non-dimensional quantities are introduced for generality:

$$\overline{x} = \frac{x}{L}, \quad \overline{y} = \frac{y}{L}, \quad \overline{x^*} = \frac{x^*}{L}, \quad \overline{y^*} = \frac{y^*}{L}, \quad \overline{s} = \frac{s}{L}, \quad \overline{P} = \frac{PL^2}{EI}.$$
 (3a,b,c,d,e,f)

- In view of eqs. (1) and (2a), and upon differentiating eq. (2a) with respect to arc-length s, one obtains the following non-dimensional equations:
- 45 Case I:  $\theta_{\rm C} \le \theta \le \theta_{\rm A}$

$$\frac{d^2\theta}{d^{-2}s} = -\overline{P}\left[\left(\sin\left(\theta_{\rm C} + \gamma\right) - \delta\tan\theta_{\rm B}\right)\sin\theta + \left(\cos\left(\theta_{\rm C} + \gamma\right) - \delta\right)\sin\theta\right],\tag{4a}$$

46 Case II:  $\theta_{\rm B} \le \theta \le \theta_{\rm C}$ 

$$\frac{d^2\theta}{d^{-2}s} = -\overline{P}\left[-\left(\delta \tan \theta_{\rm B}\right) \sin \theta - \delta \cos \theta\right],\tag{4b}$$

where the symbol  $\delta$  in eqs. (4a) and (4b) is defined by the following equation:

$$\delta = \overline{x^*} \cos(\theta_C + \gamma) + \overline{y^*} \sin(\theta_C + \gamma). \tag{5}$$

Multiplying eqs. (4a) and (4b) by  $d\theta/d\bar{s}$  and integrating with respect to  $\theta$ , one obtains the following first-order differential equations:

$$\frac{d\theta}{ds} = \pm \sqrt{2\overline{P}\left\{\left(-\cos\left(\theta_{C} + \gamma\right) + \delta\right)\sin\theta + \left(\sin\left(\theta_{C} + \gamma\right) - \delta\tan\theta_{B}\right)\cos\theta + C_{1}\right\}}, \quad \theta_{C} \le \theta \le \theta_{A}, \tag{6a}$$

$$\frac{d\theta}{d\bar{s}} = \pm \sqrt{2\bar{P} \left\{ \delta \sin \theta - \delta \tan \theta_{\rm B} \cos \theta + C_2 \right\}}, \quad \theta_{\rm B} \le \theta \le \theta_{\rm C}. \tag{6b}$$

50 Geometric relations eqs. (2a,b) are rewritten as

$$\frac{d\overline{x}}{d\overline{s}} = \cos\theta, \quad \frac{d\overline{y}}{d\overline{s}} = \sin\theta. \tag{7a,b}$$

Eqs. (6) and (7) are the set of differential equations for solving the problem. The arbitrary constants  $C_1$  and  $C_2$  in eqs. (6a) and (6b) are evaluated by the following boundary conditions:

$$\frac{d\theta}{d\overline{s}}\Big|_{\theta=\theta_{\rm A}}=0 \quad \text{for} \quad C_1, \qquad \frac{d\theta}{d\overline{s}}\Big|_{\theta=\theta_{\rm B}}=0 \quad \text{for} \quad C_2.$$
 (8a,b)

Applying these boundary conditions (eqs. (8a) and (8b)), the arbitrary constants  $C_1$  and  $C_2$  are evaluated and obtained as

$$C_1 = \sin(\theta_{\rm A} - \theta_{\rm C} - \gamma) - \delta \frac{\sin(\theta_{\rm A} - \theta_{\rm B})}{\cos\theta_{\rm B}}, \quad C_2 = 0. \tag{9a,b}$$

- In view of eqs. (6a) and (6b), the minus sign (--) is applied into these equations because the angle  $\theta$  decreases as the arc-length  $\sigma$  increases.
- Substitution of  $C_1$  and  $C_2$  into eqs. (6a) and (6b) yields the curvature expression of the beam as follows:

$$\frac{d\theta}{ds} = -\frac{1}{\lambda} \left( \sqrt{\mu_1 + \mu_2 \sin \theta + \mu_3 \cos \theta} \right), \quad \theta_{\rm C} \le \theta \le \theta_{\rm A}, \tag{10a}$$

$$\frac{d\theta}{ds} = -\frac{1}{\lambda} \left( \sqrt{\mu_4 \sin \theta + \mu_5 \cos \theta} \right), \quad \theta_{\rm B} \le \theta \le \theta_{\rm C}, \tag{10b}$$

57 where

$$\mu_1 = \sin(\theta_A - \theta_C - \gamma) - \delta \frac{\sin(\theta_A - \theta_B)}{\cos\theta_B}, \quad \mu_2 = -\cos(\theta_C + \gamma) + \delta, \tag{11a,b}$$

$$\mu_3 = \sin(\theta_C + \gamma) - \delta \tan \theta_B, \quad \mu_4 = \delta, \quad \mu_5 = -\delta \tan \theta_B, \quad \lambda = \frac{1}{\sqrt{2P}}.$$
 (11c,d,e,f)

Considering curvature expressions (eqs. (10a) and (10b) and two geometric relations (eqs. (7a) and (7b)), one can express  $d\overline{s}$ ,  $d\overline{x}$ , and  $d\overline{y}$  as functions of  $\theta$  and these expressions can be integrated using the elliptic integral technique. The closed-form solutions in the terms of elliptic integrals of the first kind  $F(\phi, k)$  and the second kind  $E(\phi, k)$  [10] are obtained.

61 Case I:  $\theta_{\rm C} \leq \theta \leq \theta_{\rm A}$ 

$$\overline{s} = \int_{\theta_{A}}^{\theta} \frac{\lambda d\theta}{\sqrt{\mu_{1} + \mu_{2} \sin \theta + \mu_{3} \cos \theta}} \begin{cases} = \eta_{1} \left\{ F\left(\frac{\pi}{2}, k\right) - F\left(\phi, k\right) \right\}, & \theta \geq \varphi_{1}, \\ = \eta_{1} \left\{ F\left(\phi, k\right) - F\left(\frac{\pi}{2}, k\right) \right\}, & \theta < \varphi_{1}, \end{cases} \tag{12}$$

$$\overline{x} = \int_{\theta_{A}}^{\theta} \frac{\lambda \cos \theta d\theta}{\sqrt{\mu_{1} + \mu_{2} \sin \theta + \mu_{3} \cos \theta}} \begin{cases}
= \eta_{2} \left\{ \left( F\left(\phi, k\right) - F\left(\frac{\pi}{2}, k\right) \right) \\
- 2 \left( E\left(\phi, k\right) - E\left(\frac{\pi}{2}, k\right) \right) - 2 \frac{k\mu_{2}}{\mu_{3}} \left( \cos(\phi) \right) \right\}, & \theta \geq \varphi_{1}, \\
= \eta_{2} \left\{ 2 \left( E\left(\phi, k\right) - E\left(\frac{\pi}{2}, k\right) \right) \\
- \left( F\left(\phi, k\right) - F\left(\frac{\pi}{2}, k\right) \right) - \frac{2k\mu_{2}}{\mu_{3}} \cos(\phi) \right\}, & \theta < \varphi_{1},
\end{cases} \tag{13}$$

$$\overline{y} = \int_{\theta_{A}}^{\theta} \frac{\lambda \sin \theta d\theta}{\sqrt{\mu_{1} + \mu_{2} \sin \theta + \mu_{3} \cos \theta}} \begin{cases}
= \eta_{3} \left\{ \left( F\left(\phi, k\right) - F\left(\frac{\pi}{2}, k\right) \right) \\
- 2\left( E\left(\phi, k\right) - E\left(\frac{\pi}{2}, k\right) \right) + \frac{2k\mu_{3}}{\mu_{2}} \cos(\phi) \right\}, & \theta \geq \varphi_{1}, \\
= \eta_{3} \left\{ 2\left( E\left(\phi, k\right) - E\left(\frac{\pi}{2}, k\right) \right) \\
- \left( F\left(\phi, k\right) - F\left(\frac{\pi}{2}, k\right) \right) + \frac{2k\mu_{3}}{\mu_{2}} \cos(\phi) \right\}, & \theta < \varphi_{1},
\end{cases} \tag{14}$$

62 where

$$\phi = \sin^{-1} \sqrt{\frac{\left(\sqrt{\mu_2^2 + \mu_3^2}\right) - \mu_2 \sin \theta - \mu_3 \cos \theta}{\mu_1 + \sqrt{\mu_2^2 + \mu_3^2}}},$$
(15)

$$k = \sqrt{\frac{\mu_1 + \sqrt{\mu_2^2 + \mu_3^2}}{2\sqrt{\mu_2^2 + \mu_3^2}}},\tag{16}$$

$$\varphi_1 = \sin^{-1}\left(\frac{\mu_2}{\sqrt{\mu_2^2 + \mu_3^2}}\right),\tag{17}$$

$$\eta_1 = \frac{\sqrt{2}\lambda}{\left(\mu_2^2 + \mu_3^2\right)^{1/4}}, \quad \eta_2 = \frac{\sqrt{2}\lambda\mu_3}{\left(\mu_2^2 + \mu_3^2\right)^{3/4}}, \quad \eta_2 = \frac{\sqrt{2}\lambda\mu_2}{\left(\mu_2^2 + \mu_3^2\right)^{3/4}}, \tag{18a,b,c}$$

63 Case II:  $\theta_{B} \leq \theta \leq \theta_{C}$ 

$$\overline{s} = \beta - \int_{\theta_{C}}^{\theta} \frac{\lambda d\theta}{\sqrt{\mu_{4} \sin \theta + \mu_{5} \cos \theta}} \begin{cases}
= \beta - \eta_{4} \left\{ F\left(\phi, \frac{1}{\sqrt{2}}\right) - F\left(\phi_{C}, \frac{1}{\sqrt{2}}\right) \right\}, & \theta \ge \varphi_{2}, \\
= \beta - \eta_{4} \left\{ F\left(\phi_{C}, \frac{1}{\sqrt{2}}\right) - F\left(\phi, \frac{1}{\sqrt{2}}\right) \right\}, & \theta < \varphi_{2},
\end{cases}$$
(19)

$$\overline{x} = \overline{x^*} - \eta_5 \left\{ 2 \left( E \left( \phi, \frac{1}{\sqrt{2}} \right) - E \left( \phi_C, \frac{1}{\sqrt{2}} \right) \right) - \left( F \left( \phi, \frac{1}{\sqrt{2}} \right) - E \left( \phi_C, \frac{1}{\sqrt{2}} \right) \right) + \frac{\sqrt{2}\mu_4}{\mu_5} (\cos \phi - \cos \phi_C) \right\}, \qquad \theta \ge \varphi_2,$$

$$= \overline{x^*} - \eta_5 \left\{ \left( F \left( \phi, \frac{1}{\sqrt{2}} \right) - F \left( \phi_C, \frac{1}{\sqrt{2}} \right) \right) - 2 \left( E \left( \phi, \frac{1}{\sqrt{2}} \right) - E \left( \phi_C, \frac{1}{\sqrt{2}} \right) \right) + \frac{\sqrt{2}\mu_4}{\mu_5} (\cos \phi - \cos \phi_C) \right\}, \qquad \theta < \varphi_2,$$

$$\overline{y} = \overline{y^*} - \int_{\theta_C}^{\theta} \frac{\lambda \cos \theta d\theta}{\sqrt{\mu_4 \sin \theta + \mu_5 \cos \theta}} \left\{ = \overline{y^*} - \eta_6 \left\{ 2 \left( E \left( \phi, \frac{1}{\sqrt{2}} \right) - E \left( \phi_C, \frac{1}{\sqrt{2}} \right) \right) - \left( F \left( \phi, \frac{1}{\sqrt{2}} \right) - F \left( \phi_C, \frac{1}{\sqrt{2}} \right) \right) - \frac{\sqrt{2}\mu_5}{\mu_4} (\cos \phi - \cos \phi_C) \right\}, \qquad \theta \ge \varphi_2,$$

$$= \overline{y^*} - \eta_6 \left\{ \left( F \left( \phi, \frac{1}{\sqrt{2}} \right) - F \left( \phi_C, \frac{1}{\sqrt{2}} \right) \right) - 2 \left( E \left( \phi, \frac{1}{\sqrt{2}} \right) - E \left( \phi_C, \frac{1}{\sqrt{2}} \right) \right) - 2 \left( E \left( \phi, \frac{1}{\sqrt{2}} \right) - E \left( \phi_C, \frac{1}{\sqrt{2}} \right) \right) - \frac{\sqrt{2}\mu_5}{\mu_4} (\cos \phi - \cos \phi_C) \right\}, \qquad \theta < \varphi_2,$$

$$= \sqrt{2}\mu_5 \left( \cos \phi - \cos \phi_C \right) \right\}, \qquad \theta < \varphi_2,$$

$$= \sqrt{2}\mu_5 \left( \cos \phi - \cos \phi_C \right) \right\}, \qquad \theta < \varphi_2,$$

64 where

$$\phi = \sin^{-1} \sqrt{\frac{\sqrt{(\mu_4^2 + \mu_5^2)} - \mu_4 \sin \theta - \mu_5 \cos \theta}{\sqrt{\mu_4^2 + \mu_5^2}}},$$
(22)

$$\varphi_2 = \sin^{-1}\left(\frac{\mu_4}{\sqrt{\mu_4^2 + \mu_5^2}}\right),\tag{23}$$

$$\phi_{\rm C} = \sin^{-1} \sqrt{\frac{\sqrt{(\mu_4^2 + \mu_5^2)} - \mu_4 \sin \theta_{\rm C} - \mu_5 \cos \theta_{\rm C}}{\sqrt{\mu_4^2 + \mu_5^2}}},$$
(24)

$$\overline{x^*} = \int_{\theta_{\rm A}}^{\theta_{\rm C}} \frac{-\lambda \cos \theta d\theta}{\sqrt{\mu_1 + \mu_2 \sin \theta + \mu_3 \cos \theta}},\tag{25}$$

$$\overline{y}^* = \int_{\theta_A}^{\theta_C} \frac{-\lambda \sin \theta d\theta}{\sqrt{\mu_1 + \mu_2 \sin \theta + \mu_3 \cos \theta}},$$
(26)

$$\eta_4 = \frac{\sqrt{2}\lambda}{\left(\mu_4^2 + \mu_5^2\right)^{1/4}}, \quad \eta_5 = \frac{\sqrt{2}\lambda\mu_5}{\left(\mu_4^2 + \mu_5^2\right)^{3/4}}, \quad \eta_6 = \frac{\sqrt{2}\lambda\mu_4}{\left(\mu_4^2 + \mu_5^2\right)^{3/4}}.$$
 (27a, b, c)

The integral terms in eqs. (25) and (26) can be transformed into elliptic integral forms by setting  $\phi = \phi_C$  in eqs. (13) and (14) and replacing  $\overline{x}$  by  $\overline{x^*}$  and  $\overline{y}$  by  $\overline{y^*}$ .

Assigning a value of load  $\overline{P}$  into the foregoing elliptic integral formulations, there are five unknowns  $(\theta_A, \theta_B, \theta_C, \overline{x^*})$ , and  $\overline{y^*}$  to be evaluated for the solutions in which five equations are needed.

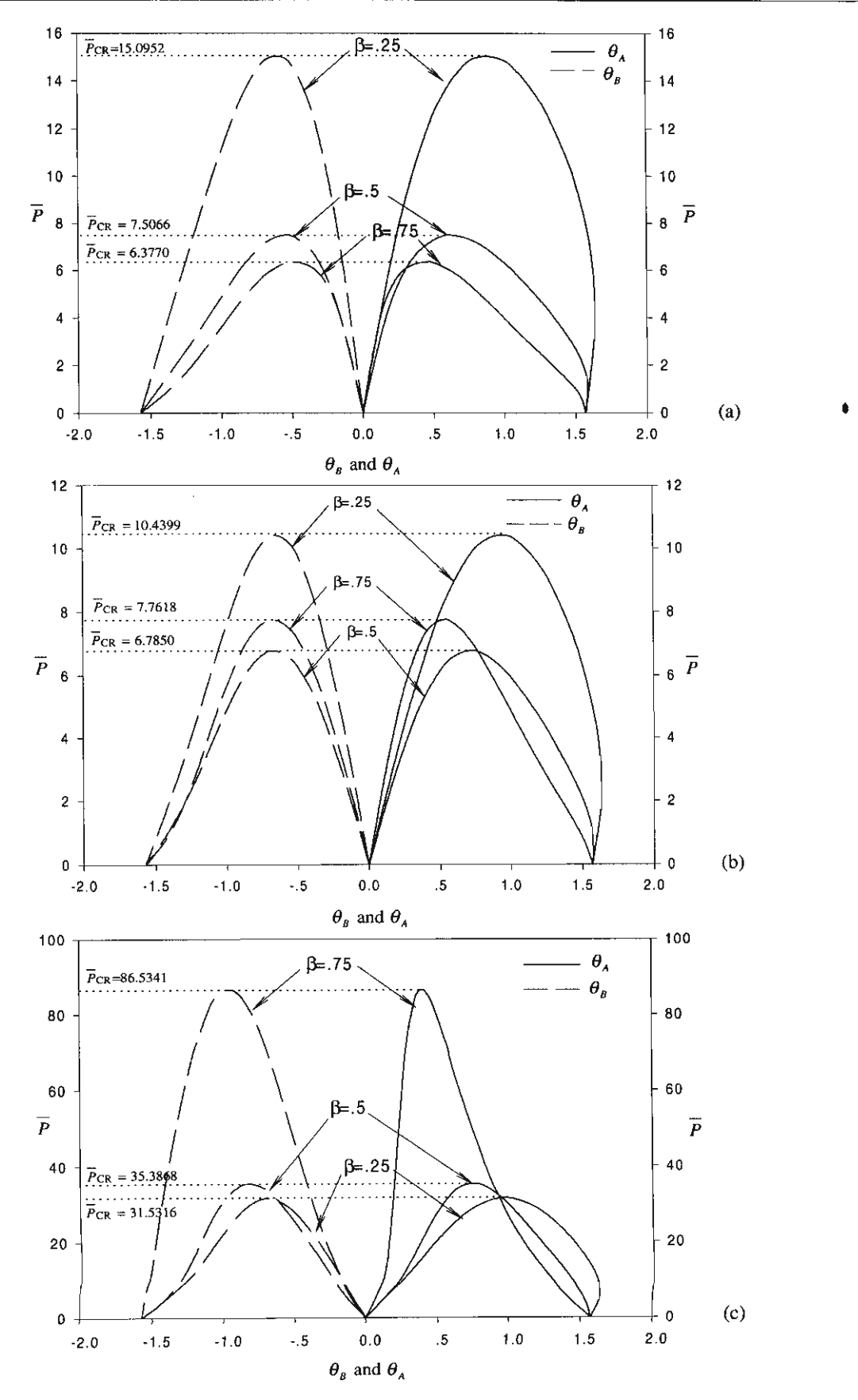


Fig. 2 Load-deflection curves when (a)  $\gamma=1.047$ ; (b)  $\gamma=0$ ; (c)  $\gamma=-1.047$ .

The first equation is obtained by setting  $\overline{x} = \overline{x^*}$  and  $\theta = \theta_C$  in eq. (13). This results in

$$f_1 = \overline{x^*} + \int_{\theta_A}^{\theta_C} \frac{\lambda \cos \theta d\theta}{\sqrt{\mu_1 + \mu_2 \sin \theta + \mu_3 \cos \theta}} = 0.$$
 (28)

The second equation is obtained by setting  $\bar{x} = 1$  and  $\theta = \theta_B$  in eq. (20).

$$f_2 = \int_{\theta_A}^{\theta_C} \frac{\lambda \cos \theta d\theta}{\sqrt{\mu_1 + \mu_2 \sin \theta + \mu_3 \cos \theta}} + \int_{\theta_C}^{\theta_B} \frac{\lambda \cos \theta d\theta}{\sqrt{\mu_4 \sin \theta + \mu_5 \cos \theta}} + 1 = 0.$$
 (29)

The third equation is obtained by using the continuity of the moment at  $\theta = \theta_C$ , which gives

$$f_3 = \sin\left(\theta_{\rm A} - \theta_{\rm C} - \gamma\right) - \frac{\sin\left(\theta_{\rm A} - \theta_{\rm B}\right)}{\cos\theta_{\rm B}}\delta + \sin\gamma = 0. \tag{30}$$

The fourth equation is obtained by setting  $\theta = \theta_B$  and  $\overline{y} = 0$  in eq. (21).

$$f_4 = \int_{\theta_A}^{\theta_C} \frac{\lambda \sin \theta d\theta}{\sqrt{\mu_1 + \mu_2 \sin \theta + \mu_3 \cos \theta}} + \int_{\theta_C}^{\theta_B} \frac{\lambda \sin \theta d\theta}{\sqrt{\mu_4 \sin \theta + \mu_5 \cos \theta}} = 0.$$
 (31)

The last equation is obtained by using the condition that the arc-length AC is always equal to  $\beta L$ :

$$f_5 = \beta + \int_{\theta_A}^{\theta_C} \frac{\lambda d\theta}{\sqrt{\mu_1 + \mu_2 \sin \theta + \mu_3 \cos \theta}} = 0. \tag{32}$$

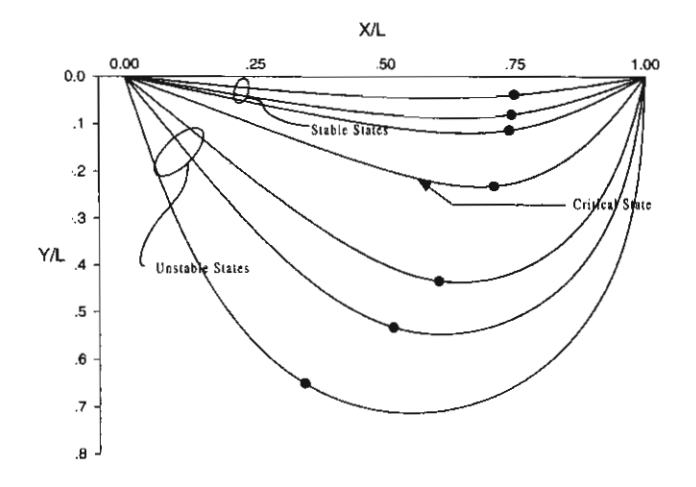
The above equations are the system of nonlinear equations and the Newton-Raphson procedure has been used to determine the solutions  $\theta_A$ ,  $\theta_B$ ,  $\theta_C$ ,  $\overline{x^*}$ , and  $\overline{y^*}$  for a given value of a load  $\overline{P}$ . Difficulties may arise when load  $\overline{P}$  is used as the control variable. The value of the critical load  $\overline{P}_{CR}$  is necessary to determine before assigning load  $\overline{P}$ . If load  $\overline{P} > \overline{P}_{CR}$  is assigned, then the iterative procedure does not converge. Therefore, an alternative procedure is recommended. In this procedure, angle  $\theta_B$  is chosen to be the control variable instead of load  $\overline{P}$ . The Newton-Raphson iterative scheme is utilized in the procedure of solving the nonlinear equations (eqs. (28)–(32). The first step is to assign a value of angle  $\theta_B$  ( $0 \le |\theta_B| \le \frac{\pi}{2}$ ) and then to estimate the initial value of  $\overline{x^*}, \overline{y^*}, \theta_A, \theta_C$ , and  $\overline{P}$ . After that, substitute these parameters into eqs. (28)–(32) and examine values of  $f_i$ , where  $i=1,\ldots,5$ , in eqs. (28)–(32). If  $|f_i| \le 10^{-14}$ , then the solutions of the nonlinear equations are correct. By varying angle  $\theta_B$ , the curves of  $\overline{P}$  versus  $\theta_A$  and  $\theta_B$  can be created.

#### 3 Results and comments

Figs. 2a–2c show the variations of load  $\overline{P}$  with respect to the end slopes  $(\theta_A \text{ and } \theta_B)$  for  $\gamma=1.047,0$  and -1.047 and  $\beta=0.25,0.5$  and 0.75. Load  $\overline{P}$  and the end rotation  $(\theta_A \text{ or } |\theta_B|)$  are initially increasing from zero. When  $\overline{P}$  reaches a critical value  $\overline{P}_{CR}$ , the maximum load that the beam can resist, an infinitesimal increase in  $\overline{P}$  will result in continuous beam motion. Beyond this critical load, as  $(\theta_A \text{ or } |\theta_B|)$  increases,  $\overline{P}$  decreases and becomes zero when  $\theta_A=|\theta_B|=\frac{\pi}{2}$ . At this point, the beam shows symmetrical configuration about mid-span of the beam and the total arc-length  $\overline{L}$  is 2.1884 [2,8] for every value of  $\gamma$  and  $\beta$ . Observing the curves in Figs. 2a, 2b, and 2c it can be seen that, for a given value of load  $\overline{P}$  and angle  $\gamma$ , there are two values of angle  $\theta_A$  and  $\theta_B$  representing two states of the equilibrium configurations. The configuration with smaller  $|\theta_B|$  (or  $\theta_A$ ) is stable state while larger  $|\theta_B|$  (or  $\theta_A$ ) is unstable state. It is worth noticing that  $\overline{P}_{CR}$  tends to decrease as  $\beta$  increases for  $\gamma \geq 0$ , but  $\overline{P}_{CR}$  increases as  $\beta$  increases for  $\gamma$  is negative. This can be explained that force P changes from pushing to pulling with respect to the support A. Thus, the left portion of the beam is in tension state rather than in compression state. The deformed shapes of beams corresponding to  $\gamma=-1.047$  and  $\beta=0.75$  is shown in Fig. 3.

The relationship between critical load  $\overline{P}_{CR}$  (using Dichotomous search algorithm [12]) and  $\beta$  is shown in Table 1, in which the value of position  $\beta$  is varied between 0.1 and 0.9, and angle  $\gamma=1.5707, 1.047, 0.5235, 0, -0.5235$ , and -1.047. Table 1 shows that the solution for  $\overline{P}_{CR}$  does not exist for  $\beta=0.9$  and  $\gamma=-1.047$ . The reason for this is that the beam changes from compression state to tension state. It also shows that  $\overline{P}_{CR}$  decreases with increasing  $\beta$  and then increases after a certain value of  $\beta$  for all values  $\gamma$  except  $\gamma=\pi/2$ . When  $\gamma=\pi/2$  and  $\beta=0.9$  the beam behaviour is almost identical to a classical pin-ended column under axial compressive force and the corresponding  $\overline{P}_{CR}$  is close to  $\pi^2$  or the well-known Euler buckling load. The results of  $\overline{P}_{CR}$  versus  $\beta$  as shown in Table 1 are plotted in Figs. 4a and 4b.

The paths of the follower force  $(x^*$  and  $y^*)$  for six values of  $\gamma$  (1.5707, 1.047, 0.5235, 0, -0.5235, -1.047) are shown in Fig. 5 for  $\beta=0.25, 0.5$ , and 0.75. For small  $\beta$  the paths almost coincide with each other and they become more separated for larger  $\beta$ . Table 2 shows comparison results of the follower force and non-follower force [2] of equal magnitude for  $\gamma=0$  and  $\beta=0.5$ . The results are close to each other when the beams are in stable state, but they are distinct in unstable state. Some of these results are demonstrated in Fig. 6 which shows comparisons of the deformed shapes of beams for  $\overline{P}=6.3114$  (stable equilibrium) and for  $\overline{P}=4.6525$  (unstable equilibrium).



Equilibrium State	Loading Steps = -1.047 P
	$\gamma_{10.0000}$
Stable State	30.0000
	50.0000
Critical State	86.5341
	50.0000
Unstable State	30.0000
	10.0000

Fig. 3 Deformed shapes of the beam for  $\beta = 0.75$  and  $\gamma = -1.047$ .

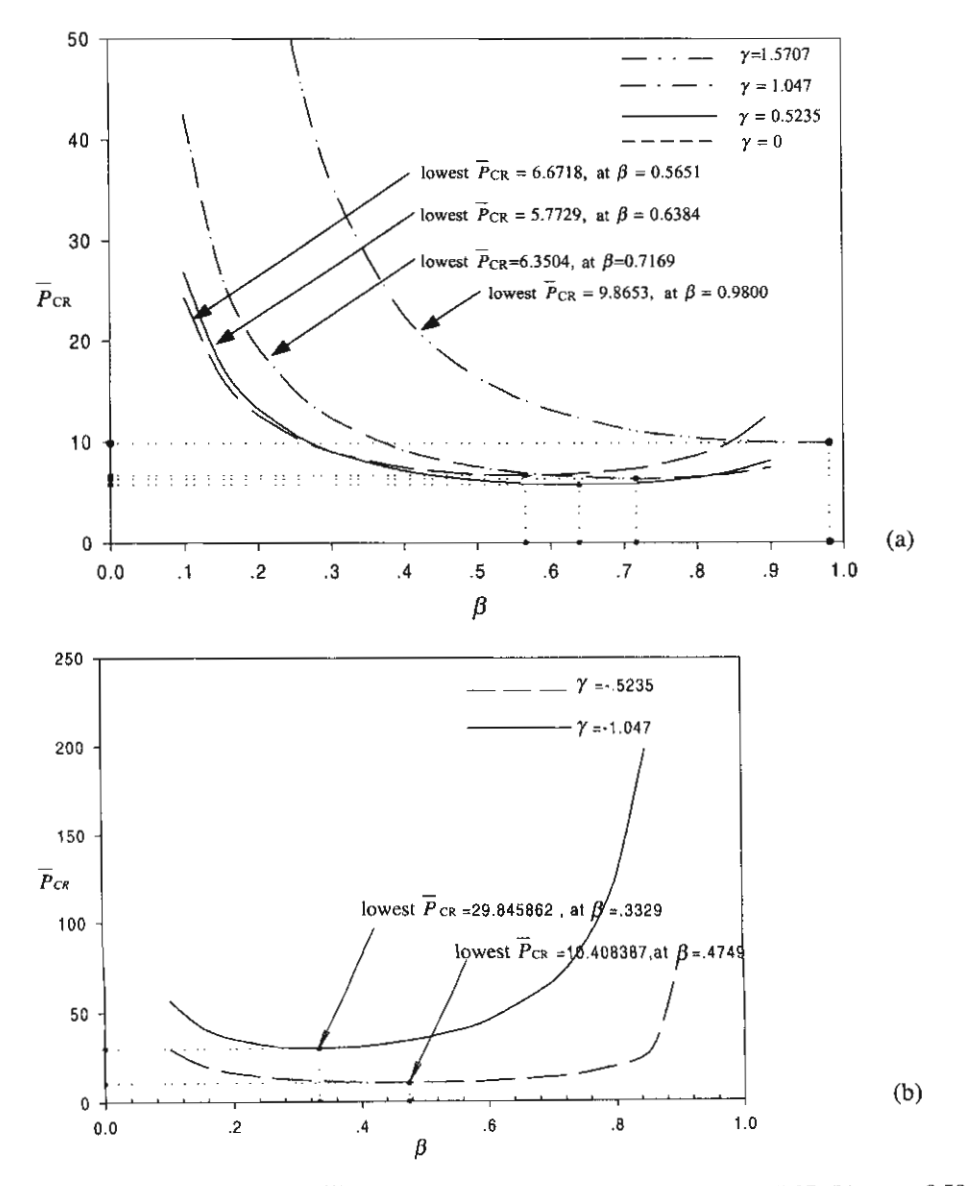


**Fig. 4** Relationship between  $\overrightarrow{P}_{CR}$  and  $\beta$  for (a)  $\gamma = 1.047, 0.5235, 0$ , and 1.5707; (b)  $\gamma = -0.5235, -1.047$ .

**Table 1** Relationship between  $\overline{P}_{CR}$  and  $\beta$ .

β	$\overline{P}_{ ext{CR}}$									
	$\gamma = 1.5707$	$\gamma = 1.047$	$\gamma=0.5235$	$\gamma = 0$	$\gamma = -0.5235$	$\gamma = -1.047$				
0.1	266.8828	42.4977	26.8546	24.3682	29.5311	56.5664				
0.2	73.2403	19.4413	13.3125	12.6679	16.1726	34.8599				
0.3	36.0234	12.3296	9.0532	9.0258	12.1852	30.0855				
0.4	22.6555	9.1427	7.1345	7.4516	10.6944	30.7485				
0.5	16.4151	7.5066	. 6.1914	6.7850	10.4393	35.3868				
0.6	13.1021	6.6685	5.8043	6.7047	11.2213	45.3139				
0.7	11.2659	6.3571	5.8582	7.2067	13.4938	66.3166				
8.0	10.3047	6.5267	6.4433	8.6471	19.3419	122.3383				
0.9	9.9192	7.4364	8.0959	12.7527	79.3274	NA				

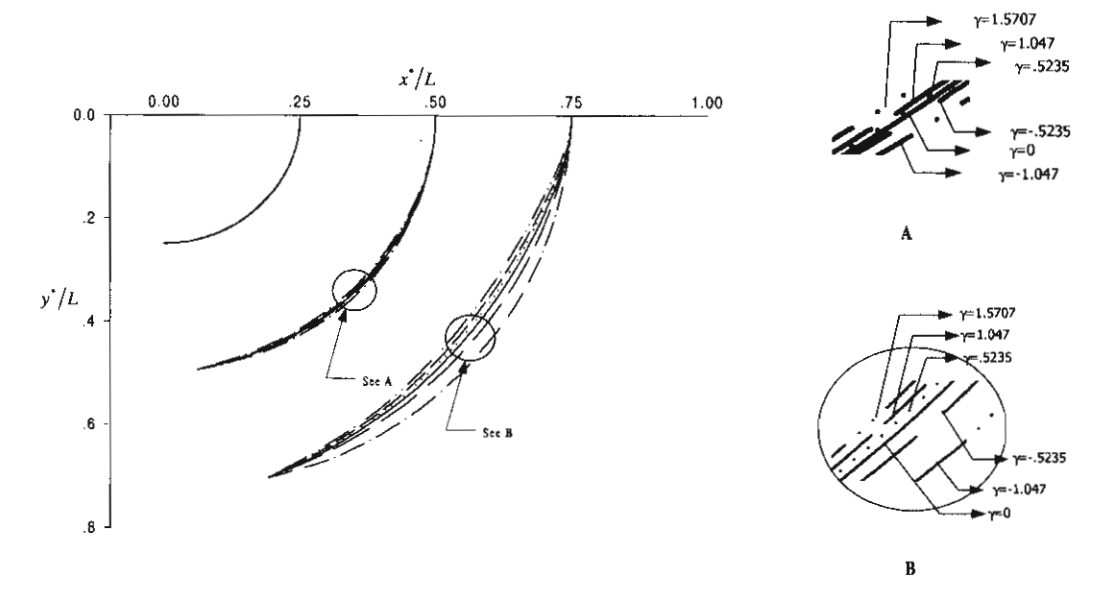


Fig. 5 Paths of the follower force at  $\beta = 0.25, 0.5$ , and 0.75.

**Table 2** Comparison of the results between follower and non-follower force [1] for  $\gamma = 0$  and  $\beta = 0.5$ .

	$ heta_{A}$			$ heta_{ extsf{B}}$		$\overline{Y}_{Max}$	$\overline{L}$		
$\overline{P}$	Follower force	Non-follower force [2]	Follower force	Non-follower force [2]	Follower force	Non-follower force [2]	Follower force	Non-follower force [2]	
2.7084	0.1750	0.1745	-0.1740	-0.1745	0.0584	0.0584	1.0082	1.0081	
4.9358	0.3523	0.3491	-0.3449	-0.3491	0.1182	0.1184	1.0332	1.0332	
6.3114	0.5287	0.5236	-0.5051	-0.5236	0.1789	0.1816	1.0749	1.0771	
6.6571	0.6177	0.6891	-0.5815	-0.6891	0.2102	0.2503	1.1026	1.1431	
6.0206	0.9887	0.8727	-0.8694	-0.8727	0.3491	0.3270	1.2704	1.2369	
4.6525	1.2044	1.0472	-1.0242	-1.0472	0.4428	0.4158	1.4187	1.3676	
2.9334	1.4148	1.2217	-1.1911	-1.2217	0.5601	0.5225	1.6328	1.5497	
0.6565	1.5812	1.3963	-1.4660	-1.3963	0.7659	0.6565	2.0458	1.8084	

109

111

112

113

117

118

119

120

121

123

125

127

128

129

130

131

132

133

134

135

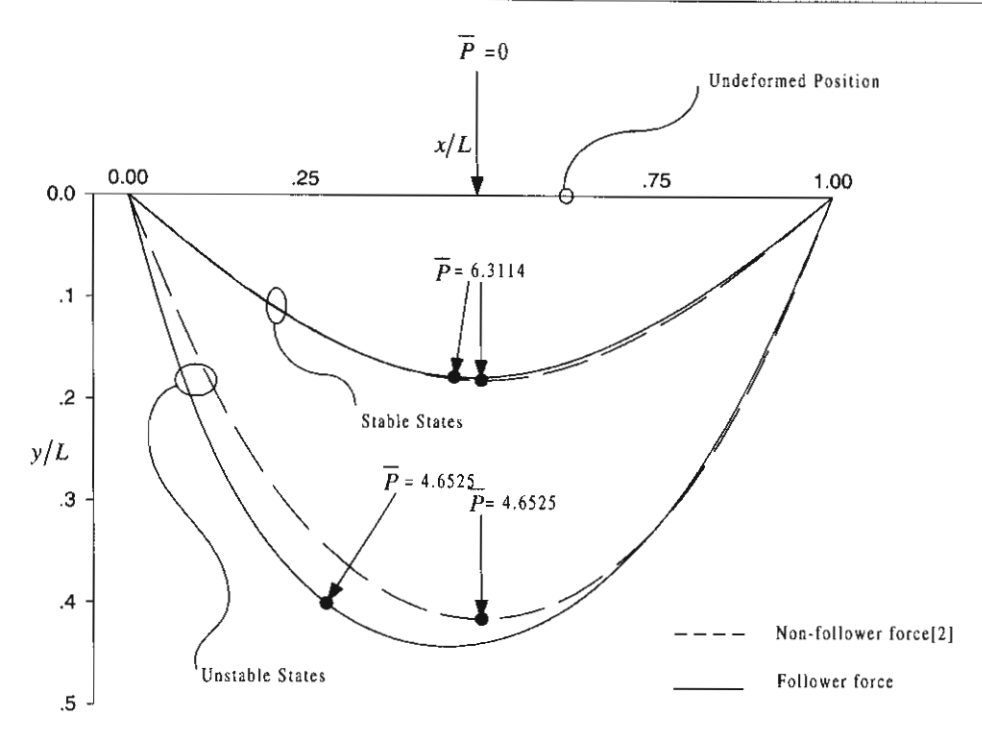


Fig. 6 Deformed shapes of beam subject to follower force ( $\gamma = 0$ ) and non-follower vertical force at mid-span,

#### 4 Conclusion

Exact-closed form solutions using elliptic integrals are obtained for elastica of the beam with variable arc-length subjected to an inclined follower force. The beam exhibits two equilibrium configurations when inclined angle  $(\gamma)$  is positive or small negative value for all values of location of applied force  $(\beta)$ , but it has only one equilibrium configuration for large negative value of  $\gamma$  and large value of  $\beta$ . Comparing the results with that of the beam subject to non-follower (vertical) force, they deviate when both beams are in unstable equilibrium configurations.

Acknowledgements This work was financially supported by Thailand Research Fund (TRF) under Grant No. RTA/03/2543.

Author, please note: & in the reference list means: this journal is not contained in the INSPEC-list and cross-linking will not work. Please check.

Author, please clarify missing parts of the references; the black squares ( should be replaced by the respective element (e.g., initials or author's name; abbreviated journal title, volume number, pages and year for journal citations; book and/or series title, editors, publishing house, place of publication and year for book citations)

#### References

- S. Chucheepsakul and T. Huang, Finite element solution of variable-arc-length beams under a point load, J. Struct. Eng. 123(7), 968-970 (1997).
- [2] S. Chucheepsakul, G. Thepphitak, and C. M. Wang, Large deflection of simple variable-arc-length beam subjected to a point load, Struct. Eng. Mech. 4(1), 49-59 (1996).
- [3] C. M. Wang, K. Y. Lam, X. Q. He, and S. Chucheepsakul, Large deflection of an end supported beam subjected to a point load, Int. J. Non-Linear Mech. 32, 63-72 (1996).
- [4] W. Hartono, Elastica of cantilever beam under two follower forces, J. Adv. Struct. Eng. 1(2), 159-165 (1997).
- [5] B. N. Rao and G. V. Rao, Large deflections of a cantilever beam subjected to a rotational distributed loading, Forsch. Ingenieurw. 55(4), 116–120 (1989).
- [6] B. S. Shwartsman, Direct method for analysis of flexible beam under a follower load, in: Proceedings of Computational of Mechanics for the Next Millennium, ■■, 1999, ■■, Vol. 1, pp. 155–160.
- [7] B. N. Rao, B. P. Shastry, and G. V. Rao, Large deflections of cantilever beam subjected to a tip concentrated rotational load, J. Aeronaut. 90(897), 262–266 (1986).
- [8] C. M. Wang, K. Y. Lam, and X. Q. He, Instability of variable arc-length elastica under follower force, Mech. Res. Commun. 25(2), 189-194 (1998).

138

139

140

141

- [9] W. Hartono, Behavior of variable length elastica with frictional support under follower force, Mech. Res. Commun. 27(6), 653–658 (2000).
- [10] S. Chucheepsakul and T. Monprapussorn, Divergence instability of variable-arc-length elastica pipes transporting fluid, J. Fluid Struct. 14, 895–916 (2000).
- [11] P.F. Byrd and M. D. Friedman, Handbook of Elliptic Integrals for Engineers and Scientists (Springer-Verlag, Berlin, New York, 1971).
- [12] J. Kempf, Numerical Software Tool in C (Prentice-Hall, Inc., Englewood Cliffs, New Jersey, 1987).

# Large Amplitude Three-Dimensional Free Vibrations of Inclined Sagged Elastic Cables

NARAKORN SRINIL1, GIUSEPPE REGA2.\*, and SOMCHAI CHUCHEEPSAKUL1

<sup>1</sup>Department of Civil Engineering, King Mongkut's University of Technology Thonburi, Bangmod, Toongkru, Bangkok 10140, Thailand

(Received: 2 January 2003; accepted: 23 July 2003)

Abstract. The nonlinear characteristics in the large amplitude three-dimensional free vibrations of inclined sagged elastic cables are investigated. A model formulation which is not limited to cables having small sag-to-span ratios and takes into account the axial deformation effect is considered. Based on a multi-degree-of-freedom cable model, a finite difference discretization is employed within a numerical solution of the governing equations of three-dimensional coupled motion. Various numerical examples of arbitrarily inclined sagged cables with initial out-of-plane or in-plane motions are carried out for the case of a specified end tension. The major findings consist of highlighting the extent of two-and three-dimensional nonlinear couplings, the occurrence of nonlinear dynamic tensions, and the meaningfulness of modal transition phenomena ensuing from the activation of various internal resonance conditions. The influence of cable inclination on the nonlinear dynamic behavior is also evaluated. Comprehensive discussion and comparison of large amplitude free vibrations of horizontal and inclined sagged cables are presented.

Keywords: Inclined cable, multi-degree-of-freedom model, large amplitude three-dimensional free vibration, internal resonance, modal transition, dynamic tension.

#### 1. Background and Motivation

Problems related to the vibrations of cable structures are encountered in a wide variety of engineering applications [1]. Amongst them, large amplitude nonlinear vibrations are of great theoretical and practical interest. Indeed, according to linear theory [2, 3], the natural frequencies and mode shapes are independent of vibration amplitude, but if the amplitudes become large enough to introduce significant nonlinear behaviors, this does not hold any more, and cable nonlinear dynamics have to be analyzed.

Most research studies in the field have been devoted to a suspended cable with fixed supports at the same level. Nonlinear free and forced vibrations have been widely investigated both theoretically [4–16] and experimentally [17, 18]. The importance of internal resonance conditions occurring in multi-degree-of-freedom (MDOF) systems when the natural frequencies are commensurable with each other has been highlighted. Internal resonances cause strong modal coupling effects and result in multi-mode and multi-frequency responses. In addition, they may cause mode transition phenomena where the cable vibrates, e.g. in a purely free planar dynamics, with two companion modes which interact and combine with each other in a hybrid mode during time evolution [16].

<sup>&</sup>lt;sup>2</sup>Dipartimento di Ingegneria Strutturale e Geotecnica, Università di Roma La Sapienza, via A. Gramsci 53, I-00197 Roma, Italy

<sup>\*</sup> Author for correspondence. E-mail: giuseppe.rega@uniroma.it.

Nevertheless, in several practical applications, cable structures can span over great distances, and inclined sagged cables are encountered. When such a cable is subjected to overall environmental loading, such as wind force or hydrodynamic drag excitations, it may experience inherently three-dimensional (3-D) vibrations. Therefore, a 3-D nonlinear dynamic analysis of inclined sagged cables is needed to determine the main features of the relevant response.

Linear vibrations of inclined cables [3, 19] exhibit interesting dynamic features, such as frequency avoidance (or veering) and the associated hybrid mode shapes [3, 19], which characterize them (as well as other asymmetric structural systems) with respect to horizontal symmetric cables. As regards nonlinear vibrations, very little work has appeared regarding both theoretical formulation and investigation of structural behavior. Cai and Chen [20] investigated parametric and external resonances in an inclined elastic cable for application to a stack/wire system. Warnitchai et al. [21] developed a nonlinear dynamic model of an inclined cable in the framework of a cable-structure system. Zhao et al. [22] made a perturbation analysis of the coupling between in-plane and forced out-of-plane vibrations in a two-degreeof-freedom model of inclined cable under 1:1 internal resonance. In all cases, very small values of cable sag-to-span ratios were considered. Takahashi and Konishi [23] examined nonlinear free vibrations of inclined sagged cables and briefly discussed geometrically nonlinear effects arising from system quadratic and cubic nonlinearities, but they did not address such important effects as cable inclination, cable extensibility, and internal resonances. Their effects on the system dynamic behavior will be discussed in this study. Indeed, due to the asymmetry of equilibrium configuration of inclined sagged cables - and to the ensuing linear dynamics features - their nonlinear dynamic characteristics may be different from those characterizing horizontal cables. Therefore, a relevant systematic investigation seems to be worthwhile from both a theoretical and a technical point of view.

The nonlinear characteristics of the large amplitude 2-D and 3-D free vibrations of elastic cables with arbitrary sags and arbitrary inclinations are analyzed numerically. To this aim, a realistic 3-D cable model accounting for cable extensibility and large sag effects [16] is implemented for inclined cables (Section 2). A MDOF model is then considered by discretizing through finite differences and solving the nonlinear equations of 3-D coupled motion (Section 3). Qualitative and quantitative results obtained under prescribed initial conditions for different values of the elasto-geometrical cable parameter are discussed in detail, distinguishing between 3-D nonlinear coupling (Section 4) and modal transition phenomena occurring in planar nonlinear dynamics (Section 5). Emphasis is placed on investigating: (i) how significant 3-D and 2-D nonlinear interactions are; (ii) which internal resonances are actually activated at different frequency avoidance regions; and (iii) whether and how a dominant internal resonance plays a major role in system nonlinear dynamics. In turn, the influence of cable inclination is analyzed in Section 6, by looking at the overall nonlinear behaviors against those previously outlined for the horizontal cable [16]. The paper ends with a summary of results and with some general conclusions.

#### 2. Cable Model and Equations of Motion

Figure 1 illustrates the inclined cable under consideration with horizontal span  $X_H$  and vertical span  $Y_H$ . Cable inclination, measured clockwise from the horizontal span to the cable chord line between two supports at different level, is represented by the angle  $\theta_C$ . The horizontal

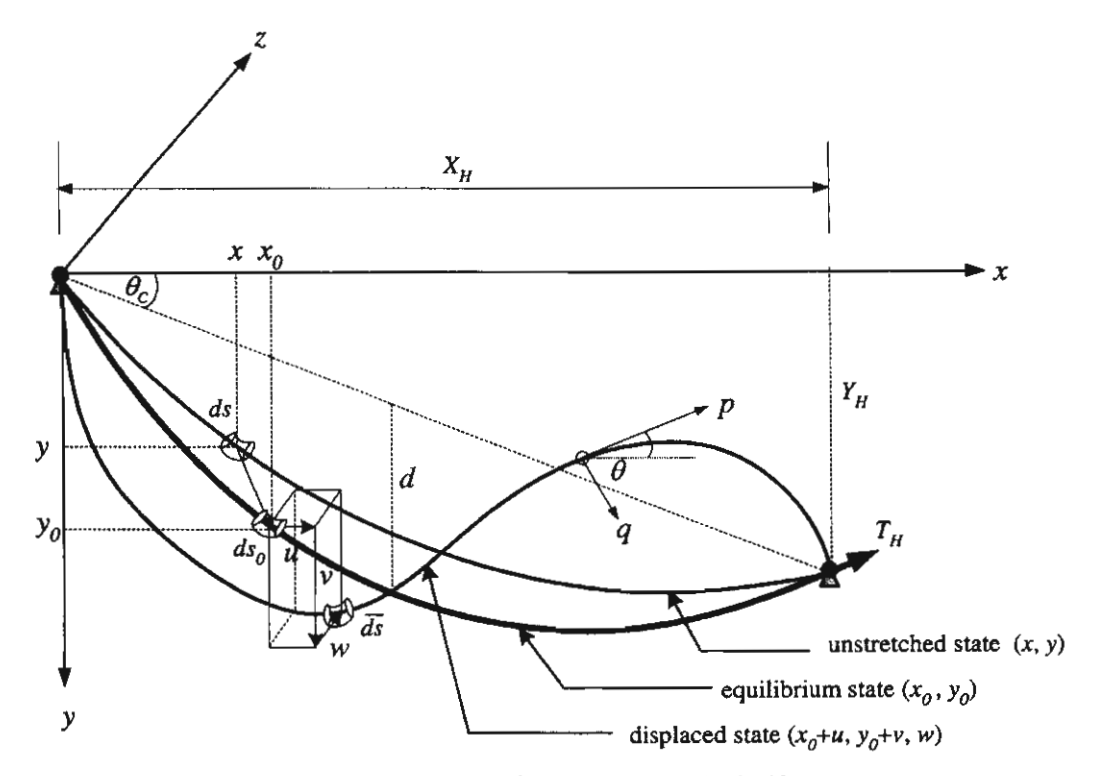


Figure 1. Reference configurations of an inclined cable.

cable can be obtained by setting  $\theta_C$  or  $Y_H$  equal to zero. The upper left end is fixed while the lower right end is the position where the specified tension  $T_H$  is applied to maintain the cable in its static configuration.

A Cartesian (global) coordinate reference frame fixed in 3-D space is established for describing displacement components and cable tension. As defined in [16], three distinct configurations of the cable element are considered, namely the unstretched (natural) state ds, the stretched (equilibrium) state ds<sub>0</sub>, and the displaced (dynamic) state d $\bar{s}$ , denoting with u, v and w and the components of displacement measured from the equilibrium configuration  $(x_0, y_0)$  in the longitudinal X, vertical Y and out-of-plane Z directions, respectively. A local reference frame attached to the cable at any point is also employed to characterize the natural mode shapes of the cable. Introducing orthogonal coordinates, the local displacement field for the in-plane motion is described using the two variables p and q in the tangential and normal directions, which in terms of global displacement components read:

$$p = u \cos \theta + v \sin \theta, \quad q = -u \sin \theta + v \cos \theta,$$
 (1)

where  $\sin \theta$  and  $\cos \theta$  are functions of both space and time given by

$$\cos \theta = \frac{\mathrm{d}x_0 + \mathrm{d}u}{\mathrm{d}\bar{s}} = \frac{(1+u')}{\sqrt{(1+u')^2 + (y_0' + v')^2 + w'^2}},\tag{2}$$

$$\sin \theta = \frac{\mathrm{d}y_0 + \mathrm{d}v}{\mathrm{d}\bar{s}} = \frac{(y_0' + v')}{\sqrt{(1 + u')^2 + (y_0' + v')^2 + w'^2}}.$$
 (3)

Here,  $\theta$  is the angle in the vertical plane between the horizontal line and the tangential displacement vector at any point along the cable, whereas a superscript prime indicates differentiation with respect to  $x_0$ . Of course, the out-of-plane displacement w is independent of any coordinate system.

In deriving the equations of motion by the virtual work-energy principle, the cable is considered to be a perfectly flexible, homogeneous, linearly elastic, one-dimensional continuum with negligible torsional, bending and shear rigidities. Therefore, the strain energy is due only to stretching of the cable axis. The total strain of the cable centerline at the displaced state reads:

$$\bar{\varepsilon} = \frac{d\bar{s} - ds}{ds} = \frac{(1 + \varepsilon_0)}{\sqrt{1 + y_0'^2}} \sqrt{(1 + u')^2 + (y_0' + v')^2 + w'^2} - 1,$$
(4)

where  $\varepsilon_0$  is the initial static strain. Following [16], the governing equations of motion in the global coordinate system read

$$\left(\frac{EA + EA(1 + \varepsilon_0)u'}{\sqrt{1 + y_0'^2}} - \frac{EA(1 + u')}{\sqrt{(1 + u')^2 + (y_0' + v')^2 + w'^2}}\right)' = \frac{w_C}{g(1 + \varepsilon_0)} \ddot{u},\tag{5}$$

$$\left(\frac{EAy_0' + EA(1+\varepsilon_0)v'}{\sqrt{1+y_0'^2}} - \frac{EA(y_0' + v')}{\sqrt{(1+u')^2 + (y_0' + v')^2 + w'^2}}\right)' = \frac{w_C}{g(1+\varepsilon_0)} \ddot{v},$$
(6)

$$\left(\frac{EA(1+\varepsilon_0)w'}{\sqrt{1+y_0'^2}} - \frac{EA(w')}{\sqrt{(1+u')^2 + (y_0'+v')^2 + w'^2}}\right)' = \frac{w_C}{g(1+\varepsilon_0)}\dot{\ddot{w}},\tag{7}$$

where the dot denotes differentiation with respect to time t, g is the gravitational force, E is Young's modulus of the cable, A is the cross-sectional area, and  $w_C$  is the cable weight per unit unstretched length. This system, involving geometrical nonlinearities and coupled through the static equilibrium configuration, is useful for analyzing 3-D, undamped, large amplitude free vibrations under specified initial conditions. The boundary conditions corresponding to hinged-hinged cable ends are

$$u(0,t) = v(0,t) = w(0,t) = u(X_H,t) = v(X_H,t) = w(X_H,t) = 0.$$
(8)

It is worth noticing that Equations (5–8) reduce themselves to those obtained by Leissa and Saad [24] in the case of a horizontal string (i.e., no initial sag) vibrating with large amplitude in the longitudinal and vertical directions. Also, they are similar to the equations of motion obtained by Takahashi and Konishi [23] for an arbitrarily sagged and inclined cable, which however are formulated in the local coordinate system instead of the global one used in this study.

#### 3. Numerical Investigation

Prior to analyzing the nonlinear free vibration characteristics of cable system, the equilibrium configuration with arbitrary sag and inclination angle, and the static tension at any point,

are evaluated. The nonlinear equilibrium equations (see, e.g., [16]) were successfully solved by the shooting method [25] in conjunction with the fourth-order Runge-Kutta integration scheme for the problem of a specified end tension [25, 26].

A finite difference discretization, coupled with a predictor-corrector method, was then employed to solve Equations (5-8). Central differences were used for approximating all spatial derivatives as well as second-order temporal derivatives, leading to an explicit discrete form of the governing equations for the unknown displacements. The displacements obtained were then used as initial trial value of the next process by means of a predictor-corrector iterative algorithm. The simulation results over each time step were iterated until the convergence was satisfactory, and the allowable tolerance was achieved by the criterion of the second order vector norm. The values of space and time discretizations were also examined through convergence tests based on the desired accuracy in the solution. Using this numerical technique, accurate results were obtained for horizontal cables in [16], where good agreement with theoretical predictions [27] of system dynamics is highlighted. The major advantage of using a finite difference approach is in capturing the spatial richness of the response and its time-varying content, as well as in obtaining reliable predictions of the significant involvement of higher-order modes, which ensues from the considered MDOF model.

A continuous cable similar to that of Srinil et al. [16] is used in the numerical simulation. The relevant parameter values are as follows:  $A = 0.1159 \text{ m}^2$ , cable density equal to  $8,337.9 \text{ kg/m}^3$ ,  $E = 1.794 \times 10^8 \text{ kN/m}^2$ . The cable is discretized into 50 segments and the integration is performed with a time step equal to 0.00001. The horizontal span  $X_H$ , equal to 850 m, is fixed, whereas the vertical span  $Y_H$  is varied to attain an arbitrary inclination angle. The extent of 2-D and/or 3-D nonlinear interactions in cable motion strongly depends on system parameters, but it is always enhanced by the occurrence of some internal resonance conditions. Accordingly, attention is focused on internally resonant cables.

Internal resonances are characterized by (perfect) tuning of system natural frequencies, a situation being nearly realized for inclined cables in the so-called avoidance regions of natural frequencies  $\omega/\pi$ , which occur for well established values of the system elasto-geometrical parameter  $\lambda/\pi$  [2, 3]. This parameter accounts for also the cable inclination angle  $(\theta_C)$  and is defined [3] as  $\lambda^2 = [(w_C S_0)^2 E A / T_a^3] \cos(\theta_C)$ , in which  $S_0$  is the cable equilibrium length and  $T_a$  is the static tension at the cable nodal point where the static angle is equal to  $\theta_C$ . Note that for given values of EA,  $w_C$ , and  $\theta_C$ ,  $\lambda^2$  (the sag) mostly depends on the applied  $T_a$  ( $T_H$ ), the greater  $\lambda^2$  (sag) the smaller  $T_a$  ( $T_H$ ), whereas  $S_0$  slightly affects  $\lambda^2$  because most of the considered cables have small initial strain.

In Figure 2, nondimensionalizing the natural frequencies with respect to the fundamental frequency of an equally inclined taut string, the frequency spectrum for the cable with  $\theta_C$ 30°, obtained by a finite element analysis [26], is exemplified for the first three avoidance regions ( $\lambda \approx 2n\pi$ , n=1,2,3). Over each avoided crossing (or veering) region, two in-plane frequencies (solid lines: I) become nearly close - but never equal - to each other, and the corresponding modes become hybrid (H1-H6) due to a mixture of symmetric/anti-symmetric modal shapes. In contrast, the out-of-plane frequencies (dashed lines: O) are independent of the system parameter  $\lambda/\pi$ . Various frequency commensurabilities do coexist over the veering regions. For instance, at first avoidance point  $(\lambda/\pi \approx 2)$  the natural frequencies of the first (H1) and second (H2) hybrid in-plane modes are markedly close to each other and nearly twice the natural frequency of the first symmetric out-of-plane mode (O1). Moreover, the angle  $\theta_C$ has a significant effect on the extent of the avoided crossing zone, as illustrated in Figure 3 for the first avoided crossing. The approaching frequencies are seen to remain as more apart from

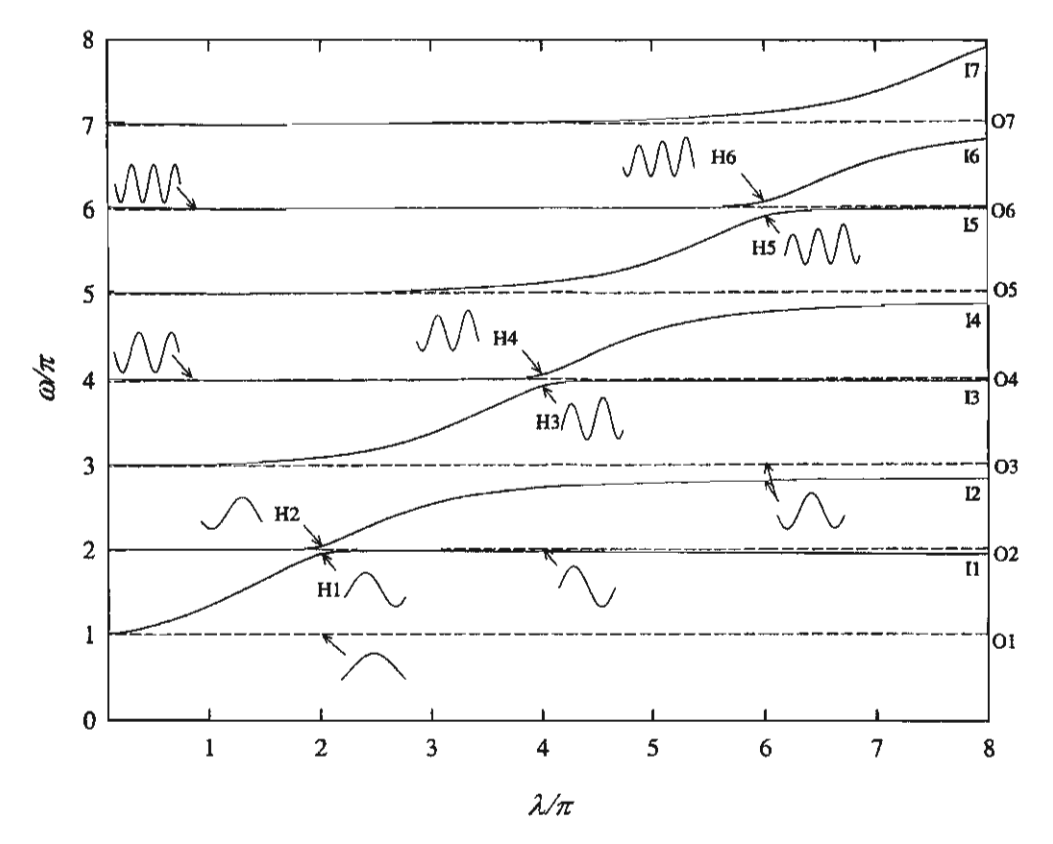


Figure 2. Natural frequency spectrum around the first three avoidance regions for inclined cable with  $\theta_C = 30^\circ$ : — in-plane frequencies (I); - - - out-of-plane frequencies (O).

each other as greater  $\theta_C$  is: this corresponds to a progressive decrease of the frequency ratio of first and second hybrid modes (Table 1), which is approximately equal to 0.958, 0.924 and 0.878 for  $\theta_C = 30^\circ$ , 45° and 60°, respectively.

Considering the first three avoidance regions and three different values of  $\theta_C$ , the cable properties obtained by varying the specified tension  $T_H$  are given in Table 1. For each value of the cable parameter  $\lambda/\pi$ , they include, besides  $T_H$  and  $S_0$ , the maximum static tension  $T_M$ , and the cable sag-to-span ratio  $d/X_H$  corresponding to different inclination angles. As the latter increases, the cable sag-to-span ratio becomes greater. The linear out-of-plane and in-plane frequencies are also documented for all cases. The properties listed in Table 1 are representative of long, either shallow or large-sagged cables, as well as low-, medium- or high-inclined cables.

To the aim of highlighting the extent of nonlinear interactions, single-mode initiations are considered and the involvement of other modes due to some internal resonances is investigated. Nonzero values of initial displacements and zero values of initial velocities are prescribed. The initial displacement vectors are assumed proportional to the linear eigenfunction vectors [26] of either in-plane or out-of-plane modes, normalized in such a way that the maximum amplitude of nodal displacement is equal to unity, and they are subsequently multiplied by the initial amplitude (a) specified in each case. It is important to note that the

Table 1. Cable properties and corresponding linear frequencies.

$N\pi$	$\theta_c$	$T_{\scriptscriptstyle H}$	$T_M$	d/X <sub>H</sub>	S <sub>o</sub>			Linear	natural fi	Linear natural frequencies (Hz)	s (Hz)		
	(deg.)	(kN)	(KN)		(m)	Out-of-p	Out-of-plane: O			In-plane: I	ane: I		. –
						10	05	11	12	13	14	15	16
	30	30480	35138	0.041	984.0	0.093	0.187	0.182 <sup>H</sup>	0.190 <sup>H</sup>	0.288	0.373	0.468	0.560
2	45	28790	36858	0.062	1205.2	0.076	0.152	0.146 <sup>H</sup>	0.158 <sup>B</sup>	0.236	0.304	0.382	0.457
	9	26200	40135	0.124	1704.4	0.054	0.108	0.101 <sup>H</sup>	0.115 <sup>H</sup>	0.167	0.216	0.270	0.324
	30	18700	23356	0.065	8.786	0.074	0.148	0.146	0.202	0.290 <sup>H</sup>	н006.0	0.379	0.444
4	45	17100	25164	0.098	1209.9	090.0	0.121	0.118	0.165	0.236 <sup>H</sup>	0.250 <sup>H</sup>	0.310	0.363
	60	14830	28797	0.194	1711.0	0.043	0.086	0.082	0.117	0.166 <sup>H</sup>	0.184 <sup>H</sup>	0.223	0.259
	30	13985	18639	980.0	992.4	0.065	0.129	0.126	0.182	0.257	0.308	0.381 <sup>H</sup>	0.392 <sup>H</sup>
9	45	12550	20612	0.128	1215.4	0.053	0.106	0.102	0.148	0.209	0.253	0.311 <sup>H</sup>	0.328 <sup>H</sup>
	09	10240	24204	0.256	1719.3	0.038	0.075	0.070	0.104	0.147	0.180	0.221 <sup>H</sup>	0.245 <sup>H</sup>
H. hwhrid	H. hishrid mode at frequence	trion conditions	1										

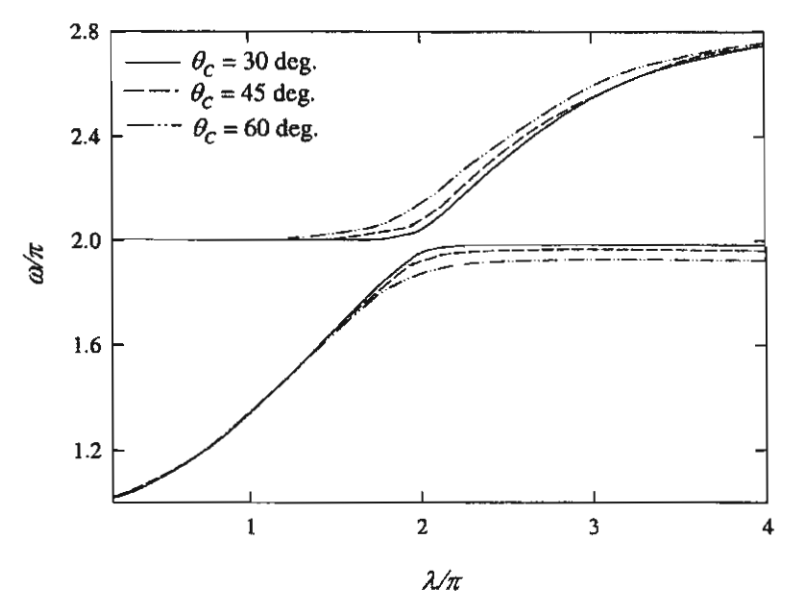


Figure 3. Effect of cable inclination on the extent of first avoided crossing region.

assigned amplitude must be large enough to produce significant nonlinear behavior, but in any case such to avoid compression in the cable.

In the following, analysis results are presented and discussed in terms of three different – and complementary – representation tools: (i) time histories of the responses at selected points giving the most significant contributions to the overall dynamics; (ii) time-varying spatial profiles (displayed *versus* the cable arc length in the local coordinate system) selected within the neighbourhood of the time instant where the nonlinear dynamic responses reveal remarkable changes with respect to prescribed initiations, due to any kind of nonlinear interaction; (iii) frequency response measures suitable to describe specific features of system dynamics. Response amplitudes and time are nondimensionalized relative to the horizontal span and to the period of each prescribed mode, respectively. Of great importance from the engineering viewpoint, the cable total tension response (summation of static and dynamic tensions) is also evaluated by the present model, which can capture both spatial and temporal variations in cable tension. This is accomplished by calculating  $T_D = E A\bar{\varepsilon}$  from the displacements through Equation (4); consequently, their maximum and minimum values relative to the maximum static tension ( $T_M$ ) are plotted.

In the following, we will start by analyzing the 3-D nonlinear coupling ensuing from application of an out-of-plane mode as initial displacement condition.

### 4. Features of Three-Dimensional Nonlinear Coupling

Let us first consider initial condition of the first symmetric out-of-plane (first S-O) mode with a=10 m at first avoidance ( $\lambda/\pi\approx 2$ ) for the cable with  $\theta_C=45^\circ$ . The longitudinal, vertical and out-of-plane responses at quarter span from left (solid line) and right (dashed line) ends, and the cable maximum (solid line) and minimum (dashed line) total tension responses, are plotted in Figure 4.

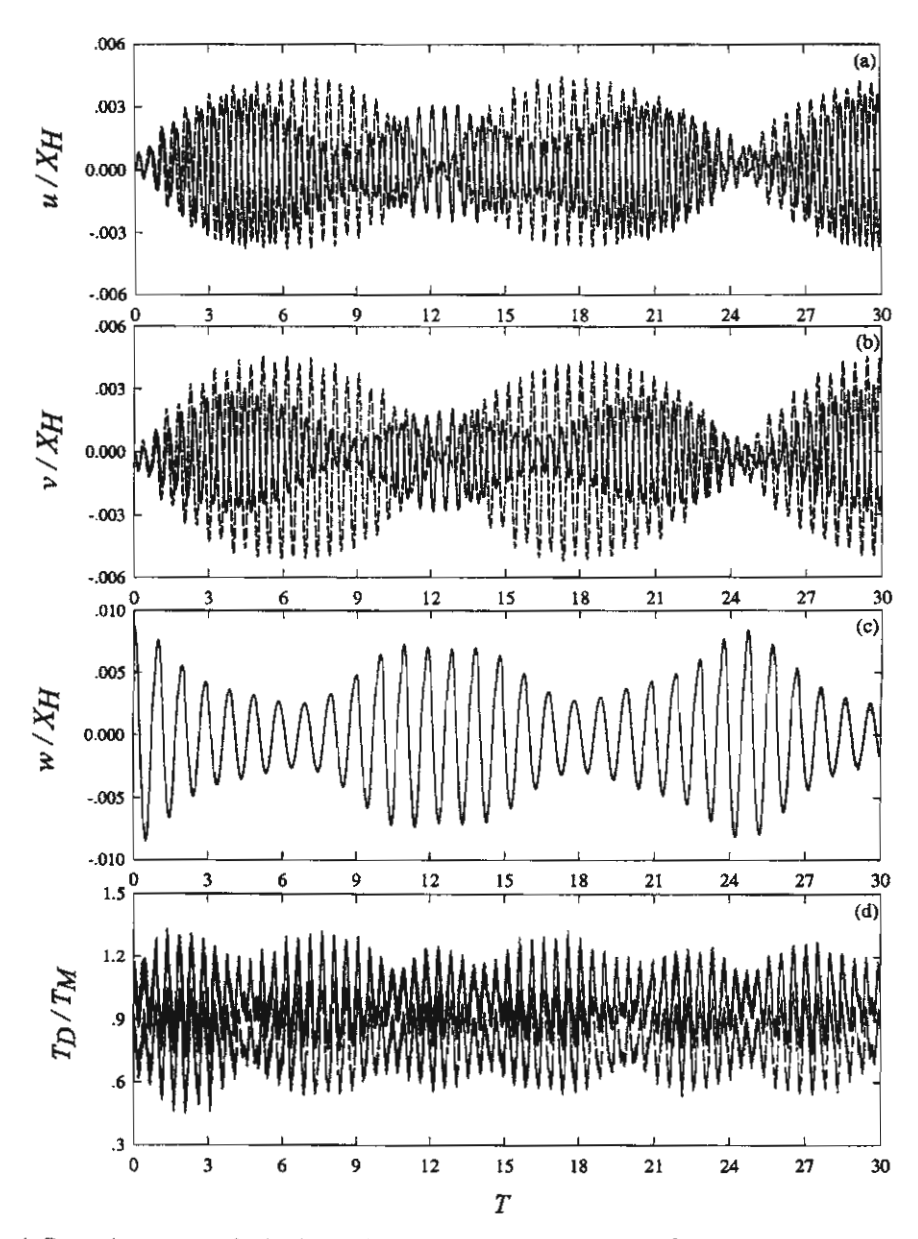


Figure 4. Dynamic responses for inclined cable with  $\lambda/\pi\approx 2$  and  $\theta_C=45^\circ$  under first S-O mode initiation: (a) longitudinal; (b) vertical; (c) out-of-plane: at quarter-span, — from left end; - - - from right end; (d) total tension: — maximum, - - - minimum.

An asymmetric feature of system dynamics is evident in both the driven longitudinal (Figure 4a) and vertical responses (Figure 4b), whose amplitudes at quarter span from the left end are unequal to those at quarter span from the right end. Conversely, the exciting out-of-plane responses are unaffected by the system asymmetry, the amplitudes at those points being equal (Figure 4c). However, a beating-type exchange with amplitude-modulated 3-D motion is observed in all responses. In particular, the out-of-plane amplitudes decrease due to the interaction with the driven longitudinal and vertical amplitudes, both of which are periodically excited through geometrically nonlinear coupling with the out-of-plane motion and are considerably greater than those obtained for cables away from avoided crossings. In addition, the longitudinal amplitudes are comparable to the vertical ones, thus meaningfully contributing to the interaction with the out-of-plane amplitudes, and to the increase of cable total tension. As a matter of fact, substantial cable tension responses are induced and enhanced in the nonlinear range (Figure 4d) due to the corresponding driven in-plane vibration amplitudes, unlike the zero tension occurring in the linear theory due to first-order cable stretching assumption.

When initiating the first anti-symmetric out-of-plane (first A-O) mode at second avoidance, the overall responses yield the same nonlinear behaviors as those explained for the first S-O mode initiation. To characterize the driven in-plane responses actually interacting with the initiated out-of-plane modes, their MDOF normal amplitudes q are plotted in Figures 5a and 5b versus the normalized arc-length coordinate at selected times, for the first S-O (at  $\lambda/\pi \approx 2$ for a=10 m and  $\theta_C=45^\circ$ ) and first A-O (at  $\lambda/\pi\approx 4$  for a=5 m and  $\theta_C=60^\circ$ ) mode initiations, respectively. In Figure 5a ( $T \approx 2.8, 3.0$ ), the dominant mode is, evidently, the second hybrid mode (H2), whose longitudinal and vertical amplitudes at quarter span from right end being greater than those at quarter span from left end (Figures 4a and 4b) is explained. They are subsequently enhanced to attain maximum values when  $T \approx 7.1$  and 7.4. Correspondingly, the out-of-plane amplitude is decreased considerably due to a beating phenomenon. It is worth observing that the first hybrid mode (H1) may take place in some time intervals ( $T \approx 11.6, 11.9$ ), where the amplitudes at quarter span from left end become the greatest (Figures 4a and 4b). Nevertheless, due to their small amplitudes, the corresponding out-of-plane responses are unaffected by this in-plane mode interaction, as shown by the steady maximum amplitude in Figure 4c. Though various frequency commensurabilities do coexist at first avoidance point, the dynamic characteristics and modal interaction observed in Figures 4 and 5a illustrate how the meaningful one involving the initiated first S-O mode is the nearly tuned 2:1 internal resonance between the second hybrid and first S-O modes.

In Figure 5b, the mode shapes of the excited in-plane response under first A-O mode initiation may be either the third hybrid (H3: see, e.g., at  $T \approx 5.5$ , 5.8) or the fourth hybrid modes (H4: see, e.g., at  $T \approx 2.3$ , 2.5, 9.3, 9.5). Since their amplitudes are comparable to each other (see, e.g., at  $T \approx 2.3$  for the H4 mode and at  $T \approx 5.5$  for the H3 mode), both of them are involved in the interaction with the out-of-plane amplitudes. Figure 5b highlights how both the existing, nearly tuned, 2:1 internal resonances – between the third (or fourth) hybrid mode and the first A-O mode – are actually activated. Consistent with a comparable phenomenon observed for the horizontal cable [16], this is likely to occur because a high frequency hybrid (instead of symmetric) in-plane mode – out of the two nearly coexisting at second avoidance – is involved in each internal resonance, though no theoretical expectation comparable to the companion horizontal cable [16] is available. The hybrid character follows from the lack of symmetry in the equilibrium of the inclined cable, which entails high modal density and asymmetric system dynamics.

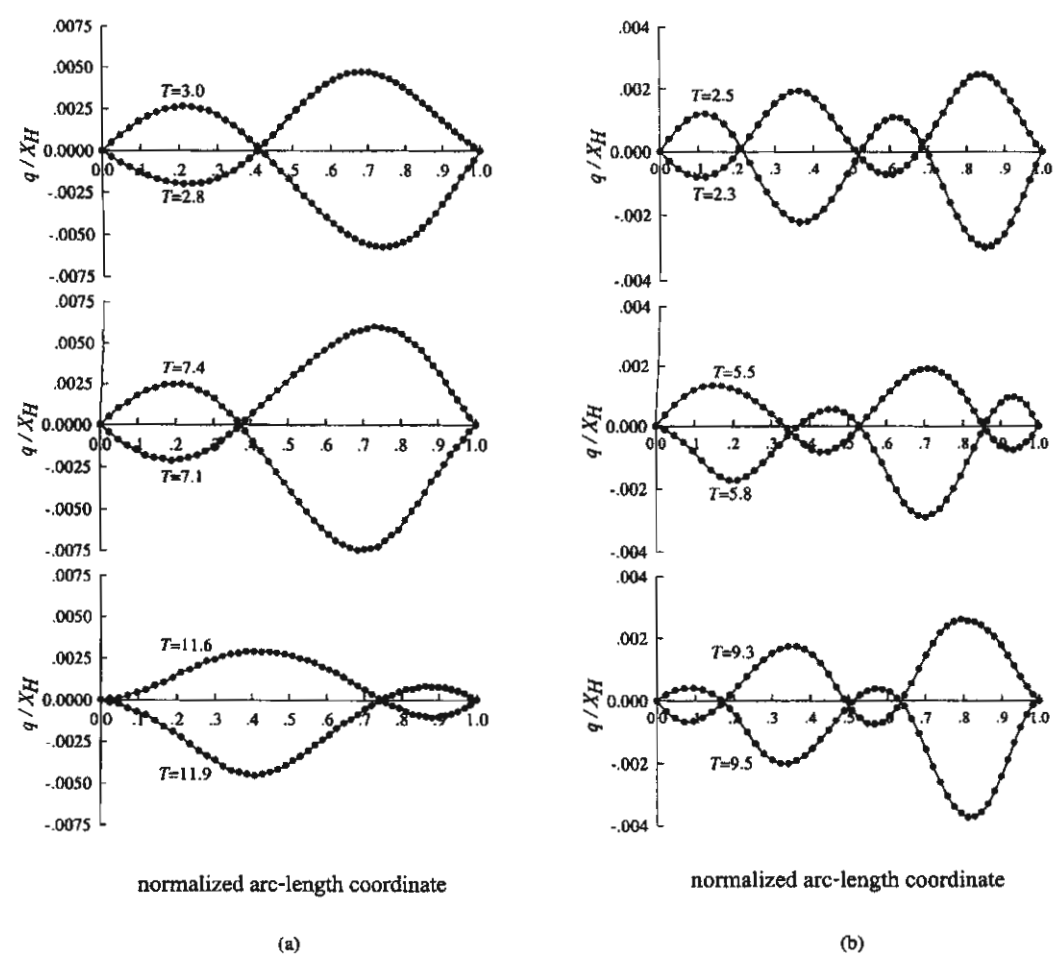


Figure 5. Cable vibration profiles at selected times for inclined cable with: (a)  $\lambda/\pi \approx 2$  and  $\theta_C = 45^\circ$  under first S-O mode initiation; (b)  $\lambda/\pi \approx 4$  and  $\theta_C = 60^{\circ}$  under first A-O mode initiation.

Consider now the cable with  $\theta_C = 45^\circ$  at third avoidance ( $\lambda/\pi \approx 6$ ). By initiating the first S-O mode with a = 10 m, the driven longitudinal and vertical responses at mid-span (Figures 6a and 6b) are markedly nonperiodic, unlikely the periodically driven responses in Figure 4, which are dominated by the stricter 2:1 internal resonances. Because of the high modal densities of inclined cable suspensions, significant higher order in-plane modes may be involved in the response when a single out-of-plane mode is initiated, even for a cable having a relatively low sag-to-span ratio ( $d/X_H = 0.128$ ). This multi-harmonic character shows the need to consider a MDOF cable model in order to obtain reliable response predictions, and is similar to that occurring for nonresonant horizontal cables with either small or, mostly, large values of sag-to-span ratio [16]. The difference here is that the spatial profiles of the driven nonperiodic responses are, of course, asymmetric. In contrast, the periodic out-ofplane response (at mid span) involves a single mode/frequency, and a nearly steady amplitude

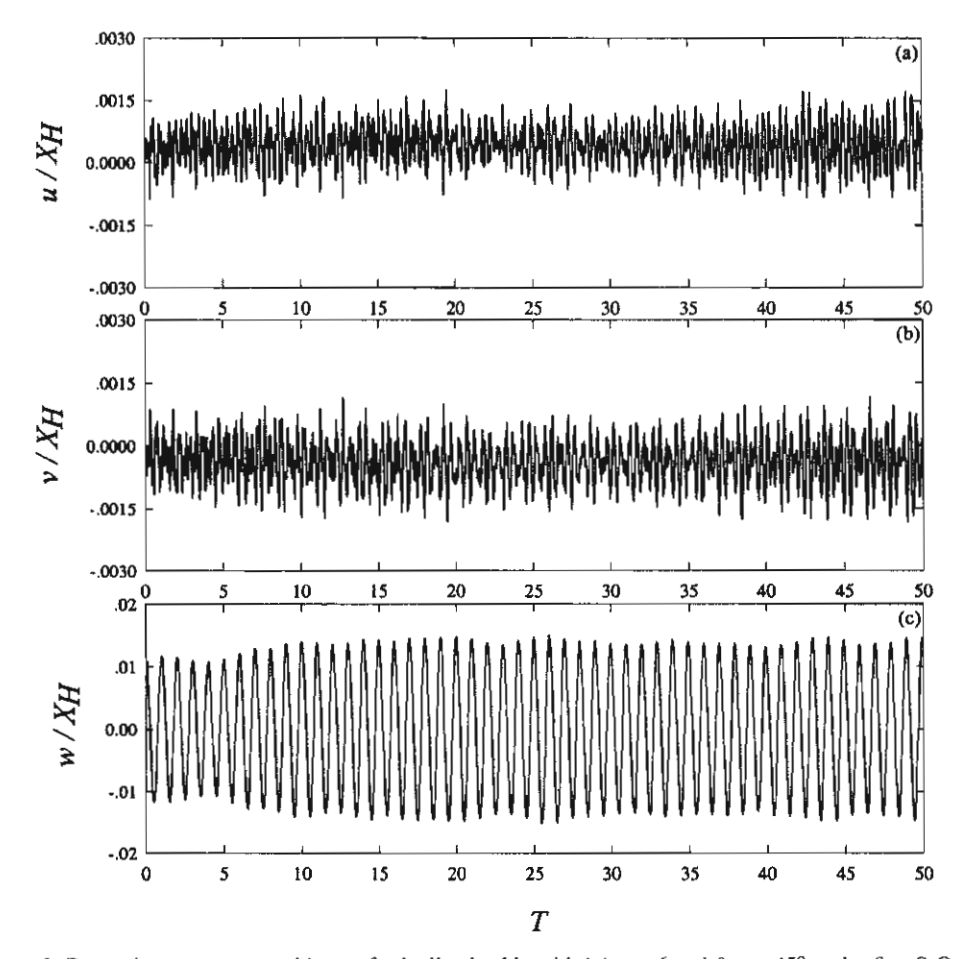


Figure 6. Dynamic responses at mid-span for inclined cable with  $\lambda/\pi \approx 6$  and  $\theta_C = 45^\circ$  under first S-O mode initiation: (a) longitudinal; (b) vertical; (c) out-of-plane.

(Figure 6c). This highlights how no one of the underlying internal resonances (Table 1) comes actually into play when initiating the (low-frequency) first S-O mode for this  $\lambda/\pi$ .

As a summary, it can be stated that apart from the *hybrid* character of the driven inplane responses, the involved modal interactions and periodical energy transfers in the 1:2 internal resonances at first and second avoidance points are *similar* to those highlighted for the horizontal cable at corresponding crossovers [16], where the first and second symmetric in-plane modes are excited.

# 5. Modal Transition Phenomena in Planar Dynamics

Modal transition has been observed in various crossover cables [16] when considering monofrequent in-plane vibrations. A companion analysis is pursued herein for inclined cables to determine how the main changes in the spatial content of the responses evolve when the frequency crossover phenomenon is replaced by the frequency avoidance typical of these

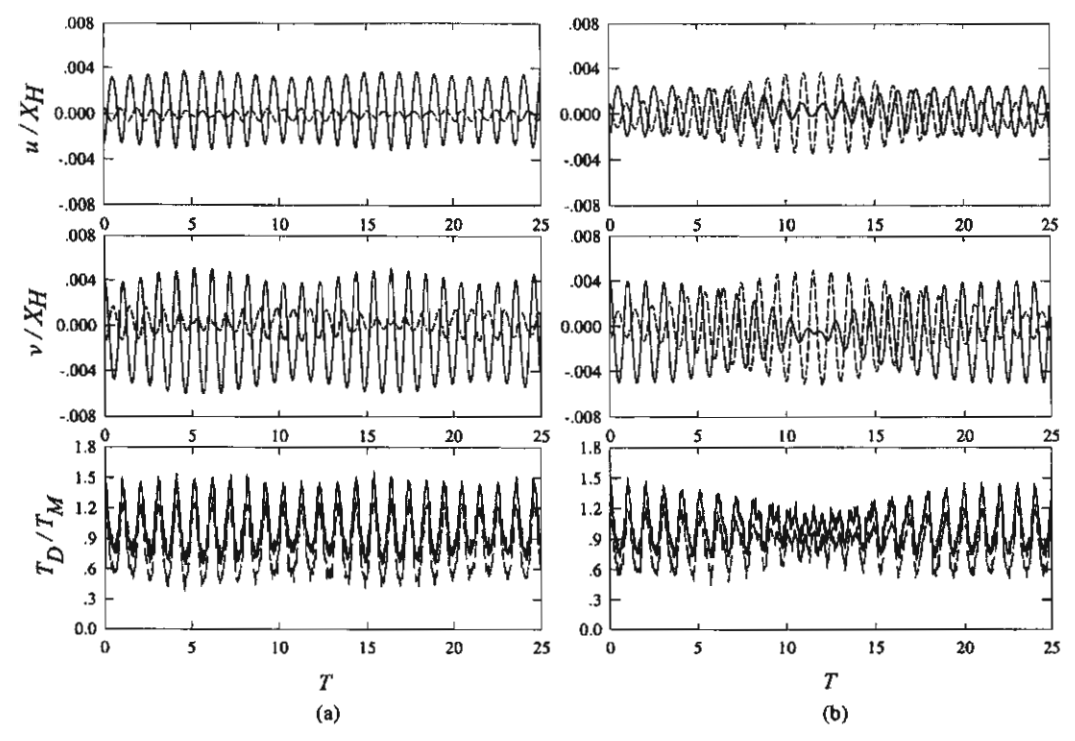


Figure 7. Longitudinal and vertical responses for inclined cable with  $\lambda/\pi \approx 2$  and  $\theta_C = 45^{\circ}$  under (a) first hybrid mode initiation: — at mid-span; - - - at quarter-span from right end; (b) second hybrid mode initiation: at mid-span; - - - at quarter-span from left end, and corresponding total tension responses: — maximum; - - - minimum.

cables. This is accomplished by considering a cable subject to initial conditions of in-plane modes, which entail no coupling with out-of-plane motions.

Various kinds of modal transition are likely to occur for a given inclined cable. In the following, we will discuss mainly the transition features occurring at each avoidance region as a consequence of a dominant internal resonance, analyzing them against the background of interaction phenomena highlighted for the horizontal cable [16].

### FIRST AVOIDANCE FREQUENCY $(\lambda/\pi \approx 2)$

The cable with  $\theta_C = 30^{\circ}$  is considered in this section. Some remarkable nonlinear aspects of system dynamics are revealed. By applying the initial condition of the first hybrid mode (H1) with a = 5 m, the longitudinal and vertical amplitudes at mid-span (solid lines) and quarter-span from right end (dashed lines) are shown in Figure 7a. No outstanding features are observed, different from the horizontal cable at first crossover, for which the first antisymmetric mode is accommodated into the response initiated by the first symmetric mode [16]. Both longitudinal and vertical responses are periodic and their amplitudes increase slightly in some intervals: the *nearly* tuned 1:1 internal resonance occurring at first avoidance frequency does not meaningfully affect the system dynamics. Also, the cable tension responses have a steady maximum value. In contrast, when initiating the second hybrid mode (H2) with the same assigned amplitude, the longitudinal and vertical amplitudes at mid-span

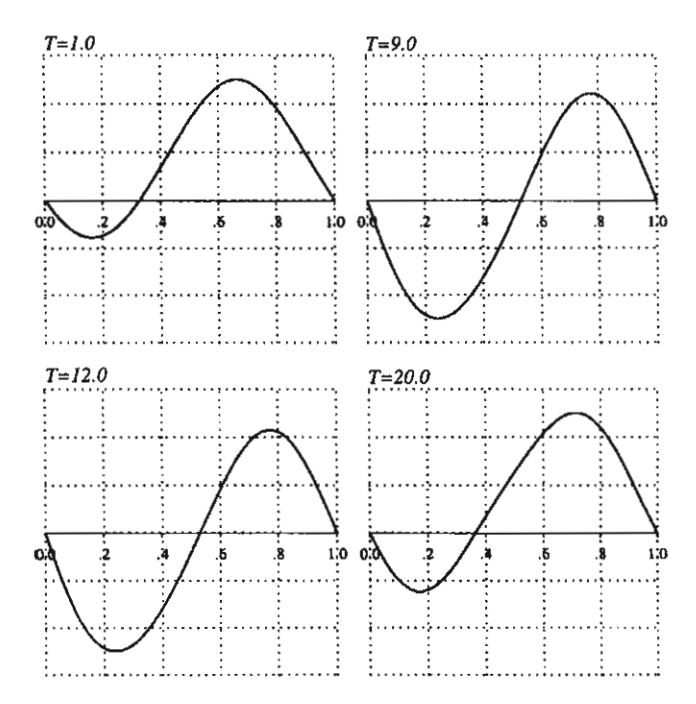


Figure 8. Modal transition for inclined cable with  $\lambda/\pi \approx 2$  and  $\theta_C = 30^\circ$  at different instants under second hybrid mode initiation.

(solid lines), which are initially greater than those at quarter-span from left end (dashed lines), are reduced up to approaching nearly zero values in some intervals (Figure 7b). Correspondingly, both longitudinal and vertical amplitudes at quarter span are increased considerably due to an amplitude exchange with corresponding mid-span quantities, and their magnitudes are grown up to 3.63 and 4.56 times their initial values, respectively.

Even though the modal shapes of both initiated modes are hybrid, Figure 7 highlights how the (beating-like) amplitude exchange phenomenon becomes evident only when initiating the second hybrid mode. To understand what kind of response occurs in this amplitude exchange interval, the vibration profiles at selected times are reported in Figure 8. Only the dominant normal displacement q is illustrated. Starting from  $T \approx 1.0$ , the vibration profile corresponds to the initiated second hybrid mode (H2) at first avoidance. Then, it develops smoothly towards an anti-symmetric shape when  $T \approx 9.0$ , which accounts for a superimposition of first and second hybrid modes, and dominates the response up to  $T \approx 12.0$ . The original shape of the second hybrid mode is completely recovered at  $T \approx 20.0$ . The contemporaneous decrease and increase of the amplitude at mid and quarter spans (Figure 7b) is thus explained. In turn, though remaining appreciable, the maximum tension response is slightly decreased when the resulting anti-symmetric mode takes place (Figure 7b), which is the nonlinear counterpart of the no-tension effect of the anti-symmetric modes occurring in the linear range. Therefore, Figures 7b and 8 highlight how the first hybrid mode is excited and accommodated into the response when initiating the second hybrid mode: contrary to the previous case, this is a visible effect of the nearly tuned 1:1 internal resonance in which they are involved. This kind of modal interaction looks similar to that induced on the first anti-symmetric mode by the perfectly

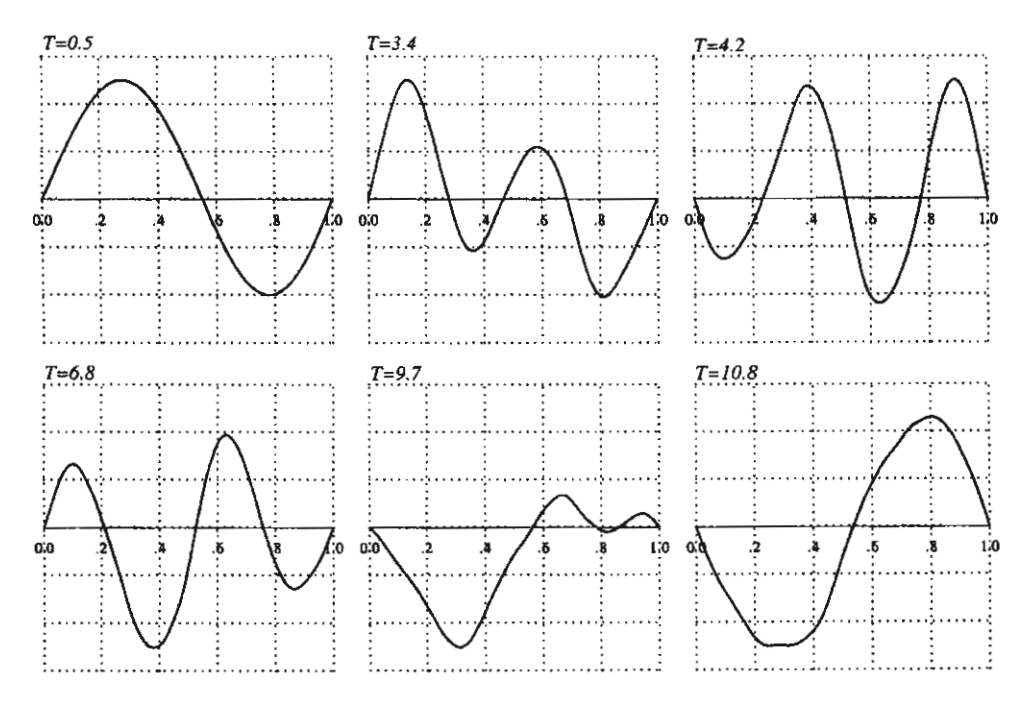


Figure 9. Modal transition for inclined cable with  $\lambda/\pi \approx 4$  and  $\theta_C = 45^\circ$  at different instants under first anti-symmetric in-plane mode initiation.

tuned 1:1 internal resonance occurring at first crossover for horizontal cable, when the first symmetric mode is initiated [16]. However, the spatial character of both the driving and the excited modes is herein hybrid.

# 5.2. SECOND AVOIDANCE FREQUENCY $(\lambda/\pi \approx 4)$

In this section, the cable with  $\theta_C = 45^{\circ}$  is considered. Having in mind the interaction phenomena of the horizontal cable, the first anti-symmetric mode (II) with a = 5 m is initiated, first. The ensuing longitudinal, vertical and nonlinear tension responses show a continuous exchange of energy between driving and excited modes: it produces decrement in magnitude and increment in frequency of the longitudinal and vertical responses, and is likely governed by an internal resonance existing at second avoidance.

To gain insight into the response, the vibration profiles are drawn comparatively. As shown in Figure 9, the shape of the initiated anti-symmetric profile ( $T \approx 0.5$ ) rapidly changes into an asymmetric mode shape ( $T \approx 3.4$ ), and further evolves at  $T \approx 4.2$  and  $T \approx 6.8$ . These shapes are seemingly associated with the involvement of higher-order hybrid in-plane modes in the cable response, and result in an asymmetric vibration profile due to a participation of the fourth hybrid mode ( $T \approx 4.2$ ), and of the third hybrid mode ( $T \approx 6.8$ ). After attaining a further asymmetric shape ( $T \approx 9.7$ ), the anti-symmetric mode resettles again ( $T \approx 10.8$ ), with the relevant response being now opposite in phase with respect to the original one ( $T \approx$ 0.5). Therefore, Figure 9 reveals how the higher hybrid modes nearly coexisting at second avoidance are both excited by the initiated first anti-symmetric mode due to their involvement in a nearly tuned 2:1 internal resonance, like the out-of-plane/in-plane interaction discussed

in Section 4 with the first A-O mode initiation. However, due to the high modal density in the frequency range of the excited modes, no one of them can dominate the spatial shape of the system in any interval. Apart from the different (*hybrid*) character of the driven in-plane modes, this behavior looks *similar* to that occurring for the horizontal cable at second crossover [16], where the second symmetric mode is excited.

On the contrary, when initiating one of the two higher-order hybrid modes (the third and fourth modes) nearly coexisting at second avoidance, the lower first anti-symmetric mode is driven according to the nearly tuned 2:1 internal resonance, irrespective of the order of the initiated modes. To highlight this phenomenon, the modal transitions of the vibration profiles under initial conditions of third (H3) and fourth (H4) hybrid modes with the same assigned amplitude (a = 2.5 m) are displayed comparatively in Figures 10a and 10b. The first one illustrates the transition from the third hybrid mode ( $T \approx 4.6$ ) to the lower excited antisymmetric mode ( $T \approx 41.0$ ), whereas the second one illustrates the transition from the fourth hybrid ( $T \approx 5.2$ ) mode to the lower excited anti-symmetric mode ( $T \approx 44.4$ ). During these transitions, there occurs a different kind of mode superimposition between the two involved modes giving rise to various asymmetric mode shapes (see, e.g., at  $T \approx 31.0$  in Figure 10a and at  $T \approx 34.6$  in Figure 10b). Afterwards, both initiated modes will dominate again the vibration profiles and the whole processes will repeat themselves as long as no external disturbances are imposed to the cable. It is worth noticing that the outcomes of the nearly internal resonance occurring at second avoidance are different from those obtained for the horizontal cable, whose lower first anti-symmetric mode is excited only when the second symmetric mode – out of the two modes coexisting at second crossover – is initiated [16]. Again, this is a consequence of the hybrid character of the two modes at second avoidance. Nevertheless, those results were numerical confirmations of theoretical predictions, whereas just the present numerical results are available for the inclined cable.

To verify the actual activation of the 2:1 internal resonance, the nonlinear frequencies dominating the system responses are evaluated using the Fourier amplitude spectral densities. Considering initiations of first anti-symmetric, third hybrid, and fourth hybrid modes, Figures 11a–11c show the frequency contents of their dominant vertical amplitudes at quarter-span from right end, respectively. Evidently, all power spectra show two major peaks, approximately equal to (0.122) and 0.249 Hz in Figure 11a, 0.117 and (0.230) Hz in Figure 11b, 0.122 and (0.249) Hz in Figure 11c. All of these frequency ratios are commensurable to a nearly tuned 2:1 internal resonance. By comparing the nonlinear frequencies of the initiated modes (the values in parenthesis) with those of the corresponding linear ones (Table 1), it is seen that the first anti-symmetric initiation produces hardening behavior, whereas both higher-order hybrid initiations produce softening behavior. Moreover, instead of having two distinct peaks corresponding to the exciting and driven modes, dominant peaks with side frequencies are sometimes observed (see, e.g., Figure 11a). These sideband frequencies are a direct result of the nonlinear interactions, and because they are not symmetric about the main peaks, the response is both amplitude- and phase-modulated [28].

## 5.3. Third Avoidance Frequency $(\lambda/\pi \approx 6)$

It is of interest to analyze the effect of internal resonances at third avoidance frequency, where higher-order modes are involved in the dynamics. The cable with  $\theta_C = 30^{\circ}$  is considered.

When applying the initial condition of the first symmetric mode (I2) with a=3 m, the amplitude responses are disturbed by a number of higher frequencies, as shown by the Fourier

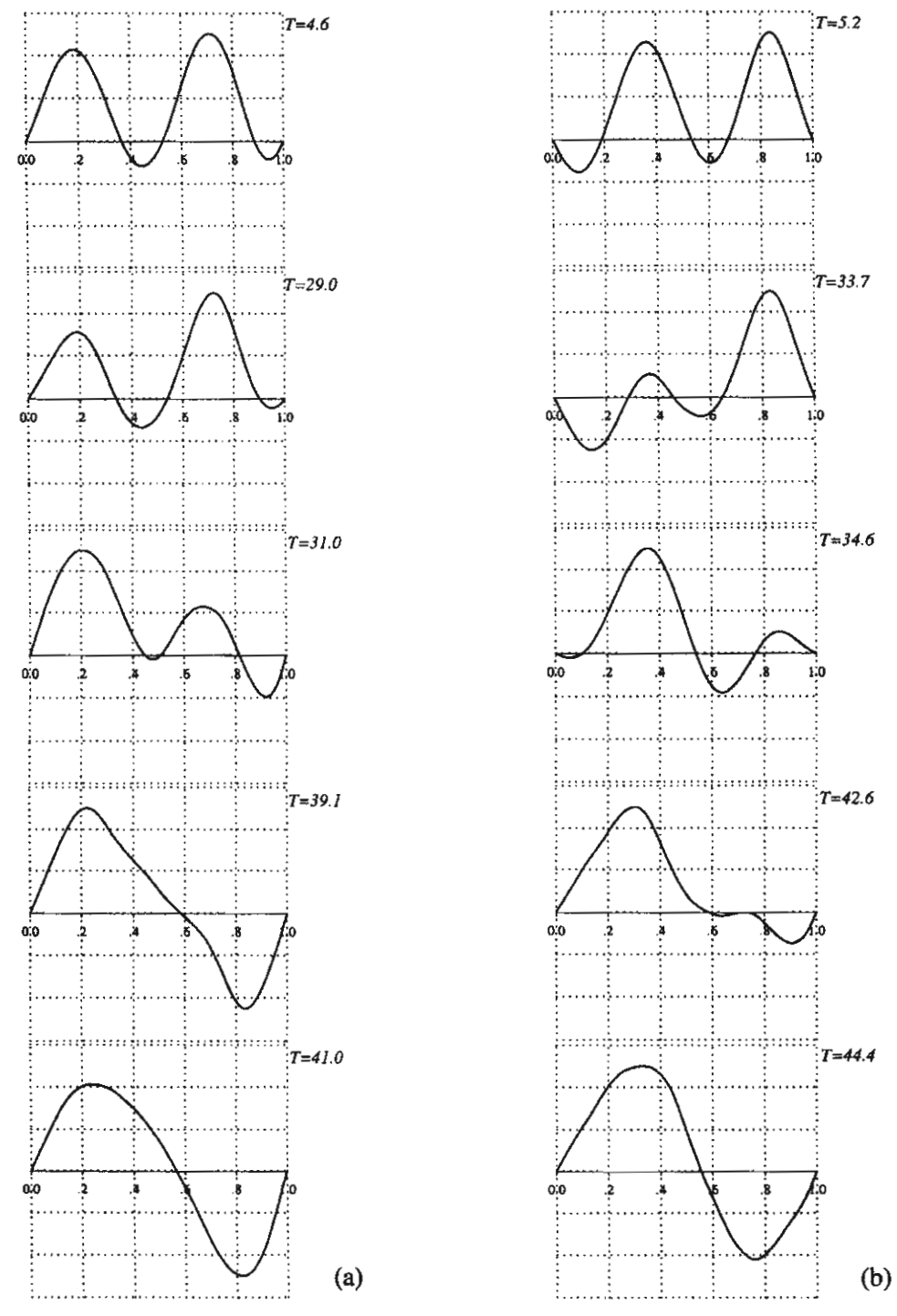


Figure 10. Modal transition for inclined cable with  $\lambda/\pi \approx 4$  and  $\theta_C = 45^\circ$  at different instants under (a) third hybrid mode initiation and (b) fourth hybrid mode initiation.

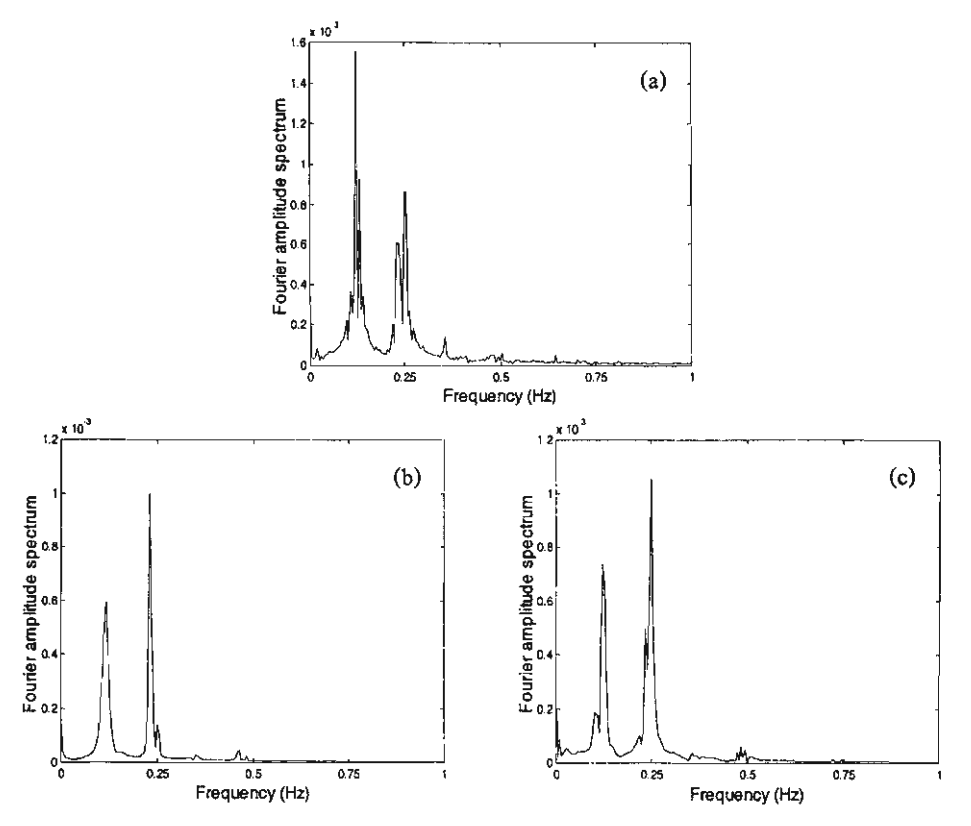


Figure 11. Fourier amplitude spectra for inclined cable with  $\lambda/\pi \approx 4$  and  $\theta_C = 45^\circ$  under initial conditions of: (a) first anti-symmetric; (b) third hybrid; (c) fourth hybrid, in-plane modes.

spectrum of the dominant vertical amplitude at mid-span (Figure 12a). No peaks exist corresponding exactly to a perfectly tuned internal resonance. In other words, no single higher order mode enters the system dynamics. Accordingly, the modal profiles in different time intervals display various kinds of asymmetric shapes due to participation of higher order modes. Again, these dynamic characteristics ensue from the high modal density of the inclined cable, and result in a behavior *different* from that of the horizontal cable at third crossover, for which only the third symmetric mode is driven by the initiated first symmetric, according to the stricter 2:1 internal resonance [16].

Conversely, when initiating the fifth hybrid mode (H5) with reduced amplitude  $a=1.5\,\mathrm{m}$ , some worthy phenomena are noticed. There is a sort of energy exchange involving frequency-and amplitude-modulation features, and suggesting likely activation of some kind of internal resonance. Accordingly, the Fourier amplitude spectrum of the dominant vertical amplitude at mid-span (Figure 12b) indicates apparently three major peaks, one corresponding to the exciting mode (0.371 Hz), and the others corresponding to the driven lower (0.186 Hz) and higher (0.742 Hz) modes. This highlights how lower and higher modes are simultaneously accommodated into the response when the fifth hybrid mode is initiated, due to their frequency commensurability according to a nearly tuned multiple (1:2:4) internal resonance. Indeed, the driven lower and higher frequencies are associated with the first symmetric (I2) and the sixth anti-symmetric modes, respectively.

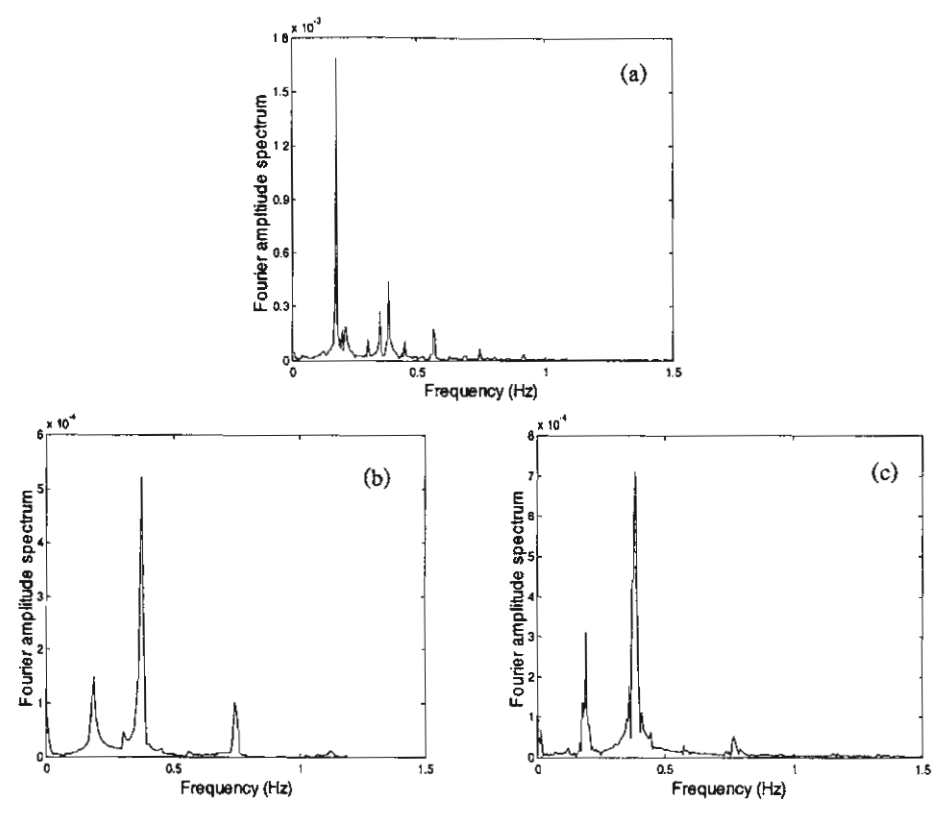


Figure 12. Fourier amplitude spectra for inclined cable with  $\lambda/\pi \approx 6$  and  $\theta_C = 30^\circ$  under initial conditions of: (a) first symmetric; (b) fifth hybrid; (c) sixth hybrid, in-plane modes.

It is worth analyzing the vibrational profiles of this multiple resonant cable at different instants. As shown in Figure 13, apart form the fifth hybrid mode assigned initially ( $T \approx 0.0$ ), none of the driven lower or higher modes dominates the system dynamics. In particular, the vibration profiles manifest themselves as a combination of contributions from higher (sixth anti-symmetric) and lower (first symmetric) modes, with either the former ( $T \approx 26.1$  and  $T \approx 28.1$ ) or the latter ( $T \approx 32.2$  and  $T \approx 43.2$ ) being more apparent in the spatial shape. However, because of the high modal density of inclined cables including various kinds of symmetric/anti-symmetric modes - which becomes even stronger for cables sagging significantly - and of the high order of the mode being initiated at third avoidance, the driven lower and higher modes cannot dominate the response in any interval. This circumstance is markedly different from the case of second avoidance where the first anti-symmetric mode, excited by both the third and fourth hybrid modes, clearly dominates the response in some intervals.

Qualitative difference is observed when initiating the sixth hybrid mode (H6), nearly coexisting with the fifth one at third avoidance, with the same amplitude as before. In Figure 12c, the frequency response highlights only two main peaks, one corresponding to the exciting mode (0.371 Hz), and the other corresponding to the lower driven first symmetric mode (0.186 Hz). Therefore, no one of the higher-order modes is excited, unlike the previous case of fifth mode initiation. Apart from the hybrid character of the initiated mode, the system response is now governed by the nearly tuned 2:1 internal resonance, similar to the corresponding case

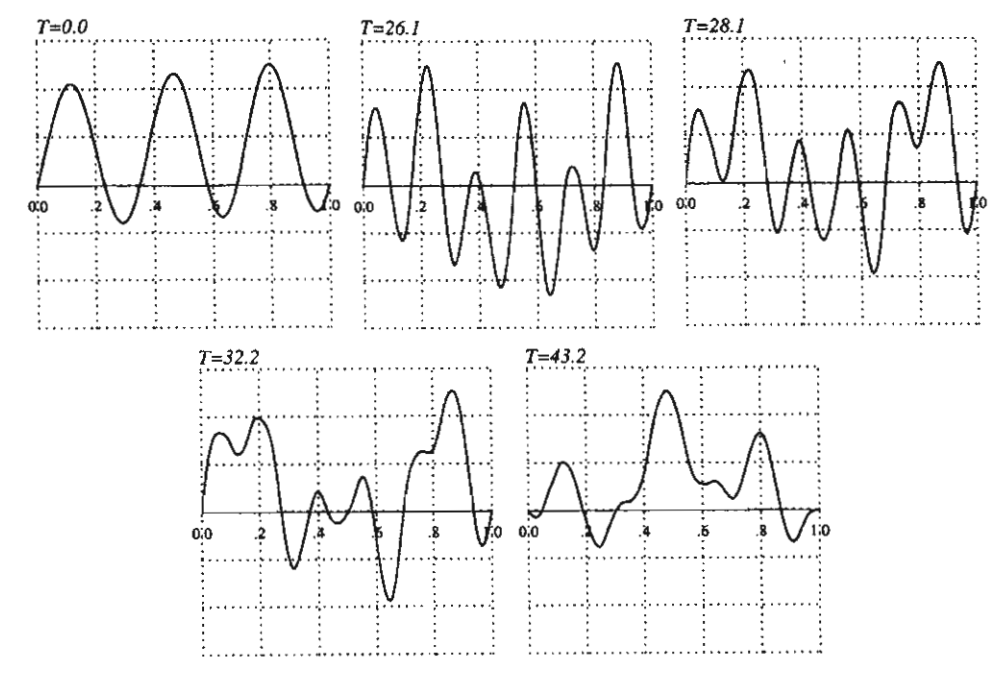


Figure 13. Modal transition for inclined cable with  $\lambda/\pi \approx 6$  and  $\theta_C = 30^\circ$  at different instants under fifth hybrid mode initiation.

of horizontal cable at third crossover [16]. Nevertheless, the driven lower (symmetric) mode cannot dominate the vibration profile in any interval, as with the fifth mode initiation.

## 6. Influence of Cable Inclination

It is now interesting to investigate the influence of cable inclination on its behavior. The first relevant issue is discussed with reference to Figures 14a and 14b, which show the maximum dynamic tensions, computed by subtracting the static tension  $T_M$  from the total one  $T_D$ , for the cable under initial conditions of first S-O and first A-O modes. With the same assigned amplitude as used in Section 4 and the same time duration measured, the dynamic tensions for six  $\lambda/\pi$  values and four angles  $\theta_C$  including the horizontal cable ( $\theta_C = 0^\circ$ ) are given. It is shown that, for each  $\theta_C$ , the dynamic tensions are increased substantially when the cable parameters are associated with the first  $(\lambda/\pi \approx 2)$  and second  $(\lambda/\pi \approx 4)$  avoidance (crossover) points, where the first S-O and first A-O modes are initiated, respectively. In both cases, the highest peak occurs for the horizontal cable, which corresponds to the perfectly tuned 2:1 resonance at each crossover. Overall, the enhancement in cable dynamic tension is due to the increased inplane vibration amplitudes resulting from nearness to the 2:1 internal resonance between the driving out-of-plane and the excited in-plane modes at avoidance (crossover) points. However, the peak of maximum tension for each resonant case is seen to decrease considerably as the inclination increases, up to becoming nearly equal to that of a generic (nonresonant) case for  $\theta_C = 60^{\circ}$ , though being the 2:1 internal resonance generally activated for all  $\theta_C$ .

As a second issue, the 1:1 resonant cable at  $\lambda/\pi \approx 2$  is considered again with the same prescribed amplitude of the second hybrid mode as in Section 5.1, but with larger inclinations,

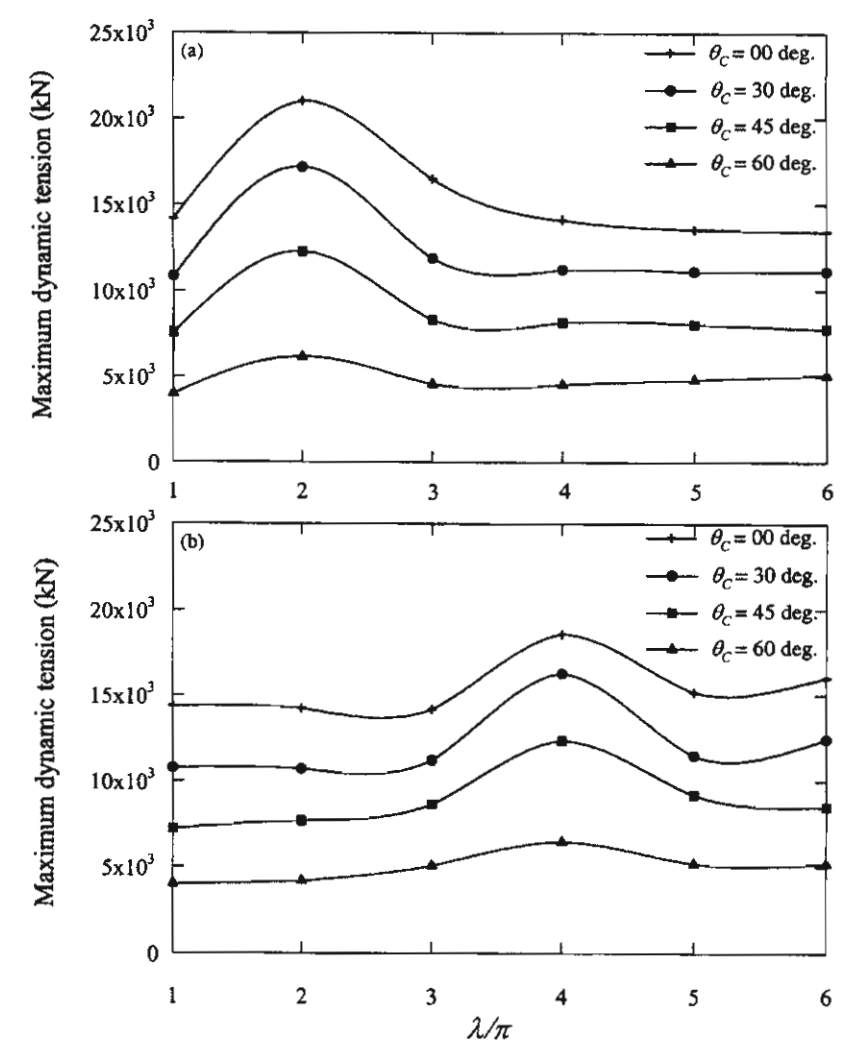


Figure 14. Effect of cable inclination on the maximum dynamic tension under initial conditions of (a) first S-O mode; (b) first A-O mode.

i.e.  $\theta_C = 45^\circ$  and  $60^\circ$ . When  $\theta_C = 45^\circ$ , the beating-type amplitude exchange is evident in Figure 15a, where a decrement in longitudinal and vertical amplitudes at mid-span (solid lines), and an increment in those at quarter-span from left end (dashed lines), are observed, just as in Figure 7b. Again, the tension responses are slightly decreased when the exchange occurs. However, being the longitudinal and vertical amplitudes at mid-span different from zero, no mode transition phenomenon resulting in the anti-symmetric mode takes place and only amplitude-modulated responses are observed. This is different from the corresponding case with lower inclination ( $\theta_C = 30^{\circ}$ , Figure 7b) where the anti-symmetric mode settles down (Figure 8).

The effect of cable inclination becomes definitely evident when  $\theta_C = 60^{\circ}$ . Firstly, the longitudinal amplitude is greater than the vertical one, as shown in Figure 15b, and dominates

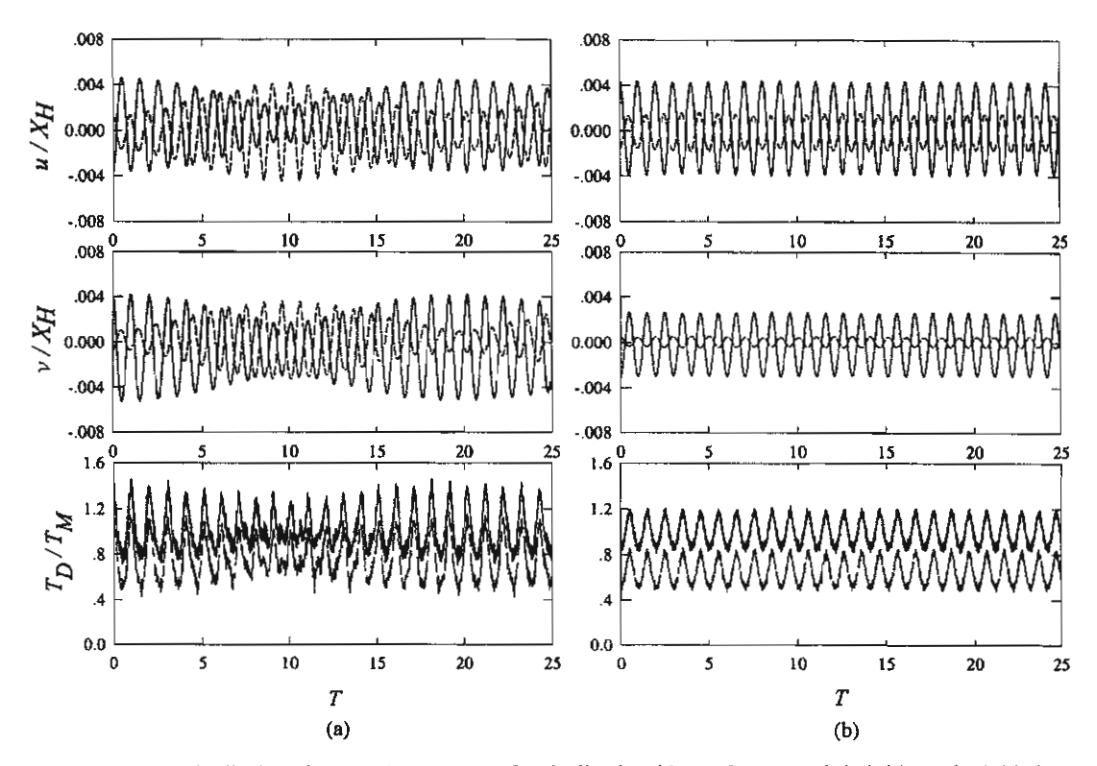


Figure 15. Longitudinal and vertical responses for inclined cable under second hybrid mode initiation: (a)  $\lambda/\pi \approx 2$  and  $\theta_C = 45^\circ$ ; (b)  $\lambda/\pi \approx 2$  and  $\theta_C = 60^\circ$ , — at mid-span; - - - at quarter-span from left end, and corresponding total tension responses: — maximum; - - - minimum.

the cable mode shape. As a result, the tension responses are mainly due to the longitudinal amplitude. Secondly, the difference in amplitude of maximum and minimum tensions is enhanced, thus highlighting the importance of accounting for axial deformation or strain variations in the analysis of inclined cables. Finally, there is no beating-like phenomenon, as well as no correlated mode transition, since the response amplitudes are perfectly periodic and steady. This ensues from the 1:1 internal resonance being just barely tuned when the cable inclination increases.

Additional information about internal resonance activation at frequency avoidance points are given in Table 2, where all of the previously discussed behaviors obtained from numerical analysis – as well as others not reported – are summarized, and a comparison with the horizontal cable at crossovers is given [16]. To this aim, the first three crossovers and first three avoidance points are dealt with comparatively in Tables 2a and 2b, where information about the spatial content of the interacting modes are also provided for each activated resonance. It is worth noticing that the reported values of the angle  $\theta_C$  are those for which the internal resonance is activated. By distinguishing between out-of-plane/in-plane interactions, between frequency avoidance/crossover points, and between low/high mode initiations, the following general observations are made.

(i) Apart from the hybrid character of driven in-plane modes, 1:2 internal resonance in-volving the initiated out-of-plane mode is activated at *all* avoidance points and for *all* cable inclinations, similar to that occurring for horizontal cable at *all* crossover points.

Table 2. A comparison in activated internal resonances between (a) horizontal (crossover) and (b) inclined (avoidance) cables.

<u>a)</u> λ/π	Type of internal	Interaction	Involved Modes
	resonance		Lower: Higher
2	1:2	(Out):In	(1st symm):1st symm
	1:1	In:(In)	1 <sup>st</sup> anti-symm:(1 <sup>st</sup> symm)
4	1:2	(Out):In	(1st anti-symm):2nd symm
	1:2	(In):In	(1 <sup>st</sup> anti-symm):2 <sup>nd</sup> symm
	1:2	In:(In)	1 <sup>st</sup> anti-symm:(2 <sup>nd</sup> symm)
6	1:2	(Out):In	(2 <sup>nd</sup> symm):3 <sup>rd</sup> symm
	1:2	(In):In	(1 <sup>st</sup> symm):3 <sup>rd</sup> symm
	1:2	In:(In)	1 <sup>st</sup> symm:(3 <sup>rd</sup> symm)

<sup>(...)</sup> Exciting mode; ... Driven mode

<u>(b)</u>				
λ/π	Type of internal resonance	Interaction	Involved Modes Lower: Higher	Inclination angle: $\theta_C$
2	1:2	(Out):In In:(In)	(1 <sup>st</sup> symm):2 <sup>nd</sup> hyb 1 <sup>st</sup> hyb:(2 <sup>nd</sup> hyb)	30,45,60 30,45
4	1:2 1:2 1:2 1:2	(Out):In (In):In In:(In) In:(In)	(1 <sup>st</sup> anti-symm):3 <sup>rd</sup> and/or 4 <sup>th</sup> hyb (1 <sup>st</sup> anti-symm):3 <sup>rd</sup> and/or 4 <sup>th</sup> hyb 1 <sup>st</sup> anti-symm:(3 <sup>rd</sup> hyb) 1 <sup>st</sup> anti-symm:(4 <sup>th</sup> hyb)	30,45,60 30,45,60 30,45,60 30,45
6	1:2 1:2:4 1:2	(Out):In In:(In):In In:(In)	(2 <sup>nd</sup> symm):5 <sup>th</sup> and/or 6 <sup>th</sup> hyb 1 <sup>st</sup> symm:(5 <sup>th</sup> hyb):6 <sup>th</sup> anti-symm 1 <sup>st</sup> symm:(6 <sup>th</sup> hyb)	30,45,60 30,45,60 30

(...) Exciting mode; ... Driven mode

- (ii) When initiating a lower pure in-plane mode, a nearly tuned 1:2 internal resonance is activated only at second avoidance but for all cable inclinations, similar to that occurring for horizontal cable at second and third crossovers.
- (iii) When initiating a higher hybrid in-plane mode, a nearly tuned 1:1 (1:2) resonance is activated at first (second) avoidance point, whereas a nearly tuned 1:2:4 resonance or a 1:2 resonance may be activated at third avoidance point. In any case, internally resonant behavior between in-plane modes does not occur when the cable inclination becomes greater and/or the order of considered mode becomes higher (see, e.g., the 1:1 resonance at first avoidance, the 1:2 resonance between first anti-symmetric and fourth hybrid modes at second avoidance, and the 1:2 resonance between first symmetric and sixth hybrid modes at third avoidance).

## 7. Summary and Conclusions

The nonlinear characteristics of the large amplitude free vibrations of inclined sagged elastic cables have been investigated numerically, based on a 3-D model formulation not restricted to cables having small sag-to-span ratios and taking into account the axial deformation effect. A finite difference discretization in both space and time has been implemented to obtain time histories and time-varying spatial profiles of the nonlinear response of a MDOF cable model. Various numerical examples of arbitrarily inclined cables with initial out-of-plane or in-plane displacements have been carried out for the case of a specified end tension. The overall nonlinear behavior is remarkably influenced by the high modal density of the system and by the ensuing hybrid modal character at avoidance points.

In the case of out-of-plane initial displacement conditions, the following main results are summarized:

- Multi-harmonic responses characterized by driven nonperiodic in-plane displacements
  do occur for nonresonant cables under periodic out-of-plane initiations. Though occurring regardless of cable sag and inclination angle, these features are enhanced for cables
  sagging significantly and/or with high inclination. This highlights the need to account for
  a MDOF model in the analysis of inclined cables.
- Strong coupling phenomena are observed for cables at first two (or three) avoided crossing points. They are associated mostly with 1:2 internal resonance conditions activated for all inclination angles and involving different modes in the various cases. Apart from the hybrid character of the driven in-plane modes, the involved modal interactions and periodical energy transfers are similar to those highlighted at corresponding crossovers for the horizontal cable [16]. Overall, the observed periodic interactions do confirm the constraining (in terms of modal content) and regularizing effects induced by internal resonances on system dynamics.
- In any case, internal resonance conditions enhance both 3-D nonlinear coupling and cable nonlinear tension, the latter effect being mainly due to the increased in-plane vibration amplitudes. In turn, the induced dynamic tension is considerably reduced as cable inclination increases.

In the case of in-plane initial displacement conditions, various mode transition phenomena take place during the ensuing in-plane vibrations, depending on the spatial character of the involved two (three) modes nearly coexisting at avoidance points, on the order of mode considered, and on the magnitude of prescribed amplitude. Indeed, besides the activation of a nearly tuned 1:1 internal resonance at first avoided crossing and 2:1 internal resonances at second and third avoided crossings, a multiple 1:2:4 internal resonance may be activated at third avoided crossing, where a higher and a lower mode are simultaneously accommodated into the response initiated by a single mode. Apart from the hybrid character of the involved modes, some general features of the observed two-mode (1:1 and 1:2) internally resonant interactions are similar to those occurring for the horizontal cable. However, meaningful differences also occur, which are likely connected just with the hybrid character of the linear modes at avoidance points: see, e.g., the accommodation of a lower anti-symmetric mode into the 1:2 internally resonant response at second avoidance, irrespective of the higher-order hybrid mode being excited. In turn, the three-mode (1:2:4) interaction at third avoidance seems to be peculiar of inclined cables.

Cable inclination also plays a major role in system dynamic behaviors, especially with respect to the energy being periodically transferred between the involved in-plane modes. The following points are summarized:

 As regards 1:1 internal resonance, there can be amplitude exchange and shape modal transition (low inclination), only amplitude exchange (medium inclination), no amplitude exchange (high inclination), depending on the extent of the avoided crossing zone – which is as higher as the sag is larger and the cable is more inclined - as well as on the ensuing closeness/separateness of the relevant frequency ratio to/from perfect tuning.

- As regards 1:2 internal resonance, it does not play any role when the cable inclination and/or the order of mode increase.
- The longitudinal amplitude becomes greater than the vertical one as cable inclination increases, thus having a major influence on cable total tension. Moreover, the increasing difference in magnitude between maximum and minimum total tensions confirms the need to account for strain variations (axial deformation effect) in the inclined cable model.

Besides providing worthwhile information about which one of the nearly coexisting internal resonances are actually activated at avoided crossing points, the numerical results highlight how most of the modifications induced by cable inclination are concerned with planar dynamics interaction. This is a somehow expected circumstance, since the modification from crossover to avoidance in linear dynamics - and the ensuing passage from pure to hybrid mode shapes - are actually planar issues. They make the nonlinear dynamics features of inclined cables meaningfully different from those characterizing horizontally suspended cables.

### Acknowledgements

The authors gratefully acknowledge the financial support of the Thailand Research Fund (TRF) under Grants PHD/0167/2543 and RTA/03/2543.

#### References

- 1. Triantafyllou, M. S., 'Dynamics of cables, towing cables, and mooring systems', Shock and Vibration Digest 23, 1991, 3-8.
- 2. Irvine, H. M. and Caughey, T. K., 'The linear theory of free vibrations of a suspended cable', Proceedings of the Royal Society of London, Series A 341, 1974, 229-315.
- 3. Triantafyllou, M. S. and Grinfogel, L., 'Natural frequencies and modes of inclined cables', ASCE Journal of Structural Engineering 112, 1986, 139-148.
- 4. Hagedorn, P. and Schafer, B., 'On non-linear free vibrations of an elastic cables', International Journal of Non-Linear Mechanics 15, 1980, 333-340.
- 5. Luongo, A., Rega, G., and Vestroni, F., 'Planar non-linear free vibrations of an elastic cable', International Journal of Non-Linear Mechanics 19, 1984, 39-52.
- 6. Benedettini, F., Rega, G., and Vestroni, F., 'Modal coupling in the free nonplanar finite motion of an elastic cable', Meccanica 21, 1986, 38-46.
- 7. Benedettini, F. and Rega, G., 'Non-linear dynamics of an elastic cable under planar excitation', International Journal of Non-Linear Mechanics 22, 1987, 497-509.
- 8. Rao, G. V. and Iyengar, R. N., 'Internal resonance and non-linear response of a cable under periodic excitation', Journal of Sound and Vibration 149, 1991, 25-41.
- 9. Perkins, N. C., 'Modal interactions in the non-linear response of elastic cables under parametric/external excitation', International Journal of Non-Linear Mechanics 27, 1992, 233-250.
- 10. Lee, C. L. and Perkins, N. C., 'Nonlinear oscillations of suspended cables containing a two-to-one internal resonance', Nonlinear Dynamics 3, 1992, 465-490.
- 11. Lee, C. L. and Perkins, N. C., 'Three-dimensional oscillations of suspended cables involving simultaneous internal resonances', Nonlinear Dynamics 8, 1995, 45-63.
- 12. Benedettini, F., Rega, G., and Alaggio, R., 'Nonlinear oscillations of a four-degree-of freedom model of a suspended cable under multiple internal resonance conditions', Journal of Sound and Vibration 182, 1995, 775-798.

- Rega, G., Lacarbonara, W., Nayfeh, A. H., and Chin, C. M., 'Multiple resonances in suspended cables: Direct versus reduced-order models', *International Journal of Non-Linear Mechanics* 34, 1999, 901–924.
- Nayfeh, A. H., Arafat, H. N., Chin, C. M., and Lacarbonara, W., 'Multimode interactions in suspended cables', Journal of Vibration and Control 8, 2002, 337–387.
- Chucheepsakul, S. and Wongsa, S., 'Effect of axial stretching on large amplitude free vibration of a suspended cable', Structural Engineering and Mechanics 11, 2001, 185-197.
- Srinil, N., Rega, G., and Chucheepsakul, S., 'Three-dimensional nonlinear coupling and dynamic tension in the large amplitude free vibrations of arbitrarily sagged cables', *Journal of Sound and Vibration* 27, 2003, 781-803.
- Rega, G., Alaggio, R., and Benedettini, F., 'Experimental investigation of the nonlinear response of a hanging cable. Part I: Local analysis', Nonlinear Dynamics 14, 1997, 89–117.
- Benedettini, F. and Rega, G., 'Experimental investigation of the nonlinear response of a hanging cable. Part II: Global analysis', Nonlinear Dynamics 14, 1997, 119-138.
- Yamaguchi, H. and Ito, H., 'Linear theory of free vibrations of an inclined cable in three dimensions', Proceedings of the Japanese Society of Civil Engineers 286, 1979, 29–36.
- Cai, Y. and Chen, S. S., 'Dynamics of elastic cable under parametric and external resonances', ASCE Journal
  of Engineering Mechanics 120, 1994, 1786–1802.
- Warnitchai, P., Fujino, Y., and Susumpow, T., 'A non-linear dynamic model for cables and its application to a cable-structure system', *Journal of Sound and Vibration* 187, 1995, 695-712.
- Zhao, Y. Y., Wang, L. H., Chen, D. L., and Jiang, L. Z., 'Non-linear dynamic analysis of the two-dimensional simplified model of an elastic cable', *Journal of Sound and Vibration* 255, 2002, 43–59.
- Takahashi, K. and Konishi, Y., 'Non-linear vibrations of cables in three dimensions. Part 1: Non-linear free vibrations', Journal of Sound and Vibration 118, 1987, 69–84.
- Leissa, A. W. and Saad A. M., 'Large amplitude vibrations of strings', ASME Journal of Applied Mechanics 61, 1994, 296–301.
- Chucheepsakul, S., Srinil, N., and Petchpeart, P., 'A variational method for three-dimensional model of
  extensible marine cables with specified top tension', Applied Mathematical Modelling 27, 2003, 781–803.
- Chucheepsakul, S. and Srinil, N., 'Free vibrations of three-dimensional extensible marine cables with specified top tension via a variational method', Ocean Engineering 29, 2002, 1067–1097.
- Lacarbonara, W. and Rega, G., 'Resonant nonlinear normal modes. Part II: Activation/orthogonality conditions for shallow structural systems', *International Journal of Non-Linear Mechanics* 38, 2003, 873–887.
- 28. Nayfeh, A. H., and Balachandran, B., Applied Nonlinear Dynamics, Wiley, New York, 1995.



Available online at www.sciencedirect.com



Journal of Sound and Vibration # (\*\*\*\*) \*\*\*\*-\*\*\*

JOURNAL OF SOUND AND VIBRATION

www.elsevier.com/locate/jsvi

# Three-dimensional non-linear coupling and dynamic tension in the large-amplitude free vibrations of arbitrarily sagged cables

Narakorn Srinila, Giuseppe Regab, Somchai Chucheepsakula.\*

<sup>a</sup> Department of Civil Engineering, King Mongkut's University of Technology Thonburi, 48 Bangmod, Toongkru, Bangkok 10140, Thailand

Received 24 May 2002; accepted 23 January 2003

### Abstract

This paper presents a model formulation capable of analyzing large-amplitude free vibrations of a suspended cable in three dimensions. The virtual work-energy functional is used to obtain the non-linear equations of three-dimensional motion. The formulation is not restricted to cables having small sag-to-span ratios, and is conveniently applied for the case of a specified end tension. The axial extensibility effect is also included in order to obtain accurate results. Based on a multi-degree-of-freedom model, numerical procedures are implemented to solve both spatial and temporal problems. Various numerical examples of arbitrarily sagged cables with large-amplitude initial conditions are carried out to highlight some outstanding features of cable non-linear dynamics by accounting also for internal resonance phenomena. Non-linear coupling between three- and two-dimensional motions, and non-linear cable tension responses are analyzed. For specific cables, modal transition phenomena taking place during in-plane vibrations and ensuing from occurrence of a dominant internal resonance are observed. When only a single mode is initiated, a higher or lower mode can be accommodated into the responses, making cable spatial shapes hybrid in some time intervals.

© 2003 Elsevier Science Ltd. All rights reserved.

### 1. Introduction

Cable systems are of great interest in a wide range of practical applications for supplying both support and stability to large structures. Moreover, they are of interest from a theoretical point of

<sup>&</sup>lt;sup>b</sup> Dipartimento di Ingegneria Strutturale e Geotecnica, Universita' di Roma La Sapienza, via A. Gramsci, 53 Roma 00197, Italy

<sup>\*</sup>Corresponding author. Tel.: +662-470-9134-36; fax: +662-427-9063.

E-mail addresses: narakorns@hotmail.com (N. Srinil), giuseppe.rega@uniroma1.it (G. Rega), somchai.chu@kmutt.ac.th (S. Chucheepsakul).

view, owing to many fundamental non-linear phenomena induced by the overall slenderness and inherent flexibility of cable structural systems. As a result of dynamical susceptibility to excitation from surrounding mediums, cable vibrations of large amplitudes may happen in some circumstances, and may eventually degrade the system performance. To reach a fundamental understanding of cable behaviors, three-dimensional (3-D) modelling and geometrically non-linear characteristics should be fully accounted for in the analysis.

Non-linear free vibrations of a suspended cable have been investigated by a number of researchers, which include Hagedorn and Schafer [1], Luongo et al. [2,3], Rega et al. [4], and Benedettini et al. [5]. All of them deal with simple cable models, with one or two degrees of freedom, developed and utilized to obtain analytical solutions. In the same theoretical framework, both single-degree-of-freedom [6,7] and multi-degree-of-freedom (m.d.o.f.) [8–12] models have been considered to explore numerous non-linear phenomena arising in cable forced vibrations. These include the meaningful effects of non-linear modal coupling under various external/internal resonance conditions and the possibility of non-periodic responses. The richness of cable non-linear dynamics has been further highlighted through systematic experimental investigations [13,14]. In all theoretical models, a certain number of assumptions have been introduced to simplify the analytical treatment. Namely, the initial static strain is disregarded so as to obtain an inextensible parabolic profile of the cable equilibrium configuration where the sag-to-span ratio is of the order of  $\frac{1}{8}$  or less. Moreover, the dynamic tension is defined as a function of time only, thus being spatially uniform, which ensues from the inertial force in the longitudinal direction being neglected according to a quasi-static stretching model of the cable in motion.

However, Behbahani-Nejad and Perkins [15] have illustrated that the analysis of tension waves propagating freely along the cable length cannot be accomplished using simple models. Pakdemirli et al. [16] and Rega et al. [17] have documented that the results obtained by analyzing reduced-mode discretized models of cable may be quantitatively erroneous for cables with nonzero sag. Moreover, several studies have highlighted how, depending on system elasto-geometric properties, the effect of axial deformation on the dynamic behaviors can be significant and should be considered in the analysis [18 24]. For arbitrarily supported cables or cables with large curvature, the investigation may require further numerical implementations [25,26]. Takahashi and Konishi [27] examined sagged cables with either horizontal or inclined supports qualitatively, and discussed geometrically non-linear effects, but they overlooked the significance of cable extensibility. Recently, Luo and Mote [28] developed a comprehensive 3-D model governing the steady response of a travelling, arbitrarily sagged, elastic cable, and obtained exact, closed-form solutions for steady motion under various loadings. Nevertheless, it seems worth investigating further 3-D non-linear coupling, as well as the variability of dynamic tension during vibration, by considering a m.d.o.f. model which accounts for cable extensibility and non-uniform dynamic tension, and which is not restricted to low values of the sag-to-span ratios.

The objective of the present study is to analyze numerically the large-amplitude free vibrations of arbitrarily sagged elastic cables through a rigorous formulation, which takes into account the axial deformation effect. Based on the principle of virtual work-energy, the non-linear equations of 3-D coupled motions are derived in Section 2. A m.d.o.f. model, which is not limited to cables having small sag-to-span ratios, is utilized within a numerical solution of the spatial and temporal problems (Section 3). The attention is then placed on the investigation of the cable 3-D non-linear free dynamics ensuing from a given set of initial conditions (Section 4). With this aim, the linear

modal coordinates of each vibration mode achieved from the previous study of Chucheepsakul and Srinil [24] are assumed as initial conditions for spatial displacements. The aim is to analyze: (i) how the cable non-linear response evolves, also in terms of dynamic tension; (ii) how significant the coupling of 3-D motion is; and (iii) whether and how the internal resonance conditions affect the dynamics. The non-linear free vibration characteristics of out-of-plane and in-plane vibrations are examined comprehensively and are discussed in detail.

# 2. Derivation of equations of motion

Fig. 1 displays the typical reference configuration of a suspended cable of horizontal span  $X_H$  with two immovable pinned-supports at the same ground level. One end of the cable is fixed while the other one is the position where the specified tension  $T_H$  is applied to maintain the cable in its static configuration. The coordinates of any point along the cable are represented using the Cartesian system. Three different states of cable configuration are distinguished, namely the unstretched, the equilibrium and the dynamic states. The cable forms a catenary suspension under its own weight at the initial unstretched state (x, y). Due to axial stretching, the cable moves to the equilibrium position  $(x_0, y_0)$ , which is considered as the initial configuration for cable dynamics. Owing to disturbances from external excitation, the cable then moves to the dynamic or displaced state, in which u, v and w are the components of displacement measured from the equilibrium configuration in the direction of X-, Y- and Z-axis, respectively.

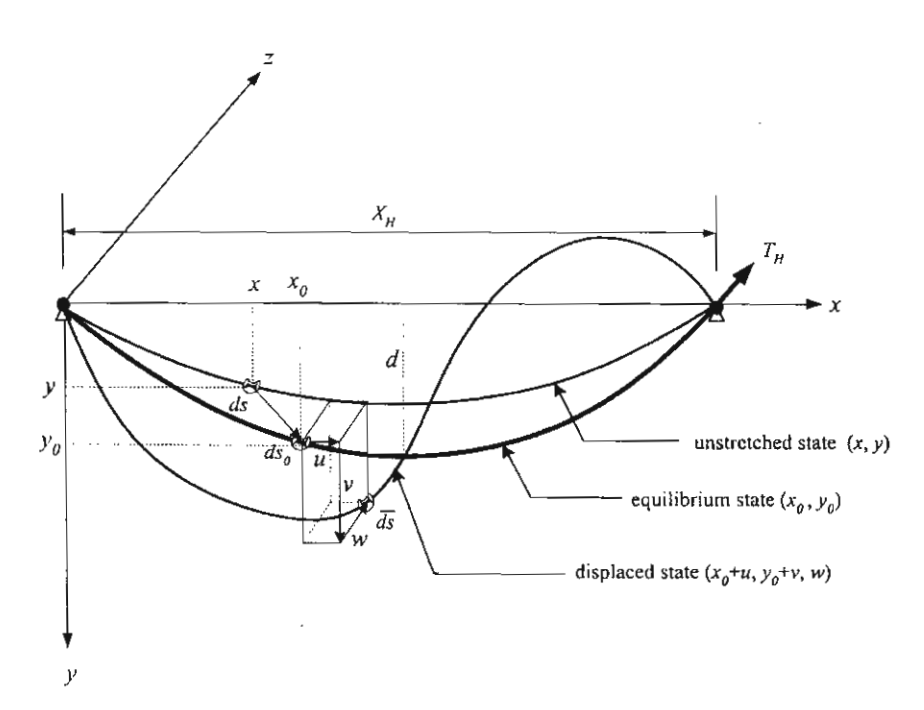


Fig. 1. Reference configurations of a suspended cable.

The length  $ds_0$  of an infinitesimal cable element at the equilibrium state can be written as

$$ds_0 = \sqrt{1 + y_0^{\prime 2}} \, dx_0, \tag{1}$$

where a superscript prime denotes a differentiation with respect to  $x_0$ . Using Lagrangian-strain definition, the cable segments at the unstretched state ds and displaced state d $\bar{s}$  are expressed, respectively, as

$$ds = \frac{\sqrt{1 + y_0'^2}}{1 + \varepsilon_0} dx_0,$$
 (2)

$$d\bar{s} = \sqrt{(1+u')^2 + (y_0' + v')^2 + w'^2} dx_0,$$
(3)

in which  $\varepsilon_0$  is the initial static strain. The total strain at the displaced state is

$$\bar{\varepsilon} = \frac{(1+\varepsilon_0)}{\sqrt{1+y_0'^2}} \sqrt{(1+u')^2 + (y_0' + v')^2 + w'^2} - 1. \tag{4}$$

The strain energies caused by bending, torsional and shear rigidities are neglected based on the assumption of a perfectly flexible cable. Hence, the strain energy is due only to the stretching of the cable axis. In view of the application of the principle of virtual work, the strain energy variation is written as

$$\delta U = \int_0^S E A \bar{\epsilon} \delta \bar{\epsilon} \, \mathrm{d}s,\tag{5}$$

where S is the total undeformed arc-length, E Young's modulus of the cable, and A its cross-sectional area, which is assumed to be constant. Substituting Eq. (4) and its variational expression into Eq. (5) yields

$$\delta U = \int_{0}^{X_{H}} \left\{ \frac{EA(1+\varepsilon_{0})(1+u')}{\sqrt{1+y_{0}'^{2}}} - \frac{EA(1+u')}{\sqrt{(1+u')^{2}+(y_{0}'+v')^{2}+w'^{2}}} \right\} \delta u' + \left\{ \frac{EA(1+\varepsilon_{0})(y_{0}'+v')}{\sqrt{1+y_{0}'^{2}}} - \frac{EA(y_{0}'+v')}{\sqrt{(1+u')^{2}+(y_{0}'+v')^{2}+w'^{2}}} \right\} \delta v' + \left\{ \frac{EA(1+\varepsilon_{0})(w')}{\sqrt{1+y_{0}'^{2}}} - \frac{EAw'}{\sqrt{(1+u')^{2}+(y_{0}'+v')^{2}+w'^{2}}} \right\} \delta w' \right\}$$

The virtual work done by the cable weight  $w_C$  per unit unstretched length is expressed as

$$\delta W_e = \int_0^{X_H} \frac{w_C \sqrt{1 + y_0'^2}}{1 + \varepsilon_0} \, \mathrm{d}x_0 \, \delta v. \tag{7}$$

In turn, the virtual work done by the inertial forces is given by

$$\delta W_i = -\int_0^{X_H} \frac{w_C \sqrt{1 + y_0'^2}}{g(1 + \varepsilon_0)} (\ddot{u}\delta u + \ddot{v}\delta v + \ddot{w}\delta w) \, \mathrm{d}x_0, \tag{8}$$

where  $w_C\sqrt{1+y_0'^2/g(1+\epsilon_0)}$  is the cable mass per unit stretched length, g is the gravitational force,  $\ddot{u}$ ,  $\ddot{v}$  and  $\ddot{w}$  are the accelerations in the direction of X-, Y- and Z-axis, respectively. Utilizing the standard principle of virtual displacement, the total virtual work-energy of the cable system is expressed as

$$\delta\Pi = \delta U - (\delta W_e + \delta W_i) = 0. \tag{9}$$

After substitution of Eqs. (6)–(8) into Eq. (9), and integration by parts of the latter with application of the boundary conditions  $\delta u = \delta v = \delta w = 0$  at  $x_0 = 0$  and  $x_0 = X_H$ , Euler's equations associated with the virtual displacements  $\delta u$ ,  $\delta v$  and  $\delta w$  read, respectively:

$$\left(\frac{EA(1+\varepsilon_0)(1+u')}{\sqrt{1+y_0'^2}} - \frac{EA(1+u')}{\sqrt{(1+u')^2+(y_0'+v')^2+w'^2}}\right)' - \frac{w_C\sqrt{1+y_0'^2}}{g(1+\varepsilon_0)}\ddot{u} = 0,$$
(10)

$$\left(\frac{EA(1+\varepsilon_0)(y_0'+v')}{\sqrt{1+y_0'^2}} - \frac{EA(y_0'+v')}{\sqrt{(1+u')^2+(y_0'+v')^2+w'^2}}\right)' - \frac{w_C\sqrt{1+y_0'^2}}{g(1+\varepsilon_0)}\ddot{v} + \frac{w_C\sqrt{1+y_0'^2}}{1+\varepsilon_0} = 0, \quad (11)$$

$$\left(\frac{EA(1+\varepsilon_0)(w')}{\sqrt{1+y_0'^2}} - \frac{EA\,w'}{\sqrt{(1+u')^2 + (y_0'+v')^2 + w'^2}}\right)' - \frac{w_C\sqrt{1+y_0'^2}}{g(1+\varepsilon_0)}\ddot{w} = 0. \tag{12}$$

By substituting the equilibrium conditions  $u = v = w = u' = v' = w' = u'' = v'' = w'' = \ddot{u} = \ddot{v} = 0$  into Eqs. (10)–(12), one can obtain Euler's equations corresponding to the equilibrium state in the direction of virtual displacements  $\delta u$  and  $\delta v$ :

$$\left(EA\,\varepsilon_0/\sqrt{1+y_0'^2}\right)'=0,\tag{13}$$

$$\left(EA\,\varepsilon_0 y_0'/\sqrt{1+y_0'^2}\right)' + w_C \sqrt{1+y_0'^2}/(1+\varepsilon_0) = 0. \tag{14}$$

Subtracting Eq. (10) by Eq. (13), and Eq. (11) by Eq. (14), the governing equations of motion corresponding to the displacements in the directions u, v and w, respectively, are

$$\left(\frac{EA + EA(1 + \varepsilon_0)u'}{\sqrt{1 + y_0'^2}} - \frac{EA(1 + u')}{\sqrt{(1 + u')^2 + (y_0' + v')^2 + w'^2}}\right)' = \frac{w_C\sqrt{1 + y_0'^2}}{g(1 + \varepsilon_0)}\ddot{u}, \tag{15}$$

$$\left(\frac{EAy_0' + EA(1+\varepsilon_0)v'}{\sqrt{1+y_0'^2}} - \frac{EA(y_0' + v')}{\sqrt{(1+u')^2 + (y_0' + v')^2 + w'^2}}\right)' = \frac{w_C\sqrt{1+y_0'^2}}{g(1+\varepsilon_0)}\ddot{v},\tag{16}$$

$$\left(\frac{EA(1+\varepsilon_0)w'}{\sqrt{1+y_0'^2}} - \frac{EA(w')}{\sqrt{(1+u')^2 + (y_0'+v')^2 + w'^2}}\right)' = \frac{w_C\sqrt{1+y_0'^2}}{g(1+\varepsilon_0)}\ddot{w}.$$
(17)

These equations are highly non-linear and are coupled through the cable equilibrium configuration. The associated boundary conditions read

$$u(0,t) = v(0,t) = w(0,t) = u(X_H,t) = v(X_H,t) = w(X_H,t) = 0.$$
(18)

This system is useful for analyzing 3-D undamped large-amplitude free vibrations under specified initial conditions. It is worth noticing that the formulation considered could be accounted for also in a local coordinate reference frame by using the relevant coordinate transformation relationship [24] or suitable Euler-angle formulations [22].

### 3. Method of solution

Cable equilibrium configuration is to be evaluated. The shooting method is used to solve the non-linear equilibrium Eqs. (13) and (14). Since a specified tension is imposed at one end of the cable, in the computation it is more convenient to use an expression for the tension at any point along the cable in place of Eq. (14). For this purpose, the equilibrium condition of a cable segment in the tangential direction is used and is then converted into the following integral expression:

$$T(x_0) = T_H - \int_{X_H}^{X_0} \frac{w_C}{(1 + \varepsilon_0)} y_0' \, \mathrm{d}x_0.$$
 (19)

Using Eqs. (13) and (19), the proposed algorithm reveals itself to be efficient for solving the cable problem with a specified end tension [29]. Each step of spatial integration is performed through the fourth order Runge-Kutta scheme.

In order to analyze the free vibration problem, each partial differential equation (Eqs. (15)–(17)) is differentiated term by term with respect to the spatially independent variable  $x_0$ . The ensuing equations of motion are written as follows:

$$(\Theta/\Psi)u'' + (1/\Psi)F(u', u'', v', v'', w', w'') = \ddot{u}, \tag{20}$$

$$(\Theta/\Psi)v'' + (1/\Psi)G(u', u'', v', v'', w', w'') = \ddot{v}, \tag{21}$$

$$(\Theta/\Psi)w'' + (1/\Psi)H(u', u'', v', v'', w', w'') = \ddot{w}, \tag{22}$$

where the spatial variables 
$$\Theta = (1 + \varepsilon_0) / \sqrt{(1 + y_0'^2)}$$
 and  $\Psi = w_C \sqrt{1 + y_0'^2} / EA g(1 + \varepsilon_0)$  are defined, and the functions  $F(..)$ ,  $G(..)$  and  $H(..)$  of the displacement variables read:
$$F(..) = \begin{cases} \frac{\varepsilon_0' u'}{(1 + y_0'^2)^{1/2}} - \frac{(1 + u' + \varepsilon_0 u') y_0' y_0''}{(1 + y_0'^2)^{3/2}} \\ - \frac{[y_0' + v')^2 u'' + w'^2 u'' - (1 + u')(y_0' + v')(y_0'' + v'') - (1 + u')w'w''}{((1 + u')^2 + (y_0' + v')^2 + w'^2)^{3/2}} \end{cases}, (23)$$

$$G(..) = \left\{ \begin{bmatrix} \frac{y_0'' + \varepsilon_0' v'}{(1 + y_0'^2)^{1/2}} - \frac{(y_0' + v' + \varepsilon_0 v') y_0' y_0''}{(1 + y_0'^2)^{3/2}} \\ - \left[ \frac{(1 + u')^2 (y_0'' + v'') + w'^2 (y_0'' + v'') - (1 + u') (y_0' + v') u'' - (y_0' + v') w' w''}{((1 + u')^2 + (y_0' + v')^2 + w'^2)^{3/2}} \right] \right\}, (24)$$

$$H(..) = \left\{ \begin{bmatrix} \frac{\varepsilon_0'w'}{(1+y_0'^2)^{1/2}} - \frac{(w'+\varepsilon_0w')y_0'y_0''}{(1+y_0'^2)^{3/2}} \\ - \left[ \frac{(1+u')^2w'' + (y_0'+v')^2w'' - w'(1+u')u'' - w'(y_0'+v')(y_0''+v'')}{((1+u')^2 + (y_0'+v')^2 + w'^2)^{3/2}} \right] \right\}.$$
 (25)

Numerical solutions to Eqs. (20)-(22) were obtained using finite difference discretization in both space and time. Central differences were used for approximating spatial derivatives and the second temporal derivatives. This led to a simple explicit form of the equations of motion for a solution of the unknown displacements. The obtained displacements were then utilized as initial guess of the next process by means of a predictor-corrector iterative algorithm. The solution over each time step was iterated repeatedly until the convergence was satisfactory, and the allowable tolerance was accomplished by the criterion of the second order vector norm.

# 4. Numerical results and discussions

A long suspended cable with horizontal span  $X_H = 850 \,\mathrm{m}$  is analyzed in order to better highlight the effect of strain variation on non-linear dynamics. The cable has a cross-sectional area  $A = 0.1159 \,\mathrm{m}^2$ , cable density equal to  $8337.9 \,\mathrm{kg/m}^3$ , and modulus of elasticity  $E = 1.794 \times 10^7 \,\mathrm{kN/m}^2$ . The cable is discretized into 50 segments. Integration was performed in all cases with a time step equal to 0.00001. The linear eigenvector is evaluated and normalized in such a way that the maximum amplitude of nodal displacement is equal to unity [24]. Subsequently, each nodal displacement is multiplied by the initial amplitude ( $\Delta$ ) specified in each case. Without structural damping, this amplitude has been chosen to attain a moderately large value to ensure that the summation of the cable static tension and the additional dynamic one does not become a compressive force. The initial velocities for all directions are assumed to be identically zero throughout the present study.

Table 1 Cable properties and corresponding linear frequencies for four different cables

Cable	$\lambda/\pi$	$T_H$ (kN)	$\varepsilon_m$	d (m)	S (m) S	$S_0$ (m)	Linear natural frequencies (Hz)					
							Out-of-pla	ne mode: O	In-plan	e mode:	[	
							1st S-O	1st A-O	1st S–I	1st A–I	2nd S-I	2nd A-I
A	0.72	30 000	0.01443	28.39	840.48	852.53	0.104	0.208	0.123	0.206	0.312	0.414
В	2.00	15642	0.00752	56.59	853.69	859.96	0.074	0.147	0.145	0.145	0.226	0.292
C	4.00	10 500	0.00505	89.57	870.51	874.67	0.058	0.115	0.158	0.112	0.222	0.229
D	10.01	7000	0.00337	164.11	926.65	929.31	0.043	0.085	0.119	0.076	0.206	0.165

S: symmetric mode; A: antisymmetric mode.

Table 1 gives the physical properties of four different cables, including the specified end tension  $T_H$ , maximum static strain  $\varepsilon_m$ , cable sag d, cable unstretched length S and cable equilibrium length  $S_0$ , which are all governed by the unique cable parameter governing the linear frequency spectrum [20,30], i.e.,  $\lambda/\pi = \sqrt{(w_C S_0)^2 EA/T_a^3/\pi}$  ( $T_a$  is the static tension at cable mid-span). The corresponding linear out-of-plane and in-plane frequencies are also documented. The specified tensions have been selected to guarantee the existence of 1:1 internal resonance conditions between symmetric and antisymmetric in-plane frequencies at the first and second crossover points in the spectrum ( $\lambda/\pi = 2$ , 4 for cables B and C, respectively), in comparison with noncrossover points (cables A and D). By altering this specified tension, the influence of cable extensibility (strain variation) and cable sag can be seen. Obviously, the maximum extensibility is that of cable A, whereas the maximum sag is that of cable D. Emphasis is placed on a prescribed initial displacement condition according to the first four natural modes, namely the first symmetric and antisymmetric modes of the in-plane and out-of-plane vibrations. Attention is focused, on one side, on crossover cables, whose actual dynamic behaviors are analyzed versus the background of theoretical conditions for activation of the existing internal resonances obtained within an infinite dimensional analytical framework [31]; on the other side, attention is focused on a large sag cable exhibiting higher multi-mode and axial extensibility effects. The analysis is performed basically in terms of time histories of dynamic responses. In addition, spatial or phaseportrait representations of cable motion and frequency response measures are provided to describe specific features of system dynamics.

The 3-D non-linear responses at mid and quarter spans non-dimensionalized by the horizontal span  $(X_H)$  are typically shown. Time (T) is non-dimensionalized by the fundamental period of each linear frequency. The cable total tension  $T_D = EA\bar{\epsilon}$  is readily computed from the displacements through Eq. (4), and is then non-dimensionalized by the value of the maximum static tension  $(T_H)$ . Total tension responses inclusive of the initial static strain are presented rather than simple additional dynamic tension. Moreover, not only the maximum tension—which is of interest to the designer for evaluating the tensile strength capability—is investigated, but also the minimum tension so as to search for the position where compression possibly happens. The dynamic strain being a function of both space and time, the positions at which maximum and minimum tensions occur may change, depending on how the nodal points vibrate in each time step.

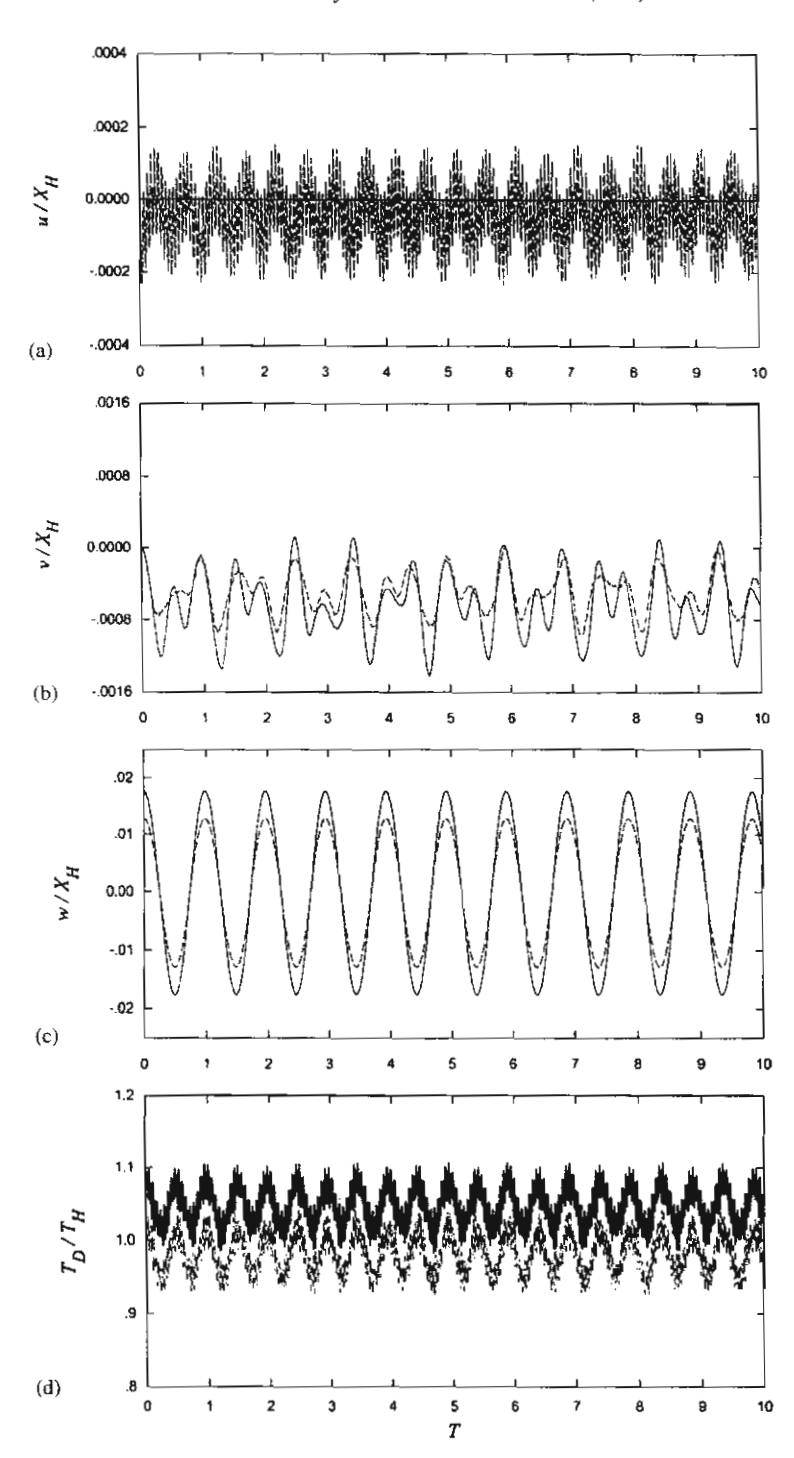


Fig. 2. Dynamic responses of cable A under initial condition of the 1st S-O mode: (a) longitudinal response; (b) vertical response; (c) out-of-plane response: —— mid-span, —— quarter span; (d) cable tension response: —— maximum, —— minimum

# 4.1. Large-amplitude out-of-plane free vibrations

The analysis starts by considering out-of-plane initial conditions with either symmetric or antisymmetric spatial shapes.

# 4.1.1. First symmetric out-of-plane mode (1st S-O mode)

The assigned amplitude  $\Delta$  is equal to 15 m for each cable. Starting from taut cable A, the out-of-plane response is perfectly periodic (Fig. 2(c)). The energy driven by the out-of-plane response geometrically induces longitudinal and vertical responses through kinematic coupling of 3-D motion. The vertical non-periodic response is disturbed by a higher frequency (Fig. 2(b)), while the longitudinal one has a considerably lower amplitude (Fig. 2(a)). The out-of-plane motion does not involve any first order cable stretching in the linear theory [30], corresponding substantially to a pendulum-like motion. In contrast, Fig. 2(d) displays the additional forces induced in the non-linear range.

Cable B corresponds to the first crossover ( $\lambda/\pi = 2$ ), where various internal resonances do coexist. However, the meaningful one involving the initiated out-of-plane mode is the 2:1 resonance between 1st S-I and 1st S-O modes, which is actually activable due to nonorthogonality of the relevant non-linear normal modes, which are both symmetric [31]. Consistently, a beating phenomenon is observed in the relevant responses (Fig. 3), as already highlighted in Ref. [5] for a two-degree-of-freedom cable model. The maximum out-of-plane amplitude decreases to about 0.64 times its initial value (Fig. 3(c)) due to the interaction with the corresponding in-plane response, whose maximum amplitude rises from zero to about 43.74% of the maximum out-of-plane amplitude. Correspondingly, the cable maximum tensions in Fig. 3(d) are enhanced considerably, and are greater than those obtained for cable A, being associated mostly with the increased in-plane vibration (Fig. 2(d)). The relationship between vertical and outof-plane displacements at mid-span is depicted in Fig. 4(a). It can be seen that the out-of-plane component vibrates nearly symmetrically about the in-plane axis. The in-plane amplitude reaches the maximum negative value when the out-of-plane amplitude is close to zero. This implies that the cable configuration drifts upwards when the cable vibrates close to the vertical plane, as shown by the cable 3-D profiles in Fig. 4(b) for  $T \approx 0 - 5$ .

Consider now cable D sagging significantly  $(d/X_H \approx 1/5)$ . The relevant longitudinal and vertical responses contain many high-frequency components and are definitely non-periodic (Figs. 5(a) and (b)), whereas the out-of-plane response in Fig. 5(c) is still periodic. The maximum amplitude of tension response is lower than that obtained for the resonant cable B. Since the out-of-plane response of each cable has a single (low) frequency, the Fourier amplitude spectral densities of the driven vertical responses are illustrated in Fig. 6 against those of cables A and B, in order to check the dominant frequency of the vibrations. Evidently, the vertical responses of cables A and D contain a number of higher frequency components (Figs. 6(a) and (c)) relevant to their non-periodic nature. In contrast, cable B attains a single frequency (0.156 Hz) twice that of the out-of-plane one (0.078 Hz), due to the energy being periodically transferred between the driving and excited modes of the 2:1 resonant cable (Fig. 6(b)).

It is worth analyzing the spatial shape of non-periodic responses by focusing attention on the large sag cable D, whose longitudinal, vertical and transversal vibration profiles at different instants ( $T \approx 6.0-6.5$ ) are illustrated in Fig. 7. Apparently, the in-plane response profiles manifest

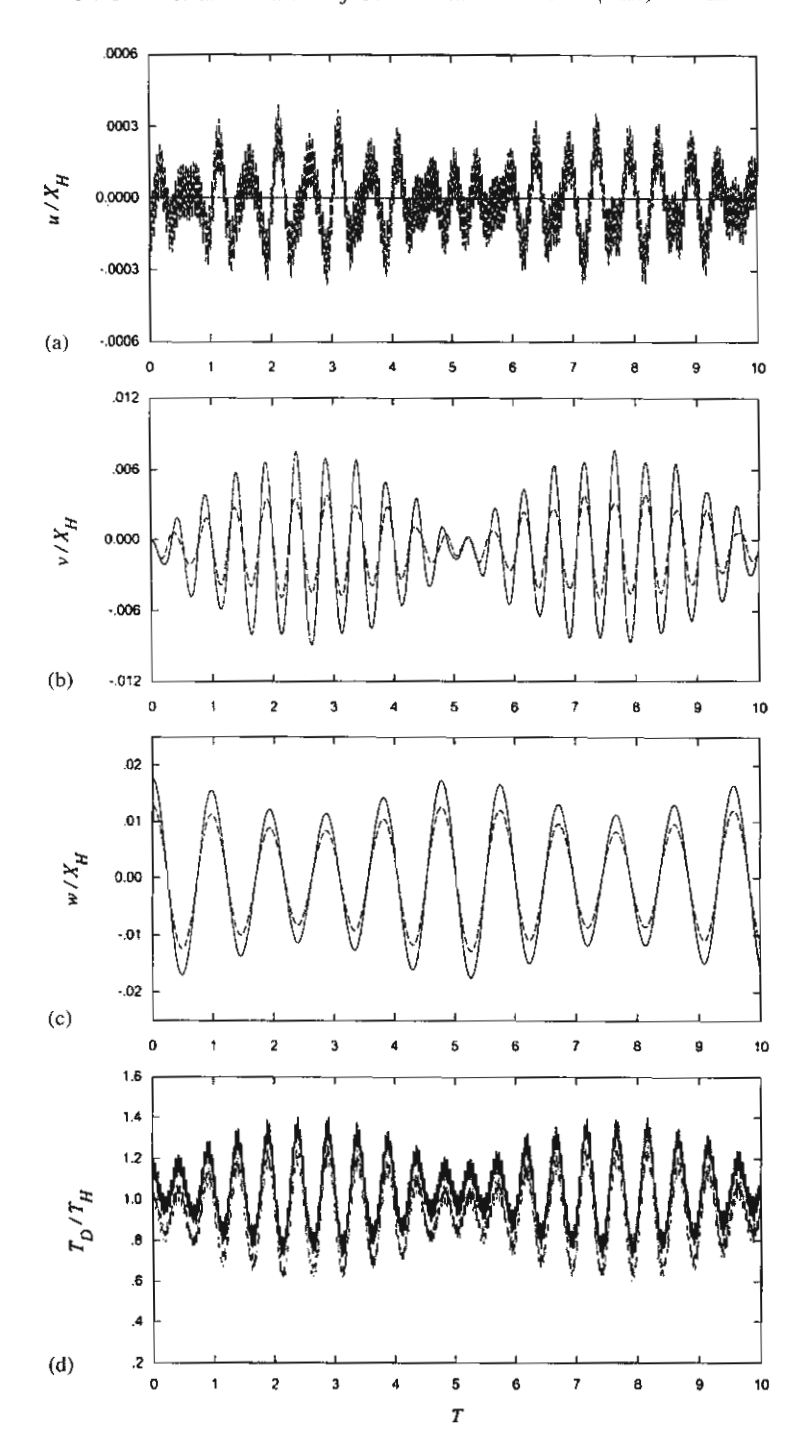


Fig. 3. Dynamic responses of cable B under initial condition of the 1st S-O mode: (a) longitudinal response; (b) vertical response; (c) out-of-plane response: —— mid-span, —— quarter span; (d) cable tension response: —— maximum, —— minimum.

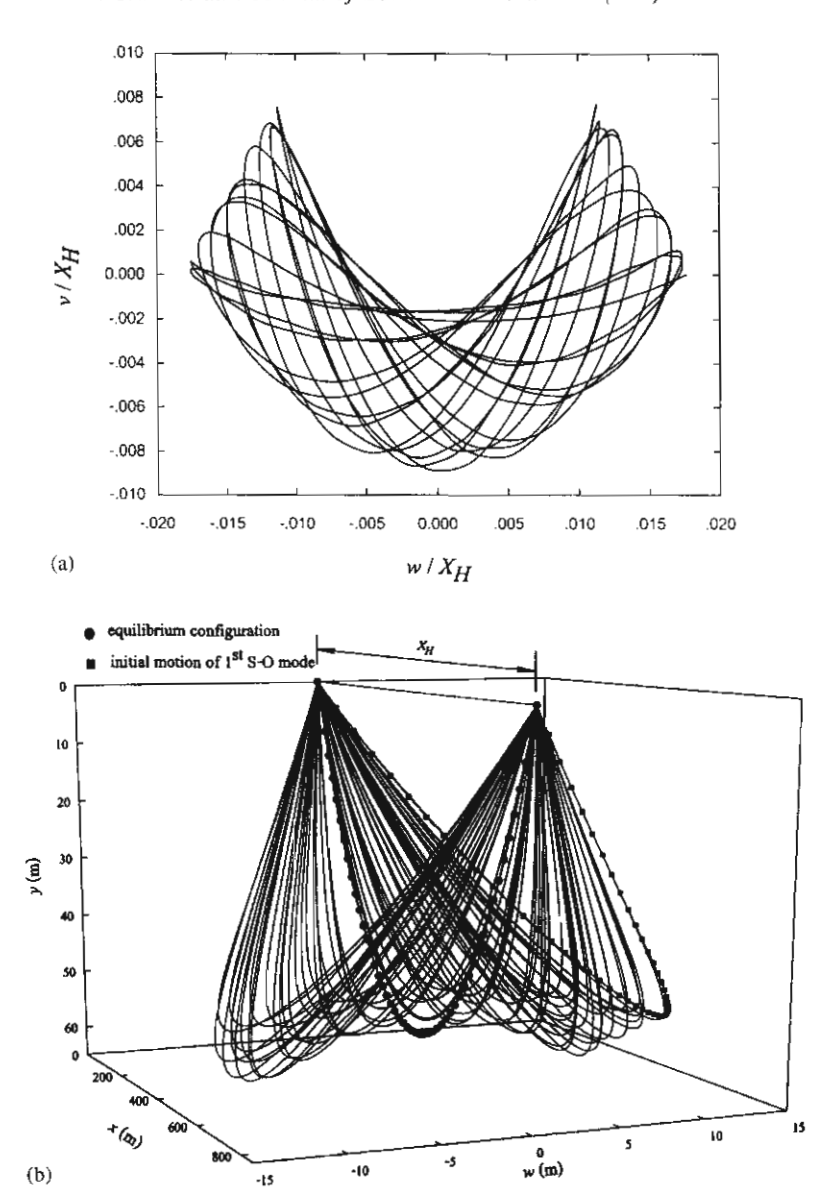


Fig. 4. Response of cable B under initial condition of the 1st S-O mode: (a) relationship plot between vertical and out-of-plane displacements at mid-span; (b) 3-D profiles  $(T \approx 0 - 5)$ .

themselves as a combination of contributions from many modes (Figs. 7(a) and (b)), different from the nearly unimodal out-of-plane profile (Fig. 7(c)). Because of the high modal densities of cable suspensions, significant higher order in-plane modes are generated when a single-mode out-of-plane amplitude is initiated. This multi-harmonic character of the driven in-plane response occurs even for the shallower cables, though to a minor extent. This highlights the need of utilizing a m.d.o.f. cable model in order to obtain detailed and reliable non-linear response predictions, mostly for a relatively large sag cable.

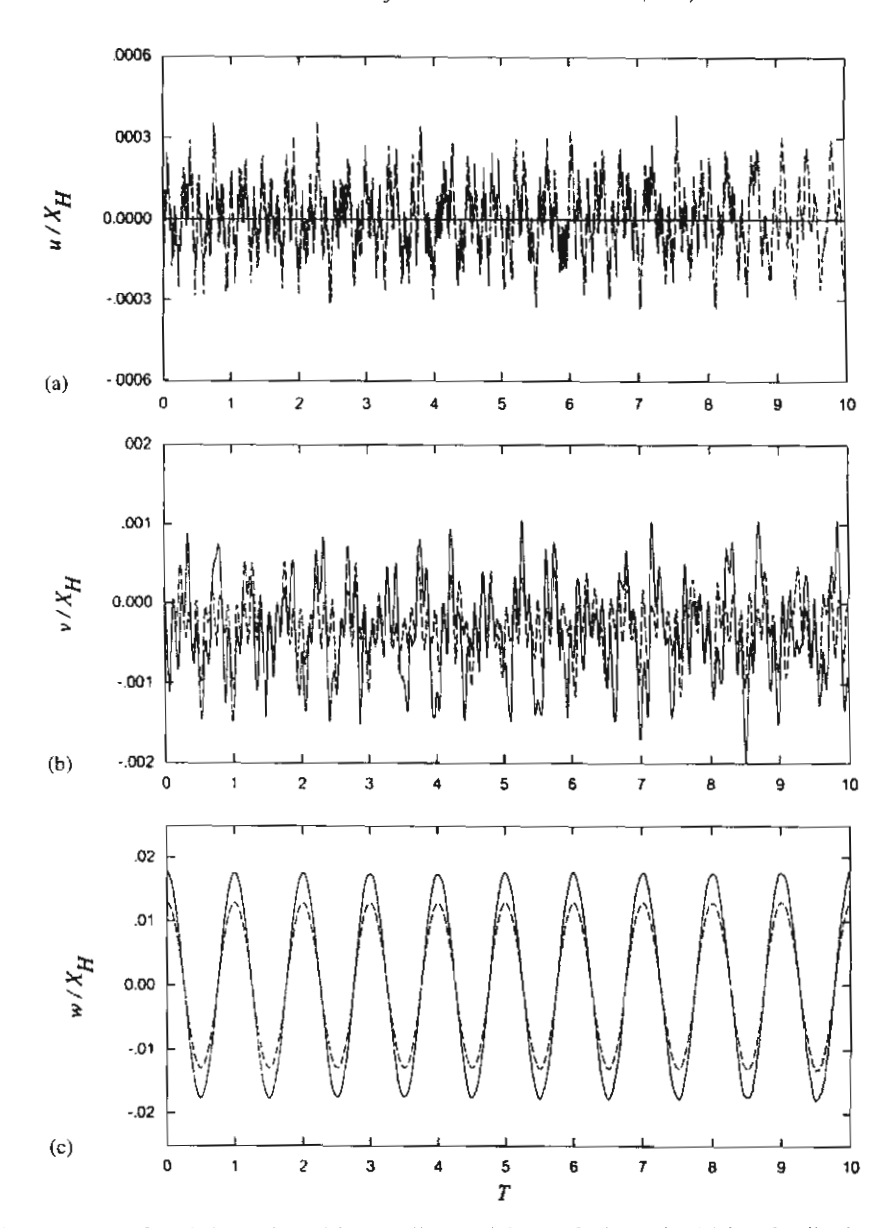


Fig. 5. Dynamic responses of cable D under initial condition of the 1st S-O mode: (a) longitudinal response; (b) vertical response; (c) out-of-plane response: —— mid-span, —— quarter span.

# 4.1.2. First antisymmetric out-of-plane mode (1st A-O mode)

For cable B with  $\Delta=15\,\text{m}$ , the longitudinal and vertical displacements—the former still exhibiting much lower amplitude values—are disturbed by high-frequency components. The inplane response is that of the 2nd S-I mode, which is supposed to be excited according to a super-harmonic coupling (of the order of  $\frac{3}{2}$  approximately) induced by the driving 1st A-O mode, whereas the out-of-plane response is perfectly periodic and its maximum amplitude is of course greater than that occurring at quarter-span when exciting the 1st S-O mode (Fig. 3(c)).

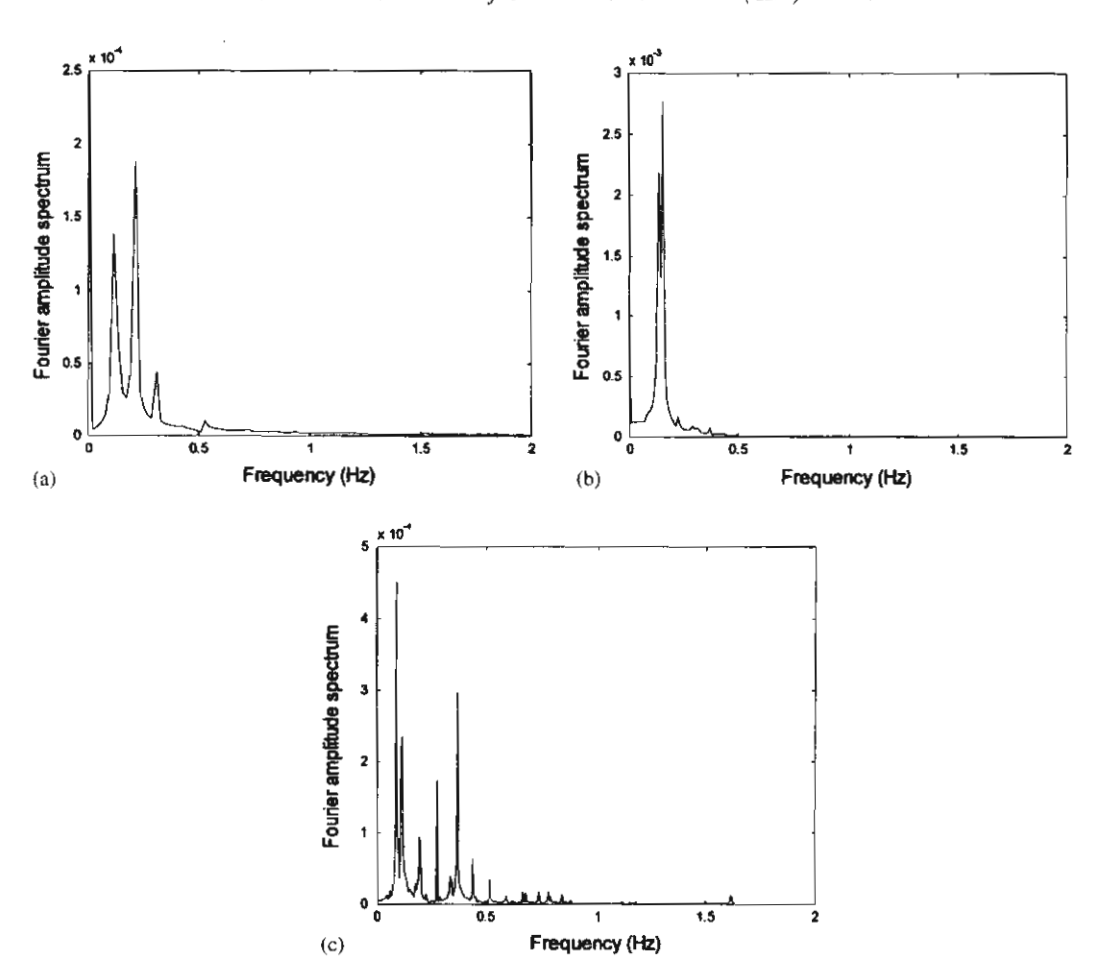


Fig. 6. Fourier amplitude spectra of cable vertical responses under initial condition of the 1st S-O mode: (a) cable A; (b) cable B; (c) cable D.

When considering cable C with  $\Delta=5\,\mathrm{m}$ , the beating phenomenon is observed again for the overall responses (Fig. 8), resembling that obtained for the first resonant cable B in Fig. 3. The associated cable parameter is that of the second crossover where various frequency commensurabilities do occur. Amongst them, the nearly 2:1 internal resonance between the 2nd S-I and 1st A-O modes is actually activable for involving a high-frequency symmetric in-plane mode [31] and, indeed, it plays an important role, as shown by the spatial shapes of the longitudinal and vertical responses of the excited 2nd S-I mode reported in Figs. 9(a) and (b), respectively ( $T \approx 2.4-3.4$ ). The graphs in Figs. 8 and 9 confirm how the non-linear coupling is enhanced due to the internal resonance, which also entails a regularization of the in-plane response—towards which the energy is periodically transferred—with respect to cable B. In particular, the maximum amplitude of the out-of-plane response is reduced to about 0.79 times its initial value, whereas the maximum vertical amplitude rises from zero to about 33% of the maximum out-of-plane amplitude.

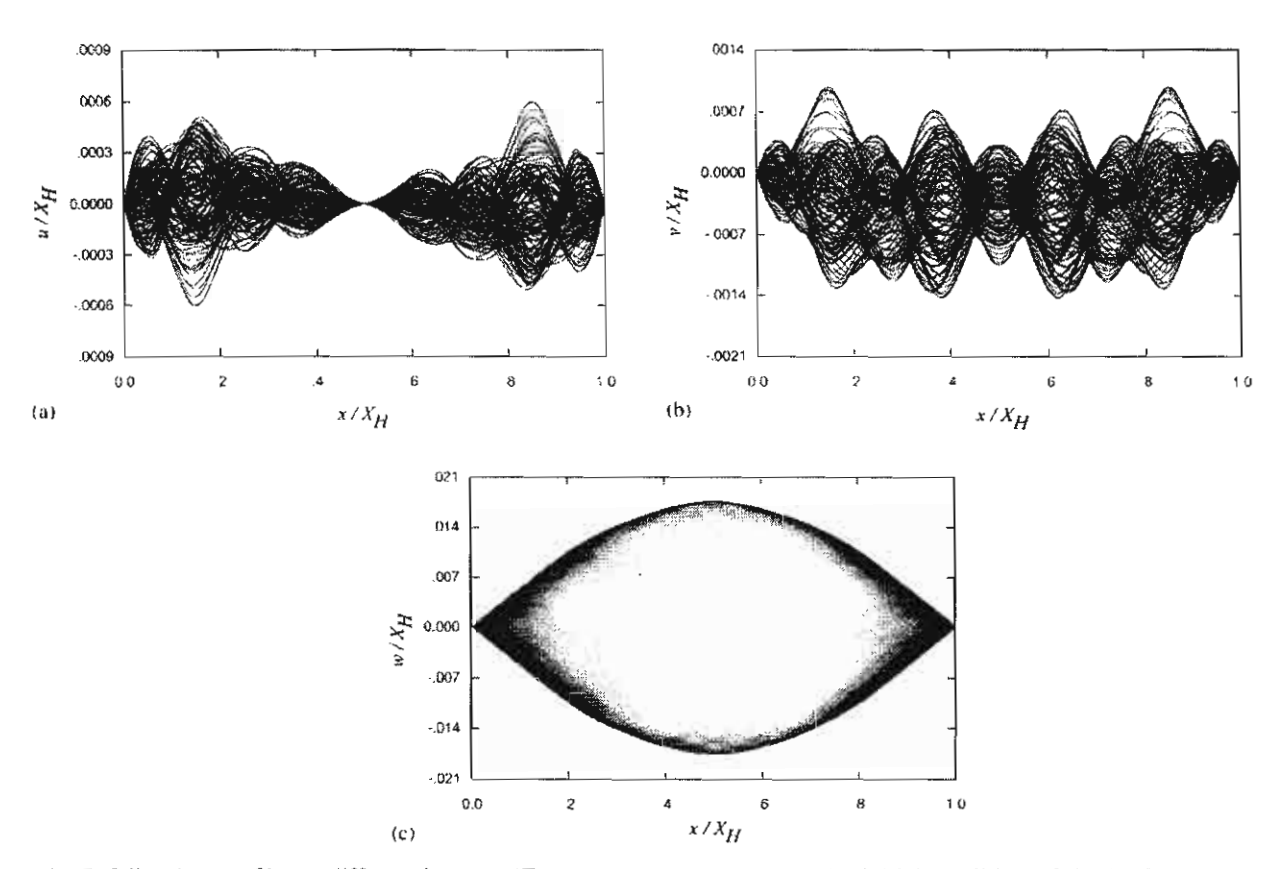


Fig. 7. Vibration profiles at different instants ( $T \approx 6.0 - 6.5$ ) for cable D under initial condition of the 1st S-O mode: (a) longitudinal response; (b) vertical response; (c) out-of-plane response.

With the same initial amplitude, a combination of high-frequency components occurs again in the in-plane responses of cable D for which no internal resonance exists. The Fourier amplitude spectrum of the corresponding in-plane response is illustrated in Fig. 10 against those of cables B and C. The driven vertical responses of cables B and, mostly, D contain higher frequency components (Figs. 10(a) and (c)). Due to a 2:1 resonant condition, the vertical response of cable C has a single frequency (Fig. 10(b)), whose value (0.234 Hz) is approximately twice that of the out-of-plane one (0.117 Hz). These results highlight the fact that, apart from the regularizing effects entailed by the internal resonance condition, the in-plane response excited by the out-of-plane motion for a generic (non-resonant) cable is non-periodic, due to a combination of high-frequency components, irrespective of cable sag condition. The multi-harmonic longitudinal and vertical responses of cable D are displayed in Figs. 11(a) and (b) ( $T \approx 4.0-4.5$ ) against the harmonic out-of-plane one (Fig. 11(c)), with the amplitude of the longitudinal response being now nearly comparable to that of the vertical one due to the large sag effect.

From the numerical results obtained in Section 4.1, non-zero values of vertical responses are obtained at cable mid-span. While highlighting that symmetric in-plane modes are excited by a prescribed out-of-plane mode, either symmetric or antisymmetric, this also confirms numerically

# N. Srinil et al. / Journal of Sound and Vibration & (\*\*\*\*) 331-831

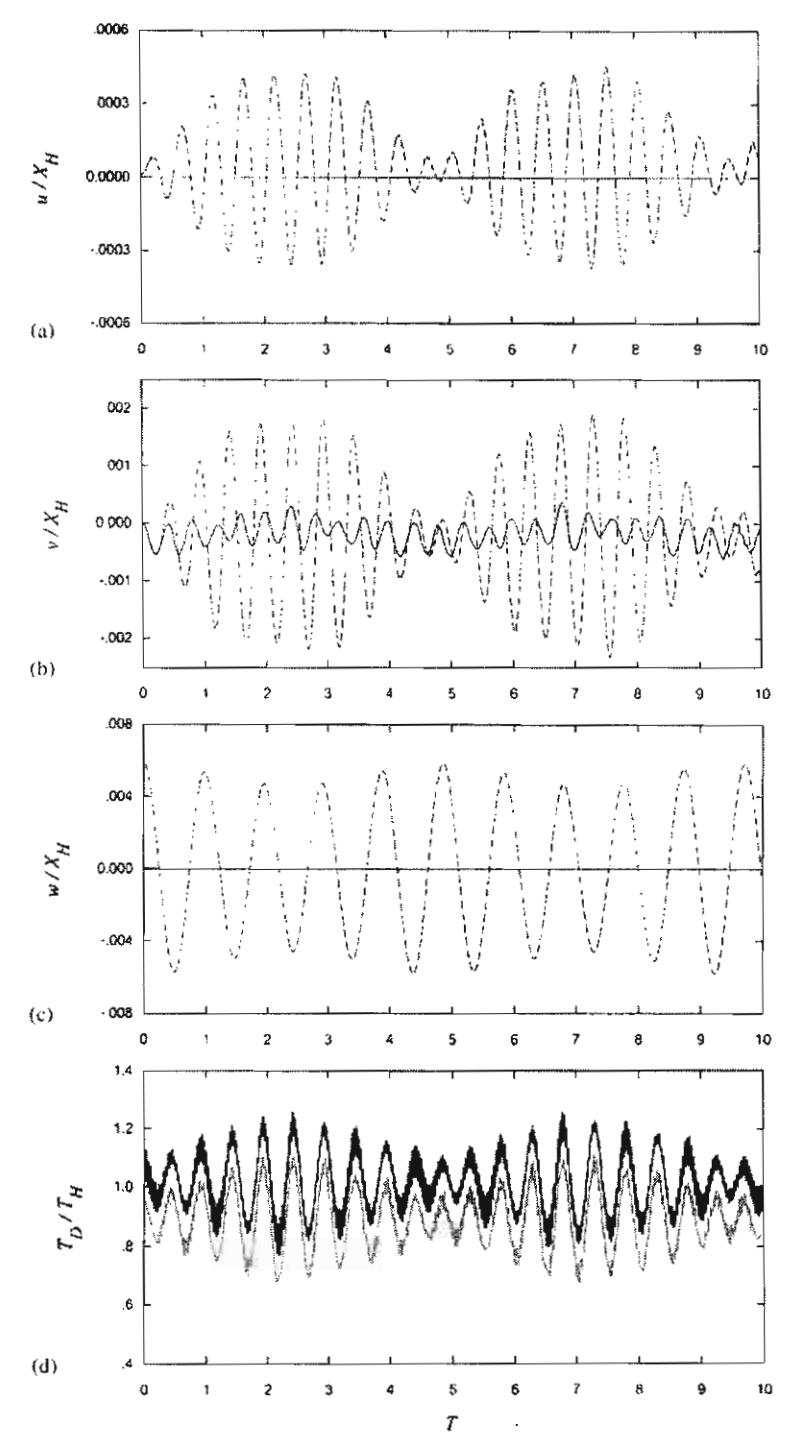


Fig. 8. Dynamic responses of cable C under initial condition of the 1st A-O mode: (a) longitudinal response; (b) vertical response; (c) out-of-plane response: —— mid-span, —— quarter-span; (d) cable tension response: —— maximum, —— minimum.



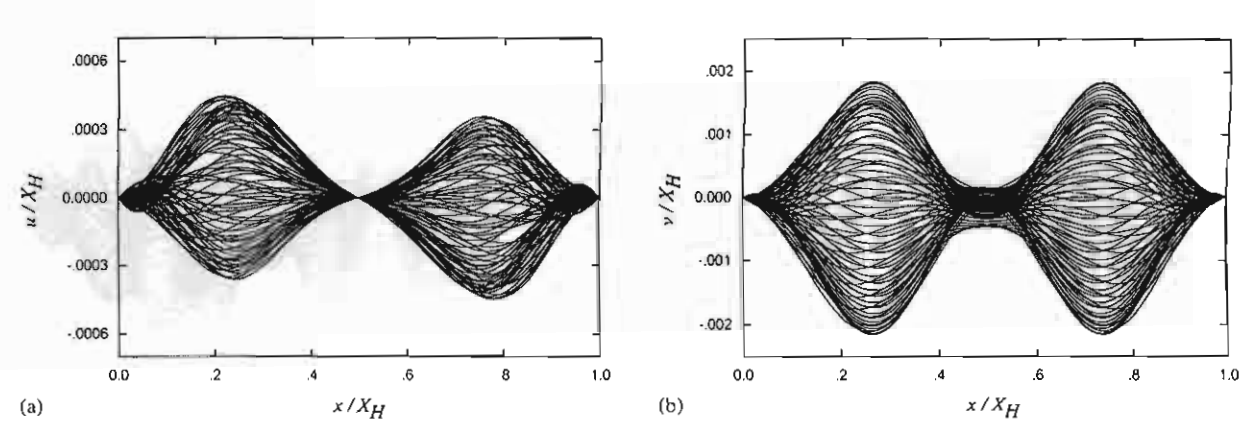


Fig. 9. Vibration profiles at different instants ( $T \approx 2.4 - 3.4$ ) for cable C under initial condition of the 1st A-O mode: (a) longitudinal response; (b) vertical response.

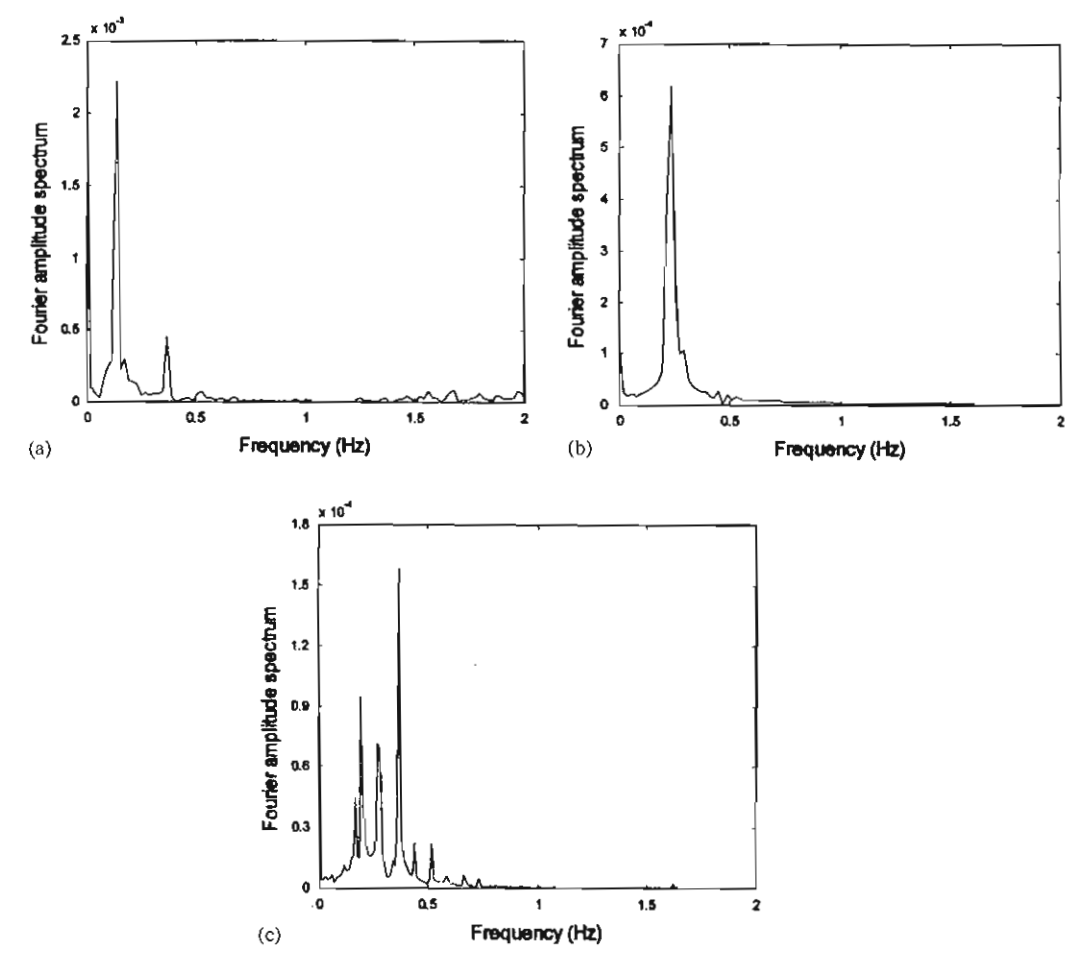


Fig. 10. Fourier amplitude spectra of cable vertical responses under initial condition of the 1st A–O mode: (a) cable B; (b) cable C; (c) cable D.

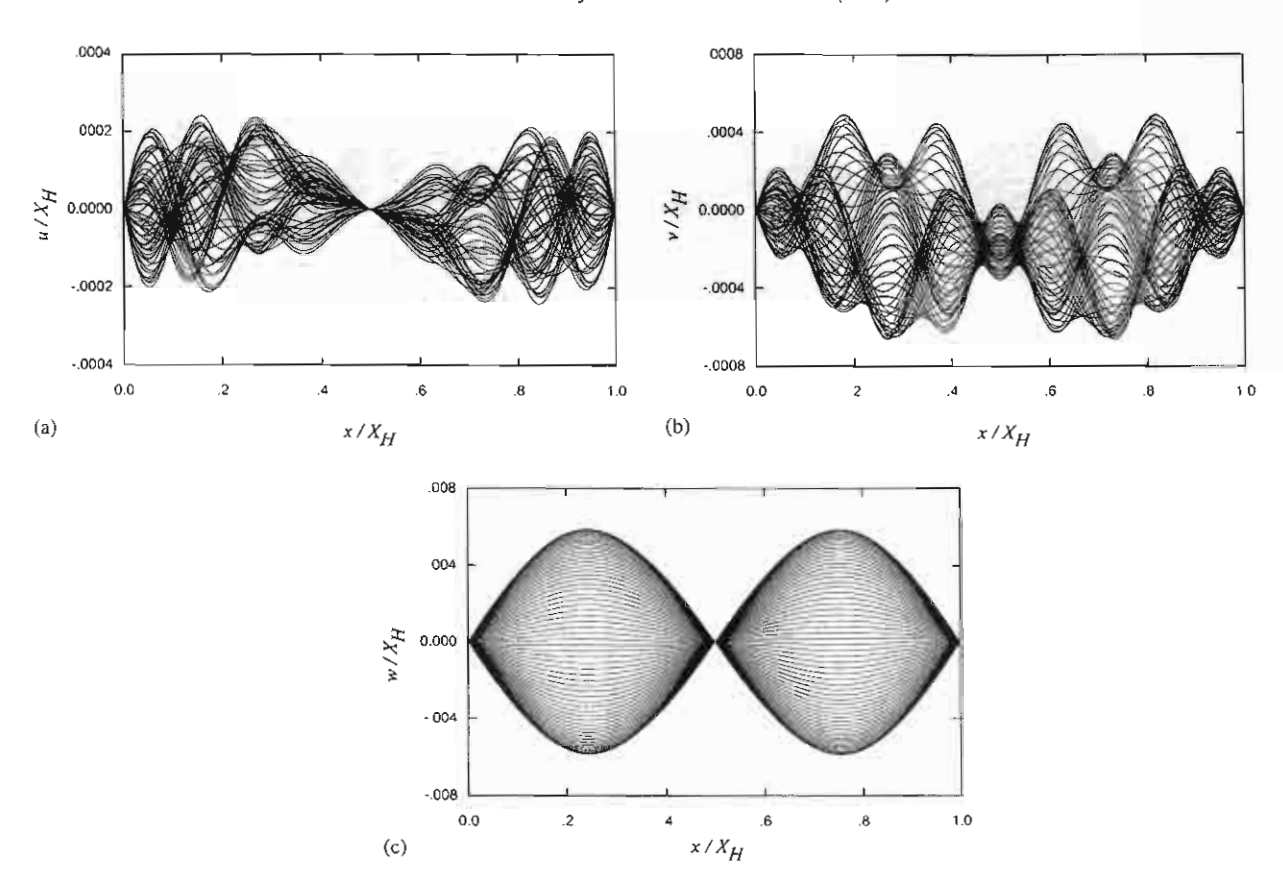


Fig. 11. Vibration profiles at different instants ( $T \approx 4.0 - 4.5$ ) for cable D under initial condition of the 1st A-O mode: (a) longitudinal response; (b) vertical response; (c) out-of-plane response.

the theoretically predicted role [31] of symmetric in-plane modes in the actual activation of 2:1 internal resonances at crossover points. As regards cables with significant sag, it is worth noticing that the occurrence of a multi-harmonic response in the driven displacement components justifies the consideration of a m.d.o.f. cable model.

#### 4.2. Large-amplitude in-plane free vibrations

Without any external excitation, no 3-D coupling occurs when only in-plane amplitude is initiated. This is because of the existence of monofrequent in-plane vibrations [2], consistent with the vanishing of all terms in the coupled equation of motion (Eq. (22)) when the variables corresponding to the out-of-plane displacement are set to zero. Nevertheless, there occur some interesting interaction behaviors, which are discussed below.

#### 4.2.1. First symmetric in-plane mode (1st S-I mode)

When considering cable A with  $\Delta = 15 \,\mathrm{m}$ , the longitudinal responses are very low, the vertical responses are periodic, and the maximum tension has a steady maximum value greater than that

18

N. Srinil et al. I Journal of Sound and Vibration 1 (1111) 111-111

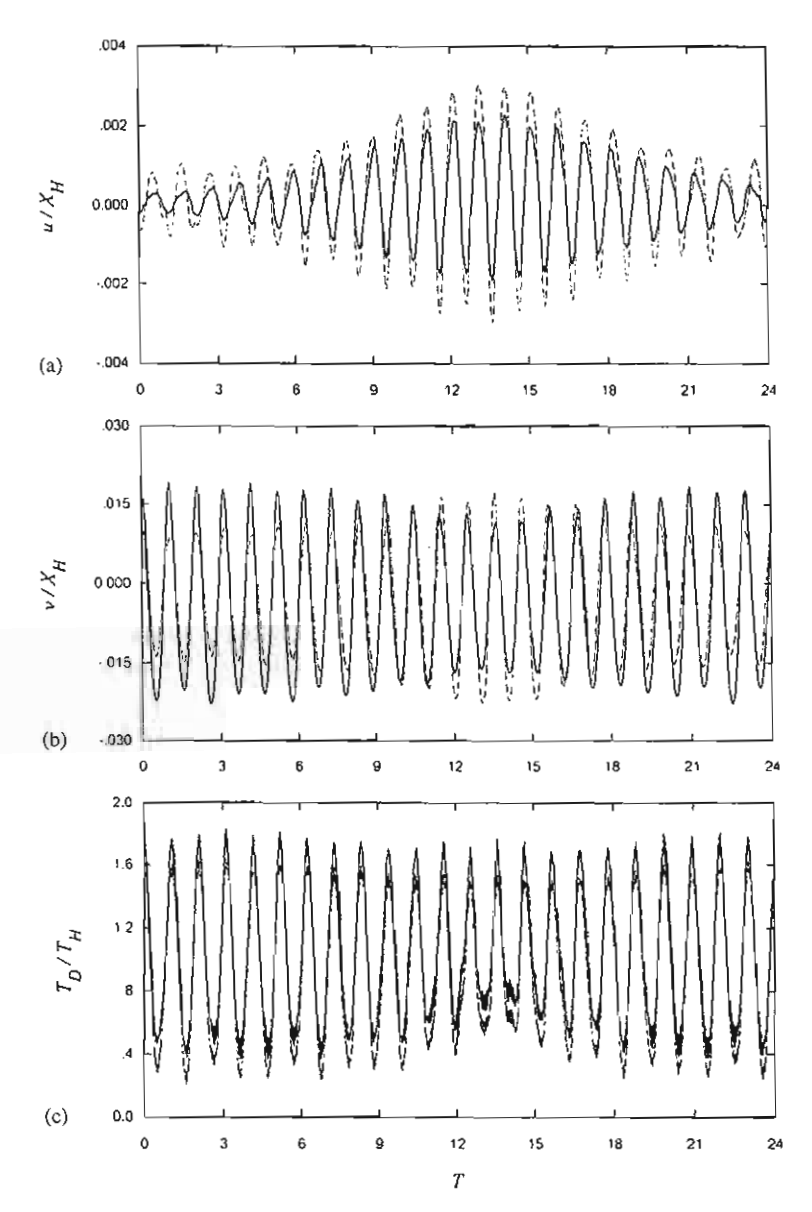


Fig. 12. Dynamic responses of cable B under initial condition of the 1st S-I mode: (a) longitudinal response; (b) vertical response: — mid-span, — quarter span; (c) cable tension response: — maximum, —— minimum.

induced by the symmetric out-of-plane mode. In contrast, when considering cable B with the same initial amplitude, some outstanding characteristics are observed in the responses (Fig. 12). The vertical amplitude at mid-span, which is of course larger than the amplitude at quarter-span, is reduced evidently in some intervals ( $T \approx 12-15$ ). Correspondingly, the longitudinal amplitude is increased due to a beating-like exchange. In contrast, both longitudinal and vertical amplitudes at quarter-span increase up to 4.74 and 2.00 times their initial values, respectively.

N. Srinil et al. | Journal of Sound and Vibration 1 (1111) 111-111

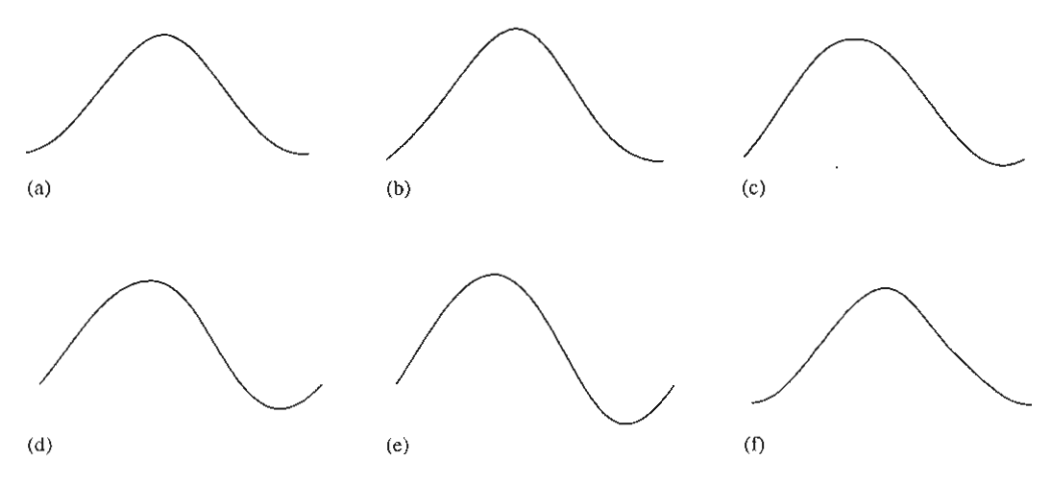


Fig. 13. Modal transition of cable B at different instants under initial condition of the 1st S-I mode: (a)  $T \approx 2.1$ ; (b)  $T \approx 5.2$ ; (c)  $T \approx 8.4$ ; (d)  $T \approx 10.5$ ; (e)  $T \approx 12.6$ ; (f)  $T \approx 23.0$ .

For the sake of convenience, the transition of the vibration profile is shown to explain what occurs during this time duration. Only the dominant vertical displacements are displayed. As exemplified in Fig. 13, initially  $(T \approx 2.1)$  the vibration profile corresponds closely to the symmetric in-plane mode at the first crossover, namely it is tangential to the equilibrium cable profile at each support (Fig. 13(a)). The associated antisymmetric longitudinal displacement is nearly zero at mid-span. Then, the vibration profile evolves smoothly towards a hybrid asymmetric shape (Figs. 13(d) and (e)) which accounts for a superimposition of the first symmetric and antisymmetric modes. Accommodation of the latter into the response ensues from cable B corresponding to a perfectly tuned 1:1 internal resonance between the two in-plane modes and from 1:1 internal resonances being always activable at crossover points [31]. Due to the antisymmetric vertical displacement accompanied by a symmetric longitudinal one with maximum value at quarter-span [30], the simultaneous increase of both corresponding amplitudes in Figs. 12(a) and (b) is explained. Afterwards, the vibration profile returns back to the symmetric mode ( $T \approx 23.0$ , Fig. 13(f)). In turn, the tension responses—which attain rather large values, on average—change slightly when the hybrid mode phenomenon takes place (Fig. 12(c)). The previous results further confirm some points made in the literature (see, e.g., Refs. [11,14]) about the antisymmetric mode being driven in the response by an existing symmetric one due to non-linear modal coupling and a mechanism of induced dynamic tension. The difference here is that the in-plane coupled dynamics are non-stationary.

Exciting the large-sagged cable D with a reduced initial amplitude ( $\Delta = 5 \,\mathrm{m}$ ), the longitudinal and vertical responses are slightly disturbed by high-frequency components. This implies that the cable sag has an influence also on the in-plane response besides the out-of-plane one. Moreover, the difference in magnitude occurring between maximum and minimum tensions (Fig. 14) justifies the need to take into account strain variations in the non-linear cable model.

#### 4.2.2. First antisymmetric in-plane mode (1st A–I mode)

No special features are observed in the dynamic response of the 1:1 resonant cable B with  $\Delta = 15 \,\text{m}$ , different from the previous case of excitation with symmetric mode, in particular no



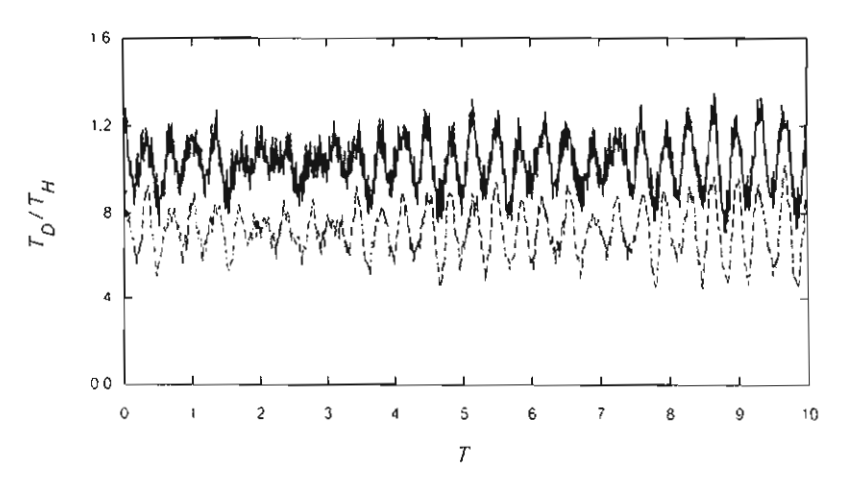


Fig. 14. Cable tension responses of cable D under initial condition of the 1st S-I mode: —— maximum, --- minimum.

other modes enter the response. Considering cable C with  $\Delta = 5 \,\mathrm{m}$ , the beating phenomenon is clearly observed in the force responses (Fig. 15(c)), while some noteworthy characteristics occur in the displacement time histories, too (Figs. 15(a) and (b)). The observed behavior is governed by a kind of internal resonance existing at the second crossover. The vibration profiles at different times are displayed comparatively in Fig. 16. Evidently, the shape of vertical response evolves from the initial antisymmetric mode, occurring when  $T \approx 1.0$  (Fig. 16(a)), to the second symmetric mode (Fig. 16(b)), up to a hybrid profile accounting for the two modes when  $T \approx 4.7$  (Fig. 16(d)). Then, the shape returns to the second symmetric mode (Fig. 16(e)), and eventually develops to become again the original antisymmetric mode when  $T \approx 6.7$  (Fig. 16(f)). Thus, Fig. 16 reveals how the 2nd S-I mode is excited and accommodated into the response initiated by the 1st A-I mode due to their involvement in a 1:2 internal resonance, which is again activated because of the higher-frequency mode being symmetric [31]. This higher mode is seen to substantially dominate the cable vibration profile in some intervals of the considered time stepping, and to cause meaningful increases in the magnitude of cable tension responses (Fig. 15(c)). The non-linear frequencies dominating the longitudinal and vertical responses are evaluated using the Fourier amplitude spectral densities, as shown in Figs. 17(a) and (b). They are approximately equal to 0.115 and 0.225 Hz, thus being both greater than the corresponding linear frequencies of first antisymmetric and second symmetric modes (Table 1), respectively: the system is thus seen to exhibit a weakly hardening non-linear behavior.

Two points are worth noticing for the present cable C at the second crossover, where various internal resonances occur. (i) The (coexisting) 2:1 resonance between the 2nd A–I mode and the initiated 1st A–I mode does not play any role, which ensues from the activation of 2:1 in-plane resonances requiring contribution from at least one (higher-frequency) symmetric mode [31]. (ii) The activable 1:1 internal resonance involving the 2nd S–I and 2nd A–I modes—and characterizing the second crossover—also occurs, but it does not play any role, too, since the 1st A–I mode is initiated. Consequently, it seems worth analyzing how the motion behaves when applying the 2nd S–I mode as the initial condition, instead. Fig. 18 shows the overall responses

#### N. Srinil et al. / Journal of Sound and Vibration 1 (1111) 111-111

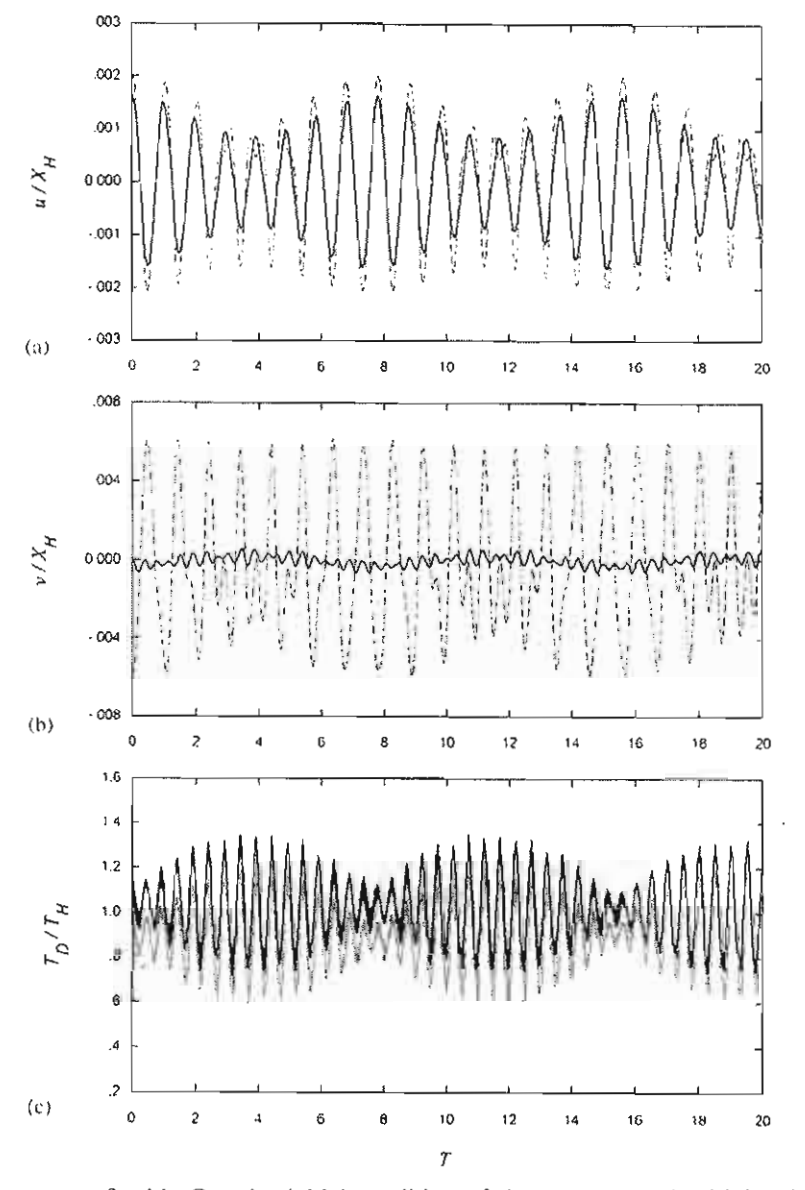


Fig. 15. Dynamic responses of cable C under initial condition of the 1st A-I mode: (a) longitudinal response; (b) vertical response: —— mid-span, —— quarter span; (c) cable tension response: —— maximum, —— minimum.

under this initiation with the same assigned amplitude ( $\Delta = 5 \,\mathrm{m}$ ) as before. Two interesting features are observed. (i) The longitudinal and vertical amplitudes at quarter-span are both increased to about 3.23 and 1.54 times their initial value, respectively; (ii) correspondingly, the relevant non-linear frequencies both decrease.

To explain the first point, the transition of the vibration profiles associated with the vertical amplitudes is displayed in Fig. 19 for those particular time intervals. Starting from  $T \approx 11.4$ , the

N. Srinil et al. | Journal of Sound and Vibration 1 (1111) 111-111

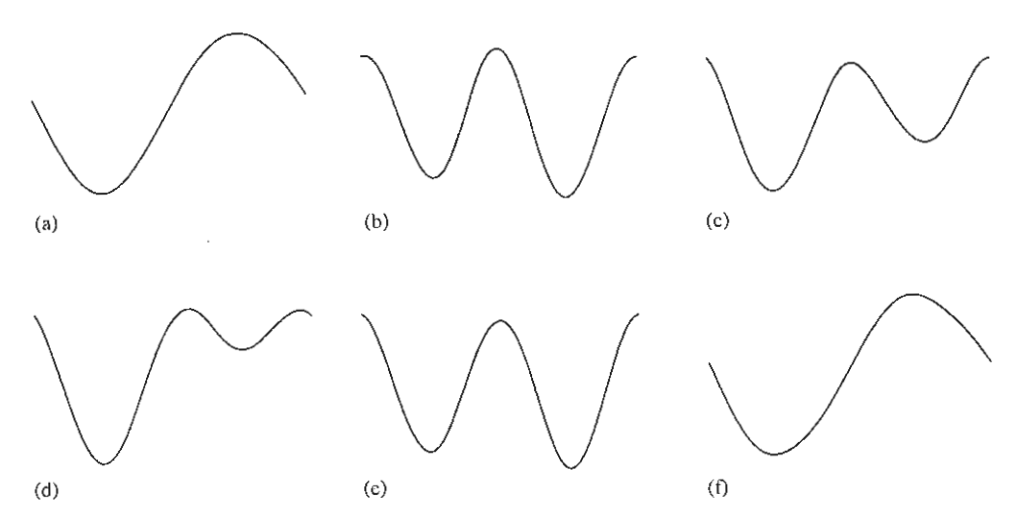


Fig. 16. Modal transition of cable C at different instants under initial condition of the 1st A-I mode: (a)  $T \approx 1.0$ ; (b)  $T \approx 2.7$ ; (c)  $T \approx 3.7$ ; (d)  $T \approx 4.7$ ; (e)  $T \approx 5.1$ ; (f)  $T \approx 6.7$ .

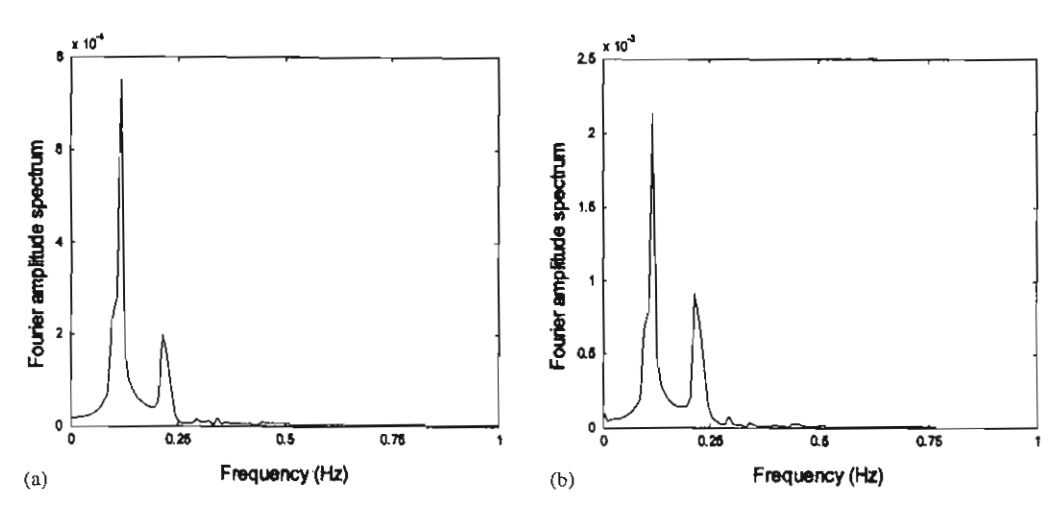


Fig. 17. Fourier amplitude spectra of cable C under initial condition of the 1st A-I mode: (a) longitudinal response at quarter span; (b) vertical response at quarter span.

profile corresponds to the 2nd S-I mode (Fig. 19(a)), then it evolves to a hybrid profile when  $T \approx 20.7$  (Fig. 19(b)), up to changing completely into the 1st A-I mode when  $T \approx 22.6$  and 24.3 (Figs. 19(c) and (d)). After attaining a further hybrid shape (Fig. 19(e)), the 2nd S-I mode resettles again at  $T \approx 30.4$  (Fig. 19(f)). This phenomenon of modal transition repeats itself as long as no external disturbance is imposed on the cable. Thus, Fig. 19 reveals how the lower order antisymmetric mode is excited and accommodated into the cable response due to the 2:1 internal resonance condition. During the time interval where the vertical profile coincides approximately with the antisymmetric mode, the cable tension in Fig. 18(c) diminishes by about 40% with respect to its maximum value, as expected from the linear theory since antisymmetric modes entail

#### N. Srinil et al. / Journal of Sound and Vibration I (IIII) III-III

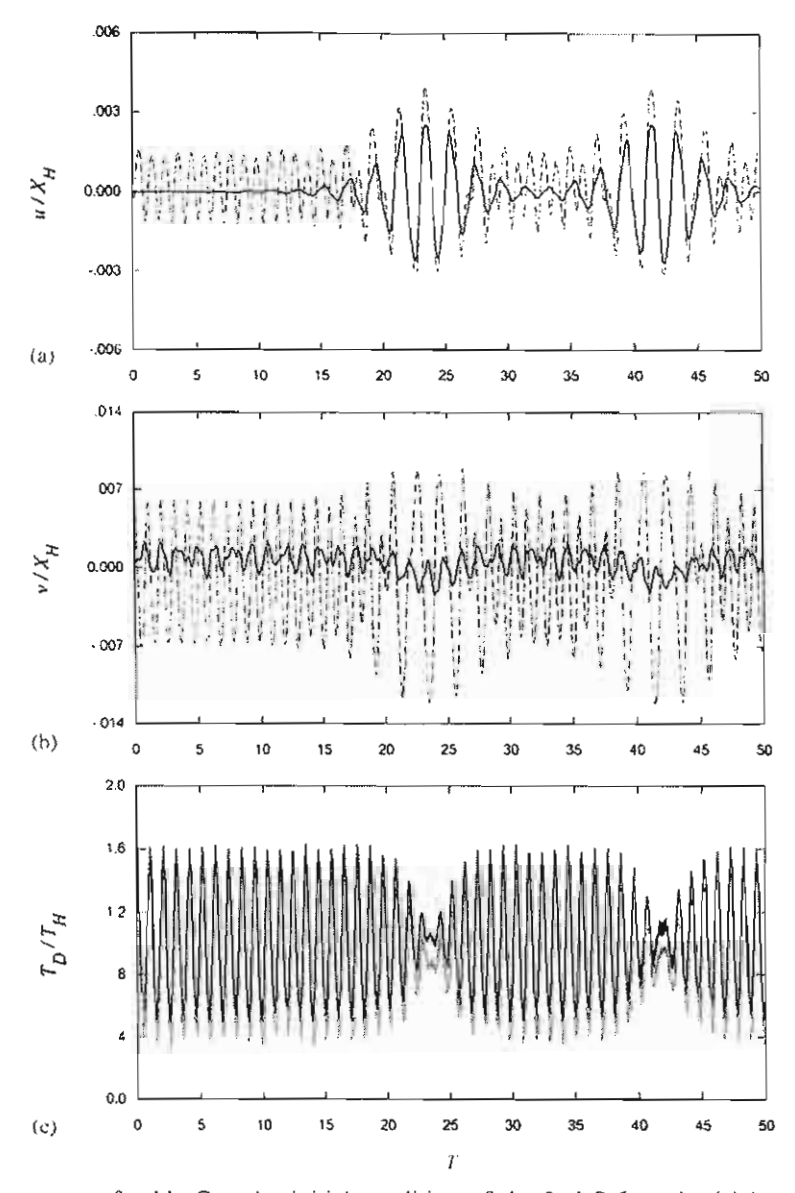
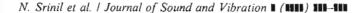


Fig. 18. Dynamic responses of cable C under initial condition of the 2nd S-I mode: (a) longitudinal response; (b) vertical response: —— mid-span, —— quarter span; (c) cable tension response: —— maximum, —— minimum.

no first order axial stretching. The obtained results (Figs. 18 and 19) are substantially the reverse of those in Figs. 15 and 16, with the role of the two involved modes being exchanged with each other during the transition interval. A difference is represented by the amplitude decrease (increase) of both the longitudinal and vertical responses occurring in the transition interval when the first antisymmetric (second symmetric) mode is initiated. Besides ensuing from the specific profile changes, it also expresses the circumstance of the 2nd S–I mode being more constrained



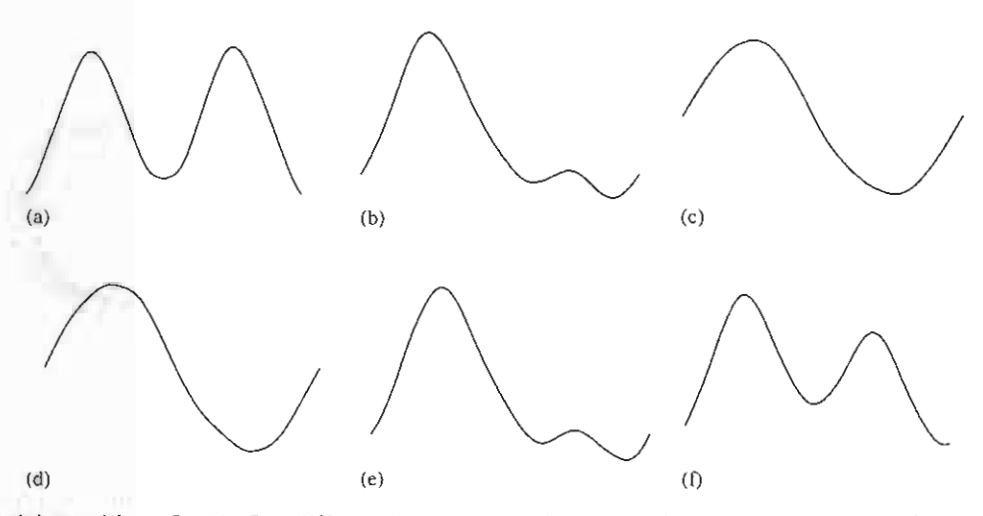


Fig. 19. Modal transition of cable C at different instants under initial condition of the 2nd S–I mode: (a)  $T \approx 11.4$ ; (b)  $T \approx 20.7$ ; (c)  $T \approx 22.6$ ; (d)  $T \approx 24.3$ ; (e)  $T \approx 26.3$ ; (f)  $T \approx 30.4$ .

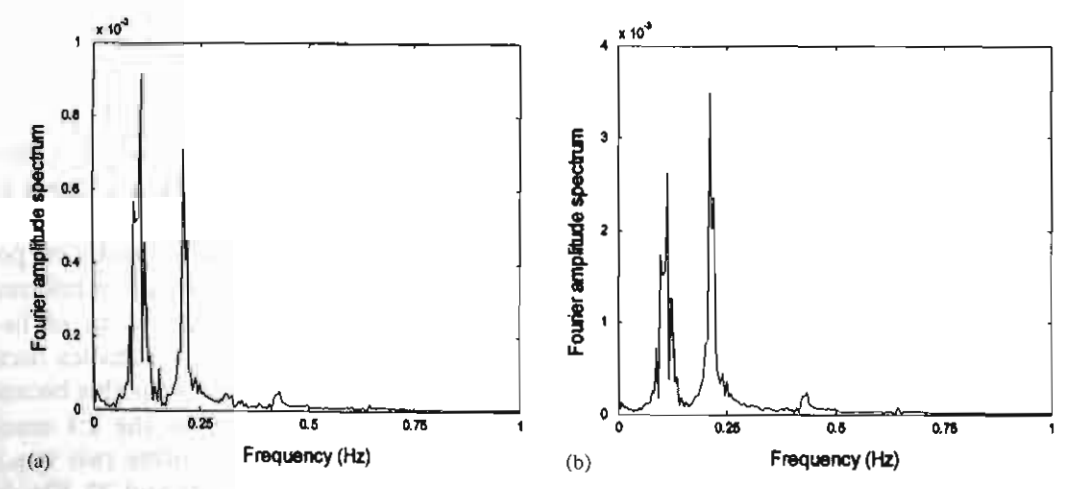


Fig. 20. Fourier amplitude spectra of cable C under initial condition of the 2nd S-I mode: (a) longitudinal response at quarter span; (b) vertical response at quarter span.

than the 1st A-I one, which entails a lower amplitude of the former with respect to the latter at a given energy level. Thus, one can conclude that the dominant internal resonance is the 2:1 one even when initiating the 2nd S-I mode. The possible activation of the 2nd A-I mode involved in the 1:1 resonance with the excited symmetric one does not actually occur, since the 2:1 resonance usually dominates instead of the coexisting 1:1 [14].

To check the frequency of longitudinal and vertical responses in the transition interval, the Fourier amplitude spectra are illustrated (Figs. 20(a) and (b)). The non-linear frequencies are equal to 0.107 and 0.210 Hz, approximately, and denote a weakly softening non-linear behavior, contrary to the first antisymmetric initiation. Phase-plane portraits are also reported in Fig. 21,

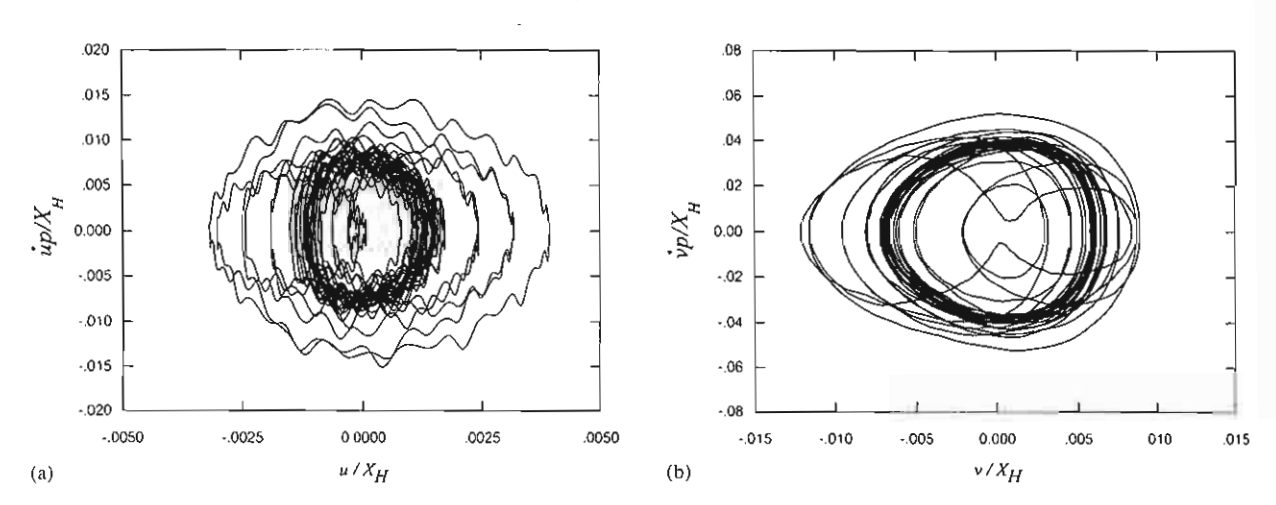


Fig. 21. Phase-plane portraits of cable C under initial condition of the 2nd S-I mode: (a) longitudinal response at quarter span; (b) vertical response at quarter span.

whose variable p in the vertical axis is the linear period of the initiated mode. They exhibit elliptical trajectories of maximum displacements with features of amplitude modulation of both longitudinal and vertical responses, as well as of small perturbations of the former. Fig. 21 shows how the energy of the motion changes through the dominant resonant condition, namely the inner repeated ellipses indicate the motion on the second symmetric mode, whereas the outer ellipses correspond to the first antisymmetric mode.

This section is concluded with a further short comment about numerical checks on possible activation/non-activation of coexisting internal resonances. Another cable yet to be referred (not reported in Table 1) corresponds to the 3rd crossover point (namely,  $\lambda/\pi=6$ ) of in-plane frequencies. In such a case, theoretical predictions [31] suggest that the 3:1 resonance occurring between 3rd S-I mode ( $\omega \approx 0.281$  Hz) and 1st A-I mode ( $\omega \approx 0.094$  Hz) is not activable because the involved modes are of a different type (symmetric-antisymmetric), whereas the 2:1 resonance between 3rd S-I and 1st S-I ( $\omega \approx 0.141$  Hz) could be activated since it involves two symmetric modes. Numerical results confirm these predictions, as highlighted in Figs. 22 and 23. The former shows the overall responses of this new cable due to 3rd S-I initiation; the vibration profiles in the latter show the accommodation of the 1st S-I mode (Fig. 23(d)) in the response dominated by the 3rd S-I mode (Figs. 23(a) and (f)), within the transition interval of Figs. 22(b) and (c) where the vertical amplitude at mid-span increases and the dynamic tension decreases.

#### 5. Conclusions

A 3-D model formulation capable of analyzing the large-amplitude free vibrations of a suspended cable has been developed. According to a m.d.o.f. model of cable, which accounts for the axial deformation effect, the formulation is not restricted to cables having small sag-to-span ratios. A finite difference discretization of the equations of motion in both space and time has

#### 

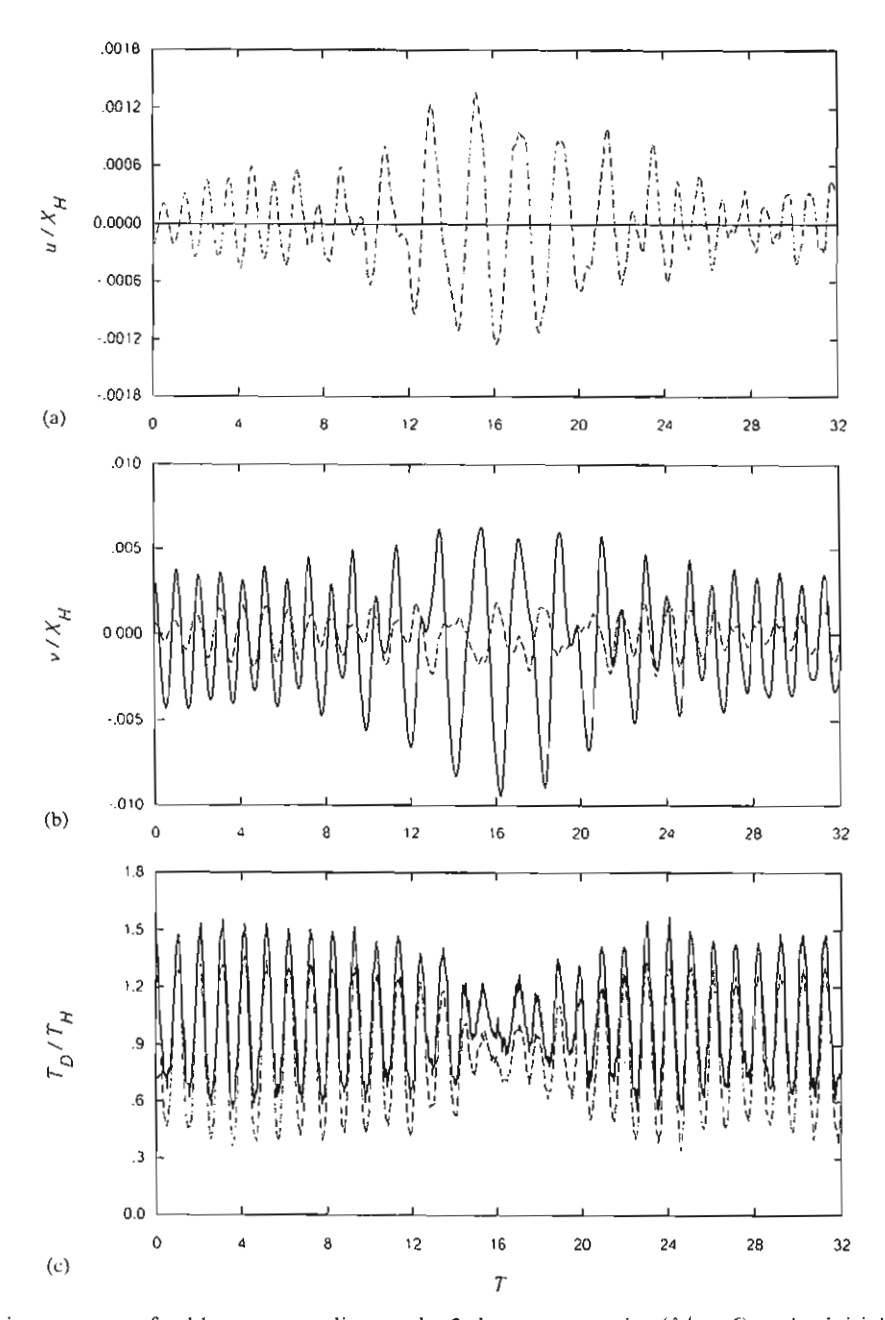


Fig. 22. Dynamic responses of cable corresponding to the 3rd crossover point  $(\lambda/\pi \approx 6)$  under initial condition of the 3rd S-I mode: (a) longitudinal response; (b) vertical response: mid-span, --- quarter span; (c) cable tension response: maximum, minimum.

been performed and numerically implemented to obtain time histories of non-linear dynamic response. Numerous examples of cables subjected to initial large-amplitude out-of-plane or in-plane vibrations have been discussed in the case of a specified end tension.

N. Srinil et al. I Journal of Sound and Vibration I (IIII) III-III

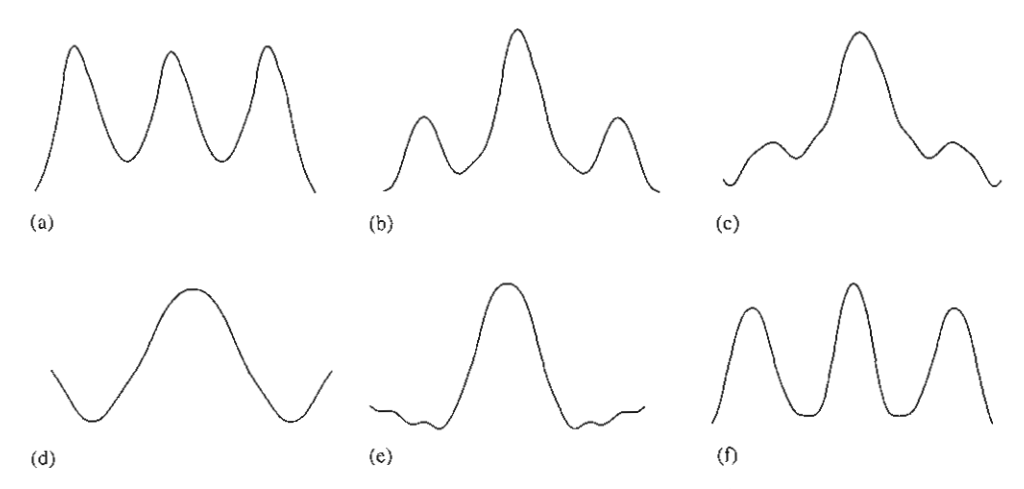


Fig. 23. Modal transition of cable corresponding to the 3rd crossover point  $(\lambda/\pi \approx 6)$  at different instants under initial condition of the 3rd S-I mode: (a)  $T\approx 6.2$ ; (b)  $T\approx 9.3$ ; (c)  $T\approx 11.3$ ; (d)  $T\approx 15.3$ ; (e)  $T\approx 19.0$ ; (f)  $T\approx 28.2$ .

Based on the analysis results, the following points on cable non-linear behaviors are drawn, in the case of out-of-plane initial displacement conditions.

- Symmetric in-plane modes are excited irrespective of the initiating out-of-plane motion being symmetric or antisymmetric, with the latter case involving higher symmetric modes.
- Regardless of cable sag condition, the driven in-plane response of a non-resonant cable is non-periodic, unlike the periodically driven response of an internally resonant cable. In turn, non-linear 3-D coupling is enhanced by the occurrence of an internal resonance condition.
- The cable tension is augmented mostly due to the occurrence of increased in-plane vibration amplitudes, and is further enhanced when the cable exhibits internally resonant frequencies.
- For a cable sagging significantly, the cable vibration profiles exhibit qualitatively multiharmonic responses due to geometric non-linearities: this accounts for the need to consider m.d.o.f. cable models. In addition, the longitudinal response tends to become nearly comparable to the vertical one, though being an order of magnitude lower than that for low-sagged cables.

In the case of in-plane initial displacement conditions, depending on driving mode and on magnitude of specified initial amplitude, worthwhile phenomena of modal transition may take place for crossover cables during the ensuing in-plane vibrations. Indeed, due to the occurrence of a dominant internal resonance, a higher or lower mode can be accommodated into the response initiated by a single mode, making the cable vibration profile hybrid in some intervals of the considered time marching. Besides the well-known 1:1 internally resonant cable at the first crossover, whose first antisymmetric mode is excited when the first symmetric mode is initiated, various modal transition phenomena occur for 2:1 resonant cables. E.g., at the second crossover, the second symmetric (first antisymmetric) mode is excited when the first antisymmetric (second symmetric) mode is initiated: the excited symmetric (antisymmetric) mode may dominate substantially the cable vibration profile, as well as induce meaningful increase (decrease) in the

magnitude of cable tension responses. Moreover, the difference in magnitude between maximum and minimum tensions increases for a cable with significant sag, which highlights the need to account for strain variation in the cable model.

All of the numerical results obtained for cables at crossovers have been discussed against the background of the theoretical predictions about activation of 1:1 or 2:1 internal resonances made within an infinite dimensional analytical framework [31]. Besides highlighting the dynamic effects entailed by their actual activation, numerical results provide worthwhile information about which one of the coexisting internal resonances actually governs the system dynamics.

#### Acknowledgements

The authors gratefully acknowledge the financial support of the Thailand Research Fund (TRF) under Grants PHD/0167/2543 and RTA/03/2543.

#### References

- [1] P. Hagedorn, B. Schafer, On non-linear free vibrations of an elastic cables, International Journal of Non-linear Mechanics 15 (1980) 333-340.
- [2] A. Luongo, G. Rega, F. Vestroni, Monofrequent oscillations of a non-linear model of a suspended cable, Journal of Sound and Vibration 82 (1982) 247-259.
- [3] A. Luongo, G. Rega, F. Vestroni, Planar non-linear free vibrations of an elastic cable, International Journal of Non-linear Mechanics 19 (1984) 39-52.
- [4] G. Rega, F. Vestroni, F. Benedettini, Parametric analysis of large amplitude free vibrations of a suspended cable, International Journal of Solids and Structures 20 (1984) 95–105.
- [5] F. Benedettini, G. Rega, F. Vestroni, Modal coupling in the free nonplanar finite motion of an elastic cable, Meccanica 21 (1986) 38-46.
- [6] F. Benedettini, G. Rega, Non-linear dynamics of an elastic cable under planar excitation, International Journal of Non-linear Mechanics 22 (1987) 497-509.
- [7] G. Rega, F. Benedettini, Planar non-linear oscillations of elastic cables under subharmonic resonance conditions, Journal of Sound and Vibration 132 (1989) 367–381.
- [8] G.V. Rao, R.N. Iyengar, Internal resonance and non-linear response of a cable under periodic excitation, Journal of Sound and Vibration 149 (1991) 25-41.
- [9] N.C. Perkins, Modal interactions in the non-linear response of elastic cables under parametric/external excitation, International Journal of Non-linear Mechanics 27 (1992) 233–250.
- [10] C.L. Lee, N.C. Perkins, Nonlinear oscillations of suspended cables containing a two-to-one internal resonance, Nonlinear Dynamics 3 (1992) 465–490.
- [11] C.L. Lee, N.C. Perkins, Three-dimensional oscillations of suspended cables involving simultaneous internal resonances, Nonlinear Dynamics 8 (1995) 45–63.
- [12] F. Benedettini, G. Rega, R. Alaggio, Nonlinear oscillations of a four-degree-of freedom model of a suspended cable under multiple internal resonance conditions, Journal of Sound and Vibration 182 (1995) 775–798.
- [13] G. Rega, R. Alaggio, F. Benedettini, Experimental investigation of the nonlinear response of a hanging cable Part I: Local analysis, Nonlinear Dynamics 14 (1997) 89–117.
- [14] F. Benedettini, G. Rega, Experimental investigation of the nonlinear response of a hanging cable. Part II: Global analysis, Nonlinear Dynamics 14 (1997) 119–138.
- [15] M. Behbahani-Nejad, N.C. Perkins, Freely propagating waves in elastic cables, Journal of Sound and Vibration 196 (1996) 189-202.

#### N. Srinil et al. | Journal of Sound and Vibration 1 (1111) 111-111

- [16] M. Pakdemirli, S.A. Nayfeh, H.A.H. Nayfeh, Analysis of one-to-one autoparametric resonance in cablesdiscretization vs. direct treatment, Nonlinear Dynamics 8 (1995) 65–83.
- [17] G. Rega, W. Lacarbonara, A.H. Nayfeh, C.M. Chin, Multiple resonances in suspended cables: direct versus reduced-order models, International Journal of Non-linear Mechanics 34 (1999) 901–924.
- [18] J.V. Huddleston, Computer analysis of extensible cables, Journal of Engineering Mechanics, American Society of Civil Engineers 107 (1981) 27–37.
- [19] B. Shih, I.G. Tadjbakhsh, Small-amplitude vibrations of extensible cables, Journal of Engineering Mechanics, American Society of Civil Engineers 110 (1984) 569-576.
- [20] J.J. Burgess, M.S. Triantafyllou, The elastic frequencies of cables, Journal of Sound and Vibration 120 (1988) 153-
- [21] M.S. Triantafyllou, D.K.P. Yue, Damping amplification in highly extensible hysteretic cables, Journal of Sound and Vibration 186 (1995) 355–368.
- [22] A.A. Tjavaras, Q. Zhu, Y. Liu, M.S. Triantafyllou, D.K.P. Yue, The mechanics of highly extensible cables, Journal of Sound and Vibration 213 (1998) 709-737.
- [23] S. Chucheepsakul, S. Wongsa, Effect of axial stretching on large amplitude free vibration of a suspended cable, Structural Engineering and Mechanics 11 (2001) 185-197.
- [24] S. Chucheepsakul, N. Srinil, Free vibrations of three-dimensional extensible marine cables with specified top tension via a variational method, Ocean Engineering 29 (2002) 1067–1097.
- [25] W.M. Henghold, J.J. Russell, Equilibrium and natural frequencies of cable structures (a nonlinear finite element approach), Computers and Structures 6 (1976) 271–276.
- [26] F. Rosenthal, Vibrations of slack cables with discrete masses, Journal of Sound and Vibration 78 (1981) 573-583.
- [27] K. Takahashi, Y. Konishi, Non-linear vibrations of cables in three dimensions. Part 1: Non-linear free vibrations, Journal of Sound and Vibration 118 (1987) 69-84.
- [28] A.C.J. Luo, C.D. Mote Jr., Equilibrium solutions and existence for traveling, arbitrarily sagged elastic cables, American Society of Mechanical Engineers, Journal of Applied Mechanics 67 (2000) 148-154.
- [29] S. Chucheepsakul, N. Srinil, P. Petchpeart, A variational approach for three-dimensional model of extensible marine cables with specified top tension, Applied Mathematical Modelling, 2003, accepted.
- [30] H.M. Irvine, T.K. Caughey, The linear theory of free vibrations of a suspended cable, Proceedings of the Royal Society of London Series A 341 (1974) 229-315.
- [31] W. Lacarbonara, G. Rega, Resonant nonlinear normal modes. Part II: Activation/orthogonality conditions for shallow structural systems, International Journal of Non-linear Mechanics 38 (2003) 873–887.

# ARTICLE IN PRESS



Available online at www.sciencedirect.com

SCIENCE DIRECTS

Computers & Structures

Computers and Structures xxx (2003) xxx-xxx

www.elsevier.com/locate/compstruc

# Plates on two-parameter elastic foundations with nonlinear boundary conditions by the boundary element method

Somchai Chucheepsakul \*, Boonme Chinnaboon

Department of Civil Engineering, King Mongkut's University of Technology Thonburi, Bangmod, Toongkru, Bangkok 10140, Thailand

Received 25 June 2002; accepted 23 July 2003

#### Abstract

A boundary element method is developed for the bending analysis of plates having nonlinear boundary conditions and resting on two-parameter elastic foundations. The nonlinearity of the problem arises from the normal bending moment of plates which is assumed to be nonlinear function of the boundary slope recognized as a support model with nonlinear rotational restraint. Thus, the solution can be treated all cases of the boundary conditions ranging from simple support to completely fixed support. The kernels of the boundary integral equations are conveniently established which the fundamental solution for the linear plate theory is used. The surface integration of the kernels for the foundation pressure is evaluated by using the property of Dirac delta function. The system of nonlinear equations is established and solved by the Newton-Raphson iterative process. The application of high-order elements, i.e. cubic elements, for improving the solution is adopted. Numerical results of several problems are given to demonstrate the accuracy and applicability of the proposed method.

© 2003 Published by Elsevier Ltd.

Keywords: Boundary element method; Plates; Two-parameter elastic foundations; Nonlinear boundary conditions; Domain integrals; Cubic elements

#### 1. Introduction

Recently, a number of research studies have been carried out on the problem of plates on two-parameter elastic foundations using the boundary element technique. The two-parameter foundation models may be considered as the Filonenko-Borodich, Pasternak, Generalized, Vlasov and Winkler models. A brief review of the past and recent investigations using boundary integral method and boundary element technique to solve the plate problems is mentioned herein. The plates on one-parameter foundations have been extensively studied by many researchers [1–7], and the bending behavior

of plates on Winkler foundation is the major concerns in those studies. While the plates on two-parameter foundations have been treated by a limited number of researchers. Balas et al. [8] presented a boundary integral formulation for plates of any shape, and they employed Fourier integral transform for the derivation of fundamental solutions. Katsikadelis and Kallivokas [9] used the boundary element method for plates on Pasternaktype elastic foundation with clamped boundary, and the same authors [10] presented a boundary differential integral equation (BDIE) method for the analysis of plates with free boundaries of any shape resting on biparametric elastic foundations. Chucheepsakul and Chinnaboon [11] presented the alternative domain/boundary element technique for solving the plates with various boundary conditions as well as mixed boundary conditions. All of the aforementioned works have been carried out based upon the conventional boundary conditions. These boundary conditions are very important as they

<sup>\*</sup>Corresponding author. Tel.: +662-470-9134-36; fax: +662-427-9063.

E-mail address: somchai.chu@kmutt.ac.th (\$. Chucheepsa

are the limiting conditions. It is known, however, that in many structural engineering applications, such as ship, aircraft, and other structures do not have simply supported or clamped edges but in general they are restrained elastically against rotation at the boundaries. In the open literature, it has been observed that the plates on two-parameter elastic foundations with nonlinear boundary conditions have not been treated elsewhere using the boundary element method.

In the present paper, a boundary element method is developed for analyzing plates with nonlinear boundary conditions on two-parameter elastic foundations. In the analysis, the normal bending moment of the plate is assumed to be nonlinear function of the boundary slope which is recognized as a kind of support model with nonlinear rotational restraint. Thus, the solution can be treated all cases ranging from simple support to complete fixity of the boundary. The proposed method uses the fundamental solution of linear plate theory and treats the subgrade reactions as unknown domain forces. Thus, the kernels of the boundary integral equations are conveniently established and evaluated. The technique for evaluating the surface integration of the kernels for the foundation pressure is presented. The obtained system of nonlinear equations is solved by the Newton-Raphson method. In integrating over the boundaries, cubic elements are employed for improving the solution. Numerical results of several problems are given to demonstrate the accuracy and applicability of the proposed method.

#### 2. Formulation of the boundary value problem

Fig. 1 shows a plate with bending rigidity D resting on the Pasternak model of elastic foundation and subjected to a transverse loading intensity q. Let S be the interior of the plate and  $\Gamma$  its boundary. Assuming that the plate maintains contact with the subgrade and that there is no friction force at the interface, its transverse deflection w(P) at any point  $P \in S$  satisfies the following differential equation:

$$\nabla^4 w + \frac{p_s}{D} = \frac{q}{D} \tag{1}$$

where  $p_s$  is the interaction pressure between plate and subgrade and defined as

$$p_{\rm s} = kw - G\nabla^2 w \tag{2}$$

Eq. (1) can be considered in a more general form as

$$Lw = \frac{q}{D} \tag{3}$$

where L is an operator defined as

$$L = \nabla^4 - \frac{G}{D}\nabla^2 + \frac{k}{D} \tag{4}$$

where

$$\nabla^2 = \frac{\partial^2}{\partial x^2} + \frac{\partial^2}{\partial y^2}, \quad \nabla^4 = (\nabla^2)^2,$$
$$D = Eh^3/12(1 - v^2)$$

is the flexural rigidity of the plate, G is the shear modulus, and k is the modulus of subgrade reaction.

The commonly used boundary conditions of the plates are known to be specified by respectively two boundary values:

simple support: 
$$w = 0$$
 and  $M_n = 0$  (5.1)

clamped support: 
$$w = 0$$
 and  $\frac{\partial w}{\partial n} = 0$  (5.2)

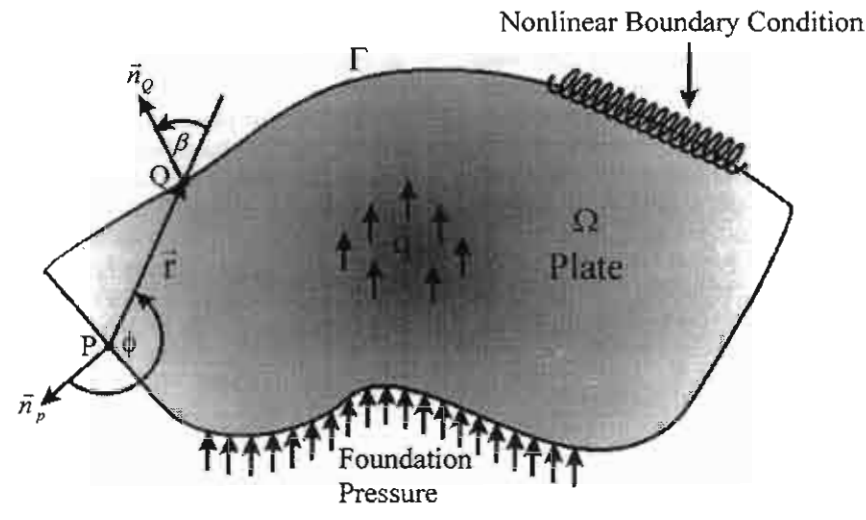


Fig. 1. Plate on two-parameter elastic foundation with nonlinear boundary condition and notation.

S. Chucheepsakul, B. Chinnaboon I Computers and Structures xxx (2003) xxx-xxx

free support: 
$$V_n = 0$$
 and  $M_n = 0$  (5.3)

where w,  $V_n$ ,  $M_n$ ,  $\frac{\partial w}{\partial n}$  are the deflection, equivalent shear force, normal bending moment and slope at the boundary, respectively.

#### 2.1. Nonlinear boundary conditions

Eqs. (5.1)–(5.3) are the boundary conditions used in the conventional engineering practice. However, in general the plate elements of structures behave more complicated in many practical problems, since they are restrained elastically against rotation at the boundary supports. The normal bending moments have been assumed to be proportional to the rotations of these boundaries with a coefficient c as follows:

$$M_n = c \frac{\partial w}{\partial n} \tag{6}$$

The values of c vary between 0 for a simply supported edge and  $\infty$  for a clamped edge. However, this boundary condition in Eq. (6) is still linear, so it does not require nonlinear treatment. For more general cases, the proportional coefficient c in Eq. (6) is reasonable to be considered as deformation-dependent. Then the coefficient c may be expressed as a function of the slope at the boundary as follows [12]:

$$c = f\left(\frac{\partial w}{\partial n}\right) \tag{7}$$

Thus, the normal bending moment  $M_n$  depends nonlinearly on the boundary slope  $\frac{\partial w}{\partial n}$ .

#### 3. Boundary element method

The integral representation of the solution can be obtained by combining the Rayleigh-Green identity for the biharmonic equation with classical Green identity for the harmonic equation. This identity can be written as

$$\int_{\Omega} \int (uLw - wLu) dS$$

$$= \frac{1}{D} \int_{\Gamma} \left[ wV_n(u) - \frac{\partial w}{\partial n} M_n(u) + \frac{\partial u}{\partial n} M_n(w) - uV_n(w) - Gu \frac{\partial w}{\partial n} + Gw \frac{\partial u}{\partial n} \right] d\Gamma$$
(8)

where  $u, w, V_n, M_n$  are deflections, equivalent shear force, normal bending moment and  $\partial/\partial n$  denotes the outward normal derivative.

Normally, the problem of plate on two-parameter elastic foundation consists of taking the suitable fun-

damental solution to Eq. (1), that is a singular particular solution of the following differential equation

$$Lu = \delta(Q - P)/D \tag{9}$$

in which  $\delta(Q-P)$  is the Dirac delta function, Q is the field point, P is the source point. The nature of the solution to Eq. (9) involves the zero-order Hankel function of the first kind that can not be evaluated easily because of its mathematical complexity. This formulation has been used by many authors [5,8–10] who have treated this problem by the boundary integral equation method.

The formulation proposed herein uses the classical fundamental solution for plate flexure problem that is

$$\nabla^4 u = \delta(Q - P)/D \tag{10}$$

and represents the pressure distribution in the foundation interface by the load applied at each node of a mesh used to discretize the plate domain.

The fundamental solution of Eq. (10) is given as

$$u_{\rm F}(P,Q) = w_{\rm F}(r) = \frac{1}{8\pi D} r^2 \ln r$$
 (11)

where  $r = |\overrightarrow{PQ}|$  and the subscript F denotes the fundamental solution corresponding to a concentrated unit force. Substituting Eqs. (10) and (11) into Eq. (8), one gets the deflection for any point P inside the domain as follows:

$$w_{P \in S} = -\int_{\Gamma} \left[ w(V_{\rm F} + GN_{\rm F}) - \frac{\partial w}{\partial n} (M_{\rm F} + Gu_{\rm F}) + M_n N_{\rm F} - V_n u_{\rm F} \right] d\Gamma - \int_{\Omega} \int (k u_{\rm F} - G\nabla^2 u_{\rm F}) w dS + \int_{\Omega} \int q u_{\rm F} dS$$
(12)

where the equivalent shear force  $V_F$ , normal bending moment  $M_F$ , normal slope  $N_F$  and  $\nabla^2 u_F$  resulting from the fundamental solution of Eq. (11) can be found in Chucheepsakul and Chinnaboon [11].

Letting point P tend to Q on the boundary and taking the limit value of the integral, the following equation for a regular point P on the boundary is obtained as

$$0.5w_{P\in\Gamma} = -\int_{\Gamma} \left[ w(V_{F} + GN_{F}) - \frac{\partial w}{\partial n} (M_{F} + Gu_{F}) + M_{n}N_{F} - V_{n}u_{F} \right] d\Gamma - \int_{\Omega} \int (ku_{F} - G\nabla^{2}u_{F})w dS + \int_{\Omega} \int qu_{F}dS$$

$$(13)$$

In addition to the solution in Eq. (11), a second fundamental solution is required. This solution corresponds to a concentrated unit moment applied at P that is

$$\nabla^4 u = \frac{\partial}{\partial u} \delta(Q - P)/D \tag{14}$$

S. Chucheepsakul, B. Chinnaboon / Computers and Structures xxx (2003) xxx-xxx

The solution of Eq. (14) is

$$u_{\rm m} = w_{\rm m}(r) = \frac{1}{2\pi D} r \ln r \cos \phi \tag{15}$$

where  $\phi$  is the angle of rotation of r with respect to a local coordinate  $\eta\xi$  applied at point P. Substituting Eqs. (14) and (15) into Eq. (8) and taking  $\xi$  in the direction of the normal, the normal derivative of w at point P along the boundary is obtained:

$$-\frac{\partial w}{\partial n_{P \in \Gamma}} = -\int_{\Gamma} \left[ (w - w|_{P})(V_{m} + GN_{m}) - \frac{\partial w}{\partial n}(M_{m} + Gu_{m}) + M_{n}N_{m} - V_{n}u_{m} \right] d\Gamma$$
$$-\int_{\Omega} \int (ku_{m} - G\nabla^{2}u_{m})w dS + \int_{\Omega} \int qu_{m}dS$$
(16)

where the equivalent shear force  $V_m$ , normal bending moment  $M_m$ , normal slope  $N_m$  and  $\nabla^2 u_m$  resulting from the fundamental solution of Eq. (15) can be found in Chucheepsakul and Chinnaboon [11] as well. The subscript m denotes the fundamental solution corresponding to a concentrated unit moment. Using Eqs. (12), (13) and (16) with the prescribed boundary conditions, one can solve for the unknowns along the boundary and the unknown deflections inside domain.

# 3.1. Evaluation of domain integrals for foundation pressure

In view of Eqs. (12), (13) and (16), to solve the problem by the present method it is necessary to evaluate the domain integrals:

$$\int_{\Omega} \int (ku - G\nabla^2 u) w \, \mathrm{d}S$$

The steps to solve these domain integrals are as follows:

- Step 1. Discretize the plate domain into m finite panels.
- Step 2. Assume the value of the deflection w of each panel is constant and is defined at the center point of each panel (see Fig. 2).
- Step 3. Use the following property of Dirac delta function.

$$\int f(t)\delta(t-t_0)dt = f(t_0)$$
(17)

then

$$\int_{\Omega} \int (ku - G\nabla^2 u) w \, dS$$

$$= \sum_{i=1}^{m} [kA_{si} u(p, Q_i) - GA_{si} \nabla^2 u(p, Q_i)] w_i$$
(18)

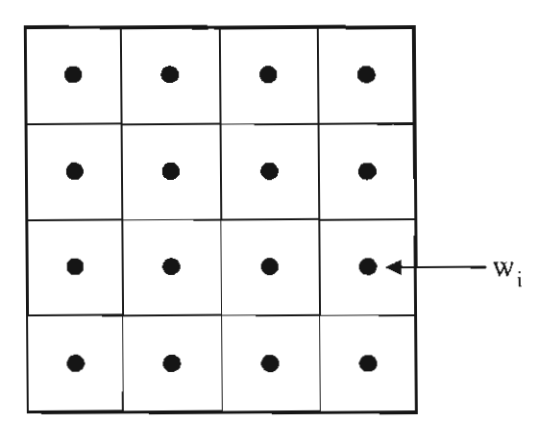


Fig. 2. Domain discretization for unknown deflections.

where P is the source point,  $Q_i$  is the center point of each panel,  $A_{si}$  is the area of each panel, and  $w_i$  is the unknown deflection inside the domain.

When the source point P and the field point  $Q_i$  are at the same point then the domain integrals

$$\int_{\Omega} \int (ku - G\nabla^{2}u)w \, dS$$

$$= w_{i} \frac{G}{4\pi D} \left[ A_{si} \left( \ln \left( \frac{a^{2} + b^{2}}{4} \right) - 1 \right) + a^{2} \tan^{-1} \left( \frac{b}{a} \right) + b^{2} \tan^{-1} \left( \frac{a}{b} \right) \right]$$
(19)

where a and b are the width and length of each panel.

Obviously, along with this method, the integral representation for the foundation pressure does not require the surface integration of kernels by Gauss-Legendre method, therefore the computer time is considerably reduced.

#### 4. Numerical procedure

In order to solve the boundary integral equations (12), (13) and (16) by means of the boundary element method, discretization of the boundary domain needs to be done. The boundary of the domain is partitioned into a number of boundary elements and the associated boundary functions are interpolated by piecewise polynomials. The problem, thus, reduces to the task of determining the nodal values of the unknown functions by a point collocation procedure.

Because the problem of plate bending on twoparameter elastic foundation is governed by a fourthorder differential equation. So, in order to improve the numerical solution, the high-order elements such as isoparametric cubic elements are adopted in the calculation of the unknown functions along the boundary. These functions can be expressed as S. Chucheepsakul, B. Chinnaboon | Computers and Structures xxx (2003) xxx-xxx

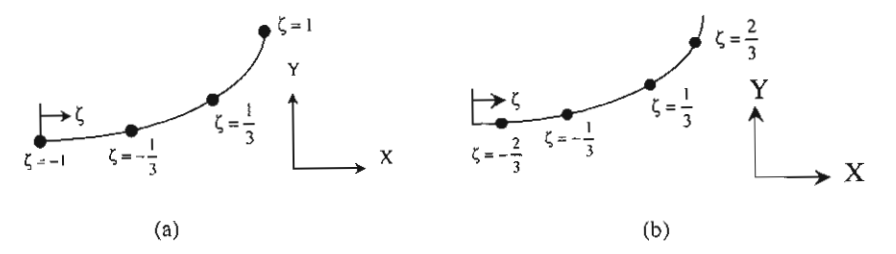


Fig. 3. Cubic elements: (a) continuous elements; (b) discontinuous elements.

$$\phi(\xi) = \sum_{i=1}^{4} F^{i}(\xi)\phi_{i} \tag{20}$$

where  $\xi$  varies between -1 and +1,  $F'(\xi)$  are the interpolation functions. The interpolation function of cubic elements, both continuous and discontinuous elements (see Fig. 3(a) and (b)), can be derived according to the procedure suggested by Kane [13] and used in the previous work [11].

Gaussian quadrature formula is used in the integration procedure to calculate the coefficients of the nodal variables. However, in integrating over boundary elements adjacent to the source point, some terms of the integrand become singular, and the integrals are generally evaluated in the Cauchy principal value sense.

### 5. Matrix formulation with nonlinear boundary conditions

A matrix formulation for Eqs. (12), (13) and (16) can be obtained by:

- (1) discretization of the boundary into a number of elements with total n nodes, of which the value of deflection w, normal slope  $\partial w/\partial n$ , normal bending moment  $M_n(w)$ , equivalent shear force  $V_n(w)$  are defined:
- (2) discretization of the domain S in m rectangular panels at the middle (nodal points), of which the value of deflections w are defined.

For Eq. (12) one obtains

$$\{w_s\} = [A_S]\{w\} + [B_S]\left\{\frac{\partial w}{\partial n}\right\} + [C_S]\{M_n\} + [D_S]\{V_n\} + [E_S]\{w_s\} + \{\bar{q}_S\}$$
 (21)

for Eq. (13):

$$\frac{1}{2}\{w\} = [\mathcal{A}_{\Gamma}^{0}]\{w\} + [\mathcal{B}_{\Gamma}^{0}]\left\{\frac{\partial w}{\partial n}\right\} + [C_{\Gamma}^{0}]\{M_{n}\} 
+ [D_{\Gamma}^{0}]\{V_{n}\} + [E_{\Gamma}^{0}]\{w_{s}\} + \{\bar{q}_{\Gamma}^{0}\}$$
(22)

and for Eq. (16):

$$-\left\{\frac{\partial w}{\partial n}\right\} = [A_{\Gamma}^{1}]\{w\} + [B_{\Gamma}^{1}]\left\{\frac{\partial w}{\partial n}\right\} + [C_{\Gamma}^{1}]\{M_{n}\} + [D_{\Gamma}^{1}]\{V_{n}\} + [E_{\Gamma}^{1}]\{w_{s}\} + \{\bar{q}_{\Gamma}^{1}\}$$
(23)

Eqs. (21)–(23) are transformed into the following set of simultaneous linear algebraic equations:

$$[A]\{w\} + [B]\left\{\frac{\partial w}{\partial n}\right\} + [C]\{M_n\} + [D]\{V_n\} + [E]\{w_s\} + \{\bar{q}\} = 0$$
 (24)

where [A], [B], [C] and [D] are 2n + m by n matrices whose coefficients stem from the curvilinear integrals of Eqs. (12), (13) and (16). [E] is a 2n + m by m matrix whose coefficients stem from the domain integral due to the foundation pressure of Eqs. (12), (13) and (16).  $\{\bar{q}\}$  is a column vector whose 2n + m components are the values of the domain integral due to external loads of Eqs. (12), (13) and (16).

For nonlinear boundary conditions, which the normal ending moments have been assumed to be proportional to the rotations of these boundaries with a coefficient c. In this paper, the proportional coefficient c is expressed as function of the slope at the boundary as follows:

$$c = c_1 \frac{\partial w}{\partial n} + c_2 \tag{25}$$

Substituting Eq. (25) into Eq. (6), one gets

$$M_n = c_1 \left(\frac{\partial w}{\partial n}\right)^2 + c_2 \frac{\partial w}{\partial n} \tag{26}$$

As can be seen, the normal bending moments depends nonlinearly on the boundary slope  $\left\{\frac{\partial w}{\partial n}\right\}$ . By substitution of Eq. (26) into Eq. (24) yields the following system of nonlinear equations as

$$|A|\{w\} + c_1[C] \left\{ \left( \frac{\partial w}{\partial n} \right)^2 \right\} + (|B| + c_2[C]) \left\{ \frac{\partial w}{\partial n} \right\}$$

$$+ |D|\{V_n\} + |E|\{w_s\} + \{\tilde{q}\} = 0$$

$$(27)$$

Supplementary use of one more prescribed boundary condition, say for the supported plate the deflection

vanishes  $\{w\} = 0$ , makes the system of nonlinear equations solvable. These systems of nonlinear equations are solved by the Newton-Raphson method starting with the known linear solution for  $c_1 = 0$  and  $c_2 = \text{const.}$  until the sufficient convergence is satisfied. The Newton-Raphson scheme can be formulated from the Taylor series expansion. The procedure to solve the system of nonlinear equations is as follows:

Step 1. Rewriting Eq. (27) in the following form:

$$\mathbf{F}(\mathbf{X}_k) = \mathbf{0} \tag{28}$$

where X are the unknowns and subscript k is the number of increment.

Step 2. Expanding the residual function as a Taylor series about an approximate solution:

$$\mathbf{F}(\mathbf{X}_{k+1}) = \mathbf{F}(\mathbf{X}_k) + \left[\frac{\partial \mathbf{F}}{\partial \mathbf{X}}\right]_k (\mathbf{X}_{k+1} - \mathbf{X}_k)$$
 (29)

Step 3. Considering that  $X_{k+1}$  is the exact solution, i.e.  $F(X_{k+1}) = 0$ , the following expression is obtained:

$$\mathbf{J}_k \Delta \mathbf{X}_{k+1} = -\mathbf{F}(\mathbf{X}_k) \tag{30}$$

in which  $J = \partial F/\partial X$  is the Jacobian matrix and  $\Delta X$  is the vector of increments.

Step 4. Starting from the linear solution for  $c_1 = 0$  and  $c_2 = \text{const.}$ , for each iteration the updated solution is obtained through the increment expression

$$X_{k+1} = X_k + \Delta X_{k+1} (31)$$

and the iteration process continues until the residual vector is sufficiently small.

#### 6. Evaluation of stress resultants inside the plate domain

When Eq. (27) is solved, all the boundary values  $\left(w, \frac{\partial w}{\partial n}, M_n, V_n\right)$  and the deflections inside the domain are obtained. Then, the deflection w(P) at any point inside the domain can be obtained from Eq. (12).

The bending moments  $M_x$ ,  $M_y$ , the twisting moment  $M_{xy}$  and the shear force  $Q_x$ ,  $Q_y$  at any point of the plate are expressed as:

$$M_{x} = -D\left(\frac{\partial^{2} w}{\partial x^{2}} + v \frac{\partial^{2} w}{\partial y^{2}}\right),$$

$$M_{y} = -D\left(\frac{\partial^{2} w}{\partial y^{2}} + v \frac{\partial^{2} w}{\partial x^{2}}\right)$$
(32a, b)

$$Q_x = -D\frac{\partial}{\partial x}\nabla^2 w, \quad Q_y = -D\frac{\partial}{\partial y}\nabla^2 w$$
 (32c, d)

$$M_{xy} = -M_{yx} = D(1-v)\frac{\partial^2 w}{\partial x \partial y}$$
 (32e)

The second- and third-order derivatives of the deflections in Eqs. (32a-e) can be evaluated from the computed values of the deflections with sufficient accuracy using numerical differentiation in which the hyper-singular domain integrals do not occur. However, the stress resultants become more accurate when they are evaluated by direct differentiation of Eq. (12) which yields the singular domain integrals. The technique to convert the singular domain integrals with kernel derivatives of the fundamental solution to regular boundary integrals can be found in Nerantzaki and Katsikadelis [14], and Katsikadelis and Nerantzaki [15].

#### 7. Numerical examples and results

A computer program based upon some modifications from a plate flexure program with cubic boundary elements has been developed. Examples aiming at validating the formulations of this method presented in this work are analyzed. Numerical results of examples are compared with those obtained from analytical or other numerical solutions. In all the cases, the boundary has been divided into 16 cubic elements as shown in Fig. 4, and the domain has been divided into  $15 \times 15$  rectangular panels. This model uses discontinuous elements at all corners as discussed by Venturini and Paiva [16]. In the following examples, the results obtained by this model are shown to be in good agreement with those from well-recognized methods.

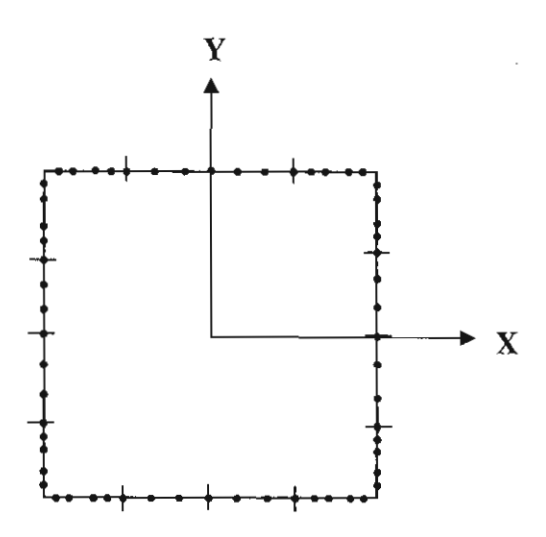


Fig. 4. Boundary discretization with 16 cubic elements.

#### 7.1. Example 1

This example demonstrates an application of the proposed method for a plate with nonlinear boundary conditions. A  $(2a \times 2a)$  square plate is subjected to a concentrated load P at center and a uniform load q respectively. Three cases are considered: (a) a plate that does not rest on an elastic foundation (k = 0, G = 0), (b) a plate on Winkler foundation with  $k = 625D/a^4$  and (c) a plate on Pasternak foundation with  $k = 625D/a^4$  and  $G = 49D/a^2$ . Each case is analyzed for a simply supported plate and a clamped plate respectively. For a simply supported plate, it can be analyzed with respect to the value of c approaching zero  $(c_1 \rightarrow 0, c_2 \rightarrow 0)$ which the results are obtained from the system of nonlinear equations solved by the Newton-Raphson method. The same analogy applied to a clamped plate, it can be analyzed with respect to the value of c approaching infinity  $(c_1 \to \infty, c_2 \to \infty)$ . The obtained results, as shown in Table 1 for a plate subjected to a concentrated load P at center and Table 2 for a plate subjected to a uniform load q, are compared with the analytical solution [17] or the boundary element method (BEM). It is obvious that the results obtained from the system of nonlinear equations solved by the Newton-Raphson method are in very good agreement with the referred solutions, thus confirming the validity and application of the proposed method.

#### 7.2. Example 2

This example is intended to show the variations of the normal bending moments and the equivalent shear forces between the simple support to complete fixity of the boundary. A  $(2a \times 2b)$  rectangular plate with b/a = 1.2 subjected to a concentrated load P at center is analyzed. A plate rests on Pasternak foundation with the subgrade reaction modulus with  $k = 625D/a^4$  and the shear modulus  $G = 49D/a^2$ . For nonlinear boundary conditions, the coefficient  $c_2 = D/a$  is applied to all cases and the coefficients  $c_1$  are varying between 0, for the case of linear spring restraint, and 100D/t. The influence coefficients for normal bending moment  $M_n = M_n/P$  and equivalent shear force  $\tilde{V}_n = V_n a/P$  are plotted in Figs. 5 and 6 respectively. Because of using cubic elements (high-order elements), it can be seen that no oscillation in the value of the equivalent shear forces occurs along the boundary supports.

#### 7.3. Example 3

Rectangular  $(2a \times 2b)$  plates with b/a = 1.0, 1.2, 1.4, 1.6, 1.8 and 2.0 subjected to a uniform load q are analyzed. Two cases are considered: (a) plates that do not rest on an elastic foundation and (b) plates on Winkler foundation with  $k = 256D/a^4$ . The influence coefficients

The influence coefficients for deflection  $\bar{w} = w/(Pa^2/D)$  of a  $(2a \times 2a)$  plate subjected to a concentrated load P

	k = 0, G = 0	r = 0, G = 0	(Fa-(L))		k=625D/	$=625D/a^4$ , $G=0$			k = 625D/	$k = 625D/a^4$ , $G = 49D/a^2$	T <sup>2</sup>	
	r 0 ↑ °	SSp	c → ∞ <sup>a</sup>	CL <sup>3</sup>	$c \rightarrow 0^a$	SS	c → ∞	CL°	$c \rightarrow 0^a$	SSc	$c \to \infty^{a}$	$C\Gamma_c$
	11.8121	11.7727	2.0641	2.0645	0.0306	0.0305	0.0393	0.0393	0.1319	0.1319	0.0924	0.092
9.0	23.2353	23.1653	6.8973	6.8980	0.3402	0.3399	0.3477	0.3477	0.3669	0.3669	0.3387	0.338
4	33.7079	33.6175	13.0068	13,0078	1.2861	1.2870	1.2889	1.2889	0.8892	0.8892	0.8720	0.872
2	42.2246	42,1231	18.9958	18.9969	3,1436	3,1441	3,1428	3.1428	1.9129	1.9129	1.9014	1.9014
0	46.5083	46.4026	22.4475	22.4469	4.9856	4.9912	4.9836	4.9836	3.2119	3.2119	3.2018	3.201

SS = Simple support, CL = Clamped support.

BEM (conventional BC).

<sup>&</sup>lt;sup>a</sup> The present method (nonlinear BC)
<sup>b</sup> The analytical solution (Ref. [17]).

S. Chucheepsakul, B. Chinnaboon | Computers and Structures xxx (2003) xxx-xxx

The influence coefficients for deflection  $\tilde{w} = w/(qa^a/D)$  of a  $(2a \times 2a)$  plate subjected to a uniform load q

	k = 0, G = 0	. 0			k = 625D/	$k = 625D/a^4, G = 0$			k = 625D/k	$k = 625D/a^4$ , $G = 49D/a^2$	$a^2$	
	$c \rightarrow 0^a$	SSp	c → ∞ <sup>a</sup>	CLb	r_0 ↑	SS <sub>P</sub>	2 ↑ 8	CL	$c \rightarrow 0^{a}$	SSc	$c \uparrow \infty$	$CL^{\mathfrak{r}}$
0.8	21.1430	21.0487	3.0697	3.0682	1.0292	1.0280	0.5089	0.5089	0.7044	0.7044	0.4135	0.4135
9.0	39.5669	39.4030	9.0780	9.0755	1.5948	1.5926	1.2126	1,2126	1.1244	1.1244	0.9040	0.9040
0.4	53.5925	53.3814	14.8828	14.8798	1.7774	1.7770	1.6292	1.6292	1.3497	1.3497	1.2084	1.2084
0.2	62.2981	62.0611	18.8534	18.8500	1.7948	1.7933	1.7937	1.7937	1.4289	1.4289	1.3328	1.3328
0.0	65.2428	64.9976	20.2468	20.2433	1.7835	1.7836	1.8281	1.8281	1,4680	1.4680	1.3839	1.3839

SS = Simple support, CL = Clamped support.

The present method (nonlinear BC).

<sup>b</sup> The analytical solution (Ref. [17]).
<sup>c</sup> BEM (conventional BC).

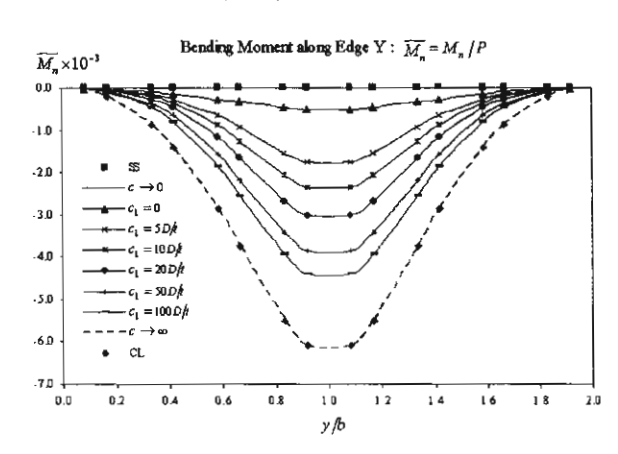


Fig. 5. The variations of normal bending moment of a plate on Pasternak foundation with  $k = 625D/a^4$  and  $G = 49D/a^2$  subjected to a concentrated load P.

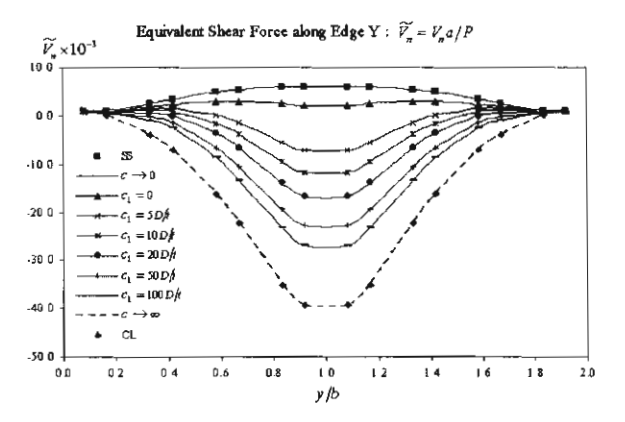


Fig. 6. The variations of equivalent shear force of a plate on Pasternak foundation with  $k = 625D/a^4$  and  $G = 49D/a^2$  subjected to a concentrated load P.

for bending moment  $M_x = M_x/qa^2$  at the plate center are shown in Fig. 7 for case (a) and Fig. 8 for case (b) respectively. The results of clamped plates and simply supported plates are compared with the analytical solution [17] except for those of clamped plates in Fig. 8. This exception is compared with those obtained from the finite element method [18]. It can be seen that the results between the proposed and well-accepted methods are insignificantly different. In Fig. 7, when the ratio b/a increases the bending moment at the plate center also increases. On the other hand, Fig. 8 shows the trend that the bending moment converges to a constant value when b/a approaches the large value. This corresponds to the case of infinite beams resting on elastic foundations.

#### 7.4. Example 4

The purpose of this example is to show the effect of nonlinear rotational restraint and the foundation S. Chucheepsakul, B. Chinnaboon | Computers and Structures xxx (2003) xxx-xxx

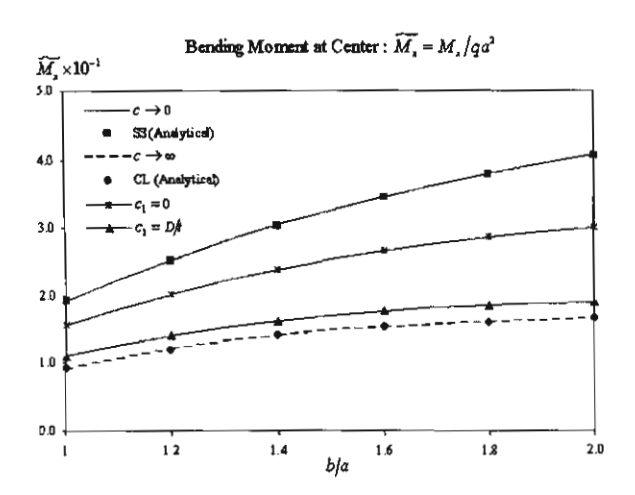


Fig. 7. The variations of central bending moments of plates that do not rest on an elastic foundation subjected to a uniform load a.

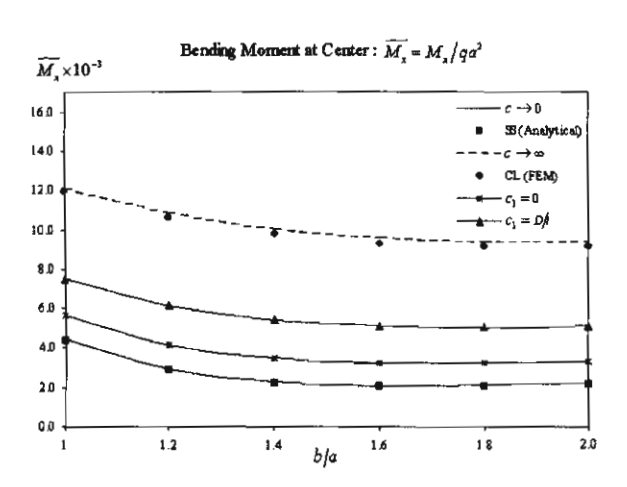


Fig. 8. The variations of central bending moments of plates on Winkler foundation  $k = 256D/a^4$  subjected to a uniform load q.

parameter to the central deflection. A  $(2a \times 2b)$  plate with b/a = 2 subjected to a uniform load q is investigated. In Fig. 9, the variations of central deflections of plates on Winkler foundation are plotted. Moreover, the variations of central deflections of plates on Pasternak foundation with a constant  $k = 16D/a^4$  are shown in Fig. 10. As may be observed, the central deflections tend to be unvaried when the foundation parameters in-

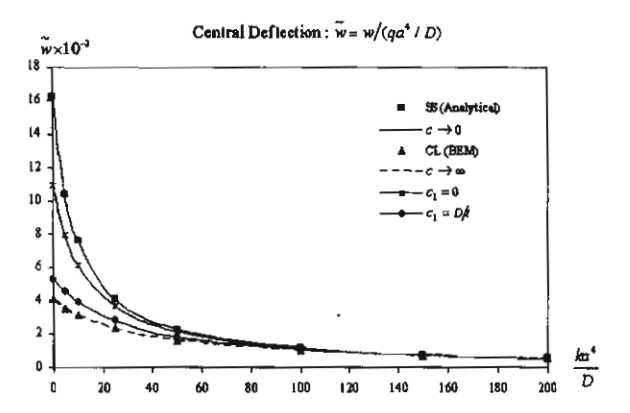


Fig. 9. The variations of central deflections of plates on Winkler foundation subjected to a uniform load q.

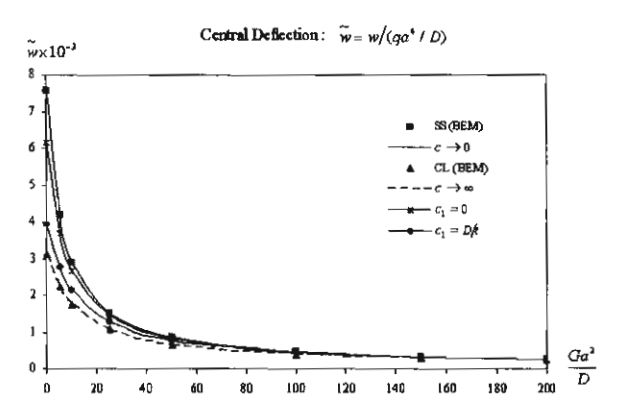


Fig. 10. The variations of central deflections of plates on Pasternak foundation with a constant  $k = 16D/a^4$  subjected to a uniform load q.

crease. The perspective of the deflection surface for the plate on Pasternak foundation with  $k = 16D/a^4$  and  $G = 25D/a^2$ , in which the coefficients of nonlinear rotational restraint are given as  $c_1 = D/t$  and  $c_2 = D/a$ , is shown in Fig. 11.

#### 8. Conclusions

The boundary element method has been extended to solve the bending analysis of plates on two-parameter elastic foundations with nonlinear boundary conditions.

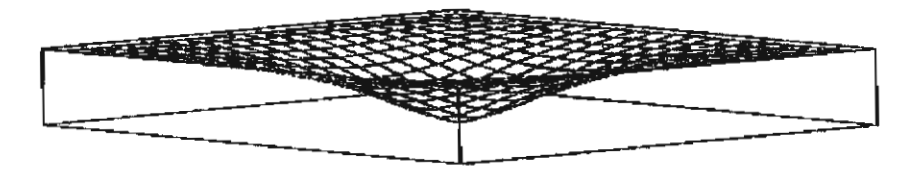


Fig. 11. The perspective of the deflection surface for the plate on Pasternak foundation with nonlinear rotational restraint.

The nonlinear boundary conditions associated in the study arise from the normal bending moment of the plate which is assumed to be nonlinear function of the boundary slope. The results from the demonstrated examples show that the proposed method can be used for analyzing plates on two-parameter elastic foundations for various degrees of fixity of the support conditions.

Furthermore, by employing the cubic elements in the calculation would help improving accuracy of the results. The proposed method is applicable not only to the plate problems considered herein, but it can also be modified to solve other engineering problems such as the nonlinear heat transfer problem with temperature-dependent convection coefficients, and radiation boundary conditions.

#### Acknowledgements

The authors are grateful for support from the Thailand Research Fund (TRF) under grants RTA/03/2543 and PHD/0057/2545.

#### References

- [1] Katsikadelis JT, Armenakas AE. Plates on elastic foundation by BIE method. J Eng Mech 1984;110(7):1086-105.
- [2] Katsikadelis JT, Armenakas AE. Analysis of clamped plates on elastic foundation by the boundary integral equation method. J Appl Mech, ASME 1984;51:574-80.
- [3] Costa JA, Brebbia CA. The boundary element method applied to plates on elastic foundations. Eng Anal 1985;2: 174-82.
- [4] Costa JA, Brebbia CA. On the reduction of domain integrals to the boundary for the BEM formulation of plates on elastic foundations. Eng Anal 1986;3:123-6.

- [5] Puttonen J, Varpasuo P. Boundary element analysis of a plate on elastic foundations. Int J Numer Meth Eng 1986;23:287-303.
- [6] Benzine G. A new boundary element method for bending of plates on elastic foundations. Int J Solids Struct 1988;24(6):557-65.
- [7] El-Zafrany A, Fadhil S, Al-Hosani K. A new fundamental solution for boundary element analysis of thin plates on Winkler foundation. Int J Numer Meth Eng 1995;38:887-903
- [8] Balas J, Sladek V, Sladek J. The boundary integral equation method for plates resting on a two parameter foundation. ZAMM 1984;64:137-46.
- [9] Katsikadelis JT, Kallivokas LF. Clamped plates on Pasternak-type elastic foundation by the boundary element method. J Appl Mech, ASME 1986;53:909-17.
- [10] Katsikadelis JT, Kallivokas LF. Plates on biparametric elastic foundation by BDIE method. J Eng Mech 1988; 114(5):847-75.
- [11] Chucheepsakul S, Chinnaboon B. An alternative domain/ boundary element technique for analyzing plates on twoparameter elastic foundations. Eng Anal 2002;26:547-55.
- [12] Chang TP, Chang HC. Vibration and buckling analysis of rectangular plates with nonlinear elastic end restraints against rotation. Int J Solids Struct 1997;34:2291-301.
- [13] Kane JH. Boundary element analysis in engineering continuum mechanics. New Jersey: Prentice-Hall; 1994.
- [14] Nerantzaki MS, Katsikadelis JT. A Green's function method for large deflection analysis of plates. Acta Mech 1988;75:211-25.
- [15] Katsikadelis JT, Nerantzaki MS. Non-linear analysis of plates by the analog equation method. Comput Mech 1994;14(2):154-64.
- [16] Venturini WS, Paiva JB. Boundary element for plate bending analysis. Eng Anal 1993;11:1-8.
- [17] Timoshenko S, Woinowsky-Krieger S. Theory of plates and shells. New York: McGraw-Hill; 1959.
- [18] Narin N. Thick plates on two-parameter elastic foundation via finite element method. Master of engineering thesis. King Mongkut's University of Technology Thonburi, Thailand; 1996.

# International Journal for Numerical Methods in Engineering

EDITORS:

ASSOCIATE EDITORS:

PROFESSOR ROLAND W. LEWIS, Department of Mechanical Engineering, University of Scales Swansea, Swansea SA2 8PP, U.K. PROFESSOR TED BELYTSCHKO, Department of Mechanical Engineering, Northwestern University, Evanston, IL 60208-3111, U.S.A. PROFESSOR RENÉ DE BORST, Koiter Institute Delft, Delft University of Technology, P.O. Box 1058, NL-2600 GB Delft, The Netherlands

PROFESSOR CHARBEL FARHAT, Chair, Department of Aerospace Engineering Sciences, Director, Center for Aerospace Structures, University of Coloraci at Boulder, Campus Box 429, Boulder, CD 80309-0429, U.S.A.

From: PROFESSOR ROLAND W. LEWIS
Department of Mechanical Engineering
University of Wales Swansea
Swansea SA2 8PP, U.K.

Tel: +44 (0)1792 295253 Fax: +44 (0)1792 295705 E-mail: G.Power@Swansea.ac.uk

14 May 2003

Prof S Chucheepsakul
Dept of Civil Engineering
King Mongkut's University of Tech. Thonburi
BANKOK 10140
THAILAND

Dear Professor Chucheepsakul

# Paper No 4491 The Coupled Radial-Axial Deformations Analysis of Flexible Pipes Conveying Fluid T Monprapussorn, S Chucheepsakul and T Huang

I am pleased to advise you that the above paper is now acceptable for publication in the Journal. However, in order that I can process your paper to be forwarded to the Publishers I will need the following:

- completed copyright transfer form (enclosed)
- a copy of the paper on electronic storage medium (please do not send via email)

Please note that, if your paper has any figures that you wish to be displayed in colour, you should supply them to me in colour so that I can include them with the hard copy of the paper for transmission to the Publishers.

The final version of your paper should not be sent electronically as the Publishers require a definitive hard copy and a copy on a storage medium for the publication process.

You need only send the listed items.

Yours sincerely,

ROLAND W LEWIS



## THE COUPLED RADIAL-AXIAL DEFORMATIONS ANALYSIS OF

#### FLEXIBLE PIPES CONVEYING FLUID

T. Monprapussorn,

Department of Civil Engineering, South-East Asia University,

Bangkok, 10160, Thailand

S. Chucheepsakul,
Department of Civil Engineering, King Mongkut's University of Technology Thonburi,
Bangkok, 10140, Thailand

T. Huang,

Department of Civil and Environmental Engineering, University of Texas at Arlington, Arlington, Texas 76019-0167, USA.

#### ABSTRACT

This paper presents large deformation analysis of flexible pipes conveying fluid in which two complicate behaviours are taken into consideration. The first is the coupling between radial and axial deformations of pipe-wall, and the other the interaction between a deformed pipe and transported fluid having variable internal flow velocity. The coupled radial-axial deformation theory of the pipes and the continuity theory of flow inside the moving deformed pipes are developed to undertake these coupling behaviours. All strong and weak forms of governing equations are obtained by carrying out the virtual work formulation. The hybrid-finite-element method is used to solve the highly nonlinear static problems, which configure the initial large deflection and large strain conditions of the pipes. The state-space-finite-element model for use in analyses of nonlinear vibration and system stability is established as well as the suggested numerical solution procedures. The numerical studies of the pipes under circumstances of intense radial loads such as deep-water risers demonstrate that even slight change of the radial deformation has significant effect in increasing nonlinear responses, and reducing stabilities of the pipes.

**KEYWORDS:** Radial deformation, axial deformation, marine risers, flexible pipes, internal flow, Poisson's ratio effect.

(A1)

#### 1. INTRODUCTION

Flexible pipes have applications in various fields of engineering industrial for years. One of those is offshore resource exploration, which use the pipes as a linkage to transport fluids that are drilled from beneath the ocean floor such as oil, gas, hydrocarbon, and other crude resources, up to the production platform or drilling ship, as shown in Figure 1.

The literature reviews by Chakrabarti and Frampton (1982), Ertas and Kozik (1987), Jain (1994), and Patel and Seyed (1995) demonstrate that analysis of flexible marine riser pipes in most work uses small deformation analysis. Particular motivation of this work is focused on the point that radial deformation of the pipe has not yet been taken into account in the analysis. Even though recent work by the authors (Chucheepsakul et al. 2003) tries to build up the large strain models that can take into consideration large axial deformation, the Poisson's ratio effect, and the transported mass effect, the work is based on the assumption that the volumetric strain of the pipe is zero, or in other words a volume of the pipe segment is always constant, in order to simplify consideration of the Poisson's ratio effect. That assumption constrains that the radial deformation depends upon magnitude of axial deformation.

However, based on the three-dimensional elasticity theory the radial deformation does not depend upon the axial deformation (Monprapussorn 2001). In fact, the radial deformation is the independent deformation induced by the radial loads to interact with the axial deformation through the Poisson's ratio effect, as depicted in Figure 2(a). Therefore, for high radial load conditions under which the effect of radial deformation is significant enough, the use of that assumption may lead to some physical errors on the models representing mechanical behaviour of the pipe. In such case, the coupled radial-axial deformations analysis, which will be presented herein, becomes another way out in seeking accuracy for large deformation analysis of flexible pipes conveying fluid.

Other factors to consider importance of the coupled radial-axial deformations analysis relate to properties and service conditions of the flexible pipes. The flexible pipes are composed of highly deformable materials, thus they could be subjected to a higher level of the Poisson's ratio effect and large deformations in both axial and radial directions than the rigid pipes. In service condition, the flexible marine pipes customarily experience high pretension, and lateral actions of vigorous external fluid pressures. In addition, to raise capability of the production system, advancement of drilling and pumping technology today try increasing the rate of fluid transportation, which induces the higher internal pressures. The conditions of the high radial loads due to the external and internal pressures all distinguish the importance of radial deformation, and so the essential of the coupled radial-axial deformations analysis.

(B1)

This paper presents the mathematical methods and the finite element solutions for the large deformation analysis of flexible pipes that takes account of the effects of axial deformation, radial deformation, and fluid transportation. Ingenuity inside the mathematical models deals with ability to handle two coupled problems: first, the coupling between axial and radial deformations of the pipe, and second, the fluid-structure interaction due to flow of transported fluid inside the pipe suffering the coupled deformations.

The former arises due to the cycle of concurrent action-reaction between radial and axial deformations of the pipe, as depicted in Figure 2(a). The Poisson's ratio effect stimulates the manner that radial deformation influences axial deformation, and vice versa. Such behaviour is said to be the coupled radial-axial deformations of the pipe. To handle the effect of this behaviour in the flexible pipe analysis, the coupled radial-axial deformations theory of the pipe is developed in Sec. 2.

The latter is the sequence of the former. As the pipe undergoes the coupled radial-axial deformations, the continuity condition of the pipe flow would constrain internal flow to change the velocity and the flow aspect in relative to the coupled deformations of the pipe. Of more interest is as shown in Figure 2(b) that the change of internal flow velocity does induce respective:

- alteration of internal pressures by conservation of energy,
- alteration of radial and axial loads by conservation of momentum,
- alteration of the coupled radial-axial deformations following Hook's law for triaxial stress,
- and then alteration of the internal flow velocity once more by conservation of mass.

These alterations loop the concurrent action-reaction between the fluid and the pipe as the cycle shown in Figure 2(b). The cycle is said to be *the transported fluid-pipe interaction* such that the coupled radial-axial deformations influences internal flow velocity, and vice versa. Analytical proof and governing equations of this interaction will be determined in Sec. 3.

The mathematical formulations taking into account the coupled behaviours are developed by the virtual work approach in Sec. 4. Generalization of the models is carried out enough for using with any kind of a flexible pipe conveying fluid. The models are applicable even to biological conveying systems such as an artery conveying blood inside human body, and a vessel rising water in the xylem of a plant. However, to give a numerical example toward engineering application, the formulations are applied to the analyses of an offshore flexible riser transporting fluid in Sec. 5.

The finite-element algorithms for solving the problem are expressed in Sec. 6, where the hybrid-finite-element method is used for determining the equilibrium configurations of the

pipe, and *the state-space-finite-element method* for the eigenvalue analysis, the nonlinear vibration analysis, and the system stability analysis. Significance of the effect of radial deformation obtained from the coupled radial-axial deformations analysis is evaluated in Sec.

- 7. The main assumptions used in this work are as follows:
- (a) Pipe materials are linearly elastic.
- (b) The pipe is thin walled.
- (c) The radial stress  $\sigma_r$  in pipe wall is negligible (for plane stress problems).
- (d) Size of cross-sections of the pipe could change.
- (e) Shape of cross-sections of the pipe does trivially change.
- (f) Flattening of bent tubes due to Brazier's effect is negligible.
- (g) Shear deformation is insignificant (for a high-slenderness-ratio pipe).
- (h) Plane section of the pipe remains plane.
- (i) Internal and external fluids are inviscid, incompressible and irrotational.
- (i) Fluid densities are uniform along the pipe length.
- (k) Internal flow is the one-dimensional plug laminar flow.
- (1) The effect of rotary inertia is negligible.
- (m) There are no residual stress and strain in the pipe wall in the undeformed state.

For effectiveness to presenting mathematical models for the large deformation analysis of flexible pipes, this work employs the following notations:

- (i) Notations identifying state of a parameter. The subscript (o) and the upper sign bar ( $\bar{}$ ) notify the equilibrium state and the undeformed state of the parameter, respectively. For example  $\bar{A}_P$ ,  $A_{Po}$ ,  $A_P$  are the cross-sectional areas of the pipe at the undeformed, the equilibrium, and the dynamic states, respectively.
- (ii) Notations identifying property of a parameter. The subscripts (e), (i), and (P) denote the properties of the external fluid column, the internal fluid column, and the pipe, respectively. For example  $A_e$ ,  $A_i$ ,  $A_p$  are the cross-sectional areas of the external fluid column, the internal fluid column, and the pipe, respectively.
- (iii) Notations identifying coordinates of a parameter. The subscript (n) denotes the normal-tangential coordinates. For example  $(u_n, v_n)$  is the displacement vector in the normal-tangential coordinates, whereas (u, v) the displacement vector in the Cartesian coordinates.

(iv) Notations identifying behaviour of a parameter. The subscripts (o) and (d) indicate the static and dynamic behaviours, respectively. For example  $(u_o, v_o)$  is the static displacement vector, and  $(u_d, v_d)$  is the dynamic displacement vector, whereas  $(u, v) = (u_o, v_o) + (u_d, v_d)$  is the total displacement vector.

In order to define a position, motion and deformation of the pipe and transported fluid for the large deformation analysis, the below physical descriptors are adopted:

- (a) Geometric descriptors. The Cartesian coordinates (CSC) of the horizontal and vertical axes (x,y) and the intrinsic coordinates (ISC) of arc-length and rotation  $(s,\theta)$  are used as the global geometric descriptors. The normal-tangential coordinates (NTC) are employed as the local one. For providing flexibility in the choice of the independent variable of the problem, this work adopts the symbol  $\alpha \in \{\bar{x}, x_o, x, \bar{y}, y_o, y, \bar{s}, s_o, s, \bar{\theta}, \theta_o, \theta\}$  to represent any independent variable, and the superscript (') to denote  $\partial(x)/\partial \alpha$ .
- (b) Kinematic and deformation descriptors. Chucheepsakul et al. (2003) exhibited that there exist the three kinds of kinematic and deformation descriptors, namely the total Lagrangian, the updated Lagrangian, and the Eulerian descriptors. In this work, the updated Lagrangian descriptor (ULD), which is referred to as the coordinate that follows motion and deformation of a deformable body with respect to the position, direction, and size of the body at the intermediate state (or the equilibrium state herein), is adopted.

# 2. THE CONSTITUTIVE EQUATIONS OF THE COUPLED RADIAL-AXIAL DEFORMATIONS OF THE PIPES

A pipe segment against external and internal pressure fields of both static and dynamic pressures is considered, as shown in Figure 3(a). Firstly, the pipe is at rest and unstretched at state-1: the undeformed state. Subsequently, when the pipe is subjected to time-independent loads such as gravitational force, steady flows of external and internal fluids, the pipe undergoes large displacements to the static equilibrium condition at state-2: the equilibrium state. Finally, under dynamic actions of the disturbances due to unsteady flows of external and internal fluids, the pipe sustains vibrations around the static equilibrium condition at state-3: the dynamic state. Schematics of axial and radial deformations are depicted in Figure 3(a) and 3(b), respectively.

The state-transitions from the state-1 → the state-2 → the state-3 result in changes of

(a) the arc length from  $d\overline{s} \rightarrow ds_o \rightarrow ds$ ;

- (b) the curvature angle from  $d\overline{\theta} \rightarrow d\theta_o \rightarrow d\theta$ ;
- (c) the cross-sectional angle from  $\overline{\phi} \rightarrow \phi_a \rightarrow \phi$ ;
- (d) the average radius of cross section of the pipe from  $\overline{R} \to R_o \to R$ .

Consequently, further properties of the pipe also modify as follows:

(e) The radial displacement alters from  $\overline{w} = 0 \rightarrow w_o \rightarrow w$  by the relations

$$w_o = \overline{w} + (R_o - \overline{R}), w = w_o + (R - R_o) = \overline{w} + (R - \overline{R}).$$
 (1a,b)

Note that the term  $R - R_o$  expresses the dynamic radial displacement  $w_d$ .

(f) The axial strain at the neutral axis alters from  $\overline{\varepsilon} = 0 \rightarrow \varepsilon_o \rightarrow \varepsilon$  by the relations

$$\varepsilon_o = \overline{\varepsilon} + \left(1 - \frac{d\overline{s}}{ds_o}\right), \ \varepsilon = \varepsilon_o + \left(\frac{ds}{ds_o} - 1\right) = \overline{\varepsilon} + \frac{ds - d\overline{s}}{ds_o}.$$
 (2a,b)

Note that the term  $ds/ds_o-1$  indicates the dynamic axial strain  $\varepsilon_d$ . Equations (2) yield the formulas of the arc-length variations:

$$\frac{d\overline{s}}{1-\varepsilon_o} = ds_o = \frac{ds}{1+\varepsilon_d}.$$
 (2c)

(g) The circumferential strain alters from  $\overline{\mathcal{E}}_{\theta} = 0 \rightarrow \mathcal{E}_{\theta o} \rightarrow \mathcal{E}_{\theta}$  by the relations

$$\varepsilon_{\theta o} = \overline{\varepsilon}_{\theta} + \left(1 - \frac{\overline{R}d\overline{\phi}}{R_{o}d\phi_{o}}\right), \ \varepsilon_{\theta} = \varepsilon_{\theta o} + \left(\frac{Rd\phi}{R_{o}d\phi_{o}} - 1\right) = \overline{\varepsilon}_{\theta} + \frac{Rd\phi - \overline{R}d\overline{\phi}}{R_{o}d\phi_{o}}. \tag{3a,b}$$

For thin-walled pipes without twist in 2D-analysis,  $\partial \overline{\phi} = \partial \phi_o = \partial \phi$ ; therefore, equations (3) become

$$\varepsilon_{\theta o} = \frac{w_o}{R_o}, \ \varepsilon_{\theta} = \varepsilon_{\theta o} + \left(\frac{w_d}{R_o}\right) = \frac{w}{R_o}.$$
 (4a,b)

where the term  $w_d/R_o$  represents the dynamic circumferential strain  $\varepsilon_{\theta d}$ .

(h) The radial strain alters from  $\overline{\varepsilon}_r = 0 \rightarrow \varepsilon_{ro} \rightarrow \varepsilon_r$  by the relations

$$\varepsilon_{ro} = \frac{dw_o}{d\overline{R}}, \ \varepsilon_r = \varepsilon_{ro} + \left(\frac{dw_d}{dR_o}\right) = \frac{dw}{dR_o}.$$
 (5a,b)

Note that the term  $dw_d/dR_o$  represents the dynamic radial strain  $\varepsilon_{nd}$ .

(i) The sectional properties of the circular pipe alter from sectional diameters:

$$\overline{D}_{\alpha} \to D_{\alpha o} = \overline{D}_{\alpha} + 2w_o \to D_{\alpha} = \overline{D}_{\alpha} + 2w,$$
 (6)

sectional areas:

$$\overline{A}_{\alpha} = \pi \overline{D}_{\alpha}^2 / 4 \rightarrow A_{\alpha \sigma} = \pi (\overline{D}_{\alpha} + 2w_{\sigma})^2 / 4 \rightarrow A_{\alpha} = \pi (\overline{D}_{\alpha} + 2w)^2 / 4,$$
 (7)

sectional area of the pipe:

$$\overline{A}_P = \overline{A}_e - \overline{A}_t \to A_{Po} = A_{eo} - A_{to} \to A_P = A_e - A_t, \tag{8}$$

moments of inertia:

$$\overline{I}_{\alpha} = \pi \overline{D}_{\alpha}^{4} / 64 \rightarrow I_{\alpha\alpha} = \pi (\overline{D}_{\alpha} + 2w_{\alpha})^{4} / 64 \rightarrow I_{\alpha} = \pi (\overline{D}_{\alpha} + 2w)^{4} / 64$$
, (9)

moment of inertia of the pipe:

$$\bar{I}_{P} = \bar{I}_{e} - \bar{I}_{i} \rightarrow I_{Po} = I_{eo} - I_{io} \rightarrow I_{P} = I_{e} - I_{i},$$
 (10)

in which the subscript  $\alpha \in \{e, i\}$ , the subscripts 'e' and 'i' indicate the properties due to 'external' and 'internal' surfaces of the pipe, respectively. For example  $D_e$  and  $D_i$  are the external and internal diameters of the pipe, respectively. Equations (6)-(10) yield the formulas of the sectional-properties variations among the three states:

$$\overline{D}_{\alpha} = \frac{D_{\alpha o}}{(1 + w_o / \overline{R}_{\alpha})} = \frac{D_{\alpha}}{(1 + w / \overline{R}_{\alpha})},\tag{11}$$

$$\overline{A}_{\alpha} = \frac{A_{\alpha o}}{\left(1 + w_{o} / \overline{R}_{\alpha}\right)^{2}} = \frac{A_{\alpha}}{\left(1 + w / \overline{R}_{\alpha}\right)^{2}},$$
(12)

$$\bar{I}_{\alpha} = \frac{I_{\alpha o}}{(1 + w_o / \bar{R}_{\alpha})^4} = \frac{I_{\alpha}}{(1 + w / \bar{R}_{\alpha})^4}.$$
 (13)

(j) The curvature alters from  $\overline{\kappa} = 0 \to \kappa_o \to \kappa$ , as well as the curvature radius from  $\overline{\Re} \to \Re_o \to \Re$  by the relations:

$$\overline{\kappa} = \frac{1}{\overline{\Re}} = \frac{d\overline{\theta}}{d\overline{s}}, \ \kappa_o = \frac{1}{\Re_o} = \frac{d\theta_o}{ds_o}, \ \kappa = \frac{1}{\Re} = \frac{d\theta}{ds}.$$
(14a-c)

- (k) The internal forces alter from axial force:  $\overline{N}_z = 0 \rightarrow N_{zo} \rightarrow N_z$ , from bending moment:  $\overline{M}_z = 0 \rightarrow M_{zo} \rightarrow M_z$ , and from shear force:  $\overline{Q}_z = 0 \rightarrow Q_{zo} \rightarrow Q_z$ .
- (1) The strain energy alters from  $\overline{U} = 0 \rightarrow U_o \rightarrow U$ .

Derivation of the constitutive equations of the coupled radial-axial deformations of the pipes involves developing respectively (i) force-stress relations, (ii) stress-strain relations, (iii) strain-displacement relations, (iv) force-displacement relations, and (v) strain energy expressions.

#### 2.1 The Force-Stress Relations

For convenience in handling hydrostatic pressure effect, analysis of underwater structures needs transformation of structural system from the real to the apparent systems. The real system that is subjected to actual axial force, actual weight, and external and internal hydrostatic pressures can be equivalent to the apparent system experiencing apparent axial force and apparent weight, as previously demonstrated by Chucheepsakul et al. (2001, 2003), and Monprapussorn (2001).

In the real system of the pipe, the force-stress relations can be expressed for the actual force and moment in the axial direction:

$$N_z = \int \sigma_z dA_{p_o} , M_z = \int \sigma_z R dA_{p_o} , \qquad (15a,b)$$

and for the actual force and moment in the circumferential direction:

$$N_{\theta} = \int \sigma_{\theta} dA_{so} , M_{\theta} = \int \sigma_{\theta} R dA_{so} = 0, \qquad (16a,b)$$

where  $A_{so}$  is the surface area of the pipe at the reference state.

In the apparent system of the pipe, the force-stress relations can be expressed for the apparent force and moment in the axial direction:

$$N_{za} = \int \sigma_{za} dA_{po} , M_{za} = \int \sigma_{za} R dA_{po} , \qquad (17a,b)$$

and for the apparent force and moment in the circumferential direction:

$$N_{\theta a} = \int \sigma_{\theta a} dA_{so} , M_{\theta a} = \int \sigma_{\theta a} R dA_{so} = 0 .$$
 (18a,b)

Note that the moment  $M_{\theta} = M_{\theta a} = 0$  because of the assumption (e) that shape of the pipe-section is trivially changed.

### 2.2 THE STRESS-STRAIN RELATIONS

From the elasticity theory, in cylindrical coordinates one has the actual stress and strain formulas in the axial direction:

$$\sigma_z = \frac{E}{(1+\nu)(1-2\nu)} \left[ (1-\nu)\varepsilon_z + \nu\varepsilon_\theta + \nu\varepsilon_r \right], \ \varepsilon_z = \frac{1}{E} \left[ \sigma_z - \nu\sigma_\theta - \nu\sigma_r \right], \tag{19a,b}$$

the actual stress and strain formulas in the circumferential direction:

$$\sigma_{\theta} = \frac{E}{(1+\nu)(1-2\nu)} \left[ (1-\nu)\varepsilon_{\theta} + \nu\varepsilon_{z} + \nu\varepsilon_{r} \right], \ \varepsilon_{\theta} = \frac{1}{E} \left[ \sigma_{\theta} - \nu\sigma_{z} - \nu\sigma_{r} \right], \tag{20a,b}$$

and the actual stress and strain formulas in the radial direction:

$$\sigma_r = \frac{E}{(1+\nu)(1-2\nu)} \left[ (1-\nu)\varepsilon_r + \nu\varepsilon_z + \nu\varepsilon_\theta \right], \ \varepsilon_r = \frac{1}{E} \left[ \sigma_r - \nu\sigma_z - \nu\sigma_\theta \right], \tag{21a,b}$$

where E is the elastic modulus, and v Poisson's ratio. By using the assumption (c) that  $\sigma_r = 0$  for plane stress problems of a thin-walled pipe, the actual stress and strain formulas of the thin-walled pipe can be derived as

$$\sigma_z = \frac{E}{(1 - v^2)} \left[ \varepsilon_z + v \varepsilon_\theta \right], \ \varepsilon_z = \frac{1}{E} \left[ \sigma_z - v \sigma_\theta \right], \tag{22a,b}$$

$$\sigma_{\theta} = \frac{E}{(1 - v^2)} \left[ \varepsilon_{\theta} + v \varepsilon_{z} \right], \ \varepsilon_{\theta} = \frac{1}{E} \left[ \sigma_{\theta} - v \sigma_{z} \right], \tag{23a,b}$$

$$\sigma_r = 0, \ \varepsilon_r = -\frac{v}{E} [\sigma_z + \sigma_\theta] = -\frac{v}{1 - v} [\varepsilon_z + \varepsilon_\theta].$$
 (24a,b)

In the apparent system, the apparent stress-strain formulas are given by

$$\sigma_{za} = E\varepsilon_z = \sigma_z - v\sigma_\theta, \ \varepsilon_z = \frac{\sigma_{za}}{E},$$
 (25a,b)

$$\sigma_{\theta a} = E \varepsilon_{\theta} = \sigma_{\theta} - v \sigma_{z}, \ \varepsilon_{\theta} = \frac{\sigma_{\theta a}}{E},$$
 (26a,b)

$$\sigma_{ra} = 0$$
,  $\varepsilon_r = -\frac{v}{(1-v)E} [\sigma_{za} + \sigma_{\theta a}].$  (27a,b)

## 2.3 STRAIN-DISPLACEMENT RELATIONS

Denoting the rotations of the pipe-section from the state-1 to 2 by  $d\varphi_o = d\theta_o - d\overline{\theta}$  and from the state-2 to 3 by  $d\varphi_d = d\theta - d\theta_o$ , the undeformed and deformed arc-lengths of pipe wall can be expressed as

$$d\overline{s}_{-} = (\overline{\Re} + \overline{R})d\overline{\theta} = \overline{\Re}d\overline{\theta} + \overline{R}(d\theta_{\alpha} - d\varphi_{\alpha}), \qquad (28a)$$

$$ds_{\tau a} = (\Re_a + R_a)d\theta_a, \tag{28b}$$

$$ds_z = (\Re + R)(d\varphi_d + d\theta_g) = \Re d\theta + R(d\varphi_d + d\theta_g). \tag{28c}$$

From equations (2c) and (14):  $\overline{\Re}d\overline{\theta} = d\overline{s} = (1 - \varepsilon_o)ds_o$ ,  $\Re d\theta = ds = (1 + \varepsilon_d)ds_o$  and  $\Re_o d\theta_o = ds_o$ , therefore equations (28) may be rewritten in the form

$$d\overline{s}_{\varepsilon} = (1 - \varepsilon_{o})ds_{o} + \overline{R}(\frac{ds_{o}}{\Re_{o}} - d\varphi_{o}) = (1 - \varepsilon_{o} + \overline{R}\kappa_{o} - \overline{R}\frac{d\varphi_{o}}{ds_{o}})ds_{o},$$
(29a)

$$ds_{zo} = \left(1 + \frac{R_o}{\Re_o}\right) ds_o = \left(1 + R_o \kappa_o\right) ds_o, \tag{29b}$$

$$ds_{z} = (1 + \varepsilon_{d})ds_{o} + R(d\varphi_{d} + \frac{ds_{o}}{\Re_{o}}) = (1 + \varepsilon_{d} + R\frac{d\varphi_{d}}{ds_{o}} + R\kappa_{o})ds_{o},$$
(29c)

where

$$\frac{d\varphi_o}{ds_o} = \frac{d\theta_o}{ds_o} - \frac{d\overline{\theta}}{d\overline{s}} \frac{d\overline{s}}{ds_o} = \kappa_o - \overline{\kappa} (1 - \varepsilon_o), \tag{30a}$$

$$\frac{d\varphi_d}{ds_o} = \frac{d\theta}{ds} \frac{ds}{ds_o} - \frac{d\theta_o}{ds_o} = \kappa (1 + \varepsilon_d) - \kappa_o, \qquad (30b)$$

$$\frac{d\varphi}{ds_o} = \frac{d\varphi_o}{ds_o} + \frac{d\varphi_d}{ds_o} = \kappa(1 + \varepsilon_d) - \overline{\kappa}(1 - \varepsilon_o). \tag{30c}$$

Using equations (4), (5), (29), and (30), the strain-displacement relations can be obtained as

$$\varepsilon_{z} = \frac{ds_{z} - d\overline{s}_{z}}{d\overline{s}_{zo}} = \frac{\varepsilon + R\left[\kappa(1 + \varepsilon_{d}) - (1 - w/R)\overline{\kappa}(1 - \varepsilon_{o})\right]}{1 + R_{o}\kappa_{o}},$$
(31a)

$$\varepsilon_{\theta} = \frac{w}{R_a}, \ \varepsilon_r = \frac{dw}{dR_a}.$$
 (31b,c)

## 2.4 FORCE-DISPLACEMENT RELATIONS

By neglecting the higher order term  $R_o \kappa_o$  in equations (29b) and (31a), and substituting equations (22a)-(27a), and (31) into (15a)-(18a), together with some manipulations, one obtains the force-displacement relations in the apparent system:

$$N_{za} = EA_{po}\varepsilon$$
,  $M_{za} = EI_{po}[\kappa(1+\varepsilon_d) - (1-w/R)\overline{\kappa}(1-\varepsilon_o)]$ , (32a,b)

$$N_{\theta a} = E \int \varepsilon_{\theta} dA_{so} , M_{\theta a} = 0 ,$$
 (32c,d)

and the force-displacement relations in the real system:

$$N_{z} = \frac{1}{1 - v^{2}} \left[ N_{za} + vE \int \varepsilon_{\theta} dA_{Po} \right] = \frac{1}{1 - v^{2}} \left[ N_{za} + \frac{vEA_{Po}w}{R_{o}} \right], M_{z} = \frac{M_{za}}{1 - v^{2}}, \quad (33a,b)$$

$$N_{\theta} = \frac{1}{1 - v^2} \left[ N_{\theta o} + vE \int \varepsilon_z dA_{so} \right], M_{\theta} = 0.$$
 (33c,d)

### 2.5 STRAIN ENERGY EXPRESSIONS

The internal virtual work done by the strain energy of the pipe is derived as

$$\delta U = \int \{\delta \varepsilon\}^{T} \{\sigma\} d\forall_{Po} = \int [\sigma_{z} \delta \varepsilon_{z} + \sigma_{\theta} \delta \varepsilon_{\theta} + \sigma_{r} \delta \varepsilon_{r}] d\forall_{Po}$$

$$= \int \int \sigma_{z} \delta \varepsilon_{z} dA_{Po} + \frac{1}{1 - v^{2}} (v N_{zo} + \int E \varepsilon_{\theta} dA_{Po}) \delta \varepsilon_{\theta} ds_{o},$$
(34)

where  $\forall_{p_o}$  is the volume of the pipe at the reference state. Inserting equations (31) into (34) together with neglecting the higher order term  $R_o \kappa_o$  in equation (31a), one obtains

$$\delta U = \int_{\alpha} \left\{ N_z \delta s' + M_z \delta \left[ \theta' - (1 - w/R) \overline{\theta}' \right] + \frac{s'_o}{1 - v^2} \left[ \frac{v N_{zo}}{R_o} + \frac{E A_{Po} w}{R_o^2} \right] \delta w \right\} d\alpha. \tag{35}$$

# 3. THE CONTINUITY EQUATIONS OF FLOW INSIDE THE COUPLED DEFORMATIONS PIPES

Derivation of the continuity equations of internal flow that undergoes the effect of the coupled radial-axial deformations of the pipe, involves developing the following relations:

- (i) relations between the pipe deformations and the local kinematics of the internal flow,
- (ii) local-global kinematics relations of the internal flow, and
- (iii) relations between the kinematics and pressure loads of the internal flow.

# 3.1 THE RELATIONS BETWEEN THE PIPE DEFORMATIONS AND THE LOCAL KINEMATICS OF THE INTERNAL FLOW

As shown in equation (12), the effect of the coupled radial-axial deformations is to change cross-section area of the pipe among the three states. From principles of fluid mechanics, this effect engenders the consequence that the flow inside the pipe has to vary the velocity to maintain conservation of system mass according to the continuity condition

$$\overline{A_i}\overline{V_i} = A_{io}(s_o)V_{io}(s_o) = A_i(s,t)V_i(s,t) + \frac{\partial \forall_{cv}(s,t)}{\partial t} = \text{a constant volume flow rate}, \quad (36)$$

where  $\overline{V}_i, V_w, V_r$  represent the internal flow velocities at the undeformed, the equilibrium, and the dynamic states, respectively. If the internal volume of a pipe element  $d \forall_r$  represents the control volume  $\forall_{cv}$ , the time rate of  $\forall_{cv}$  is derived as

$$\frac{\partial \forall_{cv}}{\partial t} = \frac{\partial (d\forall_i)}{\partial \forall_{io}} \frac{\partial \forall_{io}}{\partial s_o} \frac{ds_o}{dt} = \varepsilon_v A_{io} V_{io} = \varepsilon_v \overline{A}_i \overline{V}$$
(37)

in which the expression of the volumetric strain of the pipe  $\varepsilon_v$  is denoted by

$$\varepsilon_{v} = \frac{d\forall_{i} - d\overline{\forall}_{i}}{d\forall_{w}} = \frac{A_{i}ds - \overline{A}_{i}d\overline{s}}{A_{w}ds_{w}} = \frac{(1 + w/\overline{R})^{2}(1 + \varepsilon_{d}) - (1 - \varepsilon_{o})}{(1 + w_{o}/\overline{R})^{2}}.$$
 (38)

Utilizing equation (37), the relationship representing changes of internal flow velocities of transported fluid among the three states can be obtained from equation (36) as

$$\overline{A}\overline{V}_{i} = A_{io}V_{io} = A_{i}V_{i}/(1-\varepsilon_{v}). \tag{39}$$

This interprets that the effect of the coupled deformations of the pipe stimulates the steady uniform flow  $(\partial \overline{V}_i/\partial \alpha = \partial \overline{V}_i/\partial t = 0)$  of transported fluid at the undeformed state to change into the steady non-uniform flow  $(\partial V_{io}/\partial \alpha \neq 0, \partial V_{io}/\partial t = 0)$  at the equilibrium state, and then become the unsteady non-uniform flow  $(\partial V_i/\partial \alpha \neq 0, \partial V_i/\partial t \neq 0)$  at the dynamic state.

#### 3.2 THE LOCAL-GLOBAL KINEMATICS RELATIONS OF THE INTERNAL FLOW

Consider Figure 4. As the internal flow velocity  $V_{FP} \in \{\overline{V}_i, V_{io}, V_i\}$  of transported fluid has changed due to the effect of the coupled radial-axial deformations, the velocity  $V_F$  and the acceleration  $a_F$  of transported fluid would alter as a result, according to the relationships

$$\bar{\mathbf{V}}_{F} = \bar{\mathbf{V}}_{P} + \bar{\mathbf{V}}_{FP} = \frac{\partial \bar{\mathbf{r}}_{P}}{\partial t} + \frac{V_{FP}}{s'} \frac{\partial \bar{\mathbf{r}}_{P}}{\partial \alpha}. \tag{40}$$

$$\vec{\mathbf{a}}_{F} = \frac{D\vec{\mathbf{V}}_{F}}{Dt} = \frac{D\vec{\mathbf{V}}_{P}}{Dt} + \frac{D\vec{\mathbf{V}}_{FP}}{Dt} = \frac{D}{Dt} \left( \frac{\partial \vec{\mathbf{r}}_{P}}{\partial t} \right) + \frac{D}{Dt} \left( \frac{V_{FP}}{s'} \frac{\partial \vec{\mathbf{r}}_{P}}{\partial \alpha} \right) \\
= \left[ \underbrace{\frac{\partial^{2} \vec{\mathbf{r}}_{P}}{\partial t^{2}} + \frac{V_{FP}}{s'} \frac{\partial^{2} \vec{\mathbf{r}}_{P}}{\partial \alpha \partial t}}_{\vec{\mathbf{a}}} \right] + \underbrace{\frac{V_{FP}}{s'} \left[ \frac{\partial^{2} \vec{\mathbf{r}}_{P}}{\partial \alpha \partial t} + \frac{V_{FP}}{s'} \frac{\partial^{2} \vec{\mathbf{r}}_{P}}{\partial \alpha^{2}} \right] + \left[ \underbrace{\frac{\partial}{\partial t} \left( \frac{V_{FP}}{s'} \right) + \frac{V_{FP}}{s'} \frac{\partial}{\partial \alpha} \left( \frac{V_{FP}}{s'} \right)}_{\vec{\mathbf{a}}_{FP}} \right] \underbrace{\frac{\partial \vec{\mathbf{r}}_{P}}{\partial \alpha}}_{\vec{\mathbf{a}}} , \tag{41a}$$

$$\vec{\mathbf{a}}_{F} = \underbrace{\frac{\partial^{2} \vec{\mathbf{r}}_{P}}{\partial t^{2}}}_{(1)} + \underbrace{\left(\frac{2V_{FP}}{s'}\right) \frac{\partial^{2} \vec{\mathbf{r}}_{P}}{\partial \alpha \partial t}}_{(2)} + \underbrace{\left(\frac{V_{FP}}{s'}\right)^{2} \frac{\partial^{2} \vec{\mathbf{r}}_{P}}{\partial \alpha^{2}}}_{(3)} + \underbrace{\left(\frac{\dot{V}_{FP}}{s'}\right) \frac{\dot{V}_{FP}V'_{FP}}{\dot{s}'}}_{(4)} + \underbrace{\frac{\dot{V}_{FP}V'_{FP}}{s'^{2}}}_{(5)} - \underbrace{\frac{\dot{V}_{FP}\dot{s}'}{s'^{2}}}_{(6)} - \underbrace{\frac{\dot{V}_{FP}\dot{s}'}{s'^{3}}}_{(6)} \underbrace{\left(\frac{\partial^{2} \vec{\mathbf{r}}_{P}}{\partial \alpha}\right)}_{(6)} + \underbrace{\left(\frac{\partial^{2} \vec{\mathbf{r}}_{P}}{\partial \alpha}\right) \frac{\partial^{2} \vec{\mathbf{r}}_{P}}{\partial \alpha^{2}}}_{(4)} + \underbrace{\left(\frac{\dot{V}_{FP}}{s'}\right) \frac{\partial^{2} \vec{\mathbf{r}}_{P}}{\partial \alpha^{2}}}_{(5)} + \underbrace{\left(\frac{\dot{V}_{FP}}{s'}\right) \frac{\partial^{2} \vec{\mathbf{r}}_{P}}{\partial \alpha^{2}}}_{(6)} + \underbrace{\left(\frac{\dot{V}_{FP}}{s'}\right) \frac{\partial^{2} \vec{\mathbf{r}}_{P}}_{(6)}}_{(6)} + \underbrace{\left(\frac{\dot{V}_{FP}}{s'}\right) \frac{\partial^{2} \vec{\mathbf{r}}_{P}}{\partial \alpha^{2}}}_{(6)} + \underbrace{\left(\frac{\dot{V}_{FP}}{s'}\right) \frac{\partial^{2} \vec{\mathbf{r}}_{P}}{\partial \alpha^{2}}}_{(6)} + \underbrace{\left(\frac{\dot{V}_{FP}}{s'}\right) \frac{\partial^{2} \vec{\mathbf{r}}_{P}}_{(6)}}_{(6)} + \underbrace{\left(\frac{\dot{V}_{FP}}{s'}\right) \frac{\partial^{2} \vec{\mathbf{r}}_{$$

where  $V_{FP}$  is measured with respect to the moving frame of the pipe in local coordinates xyz,  $V_F$  is measured relative to the fixed frame of reference in global coordinates XYZ, and the position vector of the pipe-wall element is described in Figure 4 as

$$\vec{\mathbf{r}}_{p} = \vec{\mathbf{r}}_{c(XYZ)} + \vec{\mathbf{r}}_{Pc(XYZ')} = x\hat{\mathbf{i}} + y\hat{\mathbf{j}} + (\overline{R} + w)\hat{\mathbf{n}}_{c}. \tag{42}$$

It is worthwhile to note that  $\hat{\mathbf{n}}_c$  is the unit normal vector in the radial direction, and in equation (41) the term (1) is the transported mass acceleration, (2) the coriolis acceleration, (3) the centripetal acceleration, (4) the local acceleration due to unsteady flow, (5) the convective acceleration due to non-uniform flow, and (6) the relative accelerations due to rotation and displacement of the local coordinates.

In the 2-D CSC, at the dynamic state:

$$V_{EP} = V_{r}, \ \vec{\mathbf{r}}_{P} = x\hat{\mathbf{i}} + y\hat{\mathbf{j}} + (\overline{R} + w)\hat{\mathbf{n}}_{e}, \tag{43a,b}$$

$$s' = \sqrt{x'^2 + y'^2}, \quad s's'' = x'x'' + y'y'', \quad s'\dot{s}' = x'\dot{x}' + y'\dot{y}'.$$
 (43c-e)

Supposing that the higher order term  $(\overline{R} + w)\hat{\mathbf{n}}'_c = -R\theta\hat{\mathbf{t}}_c = -Rs'\kappa\hat{\mathbf{t}}_c \to 0$  is negligible, and utilizing equations (43), equations (40) and (41) can be obtained, after manipulation, as

$$\vec{\mathbf{V}}_{i,} = \left[ \dot{x} + V_i x' / s' \right] \hat{\mathbf{i}} + \left[ \dot{y} + V_i y' / s' \right] \hat{\mathbf{j}} + \left[ \dot{w} + V_i w' / s' \right] \hat{\mathbf{n}}_{c}, \tag{44}$$

$$\vec{\mathbf{a}}_{F} = \left\{ \ddot{x} + \left[ \left( \frac{2}{s'} - \frac{{x'}^{2}}{{s'}^{3}} \right) \dot{x}' - \left( \frac{{x'}y'}{{s'}^{3}} \right) \dot{y}' \right] V_{i} + \left( \frac{\kappa y'}{s'} \right) V_{i}^{2} + \left( \frac{DV_{i}}{Dt} \right) \frac{x'}{s'} \right\} \hat{\mathbf{i}}$$

$$+ \left\{ \ddot{y} + \left[ -\left( \frac{{x'}y'}{{s'}^{3}} \right) \dot{x}' + \left( \frac{2}{s'} - \frac{{y'}^{2}}{{s'}^{3}} \right) \dot{y}' \right] V_{i} - \left( \frac{\kappa x'}{s'} \right) V_{i}^{2} + \left( \frac{DV_{i}}{Dt} \right) \frac{y'}{s'} \right\} \hat{\mathbf{j}}$$

$$+ \left\{ \ddot{w} + \left( \frac{2V_{i}}{s'} \right) \dot{w}' + \left( \frac{V_{i}}{s'} \right)^{2} w'' + \left[ \frac{1}{s'} \frac{DV_{i}}{Dt} - \frac{V_{i} \dot{s}'}{s'^{2}} - \frac{V_{i}^{2} s''}{s'^{3}} \right] w' \right\} \hat{\mathbf{n}}_{c}.$$
(45)

Note that 
$$\frac{\kappa y'}{s'} = \left(\frac{y'^2}{s'^4}\right) x'' - \left(\frac{x'y'}{s'^4}\right) y''$$
, and  $-\frac{\kappa x'}{s'} = -\left(\frac{x'y'}{s'^4}\right) x'' + \left(\frac{x'^2}{s'^4}\right) y''$ . (46a,b)

In 2-D NTC, at the dynamic state:

$$V_{FP} = V_{r}, \ \vec{\mathbf{r}}_{p} = \vec{\mathbf{r}}_{c} + (\overline{R} + w)\hat{\mathbf{n}}_{c}, \ \frac{\partial \vec{\mathbf{r}}_{c}}{\partial \alpha} = s' \,\hat{\mathbf{t}}, \ \frac{\partial^{2} \vec{\mathbf{r}}_{c}}{\partial \alpha^{2}} = s' \theta' \,\hat{\mathbf{n}} + s'' \,\hat{\mathbf{t}}, \tag{47a-d}$$

$$\frac{\partial^2 \bar{\mathbf{r}}_c}{\partial t^2} = \ddot{\mathbf{u}}_n \hat{\mathbf{n}} + \ddot{\mathbf{v}}_n \hat{\mathbf{t}} , \quad \frac{\partial^2 \bar{\mathbf{r}}_c}{\partial \alpha \partial t} = s' \dot{\theta} \, \hat{\mathbf{n}} + \dot{s}' \, \hat{\mathbf{t}} . \tag{47e,f}$$

Similarly, supposing that the term  $(\overline{R} + w)\hat{\mathbf{n}}'_c = -R\theta\hat{\mathbf{t}}_c = -Rs'\kappa\hat{\mathbf{t}}_c \rightarrow 0$  is negligible, and utilizing equations (47), equations (40) and (41) can be rewritten in the form

$$\vec{\mathbf{V}}_F = \dot{u}_n \hat{\mathbf{n}} + (\dot{v}_n + V_i) \hat{\mathbf{t}} + \left[ \dot{w} + V_i w' / s' \right] \hat{\mathbf{n}}_c, \tag{48}$$

$$\vec{\mathbf{a}}_{F} = \left[ \ddot{u}_{n} + 2V_{i}\dot{\theta} + \kappa V_{i}^{2} \right] \hat{\mathbf{n}} + \left[ \ddot{v}_{n} + \frac{V_{i}\dot{s}'}{s'} + \frac{DV_{i}}{Dt} \right] \hat{\mathbf{t}} + \left\{ \ddot{w} + \left( \frac{2V_{i}}{s'} \right) \dot{w}' + \left( \frac{V_{i}}{s'} \right)^{2} w'' + \left[ \frac{1}{s'} \frac{DV_{i}}{Dt} - \frac{V_{i}\dot{s}'}{s'^{2}} - \frac{V_{i}^{2}s''}{s'^{3}} \right] w' \right\} \hat{\mathbf{n}}_{c}.$$
(49)

At the equilibrium state, the time-dependent terms vanish. Thus, one obtains  $V_{FP} = V_{io}$ ,  $(x, y, w) = (x_o, y_o, w_o)$ ,  $(s, \theta) = (s_o, \theta_o)$ ,  $u_n = v_n = 0$ , and equations (44), (45), (48), and (49) consequently become

in CSC, 
$$\vec{\mathbf{V}}_{Fo} = (V_{io}x'_{o}/s'_{o})\hat{\mathbf{i}} + (V_{io}y'_{o}/s'_{o})\hat{\mathbf{j}} + [V_{io}w'_{o}/s'_{o}]\hat{\mathbf{n}}_{co}, \tag{50}$$

$$\bar{\mathbf{a}}_{Fo} = \left\{ \left( \frac{\kappa_o y'_o}{s'_o} \right) V_{io}^2 + \frac{V_{io} V'_{io}}{s'_o} \frac{x'_o}{s'_o} \right\} \hat{\mathbf{i}} + \left\{ -\left( \frac{\kappa_o x'_o}{s'_o} \right) V_{io}^2 + \frac{V_{io} V'_{io}}{s'_o} \frac{y'_o}{s'_o} \right\} \hat{\mathbf{j}} + \left\{ \left( \frac{V_{io}}{s'_o} \right)^2 w''_o + \left[ \frac{V_{io} V'_{io}}{s'_o^2} - \frac{V_{io}^2 s''_o}{s'_o^3} \right] w'_o \right\} \hat{\mathbf{n}}_{co}, \tag{51}$$

in NTC,  $\bar{\mathbf{V}}_{Fo} = V_{io}\hat{\mathbf{t}}_{o} + \left[V_{io}w'_{o}/s'_{o}\right]\hat{\mathbf{n}}_{co}, \tag{52}$ 

$$\vec{\mathbf{a}}_{Fo} = \left[\kappa_o V_{io}^2\right] \hat{\mathbf{n}}_o + \left[\frac{V_{io} V_{io}'}{s_o'}\right] \hat{\mathbf{t}}_o + \left\{\left(\frac{V_{io}}{s_o'}\right)^2 w_o'' + \left[\frac{V_{io} V_{io}'}{s_o'^2} - \frac{V_{io}^2 s_o''}{s_o'^3}\right] w_o'\right\} \hat{\mathbf{n}}_{co}.$$
 (53)

#### 3.3 THE RELATIONS BETWEEN THE KINEMATICS AND PRESSURE LOADS OF THE INTERNAL FLOW

Based on the control volume approach of Computational Fluid Dynamics, Chucheepsakul et al. (2003) showed the derivation that the internal fluid flowing through the moving, deforming control volume of the pipe induces dynamic pressures in form of the inertial force per unit pipe-length to act on the pipe wall at the dynamic state:

$$\mathbf{\bar{f}}_I = m_{io}\mathbf{\bar{a}}_F \,, \tag{54a}$$

and at the equilibrium state:

$$\vec{\mathbf{f}}_{lo} = m_{lo} \vec{\mathbf{a}}_{Fo} \,, \tag{54b}$$

where the transported mass per unit pipe-length at the reference state is  $m_{io} = \rho_i A_{io}$ , in which  $\rho_i$  is the internal fluid density.

From the relations in equations (39), (40), (41), and (54), the transported fluid-pipe interaction shown in Figure 2(b), can be explained as follows. Firstly, the coupled deformations due to  $\varepsilon$  and w induce the alteration of the local internal flow velocity

 $V_{FP} \in \{\bar{V}_i, V_{io}, V_i\}$  following equation (39). Later, the local velocity induces the global velocity  $\bar{\mathbf{V}}_F$  and the global acceleration  $\bar{\mathbf{a}}_F$  following equations (40) and (41) due to the relativity of motion of transported mass on the moving frame of the pipe with large displacements. Then, the global acceleration  $\bar{\mathbf{a}}_F$  induces the dynamic pressure load  $\bar{\mathbf{f}}_i$  as equation (54a). Finally, the pressure load  $\bar{\mathbf{f}}_i$  induces the pipe deformations  $\varepsilon$  and w by the force-displacement relations as equations (32)-(33), and the loop of the interaction is repeated concurrently.

#### 4. VARIATIONAL FORMULATIONS

Based on the constitutive equations proposed in Sec. 2, the continuity equations derived in Sec. 3, and the method of virtual work, the coupled radial-axial deformations formulation of flexible pipes conveying fluid has the following procedure:

- Step 1: Create the equations of internal virtual work by using the strain-displacement, the force-displacement, and the energy-force-displacement relations from equations (31)-(33), and (35) in Sec. 2
- Step 2: Express the equations of external virtual work induced by the apparent weight, static and dynamic pressure forces, and inertial forces of the pipe and transported fluid. The continuity conditions from equations (39), (41), and (54) are applied to the external work done by the inertial force of transported fluid.
- Step 3: Apply the principle of virtual work to generate weak and strong formulations of the system.

In all steps, the effects of parameters changes among the three states must be taken into account by using equations (1)-(14).

#### 4.1 INTERNAL VIRTUAL WORK

Based on the basic formulas of differential geometry, and the assumption that the pipe is straight in the undeformed state, one has

$$\overline{K} = \overline{\theta}' = 0$$
,  $s'^2 = x'^2 + v'^2$ ,  $\theta' = (x''v' - x'v'')/s'^2$ . (55a-c)

Substituting equation (55a) into (32b), and taking the first variation of equations (55b) and (55c) together with coordinate transformations of the displacement vectors, one obtains

$$M_{za} = B\kappa$$
,  $B = EI_{Po}(1 + \varepsilon_d)$ , (56a,b)

in CSC: 
$$\delta s' = \left(\frac{x'}{s'}\right) \delta u' + \left(\frac{y'}{s'}\right) \delta v', \qquad (57a)$$

$$\delta\theta' = \frac{1}{s'} \left( \frac{y'}{s'} \right) \delta u'' - \left[ \kappa \left( \frac{x'}{s'} \right) + \frac{s''}{s'^2} \left( \frac{y'}{s'} \right) \right] \delta u' - \frac{1}{s'} \left( \frac{x'}{s'} \right) \delta v'' - \left[ \kappa \left( \frac{y'}{s'} \right) - \frac{s''}{s'^2} \left( \frac{x'}{s'} \right) \right] \delta v', \quad (57b)$$

in NTC: 
$$\delta s' = \delta v'_n - \theta' \delta u_n, \quad \delta \theta' = \frac{\partial}{\partial \alpha} \left[ \frac{\delta u'_n + \theta' \delta v_n}{s'} \right]. \tag{58a,b}$$

Inserting equations (56)-(58) into (35), and then taking integrations by parts twice, the three forms of the internal virtual work can be expressed below:

Form 1: in CSC,

$$\delta U = \int_{\alpha} \left\{ \frac{B\kappa}{(1-v^2)s'} \left( \frac{y'}{s'} \right) \delta u'' + \left[ \left( N_z - \frac{B\kappa^2}{1-v^2} \right) \left( \frac{x'}{s'} \right) - \frac{B\kappa}{1-v^2} \frac{s''}{s'^2} \left( \frac{y'}{s'} \right) \right] \delta u' \right\} d\alpha$$

$$+ \int_{\alpha} \left\{ -\frac{B\kappa}{(1-v^2)s'} \left( \frac{x'}{s'} \right) \delta v'' + \left[ \left( N_z - \frac{B\kappa^2}{1-v^2} \right) \left( \frac{y'}{s'} \right) + \frac{B\kappa}{1-v^2} \frac{s''}{s'^2} \left( \frac{x'}{s'} \right) \right] \delta v' \right\} d\alpha \qquad (59a)$$

$$+ \int_{\alpha} \left\{ \frac{s'_o}{1-v^2} \left[ \frac{vN_{za}}{\tilde{R}} + \frac{EA_{p_o}w}{\tilde{R}^2} \right] \delta w \right\} d\alpha,$$

in NTC, 
$$\delta U = \int_{\alpha} \left\{ \left[ -N_z \theta' \right] \delta u_n + \left[ N_z \right] \delta v_n' + \left[ M_z \right] \delta \theta' + \frac{s_o'}{1 - v^2} \left[ \frac{v N_{za}}{R_o} + \frac{E A_{Po} w}{R_o^2} \right] \delta w \right\} d\alpha$$
. (59b)

Form 2 (after the first integration by parts): in CSC.

$$\delta U = \left[ M_z \delta \theta \right]_{\alpha_o}^{\alpha_t} + \int_{\alpha} \left\{ H_z \delta u' + V_z \delta v' + \frac{s'_o}{1 - v^2} \left[ \frac{v N_{zo}}{R_o} + \frac{E A_{po} w}{R_o^2} \right] \delta w \right\} d\alpha, \qquad (60a)$$

in NTC,

$$\delta U = \left[ M_z \delta \theta \right]_{\alpha_o}^{\alpha_r} + \int_{\alpha} \left\{ -\left[ Q_z \right] \delta u_n' - \left[ N_z \theta' \right] \delta u_n + \left[ N_z \right] \delta v_n' + \left[ Q_z \theta' \right] \delta v_n \right\} d\alpha$$

$$+ \int_{\alpha} \left\{ \frac{s_o'}{1 - v^2} \left[ \frac{v N_{za}}{R_o} + \frac{E A_{p_o} w}{R_o^2} \right] \delta w \right\} d\alpha, \tag{60b}$$

where 
$$H_z = N_z \left(\frac{x'}{s'}\right) - Q_z \left(\frac{y'}{s'}\right)$$
,  $V_z = N_z \left(\frac{y'}{s'}\right) + Q_z \left(\frac{x'}{s'}\right)$ ,  $Q_z = \frac{Q_{za}}{1 - v^2}$ ,  $Q_{za} = \frac{\left(B\kappa\right)'}{s'}$ . (61a-d)

Form 3 (after the second integration by parts): in CSC,

$$\delta U = \left[ H_z \delta u + V_z \delta v + M_z \delta \theta \right]_{\alpha_o}^{\alpha_i} + \int_{\alpha} \left\{ \left[ -H_z' \right] \delta u + \left[ -V_z' \right] \delta v + \frac{s_o'}{1 - v^2} \left[ \frac{v N_{zo}}{R_o} + \frac{E A_{Po} w}{R_o^2} \right] \delta w \right\} d\alpha, \quad (62a)$$

in NTC,

$$\delta U = \left[ N_z \delta v_n - Q_z \delta u_n + M_z \delta \theta \right]_{\alpha_o}^{\alpha_i} + \int_{\alpha} \left\{ \left[ Q_z' - N_z \theta' \right] \delta u_n + \left[ -N_z' - Q_z \theta' \right] \delta v_n \right\} d\alpha$$

$$+ \int_{\alpha} \left\{ \frac{s_o'}{1 - v^2} \left[ \frac{v N_{za}}{R_o} + \frac{E A_{p_o} w}{R_o^2} \right] \delta w \right\} d\alpha.$$
(62b)

Note that  $x'/s' = \sin\theta$ ,  $y'/s' = \cos\theta$  and  $\kappa = \theta'/s' = (x''y' - x'y'')/s'^3$ .

#### 4.2 EXTERNAL VIRTUAL WORK

The external virtual work done by the force vectors  $\vec{\mathbf{f}}_w$ ,  $\vec{\mathbf{f}}_p$ ,  $\vec{\mathbf{f}}_H$ , and  $\vec{\mathbf{f}}_I$ , which are exerted by the apparent weight  $w_a$ , the static pressures  $f_p$ , the dynamic pressures  $f_H$ , and the inertial forces of the pipe and transported fluid respectively, is expressed as

$$\delta W = \iint_{\alpha} \left[ \bar{\mathbf{f}}_{w} + \bar{\mathbf{f}}_{p} + \bar{\mathbf{f}}_{H} + \bar{\mathbf{f}}_{I} \right] \cdot \delta \bar{\mathbf{u}}_{p} s_{o}' d\alpha , \qquad (63)$$

where

$$\bar{\mathbf{f}}_{w} = -w_{a}\hat{\mathbf{j}} = (w_{a}\sin\theta)\hat{\mathbf{n}} + (-w_{a}\cos\theta)\hat{\mathbf{t}}, \qquad (64a)$$

$$\bar{\mathbf{f}}_{p} = f_{p} \hat{\mathbf{n}}_{c}, \tag{64b}$$

$$\bar{\mathbf{f}}_{H} = f_{Hx}\hat{\mathbf{i}} + f_{Hy}\hat{\mathbf{j}} + f_{Hnc}\hat{\mathbf{n}}_{c} = f_{Hn}\hat{\mathbf{n}} + f_{Ht}\hat{\mathbf{t}} + f_{Hnc}\hat{\mathbf{n}}_{c}, \tag{64c}$$

$$\bar{\mathbf{f}}_{l} = -\left[m_{Po}\bar{\mathbf{a}}_{P} + m_{lo}\bar{\mathbf{a}}_{F}\right],\tag{64d}$$

$$\vec{\mathbf{u}}_{P} = u\hat{\mathbf{i}} + v\hat{\mathbf{j}} + w\hat{\mathbf{n}}_{c} = u_{n}\hat{\mathbf{n}} + v_{n}\hat{\mathbf{t}} + w\hat{\mathbf{n}}_{c}. \tag{64e}$$

Note that  $m_{p_0} = \rho_p A_{p_0}$  is the pipe mass per unit length at the reference state,  $\rho_p$  is the pipematerial density, and  $\bar{\mathbf{a}}_p$  is the acceleration vector of the pipe.

The non-vector forms of equation (63) may be expressed as: in CSC,

$$\delta W = \int_{\alpha} \left\{ s_o' \left[ f_{Hx} - m_{Po} a_{Px} - m_{io} a_{Fx} \right] \delta u \right\} d\alpha$$

$$+ \int_{\alpha} \left\{ s_o' \left[ -w_o + f_{Hy} - m_{Po} a_{Py} - m_{io} a_{Fy} \right] \delta v \right\} d\alpha$$

$$+ \int_{\alpha} \left\{ s_o' \left[ f_p - f_{Hnc} - m_{Po} a_{Pnc} - m_{io} a_{Fnc} \right] \delta w \right\} d\alpha,$$
(65)

in NTC,

$$\delta W = \int_{\alpha} \left\{ s_o' \left[ w_a \sin \theta + f_{Hn} - m_{Po} a_{Pn} - m_{no} a_{Fn} \right] \delta u_n \right\} d\alpha$$

$$+ \int_{\alpha} \left\{ s_o' \left[ -w_a \cos \theta + f_{Ht} - m_{Po} a_{Pt} - m_{no} a_{Ft} \right] \delta v_n \right\} d\alpha$$

$$+ \int_{\alpha} \left\{ s_o' \left[ f_p - f_{Hnc} - m_{Po} a_{Pnc} - m_{no} a_{Fnc} \right] \delta w \right\} d\alpha.$$
(66)

#### 4.3 TOTAL VIRTUAL WORK

Relying upon the principle of virtual work, the total virtual work of the system is zero:

$$\delta \pi = \delta U - \delta W = 0. \tag{67}$$

Since there exist the three forms of  $\delta U$  as shown in equations (59), (60), and (62), the three weak forms of the total virtual work thus are obtained as

Form 1: in CSC.

$$\delta \pi = \int_{\alpha} \left\{ \frac{B\kappa}{(1-v^{2})s'} \left( \frac{y'}{s'} \right) \delta u'' + \left[ (N_{z} - \frac{B\kappa^{2}}{1-v^{2}}) \left( \frac{x'}{s'} \right) - \frac{B\kappa}{1-v^{2}} \frac{s''}{s'^{2}} \left( \frac{y'}{s'} \right) \right] \delta u' \right\} d\alpha$$

$$+ \int_{\alpha} \left\{ -\frac{B\kappa}{(1-v^{2})s'} \left( \frac{x'}{s'} \right) \delta v'' + \left[ (N_{z} - \frac{B\kappa^{2}}{1-v^{2}}) \left( \frac{y'}{s'} \right) + \frac{B\kappa}{1-v^{2}} \frac{s''}{s'^{2}} \left( \frac{x'}{s'} \right) \right] \delta v' \right\} d\alpha$$

$$+ \int_{\alpha} \left\{ -\frac{s'_{o}}{(1-v^{2})s'} \left[ -w_{o} + f_{Hy} - m_{Po} a_{Py} - m_{lo} a_{Py} \right] \delta v \right\} d\alpha$$

$$+ \int_{\alpha} \left\{ \frac{s'_{o}}{1-v^{2}} \left[ \frac{vN_{za}}{\tilde{R}} + \frac{EA_{Po}w}{\tilde{R}^{2}} \right] - s'_{o} \left[ f_{p} - f_{Hnc} - m_{Po} a_{Pnc} - m_{lo} a_{Fm} \right] \right\} \delta w d\alpha,$$
(68a)

in NTC,

$$\delta\pi = \int_{\alpha} \left\{ -N_{z}\theta' - s'_{o} \left[ w_{a} \sin\theta + f_{Hn} - m_{Po}a_{Pn} - m_{io}a_{Fn} \right] \right\} \delta u_{n} d\alpha$$

$$+ \int_{\alpha} \left\{ \left[ N_{z} \right] \delta v'_{n} - s'_{o} \left[ -w_{a} \cos\theta + f_{Ht} - m_{Po}a_{Pt} - m_{io}a_{Ft} \right] \delta v_{n} \right\} d\alpha$$

$$+ \int_{\alpha} \left\{ \frac{s'_{o}}{1 - v^{2}} \left[ \frac{vN_{za}}{\tilde{R}} + \frac{EA_{Po}w}{\tilde{R}^{2}} \right] - s'_{o} \left[ f_{p} - f_{Hnc} - m_{Po}a_{Pnc} - m_{io}a_{Fnc} \right] \right\} \delta w d\alpha$$

$$+ \int_{\alpha} \left\{ \left[ M_{z} \right] \delta \theta' \right\} d\alpha. \tag{68b}$$

Form 2: in CSC.

$$\delta\pi = \left[ M_{z} \delta\theta \right]_{a_{a}}^{a_{r}} + \int_{\alpha} \left\{ H_{z} \delta u' - s'_{o} \left[ f_{Hx} - m_{p_{o}} a_{p_{x}} - m_{n_{o}} a_{Fx} \right] \delta u \right\} d\alpha$$

$$+ \int_{\alpha} \left\{ V_{z} \delta v' - s'_{o} \left[ -w_{a} + f_{Hy} - m_{p_{o}} a_{p_{y}} - m_{n_{o}} a_{Fy} \right] \delta v \right\} d\alpha$$

$$+ \int_{\alpha} \left\{ \frac{s'_{o}}{1 - v^{2}} \left[ \frac{v N_{za}}{\tilde{R}} + \frac{E A_{p_{o}} w}{\tilde{R}^{2}} \right] - s'_{o} \left[ f_{p} - f_{Hnc} - m_{p_{o}} a_{p_{nc}} - m_{n_{o}} a_{Fnc} \right] \right\} \delta w d\alpha,$$
(69a)

in NTC,

$$\delta\pi = \left[ M_{z} \delta\theta \right]_{a_{o}}^{a_{t}} + \int_{\alpha} \left\{ -\left[ Q_{z} \right] \delta u'_{n} - \left[ N_{z} \theta' + s'_{o} \left( w_{a} \sin\theta + f_{Hn} - m_{p_{o}} a_{p_{n}} - m_{no} a_{Fn} \right) \right] \delta u_{n} \right\} d\alpha + \int_{\alpha} \left\{ \left[ N_{z} \right] \delta v'_{n} + \left[ Q_{z} \theta' - s'_{o} \left( -w_{a} \cos\theta + f_{Ht} - m_{p_{o}} a_{p_{t}} - m_{no} a_{Ft} \right) \right] \delta v_{n} \right\} d\alpha + \int_{\alpha} \left\{ \frac{s'_{o}}{1 - v^{2}} \left[ \frac{v N_{zo}}{\tilde{R}} + \frac{E A_{p_{o}} w}{\tilde{R}^{2}} \right] - s'_{o} \left[ f_{p} - f_{Hnc} - m_{p_{o}} a_{p_{nc}} - m_{no} a_{Fnc} \right] \right\} \delta w d\alpha.$$
(69b)

Form 3: in CSC,

$$\delta\pi = \left[\underbrace{H_{z}\delta u + V_{z}\delta v + M_{z}\delta\theta}_{(1)}\right]_{a_{o}}^{a_{f}} + \int_{\alpha}^{\beta} \left\{\underbrace{\left[-H'_{z} - s'_{o}\left(f_{Hx} - m_{Po}a_{Px} - m_{to}a_{Fx}\right)\right]}_{(4)}\right\} d\alpha$$

$$+ \int_{\alpha}^{\beta} \left\{\underbrace{\left[-V'_{z} - s'_{o}\left(-w_{a} + f_{Hy} - m_{Po}a_{Py} - m_{to}a_{Fy}\right)\right]}_{(5)}\delta v\right\} d\alpha$$

$$+ \int_{\alpha}^{\beta} \left\{\underbrace{\frac{s'_{o}}{1 - v^{2}}\left[\frac{vN_{za}}{\tilde{R}} + \frac{EA_{Po}w}{\tilde{R}^{2}}\right] - s'_{o}\left(f_{p} - f_{Hinc} - m_{Po}a_{Pnc} - m_{to}a_{Fnc}\right)}_{(6)}\right\} \delta w d\alpha, \tag{70a}$$

in NTC,

$$\delta\pi = \left[\underbrace{N_{z}\delta v_{n}}_{(7)} - \underbrace{Q_{z}\delta u_{n}}_{(8)} + \underbrace{M_{z}\delta\theta}_{(3)}\right]_{\alpha_{n}}^{\alpha_{t}}$$

$$+ \int_{\alpha} \left\{ \underbrace{\left[Q'_{z} - N_{z}\theta' - s'_{o}\left(w_{a}\sin\theta + f_{Hn} - m_{p_{o}}a_{p_{n}} - m_{no}a_{p_{n}}\right)\right]}_{(9)} \delta u_{n} \right\} d\alpha$$

$$+ \int_{\alpha} \left\{ \underbrace{\left[-N'_{z} - Q_{z}\theta' - s'_{o}\left(-w_{a}\cos\theta + f_{Ht} - m_{p_{o}}a_{p_{t}} - m_{no}a_{p_{t}}\right)\right]}_{(10)} \delta v_{n} \right\} d\alpha$$

$$+ \int_{\alpha} \left\{ \underbrace{\frac{s'_{o}}{1 - v^{2}} \left[\frac{vN_{za}}{\tilde{R}} + \frac{EA_{p_{o}}w}{\tilde{R}^{2}}\right] - s'_{o}\left[f_{p} - f_{Hnc} - m_{p_{o}}a_{p_{nc}} - m_{no}a_{p_{nc}}\right]}_{(6)} \delta w d\alpha.$$

In equations (70), the terms (1), (2), (3), (7), and (8) denote the boundary conditions of the horizontal forces, vertical forces, moments, tensions, and shear forces, respectively. The terms (4), (5), (6), (9) and (10) indicate the resultant forces in the horizontal, vertical, radial, normal, and tangential directions, respectively.

#### 4.4 STRONG FORMULATIONS

The strong formulations are achieved by considering that all the terms in the right-hand side of equations (70a,b) are linearly independent. Therefore, they must be zero if equation (67) is to be valid. Because the virtual displacements  $\delta u$ ,  $\delta v$ ,  $\delta w$ ,  $\delta u_n$  and  $\delta v_n$  are nonzero, the terms (4), (5), (6), (9) and (10) in equations (70a,b) have to be zero. As a result, the governing differential equations describing the nonlinear behaviors of the pipe can be obtained as

$$\Sigma F_{x} = 0: \qquad -H'_{z} - s'_{o} \left( f_{Hx} - m_{p_{o}} a_{p_{x}} - m_{i_{o}} a_{p_{x}} \right) = 0, \tag{71}$$

A1

$$\Sigma F_{v} = 0: \qquad -V_{z}' - s_{o}' \left( -w_{a} + f_{Hy} - m_{Po} a_{Py} - m_{io} a_{Fy} \right) = 0, \tag{72}$$

$$\Sigma F_{nc} = 0: \qquad \frac{S_o'}{1 - v^2} \left[ \frac{v N_{za}}{R_o} + \frac{E A_{Po} w}{R_o^2} \right] - S_o' \left( f_p - f_{Hnc} - m_{Po} a_{Pnc} - m_{io} a_{Fnc} \right) = 0, \qquad (73)$$

$$\Sigma F_{n} = 0: \qquad Q'_{z} - N_{z}\theta' - s'_{o} \left( w_{a} \sin \theta + f_{Hn} - m_{Po} a_{Pn} - m_{io} a_{Fn} \right) = 0, \tag{74}$$

$$\Sigma F_{t} = 0: \qquad -N'_{z} - Q_{z}\theta' - s'_{o}\left(-w_{a}\cos\theta + f_{Ht} - m_{Po}a_{Pt} - m_{to}a_{Ft}\right) = 0. \tag{75}$$

In appendix A, by using the vectorial method it is demonstrated that equations (71)-(75) are identical to the equilibrium equations of the forces in the horizontal, vertical, radial, normal, and tangential directions, respectively, as shown in Figure 5. This aspect confirms the exact agreement between the variational and the vectorial formulations.

#### 5. APPLICATION TO DEEP-WATER-RISER ANALYSIS

The deep-water-riser, as shown in Figure 6, is the flexible pipe for which the effect of coupled radial-axial deformations can be important. As a long-spanned slender structure, a large amount of top tension is applied to maintain functionality and equilibrium. Behaviour of the coupled radial-axial deformations takes place in such a way that the heavy axial load induces the pipe to undergo large axial deformation, which yields significant radial deformation as a consequence of the Poisson's ratio effect, as described in Figure 2(a). On the other hand, hydrostatic and hydrodynamic pressures inside and outside the pipe exert the intense radial loads to the riser pipe wall. The radial loads magnify the radial deformation of the pipe, which produces the axial deformation by the Poisson's ratio effect, as described in Figure 2(a).

The mathematical formulations presented in Sec.4 can be directly put into operation of the deep-water-riser analysis. The external loads imposed by an offshore condition, such as apparent weight, hydrostatic and hydrodynamic pressures, and inertial forces, should be applied to equations (64). Their expressions are determined as follows.

#### 5.1 APPARENT WEIGHT

Based on the apparent tension concept (Chucheepsakul et al. 2003) the apparent weight in equation (64a) is expressed as

$$W_{o} = (\rho_{P} A_{Po} - \rho_{e} A_{eo} + \rho_{i} A_{io}) g, \qquad (76)$$

where g is the gravitational acceleration;  $\rho_P$ ,  $\rho_e$ , and  $\rho_i$  the densities of pipe material, external fluid, and internal fluid, respectively.

#### 5.2 HYDROSTATIC PRESSURES

The internal and external hydrostatic pressures induce the force acting on a unit length of the thin-walled pipe as shown in equation (64b). The expression of the force is given by

$$f_{p} = 2\pi (R_{to}\rho_{t} - R_{eo}\rho_{e})g(\overline{y}_{t} - y), \qquad (77)$$

where  $\overline{y}_i$  is the vertical distance measured from the sea surface to the bottom support of the riser, as shown in Figure 6.

#### 5.3 HYDRODYNAMIC PRESSURES

Based on the coupled Morison equation (Chucheepsakul et al. 2003), the expressions of the hydrodynamic forces in equation (64c) can be derived in the following forms:

the force in normal direction

$$f_{Hn} = -C_a^* \dot{u}_n - C_{can}^* \dot{u}_n + C_{Dn}^* V_{Hn}^2 + C_M^* \dot{V}_{Hn}, \tag{78a}$$

the force in tangential direction

$$f_{Ht} = -C_a^* \ddot{v}_n - C_{eat}^* \dot{v}_n + C_{Dt}^* V_{Ht}^2 + C_M^* \dot{V}_{Ht},$$
 (78b)

the force in radial direction

$$f_{Hnc} = C_a^* \ddot{w} + C_{conc}^* \dot{w} + C_{Dnc}^* V_{Hnc}^2 + C_M^* \dot{V}_{Hnc}, \qquad (78c)$$

the force in horizontal direction

$$f_{Hx} = -C_a^* \ddot{x} - C_{eqx}^* \dot{x} - C_{eqx}^* \dot{y} + C_{Dx}^* V_{Hx}^2 + 2C_{Dxy}^* V_{Hx} V_{Hy} + C_{Dxy2}^* V_{Hy}^2 + C_M^* \dot{V}_{Hy},$$
 (78d)

the force in vertical direction

$$f_{Hy} = -C_a^* \ddot{y} - C_{eqy}^* \dot{y} - C_{eqy}^* \dot{x} + C_{Dy}^* V_{Hy}^2 + 2C_{Dxy2}^* V_{Hy} V_{Hy} + C_{Dxy3}^* V_{Hx}^2 + C_M^* \dot{V}_{Hy}, \qquad (78e)$$

where

$$C_{eqn}^* = C_{Dn}^* [2V_{Hn} - \dot{u}_n], C_{Dn}^* = 0.5 \rho_e D_{eo} C_{Dn}. \text{sgn}(\gamma_n), \gamma_n = V_{Hn} - \dot{u}_n,$$
 (79a-c)

are the coefficient of equivalent hydrodynamic damping, the coefficient of drag force, and the velocity of the external fluid relative to the pipe in the normal direction, respectively,

$$C_{eqt}^* = C_{Dt}^* [2V_{Ht} - \dot{v}_n], \ C_{Dt}^* = 0.5 \rho_e D_{eo} \pi C_{Dt}. \operatorname{sgn}(\gamma_t), \ \gamma_t = V_{Ht} - \dot{v}_n, \tag{79d-f}$$

are the coefficient of equivalent hydrodynamic damping, the coefficient of drag force, and the velocity of the external fluid relative to the pipe in the tangential direction, respectively,

$$C_{eqnc}^* = C_{Dnc}^* [2V_{Hnc} + \dot{w}], C_{Dnc}^* = 0.5 \rho_e D_{eo} C_{Dn}. sgn(\gamma_{nc}), \gamma_{nc} = V_{Hnc} + \dot{w},$$
 (79g-i)

are the coefficient of equivalent hydrodynamic damping, the coefficient of drag force, and the velocity of the external fluid relative to the pipe in the radial direction, respectively,

$$\operatorname{sgn}(\gamma) = \begin{cases} 1 & \text{if } \gamma \ge 0 \\ -1 & \text{if } \gamma < 0 \end{cases}; \tag{79j}$$

defines the signum function,

$$C_a^* = \rho_a A_{aa} C_a$$
,  $C_M^* = \rho_a A_{aa} C_M$ ; (79k,1)

are the coefficients of added mass and inertia forces,

$$C_{eqx}^* = C_{eqn}^* \cos^2 \theta + C_{eqt}^* \sin^2 \theta, \ C_{Dx}^* = C_{Dn}^* \cos^3 \theta + C_{Dt}^* \sin^3 \theta. \tag{79m,n}$$

are the coefficient of equivalent hydrodynamic damping and the drag force coefficient in the horizontal direction,

$$C_{eqv}^* = C_{eqn}^* \sin^2 \theta + C_{eqt}^* \cos^2 \theta$$
,  $C_{Dv}^* = -C_{Dn}^* \sin^3 \theta + C_{Dt}^* \cos^3 \theta$ ; (790,p)

are the coefficient of equivalent hydrodynamic damping and the drag force coefficient in the vertical direction,

$$C_{eqxy}^* = (-C_{eqn}^* + C_{eqt}^*)\sin\theta\cos\theta; (79q)$$

is the coupling coefficient of equivalent hydrodynamic damping in the x-y plane,

$$C_{Div}^* = -C_{Di}^* \sin \theta \cos^2 \theta + C_{Di}^* \sin^2 \theta \cos \theta, \qquad (79r)$$

$$C_{Dxv2}^* = C_{Dn}^* \sin^2 \theta \cos \theta + C_{Dr}^* \sin \theta \cos^2 \theta.$$
 (79s)

are the coupling coefficients of drag forces in the x-y plane.

Note that  $D_{co}$  is the reference diameter of the external fluid column;  $C_{Dn}$  and  $C_{Dt}$  the normal and tangential drag coefficients;  $C_a$  the added mass coefficient; and  $C_M = 1 + C_a$  the inertial coefficient. It is seen that all the equivalent hydrodynamic dampings induce highly nonlinear aspect of the marine pipe vibrations.

In this study, the horizontal cross flows of current and wave are scoped, and the dynamic pressure fields are assumed uniform around the cross-section of the pipe, but vary along arclength of the pipe. Therefore

$$V_{Hx} = V_{c} + V_{w}, V_{Hy} = 0,$$
 (80a,b)

$$V_{Hn} = V_{Hnc} = V_{Hx} \cos \theta , V_{Ht} = V_{Hx} \sin \theta , \qquad (80c,d)$$

where  $V_c = V_c(y)$  is the current velocity, and  $V_w = V_w(y,t)$  the wave velocity. The profile of the current velocity may be expressed in the form of polynomial function (Larsen 1976) as

$$V_c = V_{ct} \left( \frac{y + \overline{y}_h}{\overline{y}_t + \overline{y}_h} \right)^n, \tag{81}$$

where  $V_{ct}$  is the current velocity at mean sea level, and  $\overline{y}_{t}$  and  $\overline{y}_{t}$  are defined in Figure 6. The index n can be varied from 0 to 1, depending upon the current profile. In this study, n = 1/7 is employed for the tidal current.

For the regular incoming wave, the velocity of a water particle according to Airy's wave theory could be expressed as

$$V_{w} = V_{wa} \cos \omega_{w} t , \qquad (82)$$

where t is time, and  $\omega_w$  the wave frequency. For deep water  $((\bar{y}_h + \bar{y}_t)/L \ge 0.5)$ , the velocity amplitude  $V_{wa} = V_{wa}(y)$  is given by

$$V_{wa} = \varsigma_a \omega_w e^{k[(y + \bar{y}_h) - (\bar{y}_r + \bar{y}_h)]}, \tag{83}$$

where the wave amplitude, the wave frequency, the wave number are respectively:

$$\varsigma_{a} = H/2, \ \omega_{w} = 2\pi/T, \ k = 2\pi/L,$$
 (84a-c)

in which H is the wave height, T the wave period, and L the wave length.

Substituting equation (80b) into (78d,e) yields

$$f_{Hx} = -C_a^* \ddot{x} - C_{eqx}^* \dot{x} - C_{eqxy}^* \dot{y} + C_{Dx}^* V_{Hx}^2 + C_M^* \dot{V}_{Hx},$$
 (85a)

$$f_{Hv} = -C_a^* \ddot{y} - C_{eqv}^* \dot{y} - C_{eqvx}^* \dot{x} + C_{Dxvl}^* V_{Hx}^2 + C_M^* \dot{V}_{Hv}.$$
 (85b)

Equations (78) and (85) can capture the hydrodynamic pressure effects of both steady and unsteady flows. These equations are exploited for dynamic analysis of the riser. However, for static analysis only the steady flow effects will be encountered. By eliminating the unsteady flow effects in equations (78) and (85), one obtains the hydrodynamic force equations for riser statics as

$$f_{Hno} = C_{Dno}^* (V_{co} \cos \theta_o)^2, \ f_{Hto} = C_{Dto}^* (V_{co} \sin \theta_o)^2,$$
 (86a,b)

$$f_{Hnco} = C_{Dnco}^* (V_{co} \cos \theta_o)^2, \ f_{Hxo} = C_{Dxo}^* V_{co}^2, \ f_{Hxo} = C_{Dxvlo}^* V_{co}^2,$$
 (86c-e)

where

$$C_{Dno}^* = 0.5 \rho_e \widetilde{D}_{eo} C_{Dn}, \ C_{Dto}^* = 0.5 \rho_e \widetilde{D}_{eo} \pi C_{Dt}, \ C_{Dnco}^* = 0.5 \rho_e \widetilde{D}_{eo} C_{Dn},$$
 (87a-c)

$$C_{Dxo}^* = C_{Dno}^* \cos^3 \theta_o + C_{Dno}^* \sin^3 \theta_o, \qquad (87d)$$

$$C_{Dxy1o}^* = -C_{Dno}^* \sin \theta_o \cos^2 \theta_o + C_{Dno}^* \sin^2 \theta_o \cos \theta_o, \qquad (87e)$$

$$V_{co} = V_{ci} \left( \frac{y_o + \overline{y}_b}{\overline{y}_t + \overline{y}_b} \right)^n.$$
 (87f)

#### 5.4 INERTIAL FORCES

The inertial force of the system described by equation (64d) depends upon the acceleration vectors of the pipe wall and of the transported fluid, which is measured with respect to the fixed frame of reference XYZ, as shown in Figure 4. Appendix B shows that even if the pipe wall has a motion over the moving centerline of the pipe in the perpendicular direction, the coriolis acceleration has no effect, and the acceleration of the pipe wall in equation (64d) can be simplified to

$$\vec{\mathbf{a}}_{p} = \ddot{\mathbf{u}}_{p} = \ddot{\mathbf{x}}\hat{\mathbf{i}} + \ddot{y}\hat{\mathbf{j}} + \ddot{w}\hat{\mathbf{n}}_{c} = \ddot{u}_{n}\hat{\mathbf{n}} + \ddot{v}_{n}\hat{\mathbf{t}} + \ddot{w}\hat{\mathbf{n}}_{c}. \tag{88}$$

For the transported fluid, the acceleration expression has been given in equations (41). For simplicity, this study uses the profile of internal flow velocity in equations (41) as

$$V_{FP} = V_{ia}(s_{ia}) + V_{id}(s,t),$$
 (89)

where  $V_{io}$  is the steady part of the velocity. The unsteady part of the pulsating flow  $V_{id}$  may be written as

$$V_{ut} = V_{ut}t + V_{va}\cos\omega_{v}t, (90)$$

where  $V_n$  is the linear velocity amplitude,  $V_m$  the wave velocity amplitude, and  $\omega_n$ , the forcing frequency of internal flow.

#### 6. FINITE ELEMENT SOLUTIONS

In this study, the vertical coordinate  $\alpha=y_o$  is employed as the independent variable for the problem solution. The finite element formulations are derived from the weak formulation  $\delta\pi_o=0$  for the static analysis, and  $\delta\pi=0$  for the dynamic analysis. The finite-element-solution methods for the coupled radial-axial deformations analysis are based upon the hybrid method for the nonlinear static analysis, and the state-space approach for the natural frequency and time history analysis of the nonlinear vibrations.

#### 6.1 NONLINEAR STATIC ANALYSIS VIA THE HYBRID-FINITE-ELEMENT METHOD

When the constraint conditions and corresponding field variables need to be applied along the interelement boundary of the finite elements, the finite-element formulations are referred to as the hybrid-finite-element models, and the method to solve them is called the hybrid-finite-element method. The answer to the question why this method is essential for the nonlinear static analysis of extensible flexible pipes is as follows. For the extensible analysis of most structures, the static axial strain in the weak formulation is determined from the strain-displacement relation such as

$$\varepsilon_{\alpha} = (ds_{\alpha} - d\overline{s})/ds_{\alpha}. \tag{91}$$

However, for extensible flexible pipes with large displacements this approach will not be successful, because in practice the pipes do not have the undeformed configuration  $d\bar{s}$  for reference. The equilibrium state is the only initial state or the first state of extensible flexible pipes, which is unknown initially, while the undeformed state is the ideal state, which never appears in the real situation. The way to solve this problem is using the hybrid method by establishing the static axial strain from the constitutive equations (32a) and (33a)

$$\varepsilon_o = \frac{N_{zoo}}{EA_{p_o}} = \frac{(1 - v^2)N_{zo}}{EA_{p_o}} - \frac{vw_o}{R_o} \,, \tag{92}$$

where the axial force  $N_{zo}$  as the field variable is determined from the constraint condition of the force equilibrium (75). It should be noted that the hybrid method is unnecessary for the dynamic analysis of the pipe, because the dynamic axial strain can be determined from the strain-displacement relation  $\varepsilon_d = (ds - ds_o)/ds_o$ , in which the reference configuration  $ds_o$  is known from the static analysis.

In Sec. 4, from equations (68a,b)-(70a,b) there are at least the three forms of the weak variational formulations to be used. This study employs equation (68a). By applying  $\alpha = y_o$ , and neglecting the time-dependent terms in equation (68a), the hybrid formulation for nonlinear static analysis is obtained as the objective function:

$$\delta \pi_{o} = \int_{y_{o}} \left\{ \left[ \frac{B_{o}}{(1 - v^{2}) s_{o}^{\prime 5}} \right] u_{o}^{"} \delta u_{o}^{"} + \left[ \frac{N_{zo}}{s_{o}^{\prime}} - \frac{2B_{o} u_{o}^{"2}}{(1 - v^{2}) s_{o}^{\prime 7}} \right] x_{o}^{\prime} \delta u_{o}^{\prime} + s_{o}^{\prime} \left[ -f_{Hxo} + m_{io} a_{Fxo} \right] \delta u_{o} \right\} dy_{o}$$

$$+ \int_{y_{o}} \left\{ \frac{s_{o}^{\prime} E A_{Po}}{1 - v^{2}} \left[ \frac{v \varepsilon_{o}}{R_{o}} + \frac{w_{o}}{R_{o}^{2}} \right] + s_{o}^{\prime} \left[ -f_{po} + f_{Hnco} + m_{io} a_{Fnco} \right] \right\} \delta w_{o} dy_{o} = 0,$$

$$(93)$$

subjected to the constraint condition derived from the force equilibrium equation (75):

$$N_{zo} = N_{zt} + \int_{s_o}^{\bar{y}_o} \left[ Q_{zo} \theta'_o + s'_o \left( -\frac{w_{ao}}{s'_o} + f_{Hio} - m_{io} a_{Fio} \right) \right] dy_o,$$
 (94)

where from (61c), (77), (86c,d), (51), and (53):

$$Q_{zo} = \frac{B_o}{(1 - v^2)s_o'^3} \left[ s_o'\theta_o'' - s_o''\theta_o' + \frac{3w_o's_o'\theta_o'}{R_o} \right], f_{po} = 2\pi(\rho_i R_{io} - \rho_c R_{eo})g(\bar{y}_i - y_o), \quad (95a,b)$$

$$f_{Hnco} = 0.5 \rho_e D_{eo} C_{Dn} (V_{co} / s_o')^2, \ f_{Hxo} = 0.5 \rho_e D_{co} \left( \frac{C_{Dn}}{s_o'^3} + \frac{\pi C_{Dr} x_o'^3}{s_o'^3} \right) V_{co}^2, \tag{95c,d}$$

$$a_{Fnco} = \left(\frac{V_{10}}{s_o'}\right)^2 w_o'' + \left[\frac{V_{10}V_{10}'}{s_o'^2} - \frac{V_{10}^2 s_o''}{s_o'^3}\right] w_o', \ a_{Fxo} = \frac{\kappa_o V_{10}^2}{s_o'} + \frac{V_{10}V_{10}'}{s_o'} \frac{x_o'}{s_o'}, \ a_{Fto} = \frac{V_{10}V_{10}'}{s_o'}.$$
 (95e-g)

Note that for  $\alpha = y_a$ ,

$$B_o = EI_{Po}, \ \kappa_o = \frac{u_o''}{s_o'^3}, \ \sin\theta_o = \frac{x_o'}{s_o'}, \ \cos\theta_o = \frac{1}{s_o'}$$
 (96a-d)

$$s'_{o} = \sqrt{1 + x'_{o}^{2}}, \ s''_{o} = \frac{x'_{o}u''_{o}}{s'_{o}}, \ \theta'_{o} = \frac{u''_{o}}{s'_{o}^{2}}, \ \theta''_{o} = \frac{u'''_{o} - 2s'_{o}s''_{o}\theta'_{o}}{s'_{o}^{2}}.$$
(96e-h)

Along with the essential and natural boundary conditions of the simply supported pipe

at 
$$y_o = 0$$
:  $u_o = 0$  (essential),  $u_o'' = 0$  (natural). (97a,b)

and at 
$$y_o = \overline{y}_t$$
:  $u_o = 0$  (essential),  $u_o'' = 0$  (natural), (98a,b)

and 
$$N_{zv} = T_t$$
 (essential), (98c)

the system of equations (93) and (94) is the boundary value problem (BVP) having the three dependent variables ( $u_o$ ,  $w_o$ , and  $N_{zo}$ ) and the one independent variable ( $y_o$ ).

Since  $w_o$  has the same order with the circumferential strain ( $\varepsilon_{\theta o} = w_o / R_o$ ), thus it is sufficient to approximate the displacement field of  $w_o$  by the third order shape functions. To constraint all boundary conditions of  $u_o$  from equations (97) and (98), the fifth order shape functions are used for approximating the displacement field of  $u_o$ . Thereby, the displacement vector is expressed as

$$\{\mathbf{d}_{o}\} = \{u_{o} \quad w_{o}\}^{T} = [\mathbf{N}_{o}]\{\mathbf{d}_{on}\},\tag{99}$$

where the generalized coordinates of the nodal displacements of each element are

$$\{\mathbf{d}_{on}\} = \{u_{o1} \quad u'_{o1} \quad u''_{o1} \quad w_{o1} \quad w'_{o1} \mid u_{o2} \quad u'_{o2} \quad u''_{o2} \quad w_{o2} \quad w'_{o2}\}^T, \tag{100}$$

and the shape function matrix at the equilibrium state is

$$[\mathbf{N}_{o}] = \begin{bmatrix} N_{51o} & N_{52o} & N_{53o} & 0 & 0 & N_{54o} & N_{55o} & N_{56o} & 0 & 0 \\ \hline 0 & 0 & 0 & N_{31o} & N_{32o} & 0 & 0 & 0 & N_{33o} & N_{34o} \end{bmatrix} .$$
 (101)

Note that  $N_{3w}$  and  $N_{5w}$  are the coefficients of the third and the fifth order polynomial shape functions, respectively.

From equation (100), the number of degrees of freedom per element is 10. Based on equation (67) and the calculus of variation, one has

$$\delta \pi_o^{(e)} = \sum_{i=1}^{10} \left[ \frac{\partial \pi_o^{(e)}}{\partial d_{om}} \right] \delta d_{om} = 0.$$
 (102)

Equation (102) yields the ten equilibrium equations for each element

$$\frac{\partial \pi_o^{(e)}}{\partial d_{oni}} = 0, \text{ for } i = 1, 2, \dots, 10.$$

$$(103)$$

Substituting equations (99) into (93), the matrix form of equation (103) can be obtained as

$$\int_{0}^{h} \left\{ \left[ \frac{B_{o}}{(1-v^{2})s_{o}^{\prime 5}} \right] \left[ \mathbf{N}_{o}^{\prime \prime} \right]^{T} \left\{ u_{o}^{\prime \prime} \right\} + \left[ \frac{N_{zo}}{s_{o}^{\prime}} - \frac{2B_{o}u_{o}^{\prime \prime 2}}{(1-v^{2})s_{o}^{\prime 7}} \right] \left[ \mathbf{N}_{o}^{\prime} \right]^{T} \left\{ x_{o}^{\prime} \right\} \right\} dy_{o} = 0.$$

$$\left\{ \mathbf{N}_{o}^{\prime} \right]^{T} \left\{ \frac{s_{o}^{\prime} \left[ -f_{Hxo} + m_{io}a_{Fxo} \right]}{1-v^{2}} \left[ \frac{v\varepsilon_{o}}{R_{o}} + \frac{w_{o}}{R_{o}^{2}} \right] + s_{o}^{\prime} \left[ -f_{po} + f_{Hnco} + m_{io}a_{I-nco} \right] \right\} dy_{o} = 0.$$
(104)

The system of the objective function (104) subjected to the constraint equation (94) and the boundary equations (97) and (98) can be solved by using the algorithm of the hybrid-finite-element method, as described in Figure 7. For solving the nonlinear-algebraic-finite-element equation, this study utilizes the modified Powell hybrid algorithm based on the MINPACK

subroutine HYBRD1 (More et al. 1980). The stopping criterion for the numerical iteration is to minimize the Frobenius matrix norm of the load error:  $\|\Delta \mathbf{R}_o\|_F^2 = \sum_{i=1}^{numd/s} \Delta R_o^2$ , where the load error  $\{\Delta \mathbf{R}_o\} = \{\mathbf{R}_o\} - [\mathbf{K}_o]\{\overline{\mathbf{D}}_o\}$  for the equilibrium equation  $[\mathbf{K}_o]\{\mathbf{D}_o\} = \{\mathbf{R}_o\}$ , in which  $\{\overline{\mathbf{D}}_o\}$  and  $\{\mathbf{D}_o\}$  are the calculated and the exact degrees of freedom.

#### 6.2 DYNAMIC ANALYSIS VIA THE STATE-SPACE-FINITE-ELEMENT METHOD

From equation (67):  $\delta \pi = 0$ , hence equation (68a) may be decomposed into the following three nonlinear dynamic equilibrium equations.

$$\delta \pi_{x} = 0: \int_{\alpha} \left\{ \frac{B\kappa}{(1-v^{2})s'} \left( \frac{y'}{s'} \right) \delta u'' + \left[ (N_{z} - \frac{B\kappa^{2}}{1-v^{2}}) \left( \frac{x'}{s'} \right) - \frac{B\kappa}{1-v^{2}} \frac{s''}{s'^{2}} \left( \frac{y'}{s'} \right) \right] \delta u' \right\} d\alpha = 0, \quad (105a)$$

$$\delta \pi_{y} = 0: \int_{\alpha} \left\{ -\frac{B\kappa}{(1-v^{2})s'} \left(\frac{x'}{s'}\right) \delta v'' + \left[ (N_{z} - \frac{B\kappa^{2}}{1-v^{2}}) \left(\frac{y'}{s'}\right) + \frac{B\kappa}{1-v^{2}} \frac{s''}{s'^{2}} \left(\frac{x'}{s'}\right) \right] \delta v' \right\} d\alpha = 0, \quad (105b)$$

$$\delta \pi_{nc} = 0: \int_{\alpha} \left\{ \frac{s'_o}{1 - v^2} \left[ \frac{v N_{za}}{R_o} + \frac{E A_{Po} w}{R_o^2} \right] - s'_o \left[ f_p - f_{Hnc} - m_{Po} a_{Pnc} - m_{io} a_{Fnc} \right] \right\} \delta w d\alpha = 0. \quad (105c)$$

For the vibrations with infinitesimal amplitudes, the axial force can be approximated by

$$N_z \approx N_{zo} + \frac{EA_{po}}{1 - v^2} \left( \frac{x'_o u' + y'_o v'}{s'_o^2} + \frac{v w_d}{R_o} \right).$$
 (106)

By substituting equations (45), (77), (78c), (85a,b), (88), and (106) into equations (105a-c) together with neglecting the higher order terms, eliminating the time-independent terms, and using the relations that

$$-\frac{B\kappa^{2}}{1-v^{2}}\left(\frac{x'}{s'}\right) - \frac{B\kappa}{1-v^{2}}\frac{s''}{s'^{2}}\left(\frac{y'}{s'}\right) = -\frac{B\kappa}{(1-v^{2})s'^{4}}\left[(2x'y')x'' + (y'^{2} - x'^{2})y''\right]$$
(107a)

$$-\frac{B\kappa^2}{1-v^2} \left(\frac{y'}{s'}\right) + \frac{B\kappa}{1-v^2} \frac{s''}{s'^2} \left(\frac{x'}{s'}\right) = \frac{B\kappa}{(1-v^2)s'^4} \left[ (y'^2 - x'^2)x'' - (2x'y')y'' \right]$$
(107b)

$$\int \left[ s_o' m_{io} V_i^2 \frac{\kappa y'}{s'} \right] \delta u d\alpha = \left[ \frac{s_o'}{s'} m_{io} V_i^2 \delta u \frac{x'}{s'} \right]_{\alpha_o}^{\alpha_i} - \int_{\alpha_o}^{\alpha_i} \left( \frac{s_o'}{s'} m_{io} V_i^2 \delta u \right)' \frac{x'}{s'} d\alpha$$
 (107c)

$$\int \left[ s'_{o} m_{io} V_{i}^{2} \left( -\frac{\kappa \alpha'}{s'} \right) \right] \delta v d\alpha = \left[ \frac{s'_{o}}{s'} m_{io} V_{i}^{2} \delta v \frac{y'}{s'} \right]_{\alpha_{io}}^{\alpha_{i}} - \int_{\alpha_{io}}^{\alpha_{i}} \left( \frac{s'_{o}}{s'} m_{io} V_{i}^{2} \delta v \right)' \frac{y'}{s'} d\alpha \qquad (107d)$$

$$\dot{s}' = \frac{x'\dot{u}' + y'\dot{v}'}{s'}, \ \kappa = \frac{x''y' - x'y''}{s'^3},$$
(107e,f)

equations (105a-c) can be expressed as

$$\frac{B_{\alpha}}{(1-v^{2})s_{\alpha}^{-2}} \left[ (y_{\alpha}^{-2})u^{*} - (x_{\alpha}^{-}y_{\alpha}^{-})v^{*} \right] \delta u^{*} + \left[ (N_{2\alpha} - m_{m}V_{n}^{-})u^{*} \right] \delta u^{*} + \frac{EA_{p_{\alpha}}}{(1-v^{2})^{2}} \left[ (x_{2\alpha}^{-2})u^{*} + (x_{\alpha}^{'}y_{\alpha}^{'})v^{*} + v_{\alpha}^{'}y_{\alpha}^{'}y_{\alpha}^{'} \right] \delta u^{*} + \frac{EA_{p_{\alpha}}}{(1-v^{2})^{2}} \left[ (x_{2\alpha}^{-2})u^{*} + (x_{\alpha}^{'}y_{\alpha}^{'})v^{*} + v_{\alpha}^{'}y_{\alpha}^{'}y_{\alpha}^{'} \right] \delta u^{*} + \frac{EA_{p_{\alpha}}}{(1-v^{2})^{2}} \left[ (x_{\alpha}^{'}y_{\alpha}^{'})u^{*} + (y_{\alpha}^{'2} - x_{\alpha}^{'2})v^{*} \right] \delta u^{*} + \frac{B_{\alpha}K_{\alpha}}{(1-v^{2})^{2}} \left[ (m_{p_{\alpha}} + m_{m})\ddot{u} + m_{n}V_{n} \left( \frac{2}{s_{\alpha}^{'}} - \frac{x_{\alpha}^{'2}}{s_{\alpha}^{'3}} \right) \ddot{u}^{*} + m_{m}V_{n} \left( \frac{x_{\alpha}^{'}y_{\alpha}^{'}}{s_{\alpha}^{'2}} \right) \ddot{v}^{*} \right] \delta u^{*} + \frac{EA_{p_{\alpha}}}{(1-v^{2})^{2}s_{\alpha}^{'2}} \left[ (x_{\alpha}^{'}y_{\alpha}^{'})u^{*} + (x_{\alpha}^{'2})v^{*} \right] \dot{b}v^{*} + \left[ \frac{(N_{2\alpha} - m_{m}V_{m}^{'2})v^{*}}{s_{\alpha}^{'}} \right] \delta v^{*} \right] + \frac{EA_{p_{\alpha}}}{(1-v^{2})^{2}s_{\alpha}^{'4}} \left[ (x_{\alpha}^{'}y_{\alpha}^{'})u^{*} + (x_{\alpha}^{'2})v^{*} \right] \dot{b}v^{*} + \left[ \frac{(N_{2\alpha} - m_{m}V_{m}^{'2})v^{*}}{s_{\alpha}^{'}} \right] \delta v^{*} \right] + \frac{EA_{p_{\alpha}}}{(1-v^{2})^{2}s_{\alpha}^{'4}} \left[ (x_{\alpha}^{'}y_{\alpha}^{'})u^{*} + (x_{\alpha}^{'2})v^{*} \right] \dot{b}v^{*} + \left[ \frac{(N_{2\alpha} - m_{m}V_{m}^{'2})v^{*}}{s_{\alpha}^{'}} \right] \delta v^{*} \right] + \frac{EA_{p_{\alpha}}}{(1-v^{2})^{2}s_{\alpha}^{'4}} \left[ (x_{\alpha}^{'}y_{\alpha}^{'})u^{*} + (x_{\alpha}^{'}y_{\alpha}^{'})v^{*} \right] \dot{b}v^{*} + \frac{EA_{p_{\alpha}}}{(1-v^{2})^{2}s_{\alpha}^{'4}} \left[ (x_{\alpha}^{'}y_{\alpha}^{'})u^{*} + (x_{\alpha}^{'}y_{\alpha}^{'})u^{*} + (x_{\alpha}^{'}y_{\alpha}^{'})u^{*} \right] \dot{b}v^{*} \right] + s_{\alpha}^{*} \left[ (m_{p_{\alpha}} + m_{m})\ddot{v} - m_{m}V_{m}(x_{\alpha}^{'}y_{\alpha}^{'})u^{*} + m_{m}V_{m}(2x_{\alpha}^{'}y_{\alpha}^{'})u^{*} \right] \delta v^{*} + \frac{EA_{p_{\alpha}}}{s_{\alpha}^{'}} \left[ (m_{p_{\alpha}} + m_{m})\ddot{v} - m_{m}V_{m}(x_{\alpha}^{'}y_{\alpha}^{'})u^{*} + m_{m}V_{m}(2x_{\alpha}^{'}y_{\alpha}^{'})u^{*} \right] \delta v^{*} \right] + s_{\alpha}^{*} \left[ (m_{p_{\alpha}} + m_{m})\ddot{v} - m_{m}V_{m}(x_{\alpha}^{'}y_{\alpha}^{'})u^{*} + m_{m}V_{m}(x_{\alpha}^{'}y_{\alpha}^{'})u^{*} \right] \delta v^{*} + \frac{EA_{p_{\alpha}}}{s_{\alpha}^{'}} \left[ (x_{\alpha}^{'}y_{\alpha}^{'})u^{*} + (x_{\alpha}^{'}y_{\alpha}^{'})u^{*} + m_{m}V_{m}(x_{\alpha}^{'}y_{\alpha}^{'})u^{*} \right] \delta v^{*} \right] + s_{\alpha}^{*} \left[ (x_{\alpha}^{'}y_{\alpha}^{'})\ddot{v} - m_{m}V_{m}(x_{\alpha}^{'}y_$$

Along with the boundary conditions at  $y_o = 0$ :

$$u(0,t) = v(0,t) = 0$$
 (essential), (109a)

$$u''(0,t) = v''(0,t) = 0$$
(natural), (109b)

and at 
$$y_o = \overline{y}_t$$
:  $u(\overline{y}_t, t) = v(\overline{y}_t, t) = 0$  (essential), (110a)

$$u''(\bar{y}_{t},t) = v''(\bar{y}_{t},t) = 0$$
 (natural), (110b)

and 
$$N_{ro} = T_r$$
 (essential), (110c)

and the initial conditions at time t = 0:

$$u(y_o, 0) = u_o, \ v(y_o, 0) = v_o, \ w_d(y_o, 0) = w_o,$$
 (111a-c)

$$\dot{u}(y_o, 0) = 0, \ \dot{v}(y_o, 0) = 0, \ \dot{w}_d(y_o, 0) = 0,$$
 (111d-f)

the system of partial differential equations (108a-c) is the initial-boundary-value problem, which can be transformed to the system of ordinary differential equations by performing the following three steps of the finite element method.

Step 1. By separation of variables, the displacement vector is assumed as

$$\{\mathbf{d}\} = \{u \quad v \quad w_d\}^T = [\mathbf{N}(y_o)]\{\mathbf{d}_n(t)\}, \tag{112}$$

where the generalized coordinates of the nodal displacements of an element are

$$\left\{\mathbf{d}_{n}\right\} = \left\{u_{1} \quad u_{1}' \quad u_{1}'' \quad v_{1} \quad v_{1}' \quad v_{1}'' \quad w_{1} \quad w_{1}' \quad u_{2} \quad u_{2}' \quad u_{2}'' \quad v_{2} \quad v_{2}' \quad v_{2}'' \quad w_{2} \quad w_{2}'\right\}^{T}, \quad (113)$$

and the shape function matrix at the displaced state is

$$[\mathbf{N}] = \begin{bmatrix} N_{51} & N_{52} & N_{53} & 0 & 0 & 0 & 0 & 0 & N_{54} & N_{55} & N_{56} & 0 & 0 & 0 & 0 \\ 0 & 0 & 0 & N_{51} & N_{52} & N_{53} & 0 & 0 & 0 & 0 & 0 & N_{54} & N_{55} & N_{56} & 0 & 0 \\ 0 & 0 & 0 & 0 & 0 & N_{31} & N_{32} & 0 & 0 & 0 & 0 & 0 & 0 & N_{33} & N_{34} \end{bmatrix} .$$
 (114)

Note that  $N_{3i}$  and  $N_{5i}$  are the coefficients of the third and the fifth order polynomial shape functions, respectively.

**Step 2**. Substituting equation (112) into equations (108a-c), the element equations can be obtained as

$$[\mathbf{m}^{(e)}]\{\ddot{\mathbf{d}}_{n}\} + ([\mathbf{c}^{(e)}] + [\mathbf{g}^{(e)}])\{\dot{\mathbf{d}}_{n}\} + [\mathbf{k}^{(e)}]\{\mathbf{d}_{n}\} = \{\mathbf{f}^{(e)}\},$$
(115)

where the element mass matrix is

$$\left[\mathbf{m}^{(e)}\right] = \int_{\alpha} \left\{ \left[\mathbf{N}\right]^{T} s_{o}' (m_{p_{o}} + m_{no} + C_{ao}^{*}) \begin{bmatrix} 1 & 0 & 0 \\ 0 & 1 & 0 \\ 0 & 0 & 1 \end{bmatrix} \right] d\alpha, \qquad (116a)$$

the element hydrodynamic damping matrix is

$$[\mathbf{c}^{(e)}] = \int_{\alpha} \left\{ [\mathbf{N}]^T s_o' \begin{bmatrix} C_{eqxo}^* & C_{eqxyo}^* & 0 \\ C_{eqxyo}^* & C_{eqxo}^* & 0 \\ 0 & 0 & C_{eqnco}^* \end{bmatrix} [\mathbf{N}] \right\} d\alpha,$$
 (116b)

the element gyroscopic matrix is

$$[\mathbf{g}^{(e)}] = \int_{\alpha} \left\{ [\mathbf{N}]^{T} \mathbf{m}_{io} V_{io} \begin{bmatrix} 2 - \frac{x_{o}^{\prime 2}^{2}}{s_{o}^{\prime 2}} & -\frac{x_{o}^{\prime} y_{o}^{\prime}}{s_{o}^{\prime 2}} & 0 \\ -\frac{x_{o}^{\prime} y_{o}^{\prime}}{s_{o}^{\prime 2}} & 2 - \frac{y_{o}^{\prime 2}}{s_{o}^{\prime 2}} & 0 \\ -\frac{x_{o}^{\prime} w_{o}^{\prime}}{s_{o}^{\prime 2}} & -\frac{y_{o}^{\prime} w_{o}^{\prime}}{s_{o}^{\prime 2}} & 2 \end{bmatrix} [\mathbf{N}^{\prime}] \right\} d\alpha, \qquad (116c)$$

the element stiffness matrix is

$$[\mathbf{k}^{(e)}] = [\mathbf{k}_{b1}^{(e)}] + [\mathbf{k}_{b2}^{(e)}] + [\mathbf{k}_{t1}^{(e)}] + [\mathbf{k}_{t2}^{(e)}] + [\mathbf{k}_{t3}^{(e)}] + [\mathbf{k}_{t4}^{(e)}],$$
(116d)

in which the bending stiffness matrix of the fourth order derivative is

$$[\mathbf{k}_{b1}^{(e)}] = \int_{\alpha} \left\{ [\mathbf{N''}]^T \frac{B_o}{(1-v^2)s_o^{15}} \begin{bmatrix} y_o^{12} & -x_o^{\prime}y_o^{\prime} & 0 \\ -x_o^{\prime}y_o^{\prime} & x_o^{\prime2} & 0 \\ 0 & 0 & 0 \end{bmatrix} [\mathbf{N''}] \right\} d\alpha,$$
 (116e)

the bending stiffness matrix of the third order derivative is

$$[\mathbf{k}_{b2}^{(e)}] = \int_{\alpha} \left\{ [\mathbf{N}']^T \frac{B_o \kappa_o}{(1 - v^2) s_o'^4} \begin{bmatrix} 2x_o' y_o' & y_o'^2 - x_o'^2 & 0 \\ y_o'^2 - x_o'^2 & -2x_o' y_o' & 0 \\ 0 & 0 & 0 \end{bmatrix} [\mathbf{N}''] \right\} d\alpha,$$
 (116f)

the axial and circumferential stiffness matrix of the second order derivative is

$$[\mathbf{k}_{t1}^{(e)}] = \int_{\alpha}^{\pi} \begin{bmatrix} \mathbf{N}' \end{bmatrix}^{T} \begin{bmatrix} \frac{N_{zo}}{s'_{o}} \begin{bmatrix} 1 & 0 & 0 \\ 0 & 1 & 0 \\ 0 & 0 & 0 \end{bmatrix} - \frac{m_{to}V_{to}^{2}}{s'_{o}} \begin{bmatrix} 1 & 0 & 0 \\ 0 & 1 & 0 \\ 0 & 0 & 1 \end{bmatrix} [\mathbf{N}'] \\ + [\mathbf{N}']^{T} \frac{EA_{p_{o}}}{(1 - v^{2})s'_{o}^{3}} \begin{bmatrix} x'_{o}^{2} & x'_{o}y'_{o} & 0 \\ x'_{o}y'_{o} & y'_{o}^{2} & 0 \\ 0 & 0 & 0 \end{bmatrix} [\mathbf{N}']$$

$$d\alpha, \qquad (116g)$$

the circumferential stiffness matrix of the first order derivative is

$$[\mathbf{k}_{12}^{(e)}] = \int_{\alpha} \left\{ [\mathbf{N}']^T \frac{EA_{Po}\nu}{(1-\nu^2)s_o'R_o} \begin{bmatrix} 0 & 0 & x_o' \\ 0 & 0 & y_o' \\ 0 & 0 & 0 \end{bmatrix} [\mathbf{N}] \right\} d\alpha ,$$
 (116h)

the axial and circumferential stiffness matrix of the first order derivative is

$$[\mathbf{k}_{t3}^{(e)}] = \int_{\alpha} \left\{ [\mathbf{N}]^{T} \begin{bmatrix} \frac{m_{to}V_{to}V_{to}'}{s_{o}'^{2}} \begin{bmatrix} 1 & 0 & 0 \\ 0 & 1 & 0 \\ 0 & 0 & 1 \end{bmatrix} - \frac{m_{to}V_{to}^{2}s_{o}''}{s_{o}'^{3}} \begin{bmatrix} 0 & 0 & 0 \\ 0 & 0 & 0 \\ 0 & 0 & 1 \end{bmatrix} [\mathbf{N}'] \right\} d\alpha , \qquad (116i)$$

the circumferential stiffness matrix of the zero order derivative is

$$[\mathbf{k}_{i4}^{(e)}] = \int_{\alpha}^{\pi} \left[ \mathbf{N} \right]^{T} \frac{s_{o}' E A_{p_{o}}}{(1 - v^{2}) R_{o}^{2}} \begin{bmatrix} 0 & 0 & 0 \\ 0 & 0 & 0 \\ 0 & 0 & 1 \end{bmatrix} [\mathbf{N}] + [\mathbf{N}]^{T} 2\pi g s_{o}' (\rho_{i} R_{io} - \rho_{e} R_{eo}) \begin{bmatrix} 0 & 0 & 0 \\ 0 & 0 & 0 \\ 0 & 1 & 0 \end{bmatrix} [\mathbf{N}] \right] d\alpha,$$

$$(116j)$$

the element hydrodynamic excitation vector is

$$\{\mathbf{f}^{(e)}\} = \int_{\alpha} [\mathbf{N}]^{T} s_{o}^{\prime} \left\{ C_{Dxv}^{*} (2V_{c}V_{w} + V_{w}^{2}) + C_{Mo}^{*} \dot{V}_{w} - \frac{m_{io} x_{o}^{\prime}}{s_{o}^{\prime}} \frac{DV_{ud}}{Dt} \right. \\ \left. - C_{Dnco}^{*} (2V_{c}V_{w} + V_{w}^{2}) - \frac{m_{io} y_{o}^{\prime}}{s_{o}^{\prime}} \frac{DV_{ud}}{Dt} \right. \\ \left. - C_{Dnco}^{*} (2V_{c}V_{w} + V_{w}^{2}) - C_{Mo}^{*} \dot{V}_{w} \left( \frac{y_{o}^{\prime}}{s_{o}^{\prime}} \right) - \frac{m_{io} w_{o}^{\prime}}{s_{o}^{\prime}} \frac{DV_{ud}}{Dt} \right\} d\alpha .$$
 (116k)

**Step 3**. Assembling the element equations, the global system of finite element equations can be obtained as

$$[\mathbf{M}]\{\ddot{\mathbf{D}}_{n}\} + ([\mathbf{C}] + [\mathbf{G}])\{\dot{\mathbf{D}}_{n}\} + [\mathbf{K}]\{\mathbf{D}_{n}\} = \{\mathbf{F}\}, \tag{117}$$

where  $[\mathbf{D}_n] = \sum_{i=1}^{netem} [\mathbf{d}_n], \{\dot{\mathbf{D}}_n\}, \{\mathbf{D}_n\}$  are the global nodal displacement, velocity, and acceleration vectors, respectively;  $[\mathbf{M}] = \sum_{i=1}^{netem} [\mathbf{m}^{(e)}]$  the total mass matrix;  $[\mathbf{C}] = \sum_{i=1}^{netem} [\mathbf{c}^{(e)}]$  the total hydrodynamic damping matrix;  $[\mathbf{G}] = \sum_{i=1}^{netem} [\mathbf{g}^{(e)}]$  the total gyroscopic matrix;  $[\mathbf{K}] = \sum_{i=1}^{netem} [\mathbf{k}^{(e)}]$  the total stiffness matrix; and  $[\mathbf{F}] = \sum_{i=1}^{netem} [\mathbf{f}^{(e)}]$  the total hydrodynamic excitation vector, in which *nelem* is the number of finite elements.

To obtain the state space formulation, which is central to the development of nonlinear vibration control theory, the second order model of equation (117) must be transformed to the first order model. To achieve this, the following state vector is defined:

$$\{\mathbf{X}_n\} = \begin{Bmatrix} \mathbf{D}_n \\ \mathbf{V}_n \end{Bmatrix},\tag{118}$$

where 
$$\{\mathbf{V}_n\} = \{\dot{\mathbf{D}}_n\}.$$
 (119)

Substituting equation (119) into (117), one obtains

$$[\mathbf{M}]\{\dot{\mathbf{V}}_n\} + ([\mathbf{C}] + [\mathbf{G}])\{\mathbf{V}_n\} + [\mathbf{K}]\{\mathbf{D}_n\} = \{\mathbf{F}\},$$
(120)

The system of equations (119) and (120) can be cast into the matrix form

$$\begin{bmatrix} \mathbf{I} & \mathbf{0} \\ \mathbf{0} & \mathbf{M} \end{bmatrix} \begin{bmatrix} \dot{\mathbf{D}}_{n} \\ \dot{\mathbf{V}}_{n} \end{bmatrix} + \begin{bmatrix} \mathbf{0} & -\mathbf{I} \\ \mathbf{K} & \mathbf{C} + \mathbf{G} \end{bmatrix} \begin{bmatrix} \mathbf{D}_{n} \\ \mathbf{V}_{n} \end{bmatrix} = \begin{bmatrix} \mathbf{0} \\ \mathbf{F} \end{bmatrix}. \tag{121}$$

Equation (121) can be manipulated in state space form

$$\{\dot{\mathbf{X}}_n\} = [\mathbf{A}]\{\mathbf{X}_n\} + \{\mathbf{B}\},\tag{122}$$

where the coefficient matrix or state transition matrix is

$$[\mathbf{A}] = \begin{bmatrix} \mathbf{0} & \mathbf{I} \\ -\mathbf{M}^{-1}\mathbf{K} & -\mathbf{M}^{-1}(\mathbf{C} + \mathbf{G}) \end{bmatrix}, \tag{123a}$$

and the deterministic input matrix is

$$\{\mathbf{B}\} = \left\{\begin{matrix} \mathbf{0} \\ \mathbf{M}^{-1}\mathbf{F} \end{matrix}\right\}. \tag{123b}$$

The initial-value problem of the highly nonlinear state equation (122) in association with the initial condition equations (111) can be solved to determine the nonlinear responses by the direct time integration. The scheme for the explicit time integration is described in Figure 8. The drawback to the explicit methods that they are conditionally stable due to the critical step size of time is overcome in this study by employing the Gear's stiff method that includes the automatically adaptive time-step-size algorithm (Gear 1971). This algorithm automatically improves the time-step-size during the integration process so that the absolute error criterion:

$$\max_{i=1...N} (error_i) \le tol \tag{124}$$

is achieved. In this study,  $tol = 10^{-3}$  is set forth, and the corresponding adaptive time-stepsizes are in the range  $10^{-3}$  to  $10^{-1}$  sec.

For free vibrations, equation (122) is reduced to

$$\{\dot{\mathbf{X}}_n\} = [\mathbf{A}]\{\mathbf{X}_n\},\tag{125}$$

which has the harmonic solution in the exponential form

$$\{\mathbf{X}_n\} = e^{\lambda t} \{\mathbf{X}_{na}\}, \tag{126}$$

where  $\lambda = \alpha \pm i\omega$  is the complex eigenvalue,  $\omega$  the natural frequency, and  $\{X_{na}\}$  the vector of complex coefficients or initial modal weights. Inserting equations (126) into (125) and dividing through by  $e^{\lambda t}$ , the general algebraic eigenvalue problem is obtained as

$$[\mathbf{A}]\{\mathbf{X}_n\} = \lambda\{\mathbf{X}_n\},\tag{127}$$

in which the matrix [A] is the linearized real, nonsymmetrical matrix. This equation can be solved to determine the eigenvalues and eigenvectors by the implicit double-shifted QR algorithm based on the EISPACK routine HQR2 (Smith et al.1976). The algorithm to form the finite-element equation (127) is demonstrated in Figure 9.

# 7. THE EFFECT OF RADIAL DEFORMATION ON THE FLEXIBLE PIPE BEHAVIOURS

This section is to demonstrate how important slight change of radial deformation is to influence behaviour of the flexible pipes, especially under condition of intense radial pressure loads. The deep-water riser with the input data, as shown in Figure 6, is the case studied. The hydrostatic pressures are varied, so that the riser undergoes approximately 1 mm change of the maximum static radial displacement. The parametric study is to indicate the effects of radial deformation on the nonlinear static behaviour, natural frequency, and nonlinear vibration behaviour of the riser pipe.

#### 7.1 EFFECTS OF RADIAL DEFORMATION ON NONLINEAR STATIC BEHAVIOUR OF THE PIPE

As the maximum internal hydrostatic pressure at the bottom support of the riser is varied from  $0 \rightarrow 9.806 \rightarrow 18.0430 \rightarrow 23.5344 \rightarrow 28.2020$  MPa (N/mm<sup>2</sup>), the maximum radial displacement  $w_{o(\text{max})}$  at the same position is increased from  $-0.661 \rightarrow -0.378 - 0.140 \rightarrow 0.019 \rightarrow 0.155$  mm, as shown in Fig. 10(a). Consequently, the nonlinear static behaviour of the riser is affected by the effect of radial deformation, as can be summarized as follows.

- (a) Radial deformation has the effect on increasing the large deflection of the flexible pipe. As seen in Figure 10(b),  $\sim 1$  mm escalation of the radial deformation of the pipe increases the sag of the marine pipe significantly, and the pipe changes from taut to slack.
- (b) Radial deformation has the effect on enlarging the rotation of the flexible pipe particularly at the large sag region, as shown in Figure 11(a).
- (c) Radial deformation has the effect on reducing the axial strain and axial force in the pipe, as shown in Figure 11(b) and 11(c), respectively.
- (d) Radial deformation has the effect on diminishing the statical stability of the pipe. As previously found, the axial force is reduced by the effect of radial deformation, so the axial stiffness is decreased as well as the buckling capacity of the riser system.
- (e) Radial deformation has the effect on amplifying the bending moment in the pipe especially at the large sag portion, as shown in Figure 11(d). This agrees with the effect on enlarging the rotation aforementioned in (b).

#### 7.2 EFFECTS OF RADIAL DEFORMATION ON NATURAL FREQUENCIES OF THE PIPE

As the maximum radial displacement is varied increasing up to  $\sim 1$  mm, as shown in Fig. 10(a), the natural frequencies of the riser are altered by the effect of radial deformation, as can be summarized as follows.

- (a) Radial deformation has the effect on diminishing the natural frequencies of the pipe. As shown in Figure 12(a), the natural frequencies of the pipe are decreased by an escalation of the maximum radial displacement. When the radial displacement increases continuously, the eigencurves of the fundamental vibration-mode tend to intersect the internal fluid density axis at the point where the natural frequencies are zero, and buckling of the pipe due to the effect of radial deformation can be induced.
- (b) Radial deformation has the effect on reducing the dynamical stability of the pipe. Consider the complex plane of the Argand diagram displayed in Figure 12(b). It is found that a continuous augmentation of the maximum radial deformation motivates the pipe to experience 'the statical buckling' or 'the divergence instability' at the Pitchfork bifurcation point. Based on the Liapunov indirect method (Meirovitch 1997), the complex eigenvalues of the pipe as shown in Figure 12(b) have all zero real parts, therefore free vibrations of the linearized system of the flexible riser pipe possess stable oscillations and critical behaviour. As a result, the stability of the linearized system cannot be guaranteed for the nonlinear system of the pipe. Instead, the stability of nonlinear vibrations of the pipe should be investigated by the phase space analysis based on the solutions of the nonlinear equations of motion, including the fully nonlinear hydrodynamic forces.
- (c) Radial deformation has the effect to the mode shapes of the pipe. Figures 13(a), 13(b), and 13(c) demonstrate the effect on the fundamental modes of free vibrations in the normal, tangential, and radial directions, respectively. It is seen that the radial deformation affects significantly the mode shapes of the normal and tangential free vibrations, but trivially for the mode shapes of the radial vibrations.

### 7.3 EFFECTS OF RADIAL DEFORMATION ON NONLINEAR VIBRATION BEHAVIOUR OF THE PIPE

As the maximum radial displacement is varied increasing up to  $\sim 1$  mm, as shown in Fig. 10(a), the nonlinear vibrations of the riser pipe is influenced by the effect of radial deformation, as can be summarized as follows.

- (a) Radial deformation has the effect on increasing nonlinear vibration responses of the pipe. Before increasing the radial displacement, the pipe has the nonlinear vibration responses in a time period 0-60 seconds, as shown on the left-hand side of Figure 14. After increasing up to ∼1 mm maximum radial displacement, the maximum vibration amplitudes obviously grow larger than the former, as shown on the right-hand side of the same figure.
- (b) Radial deformation has the effect on reducing steadiness of the vibrations of the pipe. Consider Figures 15(a), 15(b), and 15(c), which demonstrate the time histories of the normal vibrations of the top ( $y_o = 1800 \text{ m}$ ), middle ( $y_o = 1000 \text{ m}$ ), and bottom parts ( $y_o = 400 \text{ m}$ ) of

the pipe, respectively. It is found that over a long-term period, normal oscillations of the pipe with the low radial displacement are developed to the steady motions, while the pipe experiencing the ~1 mm radial displacement increase, still exhibits the vibrations with more unsteadiness. The unsteadiness is remarkably great at the bottom part, where the pipe has a large curvature. It is worthwhile to note that the response frequencies of the pipes are equal to  $2\pi/10$ , which are close to the wave frequency 0.6, therefore, the normal oscillations of the pipes are ordinary harmonic.

(c) Radial deformation has the effect on reducing the stability of motion of the pipe. Consider Figures 16(a), 16(b), and 16(c), which demonstrate the trajectories of the normal vibrations of the top ( $y_o = 1800 \text{ m}$ ), middle ( $y_o = 1000 \text{ m}$ ), and bottom parts ( $y_o = 400 \text{ m}$ ) of the pipe, respectively. The figures show that as a time period passes all the trajectories, which start at the initial condition of the zero normal state speed  $\dot{u}_n = 0$  and the zero normal displacement  $u_n = 0$ , tend to the orbits.

Based on the definitions of 'the orbital stability' or in other words 'the stability in sense of Poincaré' (Meirovitch 1997), it is revealed that the motions of the pipe with the low radial displacement (as shown on the left-hand side of Figure 16) are orbitally stable. This is because all trajectories remain in the neighborhood of one another for all  $t > t_o$  in which  $t_o$  is the reference time. Differently, the motions of the pipe experiencing the  $\sim 1$  mm radial displacement increase (as shown on the right-hand side of the same figure) are orbitally unstable, based on the grounds that the trajectories tend to leave the neighborhood of the others. This result indicates reduction of the stability of motion of the pipe by the effect of radial deformation.

#### 8. CONCLUSIONS

This paper proposes the novel method for large strain modeling of flexible pipes transporting fluid. The new ideas of the method deal with using the coupled radial-axial deformations theory to derive the structural stiffness equations of the pipes, and taking account of the effects of hydrostatic and hydrodynamic pressures of internal flow by employing the continuity theory of pipe flow. By adopting this approach, large strain formulations of the pipes can be undertaken more accurately than ever, and the effects of the coupled radial-axial deformations, and the influence of fluid transportation can be simply taken into consideration in the analysis and the design of the flexible pipes.

The results of parametric study show that the effect of radial deformations is very important for all behaviours of the flexible pipes under severe pressure condition such as

marine riser pipes. Therefore, the coupled radial-axial deformations analysis is highly recommended for accuracy of the analysis and the design of those pipes. It is concluded that radial deformation of the pipe has the influences on increasing large deflections and nonlinear responses, and reducing statical and dynamical stabilities of the pipe. Consequently, if radial deformation is designed excessively, the pipe may experience either poor serviceability or buckling due to overloading. Therefore, the designers are encouraged to examine the effect carefully in the design of the high-pressure pipes. It is hoped that this study will be of some value in the analysis and the design not only of the flexible pipes, but also of any kind of long slender structures that pursue rigorous treatments of extensibility, radial deformation, and transported mass.

#### 9. ACKNOWLEDGEMENT

The authors gratefully acknowledge the support of the Thailand Research Fund (TRF) under Contract No. RTA/03/2543.

#### REFERENCES

- Chakrabarti, S.K. and Frampton, R.E., 1982, "Review of Riser Analysis Techniques," **Applied Ocean Research**, Vol. 4, No. 2, pp. 73-90.
- Chucheepsakul, S. and Monprapussorn, T., 2001, "Nonlinear Buckling of Marine Elastica Pipes Transporting Fluid," International Journal of Structural Stability and Dynamics, Vol. 1, No. 3, pp. 333-365.
- Chucheepsakul, S., Monprapussorn, T. and Huang, T., 2003, "Large Strain Formulations of Extensible Flexible Marine Pipes Transporting Fluid," **Journal of Fluids and Structures**, Vol. 17, No. 2, pp. 185-224.
- Ertas, A. and Kozik, T.J., 1987, "A Review of Approaches to Riser Modeling," Journal of Energy Resources Technology, Vol. 109, No. 3, pp. 155-160.
- Gear, C.W., 1971, Numerical Initial Value Problems in Ordinary Differential Equations, New Jersey, Prentice Hall.
- Jain, A.K., 1994, "Review of Flexible Risers and Articulated Storage Systems," Ocean Engineering, Vol. 21, No. 8, pp. 733-750.
- Larsen, C.M., 1976 "Marine riser analysis," **Norwegian Maritime Research**, Vol. 4, pp. 15-26. Meirovitch, L., 1997, **Principles and Techniques of Vibrations**, New Jersey, Prentice Hall.
- Monprapussorn, T., 2001, "Influence of Axial and Radial Deformations and Fluid Transportation on Behaviors of Marine Risers with Large Displacements," **Doctor of Philosophy Dissertation**, Civil Engineering Program, King Mongkut's University of Technology Thonburi.
- More, J., Garbow, B.S. and Hillstrom, H., 1980, User guide for MINPACK-1, Illinois, Argonne National Laboratories.
- Patel, M.H. and Seyed, F.B., 1995, "Review of Flexible Riser Modelling and Analysis Techniques," **Engineering Structures**, Vol. 17, No. 4, pp. 293-304.
- Smith, B.T., Boyle, J.M., Dongarra, J.J., Garbow, B.S., Ikebe, Y., Klema, V.C. and Moler, C.B., 1976, Matrix Eigensystem Routines - EISPACK Guide, New York, Springer-Verlag.

#### APPENDIX A: NEWTONIAN DERIVATION

Consider Figure 5(a). The force equilibrium equations in the horizontal, vertical, normal, and tangential directions are derived as follows.

$$\Sigma F_{x} = 0: \qquad (H_{z} + H'_{z} d\alpha) - H_{z} + s'_{o} (f_{Hx} - m_{Po} a_{Px} - m_{io} a_{Ex}) d\alpha = 0.$$

$$-H'_{z} - s'_{o} (f_{Hx} - m_{Po} a_{Px} - m_{io} a_{Ex}) = 0. \tag{A.1}$$

$$\Sigma F_{y} = 0: \qquad (V_{z} + V_{z}' d\alpha) - V_{z} + s_{o}' \left( -w_{a} + f_{Hy} - m_{Po} a_{Py} - m_{o} a_{Fy} \right) d\alpha = 0.$$

$$-V_{z}' - s_{o}' \left( -w_{a} + f_{Hy} - m_{Po} a_{Py} - m_{o} a_{Fy} \right) = 0. \tag{A.2}$$

$$-(Q_z + Q_z'd\alpha - Q_z)\cos\left(\frac{\theta'}{2}d\alpha\right) + (N_z + N_z'd\alpha + N_z)\sin\left(\frac{\theta'}{2}d\alpha\right)$$

$$+ s_o'\left(w_a\sin\left(\theta + \frac{\theta'}{2}d\alpha\right) + f_{H_0} - m_{P_0}a_{P_0} - m_{I_0}a_{F_0}\right)d\alpha = 0.$$
(A.3)

$$(N_z + N_z'd\alpha - N_z)\cos\left(\frac{\theta'}{2}d\alpha\right) + (Q_z + Q_z'd\alpha + Q_z)\sin\left(\frac{\theta'}{2}d\alpha\right)$$

$$\Sigma F_t = 0:$$

$$+ s_o'\left(-w_a\cos\left(\theta + \frac{\theta'}{2}d\alpha\right) + f_{Ht} - m_{p_o}a_{p_t} - m_{to}a_{Ft}\right)d\alpha = 0.$$
(A.4)

The higher order terms are neglected by using the approximations that

$$(d\alpha)^2 \to 0, \sin\left(\frac{\theta'}{2}d\alpha\right) = \frac{\theta'}{2}d\alpha, \cos\left(\frac{\theta'}{2}d\alpha\right) = 1.$$
 (A.5)

Applying equation (A.5), equations (A.3) and (A.4) are reduced to

$$\Sigma F_n = 0: \qquad Q_z' - N_z \theta' - s_o' \left( w_o \sin \theta + f_{Hn} - m_{Po} a_{Pn} - m_{no} a_{Fn} \right) = 0, \qquad (A.6)$$

$$\Sigma F_{I} = 0: \qquad -N'_{I} - Q_{I}\theta' - s'_{O}\left(-w_{O}\cos\theta + f_{HI} - m_{PO}a_{PI} - m_{O}a_{FI}\right) = 0. \tag{A.7}$$

Consider Figure 5(b). The force equilibrium equation in the radial direction is derived as follows.

$$\Sigma F_{nc} = 0: \qquad -2\sigma_{\theta} h ds_o \sin\left(\frac{d\phi}{2}\right) + \left(\frac{f_p - f_{Hnc} - m_{p_o} a_{p_{nc}} - m_{to} a_{Fnc}}{2\pi}\right) d\phi ds_o = 0. \tag{A.8}$$

Since

$$\sin\left(\frac{d\phi}{2}\right) \simeq \frac{d\phi}{2},$$

and 
$$2\pi h\sigma_{\theta} = \frac{R_o}{R_o} 2\pi h\sigma_{\theta} \simeq \frac{A_{p_o}}{R_o}\sigma_{\theta} = \frac{EA_{p_o}}{R_o(1-v^2)} \left[ v\varepsilon_z + \frac{w}{R_o} \right] = \frac{1}{1-v^2} \left[ \frac{vN_{zo}}{R_o} + \frac{EA_{p_o}w}{R_o^2} \right],$$

equation (A.8) is reduced to

$$\Sigma F_{nc} = 0: \qquad \frac{s_o'}{1 - v^2} \left[ \frac{v N_{za}}{R_o} + \frac{E A_{Po} w}{R_o^2} \right] - s_o' \left( f_p - f_{Hnc} - m_{Po} a_{Pnc} - m_{to} a_{Fnc} \right) = 0. \tag{A.9}$$

#### APPENDIX B: KINEMATICS OF THE PIPE-WALL ELEMENT

From Figure 4, the position vector of the pipe-wall element is given by

$$\vec{\mathbf{r}}_P = \vec{\mathbf{r}}_{c(XYZ)} + \vec{\mathbf{r}}_{Pc(XYZ')}. \tag{B.1}$$

Differentiating equation (B.1) with respected to time yields the velocity vector of the pipewall element

$$\vec{\mathbf{V}}_{p} = \dot{\vec{\mathbf{r}}}_{c(XYZ)} + \dot{\vec{\mathbf{r}}}_{Pc(XYZ)} + \vec{\mathbf{\Omega}} \times \vec{\mathbf{r}}_{Pc(XYZ)}, \tag{B.2}$$

where  $\bar{\Omega}$  is the angular velocity of frame xyz. Note that  $\dot{\bar{r}}_{c(XYZ)}$  and  $\bar{\Omega} \times \bar{r}_{Pc(xyz)}$  are the velocities due to linear motion and rotation of frame XYZ, respectively. Similarly, differentiating equation (B.2) with respect to time yields the acceleration vector of the pipewall element

$$\vec{\mathbf{a}}_{P} = \ddot{\vec{\mathbf{r}}}_{c(XYZ)} + \ddot{\vec{\mathbf{r}}}_{Pc(xyz)} + 2\bar{\mathbf{\Omega}} \times \dot{\vec{\mathbf{r}}}_{Pc(xyz)} + \left\{ \dot{\bar{\mathbf{\Omega}}} \times \bar{\mathbf{r}}_{Pc(xyz)} + \bar{\mathbf{\Omega}} \times (\bar{\mathbf{\Omega}} \times \bar{\mathbf{r}}_{Pc(xyz)}) \right\}. \tag{B.3}$$

Since the rotary inertia due to rotations of the cross section of the pipe is assumed insignificant, the acceleration due to rotations of the frame XYZ  $\left\{ \hat{\Omega} \times \vec{\mathbf{r}}_{Pc(xyz)} + \hat{\Omega} \times (\hat{\Omega} \times \vec{\mathbf{r}}_{Pc(xyz)}) \right\}$  is negligible. In addition, because  $\hat{\Omega} = \hat{\mathbf{t}} \times \partial \hat{\mathbf{t}} / \partial t$  and  $\hat{\mathbf{r}}_{Pc(xyz)} = \dot{w}\hat{\mathbf{n}}_c$ , the coriolis acceleration  $2\hat{\Omega} \times \hat{\mathbf{r}}_{Pc(xyz)}$  vanishes as follows:

$$2\bar{\boldsymbol{\Omega}} \times \dot{\bar{\mathbf{r}}}_{Pc(xyz)} = 2\hat{\mathbf{t}} \times \left(\frac{\partial \hat{\mathbf{t}}}{\partial t} \times \dot{w}\hat{\mathbf{n}}_{c}\right) = 2(\hat{\mathbf{t}} \cdot \dot{w}\hat{\mathbf{n}}_{c})\frac{\partial \hat{\mathbf{t}}}{\partial t} - 2\left(\hat{\mathbf{t}} \cdot \frac{\partial \hat{\mathbf{t}}}{\partial t}\right)\dot{w}\hat{\mathbf{n}}_{c} = 0.$$
 (B.4)

Thereby, equation (B.3) is reduced to

$$\vec{\mathbf{a}}_{P} = \ddot{\vec{\mathbf{r}}}_{c(XYZ)} + \ddot{\vec{\mathbf{r}}}_{Pc(xvz)} = \ddot{x}\hat{\mathbf{i}} + \ddot{y}\hat{\mathbf{j}} + \ddot{w}\hat{\mathbf{n}}_{c} = \ddot{u}_{n}\hat{\mathbf{n}} + \ddot{v}_{n}\hat{\mathbf{t}} + \ddot{w}\hat{\mathbf{n}}_{c}. \tag{B.5}$$

#### LIST OF FIGURES

- Figure 1 Flexible marine riser pipes: (a) a marine riser (b) a flexible pipe (c) a hoseline.
- Figure 2 (a) The coupled radial-axial deformations behaviour of thin-walled pipes (b) The transported fluid-pipe interaction.
- Figure 3 (a) Schematic of deformations (b) radial deformations of the pipe wall.
- Figure 4 Kinematics of pipe wall and transported fluid.
- Figure 5 Free body diagrams of the pipe element: (a) in plane (b) in the radial direction.
- Figure 6 The deep-water-riser specimen.
- Figure 7 The hybrid-finite-element algorithm for the coupled radial-axial deformations analysis of the flexible-pipe statics.
- Figure 8 The state-space-finite-element algorithm for the coupled radial-axial deformations analysis of the flexible-pipe dynamics.
- Figure 9 The state-space-finite-element algorithm for determining the natural frequencies of the flexible-pipe vibrations.
- Figure 10 The parametric study: (a) increasing up to ~1 mm maximum radial displacements at the pipe base (b) the effect on the equilibrium configurations.
- Figure 11 The effect of radial deformation on (a) rotation of the pipe (b) axial strain (c) actual tension (d) bending moment.
- Figure 12 The effect of radial deformation on (a) natural frequencies (b) the complex plane.
- Figure 13 The effect of radial deformation on the fundamental mode shapes of vibrations in (a) the normal (b) the tangential (c) the radial directions.
- Figure 14 The effect of radial deformation on nonlinear responses in time 0-60 seconds.
- Figure 15 The effect of radial deformation on time histories of the normal vibrations of (a) the top (b) the middle (c) the bottom parts of the pipe.
- Figure 16 The effect of radial deformation on trajectories of the normal vibrations of (a) the top (b) the middle (c) the bottom parts of the pipe.

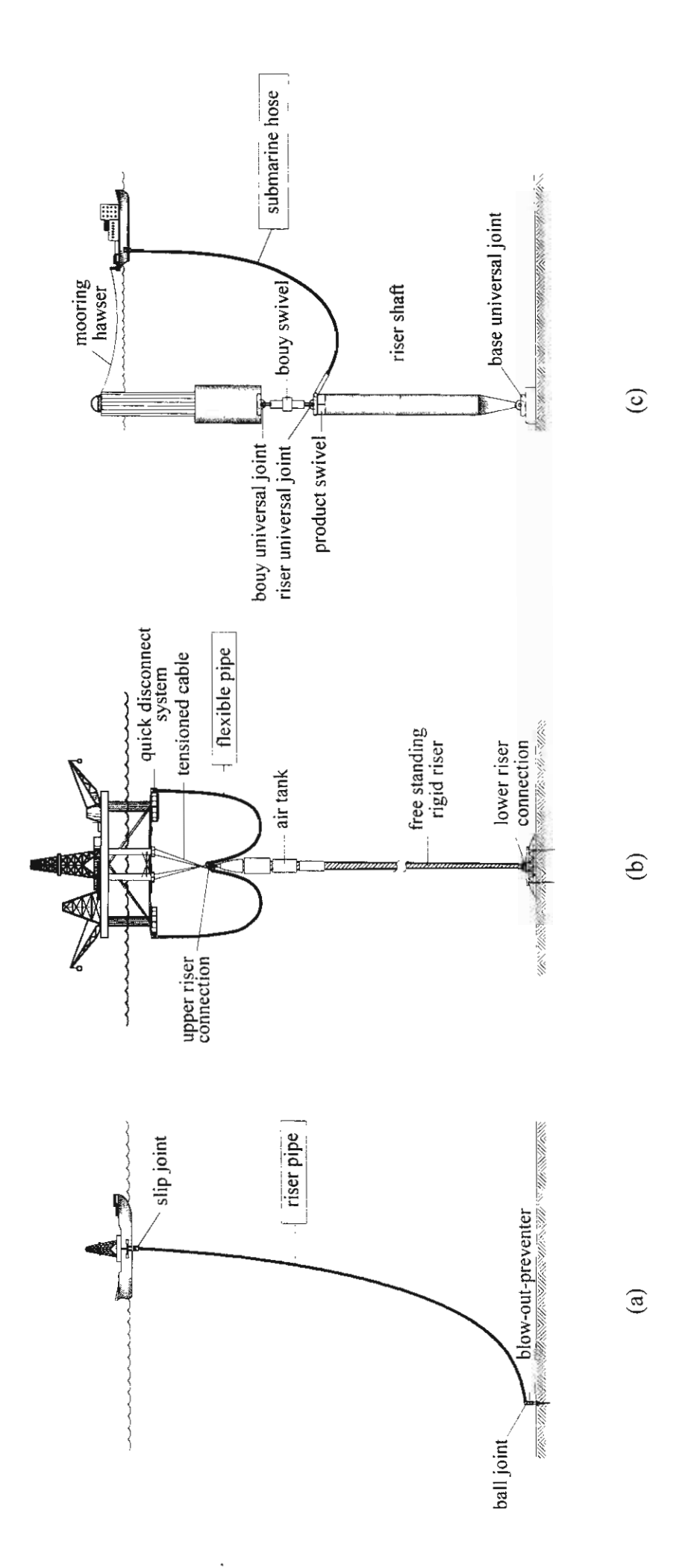
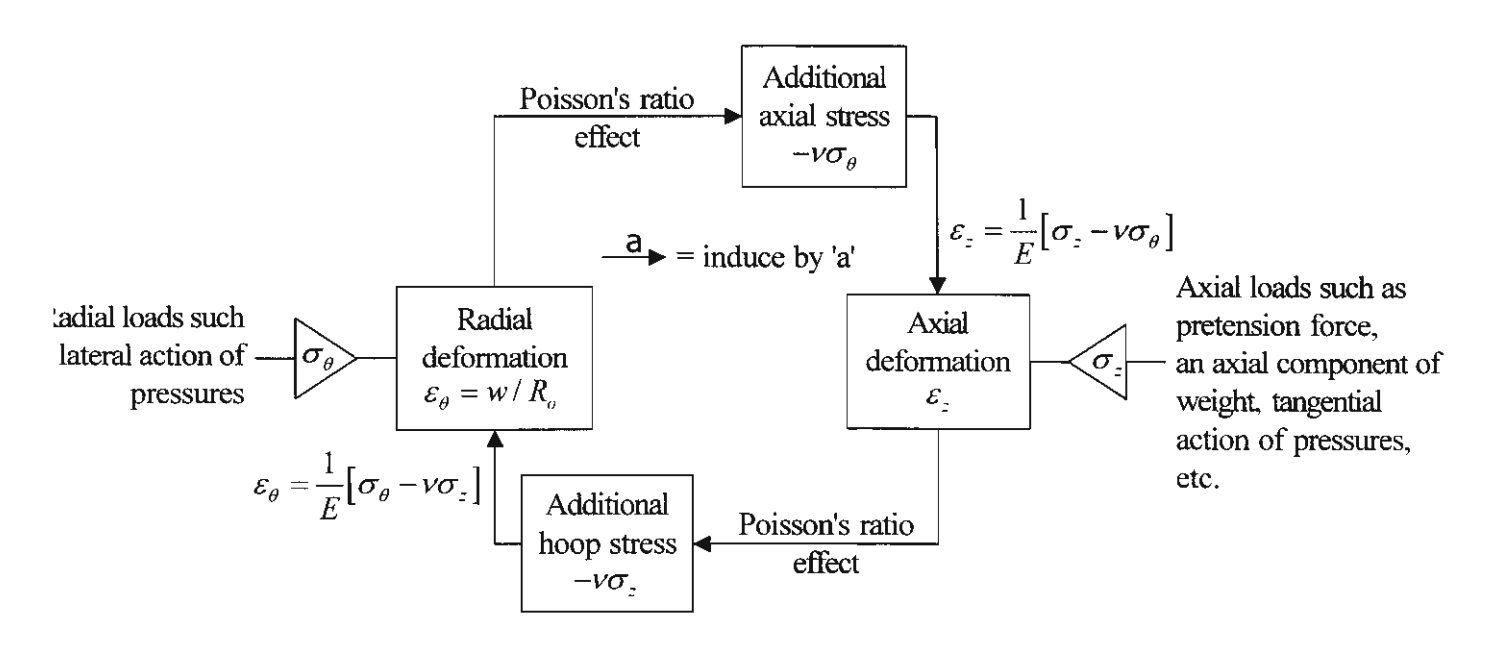
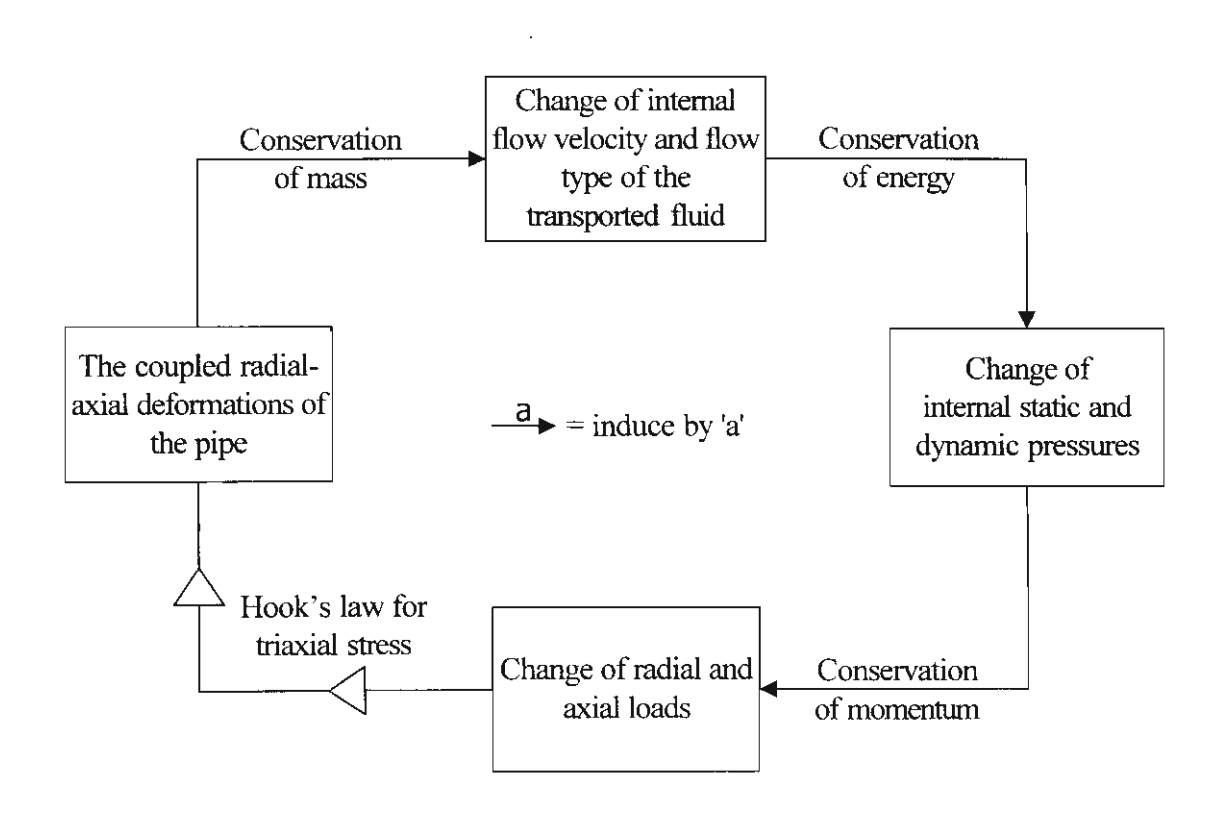


Figure 1 Flexible marine riser pipes (a) a marine riser (b) a flexible pipe (c) a hoseline



### The coupled radial-axial deformations behaviour of thin-walled pipes

(a)



### The transported fluid-pipe interaction

(b)

Figure 2

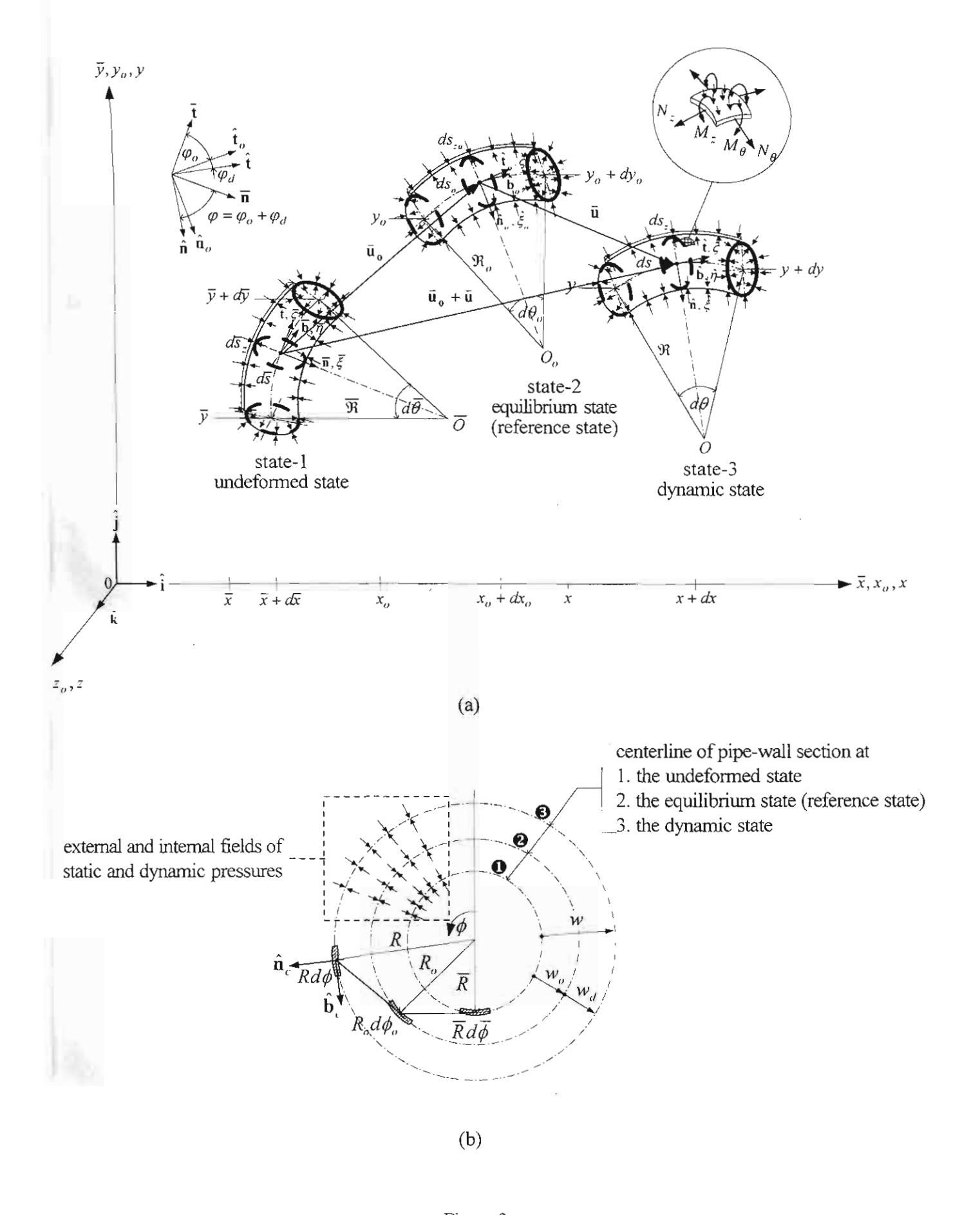


Figure 3

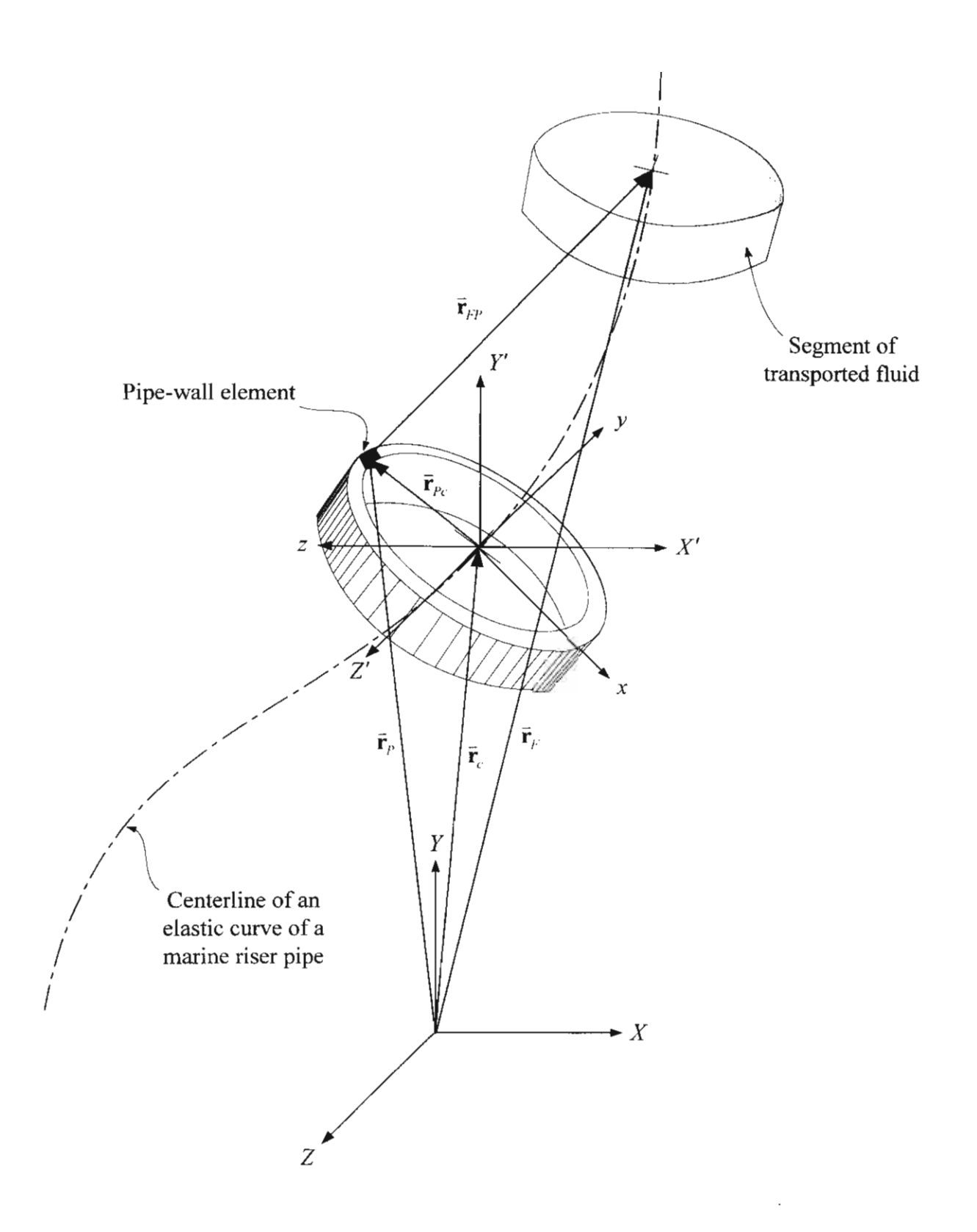


Figure 4

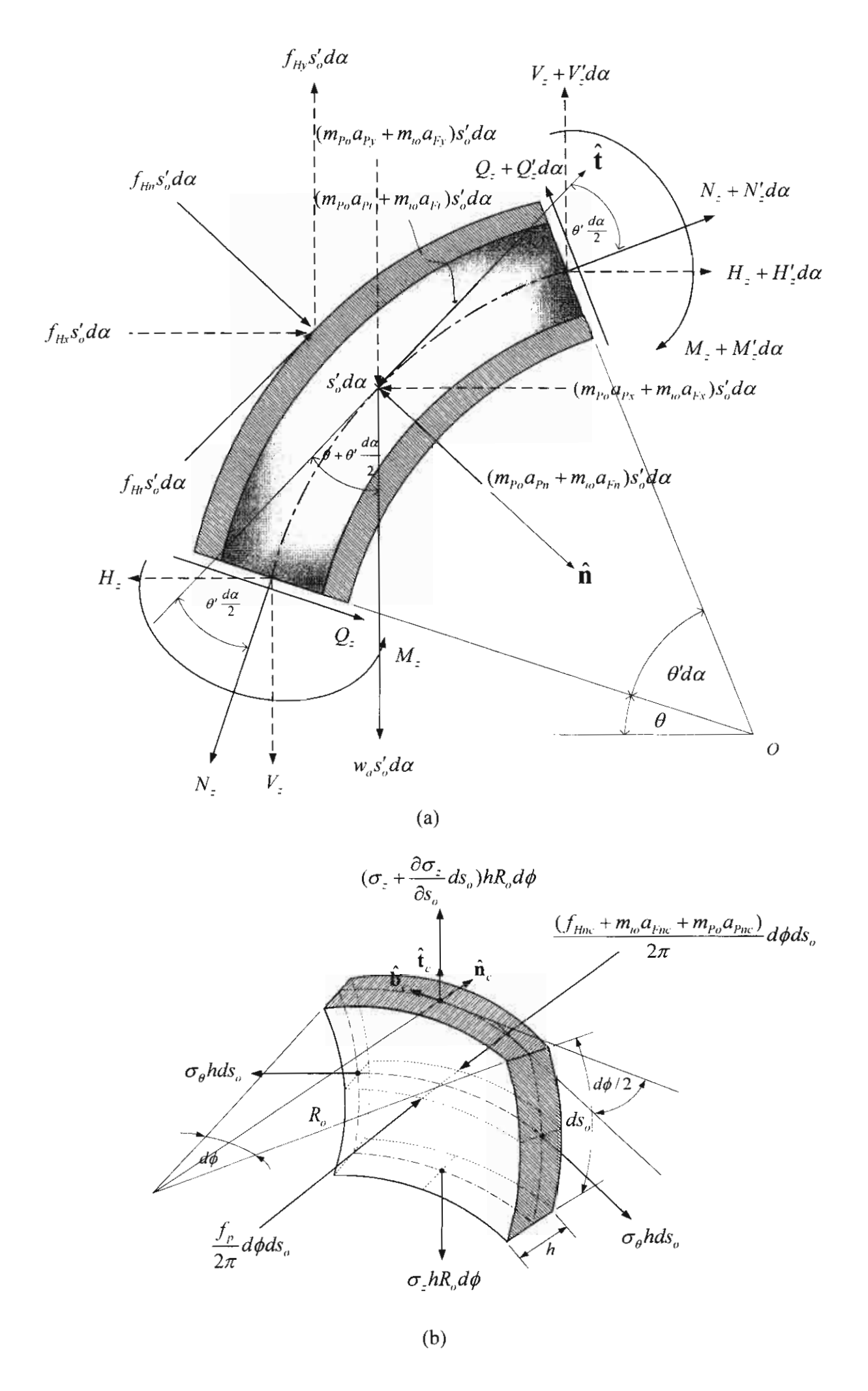
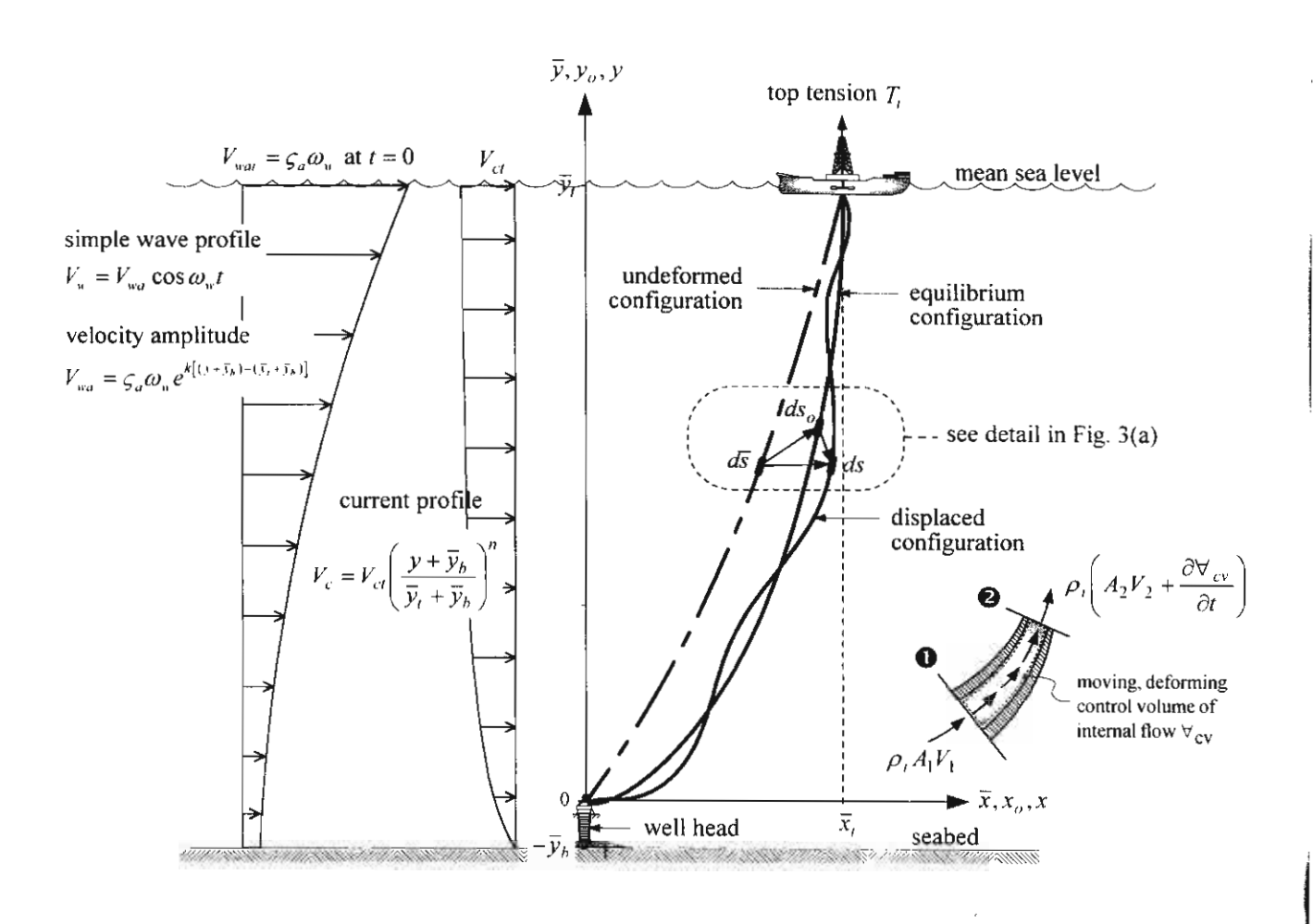
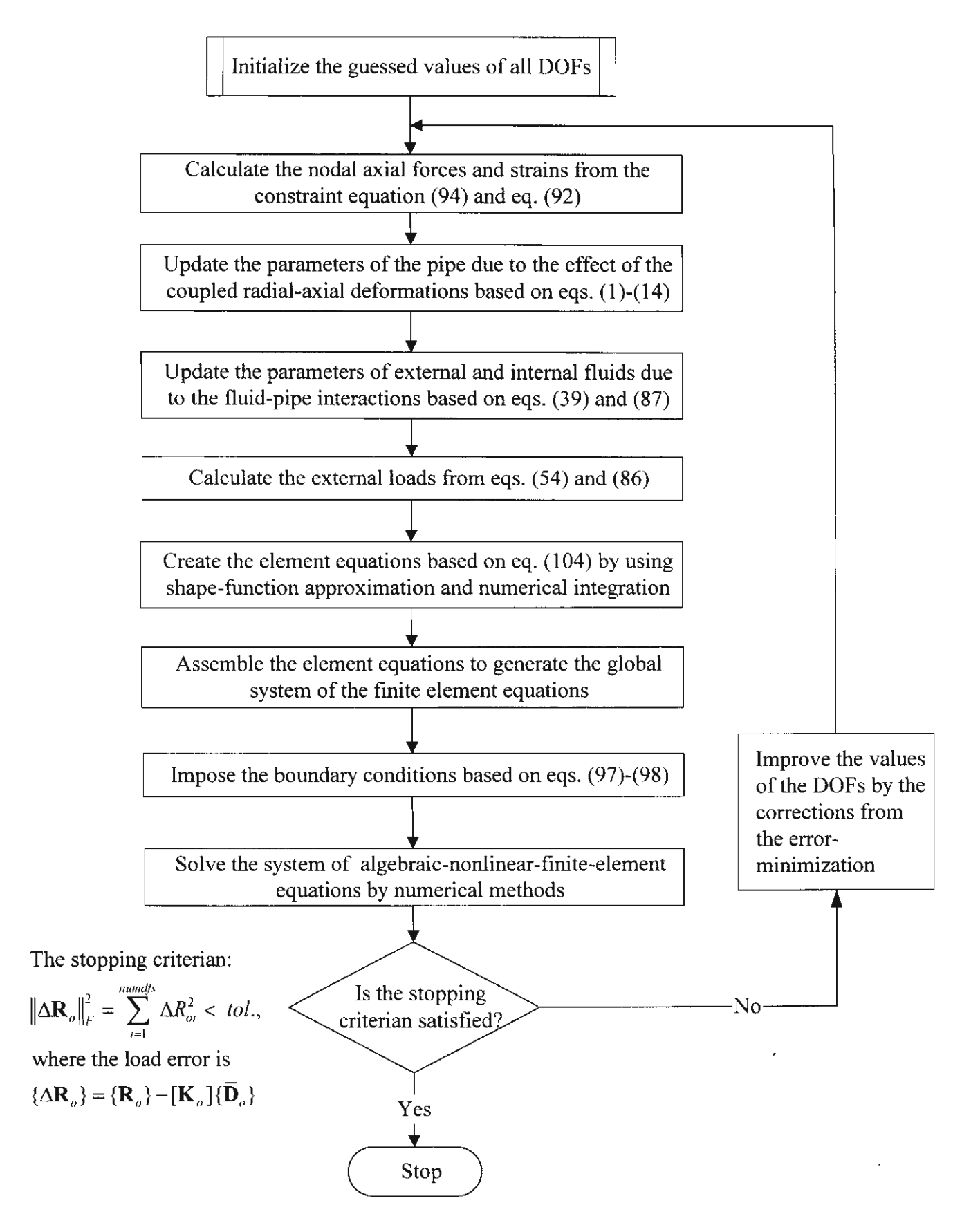


Figure 5

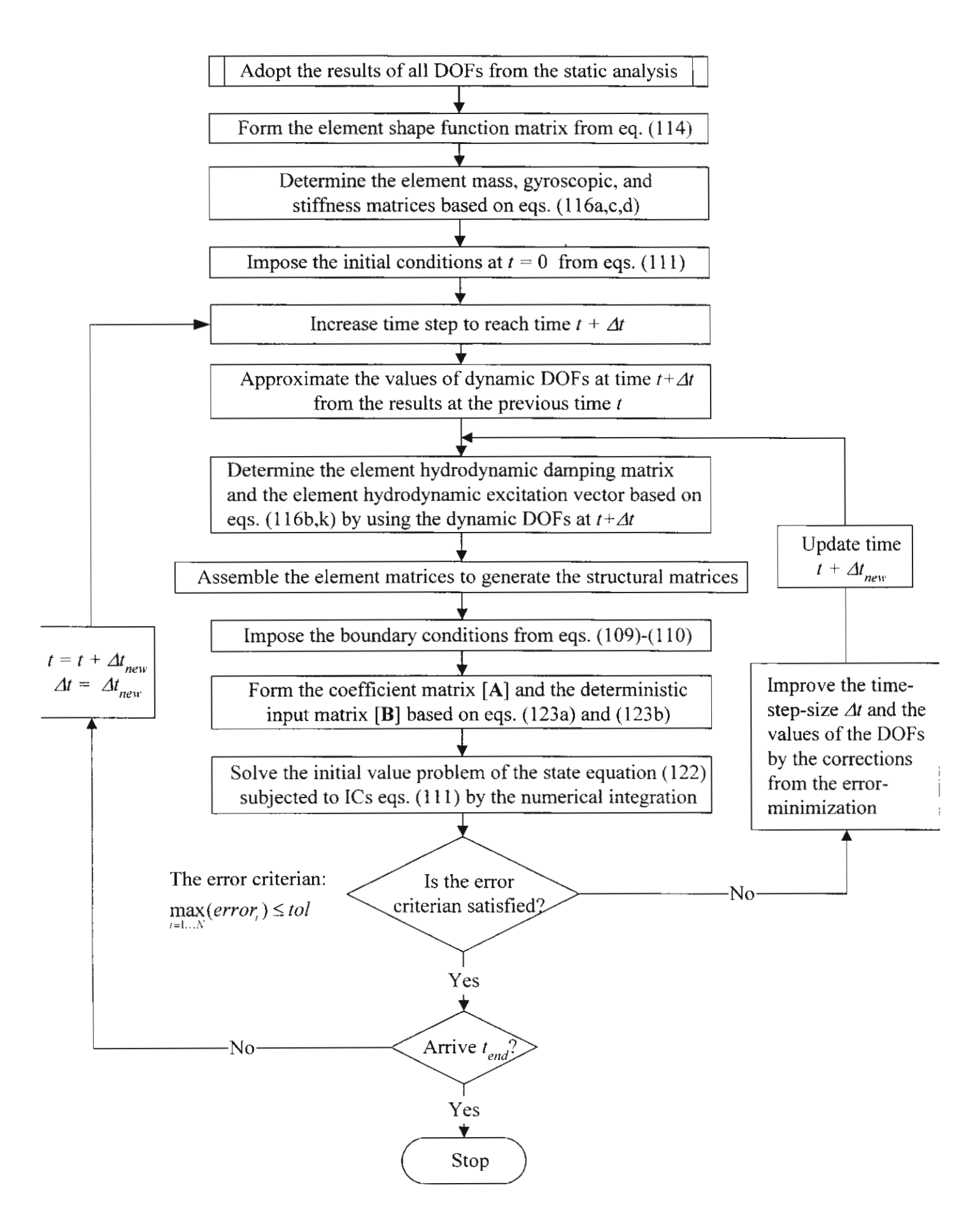


Parameter	Input Data
Elastic modulus E (N/m²)	0.207x10 <sup>12</sup>
External diameter of the pipe $\overline{\mathcal{D}}_{e}$ (m)	0.610
Internal diameter of the pipe $\overline{\mathcal{D}}_i$ (m)	0.575
Density of pipe material $ ho_{\mathbb{F}}$ (kg/m³)	8337.9
Density of external fluid $\rho_e$ (kg/m <sup>3</sup> )	1025
Density of internal fluid $\rho_i$ (kg/m <sup>3</sup> )	0,500,920,1200,1438
Poisson's ratio v	0.50
Static offset $\overline{X}_t$ (m)	100
$\overline{y}_{\varepsilon}$ (m)	2000
$\overline{y}_{b}$ (m)	~0
Applied top tension $T_t$ (N)	0.7 <b>x</b> 10 <sup>7</sup>
Normal drag coefficient $C_{Dn}$	2
Tangential drag coefficient $C_{\Gamma \tau}$	0.1
Current velocity at mean sea level $V_{\cdot,\cdot}$ (m/s)	1.5
Internal flow velocity $\overline{V}_i$ (m/s)	20
Added mass coefficient $C_3$	1.5
Wave amplitude $\varsigma_3$ (m)	6
Wave frequency $\omega_{\scriptscriptstyle W}$ (rad/sec)	0.6
Wave number k	0.03
Linear velocity amplitude of int. flow $V_{i\tau}$ (m/s)	0
Wave velocity amplitude of int. flow $V_{is}$ (m/s)	0.2
Internal flow frequency $\omega_i$ (rad/sec)	0.05

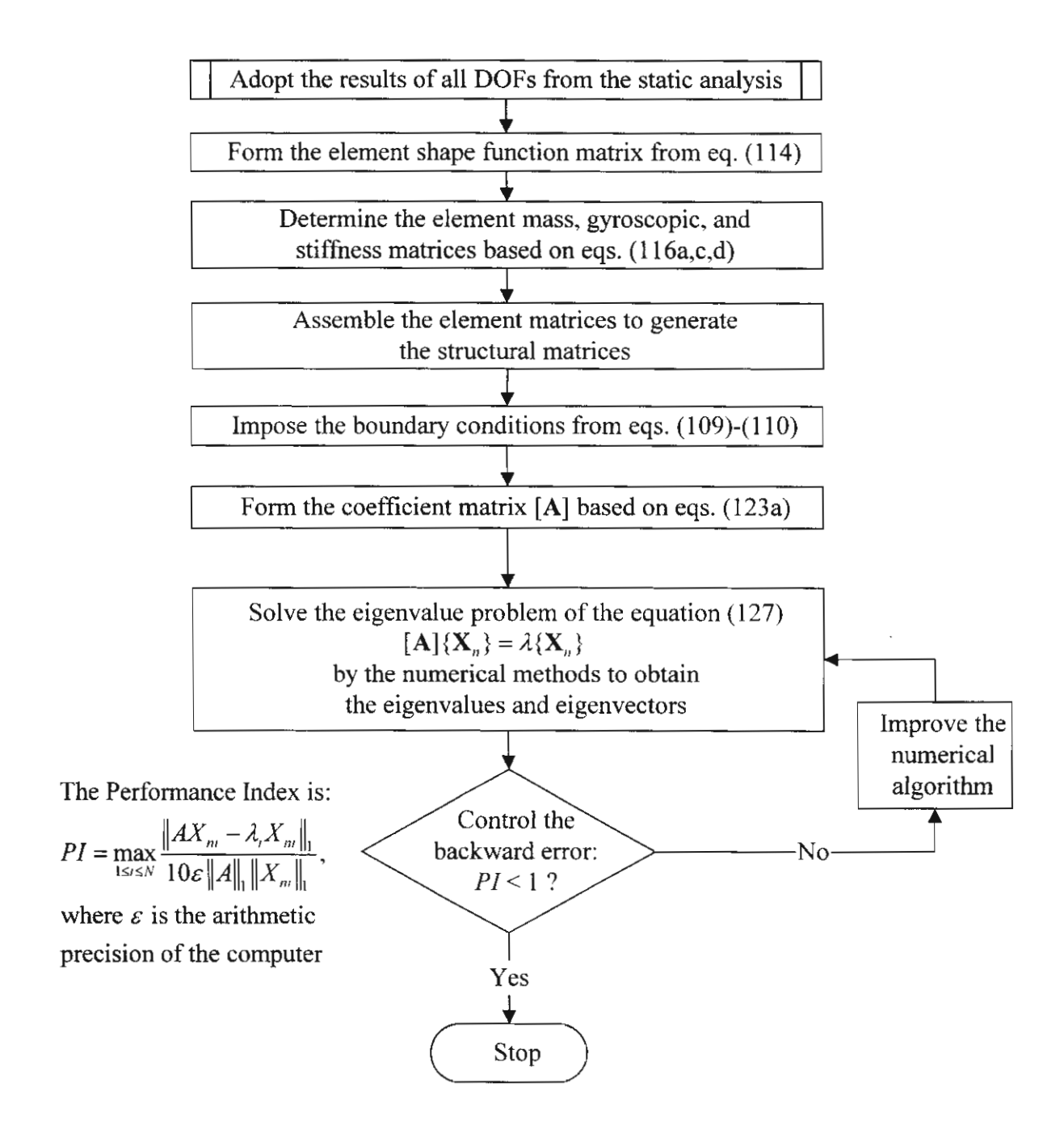
Figure 6



The hybrid-finite-element algorithm for the coupled radialaxial deformations analysis of the flexible-pipe statics



The state-space-finite-element algorithm for the coupled radialaxial deformations analysis of the flexible-pipe vibrations



The state-space-finite-element algorithm for determining the natural frequencies of the flexible-pipe vibrations

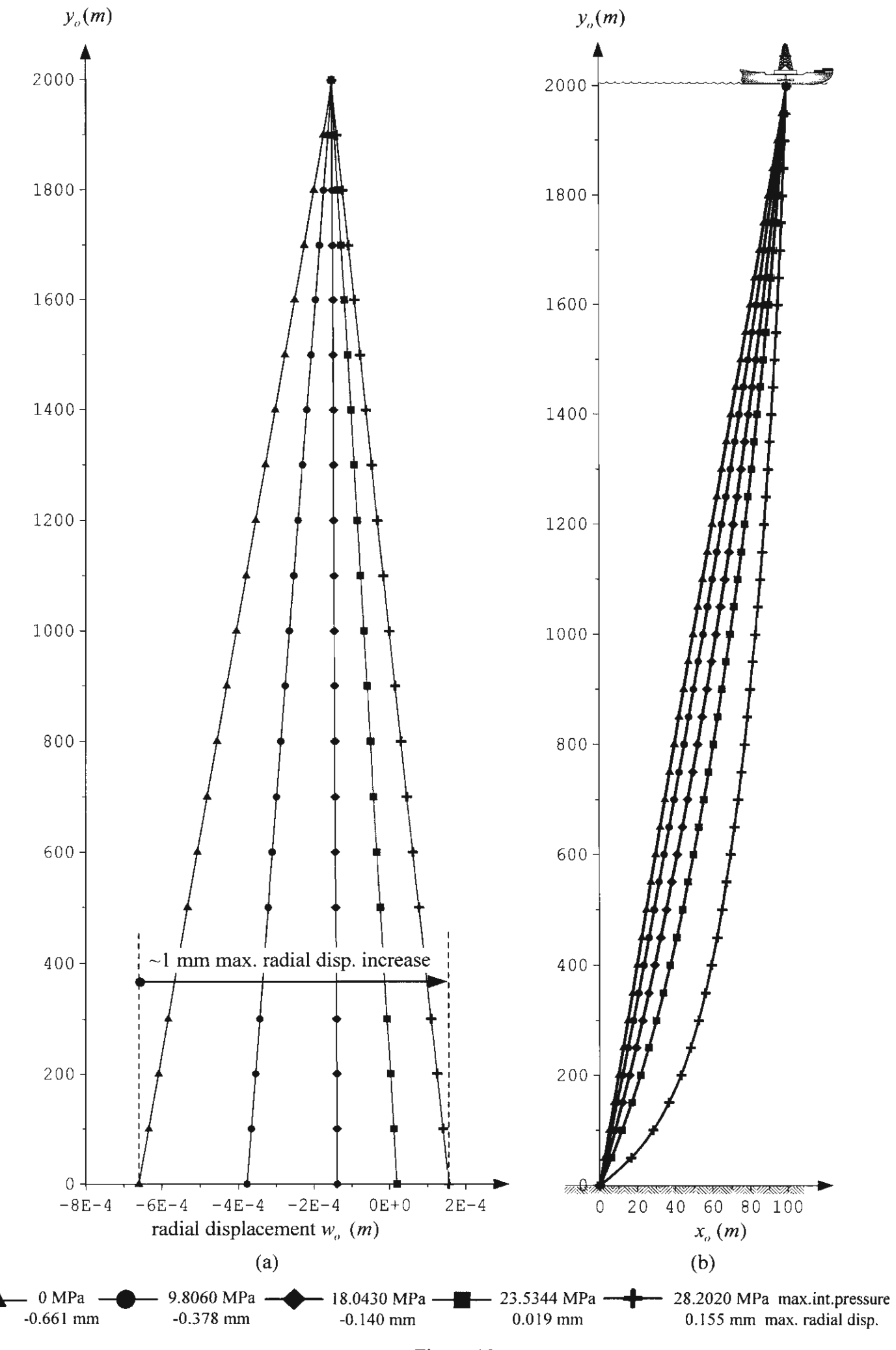


Figure 10

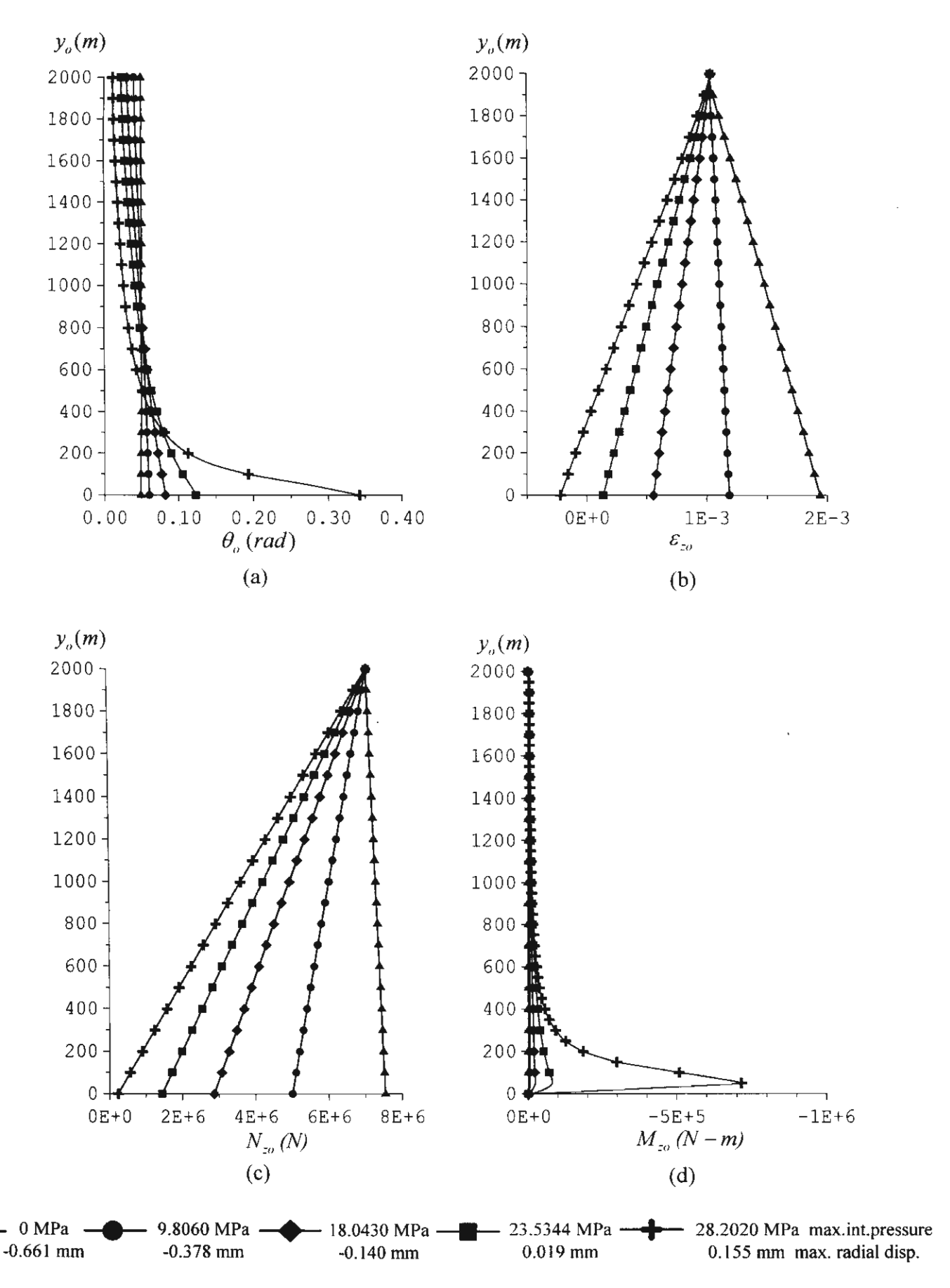
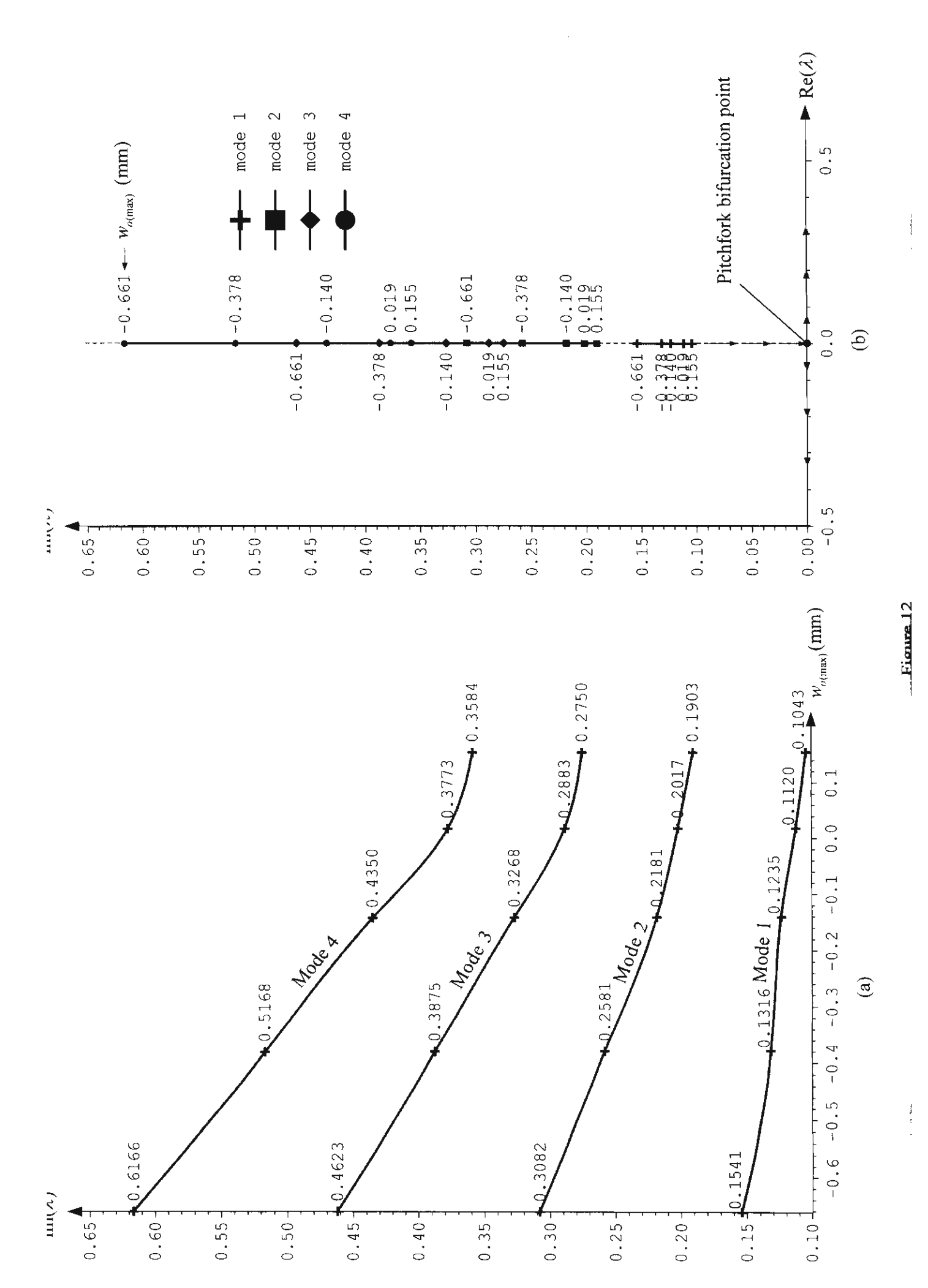


Figure 11



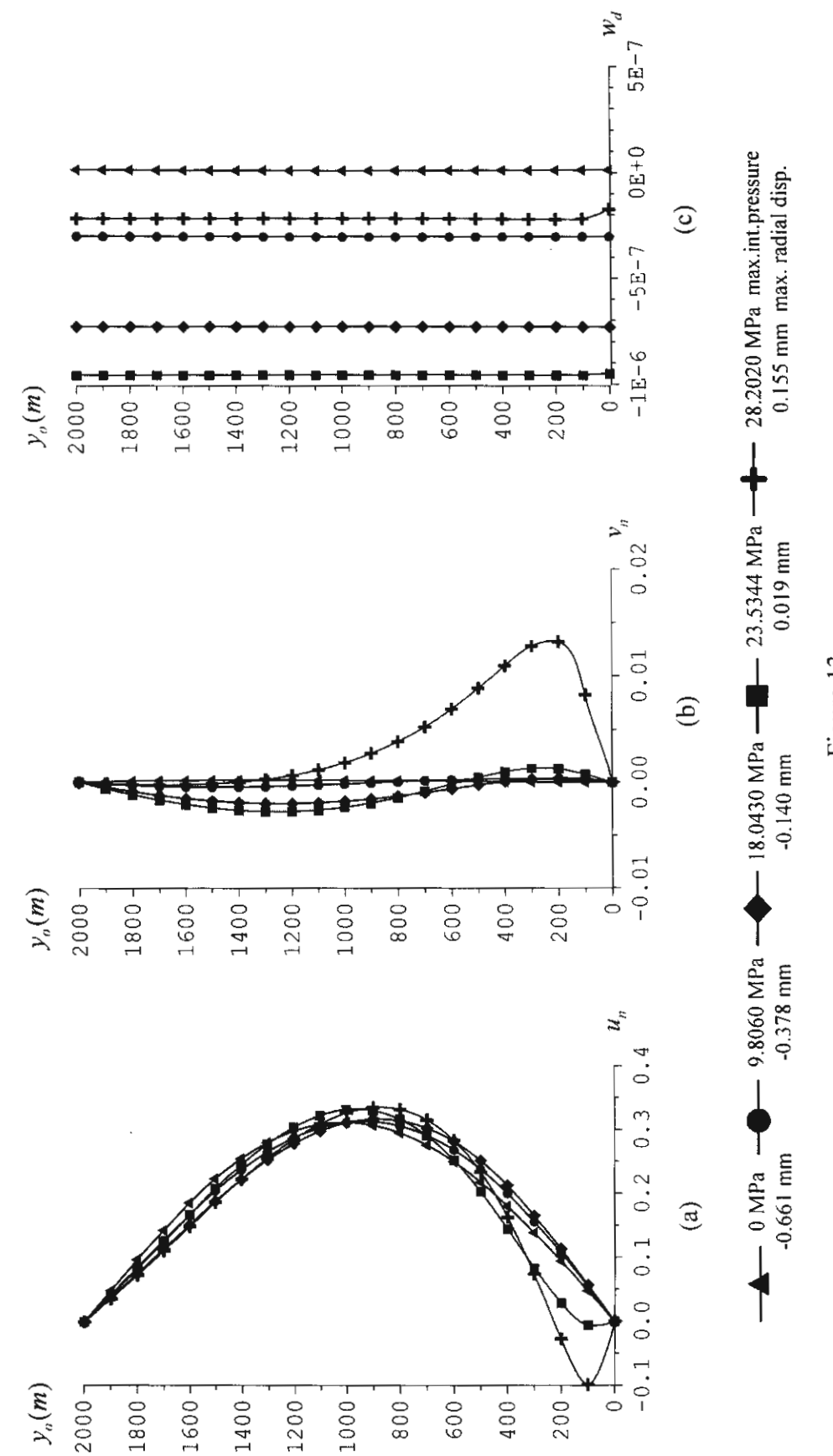


Figure 13

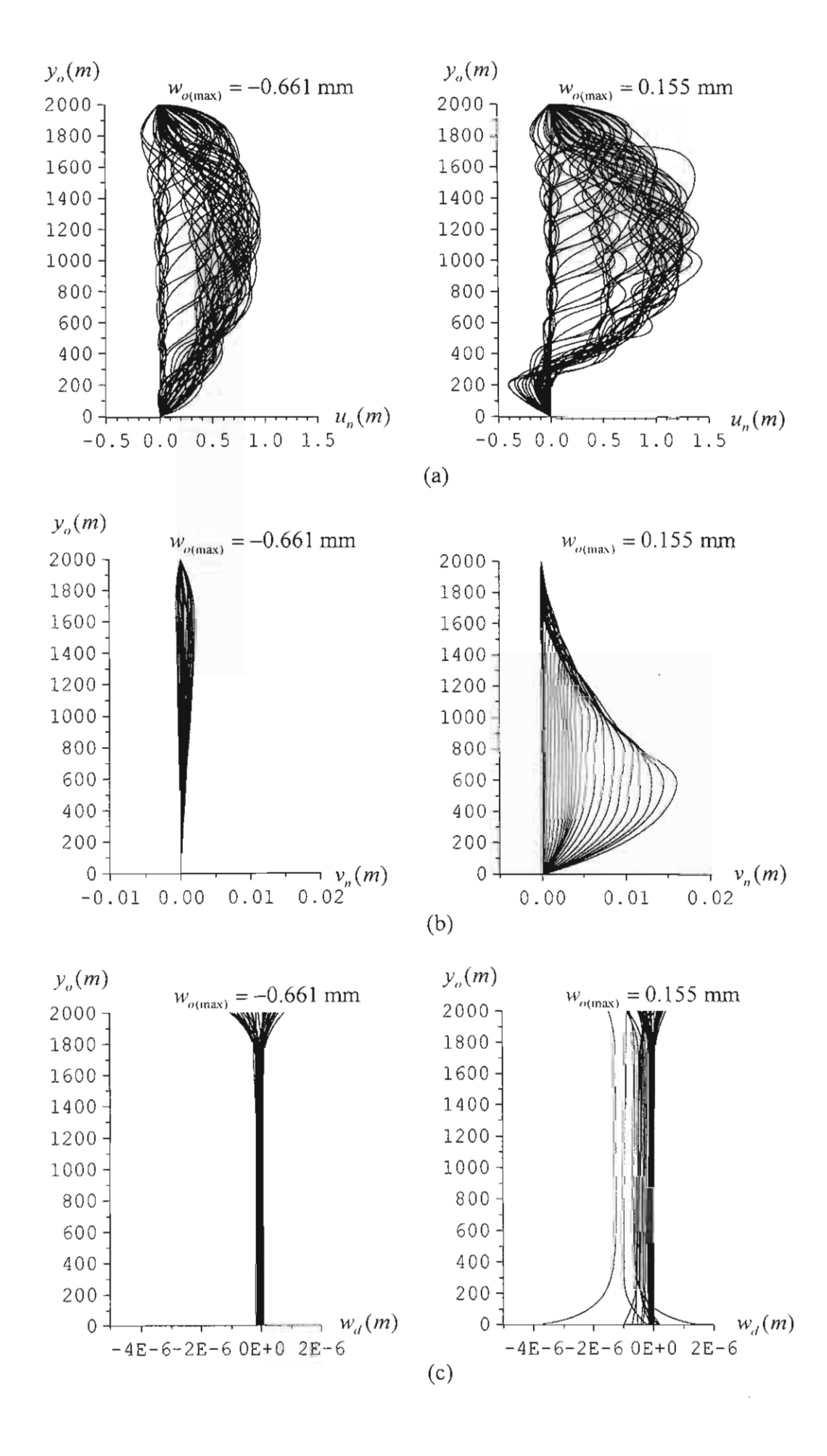
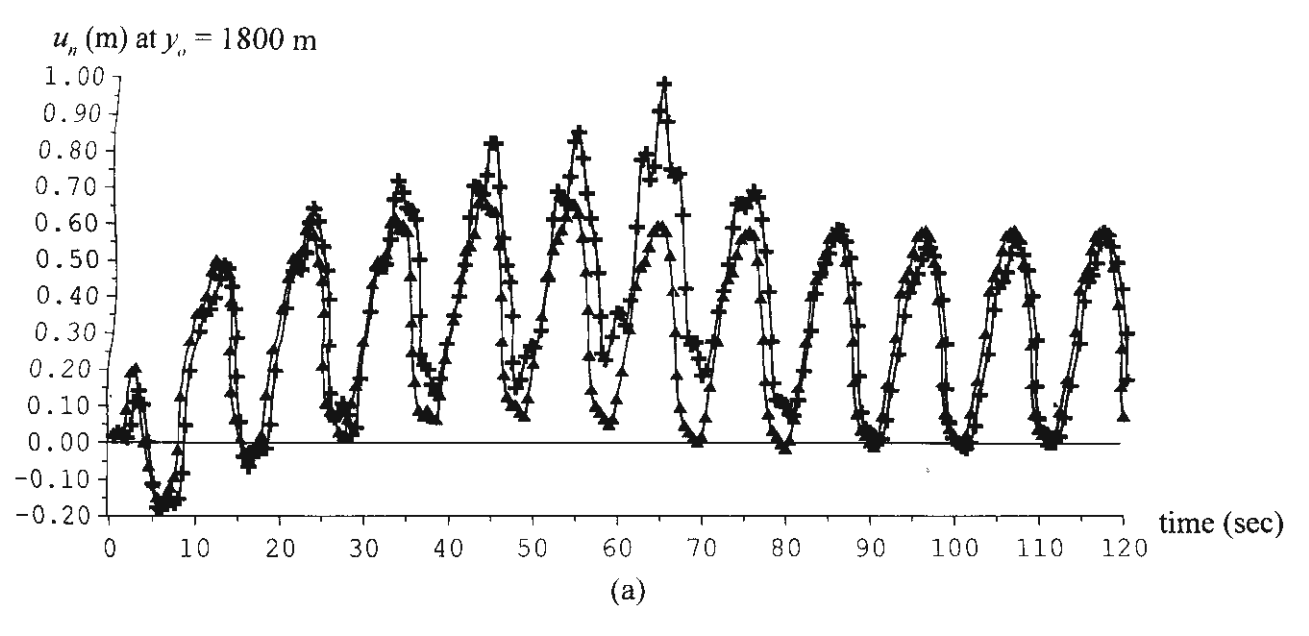
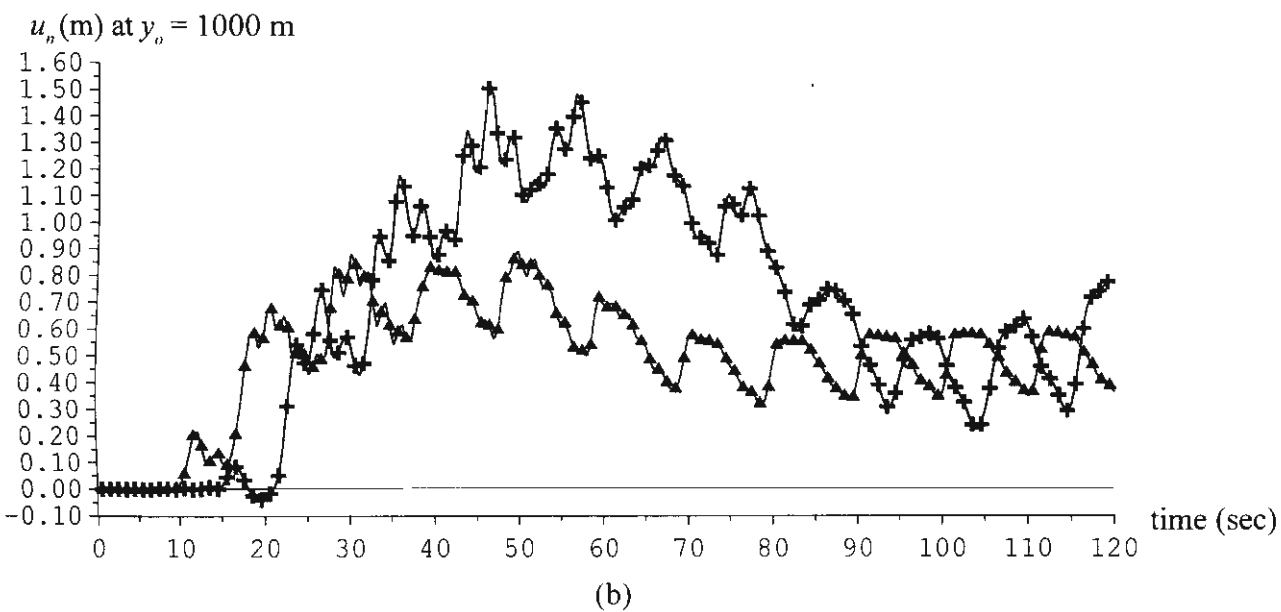


Figure 14





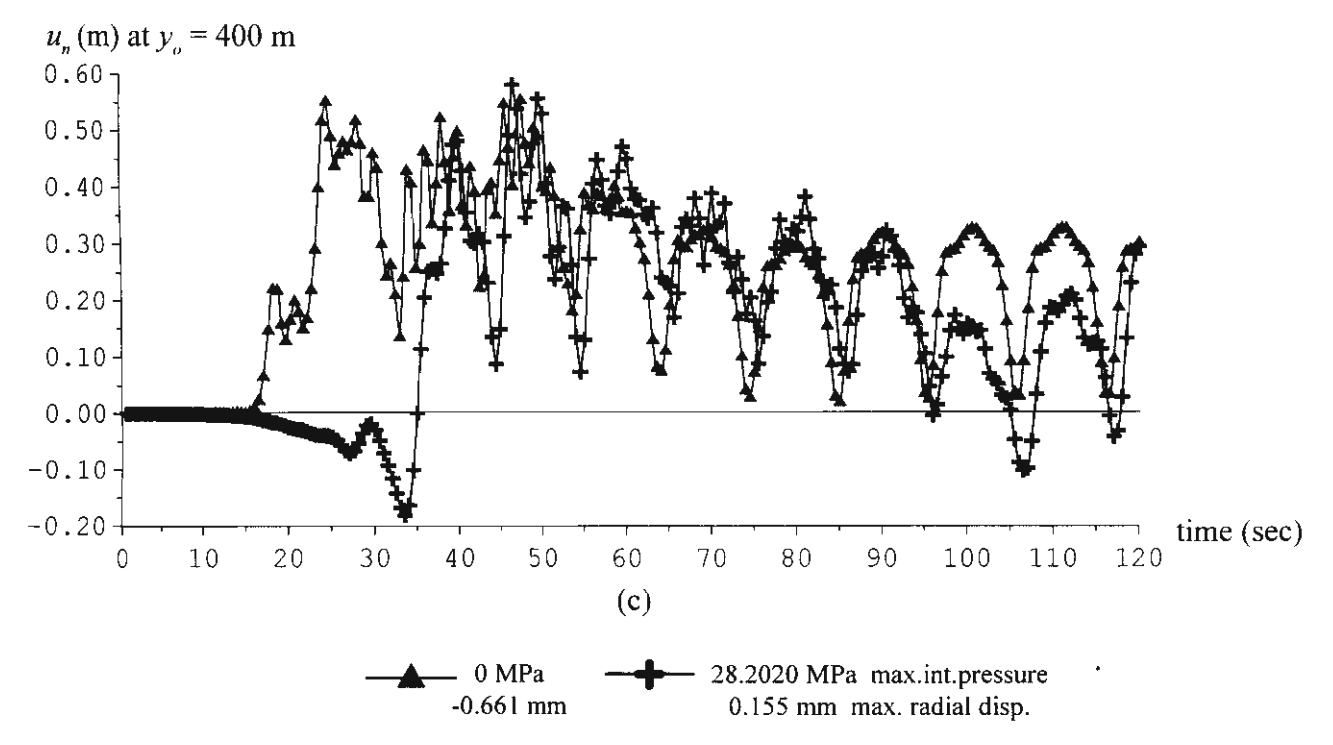
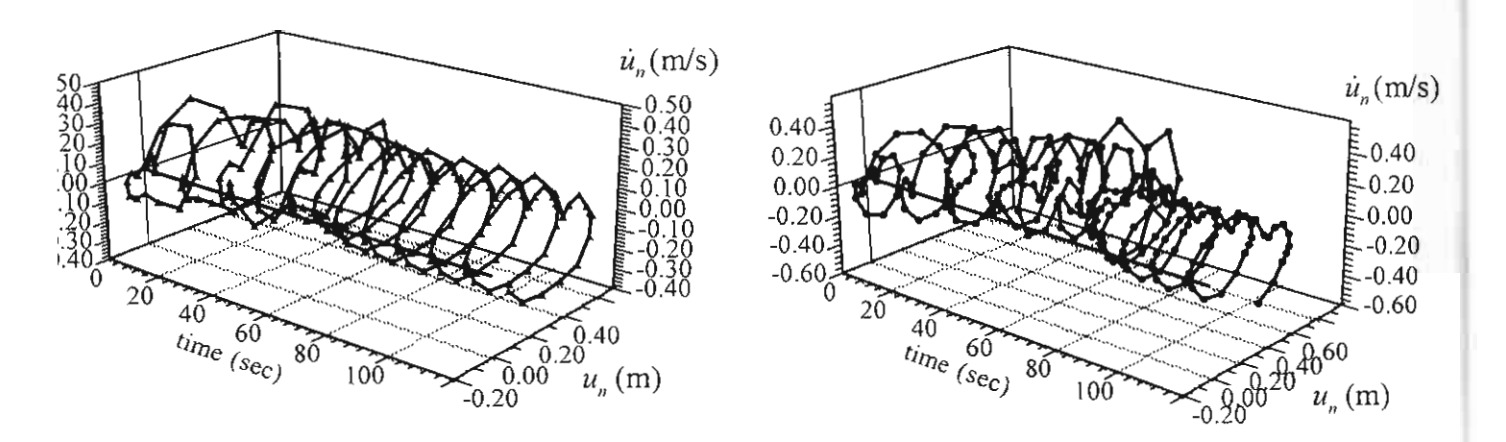
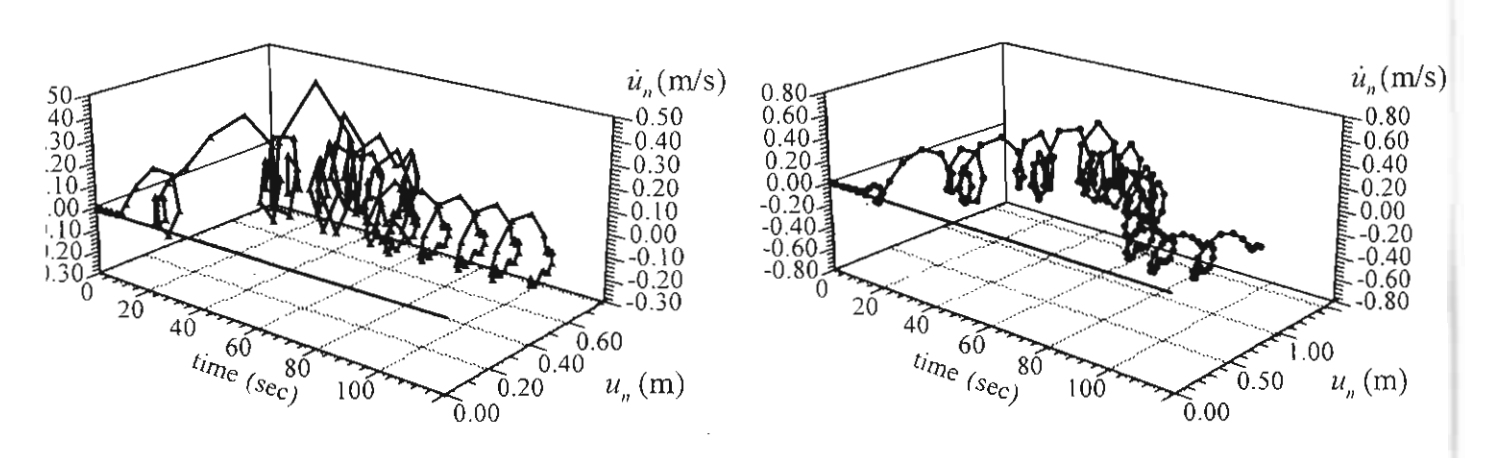


Figure 15



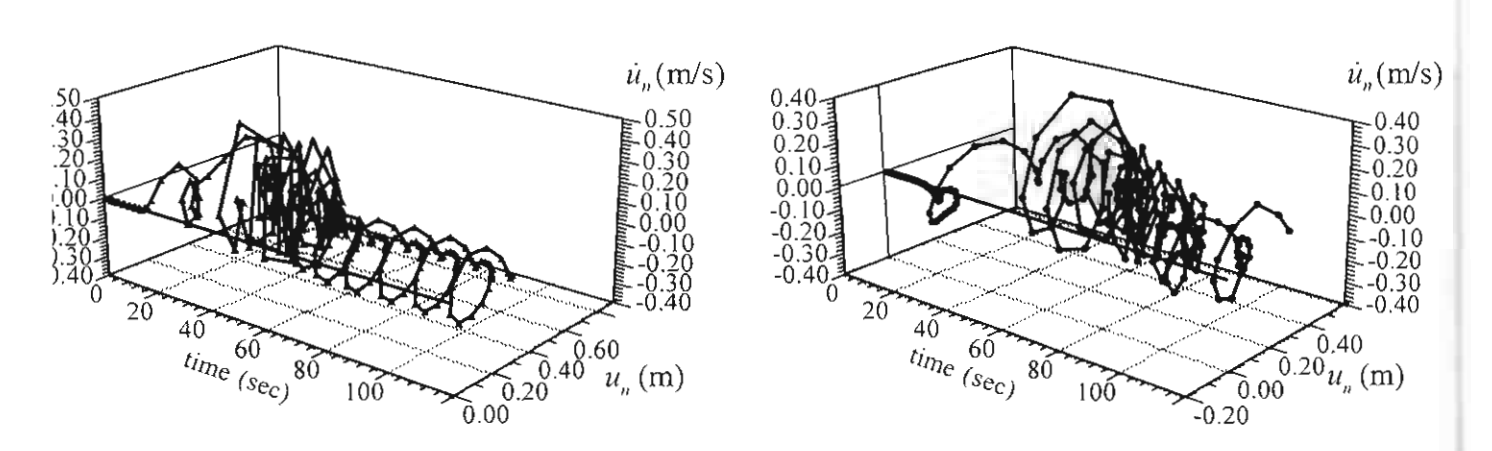
Trajectories of normal vibrations of the pipe segment at  $y_o = 1800 \text{ m}$ 

(a)



Trajectories of normal vibrations of the pipe segment at  $y_a = 1000 \text{ m}$ 

(b)



Trajectories of normal vibrations of the pipe segment at  $y_a = 400 \text{ m}$ 

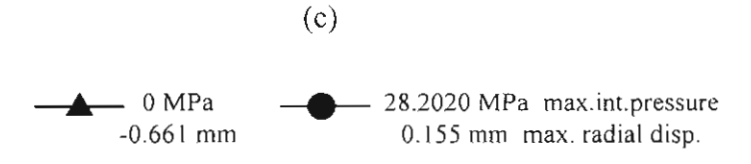


Figure 16